Diss. ETH No. 8309

THE PHOTOSPHERIC LAYERS OF SOLAR MAGNETIC FLUXTUBES

A dissertation

submitted to the

SWISS FEDERAL INSTITUTE OF TECHNOLOGY

ZÜRICH

for the degree of

Doctor of natural Science

presented by

Sami K. Solanki

Dipl. Phys. ETHZ,

born 2nd October, 1958,

citizen of Uetikon am See, Zürich.

Accepted on the recommendation of

Prof. Dr. J.O. Stenflo, examiner,

Prof. Dr. H. Nussbaumer, co-examiner.

1987

Diss. ETH No. 8309

THE PHOTOSPHERIC LAYERS OF SOLAR MAGNETIC FLUXTUBES

A dissertation

submitted to the

SWISS FEDERAL INSTITUTE OF TECHNOLOGY

ZÜRICH

for the degree of

Doctor of natural Science

presented by

Sami K. Solanki

Dipl. Phys. ETHZ,

born 2nd October, 1958,

citizen of Uetikon am See, Zürich.

Accepted on the recommendation of

Prof. Dr. J.O. Stenflo, examiner,

Prof. Dr. H. Nussbaumer, co-examiner.

1987

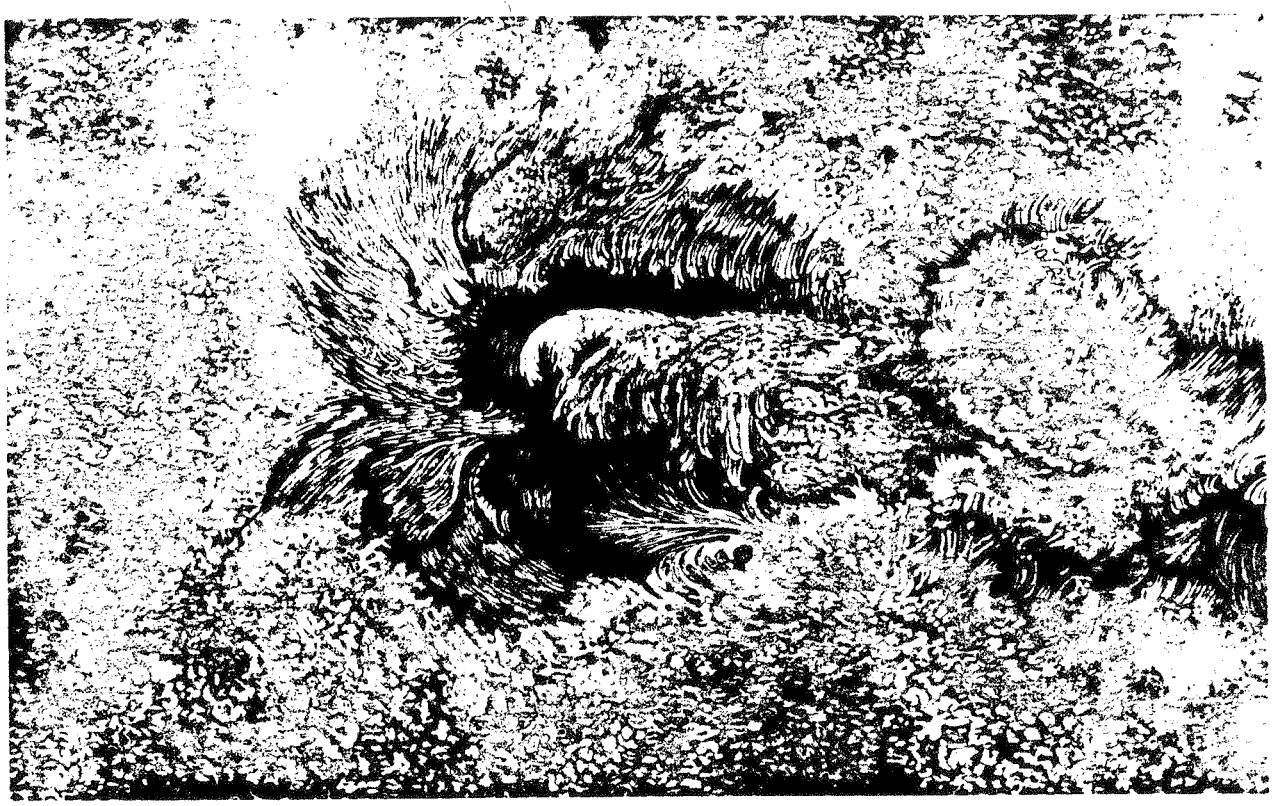

A sunspot and the surrounding photospheric faculæ observed and drawn by
S.P. Langley of Alleghany Observatory on December 23 and 24, 1873.
Engraved by Samuel Sartain of Philadelphia.

Abstract

This thesis is concerned with the structure and properties of magnetic fluxtubes in the solar photosphere. After a brief introduction outlining the importance of magnetic fields for the Sun and the stars, with particular emphasis on the role of fluxtubes, a description of polarized light, its properties, production, radiative transfer in a stellar atmosphere, and measurement is given. There follows an overview of spectroscopy and polarimetry with a Fourier transform spectrometer (FTS). The data forming the basis of the thesis, FTS spectra of Stokes I, V, and partly also Q in the visible and the infrared (1.5–1.7μ), are described and their advantages (high spectral resolution, broad spectral range) and disadvantages (low spatial and temporal resolution) relative to other data sets are discussed.

The analysis procedure is outlined. It is based on the identity $V = \Delta\lambda_H \, \mathrm{d}I/\mathrm{d}\lambda$ valid for weak fields (i.e. $\Delta\lambda_H \ll \Delta\lambda_D$), where $\Delta\lambda_H$ is the Zeeman splitting and $\Delta\lambda_D$ is the Doppler width. This relation is derived, interpreted, and tested both analytically and numerically. Its integrated form is used to determine the I_V profile, an approximation of the magnetically unsplit Stokes I inside the fluxtubes. It is also shown that similar relations for the Q and U profiles (e.g. $Q \sim \mathrm{d}^2I/\mathrm{d}\lambda^2$) are only valid in the limit of very weak lines, and are therefore of no practical value.

The lines to be analysed (a set of 450 unblended Fe I and II lines) are listed and, wherever possible, their effective Landé factors are determined from laboratory measurements, thus making the analysis independent of the validity of LS coupling. The line profiles are parameterised and a statistical analysis of these parameters is carried out. With the help of regression equations the dependences of individual parameters on Zeeman splitting, line strength, excitation potential, and wavelength are partially separated, allowing some qualitative conclusions to be drawn directly. Quantitative results are derived from detailed radiative transfer calculations in model fluxtubes. Some of the main results and conclusions are listed below:

1. The temperature in the fluxtubes of the observed active regions is found to be lower than in the fluxtubes of the quiet network, in particular in the deeper photospheric layers. Detailed models of the temperature are derived and compared to earlier models published in the literature. New diagnostic techniques for the fluxtube temperature are proposed. The importance of velocity broadening for the empirical determination of temperature is demonstrated.
2. An upper limit of 0.25 km sec^{-1} is set on stationary flows in fluxtubes from a detailed analysis of many lines at disk centre and, additionally, the centre-to-limb variation (CLV) of a few selected lines. Both, absolute wavelengths of Stokes V and wavelength shifts relative to Stokes I, give the same result. The absence of downflows is in contrast to most earlier measurements in the literature, which typically show downflows $\gtrsim 0.5$ km sec^{-1}.
3. It is proposed that the observations of downflows published in the literature may be explained by the low spectral resolution of such observations combined with the blue-red asymmetry in Stokes V. As a quantitative verification, V profiles, recorded with high spectral resolution, are smeared by convoluting them with model apparatus functions. If appropriate amounts of spectral smearing are used then the redshifts published in the literature are reproduced. Spectral smearing is found to influence other fluxtube properties determined from Stokes V quite strongly as well.
4. Extensive observations of Stokes V asymmetry, with the area and amplitude of the blue wing being different from the area and amplitude of the red wing, are described. Mechansims for producing the asymmetry are discussed and some indirect observational evidence for a connection between asymmetry and velocity is presented. The simplest mechanism giving rise to asymmetry, a stationary flow inside the fluxtube with a vertical gradient, is shown to produce profiles incompatible with the observations and is thus ruled out.
5. The presence of strong non-stationary motions in fluxtubes is deduced from the large line widths of the I_V profiles. RMS velocities of 3–4 km sec^{-1} are obtained from the most broadened lines at disk centre. These

values are considerably larger than in the quiet sun.

6. Relatively model independent statistical methods of determining the magnetic field strength in fluxtubes as well as their filling factors are proposed. Their application to the data gives values compatible with those published in the literature.
7. The importance of velocity broadening for the Stokes V 5250/5247 line ratio is demonstrated. It is also shown that the CLV of the line ratio contains little significant information on the height variation of the magnetic field. Thus both a constant magnetic field with $B = 1140$ G and a magnetic field calculated with the thin tube approximation with $B(\tau = 1) \approx 2000$ G, are consistent with the data.

Finally, MHD models of cylindrically symmetric fluxtubes are presented. The effects of magnetic tension are included via an expansion technique. Particular attention is given to the problem of merging. Thus a simple, and self-consistent formalism is developed to take the influence of neighbouring fluxtubes into account. The dependence of the merging height on various parameters of the fluxtubes is discussed. It is shown that the thin fluxtube approximation is quite reliable for fluxtubes with radii less than approximately 100 km near $\tau = 1$.

Zusammenfassung

Diese Dissertation befasst sich mit der Struktur und den Eigenschaften von solaren magnetischen Flussröhren. Zuerst wird die Rolle des Magnetfeldes der Sonne und anderer Sterne, unter besonderer Berücksichtigung seiner fibrilen Struktur, kurz skizziert. Es folgt eine Beschreibung des polarisierten Lichts, dessen Eigenschaften, Entstehungsmechanismen, Transport durch eine Atmosphäre und Messung. Besonderes Gewicht wird auf die Polarimetrie mit einem Fourier Transform Spektrometer (FTS) gelegt, da die hier benützten Daten, Spektren von Stokes I, V und teilweise auch Q im sichtbaren und infraroten (1.5–1.7μ) Wellenlängenbereich, mit einem FTS aufgenommen worden sind.

Die Analysemethode wird umrissen. Sie beruht auf der für schwache Felder (d.h. $\Delta\lambda_H \ll \Delta\lambda_D$) gültigen Identität $V = \Delta\lambda_H \mathrm{d}I/\mathrm{d}\lambda$. Dabei ist $\Delta\lambda_H$ die Zeemanaufspaltung und $\Delta\lambda_D$ die Dopplerbreite. Diese Identität wird hergeleitet, interpretiert und sowohl analytisch wie numerisch geprüft. Unter Benutzung ihrer integrierten Form wird das I_V Profil bestimmt. Dieses stellt eine Approximation des magnetisch unaufgespaltenen Stokes I Profils innerhalb der Flussröhre dar. Es wird auch gezeigt, dass ähnliche Beziehungen für die Stokes Q und U Profile (z.B. $Q \sim \mathrm{d}^2I/\mathrm{d}\lambda^2$) nur im Grenzfall sehr schwacher Linien gültig sind und ihnen deshalb keine praktische Bedeutung zukommt.

Die effektiven Landé-Faktoren der 450 ungestörten Fe I und II Linien, welche für die weitere Analyse benützt werden, werden wo immer möglich aus Labormessungen bestimmt. Dadurch wird die Analyse unabhängig von der Gültigkeit der LS-Kopplung. Die Linienprofile werden parameterisiert, und es wird eine statistische Analyse dieser Linienparameter durchgeführt. Anhand von Regressionen werden die Einflüsse von Zeemanaufspaltung, Linienstärke, Anregungspotential und Wellenlänge auf die einzelnen Linienparameter teilweise voneinander getrennt, so dass daraus direkt einige qualitative Schlüsse über Eigenschaften von Flussröhren gezogen werden können. Quantitative Resultate werden aus dem Vergleich von detaillierten Strahlungstransportberechnungen in Flussröhrenmodellen mit den Beobachtungen erzielt. Einige der Hauptresultate sind im Folgenden zusammengefasst.

1. Die Temperatur in den Flussröhren der beobachteten Netzwerk-Gebiete ist höher als in den Flussröhren der beobachteten aktiven Gebieten, vorallem in den tieferen Schichten. Detaillierte Modelle der Temperaturstruktur werden aufgestellt und mit älteren Modellen verglichen. Neue diagnostische Hilfsmittel zur Bestimmung der Flussröhrentemperatur werden vorgestellt. Die Wichtigkeit der Geschwindigkeitsverbreiterung der Spektrallinien für die empirisch bestimmte Temperaturstruktur wird gezeigt.
2. Für die Geschwindigkeit stationärer Strömungen wird eine obere Grenze von 0.25 km sek^{-1} gesetzt. Dies folgt sowohl aus einer statistischen Analyse aller Linien bei Sonnenmitte, wie auch aus der Mitte-Rand-Variation einiger ausgewählter Linien. Ferner geben sowohl die absolute Wellenlänge von Stokes V, wie auch deren Wellenlängenverschiebung gegenüber Stokes I dasselbe Resultat. Dieses Resultat steht im Widerspruch zu früheren Arbeiten, welche Abwärtsströmungen von $\gtrsim 0.5$ km sek^{-1} beobachteten.
3. Als mögliche Erklärung dieser Diskrepanz wird die schlechte spektrale Auflösung in Kombination mit der Asymmetrie des Stokes V Profils vorgeschlagen. Um diese These zu überprüfen, wird das mit hoher spektraler Auflösung gemessene V Profil künstlich verschmiert. Bei geeigneter Wahl der Verschmierung werden die älteren Beobachtungen von Abwärtsströmungen reproduziert. Auch einige andere Eigenschaften von Flussröhren, welche aus Stokes V bestimmt werden, hängen stark von der spektralen Auflösung ab.
4. Umfangreiche Beobachtungen der Stokes V Asymmetrie werden vorgestellt. Bei diesen Daten unterscheiden sich Fläche und Amplitude des blauen Flügels von denjenigen des roten. Mögliche Entstehungsmechanismen werden besprochen und Hinweise auf einen Zusammenhang mit den Massenbewegungen in den Flussröhren werden diskutiert. Der einfachste Mechanismus, eine stationäre Strömung in der Flussröhre mit einem vertikalen Gradienten, wird im Detail untersucht. Es wird gezeigt, dass dieser Mechanismus mit den Beobachtungen inkompatibel ist.

5. Aus den grossen Breiten der beobachteten I_V Profile wird auf nichtstationäre Strömungen in den Flussröhren geschlossen. Die Linien mit den grössten Verbreiterungen liefern RMS Geschwindigkeiten von 3–4 km sek^{-1} in der Nähe der Sonnenmitte. Diese Werte liegen um einiges höher als bei der ruhigen Sonne (d.h. in magnetfeldfreien Gebieten) und lassen auf das Vorhandensein von Wellen und Oszillationen mit grossen Amplituden in Flussröhren schliessen.
6. Es werden modellunabhängige statistische Methoden zur Bestimmung der Magnetfeldstärke in Flussröhren sowie des Füllfaktors (Bedeckungsgrad) vorgeschlagen und angewandt. Die Resultate stimmen gut mit denjenigen in der Literatur überein.
7. Der starke Einfluss der Geschwindigkeitsverbreiterung auf das Stokes V 5250/5247 Linienverhältnis wird untersucht. Ferner wird gezeigt, dass die Mitte-Rand-Variation dieses Linienverhältnisses nur wenig Information über die Höhenabhängigkeit der Magnetfeldstärke liefert. Dementsprechend können die Daten sowohl mit einem konstanten Magnetfeld von $B = 1140$ G als auch einem Magnetfeld welches mit der Höhe abnimmt (Dünne Flussröhren Approximation mit $B(\tau=1) \approx 2000$ G) wiedergegeben werden.

Schliesslich werden MHD Modelle von zylindersymmetrischen Flussröhren beschrieben. Der Einfluss der magnetischen Spannung wird durch eine Reihenentwicklung berücksichtigt. Besonderes Gewicht wird auf das Problem der Fusion zweier Flussröhren (merging) gelegt. Es wird ein einfacher, jedoch selbstkonsistenter Formalismus entwickelt, um den Einfluss benachbarter Flussröhren zu berücksichtigen. Die Abhängigkeit der Verschmelzungshöhe von verschiedenen Flussröhrenparametern wird beschrieben. Es wird auch gezeigt, dass die dünne Flussröhren Approximation für Flussröhren mit Radien kleiner als etwa 100 km relativ gut erfüllt ist.

Acknowledgements

First of all I wish to express my gratitude to J.O. Stenflo. He has provided much helpful advice, guidence and encouragement. His readiness to discuss any problem while at the same time allowing me a maximum of freedom have been instrumental for the successful completion of this thesis. To H. Nussbaumer go my sincere thanks for carefully reading the manuscript and for his invariably witty comments and objections. I am also indepted to many members of the solar physics community for their friendliness and help and making me feel as one of their own. In particular I wish to thank

J.W. Brault, J.W. Harvey, and R. Hubbard for assistance and collaboration in obtaining the FTS data,

J.W. Harvey for a number of fruitful discussions and also for providing data on the Kitt Peak vacuum tower telescope,

M. Hayes for informative remarks on the transition zone,

H. Holweger for clarifying comments on micro- and macro-turbulence,

M.C.E. Huber for clarifications concerning instrumentation,

C. Keller, whose assistance was invaluable for the completion of chapter 6,

G. Ladd for Fourier tranforming the data and for converting it into user format,

U. Litzén for providing unpublished measurements of Landé factors,

W. Mattig, E.H. Schröter, and H. Wöhl for helpful remarks on instrumental broadening,

Å. Nordlund for supplying the continuum opacity code and suggesting a part of the analysis in chapter 7,

G.W. Pneuman for teaching me most of what little I know about MHD and for allowing me to include many of the theoretical derivations in chapter 9,

B. Roberts for helpful discussions on some mathematical aspects of the solution of Eq. (9.57),

W. Schmutz for guidance in some questions related to radiative transfer,

M. Schüssler for pointing out the importance of the continuum intensity for the determination of filling factors and for heated and productive debates on the nature of the I_V profile,

O. Steiner for passing on some of his deep knowledge of classical greek,

E. Wiehr for valuable information on his observations,

A.D. Wittmann for providing the routine which calculates Dawson's integral,

In addition to these and other members of the international solar physics and stellar astronomy community I (last but certainly not least) gladly thank the staff of the Institut für Astronomie in Zürich for making my stay here so enjoyable.

Table of Contents

1. Introduction

The magnetism of the Sun was definitively established by Hale (1908b) when he presented conclusive evidence for the Zeeman effect in sunspots, thereby ending centuries of theorizing on their possible nature. Earlier, Lockyer (1866) had noticed split spectral lines in sunspots, but could not find any explanation for them (note that this was 30 years before Zeeman's laboratory experiments). Bigelow (1889) had also been led to hypothise on the possible existence of a solar magnetic field by photographic studies of the solar corona during the eclipse of January 1889. For many years the Sun remained the only magnetic star observed, and except for the 'invisible sunspots' of Hale (1922a, b), even it was thought to have a magnetic field largely restricted to sunspots (we disregard the spurious dipolar field of 50 G found by Hale, 1913).

A new age was heralded near the middle of the century, when Babcock (1947) discovered a strong magnetic field on the A2p star 78 Vir and the invention of the photoelectric magnetograph (Babcock and Babcock, 1952; Thiessen, 1952; Kiepenheuer, 1953) allowed the first systematic investigations of non-sunspot solar magnetic fields (Babcock and Babcock, 1955). Since then both solar and stellar magnetic fields have played an increasingly important role in the context of solar and stellar physics.

For the measurement of solar magnetic fields a wide variety of techniques have been used, and a wealth of detailed information has been obtained. The largest body of observations exists for the solar photosphere, where extensive observations in sunspots, faculæ, and the network have been carried out using the Zeeman effect, mostly via the polarization it induces in the spectral lines (cf. chapter 2). Since such observations will be quoted extensively in later chapters of this thesis, no references will be given here. A smaller number of photospheric observations also exist which make use of the Hanle effect (e.g. Stenflo, 1982; Harvey, 1986). The Hanle effect has also been used to carry out direct measurements of chromospheric magnetic fields in, for example, prominences (e.g. Bommier et al., 1981; Querfeld et al. 1985; for a review see Leroy, 1985). Above sunspots, the Zeeman effect polarization in transition region lines has yielded field strengths of 1000 G (Henze et al., 1982). The chromosphere also contains strong indirect indicators of magnetic activity, e.g. Hα structures and Ca II H and K plages. It was spectroheliograms in Hα, which first led Hale (1908a) to suspect that sunspots may be magnetic in nature. Skumanich et al. (1975) have shown that a good correlation exists between photospheric magnetic flux and Ca II emission, a result of great importance for the interpretation of stellar Ca II observations in terms of magnetic activity. Coronal fields have been measured via the Hanle effect (Querfeld, 1977). Radio observations also provide good diagnostics of the magnetic field in the higher atmosphere (Lang and Willson, 1979; Lang, 1983; see also Stenflo, 1978, for a review of older observations) and Xanthakis (1969) has derived a relation between photospheric magnetic fields and the radio emission. Another indicator of coronal magnetic fields is the X-ray flux. Golub et al. (1980, 1982) find a good correlation between coronal pressure and thermal energy content, as derived from Skylab X-ray data, and photospheric magnetic field density. In the solar wind the magnetic field has been measured *in situ* from satallites. Finally, magnetic fields are expected to penetrate to considerable depths in the convection zone (cf. Schüssler, 1984b, for a theoretical overview). So far no direct method of measuring these fields exists, although Zweibel and Bogdan (1986) point out that it is in principle possible to measure magnetic fields in the convection zone through their influence on solar oscillations. Thus, magnetic fields have been detected in all the *observable* layers of the Sun. Their fundamental importance for 'active' phenomena: sunspots, plages, prominences, spicules, flares, etc., is undoubted. It is also generally agreed that the transition region and the corona are magnetically heated (cf. Schmieder and Mein, 1981; Golub et al., 1980, 1982; recent reviews have been given by Heyvaerts, 1985, and Hammer, 1987). It has recently also been suggested that the solar wind is partly magnetically driven, since the high speed streams cannot be produced by gas pressure alone (Pneuman, 1985).

The solar magnetic field changes on all so far observed time scales, ranging from a few minutes to hundreds of years. In 1611 Galilei noticed the first indications of this variability, when he observed that sunspots have everchanging shapes and sizes (Secchi, 1871). Discovery of variability on a longer time scale followed in 1843, when Schwabe first announced a periodicity of about 10 years in the occurence of sunspots (Secchi, 1871; Clerke, 1885). This sunspot cycle has since been extensively studied. It is now known to have an average period of approximately

11.1 years, subject to considerable scatter (Wolf, 1877; Waldmeier, 1961, 1976) and a modulation over even longer periods (Eddy, 1980). However, the major discovery relating to the sunspot cycle was its correspondance to half a cycle of the solar magnetic field found by Hale et al. (1919). Today the manifold indications of the solar cycle (sunspot number, coronal shape, strength of radio emission, frequency of active regions and flares, distribution of surface magnetic flux, etc.) are interpreted as the surface manifestations of an internal change in the magnetic field geometry. A theoretical description of this evolution of the large scale structure of the Sun's magnetic field is given by the dynamo theories (Schüssler, 1983; Gilman, 1983; Belvedere 1985), which attempt an explanation in terms of induction effects in conducting fluid masses. According to these theories the main forces responsible for the generation of magnetic fields are solar differential rotation and (turbulent) convection.

Is the Sun a special case, or do magnetic fields play a similar role in other stars as well? Many stars below the main sequence, e.g. white dwarfs, have been observed to have magnetic fields considerably stronger than the Sun (Angel, 1978). But, except for Ap and Bp stars with their usually simple dipole-like magnetic field structure (e.g. Stibbs, 1950; Babcock, 1958; Borra et al., 1982; Mathys and Stenflo, 1986) no stars on or above the main sequence in the HR diagram readily show Stokes V polarization signals indicative of photospheric magnetic fields (a possible exception is ξ Boo A, which shows a weak field of 25 G; cf. Borra et al., 1984). However, this does not imply the absence of magnetic fields for all other stars, since due to the tangled nature of its magnetic field, with many bipolar regions scattered over its disk, the Sun also exhibits disappearingly small $\langle B \rangle$ values for magnetograms averaged over the whole disk. If the magnetic field of other stars were also in this tangled state, then it would necessarily be unobservable with polarization methods. An alternative is to search for the change in the unpolarized line profile due to magnetic fields. One such method, the so-called Robinson technique (Robinson, 1980), has been successfully applied to detect the presence of strong magnetic fields in a number of late type stars (Robinson et al., 1980; Marcy, 1983, 1984). Other similar techniques have been developed and applied by Giampapa et al. (1983), Gray (1984), Saar and Linsky (1985), and Saar et al. (1986). According to Linsky (1985) strong tangled magnetic fields have now been measured directly on main sequence stars with spectral types ranging from G0V to dM3.5e. On the other hand, Marcy and Bruning (1984) failed to find direct evidence for magnetic fields on late type giants.

Nevertheless, the full significance of magnetic fields for, in particular, late type stars (including giants) only becomes evident when we include the manifold indirect indicators of stellar magnetic fields. One of the most widely used of these indicators is the Ca II H and K flux (Zwaan, 1983; Noyes, 1985). Its variation over a time span of years has provided clear evidence of the presence of stellar activity cycles with periods similar to the solar cycle (Wilson, 1978; Vaughan, 1983; Baliunas and Vaughan, 1985). Short term variations of the Ca II H and K flux, visual magnitude, and flux in UV lines have been used to diagnose the presence of starspots (e.g. Baliunas and Dupree, 1982; Marstad et al., 1982; Vogt, 1983). Even their approximate position on the stellar disk and its differential rotation have in some cases been deduced (Vogt and Penrod, 1983a, b; Baliunas et al., 1985). Measurements with the EINSTEIN satellite have shown that stars of practically all spectral types along the main sequence emit significant amounts of X-rays (Vaiana, 1983). Whereas, for early type stars these observations can be explained by shocks in massive radiatively driven winds (e.g. Rosner et al., 1985), for late type stars the observed X-rays require the presence of coronæ (Vaiana, 1983; Rosner, 1986). EUV spectra obtained with the IUE satellite have also proved the existence of chromospheres and transition regions in late type stars (Linsky, 1985; Noyes, 1985). Furthermore, both EUV and X-ray measurements have shown that the coronal heating mechanism has to be magnetic in nature for all late type stars (Linsky and Ayres, 1978; Basri and Linsky, 1979; Vaiana et al., 1981). Finally, microwave emission from stellar coronæ has also been detected (Gary and Linsky, 1981, Dulk, 1985).

Fig. 1.1 gives an overview of stars which are directly or indirectly thought to be of 'solar type'. Linsky (1985) defines a 'solar type' star as a star which has a turbulent magnetic field sufficiently strong to control the dynamics and energetic in its outer atmospheric regions. He summarises the present situation as follows, ". . . evidence is accumulating rapidly that magnetic fields lie at the heart of much of the rich phenomenology of 'activity' in cool stars. This is not to say that magnetic fields control all phenomena, but rather that magnetic fields usually determine the geometry, time variability, non-radiative heating rates, inhomogeneity, and ultimately the global energy balance in stars located in a wide range of the cool half of the H–R diagram."

That the dynamo mechanism is also responsible for the magnetic fields of 'solar type' stars is indicated by the correlation between the stellar rotation rate and the X-ray emission (Pallavicini et al., 1981), and between rotation and Ca II emission (Kraft, 1967; Middelkoop and Zwaan, 1981; Middelkoop, 1982). The theory of stellar dynamos is reviewed by Schüssler (1983) and Belvedere (1985).

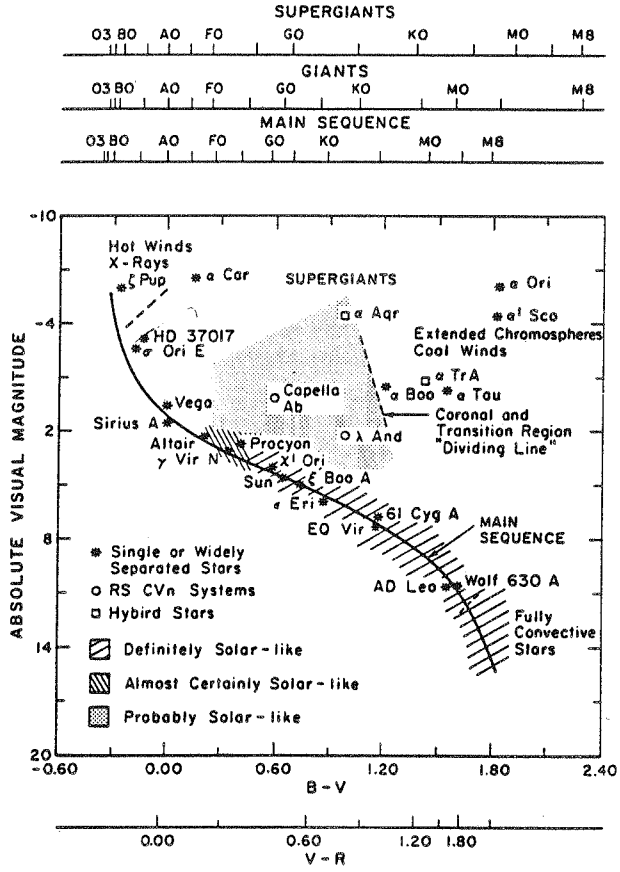

Fig. 1.1 : An H–R diagram showing schematically which types of stars are definitely or probably solar-like on the basis of direct or indirect indicators of strong, turbulent magnetic fields. Also indicated are the regions of the H–R diagram where massive winds occur and hot plasma is apparently absent (from Linsky, 1985).

So far we have briefly reviewed measurements of magnetic fields on the Sun and stars, as well as some of the consequences of such fields. An important open question is the structure of the magnetic field. In this respect the Sun, being the only star resolvable in any detail, must for the time being provide most of the information for all 'solar type' stars (with the possible exception of those few highly active stars whose rotation light curves yield some rough indirect information on the large scale geometry of their magnetic field).

Let us therefore summarize the presently accepted picture of the structure of the photospheric magnetic field on the Sun. Almost all of the magnetic field is bundled into structures with field strengths in excess of 1 kG (Stenflo, 1973; Harvey, 1977; Zwaan, 1978). Depending on the diameter or the magnetic flux of these structures, they result in sunspots, pores or (small) fluxtubes (often also called magnetic elements, or magnetic fibrils). Fluxtubes, in contrast to the much rarer sunspots and pores, are found everywhere on the solar disk, both in active regions and in quiet regions at the boundaries of supergranule cells (e.g. Leighton et al., 1962, Simon and Leighton, 1964). Since this thesis is concerned with the structure of these small magnetic elements let us briefly discuss some of their properties and the role they play in the context of solar physics and therefore also of other 'solar type' stars.

Theoretically, fluxtubes are thought to form as a result of the interaction of convection with the magnetic field. The field is expelled from the centres of turbulence elements towards their boundaries (Proctor and Weiss, 1982). This mechanism works both at the level of the supergranulation and the granulation (Nordlund, 1983, 1986; Title et al., 1987). The final concentration takes place by a convective instability. If the instability starts out as a downdraft, then the magnetic field will be greatly strengthened by the resulting evacuation of the tube. The magnetic field has a stabilising influence and once the field has been sufficiently strengthened a stable configuration can result (Spruit, 1979). Recent numerical calculations suggest that the final state is one of overstable oscillations (Hasan, 1984, 1985, 1986) as initially proposed by Spruit (1979).

From an observational point of view the critical property of fluxtubes is their size. A diameter of often less than the best presently available spatial resolution of 200–300 km (Mehltretter, 1974; Ramsey et al., 1977)

makes the rest of their properties very hard to determine by direct methods. This has led to the development of a few powerful indirect techniques which have yielded information on some of the fundamental parameters of fluxtubes, for example that they have field strengths of 1000-1500 G (Stenflo, 1973; Harvey and Hall, 1975) and that they are hotter than their surroundings (Chapman and Sheeley, 1968; Harvey and Livingston, 1969). The limits of the methods available until recently are clearly demonstrated by the following few examples of the many unanswered questions relating to fluxtubes. Very little is known about how the magnetic field and the temperature vary with height. The velocity structure in fluxtubes, their diameters, lifetimes, and evolution are even less certain. All in all, our knowledge of many aspects of these structures is very fragmentary. The main aim of this thesis is to develop new indirect methods of analysis, improve older methods (often involving model calculations), and apply these to the problem of the internal structure of solar magnetic fluxtubes in order to obtain a better idea of their magnetic field, temperature and velocity stratification.

Finally, we list a few points summarising the role of fluxtubes on the Sun.

- Over 90% of the non-sunspot magnetic flux is concentrated into small fluxtubes (Howard and Stenflo, 1972; Frazier and Stenflo, 1972).
- They are the most likely candidates for transporting the energy needed to heat the corona from the convection zone into the higher atmosphere (Spruit and Roberts, 1983). It has also been recently proposed that the chromosphere may actually exist only in fluxtubes (Ayres et al., 1986).
- They form the footpoints of chromospheric and coronal magnetic structures (cf. Altschuler and Newkirk, 1969; Altschuler et al., 1977, who calculate potential coronal fields, using the magnetic field distribution obtained from photospheric magnetograms as the lower boundary cndition).
- Spicules are concentrated in the network and are thus also associated with the magnetic fine structure (e.g. Dunn, 1972; Beckers, 1972). Theoretical calculations suggest that spicules may be one observable chromospheric manifestation of fluxtube waves (Hollweg et al., 1982; Hollweg, 1982).
- The fibril structure of the field affects the dynamo mechanism (Schüssler, 1983).
- Fluxtubes also affect solar convection, thereby changing the structure of the granulation and the heat transport, at least locally, in the upper part of the convection zone (e.g. Spruit, 1977; Deinzer et al., 1984b; Cavallini et al., 1985; Brandt and Solanki, 1987; Title et al., 1986). As a result they also affect the total luminosity of the Sun (Willson, 1984).

Perhaps, the fundamental role that small fluxtubes play for our understanding of many phenomena on the Sun and late type stars, is best described in the words of Parker (1985), "Observations show that the activity has its origin at the small scales (50–100 km) of the individual magnetic fibrils in the Sun. Hence, the observational study of stellar activity begins with the microscopy of the surface of the Sun." Such microscopy is the subject of this thesis.

2. Polarized Light

The empirical study of solar magnetic fields is intimately linked to the measurement and the interpretation of spectra in polarized light. In the presence of a magnetic field light becomes polarized through the Zeeman effect. If the light passing through the magnetic field is already polarized, then its polarization ellipse can be rotated as a result of the Faraday and Voigt effects, and the radiation can also be partially depolarized via the Hanle effect, which we shall not discuss further; see e.g., Stenflo (1971) and Leroy (1985) for additional information. In this chapter we shall consider the description of polarized light (Sect. 2.1), some processes giving rise to it and affecting it (Sects. 2.2 and 2.3), its transfer in a stellar atmosphere (Sect. 2.4) and some aspects of its measurement (Sect. 2.5).

The study of polarized radiation has a long history (cf. e.g. Robson, 1974; Clarke and Grainger, 1971). Bartholinus (1670) and Huygens (1690) discovered polarization, when they noticed that light which had passed through a piece of (doubly refracting) calcite behaved differently from ordinary light. He was able to describe the behaviour of the ordinary ray with his wave construction, but not that of the extraordinary ray. Around 1817, Young suggested that light waves are transverse rather than longitudinal vibrations, and in 1824 Fresnel showed that they are exclusively transverse waves. The resulting transverse *vector* theory allowed for the first time a description of polarization phenomena. The term 'polarization' was introduced by Malus in 1810 when describing the production of polarized light by reflection and was derived from the word 'polarity' employed earlier to describe the two-fold nature of magnetic poles.

2.1. Description of Polarized Light: Stokes Parameters

Four parameters are required for a complete and consistent description of polarized radiation (including partial polarization), and since the work of Chandrasekhar (1947, 1950) the system of four Stokes parameters has established itself as the standard representation in optical solar physics and stellar astronomy. This system has the advantage that it only contains real numbers which are directly measureable, which all have the same physical dimensions, which have a direct relationship to the physical processes of the studied object, and which allow the radiative transfer equation to be written in a straightforward manner.

In Cartesian coordinates the vibration of the electric field vector, (ξ_x, ξ_y), of light propagating in the z-direction can be written as

$$\begin{aligned} \xi_x &= \xi_{x_0} \cos(\omega t - \epsilon_x), \\ \xi_y &= \xi_{y_0} \cos(\omega t - \epsilon_y), \end{aligned} \tag{2.1}$$

where ω is the circular frequency of the vibration, ξ_{x_0} and ξ_{y_0} are the maximum amplitudes of the electric vector in the x and y directions, and ϵ_x and ϵ_y are its respective phases. In a basis of two mutually orthogonal linearly polarized vectors (e.g. the vectors with $(\xi_x, \xi_y) = (\cos\omega t, 0)$ and $(0, \cos\omega t)$ respectively), the Stokes parameters for an arbitrarily polarized beam of light can be written as

$$\begin{aligned} I &= I_x + I_y, \\ Q &= I_x - I_y, \\ U &= 2\left\langle \xi_{x_0} \xi_{y_0} \cos(\epsilon_x - \epsilon_y) \right\rangle, \\ V &= 2\left\langle \xi_{x_0} \xi_{y_0} \sin(\epsilon_x - \epsilon_y) \right\rangle. \end{aligned} \tag{2.2}$$

In Eq. (2.2) I, Q, U, and V are the Stokes parameters named after Sir George Gabriel Stokes (1819–1903), who first introduced them (Stokes, 1852). According to his principle of optical equivalence, beams of light which have the same "Stokes parameters" are indistinguishable as regards intensity, degree of polarization and polarization form. $I_x = \left\langle \xi_{x_0}^2 \right\rangle$, $I_y = \left\langle \xi_{y_0}^2 \right\rangle$, and the brackets $\langle\ \rangle$ denote averaging over time in Eq. (2.2). For *totally* polarized light the averaging over time is not necessary. It then follows directly from Eq. (2.2) that

$$I^2 = Q^2 + U^2 + V^2. \tag{2.3}$$

Therefore only three Stokes parameters are required to describe totally polarized light. In order to clarify the meaning of the different Stokes parameters somewhat more (specially U and V, whose interpretation is not obvious from Eq. (2.2)), we introduce the quantities β and φ, such that $\tan\beta = \xi_{a_0}/\xi_{b_0}$, where ξ_{a_0} and ξ_{b_0} are the magnitudes of the major and minor semi-axes, of the polarization ellipse described by the electric vector. If a and b are the direction vectors of the major and minor semi-axes respectively, then φ is defined as the angle between a and the x-direction. Fig. 2.1 illustrates these definitions.

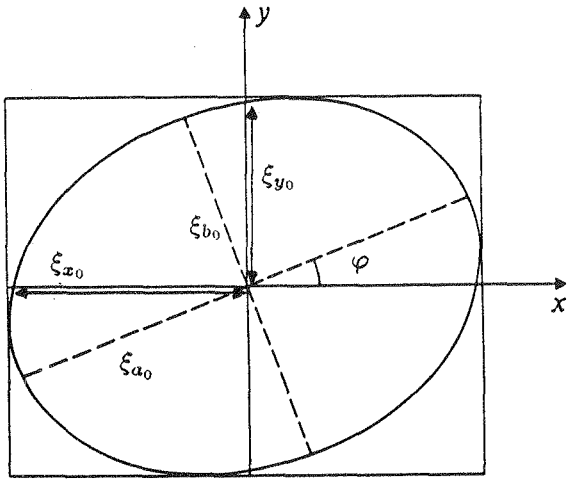

Fig. 2.1 Polarization ellipse for the electric vector (ξ_x, ξ_y). The major and minor semi-axes have lengths ξ_{a_0} and ξ_{b_0}, respectively; φ is the angle between the major axis and the x-axis (adapted from Robson, 1974).

We can now write the Stokes parameters for the general case of partially polarized light as (e.g., Wittmann, 1973b)

$$\begin{aligned} I &= I_0 + I_p, \\ Q &= I_p \cos 2\beta \cos 2\varphi, \\ U &= I_p \cos 2\beta \sin 2\varphi, \\ V &= I_p \sin 2\beta. \end{aligned} \tag{2.4}$$

Here I_0 and I_p represent the intensities of the unpolarized and the polarized fractions of the light respectively. In Eq. (2.4) the expressions for Q, U, and V bear a close resemblence to the description of a vector in three dimensional spherical coordinates. This analogy can be used to construct a simple geometrical representation of the polarized fraction of light, a representation introduced by Poincaré (1892) and which is consequently named the Poincaré sphere. We shall not consider it further here, but refer to, e.g., Robson (1974) for a short description. For partially polarized light Eq. (2.3) has to be replaced by the inequality

$$I^2 \geq I_p^2 = Q^2 + U^2 + V^2. \tag{2.5}$$

From Eqs. (2.2) and (2.4) the meanings of the four Stokes parameters can be easily reconstructed. Stokes I is obviously just the total intensity of the light, while Stokes Q, U, and V can be interpreted as follows:

$$\begin{aligned} Q &= I_{\rm lin}(\varphi = 0) - I_{\rm lin}(\varphi = \pi/2), \\ U &= I_{\rm lin}(\varphi = \pi/4) - I_{\rm lin}(\varphi = 3\pi/4), \\ V &= I_{\rm circ}({\rm right}) - I_{\rm circ}({\rm left}). \end{aligned} \tag{2.6}$$

Right circularly polarized light is defined as light with an electric vector rotating clockwise when viewed from the front at a fixed point in space. It is clear from Eqs. (2.4) and (2.6) that $V = 0$ is a necessary condition for light to be linearly polarized. Similarly $Q = U = 0$ is required for light to be circularly polarized. The quantities on the right-hand-side of Eq. (2.6) are not totally independent, since

$$I = I_{\rm lin}(0) + I_{\rm lin}(\pi/2) = I_{\rm lin}(\pi/4) + I_{\rm lin}(3\pi/4) = I_{\rm circ}({\rm right}) + I_{\rm circ}({\rm left}). \tag{2.7}$$

The polarization state of a light beam can be written in a compact form by introducing the Stokes vector $\mathbf{I}^T = (I, Q, U, V)$, where the symbol ^{T} represents the transpose. The effect of an optical device on a polarized beam

of light is equivalent to a linear transformation of the Stokes vector, as was discovered by Soleillet and expressed in matrix form by Perrin in 1942. However, it was Mueller who carried out the first extensive calculations with this formalism and solved many problems previously considered intractable. As a consequence the formalism of applying 4×4 matrices on Stokes vectors has come to be known as Mueller calculus. An example is given below. Further examples follow in Sect. 2.5.

In observational practice the angle φ is usually measured with respect to the direction of a linear polarizer. A rotation of the polarizer by the angle α, which is equivalent to a rotation of the coordinate system, will affect the Stokes vector in the following manner

$$\mathbf{I}' = \begin{pmatrix} 1 & 0 & 0 & 0 \\ 0 & \cos 2\alpha & \sin 2\alpha & 0 \\ 0 & -\sin 2\alpha & \cos 2\alpha & 0 \\ 0 & 0 & 0 & 1 \end{pmatrix} \mathbf{I}. \tag{2.8}$$

According to Eq. (2.8) Q and U are interchangeable, so that, for example on the Sun, the information content of Stokes Q and U depends strongly on the instrument and the observational procedure.

2.2. Zeeman Effect

In 1896 Pieter Zeeman (1865–1943) discovered the splitting of spectral lines in the presence of a magnetic field (Zeeman, 1897a,b,c). Although he only discussed observations of the magnetic *broadening* of the Na I D lines in his first paper, Zeeman nevertheless realised their significance due to the unique polarization signature, which was in accord with the classical theory of radiation of Lorentz. In the following two papers he described experiments in which he was finally able to observe complete splitting. A first (incomplete) quantum mechanical description of the normal Zeeman effect was given by Debye (1916) and Sommerfeld (1916). It was later extended to include the selection and polarization rules by Rubinowicz (1918a,b) and Bohr (1918). In the following we shall give a brief description of the effect and of its influence on a spectral line.

2.2.1. Zeeman Effect for an Atomic Energy Level

The Hamiltonian of an atom in an external magnetic field is to first order in $\mathbf{B}$ given by (e.g. Baym, 1969)

$$\mathrm{H} = \mathrm{H}_0 + \mathrm{H}_1 = \mathrm{H}_0 + \frac{e}{2mc}(\mathbf{L} + 2\mathbf{S})\mathbf{B}, \tag{2.9}$$

where H_0 is the Hamiltonian of the atom without any external field, e is the (positive) charge of an electron, m is its mass, c is the speed of light, $\mathbf{L}$ is the orbital angular momentum operator with $\mathbf{L}^2$ having the eigenvalues $\hbar^2 L(L+1)$ (with $L = 0, 1, 2, \ldots$), $\mathbf{S}$ is the spin angular momentum operator with $\mathbf{S}^2$ having the eigenvalues $\hbar^2 S(S+1)$ (with $S = 0, \frac{1}{2}, 1, \frac{3}{2}, 2, \ldots$), and $\mathbf{B}$ is the vector of the external magnetic field. We have assumed that LS-coupling is valid, that the magnetic moment of the nucleus can be neglected (it is at least three orders of magnitude smaller than the electronic part according to Sobel'man, 1972), and that the coupling of the atom to the external field is small compared to the spin-orbit interaction (as is the case for the magnetic field strength found on the Sun). First order time-independent perturbation theory can then be applied. It is found that the $(2J+1)$-fold degeneracy in the energy of each level disappears (here $\hbar^2 J(J+1)$ [with $J = 0, \frac{1}{2}, 1, \frac{3}{2}, 2, \ldots$] is the eigenvalue of the squared total angular momentum operator $\mathbf{J}^2$, with $\mathbf{J} = \mathbf{L} + \mathbf{S}$), due to its splitting into magnetic sublevels whose energy is given by

$$E_{J,M} = E_J + \mu_0 g M B. \tag{2.10}$$

In Eq. (2.10) E_J is the energy of the atomic level in the absence of a magnetic field (i.e. E_J is an eigenvalue of H_0), $\hbar M$ (with $M = -J, -J+1, \ldots, J$) is an eigenvalue of J_z, which is the component of the total angular momentum operator in the direction of the magnetic field, μ_0 is the Bohr magneton: $\mu_0 = e\hbar/(2mc)$, B is the absolute value of $\mathbf{B}$, and g is the Landé factor. In LS-coupling the Landé factor can be written as

$$g = 1 + \frac{J(J+1) + S(S+1) - L(L+1)}{2J(J+1)}. \tag{2.11}$$

A first version of this equation was derived by Landé (1923), but the correct physical meaning of the different quantum numbers, specially of the spin, was not realised until 1925 (Uhlenbeck and Goudsmit, 1925, 1926). If $S = 0$ (i.e. no spin) then $g = 1$, if $L = 0$ (i.e. only spin) then $g = 2$. For some levels (e.g. $^4D_{1/2}$, $^5F_1$) the Landé factor is zero and these levels do not split in the first order perturbation theory carried out here. Condon and Shortley (1964) tabulate the terms of interest, including those without Zeeman splitting. The calculation of g-factors becomes considerably more complicated when LS-coupling no longer applies. Formulæ and methods for their calculation in jj-coupling are given by e.g. Sobel'man (1972).

2.2.2. Normal and Anomalous Zeeman Effect

The normal Zeeman effect is exhibited by lines which are either formed by transitions between two levels that have equal Landé factors, for example between two singlets (which implies $g = 1$), or between a $J = 1$ and a $J = 0$ level. In the former case the two levels will split into a different number of sublevels, since the J values of the two levels are different. This is due to the dipole radiation selection rule: $\Delta L = \pm 1$ and because $L = J$ for $S = 0$. However, the separation between two sublevels of consecutive M will be the same for both levels. The M selection rules for electric dipole radiation,

$$\Delta M = 0, \pm 1, \tag{2.12}$$

with the additional constraint that

$$M = 0 \rightarrow M = 0 \quad \text{is forbidden for} \quad \Delta J = 0\,, \tag{2.13}$$

cause the spectral line to split into exactly three components (see Fig. 2.2, taken from Herzberg, 1944), having the frequencies ν_0 and $\nu_0 \pm \mu_0 g B$. g is now the Landé factor of the line and is in this case identical to the g-factor of any one of the two levels. The unshifted ($\Delta M = 0$) component is called the π-component, while the $\Delta M = \pm 1$ components are referred to as the $\sigma^{\pm}$-components. The $\Delta M = +1$ component is shifted towards the red, while the $\Delta M = -1$ component is shifted towards the blue (for a positive Landé factor).

In the case of a $J = 1 \rightarrow J = 0$ transition it is obvious that the line splits into exactly three components, since $J = 0$ does not split while the $J = 1$ level splits into three components. The g-factor of the line in this case is identical to the g-factor of the $J = 1$ level.

In the more common case of anomalous Zeeman splitting, the upper and lower levels of the transition have different g-factors. The spectral line will then usually have more than three components. However, the distinction between σ- and π-components is still made (see Fig. 2.3, taken from Herzberg, 1944). In analogy to the g-factor for a Zeeman triplet, an effective Landé factor, $g_{\rm eff}$, is defined for spectral lines showing anomalous Zeeman splitting (Shenstone and Blair, 1929), which can be written as

$$g_{\rm eff} = \frac{1}{2}(g_l + g_u) + \frac{1}{4}(g_l - g_u)(J_l(J_l+1) - J_u(J_u+1)). \tag{2.14}$$

In Eq. (2.14) the subscripts l and u denote the lower and upper levels involved in the transition respectively. The effective Landé factor $g_{\rm eff}$ is a measure of the wavelength shift of the centre of gravity of the σ-components (for example for $\Delta M = +1$) with respect to the wavelength of the unsplit line, λ_0. It should be noted that Eq. (2.14) is symmetrical with regard to the exchange of the upper and lower levels ($g_l, J_l \leftrightarrow g_u, J_u$), and that it is also valid for the normal Zeeman effect (if we set $g = 0$ for a $J = 0$ level). Neither is its validity restricted to the case of LS-coupling as long as the g_u and g_l values taken are the correct ones, as has been noted by Landi Degl'Innocenti (1982). We shall use this property of Eq. (2.14) to determine empirical $g_{\rm eff}$ values for a number of unblended solar iron lines, and thus take the effects of departure from LS-coupling on our analysis partially into account (cf. Sect. 4.3.3). Beckers (1969c) has tabulated the $g_{\rm eff}$ values for transitions between levels of many different J, L, and S values.

2.2.3. Polarization, Intensity, and Splitting of the Zeeman Components

The polarization rules for the different Zeeman components result from a straightforward derivation of the selection rules for M; cf. Eq. (2.12). However, for the sake of brevity we refer to Herzberg (1944) for a simple derivation and restrict ourselves to listing the results.

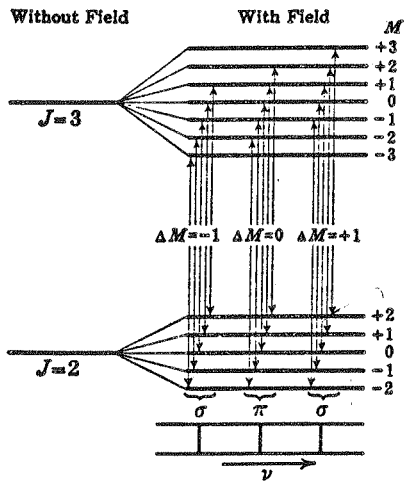

Fig. 2.2 Normal Zeeman effect for a transition $J = 3 \rightarrow J = 2$. The arrows representing the transitions form three groups of equal ΔM. The arrows in each group have equal length and therefore give rise to one and the same line in the splitting pattern visible in the lower part of figure (from Herzberg, 1944).

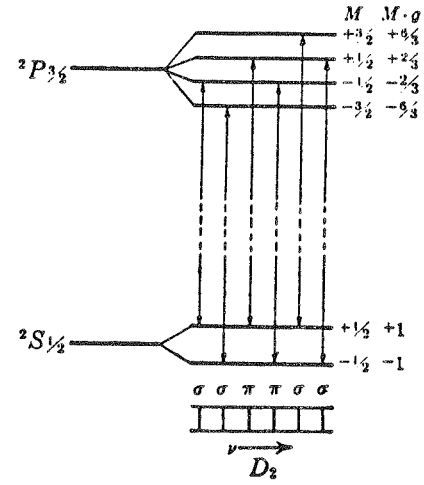

Fig. 2.3 Anomalous Zeeman effect of the Na I D_2 line, $^2P_{3/2} \rightarrow {}^2S_{1/2}$. Note that contrary to Fig. 2.2, arrows indicating transitions with equal ΔM no longer have the same length, because of the difference in splitting in the upper and lower states (from Herzberg, 1944).

- **Transversal Zeeman effect:** When the angle between the line of sight and the magnetic field vector, $\gamma = 90°$, then the π-components are linearly polarized parallel to **B** and the σ-components are linearly polarized perpendicular to **B** (σ for "senkrecht").
- **Longitudinal Zeeman effect:** For $\gamma = 0°$ or $\gamma = 180°$ no π-components are visible and the σ-components are circularly polarized. For an emission line and $\gamma = 0°$ the $\Delta M = -1$ component is left circularly polarized, while the $\Delta M = +1$ component is right circularly polarized (Condon and Shortley, 1964). For an emission line and $\gamma = 180°$, or for an absorption line and $\gamma = 0°$ the polarizations are reversed. Note: The Zeeman effect in absorption spectra is often called the reverse Zeeman effect.
- For a general direction the light is usually elliptically polarized, with the major axis of the polarization ellipse of the σ-components being perpendicular to that of the π-components.

Fig. 2.4 Illustration of the polarizations and strengths of the individual components for longitudinal and transversal Zeeman effects for the normal Zeeman triplet (from Condon and Shortley, 1964).

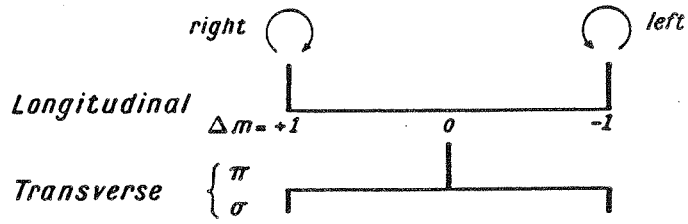

Let $S_n(M, \gamma)$ be the unnormalised relative strengths of the different Zeeman components, when viewed at the angle γ to the field, in an optically thin medium, under the assumption that all Zeeman sublevels are equally populated. $n = \Delta M = 0, \pm 1$ and $-J \leq M \leq J$. However, the exact limits to the value of M depend on ΔM and ΔJ. Both J and M refer to the initial state of the atom. $S_n(M, \gamma = \pi/2)$ values for dipole radiation are listed in Table 2.1, which has been taken from Condon and Shortley (1964). The $S_n(M, \gamma = \pi/2)$ values were first derived theoretically by Hönl (1925) and Kronig (1925) independently. Strengths for quadrupol radiation are listed by Beckers (1969b). It should be noted that the relative intensities of the Zeeman components are independent of the coupling scheme, in contrast to their shifts (i.e. the g-factor plays no role in determining the intensities). S_n should not be confused with the spin quantum number S.

Table 2.1 Unnormalised intensities $S_n(M, \gamma = \pi/2)$ of the Zeeman components

	$M \to M-1$ $(\Delta M = -1)$	$M \to M$ $(\Delta M = 0)$	$M \to M+1$ $(\Delta M = +1)$
$J \to J+1$	$(J-M+1)(J-M+2)$	$4(J+1)^2 - M^2$	$(J+M+1)(J+M+2)$
$J \to J$	$(J+M)(J-M+1)$	$4M^2$	$(J-M)(J+M+1)$
$J \to J-1$	$(J+M)(J+M-1)$	$4(J^2-M^2)$	$(J-M)(J-M-1)$

For use in radiative transfer calculations, these strengths have to be normalised such that

$$\sum_M S_n(M, \pi/2) = 1 \qquad (n = 0, \pm 1). \tag{2.15}$$

The strengths of the individual Zeeman components for an arbitrary angle γ can be determined from the strengths at $\gamma = \pi/2$ via the Seares formulæ (Seares, 1913)

$$\begin{aligned} S_0(M,\gamma) &= S_0(M,\pi/2)\sin^2\gamma, \\ S_{+1}(M,\gamma) &= S_{+1}(M,\pi/2)(1 \pm \cos\gamma)^2, \\ S_{-1}(M,\gamma) &= S_{-1}(M,\pi/2)(1 \mp \cos\gamma)^2, \end{aligned} \tag{2.16}$$

where upper and lower signs in the right-hand-side of Eq. (2.16) are applicable for right- and left-handed circular analysers respectively. For the three groups of Zeeman components ($\Delta M = 0, \pm 1$) the profiles in a stationary, optically thin medium are

$$\begin{aligned} \Phi_0 &= \sum_M S_0(M,\pi/2) H(a, v - v_0(M)), \\ \Phi_{+1} &= \sum_M S_{+1}(M,\pi/2) H(a, v - v_{+1}(M)), \\ \Phi_{-1} &= \sum_M S_{-1}(M,\pi/2) H(a, v - v_{-1}(M)), \end{aligned} \tag{2.17}$$

when viewed perpendicularly to the magnetic field. In Eq. (2.17)

$$H(a,v) = \frac{a}{\pi}\int_{-\infty}^{\infty} \frac{\exp(-y^2)}{(v-y)^2 + a^2}\,\mathrm{d}y \tag{2.18}$$

is the Voigt profile first derived by Voigt (1913), with

$$v = (\lambda - \lambda_0)/\Delta\lambda_D \tag{2.19}$$

being the dimensionless distance from the line centre wavelength, λ_0. $\Delta\lambda_D$ is the Doppler width, which for a stellar atmosphere can be written as

$$\Delta\lambda_D = \frac{\lambda_0}{c}\sqrt{\xi_{\mathrm{mic}}^2 + \frac{2kT}{M_a}}. \tag{2.20}$$

Here k is the Boltzmann constant, M_a is the mass of the atom, T is the temperature, ξ_{mic} is the microturbulence velocity (we have assumed the microturbulence to be distributed in the form of a Gaussian as well), and c is the speed of light. In Eq. (2.18)

$$a = \frac{\Gamma\lambda_0^2}{4\pi c\Delta\lambda_D}, \tag{2.21}$$

where Γ is the damping constant (see Sect. 2.4.5 for more information). More details on the physical background of $H(a,v)$ are given by Mihalas (1978). $H(a,v)$ is symmetric with regard to v,

$$H(a,-v) = H(a,v). \tag{2.22}$$

Negative values of a are unphysical. In Eq. (2.17) the quantities

$$v_n(M) = \frac{e\lambda_0^2 B}{4\pi mc^2\Delta\lambda_D} g_n(M) = 4.6686 \times 10^{-13}\frac{\lambda_0^2 B}{\Delta\lambda_D} g_n(M), \qquad (n = 0, \pm 1) \tag{2.23}$$

are the dimensionless wavelength shifts of the Zeeman components. In Eq. (2.23) λ_0, $\Delta\lambda_D$ are in Å, and B is in G. The Landé factors of individual Zeeman components of the spectral line $g_n(M)$, can be determined from the g-factors of the upper and lower levels via

$$\begin{aligned} g_0(M) &= gM - g'M, \\ g_{+1}(M) &= gM - g'(M+1), \\ g_{-1}(M) &= gM - g'(M-1), \end{aligned} \tag{2.24}$$

where g and g' are the Landé-factors of the initial and final level of the transition and may be calculated using Eq. (2.11). The maximum and minimum values of M depend on $\Delta M = n$ and ΔJ. Beckers (1969c) has tabulated the strengths, $S_n(M, \pi/2)$, and Landé factors $g_n(M)$, for all the Zeeman components of transitions between a comprehensive set of configurations.

If the medium is not optically thin, the emergent line profiles have to be determined by solving the radiative transfer equation. Then the absorption profiles given by Eq. (2.17) are proportional to the absorption coefficients, i.e. the absorption coefficient of a spectral line formed in a magnetic field splits up into the three components, $\kappa_n \sim \Phi_n$, $(n = 0, \pm 1)$. We shall return to this case in Sect. 2.4.

2.3. Anomalous Dispersion

The Zeeman effect induces not only a change in the absorption coefficient for light in a material, so that the different polarization states are absorbed differently at a particular wavelength, but also in the refractive index, so that waves in different polarization states travel at different velocities through the material. The medium thus becomes birefringent and acts similarly to certain crystals which are naturally birefringent, e.g. calcite (linearly birefringent, i.e. orthogonal linear polarizations travel at different speeds), or quartz (circularly birefringent; cf. Clarke and Grainger, 1971). This anomalous dispersion gives rise to the so called magnetooptical effects, the best known of which is Faraday rotation.

In 1845 Micheal Faraday (1791-1867) observed that the plane of polarization of linearly polarized light was rotated about its propagation axis when it passed through silicated borate of lead glass which was placed in a magnetic field parallel to the direction of propagation of the light passing through it. He described his discovery as follows. "... I recently resumed the inquiry by experiment in a most strict and searching manner, and have at last succeeded in *magnetizing and electrifying a ray of light* ..." (Faraday, 1855). This effect of a longitudinal field is now known either as Faraday rotation or as the Macaluso-Corbino effect. If the magnetic field is perpendicular to the line of sight we have linear birefringence or the so-called Voigt effect, while for an arbitrary angle we have in general elliptical birefringence. With the discovery of the Faraday effect the influence of a magnetic field on radiation was observed for the first time.

The relationship between the magnetooptical effects and the Zeeman effect is best illustrated by the dispersion relation between the refractive index n and the absorption coefficient κ. Dispersion relations are a general property of many complex functions, and we shall first write a dispersion relation in its general form. Consider a complex function of a real variable

$$f(x) = p(x) + iq(x), \tag{2.25}$$

with $p(x) = \Re f(x)$ and $q(x) = \Im f(x)$ ($\Re f$ and $\Im f$ denote the real and imaginary parts of the function f, respectively), which can be extended to cover the whole complex plane by replacing x in Eq. (2.25) by $z = x + iy$. If $f(z)$ is analytic in the upper half of the complex plane (i.e. for $y > 0$) and tends to zero at large distances from the origin, so that

$$\int_{\substack{\text{semi circle} \\ \text{of radius } R}} \frac{f(z')}{z' - z}\,\mathrm{d}z' \longrightarrow 0 \qquad \text{as} \quad R \longrightarrow \infty, \tag{2.26}$$

then it can be shown that the value of the real and imaginary parts of $f(z)$ on the real axis are related by (Corinaldesi, 1959)

$$p(x) = \frac{1}{\pi}\mathrm{P}\int_{-\infty}^{\infty} \frac{q(x')}{x' - x}\,\mathrm{d}x', \tag{2.27}$$

$$q(x) = \frac{1}{\pi}\mathrm{P}\int_{-\infty}^{\infty} \frac{p(x')}{x - x'}\,\mathrm{d}x', \tag{2.28}$$

where P denotes the Cauchy principal value of the integral. Eqs. (2.27) and (2.28) are the dispersion relations for $p(x)$ and $q(x)$.

Irrespective of the presence of a magnetic field, a medium generally has a complex refractive index defined as

$$\mathsf{n} = n + ik, \tag{2.29}$$

where n and k are the real and imaginary parts of n, namely the (real) refractive index and the extinction coefficient of the medium. They respectively determine the phase velocity and the amount of absorption of the radiation in the medium. The extinction coefficient k is related to the absorption coefficient κ used in the radiative transfer equation by

$$\kappa = \frac{4\pi\nu}{c}k. \tag{2.30}$$

Corinaldesi (1959) shows that if we consider the (non-magnetic) dispersive medium to be composed of an assembly of naturally damped oscillators then

$$\mathsf{n}(\omega) - 1 = N\frac{e^2}{2m}\frac{1}{(\omega_0^2 - \omega^2) - i\omega\Gamma}, \tag{2.31}$$

where $\omega = 2\pi\nu$ which is replaced by $\tilde{\omega} = \omega + i\omega_{\rm im}$ in order to cover the complete complex plane. ω_0 is the natural frequency of the oscillators, Γ is their natural damping constant (describing the radiative damping), and N is the number of oscillators per unit volume. A full quantum-electrodynamical treatment of a radiatively damped transition also leads to an equation similar to Eq. (2.31), the only difference to the classical result being the constants of proportionality. Eq. (2.31) satisfies Eq. (2.26) and is analytical in the upper half-plane, since its poles, the roots of the quadratic equation

$$\tilde{\omega}^2 + i\tilde{\omega}\Gamma - \omega_0^2 = 0, \tag{2.32}$$

both lie in the lower half plane. The dispersion, or Kramers-Kronig, relations (Kronig, 1926; Kramers, 1927) for n can therefore be written as follows (Corinaldesi, 1959; Huber and Sandeman, 1986),

$$k(\omega) = -\frac{2\omega}{\pi}\mathsf{P}\int_0^\infty \frac{n(\omega')}{\omega'^2 - \omega^2}\,\mathrm{d}\omega', \tag{2.33}$$

$$n(\omega) = 1 + \frac{2}{\pi}\mathsf{P}\int_0^\infty \frac{\omega' k(\omega')}{\omega'^2 - \omega^2}\,\mathrm{d}\omega'. \tag{2.34}$$

The symmetry properties of $\mathsf{n} - 1$ allow the integration to be limited to positive values of ω. Eqs. (2.33) and (2.34) demonstrate the intimate connection between n and k, i.e. between the phase velocity of light in the medium and its absorption. In particular, the Kramers-Kronig relations are also true when the absorption coefficient in the vicinity of an atomic resonance or transition (i.e. a spectral line) has a profile the shape of a Voigt function $H(a, v)$. Then the corresponding profile of $n - 1$ follows from Eq. (2.34) and is proportional to the Faraday-Voigt or dispersion profile

$$F(a, v) = \frac{1}{2\pi}\int_{-\infty}^{\infty} \frac{(v - y)\exp(-y^2)}{(v - y)^2 + a^2}\,\mathrm{d}y. \tag{2.35}$$

This follows from the fact that $H(a, v)$ and $2F(a, v)$ can be written as the real and imaginary parts of a complex function which satisfies the conditions required for the existence of the dispersion relations between H and F,

$$W(z) = H(a, v) + 2iF(a, v) = \frac{i}{\pi}\int_{-\infty}^{\infty} \frac{e^{-t^2}}{z - t}\,\mathrm{d}t, \tag{2.36}$$

where $z = v + ia$. Note that the factor before the integral in Eq. (2.35) differs from the factor of $H(a, v)$ in Eq. (2.18). In contrast to the Voigt function, $F(a, v)$ is antisymmetric in v, i.e.

$$F(a, -v) = -F(a, v). \tag{2.37}$$

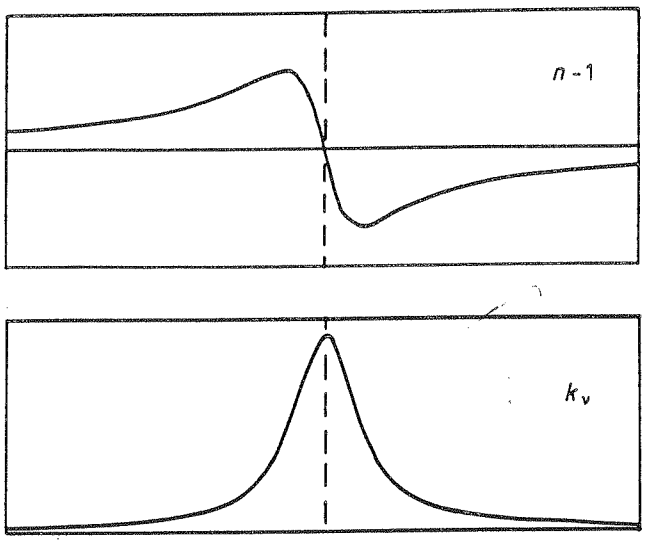

Fig. 2.5 Schematic representation of refractivity, $n-1$ (upper figure), and extinction coefficient, k (lower figure), for an isolated spectral line in the absence of a magnetic field (adapted from Huber and Sandemann, 1986).

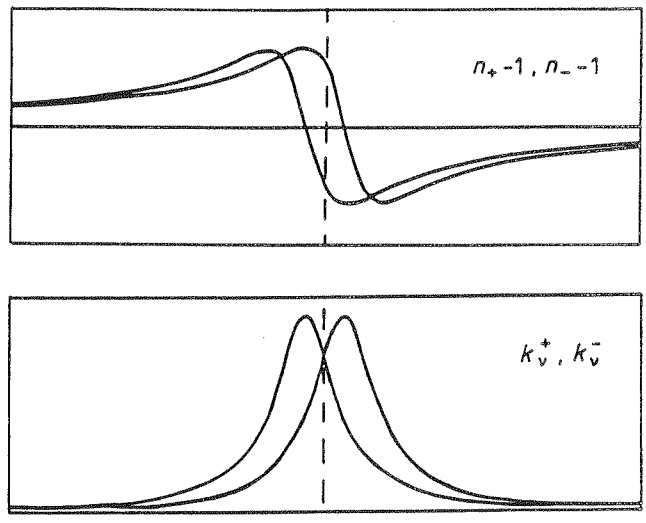

Fig. 2.6 Refractivities, $n_+ - 1$, $n_- - 1$ (upper figure) and extinction coefficients k_+, k_- (lower figure) for light beams of opposite circular polarization in the presence of a magnetic field (adapted from Huber and Sandemann, 1986).

In Fig. 2.5 $k(\nu)$ and $n(\nu) - 1$ are illustrated for a spectral line in the absence of a magnetic field. Note the antisymmetry of n.

Now consider the case of radiation passing through a medium with a magnetic field. Then a spectral line will split into its individual Zeeman components, i.e. $\kappa(\nu) \rightarrow \kappa_0 \sim \Phi_0$, $\kappa_{-1} \sim \Phi_{-1}$, $\kappa_{+1} \sim \Phi_{+1}$ (Φ_n, $n = 0, \pm 1$ are given in Eq. (2.17)). According to Eq. (2.34) this means that $n(\nu)$ will also split into "Zeeman components", which we shall call in analogy n_0, n_{-1}, n_{+1}. For a simple Zeeman triplet with **B** parallel to the line of sight the result is shown in Fig. 2.6. For a general splitting pattern we get equations similar to Eq. (2.17). The normalised magnetooptical profiles $\Psi_0 \sim n_0 - 1$, $\Psi_{+1} \sim n_{+1} - 1$, $\Psi_{-1} \sim n_{-1} - 1$ of the line, when viewing perpendicularly to the magnetic field, can then be written as

$$\begin{aligned} \Psi_0 &= 2 \sum_M S_0(M, \pi/2) F(a, v - v_0(M)), \\ \Psi_{+1} &= 2 \sum_M S_{+1}(M, \pi/2) F(a, v - v_{+1}(M)), \\ \Psi_{-1} &= 2 \sum_M S_{-1}(M, \pi/2) F(a, v - v_{-1}(M)). \end{aligned} \tag{2.38}$$

Note the factor of 2 difference with respect to Eq. (2.17). $S_n(M, \pi/2)$ ($n = 0, \pm 1$) values may be obtained from Table 2.1, with the normalisation, Eq. (2.15), taken into account, while $v_n(M)$ values can be calculated with Eq. (2.23). Ψ_n values for other angles of the magnetic field can be determined by applying the Seares formulæ. The exact relation between n_n and Ψ_n, as well as the manner in which the magnetooptical effects influence the Stokes profiles and enter into the radiative transfer equation will be discussed in the next section.

2.4. Transfer of Polarized Radiation in a Magnetic Field

2.4.1. The Equation of Transfer for the Stokes Vector

The equation of transfer for polarized light in the presence of a magnetic field and in a plane parallel atmosphere

was first derived by Unno (1956) in the notation using the Stokes parameters. It was extended to include magnetooptical effects by Rachkovsky (1962), and written to self-consistently account for the effects of departures from LTE for a two level atom by Domke (1971). In this form it reads:

$$\mu \frac{\mathrm{d}\mathbf{I}_\nu}{\mathrm{d}\tau_\nu} = (\mathbf{E} + \mathbf{\Omega})\mathbf{I}_\nu - \mathbf{S}_\nu, \tag{2.39}$$

where $\mathbf{I}_\nu$ is the Stokes vector at frequency ν, τ_ν is the continuum optical depth also at frequency ν, $\mathbf{E}$ is the unity matrix, $\mu = \cos\theta$, θ being the angle between the line of sight and the vertical direction in the atmosphere (heliocentric angle), $\mathbf{S}_\nu$ is the vector of the total (line and continuum) source function for all four Stokes parameters,

$$\mathbf{S}_\nu = \mathbf{\Omega 1} S_L + \mathbf{1} B_\nu \,. \tag{2.40}$$

Here $\mathbf{1} = (1,0,0,0)$, S_L is the source function of the line given in Eq. (2.48) for a two level atom, and B_ν is the Planck function. In Eq. (2.39) $\mathbf{\Omega}$ is the dimensionless absorption matrix at frequency ν, which, for a spectral line formed in the presence of a magnetic field, has the form

$$\mathbf{\Omega} = \begin{pmatrix} \eta_I & \eta_Q & \eta_U & \eta_V \\ \eta_Q & \eta_I & \rho_V & -\rho_U \\ \eta_U & -\rho_V & \eta_I & \rho_Q \\ \eta_V & \rho_U & -\rho_Q & \eta_I \end{pmatrix}. \tag{2.41}$$

For the case of electric dipole radiation, the elements of the matrix dealing with pure absorption are (e.g., Beckers, 1969b [who has a different sign for V]; Wittmann, 1974; Landi Degl'Innocenti, 1976),

$$\begin{aligned} \eta_I &= \frac{\eta_0}{2}\sin^2\gamma + \frac{\eta_{+1}+\eta_{-1}}{4}(1+\cos^2\gamma), \\ \eta_Q &= \left(\frac{\eta_0}{2} - \frac{\eta_{+1}+\eta_{-1}}{4}\right)\sin^2\gamma\,\cos 2\varphi, \\ \eta_U &= \left(\frac{\eta_0}{2} - \frac{\eta_{+1}+\eta_{-1}}{4}\right)\sin^2\gamma\,\sin 2\varphi, \\ \eta_V &= \frac{\eta_{-1}-\eta_{+1}}{2}\cos\gamma, \end{aligned} \tag{2.42}$$

with

$$\begin{aligned} \eta_{-1} &= \frac{\kappa_{-1}}{\kappa_c} = \frac{\kappa_L(\lambda_0)}{\kappa_c}\Phi_{-1}, \\ \eta_{+1} &= \frac{\kappa_{+1}}{\kappa_c} = \frac{\kappa_L(\lambda_0)}{\kappa_c}\Phi_{+1}, \\ \eta_0 &= \frac{\kappa_0}{\kappa_c} = \frac{\kappa_L(\lambda_0)}{\kappa_c}\Phi_0. \end{aligned} \tag{2.43}$$

Φ_{-1}, Φ_{+1}, and Φ_0 can be obtained from Eq. (2.17) for a static atmosphere, κ_c is the continuum opacity (which we do not discuss further here), and $\kappa_L(\lambda_0)$ is the line centre absorption coefficient in the absence of a magnetic field. The angles γ and ϕ are illustrated in Fig. 2.7. In LTE and for $a = 0$ (i.e. for a Gaussian line profile)

$$\kappa_L(\lambda_0) = \frac{\sqrt{\pi}e^2}{mc^2}\frac{g^* f N_l^* \lambda_0^2}{\Delta\lambda_D}\left(1 - \exp\left(-\frac{hc}{k\lambda_0 T}\right)\right). \tag{2.44}$$

Here g^* is the degeneracy of the lower level, f is the oscillator strength of the transition, and $g^* N_l^*$ is the number density of atoms in the lower level and can be determined using the Saha-Boltzmann equations (e.g. Mihalas, 1978). The expression in the brackets represents the correction for induced emission.

The terms containing ρ_Q, ρ_U, and ρ_V in $\mathbf{\Omega}$ are due to magnetooptical effects. The following expressions for them have been given, again in the case of an electric dipole, for example by Landi Degl'Innocenti (1976),

$$\begin{aligned} \rho_Q &= \left(\frac{\rho_0}{2} - \frac{\rho_{+1}+\rho_{-1}}{4}\right)\sin^2\gamma\,\cos 2\varphi, \\ \rho_U &= \left(\frac{\rho_0}{2} - \frac{\rho_{+1}+\rho_{-1}}{4}\right)\sin^2\gamma\,\sin 2\varphi, \\ \rho_V &= \frac{\rho_{-1}-\rho_{+1}}{2}\cos\gamma, \end{aligned} \tag{2.45}$$

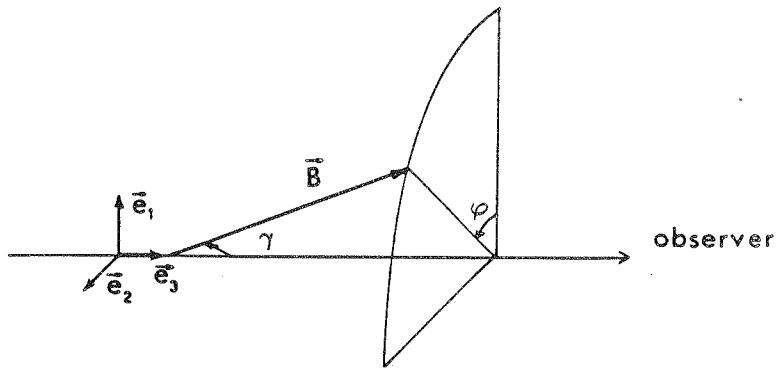

Fig. 2.7 Illustration of the angles γ and φ (from Landi Degl'Innocenti, 1976).

where ρ_0, ρ_{+1}, and ρ_{-1} are

$$\begin{aligned}
\rho_{-1} &= \frac{2\pi}{\kappa_c\lambda_0}(n_{-1}-1) = \frac{\kappa_L(\lambda_0)}{\kappa_c}\Psi_{-1},\\
\rho_{+1} &= \frac{2\pi}{\kappa_c\lambda_0}(n_{+1}-1) = \frac{\kappa_L(\lambda_0)}{\kappa_c}\Psi_{+1},\\
\rho_0 &= \frac{2\pi}{\kappa_c\lambda_0}(n_0-1) = \frac{\kappa_L(\lambda_0)}{\kappa_c}\Psi_0.
\end{aligned} \tag{2.46}$$

The Ψ_{-1}, Ψ_{+1}, and Ψ_0 are taken from Eq. (2.38) and $\kappa_L(\lambda_0)$ from Eq. (2.44). The analogues to Eqs. (2.42) and (2.45) for magnetic dipole and electric quadrupole radiation have been published by Beckers (1969b).

Let us now find a more explicit form of the source function. Using Eq. (2.41) we can rewrite Eq. (2.40) as (Domke and Staude, 1973; Stenholm and Stenflo, 1978)

$$\mathbf{S} = (B_\nu + \eta_I S_L,\ \eta_Q S_L,\ \eta_U S_L,\ \eta_V S_L). \tag{2.47}$$

For a two level atom

$$S_L = (e + \epsilon B_\nu)/(1+\epsilon), \tag{2.48}$$

where e is the scattering term,

$$e = \oint\int_0^\infty (\eta_I' I_{\nu'} + \eta_Q' Q_{\nu'} + \eta_U' U_{\nu'} + \eta_V' V_{\nu'})\,\mathrm{d}\nu'\,\frac{\mathrm{d}\omega'}{4\pi} \tag{2.49}$$

and ϵ is a measure for the importance of collisions,

$$\epsilon = \frac{C_{ij}}{A_{ij}}(1-\exp(-h\nu/kT)). \tag{2.50}$$

In Eqs. (2.49) and (2.50) ω is a solid angle, C_{ij} is the collision induced transition probability from level i to level j, and A_{ij} is the Einstein coefficient for spontaneous emission between those levels.

In LTE, which is the approximation in which the work presented in this thesis has been almost exclusively carried out, the scattering terms disappear (i.e., $\epsilon \to \infty$ and $e/\epsilon \to 0$), so that $S_L \to B_\nu$. The equation of transfer Eq. (2.39) then reduces to (Unno, 1956; Beckers, 1969a; Wittmann, 1974),

$$\mu\frac{\mathrm{d}\mathbf{I}_\nu}{\mathrm{d}\tau_\nu} = (\mathbf{E}+\mathbf{\Omega})(\mathbf{I}_\nu - \mathbf{1}B_\nu). \tag{2.51}$$

This set of four coupled equations was first derived by Unno (1956) and is often referred to as the Unno equations. A quantum mechanical derivation of the equation of transfer and of the absorption matrix has been presented by Landi Degl'Innocenti and Landi Degl'Innocenti (1972) (see also the Errata to this paper published by Landi Degl'Innocenti and Landi Degl'Innocenti, 1973, *Solar Phys.* **29**, 528), and a derivation from more general quantum electrodynamical principles has been carried out by Landi Degl'Innocenti (1983) (cf. the Errata to this paper published by Landi Degl'Innocenti, 1983, *Solar Phys.* **88**, 391), and Mathys (1983).

2.4.2. Symmetry Properties of the Stokes Parameters

The symmetries of the Stokes profiles with regard to their central wavelengths are best derived from the symmetry properties of the matrix $\mathbf{\Omega}$ defined by Eq. (2.41). The symmetry properties of the Stokes profiles have been discussed by Auer and Heasley (1978) in the absence of magnetooptical effects. Their discussion was extended by Landi Degl'Innocenti and Landi Degl'Innocenti (1981) to include magnetooptical effects. For a static atmosphere and an equal population of all the Zeeman sublevels (i.e., Eq. (2.43) is assumed to be valid) the symmetries exhibited by $\eta_0, \eta_{-1}, \eta_{+1}$ can be derived by noting that the Zeeman pattern is symmetric around the central wavelength of the unsplit line, i.e.,

$$\begin{aligned} g_{\pm 1}(-M) &= -g_{\mp 1}(M), \qquad \forall M, \\ g_0(-M) &= -g_0(M), \qquad \forall M, \end{aligned} \tag{2.52}$$

as follows directly from Eq. (2.24), and

$$\begin{aligned} S_{\pm 1}(-M) &= S_{\mp 1}(M), \qquad \forall M, \\ S_0(-M) &= S_0(M), \qquad \forall M, \end{aligned} \tag{2.53}$$

as has been shown by, e.g., Condon and Shortley (1964), or can be seen from Table 2.1. † Since the Voigt function is symmetric, cf. Eq. (2.22), it follows that

$$\begin{aligned} \eta_0(\nu_0 \pm \Delta\nu) &= \eta_0(\nu_0 \mp \Delta\nu), \\ \eta_{\pm 1}(\nu_0 \pm \Delta\nu) &= \eta_{\mp 1}(\nu_0 \mp \Delta\nu). \end{aligned} \tag{2.54}$$

The symmetries of $\rho_0, \rho_{-1}, \rho_{+1}$ follow from Eqs. (2.52), (2.53), and the antisymmetry of the Faraday-Voigt function (cf. Eq. (2.37)),

$$\begin{aligned} \rho_0(\nu_0 \pm \Delta\nu) &= -\rho_0(\nu_0 \mp \Delta\nu), \\ \rho_{\pm 1}(\nu_0 \pm \Delta\nu) &= -\rho_{\mp 1}(\nu_0 \mp \Delta\nu). \end{aligned} \tag{2.55}$$

In Eqs. (2.54) and (2.55) we have assumed that κ_c does not vary over the frequency intervall $2\Delta\nu$. Using Eqs. (2.54) and (2.55) the symmetry properties of $\eta_I, \eta_Q, \eta_U, \eta_V$, and ρ_Q, ρ_U, ρ_V can be determined via Eqs. (2.42) and (2.45). Thus under the transformation $\Delta\nu \rightarrow -\Delta\nu$ the opacity matrix $\mathbf{\Omega}(\nu_0 + \Delta\nu)$, given by Eq. (2.41), becomes

$$\mathbf{\Omega}(\nu_0 - \Delta\nu) = \begin{pmatrix} \eta_I & \eta_Q & \eta_U & -\eta_V \\ \eta_Q & \eta_I & \rho_V & \rho_U \\ \eta_U & -\rho_V & \eta_I & -\rho_Q \\ -\eta_V & -\rho_U & \rho_Q & \eta_I \end{pmatrix}, \tag{2.56}$$

where $\eta_I = \eta_I(\nu_0 + \Delta\nu)$, $\eta_Q = \eta_Q(\nu_0 + \Delta\nu)$ etc. We see that in the special case of a static atmosphere in LTE, a substitution of $\mathbf{\Omega}(\nu_0 + \Delta\nu)$ by $\mathbf{\Omega}(\nu_0 - \Delta\nu)$ in the transfer equation (2.51) results in the substitution of the solution vector $\mathbf{I}(\nu_0 + \Delta\nu) = (I, Q, U, V)$ of the former case by $\mathbf{I}(\nu_0 - \Delta\nu) = (I, Q, U, -V)$, i.e.

$$\begin{aligned} I(\nu_0 + \Delta\nu) &= I(\nu_0 - \Delta\nu), \\ Q(\nu_0 + \Delta\nu) &= Q(\nu_0 - \Delta\nu), \\ U(\nu_0 + \Delta\nu) &= U(\nu_0 - \Delta\nu), \\ V(\nu_0 + \Delta\nu) &= -V(\nu_0 - \Delta\nu). \end{aligned} \tag{2.57}$$

We have neglected the variation of B_ν over the frequency intervall $2\Delta\nu$. If one or both of the main assumptions (i.e., LTE and no mass motions) are relaxed, then Eq. (2.57) need no longer be valid. However, a velocity field independent of optical depth in a plane parallel atmosphere simply shifts $\nu_0 \rightarrow \nu_0 + \Delta\nu_v$ ($\Delta\nu_v$ is the velocity expressed in frequency units, with $\Delta\nu_v \neq \Delta\nu_v(\tau)$), leaving Eq. (2.57) unaffected if we take $\nu_0 + \Delta\nu_v$ as the new symmetry centre. Therefore, at least a horizontal, vertical, or temporal gradient in velocity, or departures from LTE are required to violate Eq. (2.57).

Since it plays a major role in chapter 8, let us next consider the integral symmetry relation for Stokes V

$$\int_{-\infty}^{\nu_0} V \, \mathrm{d}\nu = -\int_{\nu_0}^{\infty} V \, \mathrm{d}\nu, \tag{2.58}$$

† Care has to be taken when dealing with molecular lines since these need not show symmetric splitting patterns (cf. Harvey, 1973b and Illing, 1981).

or equivalently

$$\int_{-\infty}^{\infty} V \, \mathrm{d}\nu = 0. \tag{2.59}$$

For the sake of simplicity, we assume a vertical line of sight ($\mu = 1$). Horizontal velocity gradients in LTE are no longer sufficient to violate Eqs. (2.58) and (2.59) since the average profile of a horizontally inhomogeneous atmosphere can be written as

$$\langle V \rangle = \int_{y_1}^{y_2} \int_{x_1}^{x_2} V(x, y) \, \mathrm{d}x \, \mathrm{d}y. \tag{2.60}$$

In Eq. (2.60) $V(x, y)$ is always antisymmetric with respect to ν_0 for every value of (x, y) in the absence of velocity gradients along the line of sight. Integrating Eq. (2.60) over frequency, exchanging the order of the integrations, and making use of the fact that $V(x, y)$ satisfies Eq. (2.59) for every (x, y) we get

$$\int_{-\infty}^{\infty} \langle V \rangle \, \mathrm{d}\nu = 0. \tag{2.61}$$

Landi Degl'Innocenti and Landi Degl'Innocenti (1981) have also studied the symmetry properties of the Stokes profiles under the inversion of the direction of the magnetic field, and the additional assumption that $\eta_U = \rho_U = 0$. If $\mathbf{I} = (I, Q, U, V)$ is the emergent Stokes vector for a field $\mathbf{B}$ and $\mathbf{I} = (I', Q', U', V')$ the vector for $-\mathbf{B}$, then they find that

$$I' = I, \quad Q' = Q, \quad U' = -U, \quad V' = -V \tag{2.62}$$

2.4.3. Analytical Solutions of the Transfer Equations

A first attempt to analytically determine the effect of a magnetic field on a saturated line for the special case when the separation of the Zeeman components is so large that they can be treated as independent lines was made by Babcock (1949). However, the first analytical solution of Eq. (2.51) which is of consequence for the study of small magnetic fluxtubes was obtained by Unno (1956) under the assumptions of LTE, an absence of magnetooptical effects, a magnetic field strength independent of τ, a Milne-Eddington atmosphere (i.e., η_I, η_Q, η_U, and η_V independent of τ), and a Planck function linear in τ of the form

$$B_\nu = B_{\nu_0}(1 + \beta_0 \tau). \tag{2.63}$$

This equation defines the τ independent quantities B_{ν_0} and β_0. Of interest are the emergent values of the Stokes parameters normalised to the continuous background, defined as

$$\begin{aligned} r_I(\mu) &= \frac{I_c(\tau = 0, \mu) - I(\tau = 0, \mu)}{I_c(\tau = 0, \mu)}, \\ r_Q(\mu) &= \frac{Q_c(\tau = 0, \mu) - Q(\tau = 0, \mu)}{I_c(\tau = 0, \mu)}, \\ r_U(\mu) &= \frac{U_c(\tau = 0, \mu) - U(\tau = 0, \mu)}{I_c(\tau = 0, \mu)}, \\ r_V(\mu) &= \frac{V_c(\tau = 0, \mu) - V(\tau = 0, \mu)}{I_c(\tau = 0, \mu)}. \end{aligned} \tag{2.64}$$

In the above approximation the solution for the continuum is given by the Eddington-Barbier relation

$$\begin{aligned} I_c(\tau = 0, \mu) &= B_{\nu_0}(1 + \beta_0 \mu), \\ Q_c(\tau = 0, \mu) &= 0, \\ U_c(\tau = 0, \mu) &= 0, \\ V_c(\tau = 0, \mu) &= 0, \end{aligned} \tag{2.65}$$

and the solution for the emergent profiles reads

$$\begin{aligned} r_I(\mu) &= \frac{\beta_0\mu}{1+\beta_0\mu}\left(1-\frac{1+\eta_I}{(1+\eta_I)^2-\eta_Q^2-\eta_U^2-\eta_V^2}\right), \\ r_Q(\mu) &= \frac{\beta_0\mu}{1+\beta_0\mu}\frac{\eta_Q}{(1+\eta_I)^2-\eta_Q^2-\eta_U^2-\eta_V^2}, \\ r_U(\mu) &= \frac{\beta_0\mu}{1+\beta_0\mu}\frac{\eta_U}{(1+\eta_I)^2-\eta_Q^2-\eta_U^2-\eta_V^2}, \\ r_V(\mu) &= \frac{\beta_0\mu}{1+\beta_0\mu}\frac{\eta_V}{(1+\eta_I)^2-\eta_Q^2-\eta_U^2-\eta_V^2}. \end{aligned} \tag{2.66}$$

It should be noted that whereas Eqs. (2.42) and (2.43) were used to obtain these solutions, Eq. (2.44) had to be replaced so that $\kappa_L(\lambda_0) = \eta_L(\lambda_0)\kappa_c$, where $\eta_L(\lambda_0)$ is constant (independent of τ) and is a measure of the strength of the line. Rachkovsky (1962, 1967) found a solution under the same assumptions as Unno (1956), but including anomalous dispersion (see also Stenflo, 1971, Arena and Landi Degl'Innocenti, 1982).

$$\begin{aligned} r_I(\mu) &= \frac{\beta_0\mu}{1+\beta_0\mu}\left(1-\frac{(1+\eta_I)((1+\eta_I)^2+\rho_Q^2+\rho_U^2+\rho_V^2)}{D}\right), \\ r_Q(\mu) &= \frac{\beta_0\mu}{1+\beta_0\mu}\frac{(1+\eta_I)^2\eta_Q+(1+\eta_I)(\eta_V\rho_U-\eta_U\rho_V)+\rho_Q(\eta_Q\rho_Q+\eta_U\rho_U+\eta_V\rho_V)}{D}, \\ r_U(\mu) &= \frac{\beta_0\mu}{1+\beta_0\mu}\frac{(1+\eta_I)^2\eta_U+(1+\eta_I)(\eta_Q\rho_V-\eta_V\rho_Q)+\rho_U(\eta_Q\rho_Q+\eta_U\rho_U+\eta_V\rho_V)}{D}, \\ r_V(\mu) &= \frac{\beta_0\mu}{1+\beta_0\mu}\frac{(1+\eta_I)^2\eta_V+\rho_V(\eta_Q\rho_Q+\eta_U\rho_U+\eta_V\rho_V)}{D}, \end{aligned} \tag{2.67}$$

where the denominator reads

$$D=(1+\eta_I)^2((1+\eta_I)^2-\eta_Q^2-\eta_U^2-\eta_V^2+\rho_Q^2+\rho_U^2+\rho_V^2)-(\eta_Q\rho_Q+\eta_U\rho_U+\eta_V\rho_V)^2. \tag{2.68}$$

Eq. (2.67) shows that the unpolarized Stokes I profile is also affected by anomalous dispersion, although ρ_Q, ρ_U, and ρ_V do not appear in its equation of transfer directly. These terms are introduced through the coupling of Stokes I with the other Stokes parameters. For $\gamma = 0, \pi/2, \pi$, or $3\pi/2$ the non-zero magnetooptical elements in Eqs. (2.67) and (2.68) divide out. Therefore the magnetooptical effects disappear when looking parallel or perpendicular to the magnetic field. This result can also be derived directly from the absorption matrix and is valid in the general case as well.

Arena and Landi Degl'Innocenti (1982) have produced an atlas of r_I, r_Q, r_U, and r_V profiles determined with Eq. (2.67) for different values of B, γ, φ, and $\eta_L(\lambda_0)$. A variety of other analytical solutions or procedures for deriving such solutions have been proposed by a number of authors. Examples are listed below. Stepanov (1958a) derived and solved the equation of transfer for a Zeeman triplet under assumptions similar to Unno. His equations are based on a treatment of arbitrarily polarized light as a mixture of two orthogonal beams of elliptically polarized light. Stepanov (1958b) included coherent scattering in his equations and in their solution. However, Rachkovsky (1961) has shown, that the Unno formulation is more general than Stepanov's. Michard (1961) has solved the Unno equations (2.51) for a Schuster-Schwarzschild model atmosphere. Mattig (1966) found an analytical solution valid for a general model atmosphere (i.e. $\eta_L(\lambda_0)$ may be a function of τ), but limited to a Zeeman triplet in a homogeneous magnetic field, without magnetooptical effects and with a depth independent Voigt function. Kjeldseth Moe (1968) independently also discovered this solution and extended it to include coherent scattering. Staude (1969) described an iterative formalism for obtaining a solution for a general magnetic field structure and atmosphere. However, its application usually requires a computer. Göhring (1971) extended the solution of Mattig (1966) to iteratively include magnetooptical effects. He also reviewed the assumptions made in deriving previous analytical solutions. A detailed review of some of the solutions attempted before 1970 is also given by Stenflo (1971). Landi Degl'Innocenti and Landi Degl'Innocenti (1973) have determined an analytical, perturbative solution of Eq. (2.51), valid for weak magnetic fields. Its value lies mainly in the fact that it allows some qualitative conclusions to be drawn regarding the Stokes parameters. Thus

it shows that the neglect of magnetooptical effects in Q and U results in an error of the order of $\Delta\lambda_H/\Delta\lambda_D$ where $\Delta\lambda_H = 4.67 \times 10^{-13} g_{\rm eff} \lambda^2 B$, while the error in Stokes V is of the order $(\Delta\lambda_H/\Delta\lambda_D)^3$ and in Stokes I is of the order of $(\Delta\lambda_H/\Delta\lambda_D)^4$. Their analysis is valid for the case $\Delta\lambda_H/\Delta\lambda_D < 1$. Since outside sunspots this condition is fulfilled by practically all spectral lines in the visible spectral region, this means that except for Q and U magnetooptical effects are usually quite small. Finally, Landi Degl'Innocenti and Landi Degl'Innocenti (1985) have obtained an analytical solution to Eq. (2.39) for the case that Ω is constant along the line of sight (i.e. B and the Doppler width are constant). Their method of solution, which is based on Van Ballegooijen's approach (Sect. 2.4.4), is also valid for some NLTE source functions.

2.4.4. Numerical Solutions

The analytical solutions presented in the last section have been used for a number of studies of solar magnetic fields. However, the latter often do not fulfill the rather restrictive assumptions made in order to derive such solutions. Specifically, the magnetic field strength in fluxtubes is strongly dependent on depth in the atmosphere (and therefore on τ). Furthermore, the Milne-Eddington approximation is not applicable for many spectral lines. In addition, most lines are not Zeeman triplets, nor are their Voigt functions depth independent. Therefore, in general, numerical techniques are required to solve Eqs. (2.39) or (2.51). A number of such techniques have been proposed and we shall review some of them briefly in this section.

First numerical calculations were carried out by Hubenet (1954) who obtained the Stokes I profile via the formal solution for magnetic fields oriented parallel and perpendicular to the line of sight. The first code for the *general* numerical solution of Eq. (2.51) has been described by Beckers (1969a, b). It allows Stokes profiles to be calculated in LTE and including anomalous dispersion for a general model atmosphere. In particular no restrictions are placed on the variation of the magnetic field strength and direction with depth, and on the velocity structure, while the η_I, η_Q, η_U, and η_V are calculated as outlined in Sect. 2.4.1 as a function of depth. Neither are any restrictions placed on the Zeeman splitting pattern of the line to be calculated, as long as it is formed in LS-coupling. The numerical method chosen to solve the four coupled equations (2.51) is the classical fourth order Runge-Kutta technique (e.g. Abramowitz and Stegun, 1970). For the lower boundary condition an Unno type solution is chosen, similar to Eq. (2.66), except that the expressions have to be changed slightly to give I, Q, U, and V instead of r_I, r_Q, r_U, and r_V. Wittmann (1973a, b, 1974) and Landi Degl'Innocenti (1976) have given comprehensive and clear descriptions of similar codes, which also solve the Unno equations using Runge-Kutta techniques. Although the overall specifications of the three codes are very similar, they differ in a number of details, some of which are mentioned below.

The codes of Beckers and Landi Degl'Innocenti allow the contributions to the spectrum of a number of blended lines to be taken into account. The code of Wittmann was later extended to include this capability, and has actually been used to synthesise a portion of a polarized sunspot spectrum (Wittmann, 1977). The code of Landi Degl'Innocenti (1976) can take into account the effects of NLTE on a line if the departure coefficients of its upper and lower levels $\beta_u = N_u/N_u^*$ and $\beta_l = N_l/N_l^*$ are known. N_u and N_l are the NLTE populations of the upper and lower level respectively, while N_u^* and N_l^* are their LTE counterparts. The LTE line source function $S_L = B_\nu$ is then replaced by

$$S_L = \frac{2hc^2}{\lambda^5} \frac{1}{\left(\frac{\beta_l}{\beta_u} \exp\left(\frac{hc}{kT\lambda}\right) - 1\right)} \tag{2.69}$$

and the expression for the line centre absorption coefficient given in Eq. (2.44) is replaced by

$$\kappa_L(\lambda_0) = \frac{\sqrt{\pi} e^2}{mc^2} \frac{g^* f N_l^* \beta_l \lambda_0^2}{\Delta\lambda_D} \left(1 - \frac{\beta_u}{\beta_l} \exp\left(-\frac{hc}{k\lambda_0 T}\right)\right). \tag{2.70}$$

With this scheme, an NLTE solution of the Stokes profiles can be obtained if prior to running the Stokes line transfer code (in the B-field) the level populations (without the B-field) are calculated with some standard NLTE code. The process is not completely self-consistent, since Eq. (2.49) has been replaced by an integral containing I alone, but the deviation is in general very small as has been shown by Rees (1969) and Stenholm and Stenflo (1978). In addition, the code of Landi Degl'Innocenti (1976) also uses the analytical solution of Rachkovsky (1967), i.e. Eqs. (2.67, 2.68), for the lower boundary conditions.

The code of Stenholm and Stenflo (1978) calculates the Stokes profiles in NLTE assuming a two-level atom with complete redistribution among the Zeeman sublevels (no coherence effects) and complete redistribution in

frequency. Their NLTE formalism is basically a reformulation of the theory of Domke and Staude (1973a) which has been briefly presented in Sect. 2.4.1. This code is an extension of the NLTE code for Stokes I only of Stenholm and Stenflo (1977) and handles multidimensional effects explicitely by taking into account rays at different angles. The core saturation method of Rybicki (1972), extended to the multidimensional case by Stenholm (1977) is used to 'precondition' the transfer equation in order to allow it to be solved using a simple Runge-Kutta technique.

Van Ballegooijen (1985a) presents a novel approach to solving the radiative transfer equations (2.39) or (2.51). The advantage of his method of solution is that in addition to the emergent Stokes profiles, it also delivers their contribution functions. The (minor) disadvantage is that the system of differential equations to be solved is larger. In particular it would require the solution of 16 coupled differential equations if Eq. (2.51) were solved directly. By using Jones calculus, i.e. by writing the polarization in the form of a (2×2 complex) density matrix

$$\mathbf{D} = \frac{1}{2}\begin{pmatrix} I+Q & U+iV \\ U-iV & I-Q \end{pmatrix}, \tag{2.71}$$

Van Ballegooijen was able to reduce the problem to the solution of eight equations. It is of interest to note that the various Stokes parameters correspond to the four Pauli matrices which describe the spin of Spin 1/2 particles. I corresponds to the unity matrix, Q to σ_z, U to σ_x, and V to σ_y (cf. Robson, 1974, for a more detailed discussion). In this notation the radiative transfer equation for $\mathbf{D}$ reads

$$\frac{\mathrm{d}\mathbf{D}}{\mathrm{d}\tau} = \mathbf{A}\mathbf{D} + \mathbf{D}\mathbf{A}^{\dagger} - \mathbf{F}, \tag{2.72}$$

where τ is the continuum optical depth, $\mathbf{A}^{\dagger}$ is the transpose and complex conjugate of

$$\mathbf{A} = \frac{1}{2}\begin{pmatrix} 1+\eta_I+\alpha_Q & \alpha_U+i\alpha_V \\ \alpha_U-i\alpha_V & 1+\eta_I-\alpha_Q \end{pmatrix}, \tag{2.73}$$

which is the analogue to $\mathbf{E}+\mathbf{\Omega}$ in Eqs. (2.39) and (2.51), and

$$\mathbf{F} = \frac{1}{2}\begin{pmatrix} B_\nu+(\eta_I+\eta_Q)S_L & (\eta_U+i\eta_V)S_L \\ (\eta_U-i\eta_V)S_L & B_\nu+(\eta_I-\eta_Q)S_L \end{pmatrix} \tag{2.74}$$

is the analogue to $\mathbf{S}$ in Eq. (2.39), where S_L can be of the form given by Eq. (2.48). In Eq. (2.73)

$$\begin{aligned} \alpha_Q &= \eta_Q - i\rho_Q, \\ \alpha_U &= \eta_U - i\rho_U, \\ \alpha_V &= \eta_V - i\rho_V. \end{aligned} \tag{2.75}$$

To obtain the emergent intensity, $\mathbf{D}(0)$, a matrix $\mathbf{T}$ is introduced, which is defined by its differential equation

$$\frac{\mathrm{d}\mathbf{T}}{\mathrm{d}\tau} = \mathbf{A}\mathbf{T}, \qquad \text{with} \quad \mathbf{T}(\tau=0) = \mathbf{E}. \tag{2.76}$$

The problem then reduces to solving Eq. (2.76), since, once $T(\tau)$ is known, $\mathbf{D}(0)$ can be found by a simple integration

$$\mathbf{D}(0) = \int_0^\infty (\mathbf{T})^{-1}\mathbf{F}(\mathbf{T}^{\dagger})^{-1}\,\mathrm{d}\tau. \tag{2.77}$$

The contribution functions to the Stokes profiles can be extracted from the integrand in Eq. (2.77). Van Ballegooijen's code therefore calculates the emergent Stokes parameters and their contribution functions. It includes isotropic scattering with complete redistribution.

It should be noted that all these codes assume the different Zeeman sublevels to be equally populated (this assumption is already implicitely present in Eqs. (2.43) and (2.44)).

2.4.5. Some Additional Information on the Code Used in This Thesis

For the radiative transfer calculations presented in this thesis, a slightly modified and extended version of the code described by Beckers (1969a, b) has been used and shall be discussed in somewhat greater detail.

2.4.5.1. Input and Output

In its present form the code (named STOKES) requires as input a model atmosphere consisting of an optical depth scale with the following quantities defined at each optical depth point, τ: temperature T, electron pressure P_e, gas pressure P_g, absolute magnetic field strength B, angle between the magnetic field and the line of sight γ, azimuthal angle of the magnetic field φ, microturbulence velocity $\xi_{\rm mic}$ and a "global" or macroscopic velocity v (not to be confused with the macroturbulence $\xi_{\rm mac}$). A second code (MODCONVER) has been written, which can interpolate between the optical depth points of a given model atmosphere. MODCONVER can also calculate some of the missing variables, e.g. P_e from T and P_g, or the optical depth τ from κ and a height scale Z. P_e and κ are determined using the code described by Gustafsson (1973). Further details on the calculation of the (fluxtube) model atmospheres are given in chapter 4. A further input to STOKES is $\mu = \cos\theta$, θ being the angle between the line of sight and the normal to the atmosphere.

STOKES also requires the input of some atomic parameters: J_u, L_u, S_u, J_l, L_l, and S_l for the calculation of g_u and g_l using Eq. (2.11). It should be noted that except for the calculation of g_u and g_l, the quantities L_u, S_u, L_l, and S_l are not required anywhere in the code, so that lines not formed in LS-coupling can also be calculated if their g_u and g_l values are known, for example from laboratory measurements. Also input are the central wavelength of the line λ_0, its weighted oscillator strength g^*f, the atomic mass A, the ionisation stage (only neutral and singly ionized atoms are allowed), and an empirical factor to the damping constant δ_Γ (see below for further details). The partition functions should be input in the form of the coefficients of a power series in $\ln T$. They can be taken from the comprehensive list of Irwin (1981).

A number of other parameters are also input, e.g., whether magnetooptical effects should be included or not (switching them off saves CPU time and does not affect the result for $\gamma = 0°$ and $90°$), the number of lines in the spectrum (required for the calculation of blended lines), the number of separate spectra, the wavelength range, and the number of wavelength points, etc.

The output consists of the emergent Stokes profiles at equidistant wavelength points. To save computer storage space it is possible to write only a part of the Stokes parameters (e.g., I and V only). The output of STOKES is read by the code READSTO, which normalises the output to the continuum level. It can also mirror the Stokes profiles, using the symmetry properties (2.57), so that only half of each Stokes profile has to be calculated, except when models with velocity gradients are used. Additional codes have been written which create MIDAS images from the output (RADPLT), convolute the resulting Stokes profiles with a Gaussian or Voigt profile thus simulating the influence of macroturbulence (FTSCONVOL), and determine line parameters of Stokes I and V (IVPAR, see chapter 4 for more details).

2.4.5.2. Calculation of the Voigt and Faraday-Voigt Functions

Radiative transfer calculations often require a large amount of computation time, in particular if the Stokes parameters of many (anomalously split) lines are to be calculated. An efficient code is therefore not a mere luxury. By restructuring a part of the original code it was possible to speed it up by approximately a factor of three without loss of accuracy. Since a large portion of the time is required to calculate the Voigt and Faraday-Voigt functions (one should keep in mind that they must be determined individually for at least half of the Zeeman components at each depth and frequency point), it is particularly important to use a fast and reliable method for their calculation. The code uses the routine described by Hui et al. (1978), which calculates these two functions as the real and imaginary parts of the function $W(z)$ given in Eq. (2.36). $W(z)$ is closely related to the complex error function

$$w(z) = e^{-z^2}\left(1 + \frac{2i}{\sqrt{\pi}}\int_0^z e^{t^2}\,{\rm d}t\right), \tag{2.78}$$

via

$$w(z) = \begin{cases} W(z) & \Im z > 0, \\ W(z) + 2e^{-z^2} & \Im z < 0, \end{cases} \tag{2.79}$$

where $z = v + ia$. The routine approximates $w(z)$ for $a = \Im z \neq 0$ by a rational function. The version incorporated in the code has been extended by Wittmann (1986) to include the case of $a = 0$, i.e. the Gauss function and Dawson's integral (or Dawson's function, Dawson, 1898)

$$H(0, v) = e^{-v^2}, \tag{2.80}$$

$$F(0,v) = \int_0^\infty e^{-t^2} \sin 2vt \, dt = e^{-v^2} \int_0^v e^{t^2} \, dt. \tag{2.81}$$

Although this routine is not much faster than Becker's original scheme of interpolating in a table of values for $H(a,v)$ and $F(a,v)$, it is more general and accurate, the largest errors being of the order of 1% near the 'knee' between the Doppler core and the damping wings, for very small $a \neq 0$.

2.4.5.3. The Damping Constant

In Eq. (2.21) the damping constant Γ has remained unspecified. On the Sun the most important mechanism giving rise to a Lorentz or damping profile is the Van der Waals damping. Accordingly the code allows for Van der Waals broadening due to collisions of the radiating (or absorbing) atom with neutral hydrogen and helium as well as for radiative damping (see e.g. Lang, 1974 and Mihalas, 1978 for an overview of the various damping processes). The total damping constant can be written as

$$\Gamma = \Gamma_{\rm rad} + \Gamma_6 \,. \tag{2.82}$$

The radiative (or natural) damping constant $\Gamma_{\rm rad}$, resulting from the finite life times of the upper and lower states of the atom, can be expressed as

$$\Gamma_{\rm rad} = \frac{6.669 \times 10^{15}}{4} \frac{g^* f}{\lambda^2}, \tag{2.83}$$

while for the Van der Waal's damping constant Γ_6, the contributions from both hydrogen and helium can be included as follows (e.g. Steffen, 1985)

$$\Gamma_6 = \Gamma_{\rm H} + \Gamma_{\rm He} = \Gamma_{\rm H} \left(1 + 0.4133 \frac{\epsilon({\rm He})}{\epsilon({\rm H})} \right), \tag{2.84}$$

where ϵ(He) and ϵ(H) are the abundances by number of helium and hydrogen respectively, and

$$\Gamma_{\rm H} = 8.08 C_6^{2/5} \bar{v}^{3/5} N_{\rm H}. \tag{2.85}$$

Here $\bar{v}$ is the mean relative velocity of the radiating atom and the perturber, $N_{\rm H}$ is the hydrogen number density, and C_6 is the Van der Waals broadening constant of the line. $\Gamma_{\rm H}$ can also be written in terms of pressure and temperature,

$$\Gamma_{\rm H} = 0.909 \times 10^{8.6735\Theta^{0.7}} P_g C_6^{2/5} \delta_\Gamma, \tag{2.86}$$

where $\Theta = 5040/T$ (T being the temperature), P_g is the gas pressure, and δ_Γ is an empirical factor which can be varied to make the calculated value of $\Gamma_{\rm H}$ fit observed values (cf. Sect. 4.5.3 for more on δ_Γ). For the calculation of C_6 the approximation of Unsöld (1955) is used:

$$C_6 = 4.105 \times 10^{-33} \left| \frac{\overline{r_u^2}}{a_0} - \frac{\overline{r_l^2}}{a_0} \right|. \tag{2.87}$$

$\overline{r_m^2}$, the mean square orbital radius of the valence electron in state m, expressed in units of the Bohr radius a_0, can be written in the Coulomb approximation

$$\frac{\overline{r_m^2}}{a_0} = \frac{{n_m^*}^2}{2z^2} \left(5{n_m^*}^2 + 1 - 3\ell(\ell+1) \right). \tag{2.88}$$

In Eq. (2.88) ℓ is the azimuthal quantum number of the state involved, z is the effective nuclear charge, and n_m^* is the effective principal quantum number of the valence electron in state m.

$$n_m^* = z \sqrt{\frac{\chi_{\rm H}}{\chi_m - \chi_i}} \tag{2.89}$$

where $\chi_m - \chi_i$ is the energy required to ionise the m-th level of the radiating atom, and $\chi_{\rm H}$ is the ionisation potential from the ground state of hydrogen; $\chi_{\rm H} = 13.6$ eV. If the last term $3\ell(\ell+1)$ in Eq. (2.88) is neglected,

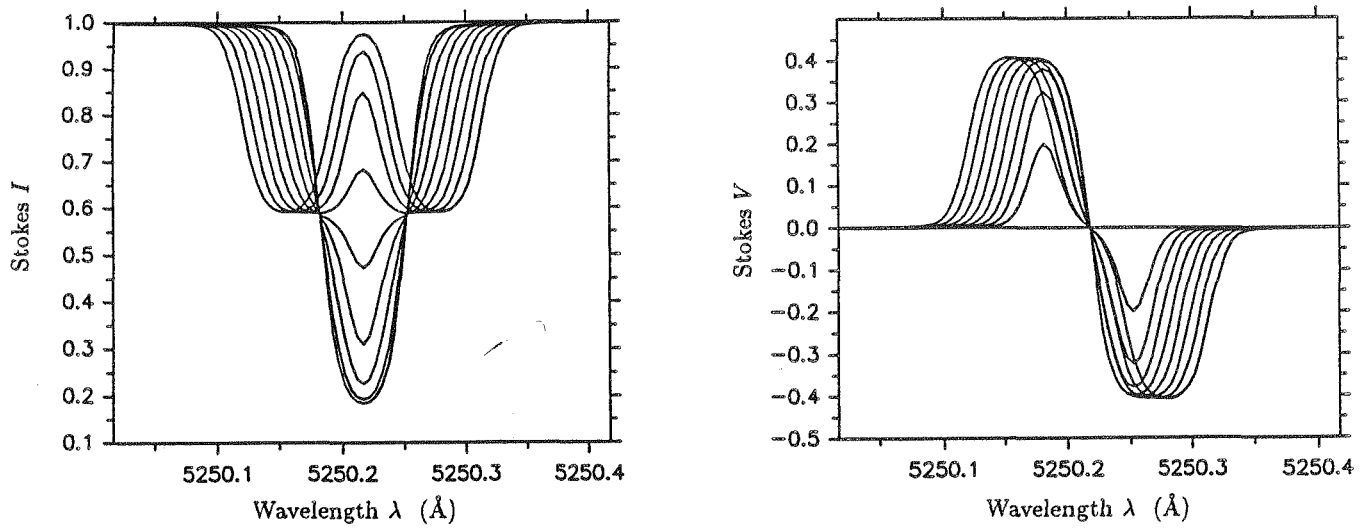

Fig. 2.8 Stokes I and V of the Fe I 5250.2 Å line, calculated using the HSRA at $\mu = 1$ for $\gamma = 0°$, and $B = 0$, 200, 400, 600, 800, 1000, 1200, 1400, and 1600 G. Note the rapid saturation of Stokes V as the field strength increases.

then Eq. (2.87) reduces to a particularly simple form as was pointed out by Unsöld (1955). Steffen (1985) has argued that the above procedure, which strictly speaking is limited to neutral atoms can also be applied to the broadening of ionic lines due to collisions with neutral hydrogen.

2.4.5.4. Numerical Stability and Examples of Profiles

Landi Degl'Innocenti (1976) has discussed the requirements to be fulfilled by the integration height step h and the optical depth of the lower boundary in order to obtain stable solutions. However, when the line of sight crosses a fluxtube boundary (as is the case for 2-D models), large changes in the model atmosphere (e.g., in T, P_g, B, $\xi_{\rm mic}$) can occur over a very small τ interval. If such changes are too large and too rapid then the numerical solution can become unstable inspite of these criteria. Therefore a routine has been introduced into STOKES which checks the atmosphere for large gradients and jumps in the atmospheric variables. If any vital quantity (e.g., temperature, magnetic field strength, angle of the field, microturbulence, macroscopic velocity) changes by too large an amount, then this routine decreases the integration height step by a factor proportional to the change. This simple procedure has a surprisingly stabilising influence on the solution and smooth profiles are obtained for jumps of more than 1000 G in B over $\Delta\tau \approx 0.1$.

Examples of Stokes profiles (Fe I 5250.2 Å) calculated with STOKES are shown in Figs. 2.8 and 2.9 for two values of γ ($\gamma = 0°$ for Fig. 2.8 and 60° for Fig. 2.9) and different values of the field strength ($B = 0$, 200, 400, 600, 800, 1000, 1200, 1400, 1600 G). In both figures $\mu = 1$ and the model atmosphere is the HSRA (Gingerich et al., 1971). For $\gamma = 0°$ only I and V are plotted since $Q = U = 0$.

2.5. Measurement of Polarized Light

2.5.1. Principle of Measurement

Let us consider the problem of how to determine the Stokes parameters of an arbitrariy beam of light. In principle, the solution can be reduced to a simple set of intensity measurements. The basic instrumental requirements are a linear polarizer and a quarter-wave plate (which converts linear polarization into circular and circular into linear). As pointed out in Sect. 2.1, any optical device acting on the Stokes parameters is equivalent to a linear transformation. In the representation of polarized light as a 4-vector, an optical device can therefore be represented by a 4×4 Mueller matrix $\mathbf{M}$, acting on an input beam with Stokes vector $\mathbf{I}$ as

$$\mathbf{I}' = \mathbf{MI}. \tag{2.90}$$

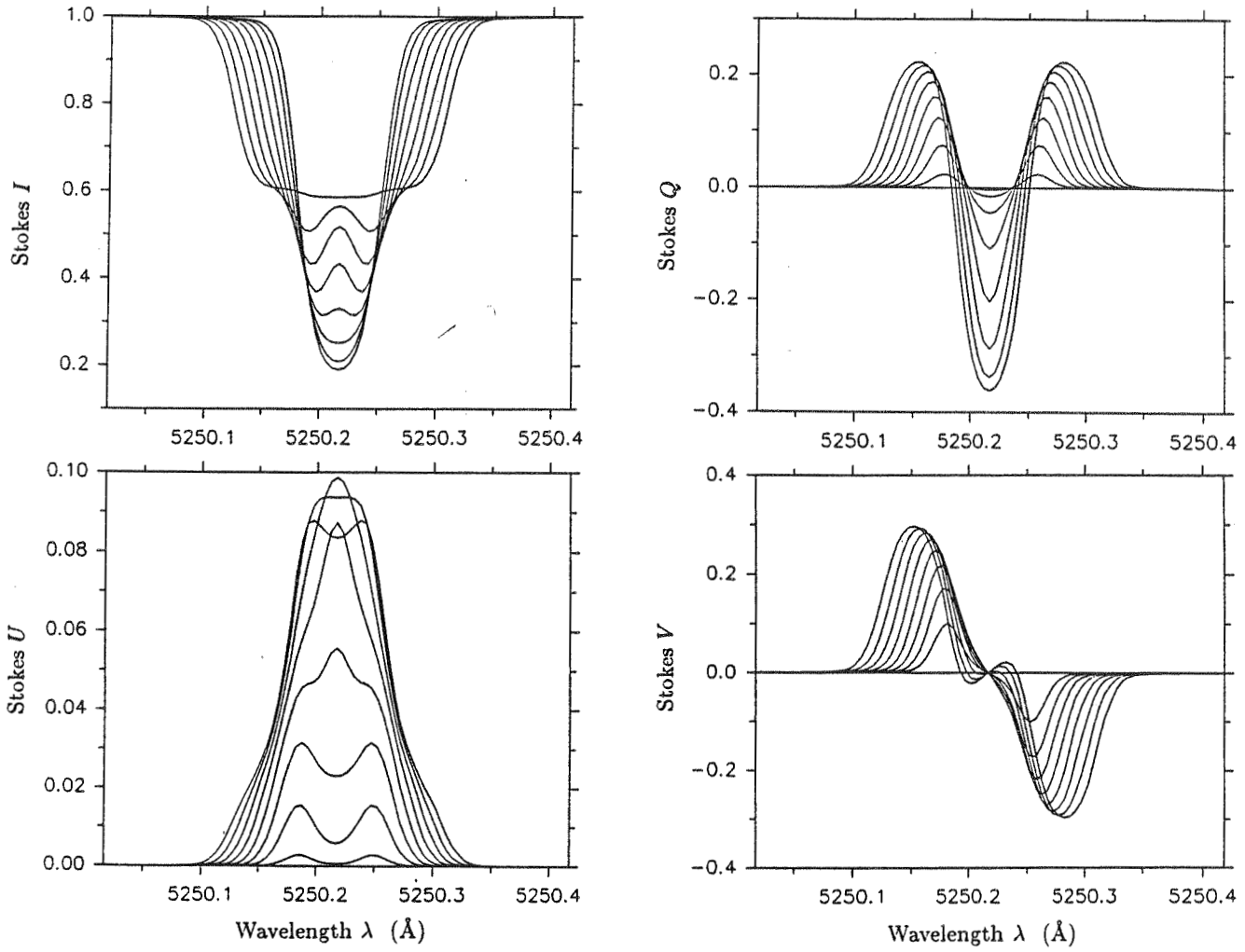

Fig. 2.9 Stokes I, V, Q, and U for the same parameters as in Fig. 2.8, except that now $\gamma = 60°$, $\varphi = 0°$. Note the magnetooptical inversion in Stokes V, and the considerably slower saturation of this profile as compared to Fig. 2.8. $U \neq 0$ is due exclusively to magnetooptical effects.

If more than one optical element intervenes in the beam, then the Mueller matrix of the total device can be written as the product of the matrices of the individual components:

$$\mathbf{M}_{\text{tot}} = \mathbf{M}_n \cdots \mathbf{M}_2 \mathbf{M}_1. \tag{2.91}$$

The light passes the individual elements in the order of the indices. Let us first write the representations of the Mueller matrices of a retarder $\mathbf{R}$ (a generalisation of a quarter wave plate) and an ideal linear polarizer $\mathbf{L}$, both with position angle $\alpha = 0$ (α is the angle at which the linear polarizer lets light pass, respectively the angle of ordinary ray polarization at the retarder) (e.g. Stenflo, 1984b)

$$\mathbf{R} = \begin{pmatrix} 1 & 0 & 0 & 0 \\ 0 & 1 & 0 & 0 \\ 0 & 0 & \cos\delta & \sin\delta \\ 0 & 0 & -\sin\delta & \cos\delta \end{pmatrix}, \tag{2.92}$$

with δ being the retardation ($\delta = \pi/2$ corresponds to a quarter wave plate), and

$$\mathbf{L} = \frac{1}{2} \begin{pmatrix} 1 & 1 & 0 & 0 \\ 1 & 1 & 0 & 0 \\ 0 & 0 & 0 & 0 \\ 0 & 0 & 0 & 0 \end{pmatrix}. \tag{2.93}$$

With the help of the transformation matrix $\mathbf{T}$, which rotates the position angle by α (compare with Eq. (2.8))

$$\mathbf{T}(\alpha) = \begin{pmatrix} 1 & 0 & 0 & 0 \\ 0 & \cos 2\alpha & \sin 2\alpha & 0 \\ 0 & -\sin 2\alpha & \cos 2\alpha & 0 \\ 0 & 0 & 0 & 1 \end{pmatrix}, \tag{2.94}$$

we can obtain Mueller matrices for an arbitrary angle α via

$$\mathbf{M}(\alpha) = \mathbf{T}(-\alpha)\mathbf{M}(0)\mathbf{T}(\alpha). \tag{2.95}$$

If we introduce

$$\begin{aligned} x &= \cos 2\alpha, & y &= \sin 2\alpha, \\ a &= \cos \delta, & b &= \sin \delta, \end{aligned} \tag{2.96}$$

then we can write for arbitrary α and δ

$$\mathbf{R}(\alpha, \delta) = \begin{pmatrix} 1 & 0 & 0 & 0 \\ 0 & x^2 + y^2 a & xy(1-a) & -yb \\ 0 & xy(1-a) & y^2 + x^2 a & xb \\ 0 & yb & -xb & a \end{pmatrix} \tag{2.97}$$

and

$$\mathbf{L}(\alpha) = \frac{1}{2} \begin{pmatrix} 1 & x & y & 0 \\ x & x^2 & xy & 0 \\ y & xy & y^2 & 0 \\ 0 & 0 & 0 & 0 \end{pmatrix}. \tag{2.98}$$

The measurement of the four Stokes parameters is carried out in six steps. First, only a linear analyser with $\alpha = 0$ is applied to the light beam to be analysed, which has the (unknown) polarization state $\mathbf{I}^T = (I_0, Q_0, U_0, V_0)$.

$$\begin{pmatrix} I_1 \\ Q_1 \\ U_1 \\ V_1 \end{pmatrix} = \frac{1}{2} \begin{pmatrix} 1 & 1 & 0 & 0 \\ 1 & 1 & 0 & 0 \\ 0 & 0 & 0 & 0 \\ 0 & 0 & 0 & 0 \end{pmatrix} \begin{pmatrix} I_0 \\ Q_0 \\ U_0 \\ V_0 \end{pmatrix} = \frac{1}{2} \begin{pmatrix} I_0 + Q_0 \\ I_0 + Q_0 \\ 0 \\ 0 \end{pmatrix}. \tag{2.99}$$

The transmitted intensity is

$$I_1 = \frac{1}{2}(I_0 + Q_0). \tag{2.100}$$

In the second step, the analyser is turned by 90° , i.e. $\alpha = \pi/2 \rightarrow x = -1,\ y = 0$ in Eq. (2.98). The intensity of the resulting beam is now

$$I_2 = \frac{1}{2}(I_0 - Q_0). \tag{2.101}$$

From Eqs. (2.100) and (2.101) it is straightforward to obtain I_0 and Q_0:

$$I_0 = I_1 + I_2 \tag{2.102}$$

and

$$Q_0 = I_1 - I_2. \tag{2.103}$$

Similarly, U_0 can be determined in two steps by placing linear analysers with $\alpha = \pi/4$ $(x = 0, y = 1)$ and $\alpha = 3\pi/4$ $(x = 0, y = -1)$ in the beam. The resulting intensities are

$$I_{3,4} = \frac{1}{2}(I_0 \pm U_0), \tag{2.104}$$

so that

$$U_0 = I_3 - I_4. \tag{2.105}$$

Finally V_0 is determined by inserting a quarter-wave plate ($\delta = \pi/2$) with orientation $\beta = \pm\pi/4$ between the light beam and the linear analyser with $\alpha = 0$. Note that not the absolute values of α and β are important, but rather $\beta - \alpha$. Then we have

$$\begin{pmatrix} I_{5,6} \\ Q_{5,6} \\ U_{5,6} \\ V_{5,6} \end{pmatrix} = \frac{1}{2} \begin{pmatrix} 1 & 1 & 0 & 0 \\ 1 & 1 & 0 & 0 \\ 0 & 0 & 0 & 0 \\ 0 & 0 & 0 & 0 \end{pmatrix} \begin{pmatrix} 1 & 0 & 0 & 0 \\ 0 & 0 & 0 & \pm 1 \\ 0 & 0 & 1 & 0 \\ 0 & \pm 1 & 0 & 0 \end{pmatrix} \begin{pmatrix} I_0 \\ Q_0 \\ U_0 \\ V_0 \end{pmatrix} = \frac{1}{2} \begin{pmatrix} I_0 \mp V_0 \\ I_0 \mp V_0 \\ 0 \\ 0 \end{pmatrix} \tag{2.106}$$

and we obtain V_0 from

$$V_0 = I_6 - I_5. \tag{2.107}$$

Thus all four Stokes parameters have been measured. Of course, this procedure can be inverted and the Mueller matrix of any optical setup can be determined with beams of known polarization

Sometimes the opposite approach to the one presented in this chapter is taken and the Stokes profiles are *defined* by the action of a set of polarization filters on them. This is the so-called operational definition. The mathematical description of Eq. (2.2) can then be derived from it.

2.5.2. Solar Magnetic Field Polarization Measurement Techniques

The measurement of solar magnetic fields basically requires three additional ingredients: a modulator, a wavelength selection device (spectrometer), and a detector. Stenflo (1978) has given a detailed review of solar polarization measurement instrumentation, and we shall therefore be very brief here, referring to the above paper for additional details and for references.

Since different optical elements are required to measure any Stokes parameter except I, either different optical channels must be used (each with its own analyser), or the analysers have to be sequentially changed (i.e. modulated). The latter method has generally been preferred in solar instrumentation, and a variety of modulation techniques have been developed, e.g., mechanical modulation (rotating $\lambda/4$ plate), electro-optical modulation (K*DP), Kerr cell switching, and piezo-optical modulation.

Since the Zeeman effect only influences atomic (and molecular) transitions, it is necessary to spectrally resolve such individual transitions for a measurement of solar magnetic fields (however, see also Kemp et al., 1987, for a broadband detection of solar polarization). The three main types of devices available for spectral analysis are grating spectrographs, narrow band filters and Fourier transform spectrometers (see Sect. 3.1.1 for more on the last named).

Finally, the importance of detectors should not be underestimated. As pointed out by Harvey (1986), it was the introduction of photoelectric detectors in the early 1950s which led to the first extensive and reliable studies of non-sunspot magnetic fields. Besides photographic film, photomultipliers (often in pairs), reticons, CCDs and vidicons are all extensively used. A more detailed account of the instrument used to obtain the data evaluated in this thesis, the McMath FTS polarimeter, is presented in Sect. 3.1.

3. Observational Data

". . . none of the activity of the Sun or any other star was anticipated theoretically. It was thrust upon us by observation."

E.N. Parker (1985)

3.1. The Fourier Transform Spectrometer as a Polarimeter

3.1.1. Basic Properties of the FTS

A Fourier transform spectrometer (FTS) is basically a modified Michelson interferometer, with an input, a beamsplitter, two retroreflectors (instead of the original plane mirrors) and one or two outputs. If the retroreflectors are positioned such that the optical path difference between them is x, then for a monochromatic plane wave with input intensity I_0, the emergent intensity $I(x)$ is

$$I(x) = \frac{1}{2}\eta_0\eta_b I_0(1 \pm \cos(2\pi\sigma x)), \tag{3.1}$$

where $\sigma = 1/\lambda$ is the wavenumber, $\eta_0 < 1$ is the reflection coefficient of the retroreflectors, and $\eta_b < 1$ is the beamsplitter efficiency. The $\pm$ signs in Eq. (3.1) signify the signals at the two possible outputs of the FTS. If we now move the reflectors such that x changes linearly with time, $v = \mathrm{d}x/\mathrm{d}t = \text{constant}$, then we can write

$$I(t) = \frac{1}{2}\eta_0\eta_b I_0(1 \pm \cos(2\pi\sigma v t)). \tag{3.2}$$

Thus the FTS modulates the input signal at a frequency of $f = \sigma v$, which for a typical instrument lies in the audio range. If instead of a monochromatic input, a source with a spectrum $I_0(\sigma)$ is observed, then, neglecting the constant term, the observed intensity upon output can be written as (e.g. Brault, 1985)

$$I(x) = \frac{1}{2}\eta_0\eta_b \int_0^\infty I_0(\sigma)\cos(2\pi\sigma x)\,\mathrm{d}\sigma. \tag{3.3}$$

Combining Eqs. (3.2) and (3.3) we see that the input optical spectrum is converted into an interferogram at audio frequencies. It also follows from Eq. (3.3) that the input spectrum $I_0(\sigma)$ and the resulting interferogram are related by the cosine transform (the real part of the Fourier transform). Thus by numerically carrying out the inverse transformation on the observed interferogram we can recover the original spectrum. In the following we briefly list some of the general properties of an FTS:

- In contrast to grating spectrographs spatial and spectral resolution are almost completely decoupled. The spectral resolution is given by the maximum path length difference L. The resolving power, R, is related to L by

  $$R \equiv \frac{\sigma}{\delta\sigma} = 2L\sigma. \tag{3.4}$$

  Of course, spatial resolution remains inversely proportional to the size of the entrance aperture, while the throughput is directly proportional to the size. The entrance aperture is often chosen in the form of a circular hole in order to maximise throughput.
- All wavelengths are sampled strictly simultaneously, the scanning is done in the Fourier domain. Thus the scan time and the wavelength range are decoupled, allowing very large wavelength ranges to be observed simultaneously.
- All the photons incident on the detector, i.e., photons of all wavelengths within the selected range, contribute to the noise at any one wavelength. In practice this sets a limit on the observed range. The noise is also influenced by the maximum resolving power, with a greater S/N ratio in the interferogram being required

to give a fixed S/N ratio in the spectrum as the resolving power is increased. This is because the noise at each point of the interferogram contributes to the noise at a given wavelength point. See also Brault (1985) and Ridgeway and Brault (1984) for more on S/N.

- The FTS has a symmetric instrumental profile of the (ideal) form

$$\psi_{\text{instr}} = 2L\,\text{sinc}(2L\sigma), \tag{3.5}$$

which gives rise to the well known 'ringing' in very narrow spectral features (e.g. telluric lines). However, according to Brault (1978, 1982) the FTS distorts the input spectrum less than any other commonly used spectrometer with apparatus function of similar width, since in the Fourier (i.e. interferogram) domain the symmetrical FTS instrumental profile stays practically constant right out to the maximum resolving power.

- A single line anywhere in the spectrum can serve as a wavelength standard for the complete spectrum.
- Scattered light, being unmodulated, is rejected by the detection system and is therefore unimportant.

More detailed information on the FTS is given by Brault (1978, 1985). It is compared with other passive spectrometers by Brault (1982), and some of the astronomical implications and uses of the FTS are reviewed by Ridgeway and Brault (1984). More specific information on the Kitt Peak FTS may be obtained from Brault (1978) and Hubbard (1982).

3.1.2. The FTS as a Polarimeter

Two methods for measuring polarized spectra with an FTS were presented by Brault (1978). A variant of the second of these, due originally to J.W. Harvey and J.O. Stenflo, was used in 1979 to obtain the Stokes I and V data discussed in Sect. 3.2. The technique has in the meantime been improved by J.W. Harvey, making it possible to measure three Stokes parameters e.g. I, Q, V, or I, U, V simultaneously, while retaining all the advantages of an FTS. This setup was used to record Stokes I, V, and Q in 1984 (also described in Sect. 3.2). A brief sketch of the modulation scheme (from Harvey, 1984) is given below.

Two optical elements are required. The first one is a sinusoidally oscillating modulator, consisting of a quartz crystal cemented to a piece of fused silica. The retardation is proportional to the amplitude of the oscillation. The second element is a linear analyser. Let us consider the case, in Mueller calculus, where I, Q, and V are measured. The case where I, U, and V are measured is described by Harvey (1984). We get the desired result if we choose the position angles α and β of retarder and analyser such that $\alpha = -45°$ and $\beta = 0°$. Then, for an input beam (I, Q, U, V), the output may be written as [Eqs. (2.97) and (2.98)]

$$\begin{pmatrix} I_{\text{obs}} \\ Q_{\text{obs}} \\ U_{\text{obs}} \\ V_{\text{obs}} \end{pmatrix} = \frac{1}{2}\begin{pmatrix} 1 & 1 & 0 & 0 \\ 1 & 1 & 0 & 0 \\ 0 & 0 & 0 & 0 \\ 0 & 0 & 0 & 0 \end{pmatrix}\begin{pmatrix} 1 & 0 & 0 & 0 \\ 0 & \cos\delta & 0 & \sin\delta \\ 0 & 0 & 1 & 0 \\ 0 & -\sin\delta & 0 & \cos\delta \end{pmatrix}\begin{pmatrix} I \\ Q \\ U \\ V \end{pmatrix} = \frac{1}{2}\begin{pmatrix} I + Q\cos\delta + V\sin\delta \\ I + Q\cos\delta + V\sin\delta \\ 0 \\ 0 \end{pmatrix}, \tag{3.6}$$

where δ is the sinusoidal retardation

$$\delta = \delta_m \sin\omega t, \tag{3.7}$$

with δ_m being the maximum amplitude of the retardation and $\omega = 20$ kHz for the Kitt Peak instrument. We can expand $\cos\delta$ and $\sin\delta$ as (e.g. Abramowitz and Stegun, 1970)

$$\cos\delta = \cos(\delta_m \sin\omega t) = J_0(\delta_m) + 2J_2(\delta_m)\cos(2\omega t) + \cdots \tag{3.8}$$

and

$$\sin\delta = \sin(\delta_m \sin\omega t) = 2J_1(\delta_m)\sin(\omega t) + \cdots. \tag{3.9}$$

The J_n are n-th order Bessel functions of the first kind. In the FTS polarimeter frequencies higher than 40 kHz are electronically rejected, so that the total observed intensity signal is

$$I_{\text{obs}} = \frac{1}{2}(I + Q\cos\delta + V\sin\delta) = \frac{1}{2}I + \frac{1}{2}QJ_0(\delta_m) + QJ_2(\delta_m)\cos(2\omega t) + VJ_1(\delta_m)\sin(\omega t). \tag{3.10}$$

We must now choose δ_m such that $J_0 = 0$, since otherwise the unmodulated part of the signal will contain a mixture of Stokes I and Q. Although it would in principle be possible to disentangle I and Q in the data reduction by using the Q from the third term, this is fortunately not required, since the first zero of J_0 also gives

values of J_1 and J_2 which are quite close to their maxima. The Q and V signals are, therefore, little affected by this choice:

$$\begin{aligned} J_0(\delta_m = 2.40) &= 0.00 \quad (\max: 1.00), \\ J_1(\delta_m = 2.40) &= 0.52 \quad (\max: 0.58), \\ J_2(\delta_m = 2.40) &= 0.43 \quad (\max: 0.49). \end{aligned} \tag{3.11}$$

The McMath telescope has a sampling frequency of 2500 Hz. It then follows from the Fourier sampling theorem that the frequency range available for the data is 0–1250 Hz. In the polarimeter mode this range is segmented into three portions with Stokes I stored in the portion with the highest frequency (833–1250 Hz), Q in the section with 417–833 Hz, and V in the 0–417 Hz segment. Q and V, which are modulated at 40 kHz and 20 kHz respectively (see Eq. (3.10)), are first simultaneously demodulated and then heterodyned to the lower frequencies. A further development of this modulation technique, which allows the measurement of all four Stokes parameters simultaneously, has been published by Stenflo (1984b).

3.2. The Data Set

3.2.1. Basic Parameters of the Data

The data were obtained during two observations runs, on April 29–30, 1979 and on May 3–7, 1984. The McMath telescope of the NSO at Kitt Peak was used, together with the 1m FTS polarimeter to simultaneously record Stokes I and V in 1979, and I, V, and Q in 1984. For a large portion of the work presented in this thesis, the data of 1979 have been used, and they will be described first. A detailed description of these data have been published by Stenflo et al. (1984). Five spectra of different regions near disk centre, which included both active plages and quiet network elements, were obtained in addition to one spectrum of a very quiet region in Stokes I only. Table 3.1 contains an overview of the data. The spatial resolution of 10″ corresponds to a circular FTS entrance aperture of 4mm diameter. Note, that in Table 3.1 (and also in Tables 3.2 and 3.3) the polarity is not absolute, since some problems exist in determining the absolute polarity with the FTS. Since the modulation transfer function of the FTS is unity out to the resolution value given in Table 3.1, (cf. Sect. 3.1.1) the solar spectrum in our data is completely resolved, i.e., it is only insignificantly broadened by the instrument. The wavelength ranges of approximately 1000-1500 Å were bounded by prefilters.

Table 3.1 Parameters of 1979 data

μ	Date	Name	Type of region	Wavelength range	Spectral resolution	Integr. time	Spatial resol.	Limb direc.	Stokes params.	Polarity
0.92	30.4.79	FTS4	Plage	4524–5580	420'000	35	10″	SW	IV	+
0.92	30.4.79	FTS5	Plage	5254–6907	500'000	21	10″	SW	IV	+
0.98	29.4.79	FTS2	Network	4566–5580	420'000	52	10″	SE	IV	+
1.00	30.4.79	FTS1	Network	4104–4942	359'000	69	10″	(SE)	IV	+
1.00	30.4.79	FTS3	Network	5254–6907	500'000	57	10″	(SE)	IV	−
1.00	29.4.79	FTS0	Quiet	4607–5588	420'000	94	10″	(–)	I	0

The data of 1984 are composed of 16 spectra, eight of them in the visible and eight in the infrared (IR). These data were obtained at different $\mu = \cos\theta$ positions right out to the solar limb (the observation at $\mu = 0.1$ is only 5″ from the limb). The spatial resolution of 5″, corresponds to a circular entrance hole of 2mm diameter. The reason for decreasing the size of the entrance aperture was to avoid poor μ resolution near the limb. Tables 3.2 and 3.3 summarise the parameters of these data. More details are to be found in Stenflo et al. (1987a, b).

The position angle of the linear analyser was chosen such that the positive Q direction is perpendicular to the limb. Except for two IR spectra of sunspot umbræ, care was taken to avoid small pores or spots by prior visual inspection of the regions to be observed. Also, regions of closely mixed polarity were avoided in the hope

Table 3.2 Parameters of 1984 visible data

μ	Date	Name	Type of region	Wavelength range	Spectral resolution	Integr. time	Spatial resol.	Limb direc.	Stokes params.	Polarity
0.10	5.5.84	PLAGE7	Plage	4883–6002	523'000	72	5″	W	IVQ	–
0.16	3.5.84	PLAGE2	Plage	4883–6002	523'000	43	5″	W	IVQ	–
0.28	3.5.84	PLAGE1	Plage	4883–6002	523'000	43	5″	W	IVQ	+
0.30	4.5.84	PLAGE6	Plage	4883–6002	523'000	58	5″	W	IVQ	+
0.45	4.5.84	PLAGE4	Plage	4883–6002	523'000	43	5″	W	IVQ	–
0.57	4.5.84	PLAGE5	Plage	4883–6002	523'000	65	5″	W	IVQ	–
0.67	4.5.84	PLAGE3	Plage	4883–6002	523'000	43	5″	W	IVQ	–
0.83	4.5.84	NETW1	Network	4883–6002	523'000	58	5″	W	IVQ	–

Table 3.3 Parameters of 1984 infrared data

μ	Date	Name	Type of region	Wavelength range	Spectral resolution	Integr. time	Spatial resol.	Limb direc.	Stokes params.	Polarity
0.15	6.5.84	PLAGE9	Plage	14676–18039	359'600	42	5″	E	IVQ	–
0.38	6.5.84	PLAGE8	Plage	14676–18039	359'600	42	5″	E	IVQ	–
0.43	6.5.84	PLAGE10	Plage	14676–18039	359'600	42	5″	W	IVQ	+
0.61	6.5.84	PLAGE11	Plage	14676–18039	359'600	48	5″	E	IVQ	–
0.76	7.5.84	NETW3	Network	14676–18039	359'600	33	5″	SW	IVQ	–
0.99	6.5.84	NETW2	Network	14676–18039	359'600	53	5″	W	IVQ	+
0.26	6.5.84	SPOT1	Umbra	14676–18039	359'600	42	5″	E	IVQ	–
0.47	7.5.84	SPOT2	Umbra	14676–18039	359'600	42	5″	E	IVQ	–

of thus selecting regions with a relatively simple geometry of the magnetic field. The method of choosing the region to be observed in the 1984 observations warrants some attention, since it is probably responsible for some selection effects. The FTS aperture was first centred on a local extremum of the Stokes V signal obtained by setting the FTS to a fixed path length difference and monitoring Stokes V on a meter. A path length difference of approximately 2cm was chosen, which corresponds roughly to the inverse of the typical width of a photospheric spectral line. Then the entrance hole was guided on this point, taking into account the law of differential rotation of photospheric magnetic fields. This procedure favours regions with large Stokes V. For observations near the limb, this means that if the magnetic field is perpendicular to the solar surface, then regions with very large filling factors are preferably observed, or if the magnetic field can be inclined, then fields inclined towards the observer will be favoured.

Fig. 3.1 illustrates this effect. In Fig. 3.1a the average of the blue and red absolute amplitudes of Stokes V, V_{max}, of Fe I 5250.2 Å is plotted for all 10 FTS recordings containing this line. If we neglect variations in the thermodynamic properties of fluxtubes with filling factor α and μ (cf. chapter 5), then $V_{max}/\cos\gamma$ is approximately proportional to α, since the magnetic field strength does not vary strongly with α (Stenflo and Harvey, 1985). Due to the theoretically expected large buoyancy of the fluxtubes, we expect $\cos\gamma \approx \cos\theta = \mu$ to be a reasonable assumption (Schüssler, 1986). Dividing V_{max} by $\cos\theta$, we get Fig. 3.1b, where the sharp increase in α towards the limb is clearly visible. However, the data also allow for the other explanation, namely that the fields near the limb are tilted towards the observer. Note: Solanki et al. (1987) have shown that at least part of this increase in $V_{max}/\cos\theta$ is induced by tilted fields. The magnetic field in the last three regions is found to be inclined towards the observer, with increasing inclination for decreasing μ.

A small part of an FTS spectrum obtained in 1984 is shown in Fig. 3.2. Plotted are Stokes I, V, and Q for a region with $\mu = 0.28$. The spectral line is Fe I 5250.2 Å (g=3), probably the most used line for polarimetric observations.

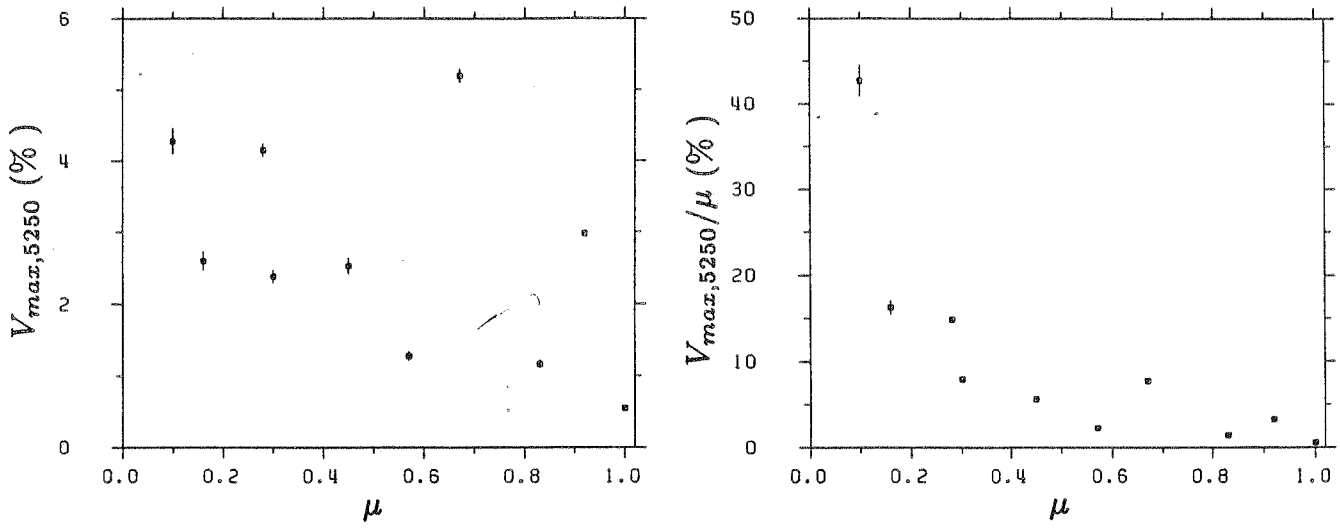

Fig. 3.1 a Average of the blue and red amplitudes of Stokes V, V_{max}, of Fe I 5250.2 Å is plotted vs. μ. b V_{max}/μ vs. μ. For a vertical field V_{max}/μ is roughly proportional to the filling factor.

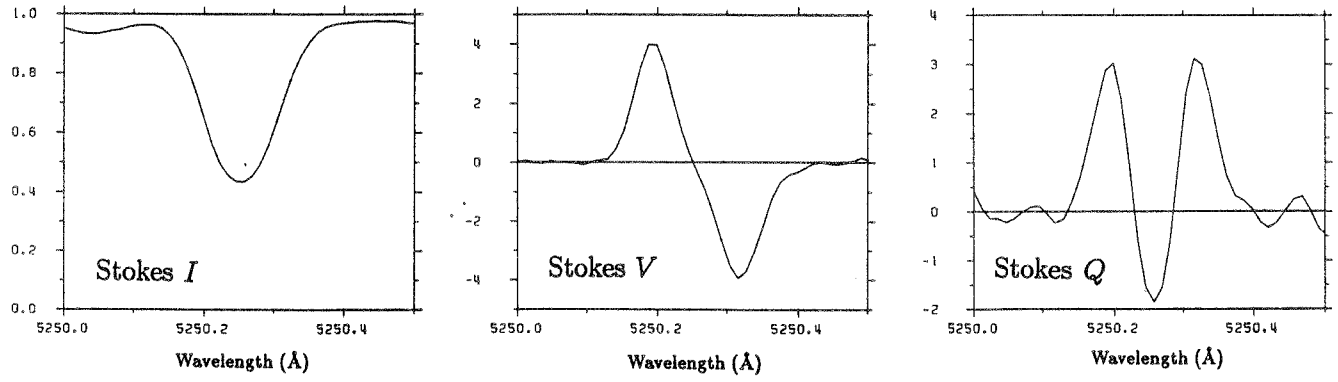

Fig. 3.2 Stokes I, V, and Q profiles of Fe I 5250.2 Å observed in an active region plage at $\mu = 0.28$.

Different wavelength ranges were chosen in 1979 in order to obtain an atlas in Stokes I and V covering a large portion of the visible spectrum. The wavelength range of the spectra in the visible of 1984 was chosen such that it contained the line pair 5247–5250 Å not too near its edge. Furthermore, a considerable number of unblended spectral lines of iron are found in this range. The wavelength range in the infrared was chosen such that it contained the $g = 3$ line Fe I 15648.5 Å. It is bounded on both sides by extensive atmospheric absorption bands. For the IR data InSb detectors cooled to approximately 73K with liquid nitrogen were used.

Note that in the rest of this thesis if nothing is said to the contrary, then the 1979 data are meant.

3.2.2. Defringing, Continuum, and Zero-Level

In the 1979 data the KD*P modulator plate caused weak interference fringes in the unpolarized data, in particular towards the blue end of the spectrum. Using numerical fits with a Fabry-Perot equation, the fringes could be successfully removed prior to the data analysis. By making all optical elements in the lightbeam slightly wedge shaped, such problems were avoided for the 1984 data (Harvey, 1985b).

The gradual decline of the prefilter transmittance near the edges of a wavelength range causes the continuum to be unreliable there. By fitting quadratic functions through the maxima of Stokes I, the continuum could be corrected to within about 0.5%, which is of sufficient accuracy for our purposes. A similar amount of uncertainty is present in the true intensity zero level (Holweger, private communication). For the 1984 data the required continuum correction was considerably smaller, due to the use of a predisperser with considerably sharper cutoff.

One effect of the gradual decrease in intensity towards the edges of the prefilter range in the 1979 data is that the noise increases considerably there, both in Stokes I and V. However, in general, noise levels in the data are quite small. Since noise is discussed in detail in Sect. 4.3.2, in connection with the selection of spectral lines, we refrain from going into greater detail here. Since the FTS has practically no stray light, no stray light correction had to be carried out.

Except from a small additive false zero-level, in V/I and Q/I (degree of circular, respectively, linear polarization), and perhaps a fixed amont of depolarization in the 1979 data, no false polarization was introduced by the instrument. It is relatively simple to subtract out this false level, by assuming that V/I and Q/I should be zero in the continuum. That this assumption is valid is demonstrated by the broadband polarization measurements of Kemp et al. (1987), who find a fractional circular polarization of $0.1\text{–}1\times10^{-6}$ and an upper limit on the linear polarization of 0.2×10^{-6} when averaging over the whole solar disk. Most of this polarization is due to the Stokes V asymmetry in spectral lines, so that the continuum polarization is even lower (cf. chapter 8 for more details). In practice we take all points with $0.98 \leq I/I_c \leq 1$, where I_c is the continuum intensity. It should be noted that V/I, respectively Q/I, should be used, and not V or Q, since the instrumental polarization contains the solar spectral features in V, respectively Q, but not in V/I or Q/I (i.e., it is spectrally flat in these quantities; cf. Stenflo et al. 1983). For the 1984 data the need for this zero-level correction was decreased by the use of the "anti-McMath" device of Harvey (1985a). The residual instrumental polarization in the raw data was generally $< 0.1\%$ in Stokes V and $< 0.2\%$ in Stokes Q. Stokes Q would have been particularly badly affected if it had been measured with the instrumental setup of 1979. After correction, the continuum polarization is considerably smaller still, being of the order of 0.01% or better for Stokes V. In particular it is lower than the noise level in every case, and is certainly completely insignificant compared to the Zeeman effect polarization of most spectral lines. Arguments in favour of some depolarization of the 1979 data have been presented by Stenflo and Harvey (1985). However, stringent tests of the instrumental setup of 1984 by Harvey (1985b) have not revealed any sources of depolarization. In any case, this depolarization only affects the filling factors determined from these data, since the rest of the analysis is independent of the absolute value of the polarization signal.

3.3. Advantages and Disadvantages of FTS Data

Due to the fact that their diameters are below the resolution limit of modern optical instrumentation, fluxtubes, like stars, require spectral methods for a proper investigation of their internal structure. Ideally, observations should combine high spatial, temporal, and spectral resolution, and cover a large spatial, temporal, and spectral range simultaneously in all four Stokes parameters. In reality, due to the limitations set by seeing and instrumentation, and in order to reach a reasonable signal to noise ratio, compromises have to be made. Over the years a large variety of data have been obtained for the study of fluxtubes. In the following we shall look at the merits and demerits of some of them for determining the internal properties of fluxtubes.

One method of investigation is to take photographs or photoelectric images of active regions or network elements in some more or less pure stretch of continuum. An advantage of continuum observations is that they allow for good spatial and temporal resolution, while enabling many spatial elements to be observed simultaneously (i.e. large spatial ranges are possible). Another advantage is that continuum data in general contain information on other levels in the fluxtube atmosphere than line spectra, and can provide estimates of the temperature in the important deeper layers. A disadvantage is that besides the temperature they cannot give any information on internal properties of fluxtubes. Strictly speaking they cannot even identify fluxtubes with certainty. All that continuum observations show are bright points of typically less than $0.5''$ diameter, although Schüssler and Solanki (1987) present some evidence in favour of identifying bright points with magnetic elements. In addition, Foukal et al. (1981) and Foukal and Duvall (1985) have pointed out that most high resolution continuum observations of fluxtubes have not been carried out in stretches of pure continuum, so that the information they give is smeared over a height range given by the number density and properties of the spectral lines in the observed window.

Although unpolarized line spectra contain in principle much more information on the fluxtube, they still suffer from the disadvantage (shared by the continuum data), that the light from the fluxtubes is, in general, strongly mingled with light from their non-magnetic surroundings. This makes spectra in unpolarized light rather less than ideal for determining the internal structure of fluxtubes. This is particularly true for spectra with low spatial resolution, and spatial resolution has often to be sacrificed if enough spectral information with good S/N

is to be gathered.

Spectra in polarized light overcome a considerable portion of the disadvantages of finite spatial resolution, since Stokes $Q = U = V = 0$ when $B = 0$, so that these Stokes parameters arise only in the magnetic part of the atmosphere. * Once more different types of polarimeter data exist, two extremes of which are listed below. Firstly, those with high spatial and temporal resolution (both are required simultaneously due to the everchanging seeing) and one or two spatial dimensions, but with only very limited spectral information (magnetograph type, or spectra in one, or at the most a few spectral lines). Secondly, those with high spectral resolution and a broad spectral range but with only moderate spatial and temporal resolution (as obtained for example with an FTS). Of course observations with properties intermediate to these two extremes exist as well.

Our FTS spectra are unique, in that each recording is a complete spectral atlas in Stokes I, V, and in some cases Q. With an appropriate analysis technique, they allow the magnetic field strength, temperature, and velocity structure of fluxtubes to be determined independently of the actual size of the spatial resolution elements. This is the main reason why 10″ and 5″ entrance apertures were chosen. Smaller entrance apertures would only have increased the noise level in the data (this is always a problem with polarimetric data outside sunspots due to the small filling factors), and would also have made the observations more sensitive to seeing fluctuations.

Of course, there are considerable limitations to the possibilities of these data. They can only provide us with average properties of fluxtubes, since usually more than one fluxtube will be present in the resolution element. Little information can be obtained on the spread of fluxtube properties, or on the detailed morphology of the field. Due to the rather long integration times, no information is obtained on the temporal evolution of the magnetic field.

Another possible problem with the FTS is that, although all the wavelengths contribute simultaneously to the recorded interferogram, the different Fourier components of each line profile are sampled at different times, which could cause a similar distortion of all line profiles in a single scan if periodic motions with a period near to the time required to record a full interferogram are present on the Sun. Problems with the ubiquitous five minute oscillations were avoided by choosing this time to be 7.2 minutes in the visible spectral range (in the IR the scan period is less fortunate, being 4 minutes 38 seconds) and by repeating the interferogram scan a number of times. This last step has the added advantage that the signal to noise ratio of the data is increased. Also, in contrast to some other such instruments, the McMath FTS samples the interferogram symmetrically, i.e. both negative and positive path length differences x are sampled. The advantage of this technique is that all x are sampled at the same *mean* epoch, thus reducing the instrumentally induced influence of changes in the solar atmosphere on the line profile shapes. Finally, a comparison of FTS Stokes I line profiles with Jungfraujoch atlas profiles shows that no significant distortions of the FTS profiles exist. Although large amplitude motions of unknown period exist in fluxtubes (see chapter 7), they are not in phase for different fluxtubes, as can be inferred from the null result of Giovanelli et al. (1978). Therefore these motions should not cause any additional distortions of the FTS Stokes V and Q profiles via the scanning in the Fourier domain.

In Table 3.4 the two extreme types of polarimeter data mentioned above are contrasted to each other and their capabilities to study different aspects of fluxtubes are summarized. Note that the table is based on present capabilities, and that future data or analysis procedures may be able to realise things now seemingly impossible. A few remarks to Table 3.4 are listed below (the places the remarks refer to are marked in the table).

[1] The observation that the IR line Fe I 15648.5 Å has a Stokes V profile whose σ components are much broader than the complete I profile, may be due to a range of magnetic fields distributed *horizontally* across the fluxtube diameter (Stenflo et al., 1987b, also see Sect. 6.5). However, at present this is not the only possible explanation and much more work is required to decide this point.

[2] It may be possible to obtain information on the Height variation of fluxtube properties from observations at various distances from the limb, or by comparing IR with visible observations, etc.

[3] α is the filling factor.

[4] It may be possible to determine diameters of fluxtubes with low resolution data off disk centre when 2-D models are used, since the line profiles may depend strongly on the fluxtube diameter and angle of inclination (cf. Van Ballegooijen, 1985b).

---

* This simple picture may no longer be true for small fluxtubes (in particular when observed near the limb), since one and the same line of sight may then pass through both magnetic and non-magnetic regions.

Table 3.4

	High spatial resolution in one spectral line	*Low spatial resolution FTS spectrum*
Internal horizontal variation of fluxtube parameters	NO (later ?)	PERHAPS[1]
Height variation of fluxtube properties	PERHAPS[2]	YES
Range of fluxtube properties	YES (between individual fluxtubes)	YES (between regions of varying α)[3]
Interaction of fluxtubes with their surroundings	YES (direct)	YES (bisectors)
Fluxtube diameters	YES ?	PERHAPS (indirect)[4]
Evolution of fluxtubes (lifetimes)	YES ?	NO
Waves, oscillations etc.	5-minutes: YES Rest: PERHAPS[5]	YES (line widths)
Geometry	YES (model dependent)	Average: YES Individual: NO
User friendliness for quantitative interpretation	Modeller's nightmare, but doable[6]	Fodder for Ph.D. students

[5] Wiehr (1985a) sees some changes in the Stokes V profile which may be part of an oscillation, but an instrumental explanation cannot be ruled out (these observations do not have high spatial resolution).

[6] The work of Brants (1985a, b) is a good example of how such data can be quantitatively interpreted.

It follows from Table 3.4, that the two types of data are complementary to each other and we need both high and low spatial resolution data in order to obtain a maximum of information on the fine scale structure of solar magnetic fields. We may also generalize from this section that high spatial resolution (e.g. magnetograph type) observations are the prime source of information on the distribution, morphology, and evolution of magnetic features, while low spatial resolution spectra (like the ones used in this thesis) are superior for determining their internal structure.

4. Data Analysis: A Statistical Approach

"There are lies, damn lies and statistics."

G.B. Shaw

4.1. Introduction

The observational procedure and the data set have been described in the last chapter. Here we shall concentrate on the analysis and present some qualitative results. Basically two approaches to the data analysis are possible, the 'few line approach', based on the detailed study of the line profiles of a few spectral lines, and the 'many line approach', which is based on an analysis of the parameters of many spectral lines. Solanki (1987) has discussed the relative merits of both approaches. To take maximum advantage of the unique features of FTS data, viz. the excellent spectral resolution and the broad spectral range, we have, for the main part, chosen the many line approach. Parameters of a large number of spectral lines (taken from a list of 400 unblended Fe I and 50 Fe II lines) are determined and analysed. One advantage of this approach is that hidden blends do not effect the analysis significantly. Parameterisation is also a simple and efficient way to get a handle on the immense amount of data (2×10^5 to 3×10^5 data points per FTS spectrum).

To allow a direct comparison between the surroundings of the fluxtube and its interior, i.e. between Stokes I and V, we introduce the I_V profile, obtained by integrating Stokes V. It is a first order approximation of the Stokes I profile arising in the fluxtube. With this step a major disadvantage of the FTS data, the low spatial resolution, is overcome. The I_V profile can, for most purposes be treated like Stokes I. In particular, I_V and I can be identically parameterised, and the rich collection of diagnostic methods developed for Stokes I can also be applied to I_V. By studying the dependence of the I_V line width and line depth, the Stokes V asymmetry and zero-crossing, etc., on the excitation potential, Landé factor, and Strength of the line, the influence of filling factor, magnetic field strength, temperature, and veloctiy on the spectrum can be, at least partially, separated, allowing a qualitative picture of these quantities inside fluxtubes to be obtained.

For more quantitative knowledge, however, model calculations are required, i.e. the emergent profiles of a number of spectral lines in a fluxtube model with some initially assumed atmospheric structure have to be calculated and compared to observed line profiles. This comparison can be used to construct an improved model. This process carried out over a number of iterative steps hopefully converges to a model with a certain semblance to reality.

Prior to this work Unno (1959) and Stenflo and Lindegren (1977) have presented a similar approach, based on the statistical analysis of the parameters of Stokes I profiles only, to estimate the strength of a turbulent or tangled magnetic field in the solar photosphere. Preston (1971) has also used the differential broadening of a few lines of different Zeeman sensitivity to determine the magnetic field strengths on Ap stars, while Brandt and Solanki (1987) have applied this technique to the determination of filling factors in solar active regions from Stokes I profiles. Finally Mathys and Stenflo (1986) have subsequently applied the concept of the I_V profile to the study of Ap stars.

The I_V profile is derived and discussed in Sect. 4.2. The unblended lines used are listed together with their atomic parameters (in particular their empirically determined Landé factors) in Sect. 4.3. In Sect. 4.4 some line parameters of Stokes I, I_V and V are defined and a first qualitative analysis with the help of regression equations is carried out. Finally, in Sect. 4.5 the models serving as the basis for the line profile calculations are briefly described.

4.2. The I_V Profile

4.2.1. A Simple Derivation of the I_V Profile: A Relationship Between Stokes I and V

Consider a normal Zeeman triplet formed at disk centre in a static atmosphere with a magnetic field which is

vertical (i.e. aligned along the line of sight) and homogeneous over the resolution element. The spectral line is then split by the magnetic field into two σ components with opposite circular polarization. Their intensities can be written as

$$I_{r,b} = \frac{1}{2}(I \pm V). \tag{4.1}$$

The Stokes I and V profiles are accordingly

$$\begin{aligned} I &= I_r + I_b \\ V &= I_r - I_b. \end{aligned} \tag{4.2}$$

Next we make use of the following relations valid in a homogeneous field along the line of sight (e.g. Unno, 1956). This is a particularly simple case of Eqs. (2.43) and (2.17).

$$\kappa_{r,b} = \frac{1}{2}\kappa(\lambda \pm \Delta\lambda_H), \tag{4.3}$$

where $\Delta\lambda_H$ is the Zeeman splitting, cf. Eqs. (2.23) and (2.24),

$$\Delta\lambda_H = 4.67 \times 10^{-13} g\lambda^2 B, \tag{4.4}$$

with λ and $\Delta\lambda_H$ in Å, and B in G. Neglecting saturation effects for the moment we obtain the following relation

$$I_{r,b} = \frac{1}{2} I_m(\lambda \pm \Delta\lambda_H). \tag{4.5}$$

I_m is the Zeeman *un*broadened Stokes I profile originating from the magnetic region, i.e. from the same region as Stokes V. Expanding the right-hand-side of the above equation in a Taylor series we get

$$I_{r,b}(\lambda) = \frac{1}{2}\sum_{n=0}^{\infty} \frac{1}{n!}\frac{\partial^n I_m(\lambda)}{\partial\lambda^n}(\pm\Delta\lambda_H)^n. \tag{4.6}$$

By combining Eq. (4.5), respectively Eq. (4.6) with Eq. (4.2) the following expressions are obtained for Stokes I and V.

$$I(\lambda) = \frac{1}{2}\left(I_m(\lambda + \Delta\lambda_H) + I_m(\lambda - \Delta\lambda_H)\right), \tag{4.7a}$$

$$V(\lambda) = \frac{1}{2}\left(I_m(\lambda + \Delta\lambda_H) - I_m(\lambda - \Delta\lambda_H)\right) \tag{4.7b}$$

and

$$I(\lambda) = \sum_{n=0}^{\infty} \frac{1}{(2n)!}(\Delta\lambda_H)^{2n}\frac{\partial^{2n}}{\partial\lambda^{2n}} I_m(\lambda), \tag{4.8a}$$

$$V(\lambda) = \sum_{n=0}^{\infty} \frac{1}{(2n+1)!}(\Delta\lambda_H)^{2n+1}\frac{\partial^{2n+1}}{\partial\lambda^{2n+1}} I_m(\lambda). \tag{4.8b}$$

As expected from the antisymmetry of Stokes V in a static atmosphere (cf. Sect. 2.4.2), only odd-powered terms are present in Eq. (4.8b), while the symmetry of I allows only even powered terms.

If the Zeeman splitting of the spectral line is much smaller than its width, the higher order terms in Eqs. (4.8) can be neglected (this is the so called weak field approximation, valid for $\Delta\lambda_H \ll \Delta\lambda_D$, $\Delta\lambda_D$ = Doppler width of the line) and they reduce to the simple expressions

$$\begin{aligned} I(\lambda) &\approx I_m(\lambda) + \frac{1}{2}\Delta\lambda_H^2 \frac{\partial^2 I_m(\lambda)}{\partial\lambda^2}, \\ V(\lambda) &\approx \Delta\lambda_H \frac{\partial I_m(\lambda)}{\partial\lambda}. \end{aligned} \tag{4.9}$$

It is therefore possible to determine Stokes V from the unsplit Stokes I profile formed in the same magnetic region. However, when investigating small solar magnetic fluxtubes we face the reverse problem, since due to their minuteness as compared with the spatial resolution, the only clean information on the fluxtubes comes from

Stokes V, the observed Stokes I being mainly formed outside the fluxtubes. Accordingly, the integrated form of Eq. (4.9) is the more useful equation (Solanki and Stenflo, 1984). If we define a profile, I_V, as

$$\frac{I_V}{I_c} = 1 + \frac{1}{\Delta\lambda_H}\int_{\lambda_1}^{\lambda} \frac{V(\lambda')}{I_c}\,\mathrm{d}\lambda', \tag{4.10}$$

then it is a good approximation of I_m in the weak field approximation, i.e. I_V is a good approximation of the unsplit line profile. Here I_c is the intensity of the continuum and λ_1 is the lower integration boundary which should in principle be at $-\infty$, but is in practice chosen sufficiently far in the blue wing for $V(\lambda_1) \approx 0$. For real data the choice of λ_1 is usually governed by noise and the proximity of neighbouring lines. The simple discussion given here for a Zeeman triplet will be extended to cover anomalous Zeeman splitting in the following section. Landi Degl'Innocenti and Landi Degl'Innocenti (1973) derived Eq. (4.9) from a perturbative solution of the radiative transfer equations.

4.2.2. Summary of a Derivation of the I_V Profile Including Anomalous Zeeman Splitting

If $\Delta\lambda_H$ for lines with anomalous Zeeman splitting is defined by replacing g in Eq. (4.4) through $g_{\rm eff}$, then a general formalism for the expansion of the absorption coefficients of the Stokes parameters $\eta_I, \eta_Q, \eta_U, \eta_V$ according to powers of $\Delta\lambda_H^* = \Delta\lambda_H/g_{\rm eff}$ can be derived (Mathys and Stenflo, 1987a). This formalism takes into account the anomalous Zeeman effect, and is valid for a general γ (the angle between the magnetic field and the line of sight). It is partly based on earlier work by Landi Degl'Innocenti (1982, 1985a). We shall restrict ourselves to describing only the results pertinent to our discussion. In its general form, the expansion can be written as

$$\begin{aligned}
\frac{\eta_I(\lambda)}{\eta(\lambda_0)} &= \frac{1}{2}\sum_{k=0}^{\infty}\left[C_0^{(2k)}\sin^2\gamma + C_1^{(2k)}(1+\cos^2\gamma)\right]\Delta\lambda_H^{*\,2k}\frac{\partial^{2k}}{\partial\lambda^{2k}}\phi(\lambda-\lambda_0),\\
\frac{\eta_Q(\lambda)}{\eta(\lambda_0)} &= \frac{1}{2}\sin^2\gamma\cos 2\varphi\sum_{k=1}^{\infty}\left[C_0^{(2k)} - C_1^{(2k)}\right]\Delta\lambda_H^{*\,2k}\frac{\partial^{2k}}{\partial\lambda^{2k}}\phi(\lambda-\lambda_0),\\
\frac{\eta_U(\lambda)}{\eta(\lambda_0)} &= \frac{1}{2}\sin^2\gamma\sin 2\varphi\sum_{k=1}^{\infty}\left[C_0^{(2k)} - C_1^{(2k)}\right]\Delta\lambda_H^{*\,2k}\frac{\partial^{2k}}{\partial\lambda^{2k}}\phi(\lambda-\lambda_0),\\
\frac{\eta_V(\lambda)}{\eta(\lambda_0)} &= \cos\gamma\sum_{k=0}^{\infty}C_1^{(2k+1)}\Delta\lambda_H^{*\,2k+1}\frac{\partial^{2k+1}}{\partial\lambda^{2k+1}}\phi(\lambda-\lambda_0),
\end{aligned} \tag{4.11}$$

where $\phi(\lambda-\lambda_0)$ is the profile of η_I in the absence of a magnetic field (λ_0 being the line centre wavelength), $\eta(\lambda_0)\phi(0)$ is the ratio of the absorption coefficient at line centre to the continuous absorption coefficient, again in the absence of a magnetic field. The coefficients $C_0^{(k)}$ and $C_1^{(k)}$ can be written in terms of the moments $\mu_n^{(i)}$ of the π and σ components

$$C_n^{(k)} = \frac{(-1)^k}{k!}\sum_{i=0}^{k}\binom{k}{i}\frac{\mu_n^{(i)}}{(\Delta\lambda_H^*)^i}(ng_{\rm eff})^{k-i} \qquad (n=0,\pm1;\, k\geq 0). \tag{4.12}$$

The $\mu_n^{(k)}$ are defined by

$$\mu_n^{(k)} = \sum_M S_n(M,\pi/2)(\Delta\lambda_n(M) - ng_{\rm eff}\Delta\lambda_H^*)^k \qquad (n=0,\pm1;\, k\geq 0). \tag{4.13}$$

$\Delta\lambda_n(M)$ is equivalent to $v_n(M)$ in Eq. (2.23) expressed now in wavelength units, and $S_n(M,\pi/2)$ represents the normalised strength of the Zeeman components arising from the transition with $n = \Delta M$ and the initial state M. Values of $S_n(M,\pi/2)$ can be determined from Table 2.1 after using Eq. (2.15). The $\mu_n^{(k)}$ satisfy the general properties

$$\mu_{-1}^{(k)} = (-1)^k\mu_1^{(k)} \tag{4.14}$$

and

$$\mu_0^{(2k+1)} = 0. \tag{4.15}$$

Values for the first few $\mu_n^{(k)}$ are listed below

$$\begin{aligned}
\mu_n^{(0)} &= 1 && (n=0,\pm1),\\
\mu_n^{(1)} &= 0 && (n=0,\pm1),\\
\mu_n^{(2)} &= X_n(g_u-g_l)^2\Delta\lambda_H^{*\,2} && (n=0,\pm1),\\
\mu_n^{(3)} &= nY_1(g_u-g_l)^3\Delta\lambda_H^{*\,3} && (n=0,\pm1),
\end{aligned} \tag{4.16}$$

where

$$\begin{aligned}
X_0 &= (3s-d^2-2)/10,\\
X_1 &= (8s-d^2-12)/80,\\
Y_1 &= d(4-d^2)/160,
\end{aligned} \tag{4.17}$$

with

$$\begin{aligned}
s &= J_u(J_u+1)+J_l(J_l+1),\\
d &= J_u(J_u+1)-J_l(J_l+1).
\end{aligned} \tag{4.18}$$

These formulae are completely symmetrical with respect to the interchange of u and l ($J_u, g_u \rightarrow J_l, g_l$). General expressions for the calculation of $\mu_0^{(k)}$, $\mu_1^{(k)}$ as well as $C_0^{(k)}$, $C_1^{(k)}$ have been derived by Mathys and Stenflo (1987a), while Mathys and Stenflo (1987b) have tabulated $\mu_0^{(k)}$, $\mu_1^{(k)}$, $C_0^{(k)}$, and $C_1^{(k)}$ for $k=0,\ldots,8$ and for a wide variety of transitions.

Since for solar magnetic fluxtubes the weak field approximation is in general satisfied, we can restrict ourselves to terms with $k \leq 2$ in Eq. (4.11)

$$\begin{aligned}
\frac{\eta_I(\lambda)}{\eta(\lambda_0)} &\approx \phi(\lambda-\lambda_0)+\frac{1}{4}\left\{\mu_0^{(2)}\sin^2\gamma+\left[\mu_1^{(2)}+\Delta\lambda_H^2\right](1+\cos^2\gamma)\right\}\frac{\partial^2}{\partial\lambda^2}\phi(\lambda-\lambda_0),\\
\frac{\eta_Q(\lambda)}{\eta(\lambda_0)} &\approx \frac{1}{4}\sin^2\gamma\cos 2\varphi\left[\mu_0^{(2)}-\mu_1^{(2)}-\Delta\lambda_H^2\right]\frac{\partial^2}{\partial\lambda^2}\phi(\lambda-\lambda_0),\\
\frac{\eta_U(\lambda)}{\eta(\lambda_0)} &\approx \frac{1}{4}\sin^2\gamma\sin 2\varphi\left[\mu_0^{(2)}-\mu_1^{(2)}-\Delta\lambda_H^2\right]\frac{\partial^2}{\partial\lambda^2}\phi(\lambda-\lambda_0),\\
\frac{\eta_V(\lambda)}{\eta(\lambda_0)} &\approx -\cos\gamma\Delta\lambda_H\frac{\partial}{\partial\lambda}\phi(\lambda-\lambda_0).
\end{aligned} \tag{4.19}$$

Except for the sign, the expression for η_V in Eq. (4.19) is very similar to the expression for Stokes V given by Eq. (4.9). The difference in sign between η_V and Stokes V is due to the fact that we are dealing with absorption lines and that therefore the absorption coefficient for right circularly polarized radiation corresponds to the emergent profile for left circularly polarized radiation. The comparison of η_V to V allows us to extend the definition of the I_V profile to general values of γ. The absence of terms due to the anomalous Zeeman effect in the expression for η_V (since $\mu_n^{(1)}=0$, cf. Eq. (4.16)) means that the simple exression for the I_V profile Eq. (4.10) originally derived only for Zeeman triplets is equally valid for lines with an anomalous Zeeman splitting pattern, if we replace the Landé factor g of the triplet by the effective Landé factor $g_{\rm eff}$ in $\Delta\lambda_H$. Thus we can write in general

$$\frac{I_c-I_V}{I_c} = -\frac{1}{\cos\gamma\Delta\lambda_H}\int_{\lambda_1}^{\lambda}\frac{V(\lambda')}{I_c}\,\mathrm{d}\lambda'. \tag{4.20}$$

Eq. (4.19) also allows I_Q and I_U profiles to be defined by putting $\eta_Q \rightarrow Q$, $\eta_U \rightarrow U$, $\phi \rightarrow I$, and integrating over the wavelength.

$$\begin{aligned}
\frac{I_c-I_Q}{I_c} &= -\frac{4}{\sin^2\gamma\cos 2\varphi(\Delta\lambda_H^2-\mu_0^{(2)}+\mu_1^{(2)})}\int_{\lambda_1}^{\lambda}\int_{\lambda_1'}^{\lambda'}\frac{Q(\lambda'')}{I_c}\,\mathrm{d}\lambda''\,\mathrm{d}\lambda',\\
\frac{I_c-I_U}{I_c} &= -\frac{4}{\sin^2\gamma\sin 2\varphi(\Delta\lambda_H^2-\mu_0^{(2)}+\mu_1^{(2)})}\int_{\lambda_1}^{\lambda}\int_{\lambda_1'}^{\lambda'}\frac{U(\lambda'')}{I_c}\,\mathrm{d}\lambda''\,\mathrm{d}\lambda'.
\end{aligned} \tag{4.21}$$

$\lambda_1' = \lambda_1$ should again be chosen far enough in the wing for $Q \approx U \approx 0$. For these profiles, the terms due to the anomalous Zeeman effect do play a role. Therefore I_Q profiles calculated without taking anomalous Zeeman

splitting into account (e.g. using the formula derived by Stenflo, 1985) will differ accordingly from corresponding I_Q profiles calculated using Eq. (4.21). There are some further problems with the I_Q and I_U profiles which make them of questionable use for application to real data. These problems will be discussed in Sect. 4.2.3.

4.2.3. Effects of Saturation on Stokes Q, U, and V: The I_V Profile for Saturated lines

Since Stokes Q and U are identical except for their different dependence on the azimuth φ, it is sufficient to consider only Stokes Q and V in this section. In Fig. 4.1 the Q profile of the medium strong line Fe I 5250 Å, calculated with the HSRA for $\gamma = 90°$, $\varphi = 0°$ and $B = 10$ G, is plotted. Although the weak field approximation is valid ($B = 1$ G still gives the same profile shape), it is clear, that since the area of the profile above the zero-line is not equal to the area below the zero-line, the continuum will lie at different levels on the blue and red side of I_Q. For such a large asymmetry between the areas of the σ and π components as exhibited by this Q profile (with $A_{\sigma_b} + A_{\sigma_r} > 2A_\pi$, these quantities are defined below), I_Q will not look even faintly similar to I. This effect is *not* due to velocity gradients, or unequally populated Zeeman sublevels as required to explain Stokes V asymmetry [The Stokes Q profile fulfills the symmetry relation Eq. (2.57)]. Rather, it is due to a combination of the Zeeman splitting and the saturation in the line.

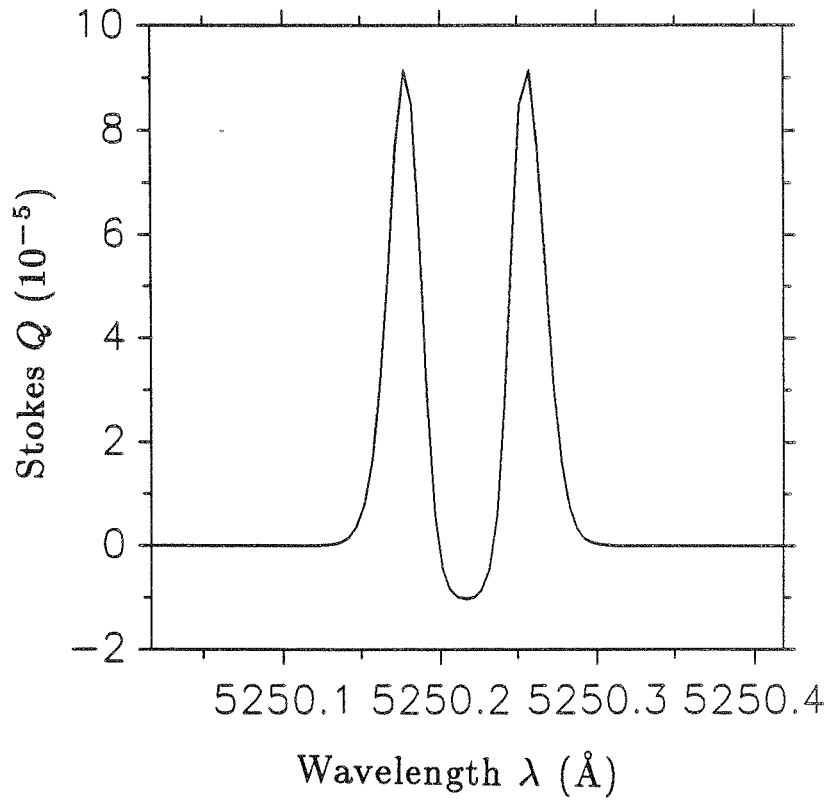

Fig. 4.1 The Stokes Q profile of Fe I 5250.2 Å, as calculated using the HSRA model atmosphere and a magnetic field vector given by $\gamma = 90°$, $\varphi = 0°$, $B = 10$ G. Note the difference in area between the π- and σ-components.

The same effect also gives rise to the broad-band linear polarization in active regions and sunspots, as was first measured by Leroy (1962), who also found the correct interpretation for his observations by considering the Unno solution for Stokes Q. Calamai et al. (1975) extended his analysis to include magnetooptical effects (by using Rachkovsky's solution).

However, the discussion of broadband polarization fails to make clear that the σ-π asymmetry of Stokes Q persists even for small field strengths, since the integrated quantity which is important for broadband linear polarization

$$\int Q \, d\lambda \to 0 \qquad \text{for} \quad B \to 0, \tag{4.22}$$

i.e. the absolute σ-π asymmetry disappears for small magnetic field strengths. However, the relative asymmetry,

defined as

$$\delta Q = \frac{A_{\sigma_b} + A_{\sigma_r} - A_\pi}{A_{\sigma_b} + A_{\sigma_r} + A_\pi} = \frac{\int Q \, \mathrm{d}\lambda}{\int |Q| \, \mathrm{d}\lambda} \tag{4.23}$$

does not disappear, as Fig. 4.1 and the following Milne-Eddington calculations show. A_{σ_b} is the absolute area of the blue σ-component of Stokes Q, A_{σ_r} the area of its red σ-component, and A_π the area of its π-component.

For simplicity, we assume that $\gamma = 90°$, $\varphi = 0°$, and a weak field, i.e. $\eta_I \gg \eta_Q$ and $\eta_U = \eta_V = 0$. No principle limitations exist to extend these calculations to a more general case. However, no qualitatively new results are obtained. It is also better to consider the general case with a proper radiative transfer code than with the simple Unno formalism. The magnetooptical effects are minute for the weak field case (cf. chapter 2), and can be neglected (for $\gamma = 0°$ they disappear anyway). Then

$$Q = -\frac{\beta_0 \mu}{1 + \beta_0 \mu} \frac{\eta_Q}{(1 + \eta_I)^2 - \eta_Q^2}. \tag{4.24}$$

We have normalised Q to the local continuum level. Using Eq. (2.42), we can rewrite Eq. (4.24) as

$$Q = -\frac{\beta_0 \mu}{1 + \beta_0 \mu} \frac{\eta_Q}{(1 + \eta_0)^2 \left(1 - \frac{2\eta_Q}{1+\eta_0}\right)} \approx -\frac{\beta_0 \mu}{1 + \beta_0 \mu} \frac{\eta_Q}{(1 + \eta_0)^2}, \tag{4.25}$$

since $(1 + \eta_0) \gg 2\eta_Q$. Using Eq. (4.19) and the fact that the Unno solution is only valid for Zeeman triplets we get

$$Q(\lambda) \approx -\frac{\beta_0 \mu}{1 + \beta_0 \mu} \frac{1}{4} \frac{\Delta\lambda_H^2}{(1 + \eta_0(\lambda))^2} \frac{\mathrm{d}^2 \eta_0(\lambda)}{\mathrm{d}\lambda^2}. \tag{4.26}$$

It is the $\eta_0(\lambda)$ in the denominator, which leads to the asymmetry even in the case of a weak magnetic field. Since we can assume that $\eta_0(\lambda)$ has the form of a Voigt function centred on the line, the denominator is larger for line centre, which reduces the area of the π component, leading to the observed asymmetry. For very weak lines $\eta_0(\lambda) \ll 1$ for all λ, so that

$$Q(\lambda) \approx -\frac{\beta_0 \mu}{1 + \beta_0 \mu} \Delta\lambda_H^2 \frac{\mathrm{d}^2 \eta_0(\lambda)}{\mathrm{d}\lambda^2}. \tag{4.27}$$

To test the validity of the I_Q profile for a saturated line we require a relation between $\mathrm{d}^2 I/\mathrm{d}\lambda^2$ and $\mathrm{d}^2\eta_0(\lambda)/\mathrm{d}\lambda^2$. We start with the Unno solution for weak fields.

$$I(\lambda) \approx \frac{\beta_0 \mu}{1 + \beta_0 \mu} \left(1 - \frac{1}{(1 + \eta_0(\lambda))}\right). \tag{4.28}$$

Then

$$\frac{\mathrm{d}I}{\mathrm{d}\lambda} \approx \frac{\beta_0 \mu}{1 + \beta_0 \mu} \frac{1}{(1 + \eta_0(\lambda))^2} \frac{\mathrm{d}\eta_0(\lambda)}{\mathrm{d}\lambda} \tag{4.29}$$

and

$$\frac{\mathrm{d}^2 I}{\mathrm{d}\lambda^2} \approx -\frac{\beta_0 \mu}{1 + \beta_0 \mu} \left(\frac{2}{(1 + \eta_0(\lambda))^3} \left(\frac{\mathrm{d}\eta_0(\lambda)}{\mathrm{d}\lambda}\right)^2 - \frac{1}{(1 + \eta_0(\lambda))^2} \frac{\mathrm{d}^2 \eta_0(\lambda)}{\mathrm{d}\lambda^2} \right). \tag{4.30}$$

If we use Eq. (4.30) to replace $\mathrm{d}^2\eta_0(\lambda)/\mathrm{d}\lambda^2$ in Eq. (4.26), then we get not only a $\mathrm{d}^2 I/\mathrm{d}\lambda^2$ term, but also a $(\mathrm{d}\eta_0/\mathrm{d}\lambda)^2$ term. For very weak lines, i.e., $\eta_0 \ll 1 \quad \forall\lambda$, Eq. (4.30) reduces to

$$\frac{\mathrm{d}^2 I}{\mathrm{d}\lambda^2} \approx \frac{\beta_0 \mu}{1 + \beta_0 \mu} \frac{\mathrm{d}^2 \eta_0(\lambda)}{\mathrm{d}\lambda^2}. \tag{4.31}$$

By combining Eq. (4.31) with (4.27) we get

$$Q(\lambda) \approx -\frac{1}{4} \Delta\lambda_H^2 \frac{\mathrm{d}^2 I(\lambda)}{\mathrm{d}\lambda^2}. \tag{4.32}$$

Thus, Eq. (4.21) is only valid for very weak (i.e. unsaturated) spectral lines (the weak field limit is a prerequisit of Eq. (4.21) in any case). We therefore conclude that the I_Q and I_U profiles are not of practical use, since most

lines of interest show at least some saturation. For larger fields the η_Q, η_U, and η_V terms in the denominator of Eq. (4.26) also play a role and modify δQ. They also lead to a certain γ dependence of the effect.

How can the Stokes Q asymmetry be understood intuitively? In the presence of a magnetic field, the two equally polarized σ components are shifted so that due to saturation their combined area is somewhat larger than that of the π component. The larger the splitting ($\sim B$), the larger the absolute asymmetry will be. However, the amount by which σ or π cancel each other in Q decreases with increasing B. This has the result that for small magnetic field values most of the signal cancels, so that the small *absolute* asymmetry between σ and π dominates the resulting signal, thus leading to a large *relative* asymmetry. For strong fields both the absolute and the relative asymmetry should approach asymptotic values depending only on the amount of saturation in the line.

Concrete calculations, including magnetooptical effects, for the Fe I 5250.2 Å line with a radiative transfer code have also been carried out and have confirmed the dependences suggested by the analytical and heuristic considerations presented above. Fig. 4.2 shows δQ vs. B for 5250.2 Å with $\log g^* f = -4.938$ (solid curve, the $g^* f$ value measured by Blackwell, Ibbetson, Petford, and Shallis, 1979) and $\log g^* f = -5.938$ (dashed curve). The abundance is the same for all three curves: $\epsilon = 7.5$. As is clearly visible from the figure, a decrease in $\log g^* f$ also results in a decrease in δQ. The figure also demonstrates the dependence of δQ on B (for $g = 3$).

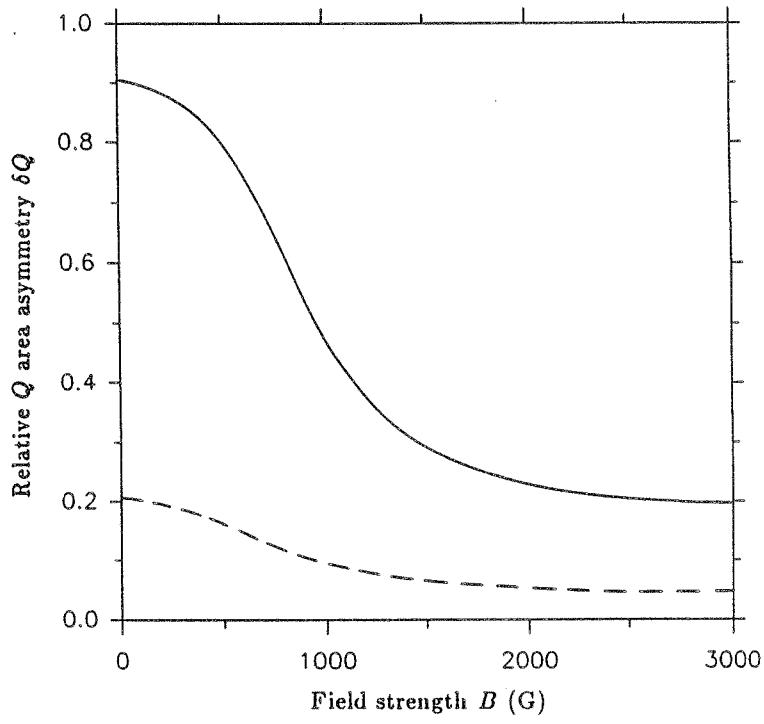

Fig. 4.2 The relative asymmetry between the summed areas of the σ- and π-components of Stokes Q, δQ, plotted vs. the field strength B. The two curves represent Fe I 5250.2 Å (solid), and a hypothetical variant of this line with the $g^* f$ value reduced by a factor of 10 (dashed).

Since the two sigma components are completely equivalent with respect to saturation in a static atmosphere, the Stokes V profile suffers no similar consequences, so that I_V can be calculated without any problems for lines of any amount of saturation. This can also be shown very simply with the Unno model for weak fields.

Comparing Eq. (4.29), which is valid for all angles in a weak field, with the weak field approximation of the Unno solution for Stokes V

$$V \approx -\frac{\beta_0 \mu}{1 + \beta_0 \mu} \frac{\eta_V}{(1 + \eta_0)^2} \tag{4.33}$$

and using Eq. (4.19), where we replace $\phi(\lambda - \lambda_0)$ by $\eta_0(\lambda)$, we get

$$V = \Delta\lambda_H \frac{\mathrm{d}I}{\mathrm{d}\lambda}. \tag{4.34}$$

We conclude that the definition of the I_V profile is *not* affected by saturation in the spectral line.

4.2.4. The I_V Profile for Real Data

A first test of the validity of the I_V profile for real data was carried out by Stenflo et al. (1984) when they compared the observed $\partial I/\partial\lambda$ and Stokes V profiles with each other for a number of lines. An example is shown in Fig. 4.3, where the Na I D_1 line at 5895.93 ($g_{\rm eff} = 1.33$) is used. $-\partial I/\partial\lambda$ (thick line) has been normalised so that its blue peak coincides with the blue peak of Stokes V.

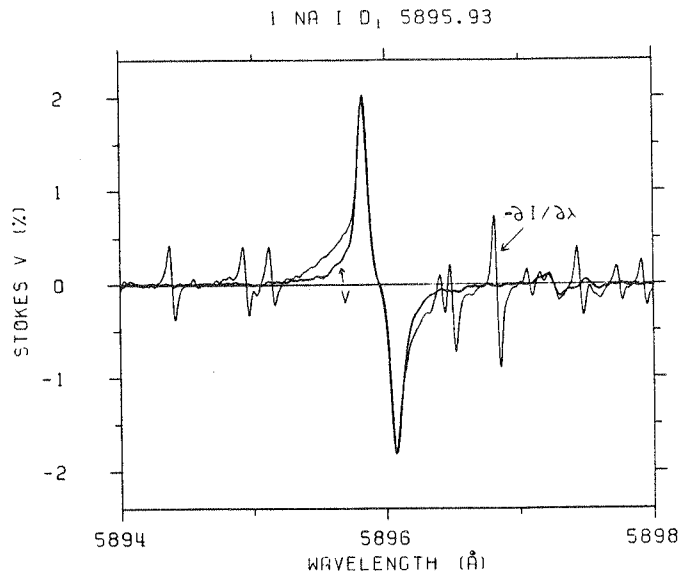

Fig. 4.3 Stokes V (thick curve) and $-\partial I/\partial\lambda$ (thin curve) of Na I D_1 recorded in a strong plage at $\mu = 0.92$. $-\partial I/\partial\lambda$ has been normalised to the same amplitude as Stokes V of the Na line. Notice the strong water vapour components in $-\partial I/\partial\lambda$ which are absent in Stokes V.

Except for the far wings of the line (where V is smaller than $-\partial I/\partial\lambda$), both profiles are identical. Stenflo et al. proposed that water vapour may be the cause of this difference. Another possible explanation is that due to the higher temperature in the fluxtube (cf. chapter 5), the strength of the line in the fluxtube is smaller than its strength in the quiet atmosphere. For a line as strong as Na I D_1 this would mostly result in a decrease of the line wings. It should be kept in mind that, due to the generally small filling factor, Stokes I is formed mostly outside the fluxtube.

The good agreement between $-\partial I/\partial\lambda$ and Stokes V for the Na I D_1 line is not surprising, since this line is so broad that the weak field approximation is certainly valid and any differences between the two profiles have to be due to differences in the atmospheres they are formed in (i.e. due to differences in temperature, pressure, velocity, or magnetic field). The presence of terrestrial water vapour is readily visible in the large number of H_2O lines present in $-\partial I/\partial\lambda$ but absent from Stokes V. Thus we see how a comparison between $\partial I/\partial\lambda$ and Stokes V allows telluric lines to be recognised easily by their absence in Stokes V. Of course $g_{\rm eff} = 0$ solar lines would also disappear to first order, but are so rare that they can be neglected.

More relevant examples for checking the validity of I_V are shown in Fig. 4.4, where the $-\partial I/\partial\lambda$ and Stokes V profiles of the Fe I lines at 5247.1 Å ($g_{\rm eff} = 2$) and 5250.2 Å ($g = 3$) measured in a plage region are compared to each other (thick curve: Stokes V, thin curve: $-\partial I/\partial\lambda$, which is again normalised to the blue peak of Stokes V). For the Fe I 5247.1 Å line shown on the left, the I_V and Stokes V curves match each other quite well, with the exception of the pronounced asymmetry in Stokes V, which can of course not be reproduced by $-\partial I/\partial\lambda$. In contrast to this nice correspondence, Fe I 5250.2 Å shows distinct differences between Stokes V and $-\partial I/\partial\lambda$. One interpretation of these differences would be, that due to its larger Landé factor, Fe I 5250.2 Å no longer fulfills the weak field approximation. We may thus be tempted to conclude that the weak field approximation is valid for lines with $g_{\rm eff} \leq 2$, but not for lines with $g_{\rm eff} = 3$.

Unfortunately, the Stokes I profiles inside and outside the fluxtube are not identical, (see e.g. Harvey and Livingston, 1969; Frazier and Stenflo, 1978). It is therefore not necessary for $-\partial I/\partial\lambda$ and Stokes V to overlap completely. From this we conclude that, although it is encouraging that the two profiles match each other for Fe I 5247.1 Å, this does not constitute a stringent test for the validity of the weak field approximation. A proper test would require that I and V profiles be calculated with a radiative transfer code in the same magnetic atmosphere, and the resulting I_V and I profiles be compared with each other [or more accurately the I profile calculated via Eq. (4.8a) with the I profile resulting directly from the radiative transfer]. A simple test of this kind is presented

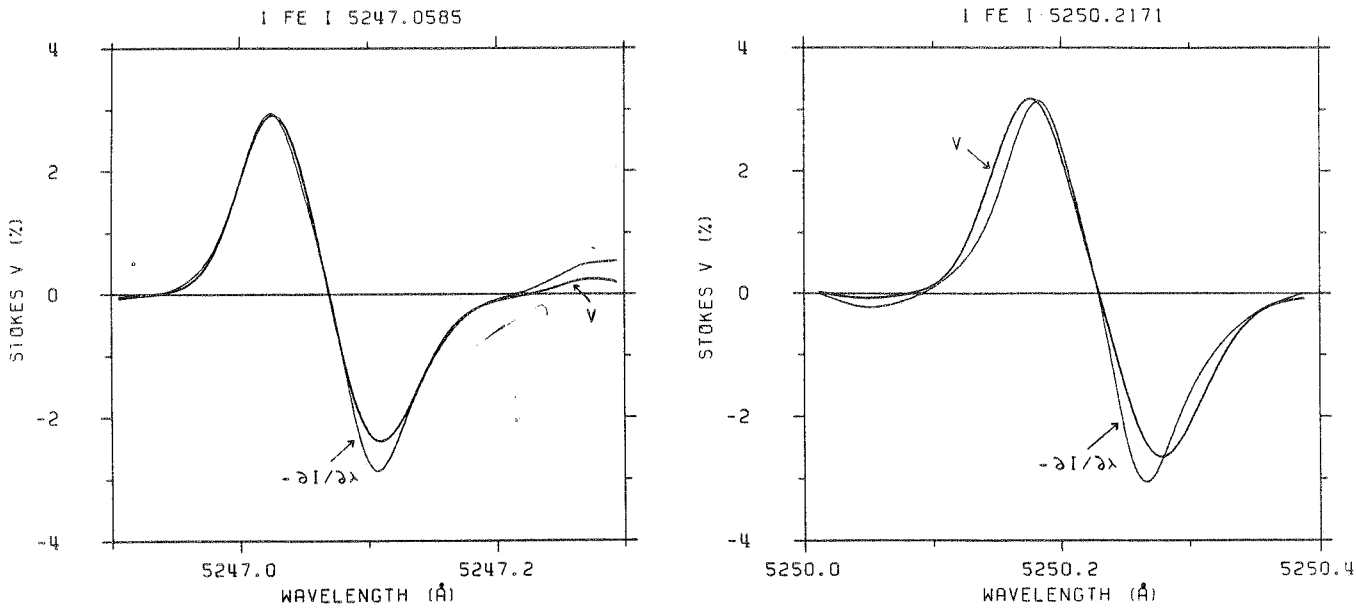

Fig. 4.4 Stokes V (thick curve) and $-\partial I/\partial\lambda$ (thin curve) of Fe I 5247.1 Å and 5250.2 Å from data recorded in a strong plage ($\mu = 0.92$). The $-\partial I/\partial\lambda$ curves have been normalised such that the amplitudes of their blue wings are the same as of those of Stokes V.

in Sect. 4.2.6. For the present we shall concentrate on the actual calculation of I_V from the observations and on its interpretation. We shall follow the discussion given by Solanki and Stenflo (1984, 1985) and Solanki (1986).

Since most fluxtubes have diameters below the best presently available spatial resolution, and our observations of 10″ (respectively 5″) resolution probably contain more than one fluxtube in the resolution element, we have to replace the different quantities in Eq. (4.20) by their spatial averages. Stokes V has to be replaced by $\langle V\rangle$ and $B\cos\gamma$ by $\langle B\cos\gamma\rangle$. For a simple two-component model of a magnetic region, composed of a magnetic component with no horizontal variations and with field strength B covering a fraction α (the magnetic filling factor) of the surface, and field free regions covering a fraction $(1-\alpha)$, we have $\langle B\cos\gamma\rangle = \cos\gamma\,\alpha B$ and $\langle V\rangle = \alpha V$, so that $\langle I_V\rangle = I_V$. In a more realistic model $\langle V\rangle$ can be written as

$$\langle V\rangle = \frac{\iint V(x,y)\,\mathrm{d}x\,\mathrm{d}y}{\iint \mathrm{d}x\,\mathrm{d}y} \approx 4.67\times10^{-13} g\lambda^2 \left\langle B(x,y)\cos\gamma\,\frac{\partial I_V(x,y)}{\partial\lambda}\right\rangle, \tag{4.35}$$

where x and y are coordinates in the plane perpendicular to the line of sight. We can also write Eq. (4.35) as

$$\langle V\rangle \approx 4.67\times10^{-13} g\lambda^2 \langle B\cos\gamma\rangle \frac{\partial\langle I_V(x,y)\rangle}{\partial\lambda} = \langle\Delta\lambda_H\cos\gamma\rangle\frac{\partial\langle I_V(x,y)\rangle}{\partial\lambda}, \tag{4.36}$$

with

$$\langle B\cos\gamma\rangle = \frac{\iint B(x,y)\cos\gamma(x,y)\,\mathrm{d}x\,\mathrm{d}y}{\iint \mathrm{d}x\,\mathrm{d}y} \tag{4.37}$$

and

$$\langle I_V\rangle \approx \frac{\iint B(x,y)\cos\gamma(x,y) I(x,y)\,\mathrm{d}x\,\mathrm{d}y}{\iint B(x,y)\cos\gamma(x,y)\,\mathrm{d}x\,\mathrm{d}y}. \tag{4.38}$$

($\langle B\cos\gamma\rangle$ is proportional to the magnetic flux), and we can retrieve Eq. (4.20) if we replace V by $\langle V\rangle$, $B\cos\gamma$ by $\langle B\cos\gamma\rangle$, and I_V by $\langle I_V\rangle$. Note that I occurs without index V under the integral sign in Eq. (4.38), since it is weighted by B. According to Eq. (4.38) the I_V profile obtained from Eq. (4.20) can be interpreted as a weighted average of the true Stokes I profile over the fluxtube cross-section. Regions which have a stronger magnetic field give a larger contribution, since Stokes V scales approximately linearly with $B\cos\gamma$, (exactly linearly in the weak-field approximation), it follows directly from Eq. (4.38) that $\langle I_V\rangle$ gets no contributions from a field free region where $V = 0$. $B(x,y)$ and $\langle B\rangle$ refer to the field strength at the height of maximum contribution to the line. We assume that B does not vary too strongly over the height range of formation of the line. Of course, for a realistic fluxtube geometry many lines of sight will pass through both magnetic and non-magnetic parts of the

atmosphere, and the simple interpretation given above to the I_V profile loses its meaning, since for a particular ray $B(x,y)$ can vary rapidly over small distances along the line of sight. The validity of the I_V profile will in this case have to be checked numerically using a 2-D model and radiative transfer along many lines of sight.

In addition to this averaging over the resolution element, the Stokes V and therefore the I_V profiles are also averaged over the time span of the measurement, over which period individual fluxtubes may have evolved or moved. For most of the following analysis we will use the symbols B, $\langle B \rangle$, $\Delta\lambda_H$, $\langle \Delta\lambda_H \rangle$, $\cos\gamma$, $\langle \cos\gamma \rangle$, $\langle I_V \rangle$, and I_V as representing the simple two component model. However, we shall often simply refer to Stokes V or V when implying $\langle V \rangle$. Since $\langle V \rangle = \alpha V$, we can always do this except for the rare cases when the filling factor plays a direct role. In particular, as most of the following analysis depends only on the comparison between the profiles of different lines. We have also implicitely assumed that the continuum intensity inside the fluxtube is equal to the continuum intensity outside. This need not necessarily be the case and in general $\langle V \rangle = \alpha\delta_c V$, where $\delta_c = I_c^{\text{Fluxtube}} / I_c^{\text{Photosphere}}$ is the ratio of the continuum intensities of the fluxtubes to that of their surroundings if $\alpha \ll 1$. Except for the determination of α, δ_c plays no role and due to the large uncertainty in the true I_c^{Fluxtube} we set it to unity for the rest of the analysis (see also Grossmann-Doerth et al., 1987; Schüssler and Solanki, 1987, for detailed discussions).

In the derivation carried out in Sect. 4.2.1, it was assumed that the magnetic field strength remains constant with height ($B(z) = \text{constant}$). In the weak field approximation, this is equivalent to requiring that the magnetic flux remains constant with height ($\langle B(z) \rangle = \text{constant}$), so that the magnetic field strength may vary, as long as this variation is compensated by an inverse variation of the area covered by the field, and as long as $\Delta\lambda_H / \Delta\lambda_D \ll 1$ (with $\Delta\lambda_H \sim B$ and not $\sim \langle B \rangle$). This makes $\langle \Delta\lambda_H \rangle$ independent of height, and therefore also of the wavelength in the line, allowing it to be moved in front of the integration. Due to our spatial resolution of 10″, respectively 5″, which is much larger than the diameter of a fluxtube, the condition of $\langle \Delta\lambda_H \rangle$ independent of z is almost certainly fulfilled for our observations. It can only be invalidated by the presence of very large canopies with diameters much larger than the resolution element, such as the ones proposed by Giovanelli (1980). However, since practically all the lines considered in this thesis are formed below the height of the temperature minimum, $T_{\min}$, and thus below such canopies, we need not worry about their effects here.

$\langle B \rangle$ in the expression for $\langle \Delta\lambda_H \rangle$ acts as a scaling factor for the fluxtube line profiles I_V. However, the determination of $\langle B \rangle$ cannot be carried out in an unambiguous manner. Since we use Fe I and II lines for the later analysis, let us briefly consider their respective potentials for the determination of $\langle B \rangle$. The strengths of the Fe I lines are strongly temperature dependent, so that they cannot be used to determine $\langle B \rangle$ with any measure of accuracy without taking recourse to model calculations. Although Fe II lines are much less sensitive to temperature, and $\langle B \rangle$ values determined from them are also considerably less model dependent, any uncalibrated depolarization in the instrument may still falsify the values of $\langle B \rangle$ determined from Stokes V. Stenflo and Harvey (1985) have proposed a depolarization by a factor of two for our 1979 data, while later tests of the telescope, the polarisation measurement procedure for the FTS, and the Fourier inverse transformation procedure by Harvey (1985b) have not been able to detect the source of this circular depolarization. Consequently, some uncertainty in the polarization scale is unavoidable at present.

In view of these uncertainties, $\langle B \rangle$ is arbitrarily set to 1 G for all the observed regions. The derived line depths are accordingly incorrect by a factor equal to the actual value of $\langle B \rangle$. As this correction factor is the same for all the lines in a particular spectrum it does *not* affect the investigation of profiles of different lines relative to each other.

4.2.5. The Influence of the Area Asymmetry of Stokes V on I_V

As is clearly visible from Fig. 4.4, the observed Stokes V profiles of photospheric lines do not fulfill either of the symmetry relations Eqs. (2.57) or (2.58). Whereas the invalidity of Eq. (2.57) alone would only lead to a curved bisector of the I_V profile, the invalidity of Eq. (2.58) leads to an unphysical result, namely that the level of the continuum on the blue and red sides of I_V is different. This simply reflects the fact that Eq. (4.20) was derived for a static atmosphere and for symmetric populations of the Zeeman sub-levels, whereas the presence of an asymmetry in the areas of the Stokes V wings requires either a veloctiy gradient along the ray path, or an asymmetry in the populations (cf. Sect. 2.4.2). For more details on Stokes V asymmetry see chapter 8.

In our later analysis we wish to compare I and I_V with a minimum of bias. This requires the identical parameterisation of both spectra, which is not possible, as long as I_V shows an unphysical continuum jump. We therefore require that the continuum on both sides of the I_V profile be forced to have the same value. An

attempt to derive a version of Eq. (4.20) including the effects of a general velocity field, showed that full prior knowledge of the velocity field is needed if the asymmetry of Stokes V is to be properly compensated. This is obviously unfeasable. An alternative to this approach is to write Eq. (4.20) as

$$\frac{I_c - I_V(\lambda)}{I_c} = -\frac{1}{\cos\gamma\,\langle\Delta\lambda_H\rangle}\int_{\lambda_1}^{\lambda}\frac{\omega(\lambda')\,\langle V(\lambda')\rangle}{I_c}\,\mathrm{d}\lambda', \tag{4.39}$$

where $\omega(\lambda)$ is a weighting function required to make the continuum on the red and blue sides of I_V lie at the same level. Since the detailed mechanism giving rise to the asymmetry is not known, a very simple form of $\omega(\lambda)$ has been chosen,

$$\begin{aligned} \omega(\lambda) &= \sqrt{A_r/A_b} \qquad \text{for} \quad \lambda < \lambda_V, \\ \omega(\lambda) &= \sqrt{A_b/A_r} \qquad \text{for} \quad \lambda > \lambda_V, \end{aligned} \tag{4.40}$$

where λ_V is the zero-crossing wavelength of Stokes V and A_b and A_r are the areas of the blue and red wings of Stokes V respectively, defined in Sect. 4.4.1. In practice the two steps, integration and symmetrisation, are carried out separately, which is made possible by the simple form of the chosen $\omega(\lambda)$.

Fig. 4.5 shows the effect of this procedure on the Stokes V profile of Fe I 5250.2 Å observed in a network element. First Stokes V (left) is integrated (centre) and then corrected for the continuum discontinuity (right). From now on I_V will always denote the integrated and symmetrised V profile.

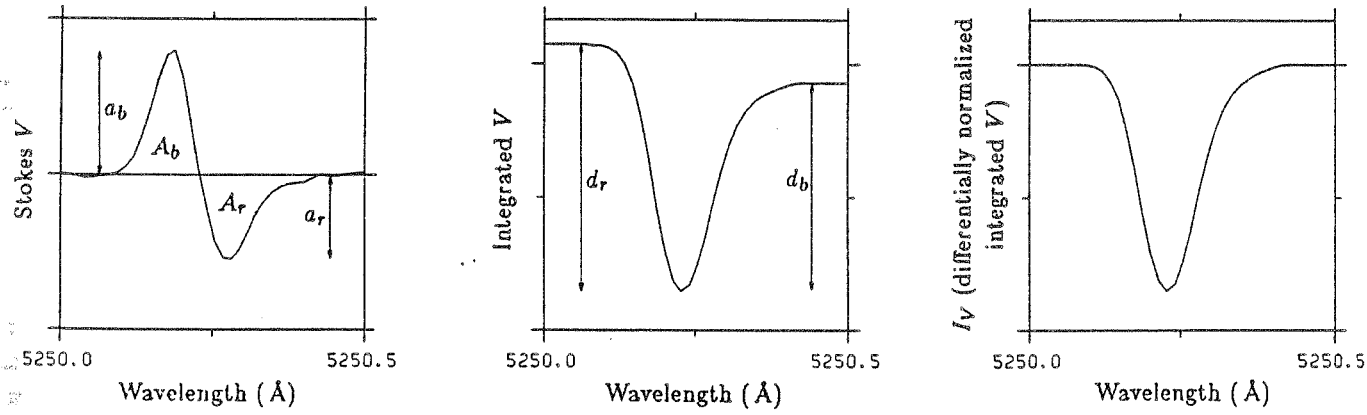

Fig. 4.5 Illustration of the transformation of a Stokes V profile into an I_V profile for the Fe I 5250.2 Å line measured in a network element. Left: Asymmetric V profile. A_b and A_r are the areas of the blue and red wings of V, respectively, while a_b and a_r are their amplitudes. Centre: Integrated V profile (before differential renormalization). d_b and d_r are the line depths measured from the blue and the red continuum, respectively. Right: I_V profile, i.e., integrated V after differential renormalization such that the continuum appears at a single level (see text).

Why carry out this conversion to I_V at all? The main reason has already been stated: in order to be able to treat the Stokes V profile on an equal basis to the Stokes I profile. The I_V profile also has certain advantages over the Stokes V profile when low spatial resolution polarimeter data are compared with *one-dimensional* fluxtube models, as is the case in a large portion of this work. Since our observations have low spatial resolution, the assumption that the magnetic flux in the field of view is the same at all heights in the photosphere is quite reasonable. For the model calculations we use the thin fluxtube approximation (cf. Sect. 4.5), which also conserves magnetic flux with height. However, the radiative transfer is carried out along only one ray (at disk centre this is the axis of the fluxtube). This one-line-of-sight approximation means that the magnetic flux as felt by the spectral lines, is not conserved with height in the model calculations. Due to the great sensitivity of the Stokes V amplitude on the amount of magnetic flux, synthetic Stokes V profiles of lines formed at different heights cannot be simultaneously compared with the respective observed profiles, so that one of the main advantages of FTS data (the large number of observed lines) is lost. With the I_V profile this problem is greatly reduced, since the data can now be compared to calculated profiles of Stokes I which are considerably less sensitive to the amount of magnetic flux.

4.2.6. How Well Does the Integrated V Profile Approximate Stokes I

The validity of the I_V profile as an approximation of the Zeeman unbroadened Stokes I profile has been tested by carrying out radiative transfer calculations for lines with varying Landé factors. I_V is determined from the synthetic Stokes V profiles and compared to the respective Stokes I profiles. The HSRA (Gingerich et al., 1971) with a height independent magnetic field of 1000 G is chosen as model atmosphere. This value of B is in accordance with the field strength determined from the line ratio analysis of chapter 6.

Six spectral lines have been calculated, all of which have the same line parameters as Fe I 5250.2 Å (cf. Table 4.4), except for the Landé factors. J, L, and S have been chosen such that all lines are Zeeman triplets and have $g = 0.5, 1.0, 1.5, 2.0, 2.5$, and 3.0 respectively. The calculations have been carried out for $\mu = 1$ and $\gamma = 0°$. In a first step, a microturbulence of 1 km sec^{-1} has been chosen as the only source of non-thermal, non-magnetic broadening.

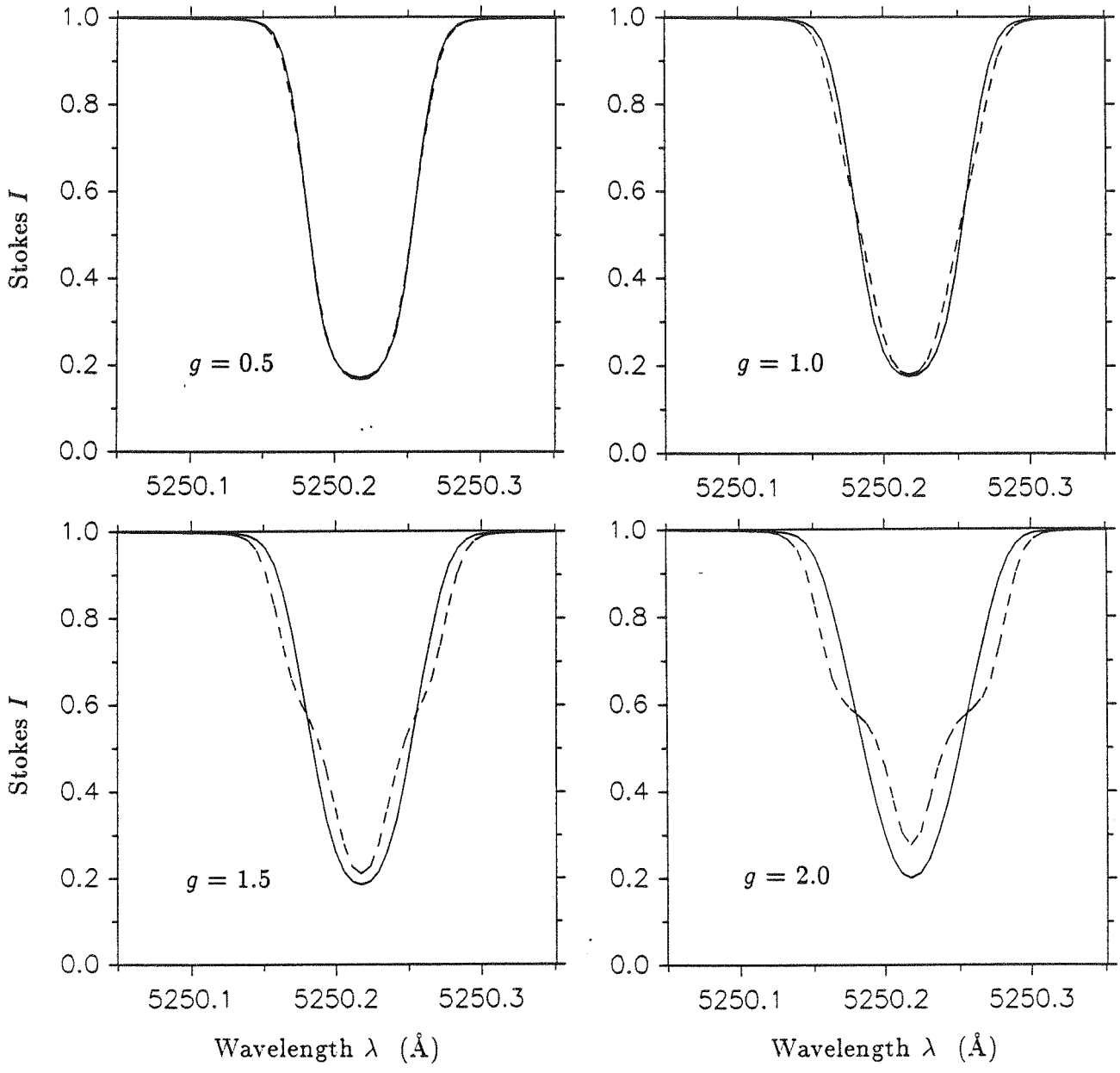

Fig. 4.6 Comparison between calculated I_V (solid) and Stokes I (dashed) profiles. The different lines are Zeeman triplets and have Landé factors $g = 0.5, 1.0, 1.5$, and 2.0 as marked in the individual figures. Otherwise all lines are identical. The model atmosphere is the HSRA with $B = 1000$ G = constant, $\xi_{\rm mic} = 1.0$ km sec^{-1} and $\xi_{\rm mac} = 0$.

First we compare I_V with the complete I profile as calculated directly by the code (i.e. including Zeeman splitting). Fig. 4.6 shows the calculated I_V (solid curves) and Stokes I (dashed curves) profiles of the lines with $g = 0.5, 1.0, 1.5$, and 2.0. The correspondence is quite good for small g values, but for $g = 1.5$ and 2.0 the I_V profile becomes of questionable use. The fits for $g = 2.5$ and 3.0 are even worse. However, so far we have neglected both, line broadening due to macroturbulence and the fact that we have to take Zeeman broadening into account via Eq. (4.7a). In accordance with the results of chapter 7 for lines of similar strength, we have in a second step convoluted the calculated line profiles with a macroturbulence velocity of 2 km $\sec^{-1}$ and have used Eq. (4.7a) to convert the I_V profile into what we call $I(V)$, which is an approximation of Stokes I. The resulting profiles are shown in Fig. 4.7. The directly calculated Stokes I profile is plotted solid, the I_V profile is plotted dashed, and the $I(V)$ profile is plotted dotted. The correspondence has improved considerably so that we can use the $I(V)$ profile as an approximation of Stokes I for $g \leq 2.5$ certainly, and perhaps even for larger g. Therefore, $I(V)$ is a good representation for practically all lines in the visible, or equivalently, I_V is a good approximation to the unsplit Stokes I profile for all lines in the visible.

Since most lines in the sample we shall use for a statistical analysis have g of the order of 1 (Stenflo and Lindegren, 1977), we conclude that the I_V profile may be used as a representation of the I profile in fluxtubes for all except a few of the lines. It should be noted that by making use of regression equations which take the effect of Zeeman splitting into account we effectively reduce all lines to the case of very small Zeeman splitting for those parts of the analysis in this thesis which make use of the I_V profile. Furthermore, by looking at the deviation of the I_V profile from Stokes I we can also learn something on the nature of the small spurious effects we may expect from using the I_V profile for lines with large splitting. Note that in general the I_V profile is narrower and deeper than the corresponding I profile. Since we take I_V profiles from the data and compare them to Stokes I profiles from radiative transfer calculations, we would therefore expect the observed profiles to be too narrow rather than too broad. Thus velocities would tend to be *underestimated.* Furthermore, the observed profiles would tend to be slightly too deep, so that the temperature would also tend to be underestimated, although only by a small amount. In any case, deviations of I_V from Stokes I cannot explain the large velocities derived in chapter 7.

4.3. Line Lists and Landé Factors

4.3.1. Lists of Lines

In order to avoid introducing uncertainties into the analysis through the uncertainties in the measured elemental abundances, the spectrum of only one atomic species, namely iron has been analysed. It is the element giving the richest contribution to the solar spectrum, with a considerable number of Fe I and Fe II lines present. Iron also has some additional advantages as pointed out by Dravins et al. (1981). It has one predominent isotope (91.8% $_{26}Fe^{56}$) which is even-even in its proton-neutron numbers, so that its nuclear spin and thus hyperfine splitting is zero. In addition iron has a large mass, so that the thermal broadening of its spectrum is minimised, allowing for the better detection of subtle magnetic field and velocity effects on the line profile. Laboratory wavelengths are also available for many Fe I and Fe II lines (see below).

Of the various lists of unblended iron lines (e.g. Holweger, 1967; Mäckle et al., 1975; Stenflo and Lindegren, 1977; Ruland et al., 1980; Rutten and van der Zalm, 1984; Dravins and Larsson, 1984), we have used the list of 402 Fe I lines of Stenflo and Lindegren (1977), and the 54 Fe II lines of Dravins and Larsson (1984) and Dravins et al. (1986). In addition to these lines the Mg I b lines at 5172.7 Å and 5183.6 Å have been used for a part of the analysis.

Table 4.1 lists all the Fe I lines used in the analysis. The first column lists the solar wavelength in Å according to Pierce and Breckinridge (1973). For the lines not present in the tables of Pierce and Breckinridge, the wavelengths are from Moore et al. (1966). The second column gives the difference between the solar and laboratory wavelength in units of 10^{-4} Å. Laboratory wavelengths have been taken from Stenflo and Lindegren (1977), who either used the wavelengths listed by Crosswhite (1975) or calculated them from the energy levels where no wavelength measurements existed. Column 3 contains the multiplet number and column 4 the excitation potential in eV. Column 5 lists the transition (from Moore, 1972), while column 6 contains the g_{eff} values calculated in LS-coupling using Eqs. (2.11) and (2.14). The values have in general been taken directly from the

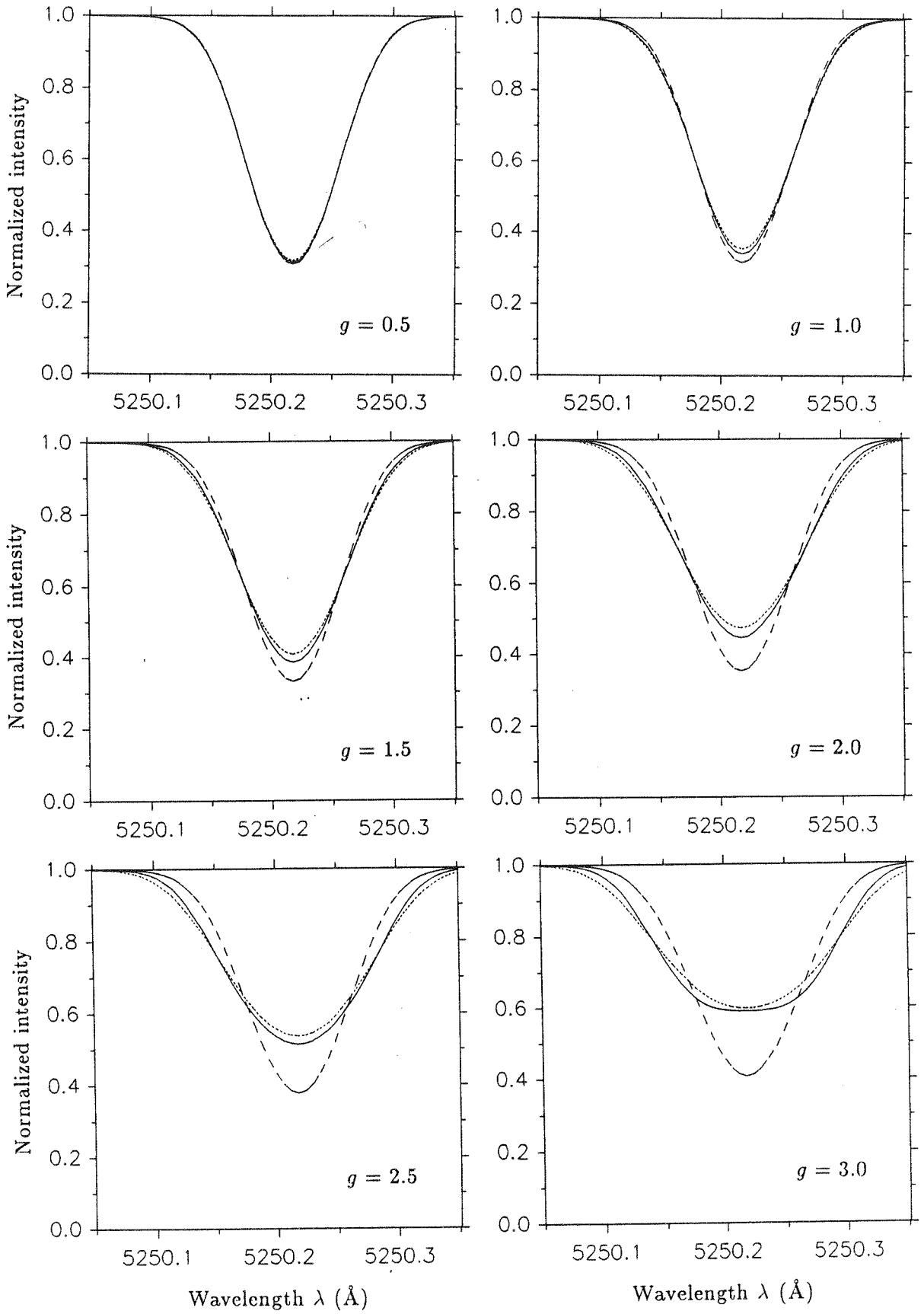

Fig. 4.7 Comparison between Stokes I (solid), I_V (long dashed), and $I(V)$ (short dashed) profiles. All lines are Zeeman triplets with Landé factors as marked in the figures. In this figure $\xi_{\rm mac} = 2$ kmsec, while the rest of the atmospheric parameters are the same as in Fig. 4.6.

table of Beckers (1969c). In column 7 the $g_{\rm eff}$ values are listed as determined from laboratory measurements of g_u and g_l for the lines for which these were available. Columns 6 and 7 are described in greater detail in Sect. 4.3.3.

In Table 4.2 the same quantities as in Table 4.1 are given for the Fe II lines chosen by Dravins and Larsson (1984) and Dravins et al. (1986). The Fe II laboratory wavelengths have been taken from Johansson (1978). For some of the Fe II lines originally chosen by Dravins and Larsson, insufficient atomic data are available to calculate their $g_{\rm eff}$ values, and these have not been included in Table 4.2 or in the further analysis.

Further useful lists of lines for solar studies have been selected by von Klüber (1947), Sistla and Harvey (1970), Harvey (1973a), and Solanki et al. (1986). Von Klüber presents brief lists of lines with large Zeeman splitting patterns, no Zeeman splittings, and simple Zeeman splittings. Sistla and Harvey give a more complete list of lines with no Zeeman splitting. Harvey lists the lines with large Zeeman splitting. Finally Solanki et al. list lines with large Stokes V amplitudes outside sunspots.

4.3.2. Noise and Blends

In order to determine the noise of the polarized signal, first the data points with $1 \geq I/I_c > 0.98$ were determined. The rms value of the Stokes V signal for these wavelengths then gives an approximate rms value of the noise (upper limit). The noise level in the data is generally low. For the data of 1979 its rms value is on the average around $2\text{–}3 \times 10^{-4}$ and can be as low as 1×10^{-4}. For the 1984 data, the levels are higher, typical values being in the range $5 \times 10^{-4}\text{–}2 \times 10^{-3}$. In the newer data, the noise increases from the red to the blue end of the spectrum by a factor of 3–4, due mainly to the deterioration of the photon statistics towards the blue. This difference between the two data sets may be due to the fact that the 1984 observations were made closer to the limb, where the spectral intensity is lower (seeing noise also increases dramatically when observing very close to the limb), and that a smaller entrance hole with a diameter of 5 arc sec was used instead of the 10 arc sec diameter hole used in 1979. A part is probably also due to the different polarization measurement instrumentation, specially the higher oscillation frequency of the piezoelectric modulator in the 1984 measurements as compared to the KD*P oscillator in the 1979 measurements. The more sophisiticated instrumental polarization compensator used for the 1984 recordings also decreases the intensity of the light beam due to the numerous reflections in it (cf. Harvey, 1985a).

Near the edge of the prefilter range (over the last 100–150 Å for the 1979 data), the noise increases and can reach values upto 0.2–0.5 % at the very edge of the 1979 data. The 1984 data show a much smaller increase in noise near the edge, due to the improved predispersor spectral profile for these data. In order to reduce the number of lines affected by noise in our data, all the lines with amplitudes of Stokes V smaller than some factor of σ of the noise are automatically dropped (typically a factor of 5 is chosen). This limit in general removes most of the lines which are heavily influenced by noise.

A few lines remain which have Stokes V amplitudes larger than this limit, but which show an untypical behaviour in the scatter plots described in Sect. 4.4. These lines have been checked and removed individually. Reasons for such untypical behaviour (besides noise) are blends, deviation from LS-coupling or a strongly anomalous Zeeman splitting. Blends make themselves felt more strongly in the I_V profile than in the Stokes I profile, because the Stokes V profile, used as the basis for calculating I_V, is in general more sensitive to blends than Stokes I (Stenflo et al., 1984), and because the complete Stokes V profile has to be integrated including the far wings. Although only few lines are completely free of blends, specially in the blue and green parts of the spectrum, the blending lines are usually quite weak and affect the Stokes V profile only slightly in the far wings. In some cases the presence of blends has required the rejection of a particular line from Tables 4.1 and 4.2. Examples are Fe I 4637.5 Å, 5022.2 Å, 5216.3 Å, and 6663.5 Å. The other two reasons for anomalous behaviour in the scatter plots are discussed in the following section.

4.3.3. Landé Factors and Anomalous Zeeman Splitting

As has been pointed out by Landi Degl'Innocenti (1982), the equation for the effective Landé factor Eq. (2.14) is also valid when LS-coupling does not apply, if the appropriate g_l and g_u values are used. Such "appropriate" values are for example, g_l and g_u from laboratory measurements, as listed by Reader and Sugar (1975), Corliss and Sugar (1982), and Litzén (1984). The empirical $g_{\rm eff}$ values for all the Fe I and II lines in the lists of Sect. 4.3.1 for which such laboratory data are available have been calculated and are given in column 7 of Tables 4.1 and 4.2 respectively. A question mark has been placed behind the empirical $g_{\rm eff}$ values of those Fe I lines for

Table 4.1 List of Fe I lines and their Landé factors

Wavelength	$\Delta\lambda$	Multiplet	χ_e	Transition	$g_{\rm eff}^{\rm LS}$	$g_{\rm eff}^{\rm emp}$
4365.9004	50	415	2.99	$b\ ^3G_4 - w\ ^3D_3^\circ$	0.625	0.601
4389.2512	67	2	0.05	$a\ ^5D_3 - z\ ^7F_2^\circ$	1.500	1.497
4423.8447	27	830	3.65	$z\ ^5P_2^\circ - e\ ^5P_2$	1.833	—
4432.5726	67	797	3.57	$a\ ^1H_5 - u\ ^3G_5^\circ$	1.100	1.070
4439.6371	31	515	3.05	$a\ ^1G_4 - x\ ^3F_3^\circ$	0.875	0.884
4439.8860	51	116	2.28	$a\ ^3P_2 - z\ ^5S_2^\circ$	1.750	1.745
4442.8357	49	69	2.18	$a\ ^5P_3 - y\ ^7P_2^\circ$	1.000	0.992
4443.1998	68	350	2.86	$b\ ^3P_0 - x\ ^3D_1^\circ$	0.500	0.556
4445.4760	55	2	0.09	$a\ ^5D_2 - z\ ^7F_2^\circ$	1.500	1.502
4447.1354	60	69	2.20	$a\ ^5P_2 - y\ ^7P_3^\circ$	2.000	1.996
4484.2266	72	828	3.60	$z\ ^5P_3^\circ - g\ ^5D_4$	1.250	1.232
4485.9708	7	825	3.65	$z\ ^5P_2^\circ - f\ ^5F_1$	2.750	—
4489.7449	60	2	0.12	$a\ ^5D_0 - z\ ^7F_1^\circ$	1.500	1.549
4502.5931	20	796	3.57	$a\ ^1H_5 - x\ ^3H_6^\circ$	1.583	1.563
4523.4015	11	829	3.65	$z\ ^5P_2^\circ - e\ ^7S_3$	2.167	2.00?
4537.6723	11	594	3.27	$b\ ^3H_5 - z\ ^1H_5^\circ$	1.017	1.025
4551.6499	8	972	3.94	$z\ ^3F_3^\circ - f\ ^5G_4$	1.250	—
4556.9275	23	638	3.25	$a\ ^3D_3 - v\ ^5P_2^\circ$	0.833	0.930
4560.0909	30	823	3.60	$z\ ^5P_3^\circ - e\ ^5G_4$	0.375	0.609
4574.2191	48	554	3.21	$z\ ^5D_4^\circ - e\ ^5F_3$	1.875	1.901
4574.7224	54	115	2.28	$a\ ^3P_2 - x\ ^5D_2^\circ$	1.500	1.503
4587.1316	36	795	3.57	$a\ ^1H_5 - x\ ^1G_4^\circ$	1.000	1.044
4593.5268	17	971	3.94	$z\ ^3F_3^\circ - f\ ^5P_2$	0.333	—
4596.4113	−26	823	3.65	$z\ ^5P_2^\circ - e\ ^5G_3$	0.000	0.753
4598.1221	44	554	3.28	$z\ ^5D_1^\circ - e\ ^5F_1$	0.750	0.751
4602.0060	58	39	1.61	$a\ ^3F_2 - y\ ^5F_1^\circ$	1.000	1.013
4602.9466	65	39	1.48	$a\ ^3F_4 - y\ ^5F_5^\circ$	1.700	1.743
4619.2932	68	821	3.60	$z\ ^5P_3^\circ - f\ ^5D_2$	1.833	1.700
4625.0514	76	554	3.24	$z\ ^5D_3^\circ - e\ ^5F_3$	1.375	1.368
4630.1258	53	115	2.28	$a\ ^3P_2 - x\ ^5D_3^\circ$	1.500	1.502
4635.8509	51	349	2.84	$b\ ^3P_1 - y\ ^5S_2^\circ$	2.250	2.087
4637.5095	61	554	3.28	$z\ ^5D_1^\circ - e\ ^5F_2$	0.750	0.739
4657.5879	26	346	2.84	$b\ ^3P_1 - w\ ^5D_1^\circ$	1.500	1.402
4658.2976	39	591	3.27	$b\ ^3H_5 - x\ ^3G_4^\circ$	1.000	0.974
4672.8364	70	40	1.61	$a\ ^3F_2 - z\ ^3P_1^\circ$	0.250	0.257
4678.8519	68	821	3.60	$z\ ^5P_3^\circ - f\ ^5D_4$	1.250	1.299
4683.5638	31	346	2.83	$b\ ^3P_2 - w\ ^5D_2^\circ$	1.500	1.515
4690.1417	63	820	3.69	$z\ ^5P_1^\circ - f\ ^7D_1$	2.750	—
4700.1590	−324	935	3.69	$b\ ^1G_4 - x\ ^3H_5^\circ$	1.100	1.156
4704.9519	48	821	3.69	$z\ ^5P_1^\circ - f\ ^5D_0$	2.500	2.487
4726.1396	23	384	3.00	$z\ ^7P_3^\circ - e\ ^5D_2$	2.333	2.313
4729.0210	37	1043a	4.07	$c\ ^3F_4 - {}^5F_5^\circ$	1.700	—
4733.5968	58	38	1.48	$a\ ^3F_4 - y\ ^5D_4^\circ$	1.375	1.375
4735.8471	53	1042	4.07	$c\ ^3F_4 - t\ ^3G_5^\circ$	1.100	1.174
4741.5341	53	346	2.83	$b\ ^3P_2 - w\ ^5D_3^\circ$	1.500	1.464
4749.9488	14	1206	4.56	$y\ ^5P_3^\circ - i\ ^5D_3$	1.583	1.538
4776.0702	12	635	3.30	$a\ ^3D_2 - y\ ^3S_1^\circ$	0.750	0.825
4779.4423	0	720	3.41	$a\ ^1P_1 - x\ ^3P_0^\circ$	1.000	0.817
4780.8132	19	633	3.25	$a\ ^3D_3 - w\ ^3D_2^\circ$	1.500	1.454
4785.9583	−8	1044	4.14	$c\ ^3F_3 - {}^5D_4^\circ$	2.125	—
4786.8127	65	467	3.02	$c\ ^3P_2 - x\ ^3D_3^\circ$	1.167	1.220
4788.7627	60	588	3.24	$b\ ^3H_6 - z\ ^3H_6^\circ$	1.167	1.182
4789.6568	69	753	3.55	$a\ ^1D_2 - z\ ^1D_2^\circ$	1.000	0.97?
4790.5627		1068	4.15	$y\ ^5D_3^\circ - f\ ^5G_2$	2.667	—
4790.7436		632	3.25	$a\ ^3D_3 - x\ ^3F_3^\circ$	1.208	1.247
4794.3571	18	115	2.42	$a\ ^3P_1 - x\ ^5D_1^\circ$	1.500	1.499
4798.2670	29	1042	4.19	$c\ ^3F_2 - t\ ^3G_3^\circ$	0.833	1.167
4798.7336	25	38	1.61	$a\ ^3F_2 - y\ ^5D_2^\circ$	1.083	1.082
4799.0698		1098	4.28	$y\ ^5F_2^\circ - f\ ^3F_2$	0.833	0.837
4799.4092	35	888	3.64	$b\ ^3D_2 - w\ ^3P_2^\circ$	1.333	—
4802.5216	−10	1206	4.61	$y\ ^5P_2^\circ - i\ ^5D_2$	1.667	—
4807.7122	41	688	3.37	$z\ ^5F_4^\circ - e\ ^3F_4$	1.300	1.321
4808.1509	42	633	3.25	$a\ ^3D_3 - w\ ^3D_3^\circ$	1.333	1.340
4809.9400	−4	793	3.57	$a\ ^1H_5 - y\ ^3H_5^\circ$	1.017	1.037
4835.8713	27	1068	4.10	$y\ ^5D_4^\circ - f\ ^5G_4$	1.325	—
4839.5500	48	588	3.27	$b\ ^3H_5 - z\ ^3H_5^\circ$	1.033	1.046
4848.8866	41	114	2.28	$a\ ^3P_2 - y\ ^3D_1^\circ$	2.000	2.012
4871.3262	90	318	2.86	$z\ ^7F_3^\circ - e\ ^7D_2$	1.000	1.017
4873.7534	8	633	3.30	$a\ ^3D_2 - w\ ^3D_2^\circ$	1.167	1.197
4874.3565	34	467	3.07	$c\ ^3P_1 - x\ ^3D_2^\circ$	1.000	1.067
4875.8815	67	687	3.33	$z\ ^5F_5^\circ - e\ ^5F_4$	1.500	1.535
4882.1484	44	687	3.42	$z\ ^5F_2^\circ - e\ ^5F_2$	1.000	0.997
4885.4361	58	966	3.88	$z\ ^3F_4^\circ - g\ ^5D_3$	0.875	0.887
4892.8624	35	1070	4.22	$y\ ^5D_1^\circ - f\ ^3D_1$	1.000	—
4907.7365	37	687	3.43	$z\ ^5F_1^\circ - e\ ^5F_2$	1.500	1.492
4909.3874	34	985	3.93	$z\ ^3D_2^\circ - g\ ^5D_2$	1.333	1.37?
4910.0222	72	687	3.40	$z\ ^5F_3^\circ - e\ ^5F_3$	1.250	1.243
4911.7808	20	984	3.93	$z\ ^3D_2^\circ - e\ ^3D_1$	1.500	1.351
4918.0152	41	1070	4.23	$y\ ^5D_0^\circ - f\ ^3D_1$	0.500	—
4938.8209	84	318	2.87	$z\ ^7F_2^\circ - e\ ^7D_3$	2.000	2.006

Wavelength	Δλ	Multiplet	χ_e	Transition	$g_{\text{eff}}^{\text{LS}}$	$g_{\text{eff}}^{\text{emp}}$
4939.6931	71	16	0.86	$a\ ^5F_5 - z\ ^5F_4^\circ$	1.500	1.491
4945.6390	25	1113	4.21	$z\ ^3P_2^\circ - f\ ^5G_3$	0.333	0.791
4946.3941	92	687	3.37	$z\ ^5F_4^\circ - e\ ^5F_4$	1.350	1.343
4950.1108	67	687	3.42	$z\ ^5F_2^\circ - e\ ^5F_3$	1.500	1.468
4962.5756	205	1097	4.18	$y\ ^5F_5^\circ - e\ ^3H_6$	0.583	0.745
4969.9228	71	1066	4.22	$y\ ^5D_1^\circ - h\ ^5D_1$	1.500	—
4979.5881		883	3.64	$b\ ^3D_2 - w\ ^3F_2^\circ$	0.917	—
4982.5063	86	1067	4.10	$y\ ^5D_4^\circ - f\ ^5P_3$	1.250	—
4983.2566	85	1067	4.15	$y\ ^5D_3^\circ - f\ ^5P_2$	1.167	—
4985.2587	73	984	3.93	$z\ ^3D_2^\circ - e\ ^3D_2$	1.167	1.146
4985.5530	72	318	2.86	$z\ ^7F_3^\circ - e\ ^7D_4$	1.875	1.868
4986.2252	8	1070	4.22	$y\ ^5D_1^\circ - f\ ^3D_2$	1.000	—
4988.9549	99	1066	4.15	$y\ ^5D_3^\circ - h\ ^5D_3$	1.500	—
4992.7870		1110	4.26	$z\ ^3P_1^\circ - g\ ^5F_1$	0.750	—
4994.1364	76	16	0.91	$a\ ^5F_4 - z\ ^5F_3^\circ$	1.500	1.500
4995.4109		1113	4.26	$z\ ^3P_1^\circ - f\ ^5G_2$	−0.250	—
4999.1135	−6	1040	4.19	$c\ ^3F_2 - x\ ^1F_3^\circ$	1.333	1.481
5001.8760	138	965	3.88	$z\ ^3F_4^\circ - e\ ^3D_3$	1.125	1.107
5002.7985	92	687	3.40	$z\ ^5F_3^\circ - e\ ^5F_4$	1.500	1.452
5012.6983		1093	4.28	$y\ ^5F_2^\circ - e\ ^5H_3$	0.000	−0.030
5014.9505	93	965	3.94	$z\ ^3F_3^\circ - e\ ^3D_2$	1.000	1.047
5016.4778	22	1089	4.26	$y\ ^5F_3^\circ - g\ ^5F_2$	1.500	—
5022.2420	67	965	3.98	$z\ ^3F_2^\circ - e\ ^3D_1$	0.750	0.622
5023.1879		1095	4.28	$y\ ^5F_2^\circ - f\ ^3D_1$	1.250	—
5029.6208	−3	718	3.41	$a\ ^1P_1 - {}^1D_2^\circ$	1.000	1.30?
5030.7807	86	585	3.24	$b\ ^3H_6 - z\ ^3I_7^\circ$	1.071	1.101
5044.2164	59	318	2.85	$z\ ^7F_4^\circ - e\ ^7D_5$	1.800	1.769
5048.4413	82	984	3.96	$z\ ^3D_1^\circ - e\ ^3D_2$	1.500	1.431
5054.6457	42	884	3.64	$b\ ^3D_2 - v\ ^3D_3^\circ$	1.500	—
5058.4987	26	884	3.64	$b\ ^3D_3 - v\ ^3D_3^\circ$	1.333	1.268
5067.1569	61	1092	4.22	$y\ ^5F_4^\circ - f\ ^5G_4$	1.250	—
5072.6767	117	1095	4.22	$y\ ^5F_4^\circ - f\ ^3D_3$	1.375	1.473
5074.7556	77	1094	4.22	$y\ ^5F_4^\circ - e\ ^3G_5$	0.900	1.056
5079.7462	77	16	0.99	$a\ ^5F_2 - z\ ^5F_1^\circ$	1.500	1.505
5083.3450	73	16	0.96	$a\ ^5F_3 - z\ ^5F_3^\circ$	1.250	1.250
5088.1559		1066	4.15	$y\ ^5D_3^\circ - h\ ^5D_4$	1.500	1.349
5090.7807	57	1090	4.26	$y\ ^5F_3^\circ - h\ ^5D_2$	1.000	—
5104.0338	47	465	3.02	$c\ ^3P_2 - w\ ^5D_3^\circ$	1.500	1.478
5104.1916		1092	4.18	$y\ ^5F_5^\circ - f\ ^5G_5$	1.333	1.319
5109.6544	47	1089	4.30	$y\ ^5F_1^\circ - g\ ^5F_2$	1.500	—
5127.3655	74	16	0.91	$a\ ^5F_4 - z\ ^5F_5^\circ$	1.500	1.497
5127.6836	29	1	0.05	$a\ ^5D_3 - z\ ^7D_2^\circ$	1.000	0.993
5129.6312	17	965	3.94	$z\ ^3F_3^\circ - e\ ^3D_3$	1.208	1.215
5136.0929	56	1036	4.19	$c\ ^3F_2 - z\ ^1P_1^\circ$	0.500	0.382
5137.3897	97	1090	4.18	$y\ ^5F_5^\circ - h\ ^5D_4$	1.200	1.381
5141.7460	73	114	2.42	$a\ ^3P_1 - y\ ^3D_1^\circ$	1.000	0.996
5143.7250	27	65	2.20	$a\ ^5P_2 - y\ ^3F_3^\circ$	0.333	0.352
5145.0993	48	66	2.20	$a\ ^5P_2 - y\ ^5P_2^\circ$	1.833	1.828
5159.0637	57	1091	4.28	$y\ ^5F_2^\circ - f\ ^5P_1$	0.250	—
5194.9477	65	36	1.56	$a\ ^3F_3 - z\ ^3F_3^\circ$	1.083	1.086
5196.0650	−370	1091	4.26	$y\ ^5F_3^\circ - f\ ^5P_2$	0.667	—
5197.9385		1091	4.30	$y\ ^5F_1^\circ - f\ ^5P_1$	1.250	—
5198.7171	57	66	2.22	$a\ ^5P_1 - y\ ^5P_2^\circ$	1.500	1.504
5213.8071	19	962	3.94	$z\ ^3F_3^\circ - e\ ^5G_4$	1.250	1.466
5216.2802	65	36	1.61	$a\ ^3F_2 - z\ ^3F_2^\circ$	0.667	0.676
5217.3972	83	553	3.21	$z\ ^5D_4^\circ - e\ ^5D_3$	1.500	1.493
5223.1851	−17	880	3.63	$b\ ^3D_1 - x\ ^3P_0^\circ$	0.500	—
5225.5332	79	1	0.11	$a\ ^5D_1 - z\ ^7D_1^\circ$	2.250	2.250
5228.3810		1091	4.22	$y\ ^5F_4^\circ - f\ ^5P_3$	0.875	—
5232.9493	99	383	2.94	$z\ ^7P_4^\circ - e\ ^7D_5$	1.300	1.261
5236.2039	25	1034	4.19	$c\ ^3F_2 - {}^3P_1^\circ$	0.250	0.39?
5242.4988	81	843	3.63	$a\ ^1I_6 - z\ ^1H_5^\circ$	1.000	1.004
5243.7823	−7	1089	4.26	$y\ ^5F_3^\circ - g\ ^5F_4$	1.500	—
5247.0585	97	1	0.09	$a\ ^5D_2 - z\ ^7D_3^\circ$	2.000	1.992
5250.2171	88	1	0.12	$a\ ^5D_0 - z\ ^7D_1^\circ$	3.000	2.999
5250.6527	80	66	2.20	$a\ ^5P_2 - y\ ^5P_3^\circ$	1.500	1.502
5253.0250	22	113	2.28	$a\ ^3P_2 - y\ ^5P_1^\circ$	1.000	1.008
5253.4693	83	553	3.28	$z\ ^5D_1^\circ - e\ ^5D_1$	1.500	1.506
5262.6246		1149	4.32	$z\ ^5G_6^\circ - e\ ^3H_6$	1.250	1.278
5263.3143	96	553	3.26	$z\ ^5D_2^\circ - e\ ^5D_2$	1.500	1.503
5279.6578	42	584	3.30	$b\ ^3H_4 - y\ ^3G_3^\circ$	0.875	0.880
5284.6100	48	1032	4.19	$c\ ^3F_2 - t\ ^3D_2^\circ$	0.917	0.911
5288.5315	36	929	3.69	$b\ ^1G_4 - y\ ^1G_4^\circ$	1.000	1.021
5293.9609	−2	1031	4.14	$c\ ^3F_3 - u\ ^3D_2^\circ$	1.000	0.976
5294.5493	23	875	3.64	$b\ ^3D_2 - v\ ^5F_2^\circ$	1.083	—
5295.3160		1146	4.41	$z\ ^5G_3^\circ - e\ ^5H_3$	0.708	0.685
5302.3074	85	553	3.28	$z\ ^5D_1^\circ - e\ ^5D_2$	1.500	1.507
5320.0381	−9	877	3.64	$b\ ^3D_3 - v\ ^5P_2^\circ$	0.833	0.912
5321.1105		1165	4.43	$z\ ^3G_4^\circ - e\ ^3H_4$	0.925	0.985
5322.0461	54	112	2.28	$a\ ^3P_2 - y\ ^3F_3^\circ$	0.667	0.666
5329.9932	59	1028	4.07	$c\ ^3F_4 - {}^1H_5^\circ$	0.500	0.65?
5332.9062	75	36	1.56	$a\ ^3F_3 - z\ ^3F_4^\circ$	1.500	1.496

Wavelength	Δλ	Multiplet	χ_e	Transition	$g_{\text{eff}}^{\text{LS}}$	$g_{\text{eff}}^{\text{emp}}$
5339.9356	74	553	3.26	$z\ ^5D_2^\circ - e\ ^5D_3$	1.500	1.513
5358.1168	50	628	3.30	$a\ ^3D_2 - x\ ^3D_2^\circ$	1.167	1.189
5364.8801	84	1146	4.44	$z\ ^5G_2^\circ - e\ ^5H_3$	0.667	0.633
5365.4063	100	786	3.57	$a\ ^1H_5 - z\ ^1G_4^\circ$	1.000	0.950
5367.4755	84	1146	4.41	$z\ ^5G_3^\circ - e\ ^5H_4$	0.875	0.92?
5369.9702	81	1146	4.37	$z\ ^5G_4^\circ - e\ ^5H_5$	1.000	1.100
5373.7136	40	1166	4.47	$z\ ^3G_3^\circ - f\ ^3F_4$	2.000	1.666
5376.8331		1132	4.29	$b\ ^1D_2 - z\ ^1P_1^\circ$	1.000	—
5379.5796	56	928	3.69	$b\ ^1G_4 - z\ ^1H_5^\circ$	1.000	1.096
5383.3792	103	1146	4.31	$z\ ^5G_5^\circ - e\ ^5H_6$	1.083	1.123
5386.3345	−4	1064	4.15	$y\ ^5D_3^\circ - e\ ^5P_2$	1.167	—
5389.4866	80	1145	4.41	$z\ ^5G_3^\circ - f\ ^5G_3$	0.917	1.014
5393.1744	76	553	3.24	$z\ ^5D_3^\circ - e\ ^5D_4$	1.500	1.517
5395.2187	29	1143	4.44	$z\ ^5G_2^\circ - g\ ^5F_1$	0.500	—
5398.2860		1145	4.44	$z\ ^5G_2^\circ - f\ ^5G_2$	0.333	—
5405.7838	97	15	0.99	$a\ ^5F_2 - z\ ^5D_1^\circ$	0.750	0.752
5406.7799		1148	4.37	$z\ ^5G_4^\circ - f\ ^3D_3$	0.875	0.870
5410.9197	96	1165	4.47	$z\ ^3G_3^\circ - e\ ^3H_4$	0.875	0.991
5412.7876		1162	4.43	$z\ ^3G_4^\circ - e\ ^5H_4$	0.975	1.00?
5415.2108	111	1165	4.39	$z\ ^3G_5^\circ - e\ ^3H_6$	1.083	1.167
5417.0405	14	1148	4.41	$z\ ^5G_3^\circ - f\ ^3D_2$	0.667	—
5422.1560		1145	4.32	$z\ ^5G_6^\circ - f\ ^5G_5$	1.500	1.609
5432.9525	65	1143	4.44	$z\ ^5G_2^\circ - g\ ^5F_2$	0.667	—
5434.5315	87	15	1.01	$a\ ^5F_1 - z\ ^5D_0^\circ$	0.000	−0.014
5436.2985	12	1161	4.39	$z\ ^3G_5^\circ - f\ ^5G_4$	1.300	—
5436.5926	53	113	2.28	$a\ ^3P_2 - y\ ^5P_3^\circ$	1.833	1.816
5441.3420		1144	4.31	$z\ ^5G_5^\circ - h\ ^5D_4$	0.800	0.784
5445.0502	78	1163	4.39	$z\ ^3G_5^\circ - e\ ^3G_5$	1.200	1.248
5460.8762	50	464	3.07	$c\ ^3P_1 - x\ ^5P_1^\circ$	2.000	1.965
5461.5530	25	1145	4.44	$z\ ^5G_2^\circ - f\ ^5G_3$	1.500	1.949
5462.9672	71	1163	4.47	$z\ ^3G_3^\circ - e\ ^3G_3$	0.750	0.816
5463.2851	102	1163	4.43	$z\ ^3G_4^\circ - e\ ^3G_4$	1.050	1.098
5464.2825	68	1030	4.14	$c\ ^3F_3 - y\ ^1D_2^\circ$	1.167	1.107
5470.0957	38	1144	4.44	$z\ ^5G_2^\circ - h\ ^5D_1$	−0.250	—
5473.1650	11	1064	4.19	$y\ ^5D_2^\circ - e\ ^5P_2$	1.667	—
5473.9076	73	1062	4.15	$y\ ^5D_3^\circ - g\ ^5D_3$	1.500	1.492
5483.1017	41	1061	4.15	$y\ ^5D_3^\circ - e\ ^3D_2$	1.833	1.859
5487.1489	50	1143	4.41	$z\ ^5G_3^\circ - g\ ^5F_3$	1.083	—
5487.7512	79	1025	4.14	$c\ ^3F_3 - t\ ^5D_2^\circ$	0.667	—
5491.8346	−17	1031	4.19	$c\ ^3F_2 - u\ ^3D_3^\circ$	2.000	1.935

Wavelength	Δλ	Multiplet	χ_e	Transition	$g_{\text{eff}}^{\text{LS}}$	$g_{\text{eff}}^{\text{emp}}$
5493.5012	42	1061	4.10	$y\ ^5D_4^\circ - e\ ^3D_3$	1.750	1.722
5494.4668	55	1024	4.07	$c\ ^3F_4 - x\ ^3H_5^\circ$	0.600	0.586
5501.4715	74	15	0.96	$a\ ^5F_3 - z\ ^5D_4^\circ$	1.875	1.880
5506.7864	88	15	0.99	$a\ ^5F_2 - z\ ^5D_3^\circ$	2.000	2.000
5517.0692	−6	1109	4.21	$z\ ^3P_2^\circ - e\ ^5P_2$	1.667	—
5522.4491	17	1108	4.21	$z\ ^3P_2^\circ - g\ ^5D_2$	1.500	1.53?
5525.5472	32	1062	4.23	$y\ ^5D_0^\circ - g\ ^5D_1$	1.500	—
5539.2824	−13	871	3.64	$b\ ^3D_3 - {}^1D_2^\circ$	1.667	—
5543.1944	476	926	3.69	$b\ ^1G_4 - x\ ^3G_5^\circ$	1.375	1.651
5543.9399	35	1062	4.22	$y\ ^5D_1^\circ - g\ ^5D_2$	1.500	1.61?
5546.5101		1145	4.37	$z\ ^5G_4^\circ - f\ ^5G_5$	1.500	1.457
5552.6919	7	1281	4.95	$x\ ^5D_3^\circ - i\ ^5D_2$	1.500	—
5560.2156		1164	4.43	$z\ ^3G_4^\circ - f\ ^3D_3$	0.625	0.863
5565.7114	74	1183	4.61	$y\ ^3F_3^\circ - f\ ^3F_3$	1.083	1.078
5568.8689	16	869	3.63	$b\ ^3D_1 - w\ ^3D_1^\circ$	0.500	—
5569.6253	76	686	3.42	$z\ ^5F_2^\circ - e\ ^5D_1$	0.750	0.747
5576.0970	96	686	3.43	$z\ ^5F_1^\circ - e\ ^5D_0$	0.000	−0.012
5577.0257		1314	5.03	$x\ ^5F_4^\circ - g\ ^5G_4$	1.250	—
5587.5755	47	1026	4.14	$c\ ^3F_3 - v\ ^3F_4^\circ$	1.500	1.206
5607.6668	31	1058	4.15	$y\ ^5D_3^\circ - e\ ^7G_4$	1.000	1.107
5611.3587	−19	869	3.63	$b\ ^3D_1 - w\ ^3D_2^\circ$	1.500	—
5618.6360	52	1107	4.21	$z\ ^3P_2^\circ - e\ ^3D_2$	1.333	1.309
5619.6002		1161	4.39	$z\ ^3G_5^\circ - f\ ^5G_6$	1.667	1.510
5624.0264		1160	4.39	$z\ ^3G_5^\circ - h\ ^5D_4$	0.600	0.874
5633.9504		1314	4.99	$x\ ^5F_5^\circ - g\ ^5G_6$	1.167	1.42?
5635.8247	5	1088	4.26	$y\ ^5F_3^\circ - e\ ^5P_2$	0.667	—
5636.6992	34	868	3.64	$b\ ^3D_2 - x\ ^3F_3^\circ$	1.000	—
5638.2675	57	1087	4.22	$y\ ^5F_4^\circ - g\ ^5D_3$	1.125	1.122
5646.6854	56	1109	4.26	$z\ ^3P_1^\circ - e\ ^5P_2$	2.000	—
5649.9878		1314	5.10	$x\ ^5F_1^\circ - g\ ^5G_2$	0.500	0.517
5650.6872		1314	5.08	$x\ ^5F_2^\circ - g\ ^5G_3$	0.833	—
5651.4716	17	1161	4.47	$z\ ^3G_3^\circ - f\ ^5G_4$	1.750	—
5652.3194	−2	1108	4.26	$z\ ^3P_1^\circ - g\ ^5D_2$	1.500	1.61?
5653.8674		1159	4.39	$z\ ^3G_5^\circ - g\ ^5F_5$	1.300	—
5655.1795		1314	5.06	$x\ ^5F_3^\circ - g\ ^5G_4$	1.000	—
5661.3480	6	1108	4.28	$z\ ^3P_0^\circ - g\ ^5D_1$	1.500	—
5662.5233	80	1087	4.18	$y\ ^5F_5^\circ - g\ ^5D_4$	1.200	1.277
5677.6875	34	1057	4.10	$y\ ^5D_4^\circ - e\ ^5G_5$	0.800	1.088
5679.0295		1183	4.65	$y\ ^3F_2^\circ - f\ ^3F_3$	1.500	1.454
5680.2441	76	1026	4.19	$c\ ^3F_2 - v\ ^3F_3^\circ$	1.500	1.515

Wavelength	Δλ	Multiplet	χ_e	Transition	$g_{\text{eff}}^{\text{LS}}$	$g_{\text{eff}}^{\text{emp}}$
5686.5372		1182	4.55	$y\ ^3F_4^\circ - e\ ^3H_5$	0.600	0.835
5701.5527	79	209	2.56	$b\ ^3F_4 - y\ ^3D_3^\circ$	1.125	1.101
5705.4677	21	1087	4.30	$y\ ^5F_1^\circ - g\ ^5D_1$	0.750	—
5712.1361	52	686	3.42	$z\ ^5F_2^\circ - e\ ^5D_3$	2.000	2.012
5717.8379	37	1107	4.28	$z\ ^3P_0^\circ - e\ ^3D_1$	0.500	0.801
5720.8950	109	1178	4.55	$y\ ^3F_4^\circ - f\ ^5G_3$	1.750	1.402
5724.4660		1109	4.28	$z\ ^3P_0^\circ - e\ ^5P_1$	2.500	2.432
5731.7666	50	1087	4.26	$y\ ^5F_3^\circ - g\ ^5D_3$	1.375	1.368
5741.8560		1086	4.26	$y\ ^5F_3^\circ - e\ ^3D_2$	1.333	1.363
5752.0377		1180	4.55	$y\ ^3F_4^\circ - e\ ^3G_4$	1.150	1.171
5753.1287	74	1107	4.26	$z\ ^3P_1^\circ - e\ ^3D_2$	1.000	0.939
5759.2637		1184	4.65	$y\ ^3F_2^\circ - e\ ^3P_2$	1.083	1.073
5760.3455		867	3.64	$b\ ^3D_3 - y\ ^3F_2^\circ$	1.167	1.208
5775.0849	54	1087	4.22	$y\ ^5F_4^\circ - g\ ^5D_4$	1.425	1.415
5778.4579	32	209	2.59	$b\ ^3F_3 - y\ ^3D_3^\circ$	1.208	1.198
5780.6041	60	552	3.24	$z\ ^5D_3^\circ - e\ ^7D_3$	1.625	1.627
5784.6614	40	686	3.40	$z\ ^5F_3^\circ - e\ ^5D_4$	1.875	1.880
5793.9178	50	1086	4.22	$y\ ^5F_4^\circ - e\ ^3D_3$	1.375	1.342
5804.0370		959	3.88	$z\ ^3F_4^\circ - e\ ^3F_3$	1.500	1.464
5807.7868	47	552	3.29	$z\ ^5D_0^\circ - e\ ^7D_1$	3.000	3.002
5809.2215		982	3.88	$z\ ^3D_3^\circ - e\ ^3F_3$	1.208	1.214
5811.9172	30	1022	4.14	$c\ ^3F_3 - x\ ^1G_4^\circ$	0.875	0.846
5814.8092	40	1086	4.28	$y\ ^5F_2^\circ - e\ ^3D_2$	1.083	1.061
5827.8794	47	552	3.28	$z\ ^5D_1^\circ - e\ ^7D_2$	2.250	2.266
5835.1018	38	1084	4.26	$y\ ^5F_3^\circ - f\ ^5F_4$	1.500	1.521?
5838.3753		959	3.94	$z\ ^3F_3^\circ - e\ ^3F_2$	1.500	1.550
5849.6864	48	922	3.69	$b\ ^1G_4 - x\ ^3F_4^\circ$	1.125	1.161
5852.2222	48	1178	4.55	$y\ ^3F_4^\circ - f\ ^5G_4$	1.200	—
5855.0803		1179	4.61	$y\ ^3F_3^\circ - e\ ^5H_4$	0.625	0.62?
5856.0913		1128	4.29	$b\ ^1D_2 - y\ ^1D_2^\circ$	1.000	—
5858.7840	53	1084	4.22	$y\ ^5F_4^\circ - f\ ^5F_5$	1.500	1.464
5859.5938		1181	4.55	$y\ ^3F_4^\circ - f\ ^3D_3$	1.125	1.228
5861.1123	55	1084	4.28	$y\ ^5F_2^\circ - f\ ^5F_3$	1.500	—
5862.3651	117	1180	4.55	$y\ ^3F_4^\circ - e\ ^3G_5$	1.100	1.252
5880.0236	−53	1201	4.56	$y\ ^5P_3^\circ - f\ ^5G_4$	0.375	—
5881.2822	28	1178	4.61	$y\ ^3F_3^\circ - f\ ^5G_3$	1.000	1.114
5902.4755	132	1234	4.59	$d\ ^3F_4 - t\ ^3G_5^\circ$	1.100	—
5905.6759		1181	4.65	$y\ ^3F_2^\circ - f\ ^3D_1$	0.750	—
5916.2535	44	170	2.45	$a\ ^3H_4 - y\ ^3F_4^\circ$	1.025	1.028
5927.7919	56	1175	4.65	$y\ ^3F_2^\circ - g\ ^5F_1$	1.000	—
5929.6802	135	1176	4.55	$y\ ^3F_4^\circ - h\ ^5D_3$	0.875	—
5930.1894		1180	4.65	$y\ ^3F_2^\circ - e\ ^3G_3$	0.833	0.996
5934.6619		982	3.93	$z\ ^3D_2^\circ - e\ ^3F_3$	1.000	1.046
5952.7212		959	3.98	$z\ ^3F_2^\circ - e\ ^3F_2$	0.667	0.652
5956.6997	74	14	0.86	$a\ ^5F_5 - z\ ^7P_4^\circ$	0.700	0.707
5976.7838		959	3.94	$z\ ^3F_3^\circ - e\ ^3F_3$	1.083	1.096
5983.6859		1175	4.55	$y\ ^3F_4^\circ - g\ ^5F_4$	1.300	—
5984.8221		1260	4.73	$y\ ^3D_3^\circ - e\ ^3P_2$	1.167	1.189
5987.0674		1260	4.79	$y\ ^3D_2^\circ - e\ ^3P_1$	1.000	0.997
6003.0188		959	3.88	$z\ ^3F_4^\circ - e\ ^3F_4$	1.250	1.269
6007.9656	51	1178	4.65	$y\ ^3F_2^\circ - f\ ^5G_3$	1.167	1.596
6008.5631		982	3.88	$z\ ^3D_3^\circ - e\ ^3F_4$	1.125	1.238
6027.0562	60	1018	4.07	$c\ ^3F_4 - v\ ^3G_5^\circ$	1.100	0.961
6034.0365	32	1142	4.31	$z\ ^5G_5^\circ - g\ ^5D_4$	0.800	0.680
6056.0114	52	1259	4.73	$y\ ^3D_3^\circ - f\ ^3F_4$	1.125	0.866
6065.4921	101	207	2.61	$b\ ^3F_2 - y\ ^3F_2^\circ$	0.667	0.675
6078.4976		1259	4.79	$y\ ^3D_2^\circ - f\ ^3F_3$	1.000	0.991
6079.0136		1176	4.65	$y\ ^3F_2^\circ - h\ ^5D_2$	1.083	—
6082.7147	63	64	2.22	$a\ ^5P_1 - z\ ^3P_1^\circ$	2.000	1.997
6089.5717		1327	5.02	$a\ ^1F_3 - v\ ^1G_4^\circ$	1.000	—
6093.6457		1177	4.61	$y\ ^3F_3^\circ - f\ ^5P_2$	0.333	—
6094.3766		1177	4.65	$y\ ^3F_2^\circ - f\ ^5P_1$	−0.250	—
6096.6682		959	3.98	$z\ ^3F_2^\circ - e\ ^3F_3$	1.500	1.532
6102.1828	235	1259	4.83	$y\ ^3D_1^\circ - f\ ^3F_2$	0.750	0.767
6136.6241	97	169	2.45	$a\ ^3H_4 - z\ ^3G_3^\circ$	0.875	0.841
6136.9992	64	62	2.20	$a\ ^5P_2 - y\ ^5D_1^\circ$	2.000	1.984
6137.7007	70	207	2.59	$b\ ^3F_3 - y\ ^3F_3^\circ$	1.083	1.079
6151.6217	51	62	2.18	$a\ ^5P_3 - y\ ^5D_2^\circ$	1.833	1.837
6157.7331	85	1015	4.07	$c\ ^3F_4 - w\ ^3F_3^\circ$	1.250	1.222
6159.3801		1175	4.61	$y\ ^3F_3^\circ - g\ ^5F_4$	1.750	—
6165.3641	61	1018	4.14	$c\ ^3F_3 - v\ ^3G_4^\circ$	1.000	0.686
6173.3433	89	62	2.22	$a\ ^5P_1 - y\ ^5D_0^\circ$	2.500	2.499
6180.2084	57	269	2.73	$a\ ^3G_4 - y\ ^3D_3^\circ$	0.625	0.641
6187.9941		959	3.94	$z\ ^3F_3^\circ - e\ ^3F_4$	1.500	1.591
6191.5680	97	169	2.43	$a\ ^3H_5 - z\ ^3G_4^\circ$	1.000	0.914
6200.3204	66	207	2.61	$b\ ^3F_2 - y\ ^3F_3^\circ$	1.500	1.509
6213.4375	86	62	2.22	$a\ ^5P_1 - y\ ^5D_1^\circ$	2.000	1.995
6219.2886	92	62	2.20	$a\ ^5P_2 - y\ ^5D_2^\circ$	1.667	1.657
6220.7867	107	958	3.88	$z\ ^3F_4^\circ - e\ ^5F_4$	1.300	1.290
6226.7403	98	981	3.88	$z\ ^3D_3^\circ - e\ ^5F_4$	1.375	1.346

Wavelength	Δλ	Multiplet	χ_e	Transition	$g_{\rm eff}^{\rm LS}$	$g_{\rm eff}^{\rm emp}$
6232.6493	100	816	3.65	$z\ ^5P_2^\circ - e\ ^5D_1$	2.000	1.993
6240.6516	65	64	2.22	$a\ ^5P_1 - z\ ^3P_2^\circ$	1.000	0.990
6246.3271	99	816	3.60	$z\ ^5P_3^\circ - e\ ^5D_3$	1.583	1.582
6252.5642	105	169	2.40	$a\ ^3H_6 - z\ ^3G_5^\circ$	1.083	0.950
6265.1412	100	62	2.18	$a\ ^5P_3 - y\ ^5D_3^\circ$	1.583	1.579
6270.2322	99	342	2.86	$b\ ^3P_0 - y\ ^3D_1^\circ$	0.500	0.493
6271.2832	68	685	3.33	$z\ ^5F_5^\circ - e\ ^7D_5$	1.500	1.492
6280.6240	77	13	0.86	$a\ ^5F_5 - z\ ^7F_5^\circ$	1.450	1.449
6297.8013	93	62	2.22	$a\ ^5P_1 - y\ ^5D_2^\circ$	1.000	0.993
6301.5091	108	816	3.65	$z\ ^5P_2^\circ - e\ ^5D_2$	1.667	1.669
6302.5017		816	3.69	$z\ ^5P_1^\circ - e\ ^5D_0$	2.500	2.487
6303.4671		1140	4.32	$z\ ^5G_6^\circ - e\ ^5G_5$	1.500	1.262
6311.5050	50	342	2.83	$b\ ^3P_2 - y\ ^3D_2^\circ$	1.333	1.324
6315.8164	73	1014	4.07	$c\ ^3F_4 - y\ ^1G_4^\circ$	1.125	1.163
6322.6936	37	207	2.59	$b\ ^3F_3 - y\ ^3F_4^\circ$	1.500	1.505
6330.8519		1254	4.73	$y\ ^3D_3^\circ - h\ ^5D_2$	1.167	—
6335.3378	97	62	2.20	$a\ ^5P_2 - y\ ^5D_3^\circ$	1.167	1.164
6336.8328	101	816	3.69	$z\ ^5P_1^\circ - e\ ^5D_1$	2.000	2.002
6338.8800		1258	4.79	$y\ ^3D_2^\circ - f\ ^3D_1$	1.500	—
6380.7483	74	1015	4.19	$c\ ^3F_2 - w\ ^3F_2^\circ$	0.667	0.677
6385.7206	49	1253	4.73	$y\ ^3D_3^\circ - g\ ^5F_3$	1.292	—
6392.5429	53	109	2.28	$a\ ^3P_2 - y\ ^5D_1^\circ$	1.500	1.513
6393.6113	95	168	2.43	$a\ ^3H_5 - z\ ^5G_4^\circ$	0.800	0.908
6408.0262	102	816	3.69	$z\ ^5P_1^\circ - e\ ^5D_2$	1.000	1.011
6411.6586	118	816	3.65	$z\ ^5P_2^\circ - e\ ^5D_3$	1.167	1.181
6419.9559		1258	4.73	$y\ ^3D_3^\circ - f\ ^3D_3$	1.333	1.291
6430.8538	98	62	2.18	$a\ ^5P_3 - y\ ^5D_4^\circ$	1.250	1.241
6436.4102	46	1016	4.19	$c\ ^3F_2 - v\ ^3D_1^\circ$	0.750	0.734
6475.6318	65	206	2.56	$b\ ^3F_4 - z\ ^3G_3^\circ$	2.000	1.901
6481.8784	89	109	2.28	$a\ ^3P_2 - y\ ^5D_2^\circ$	1.500	1.500
6494.9910	103	168	2.40	$a\ ^3H_6 - z\ ^5G_5^\circ$	0.917	1.025
6496.4738	51	1258	4.79	$y\ ^3D_2^\circ - f\ ^3D_2$	1.167	—
6498.9461	89	13	0.96	$a\ ^5F_3 - z\ ^7F_3^\circ$	1.375	1.381
6518.3736	81	342	2.83	$b\ ^3P_2 - y\ ^3D_3^\circ$	1.167	1.150
6574.2325	70	13	0.99	$a\ ^5F_2 - z\ ^7F_2^\circ$	1.250	1.252
6575.0229	49	206	2.59	$b\ ^3F_3 - z\ ^3G_3^\circ$	0.917	0.932
6581.2143	71	34	1.48	$a\ ^3F_4 - z\ ^5F_4^\circ$	1.300	1.304
6591.3175		1229	4.59	$d\ ^3F_4 - t\ ^3D_3^\circ$	1.125	—
6593.8798	88	168	2.43	$a\ ^3H_5 - z\ ^5G_5^\circ$	1.150	1.128
6608.0301	62	109	2.28	$a\ ^3P_2 - y\ ^5D_3^\circ$	1.500	1.478
6609.1189	86	206	2.56	$b\ ^3F_4 - z\ ^3G_4^\circ$	1.150	1.167
6625.0272	60	13	1.01	$a\ ^5F_1 - z\ ^7F_1^\circ$	0.750	0.767
6627.5488	93	1174	4.55	$y\ ^3F_4^\circ - g\ ^5F_3$	0.875	—
6633.4155	0	1258	4.83	$y\ ^3D_1^\circ - f\ ^3D_2$	1.500	—
6633.7562		1197	4.56	$y\ ^5P_3^\circ - e\ ^5P_3$	1.667	1.662
6646.9355	38	206	2.61	$b\ ^3F_2 - z\ ^3G_3^\circ$	0.833	0.919
6653.9110		1052	4.15	$y\ ^3D_3^\circ - e\ ^3F_3$	1.292	1.215
6663.4503	118	111	2.42	$a\ ^3P_1 - z\ ^3P_0^\circ$	1.500	1.500
6667.7206		1228	4.58	$d\ ^3F_3 - u\ ^3D_3^\circ$	1.208	—
6677.9958	66	268	2.69	$a\ ^3G_5 - y\ ^3F_4^\circ$	1.100	1.099
6699.1415		1228	4.59	$d\ ^3F_4 - u\ ^3D_3^\circ$	1.125	—
6703.5720	42	268	2.76	$a\ ^3G_3 - y\ ^3F_3^\circ$	0.917	0.921
6704.4794		1052	4.22	$y\ ^5D_1^\circ - e\ ^3F_2$	0.250	0.187
6710.3213	54	34	1.48	$a\ ^3F_4 - z\ ^5F_5^\circ$	1.700	1.689
6712.4670		1279	4.99	$x\ ^5D_2^\circ - f\ ^3F_3$	0.667	0.641
6713.7451		1255	4.79	$y\ ^3D_2^\circ - f\ ^5P_2$	1.500	—
6725.3640		1052	4.10	$y\ ^5D_4^\circ - e\ ^3F_4$	1.375	1.392
6726.6722		1197	4.61	$y\ ^5P_2^\circ - e\ ^5P_1$	1.500	1.538
6733.1567		1195	4.64	$y\ ^5P_1^\circ - g\ ^5D_0$	2.500	2.502
6737.9830	−4	1192	4.56	$y\ ^5P_3^\circ - f\ ^5F_3?$	1.258	—
6739.5243	47	34	1.56	$a\ ^3F_3 - z\ ^5F_3^\circ$	1.167	1.168
6745.1049		1227	4.58	$d\ ^3F_2 - x\ ^1D_2^\circ$	0.833	—
6745.9626	84	1005	4.07	$c\ ^3F_4 - w\ ^5G_3^\circ$	1.750	1.763
6746.9508	−22	205	2.61	$b\ ^3F_2 - z\ ^5G_2^\circ$	0.500	0.499
6750.1597	100	111	2.42	$a\ ^3P_1 - z\ ^3P_1^\circ$	1.500	1.498
6752.7107	59	1195	4.64	$y\ ^5P_1^\circ - g\ ^5D_1$	2.000	—
6786.8632		1052	4.19	$y\ ^5D_2^\circ - e\ ^3F_3$	0.667	0.719
6793.2656	133	1005	4.07	$c\ ^3F_4 - w\ ^5G_4^\circ$	1.200	1.204
6806.8491	24	268	2.73	$a\ ^3G_4 - y\ ^3F_4^\circ$	1.150	1.148
6810.2669		1197	4.61	$y\ ^5P_2^\circ - e\ ^5P_3$	1.500	1.492
6820.3730	34	1197	4.64	$y\ ^5P_1^\circ - e\ ^5P_2$	1.500	—
6828.5976	78	1195	4.64	$y\ ^5P_1^\circ - g\ ^5D_2$	1.000	1.10?
6837.0091		1225	4.59	$d\ ^3F_4 - u\ ^3G_4^\circ$	1.150	—
6839.8340	26	205	2.56	$b\ ^3F_4 - z\ ^5G_4^\circ$	1.200	1.169
6841.3450	97	1195	4.61	$y\ ^5P_2^\circ - g\ ^5D_3$	1.167	1.148
6842.6903		1197	4.64	$y\ ^5P_1^\circ - e\ ^5P_1$	2.500	2.467
6843.6606	122	1173	4.55	$y\ ^3F_4^\circ - e\ ^3D_3$	1.125	1.097
6855.1684	91	1195	4.56	$y\ ^5P_3^\circ - g\ ^5D_4$	1.250	1.226
6857.2481	49	1006	4.07	$c\ ^3F_4 - z\ ^1G_4^\circ$	1.125	1.144
6858.1540	90	1173	4.61	$y\ ^3F_3^\circ - e\ ^3D_2$	1.000	1.047

Table 4.2 List of Fe II lines and their Landé factors

Wavelength	$\Delta\lambda$	Multiplet		χ_e	Transition	$g_{\rm eff}^{\rm LS}$	$g_{\rm eff}^{\rm emp}$
4122.6625	−55	28		2.58	$b\ {}^4P_{2\frac{1}{2}} - z\ {}^4F^{\rm o}_{2\frac{1}{2}}$	1.314	1.326
4124.7842	−28	22		2.54	$a\ {}^2D_{2\frac{1}{2}} - z\ {}^4F^{\rm o}_{3\frac{1}{2}}$	1.286	1.377
4128.7410	−70	27		2.58	$b\ {}^4P_{2\frac{1}{2}} - z\ {}^4D^{\rm o}_{1\frac{1}{2}}$	1.900	1.908
4178.8590	−30	28		2.58	$b\ {}^4P_{2\frac{1}{2}} - z\ {}^4F^{\rm o}_{3\frac{1}{2}}$	0.786	0.924
4258.1590	50	28		2.70	$b\ {}^4P_{1\frac{1}{2}} - z\ {}^4F^{\rm o}_{1\frac{1}{2}}$	1.067	1.082
4369.4030	−80	28		2.78	$b\ {}^4P_{\frac{1}{2}} - z\ {}^4F^{\rm o}_{1\frac{1}{2}}$	−0.167	−0.114
4413.5941	−69	32		2.68	$a\ {}^4H_{4\frac{1}{2}} - z\ {}^4F^{\rm o}_{4\frac{1}{2}}$	1.152	1.135
4416.8245	−55	27		2.78	$b\ {}^4P_{\frac{1}{2}} - z\ {}^4D^{\rm o}_{1\frac{1}{2}}$	0.833	0.767
4491.4035	−15	37		2.85	$b\ {}^4F_{1\frac{1}{2}} - z\ {}^4F^{\rm o}_{1\frac{1}{2}}$	0.400	0.421
4508.2866	−14	38		2.85	$b\ {}^4F_{1\frac{1}{2}} - z\ {}^4D^{\rm o}_{\frac{1}{2}}$	0.500	0.503
4515.3389	−1	37		2.84	$b\ {}^4F_{2\frac{1}{2}} - z\ {}^4F^{\rm o}_{2\frac{1}{2}}$	1.029	1.044
4520.2258	18	37		2.81	$b\ {}^4F_{4\frac{1}{2}} - z\ {}^4F^{\rm o}_{3\frac{1}{2}}$	1.500	1.336
4534.1639	−41	37		2.85	$b\ {}^4F_{1\frac{1}{2}} - z\ {}^4F^{\rm o}_{2\frac{1}{2}}$	1.500	1.572
4541.5204	−36	38		2.85	$b\ {}^4F_{1\frac{1}{2}} - z\ {}^4D^{\rm o}_{1\frac{1}{2}}$	0.800	0.774
4555.8937	7	37		2.83	$b\ {}^4F_{3\frac{1}{2}} - z\ {}^4F^{\rm o}_{3\frac{1}{2}}$	1.238	1.250
4576.3377	−23	38		2.84	$b\ {}^4F_{2\frac{1}{2}} - z\ {}^4D^{\rm o}_{2\frac{1}{2}}$	1.200	1.184
4582.8330	−20	37		2.81	$b\ {}^4F_{2\frac{1}{2}} - z\ {}^4F^{\rm o}_{3\frac{1}{2}}$	1.500	1.629
4620.5160	−50	38		2.83	$b\ {}^4F_{3\frac{1}{2}} - z\ {}^4D^{\rm o}_{3\frac{1}{2}}$	1.333	1.305
4635.3100	−60	186		5.95	$d\ {}^2D_{2\frac{1}{2}} - y\ {}^2F^{\rm o}_{3\frac{1}{2}}$	1.071	—
4656.9787	−23	43		2.89	$a\ {}^6S_{2\frac{1}{2}} - z\ {}^4D^{\rm o}_{2\frac{1}{2}}$	1.686	1.673
4666.7536	−44	37		2.83	$b\ {}^4F_{3\frac{1}{2}} - z\ {}^4F^{\rm o}_{4\frac{1}{2}}$	1.500	1.512
4670.1723	−97	25		2.58	$b\ {}^4P_{2\frac{1}{2}} - z\ {}^6F^{\rm o}_{3\frac{1}{2}}$	1.143	1.169
4720.1347	−143	54		3.20	$b\ {}^2P_{1\frac{1}{2}} - z\ {}^4P^{\rm o}_{2\frac{1}{2}}$	1.800	1.788
4833.1919	−51	30		2.66	$a\ {}^4H_{5\frac{1}{2}} - z\ {}^6F^{\rm o}_{4\frac{1}{2}}$	0.455	0.419
4893.8136	−64	36		2.83	$b\ {}^4F_{3\frac{1}{2}} - z\ {}^6P^{\rm o}_{2\frac{1}{2}}$	0.429	0.386
4923.9299	29	42		2.89	$a\ {}^6S_{2\frac{1}{2}} - z\ {}^6P^{\rm o}_{1\frac{1}{2}}$	1.700	1.694
4993.3527	−53	36		2.81	$b\ {}^4F_{4\frac{1}{2}} - z\ {}^6P^{\rm o}_{3\frac{1}{2}}$	0.667	0.616
5100.6563	−77	35		2.81	$b\ {}^4F_{4\frac{1}{2}} - z\ {}^6F^{\rm o}_{3\frac{1}{2}}$	1.222	1.146
5132.6658	−32	35		2.81	$b\ {}^4F_{4\frac{1}{2}} - z\ {}^6F^{\rm o}_{4\frac{1}{2}}$	1.384	1.368
5136.7971	−49	35		2.84	$b\ {}^4F_{2\frac{1}{2}} - z\ {}^6F^{\rm o}_{1\frac{1}{2}}$	1.000	1.003
5197.5742	−28	49		3.23	$a\ {}^4G_{2\frac{1}{2}} - z\ {}^4F^{\rm o}_{1\frac{1}{2}}$	0.700	0.671
5234.6298	48	49		3.22	$a\ {}^4G_{3\frac{1}{2}} - z\ {}^4F^{\rm o}_{2\frac{1}{2}}$	0.929	0.869
5256.9346	−34	41		2.89	$a\ {}^6S_{2\frac{1}{2}} - z\ {}^6F^{\rm o}_{2\frac{1}{2}}$	1.657	1.650
5264.8074	−46	48		3.33	$a\ {}^4G_{2\frac{1}{2}} - z\ {}^4D^{\rm o}_{1\frac{1}{2}}$	0.100	0.142
5284.1091	1	41		2.89	$a\ {}^6S_{2\frac{1}{2}} - z\ {}^4F^{\rm o}_{3\frac{1}{2}}$	1.071	0.653
5325.5558	28	49		3.22	$a\ {}^4G_{3\frac{1}{2}} - z\ {}^4F^{\rm o}_{3\frac{1}{2}}$	1.111	1.135
5337.7364	44	48		3.23	$a\ {}^4G_{2\frac{1}{2}} - z\ {}^4D^{\rm o}_{2\frac{1}{2}}$	0.971	0.962
5414.0736	6	48		3.22	$a\ {}^4G_{3\frac{1}{2}} - z\ {}^4D^{\rm o}_{3\frac{1}{2}}$	1.206	1.190
5425.2523	−47	49		3.20	$a\ {}^4G_{4\frac{1}{2}} - z\ {}^4F^{\rm o}_{4\frac{1}{2}}$	1.253	1.235
5534.8451	−19	55		3.24	$b\ {}^2H_{5\frac{1}{2}} - z\ {}^4F^{\rm o}_{4\frac{1}{2}}$	0.545	0.572
5824.4065	−85	58		3.42	$a\ {}^2F_{2\frac{1}{2}} - z\ {}^4D^{\rm o}_{2\frac{1}{2}}$	1.114	1.100
5991.3749	−11	46		3.15	$a\ {}^4G_{5\frac{1}{2}} - z\ {}^6F^{\rm o}_{4\frac{1}{2}}$	0.909	0.803
6084.1061	−49	46		3.20	$a\ {}^4G_{4\frac{1}{2}} - z\ {}^6F^{\rm o}_{3\frac{1}{2}}$	0.778	0.714
6113.3221	1	46		3.22	$a\ {}^4G_{3\frac{1}{2}} - z\ {}^6F^{\rm o}_{2\frac{1}{2}}$	0.571	0.575
6149.2483	−97	74		3.89	$b\ {}^4D_{\frac{1}{2}} - z\ {}^4P^{\rm o}_{\frac{1}{2}}$	1.333	—
6238.3903	−17	74		3.89	$b\ {}^4D_{1\frac{1}{2}} - z\ {}^4P^{\rm o}_{1\frac{1}{2}}$	1.467	—
6239.9431	−99	74		3.89	$b\ {}^4D_{\frac{1}{2}} - z\ {}^4P^{\rm o}_{1\frac{1}{2}}$	2.167	—
6247.5643	73	74		3.89	$b\ {}^4D_{2\frac{1}{2}} - z\ {}^4P^{\rm o}_{1\frac{1}{2}}$	1.100	1.034
6369.4619	−1	40		2.89	$a\ {}^6S_{2\frac{1}{2}} - z\ {}^6D^{\rm o}_{1\frac{1}{2}}$	2.100	2.098
6416.9282	92	74		3.89	$b\ {}^4D_{2\frac{1}{2}} - z\ {}^4P^{\rm o}_{2\frac{1}{2}}$	1.486	1.459
6432.6831	31	40		2.89	$a\ {}^6S_{2\frac{1}{2}} - z\ {}^6D^{\rm o}_{2\frac{1}{2}}$	1.829	1.824
6446.4102	2	199		6.22	$c\ {}^4F_{3\frac{1}{2}} - x\ {}^4G^{\rm o}_{4\frac{1}{2}}$	1.056	—
6456.3878	48	74		3.90	$b\ {}^4D_{3\frac{1}{2}} - z\ {}^4P^{\rm o}_{2\frac{1}{2}}$	1.214	1.182
6516.0855	45	40		2.89	$a\ {}^6S_{2\frac{1}{2}} - z\ {}^6D^{\rm o}_{3\frac{1}{2}}$	1.071	1.069

which the empirical Landé factors of one of their levels has been measured with lower accuracy than usual. The lines with

$$\frac{|g_{\rm eff}^{\rm LS} - g_{\rm eff}^{\rm emp}|}{|g_{\rm eff}^{\rm emp}|} > 10\% \qquad \text{and} \qquad |g_{\rm eff}^{\rm LS} - g_{\rm eff}^{\rm emp}| > 0.05 \tag{4.41}$$

are also listed in Table 4.3, together with their values of $g_u^{\rm emp}$ and $g_l^{\rm emp}$ (in columns 6 and 7 respectively). These can be used instead of $g_u^{\rm LS}$ and $g_l^{\rm LS}$ in radiative transfer calculations, so that the Zeeman splittings of lines which exhibit departures from LS-coupling can also be calculated correctly, as has been mentioned in Sect. 2.4.5.1.

Solanki and Stenflo (1984) also presented a method for determining $g_{\rm eff}$ values empirically from solar data which is briefly described in the following. Since I_V scales with the Landé factor, an error in $g_{\rm eff}$ will cause it to be either too deep or too shallow. If $\ln(d_V/d_I)$ is plotted vs. S_I (where d_V and d_I are the line depths of I_V and I, while S_I is the line strength of I; see Sect. 4.4.1 for the exact definitions), then lines with sufficiently wrong $g_{\rm eff}$ values will lie some standard deviations away from the rest of the points. A Landé factor that is too small results in a value of $\ln(d_V/d_I)$ that is too large and vice versa. The correct value of $g_{\rm eff}$ is found by determining the line depth, d_V, that the line must have in order to lie on the average curve described by the rest of the points. If we denote the line depth of the I_V profile calculated using $g_{\rm eff}^{\rm LS}$ as $d_V^{\rm LS}$, the effective Landé factor determined with this method as $g_{\rm eff}^{\rm solar}$, and its corresponding I_V line depth as $d_V^{\rm solar}$, then the relation between $g_{\rm eff}^{\rm solar}$ and $g_{\rm eff}^{\rm LS}$ is of the form

$$g_{\rm eff}^{\rm solar} = g_{\rm eff}^{\rm LS} \exp\left(\ln\left(\frac{d_V^{\rm LS}}{d_I}\right) - \ln\left(\frac{d_V^{\rm solar}}{d_I}\right)\right). \tag{4.42}$$

However, the reverse is not necessarily true, since the line depth of the (unblended) I_V profile is also affected by anomalous Zeeman splitting as pointed out by Mathys and Stenflo (1987a). They find that for lines with small $g_{\rm eff}$ values and strongly anomalous Zeeman splitting, the higher order terms also play an important role, since the depths of I_V and Stokes I are not affected in the same way by them. If η_I and η_{I_V} are treated as if they represent I and I_V, formed in the same region, and LS coupling is valid, then

$$\frac{\eta_{I_V}(\lambda_0)}{\eta_I(\lambda_0)} \approx -1, \tag{4.43}$$

is valid to first order for any line, or to any order for a Zeeman triplet (the minus sign has been explained earlier). For such lines, the Stokes I and I_V profiles will have the same depth (we have assumed that $\langle B \rangle$ is exactly known). For a line with an anomalous Zeeman pattern Eq. (4.43) has to be replaced by

$$\frac{\eta_{I_V}(\lambda_0)}{\eta_I(\lambda_0)} \approx -1 - \frac{1}{12}\left(5\Delta\lambda_H^2 + 9\mu_1^{(2)} + \frac{2\mu_1^{(3)}}{\Delta\lambda_H}\right)\frac{1}{\phi(0)}\frac{{\rm d}^2}{{\rm d}\lambda^2}\phi(0), \tag{4.44}$$

if second order terms are also included. If $g_{\rm eff}$ is sufficiently small, and $\mu_1^{(2)}$, $\mu_1^{(3)}$ sufficiently large, then $\eta_{I_V}(\lambda_0)/\eta_I(\lambda_0)$ will be dominated mainly by the anomalous splitting terms, so that the depths of the I_V and Stokes I profiles will differ considerably even when LS-coupling is strictly valid. In such a case Eq. (4.42) will give wrong results. In view of this uncertainty we will not use the method of Solanki and Stenflo (1984) for determining further $g_{\rm eff}$ values.

4.4. Line Parameters and Their Statistical Analysis

4.4.1. Line Paramters

Stokes I and I_V are parameterised exactly equivalently. We shall differentiate between the parameters of Stokes I and I_V by giving the former an index I, while marking the latter with an index V. Following Stenflo and Lindegren (1977) we introduce the following parameters (see Fig. 4.8). The line *depth* (written as d_I and d_V) is determined from the minimum of a parabolic function fitted to the three lowest points. The *width* of the line at the levels $0.1d$, $0.3d$, $0.5d$, and $0.7d$ above the line bottom (written as $v_{D_I}(0.1d_I), \ldots, v_{D_I}(0.7d_I)$ and $v_{D_V}(0.1d_V), \ldots, v_{D_V}(0.7d_V)$). These widths are expressed, in velocity units, in terms of the formal Doppler width of a Gaussian that has the same width at the respective level. This way of parameterisation has the advantage that if the line profile has the shape of a Gaussian its width at any two levels will give the same

Table 4.3a List of Fe I lines showing deviations from LS coupling

Wavelength	Mult.	Transition	$g_{\rm eff}^{\rm LS}$	$g_{\rm eff}^{\rm emp}$	$g_l^{\rm emp}$	$g_u^{\rm emp}$
4443.1998	350	$b\ ^3P_0 - x\ ^3D_1^\circ$	0.500	0.556	—	0.556
4556.9275	638	$a\ ^3D_3 - v\ ^5P_2^\circ$	0.833	0.930	1.335	1.740
4560.0909	823	$z\ ^5P_3^\circ - e\ ^5G_4$	0.375	0.609	1.657	1.238
4596.4113	823	$z\ ^5P_2^\circ - e\ ^5G_3$	0.000	0.753	1.835	1.294
4779.4423	720	$a\ ^1P_1 - x\ ^3P_0^\circ$	1.000	0.817	0.817	—
4798.2670	1042	$c\ ^3F_2 - t\ ^3G_3^\circ$	0.833	1.167	0.677	0.922
4911.7808	984	$z\ ^3D_2^\circ - e\ ^3D_1$	1.500	1.351	1.168	0.801
4945.6390	1113	$z\ ^3P_2^\circ - f\ ^5G_3$	0.333	0.791	1.493	1.142
4962.5756	1097	$y\ ^5F_5^\circ - e\ ^3H_6$	0.583	0.745	1.417	1.225
4999.1135	1040	$c\ ^3F_2 - x\ ^1F_3^\circ$	1.333	1.481	0.677	1.079
5022.2420	965	$z\ ^3F_2^\circ - e\ ^3D_1$	0.750	0.622	0.682	0.801
5029.6208	718	$a\ ^1P_1 - \ ^1D_2^\circ$	1.000	1.30?	0.817	1.14?
5074.7556	1094	$y\ ^5F_4^\circ - e\ ^3G_5$	0.900	1.056	1.344	1.248
5088.1559	1066	$y\ ^5D_3^\circ - h\ ^5D_4$	1.500	1.349	1.492	1.435
5136.0929	1036	$c\ ^3F_2 - z\ ^1P_1^\circ$	0.500	0.382	0.677	1.266
5137.3897	1090	$y\ ^5F_5^\circ - h\ ^5D_4$	1.200	1.381	1.417	1.435
5213.8071	962	$z\ ^3F_3^\circ - e\ ^5G_4$	1.250	1.466	1.086	1.238
5236.2039	1034	$c\ ^3F_2 - \ ^3P_1^\circ$	0.250	0.39?	0.677	1.25?
5329.9932	1028	$c\ ^3F_4 - \ ^1H_5^\circ$	0.500	0.65?	1.264	1.06?
5373.7136	1166	$z\ ^3G_3^\circ - f\ ^3F_4$	2.000	1.666	0.791	1.141
5410.9197	1165	$z\ ^3G_3^\circ - e\ ^3H_4$	0.875	0.991	0.791	0.871
5461.5530	1145	$z\ ^5G_2^\circ - f\ ^5G_3$	1.500	1.949	0.335	1.142
5560.2156	1164	$z\ ^3G_4^\circ - f\ ^3D_3$	0.625	0.863	1.100	1.258
5587.5755	1026	$c\ ^3F_3 - v\ ^3F_4^\circ$	1.500	1.206	1.066	1.122
5619.6002	1161	$z\ ^3G_5^\circ - f\ ^5G_6$	1.667	1.510	1.248	1.323
5624.0264	1160	$z\ ^3G_5^\circ - h\ ^5D_4$	0.600	0.874	1.248	1.435
5633.9504	1314	$x\ ^5F_5^\circ - g\ ^5G_6$	1.167	1.42?	1.390	1.40?
5677.6875	1057	$y\ ^5D_4^\circ - e\ ^5G_5$	0.800	1.088	1.496	1.360
5686.5372	1182	$y\ ^3F_4^\circ - e\ ^3H_5$	0.600	0.835	1.246	1.109
5717.8379	1107	$z\ ^3P_0^\circ - e\ ^3D_1$	0.500	0.801	—	0.801
5720.8950	1178	$y\ ^3F_4^\circ - f\ ^5G_3$	1.750	1.402	1.246	1.142
5862.3651	1180	$y\ ^3F_4^\circ - e\ ^3G_5$	1.100	1.252	1.246	1.248
5881.2822	1178	$y\ ^3F_3^\circ - f\ ^5G_3$	1.000	1.114	1.086	1.142
5930.1894	1180	$y\ ^3F_2^\circ - e\ ^3G_3$	0.833	0.996	0.688	0.842
6007.9656	1178	$y\ ^3F_2^\circ - f\ ^5G_3$	1.167	1.596	0.688	1.142
6027.0562	1018	$c\ ^3F_4 - v\ ^3G_5^\circ$	1.100	0.961	1.264	1.163
6034.0365	1142	$z\ ^5G_5^\circ - g\ ^5D_4$	0.800	0.680	1.218	1.487
6056.0114	1259	$y\ ^3D_3^\circ - f\ ^3F_4$	1.125	0.866	1.324	1.141
6165.3641	1018	$c\ ^3F_3 - v\ ^3G_4^\circ$	1.000	0.686	1.066	0.914
6252.5642	169	$a\ ^3H_6 - z\ ^3G_5^\circ$	1.083	0.950	1.163	1.248
6303.4671	1140	$z\ ^5G_6^\circ - e\ ^5G_5$	1.500	1.262	1.332	1.360
6393.6113	168	$a\ ^3H_5 - z\ ^5G_4^\circ$	0.800	0.908	1.038	1.103
6494.9910	168	$a\ ^3H_6 - z\ ^5G_5^\circ$	0.917	1.025	1.163	1.218
6704.4794	1052	$y\ ^5D_1^\circ - e\ ^3F_2$	0.250	0.187	1.492	0.622

Table 4.3b List of Fe II lines showing deviations from LS coupling

Wavelength	Mult.	Transition	$g_{\rm eff}^{\rm LS}$	$g_{\rm eff}^{\rm emp}$	$g_l^{\rm emp}$	$g_u^{\rm emp}$
4178.8590	28	$b\ ^4P_{5/2} - z\ ^4F_{7/2}^\circ$	0.786	0.924	1.583	1.29
4369.4030	28	$b\ ^4P_{1/2} - z\ ^4F_{3/2}^\circ$	−0.167	−0.114	2.68	0.445
4520.2258	37	$b\ ^4F_{9/2} - z\ ^4F_{7/2}^\circ$	1.500	1.336	1.307	1.29
5284.1091	41	$a\ ^6S_{5/2} - z\ ^4F_{7/2}^\circ$	1.071	0.653	1.996	1.399
5991.3749	46	$a\ ^4G_{11/2} - z\ ^6F_{9/2}^\circ$	0.909	0.803	1.237	1.43

number. In the following, if the level to which the width refers is not explicitly stated, then the $0.5d$ level is meant (i.e. v_{D_I}, respectively v_{D_V}, refer to $v_{D_I}(0.5d_I)$, respectively $v_{D_V}(0.5d_V)$). The *line strength* (S_I and S_V) is parameterised by the area of the profile below the level $0.5d_I$, and is expressed in Fraunhofer (equivalent width in wavelength units multiplied by $10^6/\lambda$). For a Gaussian the equivalent width is $3.4336S$, while for a purely Lorentzian profile it is $5.5039S$. This parameter has been chosen instead of the full equivalent width in order to minimise the effects of small blends in the wings. The *central wavelength* of the I and I_V profiles are termed λ_I and λ_V. The Stokes I wavelength is determined using four different methods. a: From the minimum of a parabola fitted through the three lowest points. b: By determining the centre of gravity of the lower half of the line. c: From the centre of the line chord at $0.1d$ above line bottom, where d is the total line depth. d: From the centre of gravity of the lowest 10th of the line (i.e. of the area below the $0.1d$ chord). The second method does not give exactly the core wavelength, but is less susceptible to noise than the other three. It should be noted that the zero-crossing wavelength of Stokes V is identical to the wavelength of the minimum of I_V, and both are represented by the same symbol. In practice λ_V is determined directly from Stokes V.

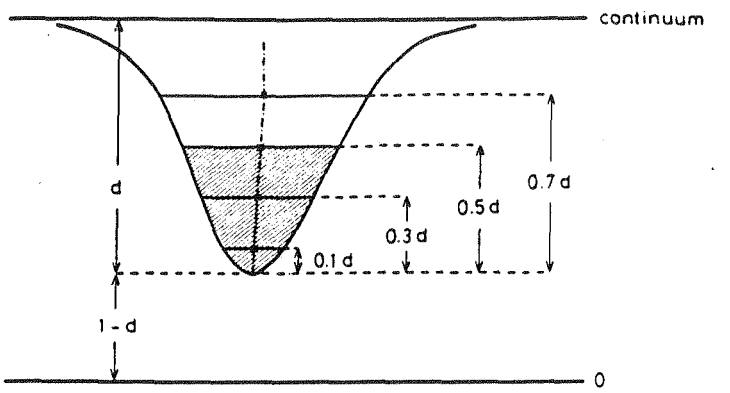

Fig. 4.8 Illustration of the line parameters described in the text. The shaded area corresponds to the line strength S. This illustration is equally valid for Stokes I and the I_V profile. In the former case all parameters have index I, in the latter case index V (from Stenflo and Lindegren, 1977).

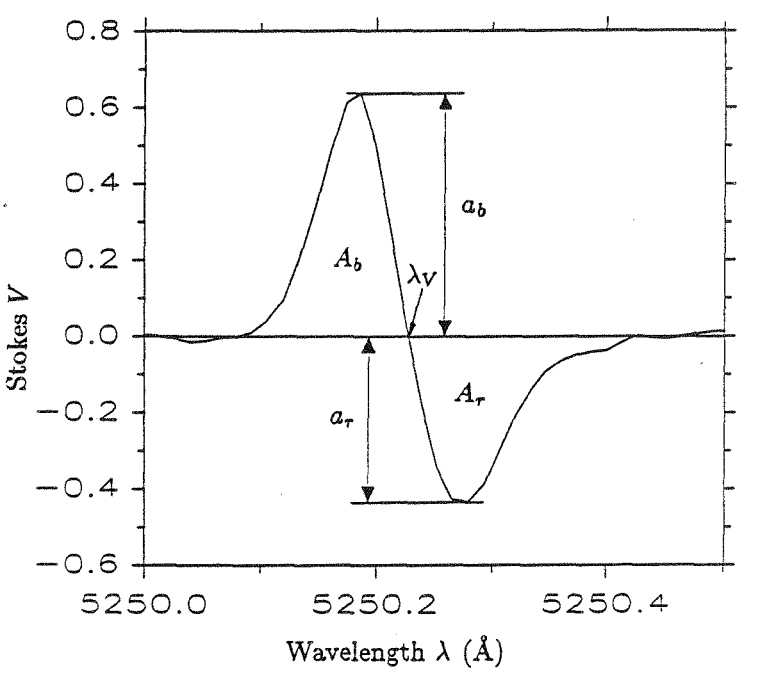

Fig. 4.9 Illustration of line parameters of the Stokes V profile (cf. text).

In addition to these parameters of I and I_V we have also determined some parameters of the Stokes V profile directly. These are illustrated in Fig. 4.9. The amplitudes a_b and a_r of the blue and red wings (in % polarization) are determined by fitting a parabolic function through the three points around the peak. The wavelength of the zero-crossing, λ_V, at which Stokes V changes sign is determined by linear interpolation; the curvature of the profile is sufficiently small near λ_V to justify this. The areas of the blue and red wings of Stokes V are represented

by A_b and A_r which are defined as

$$A_b = \int_{\lambda_1}^{\lambda_V} V(\lambda)\,\mathrm{d}\lambda,$$
$$A_r = \int_{\lambda_V}^{\lambda_2} V(\lambda)\,\mathrm{d}\lambda. \tag{4.45}$$

λ_1 and $\lambda_2 > \lambda_1$ are chosen to lie far in the wings, so that $V(\lambda_1) \approx V(\lambda_2) \approx 0$. With these definitions of a_b, a_r, A_b, and A_r we can define the following asymmetry parameters of Stokes V. *Absolute* area and amplitude asymmetry

$$\Delta A = A_b - A_r,$$
$$\Delta a = a_b - a_r, \tag{4.46}$$

and *relative* area and amplitude asymmetry

$$\delta A = \frac{A_b - A_r}{A_b + A_r},$$
$$\delta a = \frac{a_b - a_r}{a_b + a_r}. \tag{4.47}$$

The determination of line parameters has been automated to a large degree. A program, IVPAR, has been written which reads the solar FTS data, searches therein for the lines from a given line list, calculates the I_V profile for each line (including the correct setting of the continuum), and then determines the parameters described above for Stokes I, Stokes V and I_V. The code also carries out the same procedure for line profiles calculated with the radiative transfer code STOKES (described in chapter 2), so that exactly equivalent parameters are determined for observed and calculated profiles, which greatly facilitates their comparison. The extension of the code to include further parameters, or e.g., parameters of Stokes Q is quite straighforward.

In addition to these parameters, determined from the solar data, we shall also use the atomic parameters listed in Sect. 4.3.1 (which are of course identical for I_V and Stokes I), namely the laboratory wavelength of the line, λ_{lab}, the effective Landé factor, g_{eff} ($g_{\mathrm{eff_{emp}}}$ is used whenever available), and the excitation potential χ_e (in eV), or its extension χ^* defined to cover both neutral and ionised lines. $\chi^* = \chi_e + \chi_i$, with $\chi_i = 0$ eV for Fe I and $\chi_i = 7.87$ eV for Fe II (representing the ionisation potential of Fe I).

4.4.2. Scatter Plots and Regression Analysis

Once the various parameters of the selected Fe I and Fe II lines have been determined, we can search for relations between them by plotting different combinations of them against each other following Solanki and Stenflo (1984, 1985). An example is shown in Fig. 4.10, where v_{D_I} and v_{D_V} of the Fe I lines observed in a network region are plotted vs. S_I. The stars represent Fe I lines with $\chi_e < 3$ eV, the circles Fe I lines with $\chi_e \geq 3$ eV. The reason for not using S_V as the abscissa in Fig. 4.10b is the following: since the average field $\langle B \rangle$ is not known a priori, the values of S_V and S_I cannot be directly compared to each other, since the scales differ by a constant but unknown factor, as explained in Sect. 4.2.4. Using S_I as abscissa in both diagrams of Fig. 4.10 thus facilitates the comparison between Stokes I and I_V data.

Several things are apparent from Fig. 4.10. Firstly, the scatter in the v_{D_I} values in Fig. 4.10a is smaller than the scatter in Fig. 3 of Stenflo and Lindegren (1977) which illustrates the superiority of the FTS spectra over the Jungfraujoch atlas data (Delbouille et al. 1973) which was used by them. One reason for this difference may be the better instrumental profile of the Kitt Peak FTS. Another may be that the Jungfraujoch data were not obtained simultaneously, so that regions with different amounts of activity may have been observed in the data analysis.

Secondly, the v_{D_V} of the weaker I_V profiles show a considerably greater scatter than the corresponding v_{D_I} values. This is partly due to the smaller signal to noise ratio in the Stokes V data, but a large part is due to the larger Zeeman broadening of I_V. This is indicated by the fact that the scatter is mainly in the direction of greater v_{D_V} and can be verified by carrying out a regression analysis. If we neglect this scatter, then we see that although the weak and medium strong I_V profiles have a width similar to those of the I profiles (in agreement with the results of Stellmacher and Wiehr, 1971, and Harvey et al., 1972), for the strongest lines $v_{D_V} < v_{D_I}$. We will show in chapters 5 and 7 that the I_V line widths are determined by an intricate interplay of Zeeman and velocity broadening, and of temperature effects. We also note that the splitting of the v_{D_I} curve according to the excitation potential χ_e of the lines is absent for v_{D_V}.

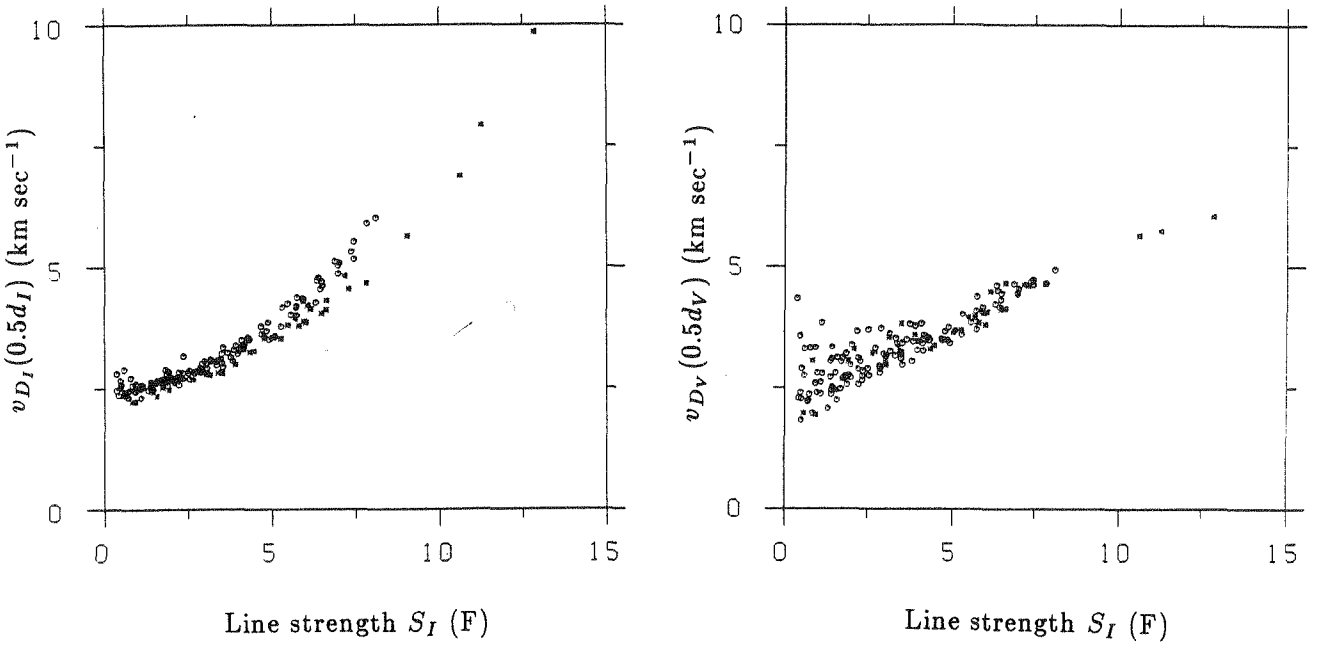

Fig. 4.10 Line width v_D (km sec^{-1}) plotted as a function of Stokes I line strength, S_I (Fraunhofer, F), for an enhanced network region. a v_{D_I} width of Stokes I, b v_{D_V}, width of I_V. Lines with $\chi_e < 3$ eV are represented by a star, those with $\chi_e \geq 3$ by a circle.

Stenflo and Lindegren showed that the dependence of v_{D_I} on line strength, excitation potential, Landé factor, and wavelength may be expressed by a regression equation of the following form:

$$v_{D_I} = x_1 + x_2 S_I + x_3 S_I^2 + x_4 v_0 \chi_e + x_5 g_{\text{eff}}^2 \lambda_I^2 / v_0 + x_6 \left\langle g_{\text{eff}}^2 \right\rangle \lambda_I^2 / v_0, \tag{4.48}$$

where the x_i are the regression coefficients and v_0 is a second order polynomial fit to v_{D_I} as a function of S_I alone

$$v_0 = y_1 + y_2 S_I^2. \tag{4.49}$$

The regression equation Eq. (4.48) can also be used to describe v_{D_V}, although the meanings of some of the coefficients will be changed.

Instead of treating v_{D_V} and v_{D_I} individually, we can also plot their difference $v_{D_V} - v_{D_I}$ vs. S_I, as has been done in Fig. 4.11. The Fe II lines have now also been plotted in addition to the Fe I lines. The data are from the same region as those in Fig. 4.10. The symbols: stars represent Fe I lines with $\chi_e < 3$ eV, circles Fe I lines with $\chi_e \geq 3$ eV, and the solid squares Fe II lines. This diagram has great value for the diagnostic of the velocity structure in fluxtubes (see chapters 5 and 7). The advantage of using differences of parameters ($v_{D_V} - v_{D_I}$ and later $\ln d_V - \ln d_I$), instead of simply the parameters of I_V themselves lies in the fact that the former are much more sensitive to small variations in the atmosphere between the fluxtubes and their surroundings.

For the Fe I lines a regression equation identical to Eq. (4.48) can be written to describe $v_{D_V} - v_{D_I}$. In principle it would be possible to extend the regression equation Eq. (4.48) to include Fe II lines as well if we replace χ_e by χ^*. However, a glance at Fig. 4.11 shows that the positions of the Fe II lines in that diagram cannot be extrapolated in a straightforward manner from the relative positions of the Fe I lines with different χ^*. We therefore refrain from extending this analysis to Fe II lines.

Perhaps we should add that the difference in width between observed Fe I lines of equal S_I, but different excitation potentials, stems mainly from the fact that the Stokes I profiles of high excitation lines are broader than of the low excitation ones. The larger average width of the medium strong and strong Fe II lines compared to the Fe I lines, on the other hand, is due mainly to the difference between the V profiles of these lines, since the relative widths of the Stokes I profiles of Fe I and II lines would tend to produce the opposite effect in the $v_{D_V} - v_{D_I}$ vs. S_I diagram.

These regression equations can be used to obtain a variety of results. They confirm that v_{D_V} is practically independent of χ_e, that v_{D_V} and $v_{D_V} - v_{D_I}$ show a significant dependence on $g_{\text{eff}}^2 \lambda^2 / v_0$ consistent with the presence

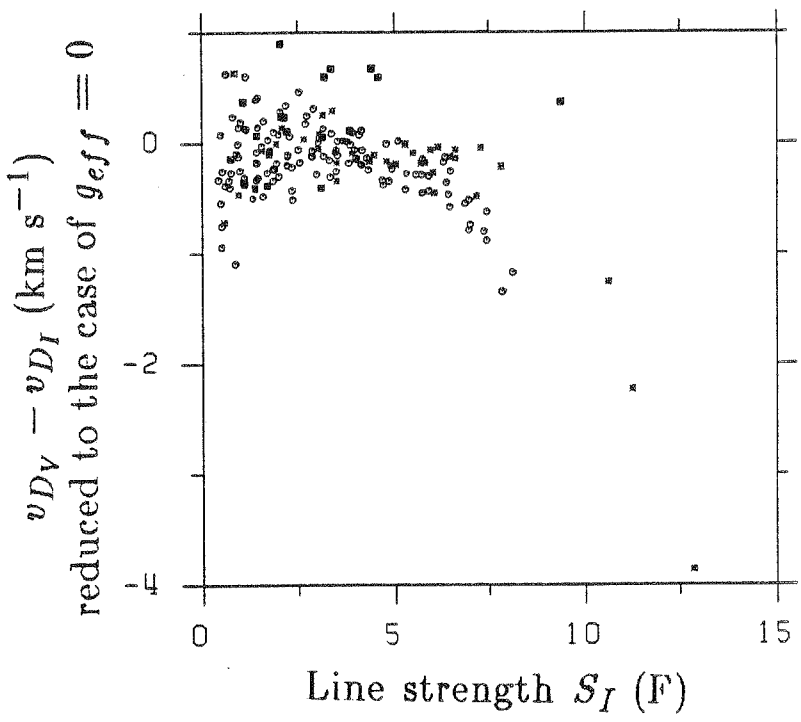

Fig. 4.11 Difference in line width of the I_V and I profiles, $v_{D_V} - v_{D_I}$, plotted vs. S_I for an enhanced network region. The line widths have been reduced to the case that $g_{\rm eff} = 0$. Fe I lines with $\chi_e < 3$ eV are represented by stars, those with $\chi_e \geq 3$ eV by circles, and the Fe II lines by filled squares.

of kG magnetic fields inside fluxtubes. This dependence when subtracted from the data in an appropriate manner leads to a decrease in the scatter of v_{D_V} and $v_{D_V} - v_{D_I}$ vs. S_I for the weak lines. The determination of field strengths with such a regression analysis will be discussed in detail in chapter 6.

Next let us turn to a short discussion of $\ln(d_V/d_I)$ vs. S_I, shown in Fig. 4.12a. The fact that $\ln(d_V/d_I)$ exhibits such large values is only an artifact of our using $\langle B \rangle = 1$ when calculating I_V for reasons stated earlier. The seemingly large scatter of the weak lines is mostly of solar origin, and mirrors the fact that $\ln(d_V/d_I)$ is strongly dependent on the excitation potential. This can be confirmed by carrying out a regression of the following form,

$$\ln(d_V/d_I) = x_1 + x_2 S_I + x_3 S_I^2 + x_4 \chi^* + x_5 \chi^* h(S_I) + x_6\, g_{\rm eff}^2 \lambda^2/v_0^2 + x_7 \left\langle g_{\rm eff}^2 \right\rangle \lambda^2/v_0^2. \qquad (4.50)$$

Here

$$h(S_I) = S_I + a_1 S_I^2 + a_2 S_I^3. \qquad (4.51)$$

Thus two additional regression coefficients a_1 and a_2 need to be determined simultaneously with the x_i coefficients. The complicated χ^* terms are necessary to correctly reproduce the χ^* dependence of both Fe I and Fe II simultaneously. Note that the x_6 and x_7 terms now contain the factor $1/v_0^2$ instead of $1/v_0$, which stems from the fact that the line depth is influenced somewhat differently from the line width by the Zeeman effect. The effect of carrying out this regression and subtracting the dependence on χ^*, $g_{\rm eff}$ and λ is shown in Fig. 4.12b. The scatter of the weak lines is greatly reduced by this procedure. Again the value of the Zeeman splitting coefficient x_6 shows the presence of kG magnetic fields in fluxtubes. More details regarding the magnetic field determination will be given in chapter 6. The shape of the data curves in the scatter plots $\ln(d_V/d_I)$ vs. S_I and $\ln(d_V/d_I)$ vs. χ^* contains information on the temperature structure (cf. chapter 5), while the absolute value of $\ln(d_V/d_I)$ is a measure of the filling factor (cf. chapter 6).

We can obtain some qualitative information on fluxtube temperature from $\ln(d_V/d_I)$ vs. S_I directly, if we note that the strongest Fe I lines in the diagram have depths relative to the continuum, d_I, close to 1 in the quiet photosphere. Therefore, due to saturation, in the fluxtube these lines cannot have significantly larger depths than outside. This gives us a limit for placing the zero line correctly in Fig. 4.12. It must lie at or above the strongest Fe I lines. Thus the depths of the weaker lines are reduced in the fluxtube, compared to outside. Further, Fe I lines are more strongly weakened than Fe II lines of equal strength. This suggests that this weakening is a temperature effect, Fe I being strongly dependent on T while Fe II is not. This is due to the fact that over 90 % of the iron atoms are ionised in the solar photosphere (e.g. Nordlund, 1984), so that when a small number of atoms changes state due to a change in T (following the Saha-Boltzmann equation), the percentage change will

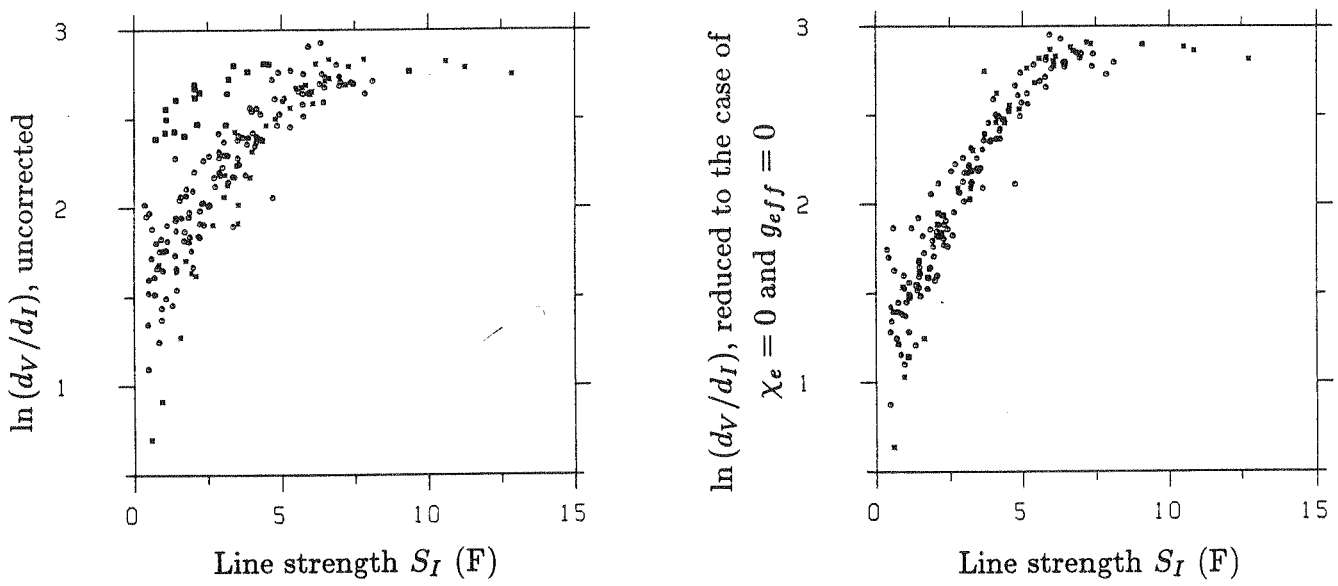

Fig. 4.12 The logarithm of the ratio of the line depths of I_V and I, $\ln(d_V/d_I)$, plotted vs. S_I for an enhanced network region. The symbols are the same as in Fig. 4.11. a Original data. b $\ln(d_V/d_I)$ reduced to the case of $\chi^* = 0$ and $g_{\rm eff} = 0$ using Eq. (4.50).

be considerabley larger for neutral iron than for ionised iron. The fact that the Fe I lines are weakened (and not strengthened) suggests that T is larger in fluxtubes than in the non-magnetic photosphere as has been suggested by a number of previous studies, e.g. Chapman and Sheeley (1968) and Harvey and Livingston (1969).

Finally, consider a pair of scatter plots providing information on the line shape. In Fig. 4.13a (for Stokes I) and b (for I_V) the line width at the $0.1d$ level has been plotted vs. the line width at the $0.5d$ level. By virtue of the definition of v_D, a line with a Gaussian profile would fall on the 45° line in the diagram. Lines with more U-shaped profiles lie above this line, whereas lines with more V-shaped profiles lie below it.

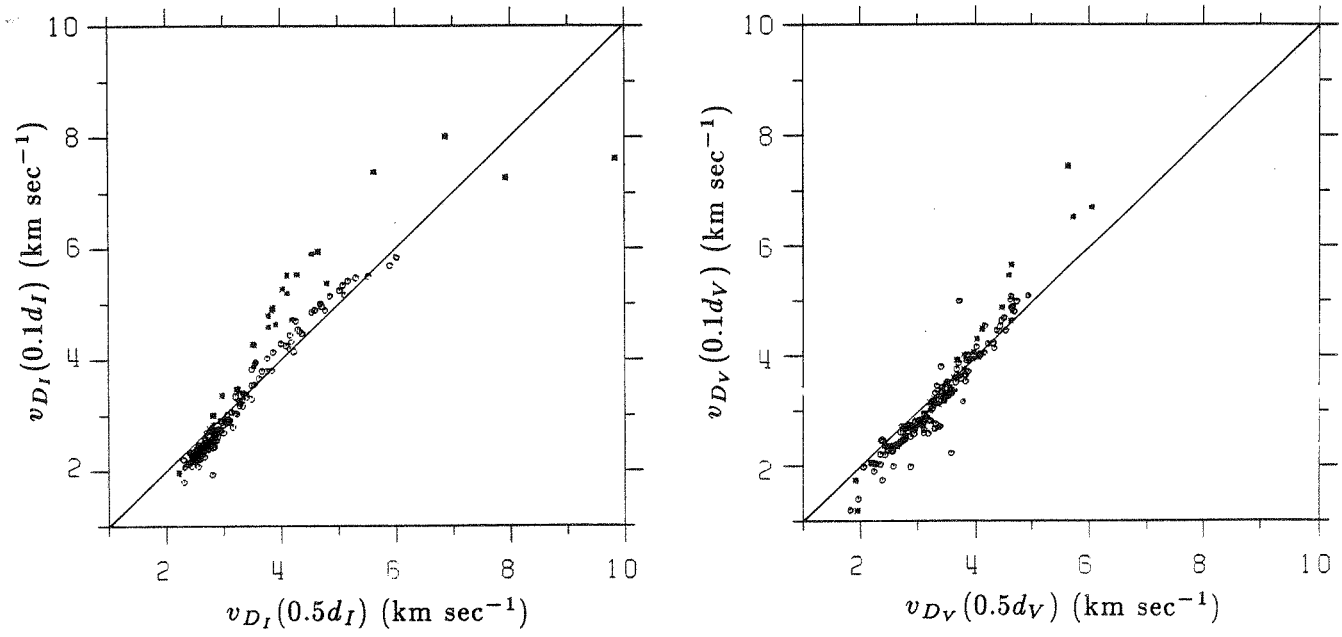

Fig. 4.13 Line widths at the level $0.1d$ plotted vs. line width at the $0.5d$ level. a Stokes I: $v_{D_I}(0.1d_I)$ vs. $v_{D_I}(0.5d_I)$. b Stokes V: $v_{D_V}(0.1d_V)$ vs. $v_{D_V}(0.5d_V)$.

The main difference between the behaviour of the I and I_V profiles appears to be that the I_V profiles do

not show any significant distinction between lines of different excitation potentials, in contrast to the Stokes I profiles. The different behaviour of $\chi_e < 3$ eV and $\chi_e \geq 3$ eV lines in Fig. 4.13a may be a non-LTE effect. The $\chi_e < 3$ eV levels, being metastable, are overpopulated as compared with the higher levels (Lites, 1972). An increase in temperature inside the fluxtube might explain the merging of the $\chi_e \geq 3$ eV and $\chi_e < 3$ eV curves of the I_V diagram, since it would raise the population of the higher levels relative to the lower ones.

4.4.3. Tests of the Influence of the Stokes V Asymmetry on the Analysis of I_V

The simple renormalisation process of the continuum of I_V discussed in Sect. 4.2.5 may affect the profiles in subtle ways, and is therefore a potential source of error for the determination of temperature, filling factor, or velocity. For example we only compensate for the area asymmetry of Stokes V, so that, e.g., the amplitude asymmetry (which is *not* linearly related to the area asymmetry, cf. chapter 8) could influence the shape of the profile. Therefore, in order to obtain a feeling for the way in which this renormalization process affects the results, test runs have been made using unrenormalized I_V profiles as the basis of the statistical analysis. The parameterisation is then no longer unique with, for example, two different line depth values possible per line (see Fig. 4.5). Using either of these values does not change the determined temperature structure by more than a few percent. Furthermore, the values of the magnetic field strength and the magnetic filling factor are not affected significantly.

The half widths of the blue and red halfs of the unrenormalised lines have also been determined and compared to the half widths of the renormalised lines. This has been carried out for a number of lines with large absolute and relative asymmetries. In all but one case the differences are found to be considerably smaller than the scatter due to noise.

The results of these tests confirm that the Stokes V area asymmetry and the simple method used to counter its effects do not have an appreciable effect on the subsequent analysis, or on the derived values of physical quantities inside fluxtubes.

4.5. Fluxtube Models for the Calculation of Stokes Line Profiles

Some qualitative properties of fluxtubes can be read directly from the scatter plots, as has been shown with the help of a few examples in the last section. However, in order to obtain more quantitative information, line profiles have to be calculated in a model of a small magnetic fluxtube and compared with the observational data. As a first step, a very simple model is required, which would allow us to study the effects of changing a small number of free parameters on the profiles of a sample of spectral lines with a wide range of properties. With such a model it is possible to fix the range of values which these parameters may possess in fluxtubes, and also to explore the diagnostic contents of the various scatter plots. Such a model for exploratory calculations is described in Sect. 4.5.2. For the later, more detailed, investigation of the fluxtube temperature and velocity structure a somewhat more sophisticated model is used. It is briefly described in Sect. 4.5.3. The spectral lines calculated with these fluxtube models are also described in Sects. 4.5.2 and 4.5.3. A considerably more sophisticated model, which may be useful for future empirical modelling, is presented in chapter 9.

4.5.1. Basic Assumptions

Both kinds of models described here are based on the same fundamental assumptions. These are:

a) The model is one dimensional: i.e. none of the physical quantities varies across the cross-section of the fluxtube, and only a one line of sight radiative transfer along the fluxtube axis is carried out. Almost all model calculations have been carried out for the centre of the solar disk and have only been compared to data with $\mu \geq 0.92$. The fluxtubes are assumed to be vertical. We wish to stress that for the many-lines analysis chosen to take maximum advantage of the FTS data, a two dimensional model would require prohibitive amounts of computer time. At this stage in the analysis it would therefore be unnecessarily restrictive, since it would not allow a sufficiently extensive grid of parameters to be tested.

b) The structure of the fluxtube is assumed to be independent of dynamical effects (static models), i.e. mass motions in it and in its immediate surroundings are assumed to have velocities which are small compared to the sound speed.

c) The so called thin fluxtube approximation is used, which assumes that magnetic tension does not affect the

structure of the fluxtube. No external magnetic field is assumed to be present. The magnetic field strength can then be determined at each height from the horizontal balance of the gas pressure.

$$\frac{B^2_{\text{fluxtube}}}{8\pi} + P_{\text{fluxtube}} = P_{\text{external}} \tag{4.52}$$

A test for the validity of this approximation is presented in chapter 9, where the thin fluxtube approximation is compared with a second order expansion solution (see also Pneuman et al., 1986).

d) As a description of the external atmosphere, the HSRASP (Chapman, 1979) or some slightly modified version of this model is used (the modifications will be described later). The HSRASP is a downwards extension of the HSRA (Gingerich et al., 1971) into the convection zone, by combining it with the convection zone model of Spruit (1974). This extension is required by the fact that, due to the Wilson depression, the light in a fluxtube may come from a deeper layer than in the surrounding atmosphere. In the following the term HSRA will in general refer to the HSRASP. By assuming such an average model for the external atmosphere, we have neglected all the inhomogeneity known to be present in it. Since we generally compare our Stokes V data with a Stokes I spectrum obtained in a quiet region, it is irrelevant for our analysis whether fluxtubes modify the structure of their surroundings or not (cf. Spruit, 1977; Deinzer et al., 1984b).

e) All empirical calculations of line profiles are carried out in LTE with the modified code of Beckers (1969a,b) described in chapter 2. Some tests on the validity of LTE in the fluxtube photosphere for Fe I and II lines are given by Solanki and Steenbock (1987).

4.5.2. A Model for Exploratory Calculations

For first exploratory calculations it is assumed that the temperature difference between the model fluxtube and its surroundings is *approximately* linear at equal τ. The exact method of calculating the temperature is slightly more complicated. First the temperature structure is prescribed in the absence of a magnetic field, i.e. with a Wilson depression $Z_W = 0$. Two parameters then describe the temperature structure:

$$\begin{aligned} \Delta T_{\text{top}} &= T_{\text{fluxtube}} - T_{\text{HSRA}} \quad \text{at} \quad \tau_{5000}(\text{HSRA}) = 10^{-4} \quad \text{and} \\ \Delta T_{\text{bot}} &= T_{\text{fluxtube}} - T_{\text{HSRA}} \quad \text{at} \quad \tau_{5000}(\text{HSRA}) = 1. \end{aligned} \tag{4.53}$$

The temperature difference at all heights Z (still for $Z_W = 0$), is found by linear interpolation between ΔT_{top} and ΔT_{bot}. The pressure inside the fluxtube is assumed equal to the pressure outside the fluxtube at equal Z. After this, the fluxtube atmosphere is shifted down by a Wilson depression Z_W, here defined as the height difference between levels of equal pressure inside and outside the fluxtube. Note that the Wilson depression defined in this manner is in general *not* equal to the difference in heights between the levels with $\tau_{5000} = 1$ inside and outside the fluxtube. The magnetic field can then be calculated in the thin fluxtube approximation Eq. (4.52). The electron pressure $P_e(P_g, T)$ is, for this exploratory model, determined through interpolation in the tables given by Bashek and Scholz (1982) and Allen (1973). Finally, the absorption coefficient $\kappa(P_e, T)$ is determined from the graphs given in Unsöld (1955), which are based on the calculations of Vitense (1951).

This exceedingly simple model, therefore, contains only three essential free paramters: Z_W, ΔT_{top}, and ΔT_{bot}. In addition the microturbulence velocity inside the fluxtube $\xi_{\text{mic}}^{\text{fluxtube}}$ is assumed to be some fixed fraction of a height dependent microturbulence velocity in the surroundings ξ_{mic}^{HSRA}. This gives another free parameter $f_{\text{mic}} = \xi_{\text{mic}}^{\text{fluxtube}}/\xi_{\text{mic}}^{HSRA}$, which is not of great consequence for the preliminary investigations carried out with this model, as long as we choose $f_{\text{mic}} \leq 1$, which is the case for all the test calculations.

No additional line broadening mechanism is assumed except collisional damping for which no empirical corrections are made. $\xi_{\text{mic}}^{\text{HSRA}}$ is determined by fitting the line profiles of a quiet region with the HSRASP as model atmosphere. A total of 96 hypothetical Fe I lines with different line strengths (i.e. g^*f values), excitation potentials (0, 3, 5 eV), and Landé factors (0, 1, 2, 3) are calculated for each set of model parameters. All the hypothetical lines have $\lambda = 5000$ Å. In addition eight hypothetical Fe II lines with $g_{\text{eff}} = 1$, $\chi_e = 3$ eV, $\lambda = 5000$ Å, and varying line strength are calculated. The modest number of hypothetical Fe II lines has been chosen due to the small number of unblended Fe II lines in the visible solar spectrum, and due to the small range of variations in g_{eff} and χ_e of these lines.

Test calculations have also been carried out for lines with $\lambda = 6000$ Å, for Fe II lines with $\chi_e = 2.5$ eV and 4 eV, and for Fe II lines with $g_{\text{eff}} = 0$ or 2. However, the resulting effects on the line profiles are found to lie

within the scatter in the observational data. We therefore refrain from using these additional hypothetical lines in the further analysis.

4.5.3. A Model for the Empirical Determination of Fluxtube Properties

In this thin fluxtube model, the temperature is first prescribed at all height points in the atmosphere, $T_{\rm fluxtube}(Z)$. No constraint is made on the form of the temperature stratification. The pressure is then calculated from hydrostatic equilibrium for a given value of $P_{\rm fluxtube}(Z=0)$,

$$P_{\rm fluxtube}(Z) = P_{\rm fluxtube}(Z=0)\exp\left(-\int_0^Z \frac{{\rm d}Z'}{H(Z')}\right), \tag{4.54}$$

where $H(Z)$ is the pressure scale height in the fluxtube given by

$$H(Z) = \frac{kT_{\rm fluxtube}(Z)R_\odot^2}{Gm_pM_\odot}. \tag{4.55}$$

In Eq. (4.55) k is Boltzmann's constant, $R_\odot$ is the solar radius, G is the gravitational constant, m_p is the mean particle mass, and $M_\odot$ is the solar mass. The value of $P_{\rm fluxtube}(Z=0)$ is fixed by the magnetic field strength prescribed at that height, or equivalently by a Wilson depression Z_W, as defined in Sect. 4.5.2. $B(Z)$ is calculated using Eq. (4.52). $P_e(Z)$ and $\kappa(Z)$ are determined using the LTE code of Gustafsson (1973). This code is very versatile with regard to the atomic data which is input to calculate these quantities. As used in this thesis, the code takes into account the contributions of H (2), He (2), C (3), N (3), O (2), Ne (2), Na (2), Mg (3), Al (4), Si (3), S (3), K (2), Ca (3), Cr (3), Fe (3), and Ni (3) to P_e and κ. The numbers in brackets are the number of ionisation stages which are considered for the particular element.

The microturbulence velocity of the model atmosphere can be prescribed independently for each height, and there is also a provision for the specification of a macroscopic flow velocity, which is useful for the calculation of Stokes V asymmetry (cf. chapter 8).

Since information on the velocity structure in fluxtubes is to be obtained with this model, some care has to be taken with the line broadening mechanisms, specially the damping. The Unsöld approximation to Van der Waals damping is generally used in the literature and we shall adopt it as well (cf. Sect. 2.4.5.3). However, there are varying claims as to the need for an empirical correction factor, δ_Γ for Γ_6 with

$$\Gamma_{\rm true} = \delta_\Gamma\Gamma_6. \tag{4.56}$$

Holweger (1979) has suggested that $\delta_\Gamma \approx 2.5$, as a result of his W_λ analysis of a large number of Fe I lines. This is in accord with the theoretical calculations of Brueckner (1971) and O'Mara (1976). Blackwell and Shallis (1979), on the other hand, find that $\delta_\Gamma \approx 1.0$ for a few strong low excitation Fe I lines for which reliable g^*f values measured by the Oxford group are available (e.g. Blackwell, Ibbetson, Petford, and Shallis, 1979, and Blackwell, Petford and Shallis, 1979). Finally Simmons and Blackwell (1982) present solar data which suggest tht δ_Γ is a function of multiplet number for Fe I, with δ_Γ increasing from 1.0 for Multiplet 1 to $\delta_\Gamma = 1.5$ for Multiplet 207, the multiplet with the highest χ_e value for which the Oxford group has measured oscillator strengths. In view of these conflicting claims many of the calculations have been carried out twice; once with $\delta_\Gamma = 1$ and once with $\delta_\Gamma = 2.5$.

Two sets of thirty hypothetical Fe I and II line profiles each, one for $\delta_\Gamma = 1$ and the other for $\delta_\Gamma = 2.5$, are calculated for each set of fluxtube model parameters. Two separate sets are needed since changing Γ_6 also changes the strengths (S_I) of the stronger lines with their prominent damping wings. Both sets of lines are divided into three groups, each containing ten lines of differing strengths. The first group is composed of ten Fe I lines with $\chi_e = 1.5$ eV, the second group of Fe I lines with $\chi_e = 4$ eV, and the third group of Fe II lines with $\chi_e = 3$ eV. All lines have $\lambda = 5000$ Å and are Zeeman triplets with $g = 0$. This value of the Landé factor can be chosen since the data are first reduced to $g_{\rm eff} = 0$ before they are compared with the calculated profiles.

In addition to these hypothetical lines, the profiles of eight Fe I and two Fe II lines, selected from Tables 4.1 and 4.2 according to criteria described below, are also calculated for part of the work. Their relevant atomic data are given in Table 4.4. These lines serve to check how well the complete line profile is reproduced by fitting a small number of line parameters. An additional reason for fitting individual lines is to see how large the effects

Table 4.4 List of lines selected for full profile comparison between models and observational data

Ion	λ (Å) [6],[14]	$\Delta\lambda$ [6], [14]	Multiplet [14]	Transition [10]	χ_e (eV) [6],[14]	$g_{\rm eff}^{\rm LS}$ [13],[14]	$g_{\rm eff}^{\rm emp}$ [13]	$\frac{g^{\rm LS}-g^{\rm emp}}{g^{\rm emp}}$ %	log g^*f(lab) [7]	log g^*f(other Solar)	log g^*f (HSRA)(†)	$\frac{g^*f({\rm HSRA})}{g^*f({\rm lab})}$	log g^*f (HM)(⋆)	$\frac{g^*f({\rm HM})}{g^*f({\rm lab})}$ (‡)	δ_Γ
Fe I	5048.4413	82	984	$z\ ^3D_1^\circ - e\ ^3D_2$	3.96	1.500	1.431	4.8	−1.19 [5]	——	−1.02	1.48	−1.09	1.26	2.5
Fe I	5083.3450	73	16	$a\ ^5F_3 - z\ ^5F_3^\circ$	0.96	1.250	1.250	0.0	−2.958[1]	−2.99 [8]	−3.01	0.89	−2.95	1.02	1.1
Fe I	5127.6836	29	1	$a\ ^5D_3 - z\ ^7D_2^\circ$	0.05	1.000	0.993	0.7	−6.125[2]	−6.13 [8]	−6.02	1.27	−6.02	1.27	1.0
Fe II	5197.5742	−28	49	$a\ ^4G_{2\frac{1}{2}} - z\ ^4F^\circ_{1\frac{1}{2}}$	3.23	0.700	0.671	4.3	−2.18 [11]	−2.38 [11]	−2.20	0.95	−2.28	0.79	2.5
Fe I	5247.0585	97	1	$a\ ^5D_2 - z\ ^7D_3^\circ$	0.09	2.000	1.992	0.4	−4.946[2]	−4.88 [8]	−4.98	0.92	−4.94	1.01	1.0
Fe I	5250.2171	88	1	$a\ ^5D_0 - z\ ^7D_1^\circ$	0.12	3.000	2.999	0.03	−4.938[2]	−4.86 [8]	−4.97	0.93	−4.92	1.04	1.0
Fe I	5293.9609	−2	1031	$c\ ^3F_3 - u\ ^3D_2^\circ$	4.14	1.000	0.976	2.5	−1.80 [9]	−1.95 [8]	−1.67	1.35	−1.77	1.07	2.5
Fe I	5383.3792	103	1146	$z\ ^5G_5^\circ - e\ ^5H_6$	4.31	1.083	1.123	3.6	+0.52 [5],[9]	+0.50 [8]	+0.37	0.71	+0.37	0.71	2.5
Fe II	5414.0736	6	48	$a\ ^4G_{3\frac{1}{2}} - z\ ^4D^\circ_{3\frac{1}{2}}$	3.22	1.206	1.190	1.3	−3.28 [3],[11]	−3.79 [3], −3.29[11]	−3.29	0.98	−3.40	0.76	2.5
Fe I	5445.0502	78	1163	$z\ ^3G_5^\circ - e\ ^3G_5$	4.39	1.200	1.248	−3.9	+0.04 [15]	−0.12 [8]	−0.06	0.79	−0.09	0.74	2.5

(†) Abundance $\epsilon = 7.54$ and microturbulence $\xi_{\rm mic} = 0.8$ km sec^{-1} assumed. Blackwell and Shallis (1979) find ϵ between 7.496–7.545, $\xi_{\rm mic}$ between 0.6–0.8 km sec^{-1}.

(⋆) Holweger and Müller (1974). Abundance $\epsilon = 7.70$ and microturbulence $\xi_{\rm mic} = 0.9$ km sec^{-1} assumed. Blackwell and Shallis (1979) find ϵ between 7.640–7.674, $\xi_{\rm mic}$ between 0.8–0.9 km sec^{-1}. [3] find $\epsilon = 7.69$, $\xi_{\rm mic} = 0.95$ km sec^{-1}

(‡) Simmons and Blackwell (1982) give empirical enhancement values only for multiplets ≤ 209, i.e. for $\chi_e \lesssim 2.6$ eV. For such lines we use their δ_Γ values, whereas for $\chi_e \gtrsim 4$ eV we assume $\delta_\Gamma = 2.5$, as suggested by Holweger (1979). For Fe II, we take $\delta_\Gamma = 2.5$.

[1] Blackwell, Petford and Shallis (1979)
[2] Blackwell, Ibbetson, Petford, and Shallis (1979)
[3] Blackwell, Shallis, and Simmons (1980)
[4] Bridges (1973)
[5] Bridges and Kornblith (1974)
[6] Dravins and Larsson (1984), Dravins et al. (1986)
[7] Fuhr et al. (1981). All the data in this column are from this reference. The numbers in square brackets after each g^*f value mark the reference of the original source.
[8] Gurtovenko and Kostik (1982)
[9] May et al. (1974)
[10] Moore (1972)
[11] Phillips (1979)
[12] Rutten and Van der Zalm (1984)
[13] Solanki and Stenflo (1985)
[14] Stenflo and Lindegren (1977)
[15] Wolnik et al. (1970)

of non-zero Landé factor and anomalous Zeeman splitting are on the derived velocities and temperatures. The following criteria have been used to select the lines:

i The lines should be unblended. The Stokes V profiles of approximately 50 candidate lines from Tables 4.1 and 4.2 were checked by eye for the presence of blends hidden in Stokes I.

ii A minimum number of lines should cover the $S_I - \chi^*$ plane as completely as possible, to maximise their diagnostic capability (cf. Fig. 4.14). Due to the absence of unblended Fe lines between $\chi^* = 5.5$ eV and $\chi^* = 10$ eV in the visible part of the solar spectrum, a gap in this region is unavoidable.

iii The chosen set should allow the determination of the magnetic field strength. Therefore both Fe I 5250.2 Å and Fe I 5247.1 Å are included. The comparison of their I_V profiles also provides a check on the validity of the weak field approximation.

iv The lines should be formed in LS coupling. Therefore only lines with $|(g_{\mathrm{eff}_{\mathrm{LS}}} - g_{\mathrm{eff}_{\mathrm{emp}}})/g_{\mathrm{eff}_{\mathrm{emp}}}| < 5\%$ have been chosen. Lines for which the empirical (laboratory) effective Landé factors are not known, have not been chosen.

v The lines should be present in our data set. In order to be able to compare model profiles, both with our data at disk centre (observations of 1979) and later also near the limb (1984 observations), the wavelength range has had to be limited to between 4900 Å and 5500 Å. It is important to have all the lines in the same FTS spectrum, since for example differences in the filling factors of two observed regions can make the intercomparison of their Stokes V profiles unreliable. In addition, a spectrum obtained near disk centre in a very quiet region, which is useful for determining the g^*f values of the lines, is available in this wavelength range.

vi The chosen lines should not be strongly affected by noise. This can be a problem for the Stokes V profiles of lines with small g_{eff} and/or small S_I values. For this reason no lines with $g_{\mathrm{eff}} < 0.7$ are to be found in the list. However, even then the signal to noise level for the Stokes V profile of very weak lines like 5127.6 Å can be as low as 10 for the 1979 data. These lines have been retained nevertheless, since they are of interest for checking the fluxtube temperature. Problems with the noise are considerably increased in the 1984 data, which we shall not consider in such detail here.

vii If possible, the laboratory wavelength should be accurately known, in order to allow detailed modelling of velocity fields if required.

viii Finally, at least one measurement of the line's oscillator strength must be available in the literature, if possible of good accuracy.

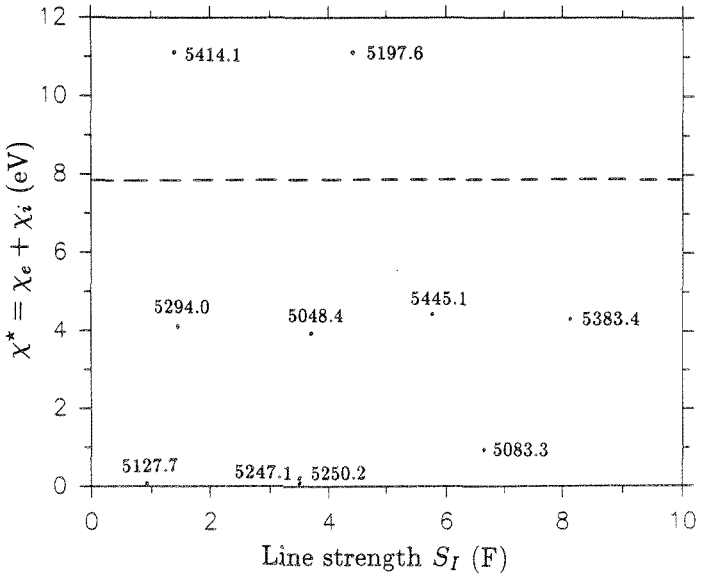

Fig. 4.14 Excitation potential, measured from the ground state of Fe I, χ^* vs. S_I of the 10 lines listed in Table 4.4. The dashed line marks the ionisation potential of Fe I.

Of course, some compromises have had to be made. For example, not all the lines have well known g^*f values, the situation being particularly precarious for Fe II. To see how well the published g^*f values reproduce the solar profiles, they have been used to calculate model profiles using the HSRA and the Holweger-Müller (HM) atmosphere models. Since the fits, specially for the former, are not always satisfactory, the g^*f values have also been derived empirically, again using these two model atmospheres and different estimates of the microturbulence.

In Table 4.4 the $\log g^* f$ values from the literature and from these solar data are tabulated and compared. The column headed $\log g^* f$(lab) contains values listed by Fuhr et al. (1981), who have gathered them from different sources, compared them, evaluated their uncertainties, and attempted to remove systematic differences. The references to the original sources of the data are marked behind the individual $g^* f$ values. The next column (headed $\log g^* f$(other Solar)) contains $g^* f$ values obtained empirically from the Sun by other authors. Note, that although in a few cases Fuhr et al. have also used solar oscillator strengths, the values in these two columns can be quite different due to the renormalisation carried out by Fuhr et al. (1981). In general the values of Fuhr et al. have been used as a standard for comparison, since their results should be more internally consistent.

The procedure used to determine empirical $g^* f$ values is to first fit the lines whose $g^* f$ values have been determined to great accuracy by Blackwell and co-workers of the Oxford group, thus getting estimates of the abundance and the microturbulence. $\delta_\Gamma \doteq 2.5$ is chosen for the empirical correction to the damping constant, in accordance with the findings of Holweger (1979). Using these values the rest of the $g^* f$ values are determined. From the columns comparing the solar with the laboratory results, it is obvious that the HM model is superiour to the HSRA for spectral line analysis, in agreement with the findings of Blackwell and Shallis (1979). On the average, the HSRA $g^* f$ values are approximately 10% stronger than the laboratory values. The standard deviation of the $g^* f$ ratios is around 35%. There also appears to be a trend towards larger ratios of solar $g^* f$ values to the laboratory ones with decreasing line strength. For the HM model the scatter is reduced to close to 20% and the average of the $g^* f$ ratio is now almost unity. The difference between Solar and laboratory oscillator strengths is less than 30% for all lines. The relatively large deviation of the strong line at 5383 Å may be due to NLTE effects. The Fe I 5127.6 Å line is the only Oxford line to show a deviation larger than 10% (this is the case for both models). This may be due to a small hidden blend. For the following analysis we shall use the empirically determined solar $g^* f$ values. This has the advantage, that the Stokes I profiles are reproduced with reasonable accuracy. Furthermore, if the radiative transfer code were to have certain inaccuracies, then it would not affect the results of the following analysis significantly, since the analysis is based on the comparison of Stokes I formed inside the fluxtube with Stokes I formed in the quiet sun and (hopefully) both profiles would be affected in the same manner.

5. Temperature

5.1. Review of Empirical Fluxtube Temperature Determinations

There has been no lack of attempts to determine the temperature inside fluxtubes. First evidence for a higher temperature in the then unknown fluxtubes compared to their surroundings was presented by St. John (1922) when he observed that although Ti I lines have the same strengths in faculæ as in the quiet photosphere, the Ti II lines are strengthened in faculæ. Local weakenings, named "line gaps" in the unpolarized profiles of Fe I lines were first observed in faculæ by McMath et al. (1956), who ascribed them to local temperature increases. Sheeley (1967) found that these line weakenings (in the unpolarized profile) are correlated with magnetic fields. Chapman and Sheeley (1968) showed that magnetic splitting is insufficient to explain the weakening in the network and that a temperature rise of 100–200 K is needed to explain this weakening. Harvey and Livingston (1969) used the ratios between the Stokes V profiles of Fe I 5250.2 Å and 5233.0 Å to determine the 'true' weakening of the Stokes I profile of Fe I 5250.2 Å inside the magnetic element. They found that a temperature increase of approximately 250 K inside small fluxtubes can explain the observed Fe I 5250.2 Å line weakening. They also observed that Fe II 5234.6 Å does not change appreciably in magnetic regions and that the amount of weakening of the unpolarised profile in fluxtubes is proportional to the amount of magnetic flux. Simon and Zirker (1974) noted that although the magnetic flux is found in patches of 1–3″ the bright filigree of Dunn and Zirker (1973) has a size of only 0.2-0.3″. Therefore, they argued, the magnetic regions are considerably larger than the bright and hot regions. However, Tarbell and Title (1977) have shown conclusively, that Simon and Zirker (1974) did not resolve individual fluxtubes, but only saw bundles of considerably smaller fluxtubes.

Besides these early determinations of temperature at a single height, a number of quantitative models of the $T(\tau)$ structure of faculæ have been made. Such models can be roughly divided into two classes, the one- and the two-component models.

The one-component models do not use the concept of a fluxtube, assuming faculæ to be horizontally homogeneous structures. These models therefore give some (ill defined) average of the properties of fluxtubes and their non-magnetic surroundings. Many of the early facular models were of this type, as are most models of chromospheric plages.

Examples of such one-component models are: Schmahl (1967, based on the centre to limb variation (CLV) of the continuum contrast), Stellmacher and Wiehr (1971, based on line weakenings), Stellmacher and Wiehr (1973, based on observations of line weakening plus continuum contrast at one μ value), Shine and Linsky (1974a, from an analysis of the damping wings of Ca II K and Ca II 8542 Å), Shine and Linsky (1974b, from the cores of Ca II H, K, and the Ca II IR triplet. This is a purely chromospheric model), Morrison and Linsky (1978, from Mg II h and k at 2802.7 Å and 2795.5 Å respectively), Hersé (1979, a simple 'step' model based on continuum contrast observations near 2000 Å), Basri et al. (1979, based on 0.8″ spatial resolution HRTS Lyα measurements. This is an upper chromosphere and lower transition region model), Vernazza et al. (1981, their model F of a bright network region is based to a large extent on the spectrum between 400 and 1400 Å. It is mainly a chromosphere and transition region model).

The two component models, which make up the other main group, suppose faculæ to be composed of, in general, a hotter component [composed of fluxtubes, which are called different things by different authors, e.g. 'microspots' (Alfvén, 1967), 'filigree' composed of 'crinkles' (Dunn and Zirker, 1974), 'magnetic elements' (Livingston and Harvey, 1969), 'magnetic knots' and 'micropores' (Beckers and Scröter, 1968a), 'facular granules' (Hirayama, 1978), 'magnetic filaments' (Stenflo, 1971), 'facular points' (Mehltretter, 1974), 'gaps' (Sheeley, 1967), 'facular granules' (Muller, 1977), 'magnetic flux concentrations' (Schüssler and Solanki, 1987)] embedded in a non-magnetic atmosphere. In the photospheric layers this is certainly the superiour approach, since both high resolution observations and indirect magnetic field measurements have shown that the magnetic field is concentrated into small fluxtubes, which are well correlated with line weakenings and higher temperatures (e.g. Sheeley, 1967; Frazier and Stenflo, 1978; Koutchmy and Stellmacher, 1978)

The first very simple two-component model was proposed by Rogerson (1961), based on obervations of

continuum contrast between $\mu = 0.1$ and 0.2. Further examples of two-component models are those of Chapman (1970, from the CLV of continuum contrast), Wilson (1971, from a reinterpretation of Chapman's data), Stenflo (1975, from the Stokes V profiles of Fe I 5247.1 Å and Fe I 5250.2 Å), Muller (1975, from the CLV of continuum contrast), Chapman (1977, 1979, from the unpolarized profiles of ten photospheric lines at disk centre), Hirayama (1978, from the CLV of continuum contrast for $\mu \lesssim 0.5$, obtained with a balloon borne telescope), Koutchmy and Stellmacher (1978, from three Fe I lines and disk centre continuum contrast measurements), Stellmacher and Wiehr (1979, based on eleven lines plus the continuum contrast as a function of wavelength. Theirs is actually a three component model since they treat granules and intergranular lanes separately), and finally the recent models of Walton (1987, based on the IR continuum contrast, eight unpolarized potospheric lines measured at two disk positions, and the Mg Ib line wings. He includes the effects of fluxtube expansion on the line profiles).

The model calculations of fluxtube temperatures presented in this thesis also belong in the category of two-component models. However, they differ in two major respects from most of the previous models. Firstly, they are based on a statistical analysis of a few hundred Fe I and II lines which have a wide range of equivalent widths and excitation potentials, whereas all previous two-component models are based on at the most a dozen spectral lines, or on continuum measurements. Secondly, they are derived from simultaneous observations of Stokes I and V. Therefore, unlike models based on Stokes I alone, they do not suffer from the handicap that the filling factor is a free parameter. Besides the models presented in sections 5.3 and 5.4 of this chapter, which are based on the work of Solanki and Stenflo (1984, 1985) and Solanki (1984, 1986), only the model of Stenflo (1975) is based on Stokes V observations. As an additional constraint on the models, their continuum intensities are also compared to observed values in the literature.

5.2. Exploratory Calculations

First exploratory calculations have been carried out with the model having approximately linear $\Delta T(\tau)$ described in Sect. 4.5.2. It is stressed again that the main aim of this section is to find the line parameters which are most sensitive to temperature, and determine their dependence on it. We also wish to find the approximate range in which the temperature difference between fluxtube and surroundings may lie, and to obtain an idea of the response of the different spectral lines to changes in the fluxtube model. The results described in this section are based on the work of Solanki and Stenflo (1984, 1985).

Since we shall use the differences and ratios of the I and I_V profiles as diagnostic tools, the quiet Sun profiles will have to be modelled first. For these exploratory calculations we assume that the line broadening is due to microturbulence alone. Using the HSRASP as our quiet Sun model, the observed Stokes I profiles in a quiet region, as represented by the v_{D_I} vs. S_I and d_I vs. S_I diagrams, can be reproduced fairly well. However, in order to fit the line widths of the stronger lines properly an increase in $\xi_{\rm mic}$ with height has to be assumed. This contradicts the determinations of $\xi_{\rm mic}(\tau)$ published in the literature, which often show a decrease of $\xi_{\rm mic}$ with τ (e.g. Holweger, 1967; Lites, 1973; Gurtovenko, 1975). This discrepancy may in part be due to the fact that we have used a too small damping constant for these calculations. However, since we are only interested in differences and ratios between the parameters of the lines formed inside and outside the fluxtube, this absolute increase in $\xi_{\rm mic}$ should not affect the results of this section significantly. In Sect. 5.4 we shall use the superiour approach of combining a depth independent microturbulence with a macroturbulence.

5.2.1. Results Based on Fe I Alone

First trial calculations have shown that the following three scatter plots are most sensitive to the temperature: $\ln(d_V/d_I)$ vs. S_I, $\ln(d_V/d_I)$ vs. χ_e, and $v_{D_V} - v_{D_I}$ vs. S_I. On the rest of the scatter plots the influence of temperature is small. Let us consider the results of some test calculations and how they compare with the data.

We will keep the parameter $f_{\rm mic} = 0.7$, $Z_W = 50$ km, and $\Delta T_{\rm top} = 500$ K fixed and calculate line profiles for $\Delta T_{\rm bot} = 0$, 250, 500, 750, 1000 K. Changing Z_W or $f_{\rm mic}$ does not affect the following discussion in any significant manner. The value for $\Delta T_{\rm top}$ has been chosen such that it is roughly comparable with the ≈ 400 K excess in the network and in plages observed by Cook et al. (1983). They observe the continuum in the UV near 1700 Å with the HRTS rocket experiment (at this wavelength the continuum is formed near $\tau = 10^{-4}$ in the external atmosphere). We shall calculate models with varying $\Delta T_{\rm top}$ in Sect. 5.2.2. As can be seen from these parameters, only models hotter than the quiet Sun at equal τ have been chosen. This choice is supported both

by previous temperature determinations in the literature, and by the fact that the $\ln(d_V/d_I)$ vs. S_I diagram can only be interpreted in terms of line weakenings (cf. Sect. 4.4.2).

Fig. 5.1 shows the smoothed mean $\ln(d_V/d_I)$ vs. S_I curves for the Fe I lines of four 1979 FTS spectra, where with the help of a somewhat simpler regression than Eq. (4.50), $\ln(d_V/d_I)$ has been reduced to the case of $\chi_e = 0$ eV, $g_{\rm eff} = 0$. The exact regression equation used reads

$$\ln(d_V/d_I) = x_1 + x_2 S_I + x_3 S_I^2 + x_4 \chi_e + x_5 S_I \chi_e + x_6 g_{\rm eff}^2 \lambda^2 / v_0^2. \qquad (5.1)$$

These data curves have been normalised such that their strongest lines coincide. Also shown are the model calculations for $\Delta T_{\rm top} = 500$ K, and $\Delta T_{\rm bot} = 0$, 250, 500, 750, 1000 K respectively. The calculated lines have $g_{\rm eff} = 0$ and $\chi_e = 0$ eV. It is obvious from the diagram that the fluxtubes in the observed network regions are hotter than those in the observed plages, at least in the deeper layers of the photosphere.

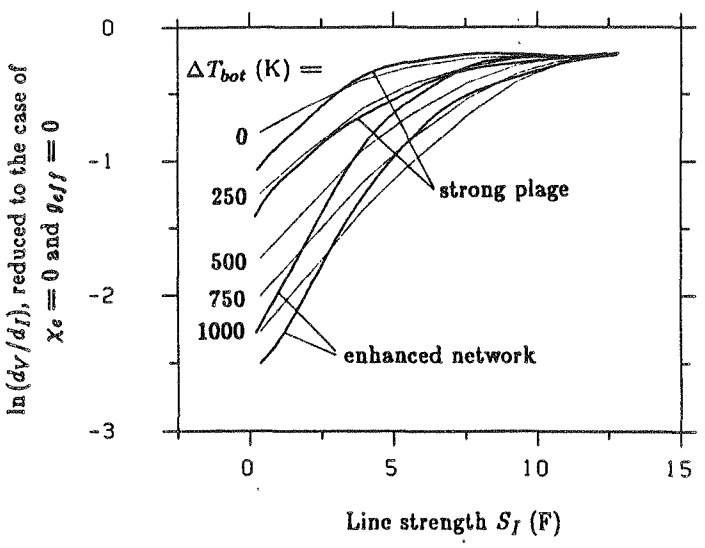

Fig. 5.1 $\ln(d_V/d_I)$ vs. S_I. The thick curves represent smoothed averages (cubic splines) of the data, reduced to the case that $\chi_e = 0$ and $g_{\rm eff} = 0$. The two steeper curves correspond to enhanced network elements, the other two to plage data. The thin lines have been calculated using models with $\Delta T_{\rm top} = 500$ K and (in the order of increasing steepness of the curve) $\Delta T_{\rm bot} = 0$, 250, 500, 750, and 1000 K. All curves have been shifted so that they coincide at the S_I of the strongest lines.

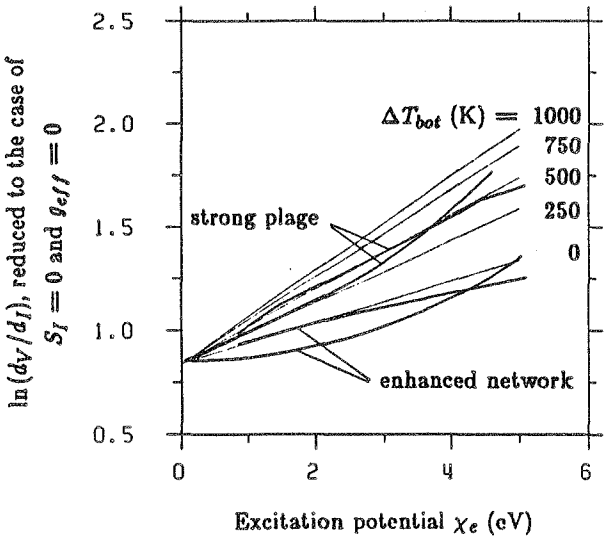

Fig. 5.2 The four thick lines represent the average (cubic spline fit) of $\ln(d_V/d_I)$ vs. χ_e when the data have been reduced to the case that $S_I = 0$ and $g_{\rm eff} = 0$. The two curves with the steeper slope correspond to enhanced network regions, the other two correspond to plages. The thin lines are theoretical curves calculated from models with $\Delta T_{\rm top} = 500$ K and $\Delta T_{\rm bot} = 0$, 250, 500, 750, and 1000 K, in the order of increasing slope, for lines with $g_{\rm eff} = 0$ and $S_I \approx 0$. The curves have been arbitrarily normalized so that they coincide at $\chi_e = 0$.

This difference in temperature between plage and network fluxtubes is supported by the plot of $\ln(d_V/d_I)$ vs. χ_e shown in Fig. 5.2. The same data, now reduced to the case $S_I = 0$ and $g_{\rm eff} = 0$ using the regression Eq. (5.1), and the parameters of model profiles with $g_{\rm eff} = 0$ and $S_I \approx 0$ are plotted. The curves have been arbitrarily normalised to make them coincide at $\chi_e = 0$ eV. In the absence of secure values of $\langle B \rangle$, only the slope or shape of $\ln(d_V/d_I)$ vs. χ_e (and $\ln(d_V/d_I)$ vs. S_I as well) contains information on the temperature, with higher fluxtube temperatures giving steeper curves. The models plotted in this figure are the same as the ones previously shown in Fig. 5.1. By comparing the two figures we see that none of these trial models can fit $\ln(d_V/d_I)$ vs. S_I and $\ln(d_V/d_I)$ vs. χ_e simultaneously. We will see in Sect. 5.3 that this is mainly due to the approximately linear $\Delta T(\tau)$ structure of the models used in this section.

Finally, Fig. 5.3 shows $v_{D_V} - v_{D_I}$ vs. S_I for data obtained in a plage region ($v_{D_V} - v_{D_I}$ is reduced to $g_{\rm eff} = 0$ only; see below), together with the calculated curves for Fe I $\chi_e = 0$ eV and Fe I $\chi_e = 3$ eV lines

for the fluxtube model with $\Delta T_{\rm top} = 500$ K and $\Delta T_{\rm bot} = 250$ K. The weak and medium strong lines in the figure have approximately the same half widths in fluxtubes as in their surroundings (compare with Fig. 4.11 and its discussion), but the strongest lines have greatly reduced widths. The qualitative form of this behaviour is intuitively clear. Since the strongest lines are heavily saturated, any temperature induced decrease in the line strength is accompanied by a corresponding decrease in the line width (in particular via the line wings). For the weak lines, on the other hand, it is the line depth which is mainly affected, since their width is dominently determined by thermal Doppler broadening. However, note that the widths of the strongest lines are only sensitive to $\Delta T(\tau)$ values $\lesssim 1000$ K, since above this temperature they are so weakened as to behave more like the weak lines. The more quantitative comparison of the model curves (of a model which reproduces $\ln(d_V/d_I)$ vs. S_I of this region relatively well) with the data shows that only the weakest and the strongest synthetic line profiles have the correct widths. The medium strong synthetic lines are too narrow. This is a first indication that the widths of spectral lines in fluxtubes may be partially determined by velocity (cf. Sect. 5.4 and chapter 7).

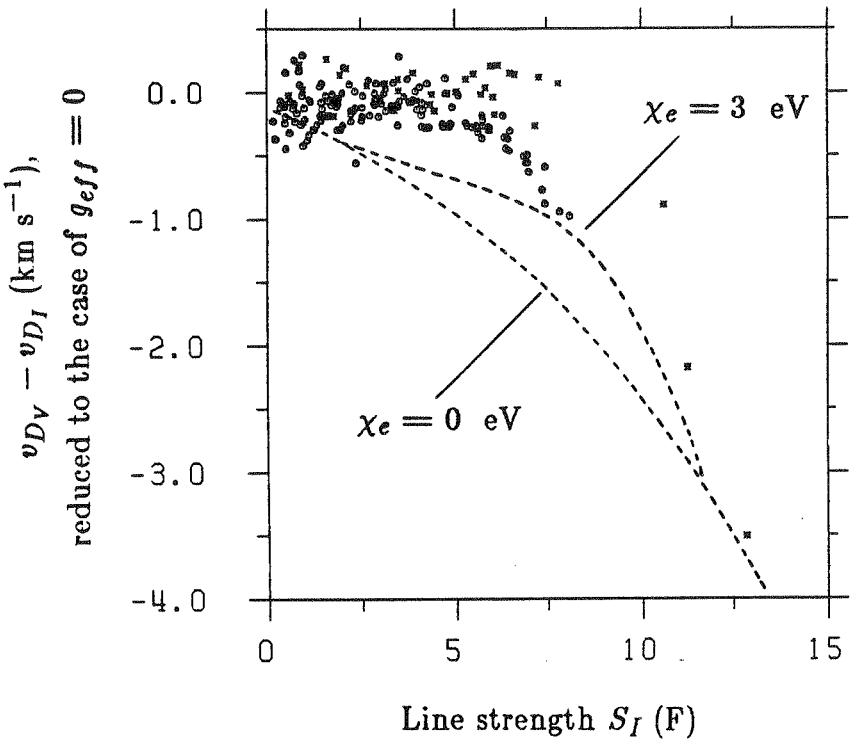

Fig. 5.3 $v_{Dv} - v_{DI}$ vs. S_I for a plage. The data points have been reduced to the case that $g_{\rm eff} = 0$ (but *not* to $\chi_e = 0$). The dashed curves have been calculated using a model with $\Delta T_{\rm top} = 500$ K and $\Delta T_{\rm bot} = 250$ K, Wilson depression $Z_W = 50$ km, and $f_{\rm mic} = \xi_{\rm mic}^{\rm fluxtube}/\xi_{\rm mic}^{\rm HSRA} = 0.7$ (best model for fitting the $\ln(d_V/d_I)$ vs. S_I plot for this plage). Both theoretical curves are for lines with $g_{\rm eff} = 0$. The lower theoretical curve has been calculated for lines with $\chi_e = 0$ eV, the upper curve for lines with $\chi_e = 3$ eV.

This notion is also supported by the fact that the data exhibit the opposite dependence on χ_e than the model calculations. This can certainly not be a temperature or magnetic field effect. It is in order to illustrate this discrepancy that the data curves have not been reduced to $\chi_e = 0$.

5.2.2. Fe I and Fe II lines

The greatly different temperature sensitivity of Fe I and Fe II is clearly illustrated by Fig. 5.4, where $\ln(d_V/d_I)$ vs. S_I is plotted for Fe I and II lines calculated with models having $Z_W = 60$ km, $f_{\rm mic} = 0.7$, $\Delta T_{\rm bot} = 750$ K, and $\Delta T_{\rm top} = 100$, 300, 500, and 900 K. As mentioned earlier, Z_W and $f_{\rm mic}$ do not have any significant effect on this diagram. For each set of parameters, ten Fe I lines with $\chi_e = 0$ eV and ten Fe II lines with $\chi_e = 3$ eV have been calculated. The Fe II lines give the almost horizontal curves near the top of the diagram. As expected the Fe II lines are hardly weakened at all. Furthermore, changing $\Delta T_{\rm top}$ simply shifts the Fe I $\ln(d_V/d_I)$ curves, instead of changing their slope. This behaviour is due to a combination of the dependence of temperature sensitivity of the line depth on the strength of the line, the fact that the stronger lines are formed higher in the atmosphere, and the temperature change induced throughout the atmosphere by the linear $\Delta T(\tau)$. We see therefore, that the Fe II lines provide us with a relatively model independent method of fixing the zero level of $\ln(d_V/d_I)$, so that both $\Delta T_{\rm top}$ and $\Delta T_{\rm bot}$ may be determined from the data.

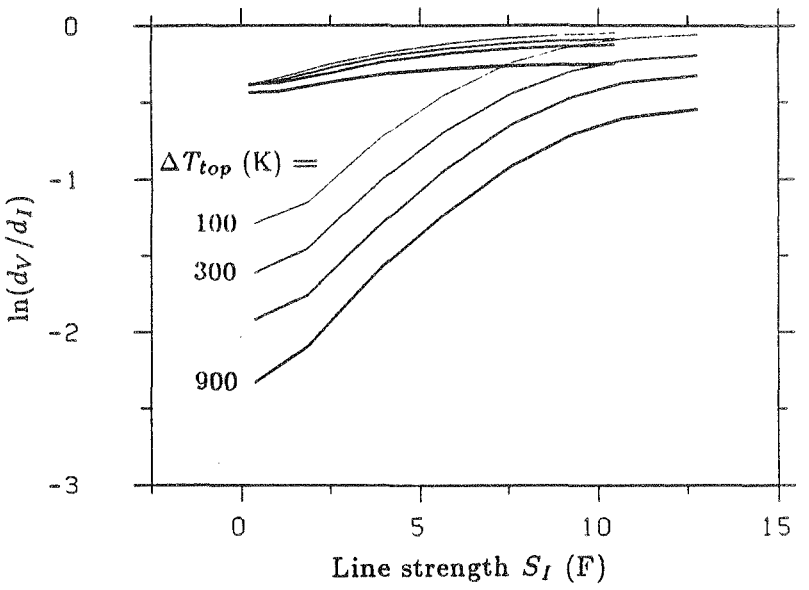

Fig. 5.4 $\ln(d_V/d_I)$ vs. S_I for four models with $f_{\rm mic} = 0.7$, Wilson depression $Z_W = 60$ km, $\Delta T_{\rm bot} = 750$ K, and $\Delta T_{\rm top} = 100$, 300, 500, and 900 K in the order of increasing thickness of the curves. The almost horizontal curves correspond to Fe II lines, the others to Fe I lines with $\chi_e = 0$ eV. All the curves are unshifted.

Fig. 5.5 illustrates the method. In Fig. 5.5a Fe I ($\chi_e < 3$ eV) and Fe II $\ln(d_V/d_I)$ data from the network have been plotted vs. S_I, together with curves for models with $\Delta T_{\rm bot} = 750$ K, which Fig. 5.1 showed to be reasonable for the network Fe I lines, and $\Delta T_{\rm top} = 100$, 300, 500, and 900 K. The observational data and model curves have been shifted, so that the results for Fe II overlap, with the Fe II curves of the model with $\Delta T_{top} = 300$ K serving as reference. Fig. 5.5b is the equivalent figure for plage data and curves calculated from models having $\Delta T_{\rm bot} = 250$ K. In this manner $\Delta T_{\rm top} = 900$ K can be ruled out. However, none of the curves really reproduces the data satisfactorily, indicating strong departures from a linear $\Delta T(\tau)$.

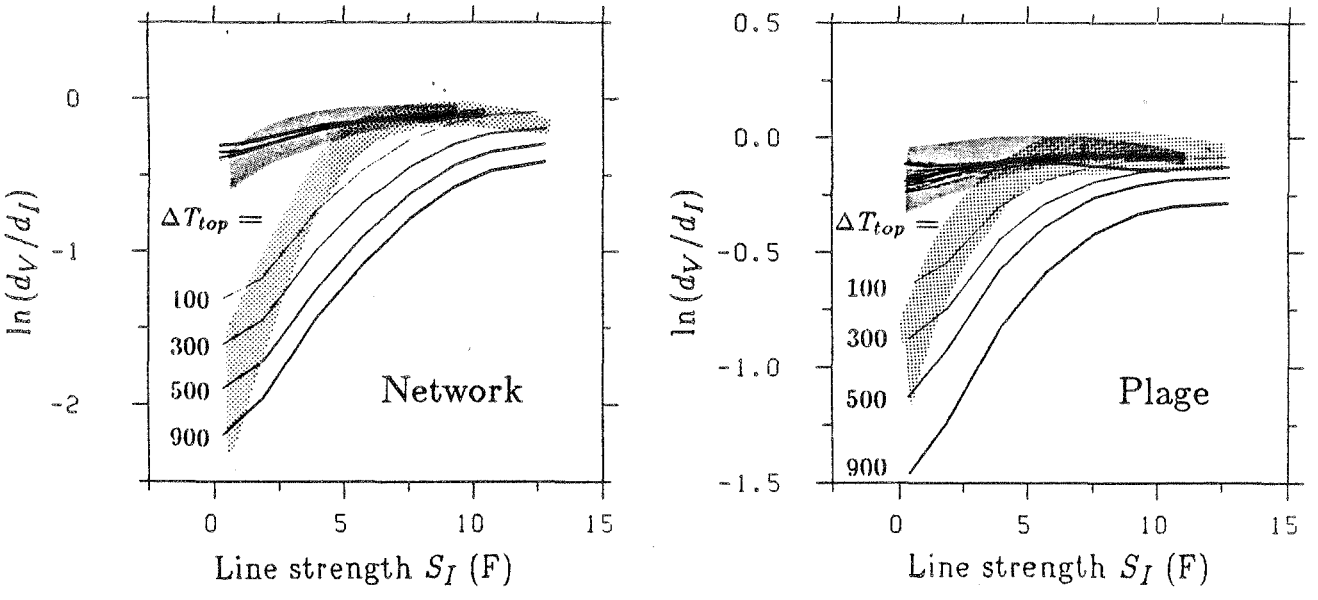

Fig. 5.5. Comparison of model calculations with observations: $\ln(d_V/d_I)$ vs. S_I. a Enhanced network data (Light shading: Fe I lines with $\chi_e < 3$ eV; dark shading: Fe II lines) plotted together with the model curves of Fig. 5.4. The empirical data and the model curves have been shifted such that the results for Fe II overlap. b Plage data (Light shading: Fe I lines with $\chi_e < 3$ eV; dark shading: Fe II lines) plotted together with model curves using $f_{\rm mic} = 0.7$, $Z_W = 60$ K, $\Delta T_{\rm bot} = 250$ km, and $\Delta T_{\rm top} = 100$, 300, 500, and 900 K (in the order of increasing thickness of the curves). All curves have been shifted such that the results for Fe II overlap.

Further inconsistency is revealed by comparing the same models to the data in a plot of $\ln(d_V/d_I)$ vs. $\chi^* = \chi_e + \chi_i$ (defined in Sect. 4.4.1), as shown for a network region in Fig. 5.6a and for a plage in Fig. 5.6b. The data have been reduced to $g_{\rm eff} = 0$ and $S_I = 0$ F. The models are the same as in Fig. 5.5a, respectively Fig.

5.5b. Data and models have been normalised in the same manner as in Fig. 5.5. In Fig. 5.6a the model with $\Delta T_{\rm top} = 900$ K gives an acceptable fit to the data, which is contrary to Fig. 5.5a. The fact that a lower $\Delta T_{\rm top}$ is required by the $\ln(d_V/d_I)$ vs. S_I data as compared to the $\ln(d_V/d_I)$ vs. χ^* data, seems to hint at the fact that $\Delta T(\tau)$ is lower, in the higher layers of the fluxtube where the stronger lines are formed [since the $\ln(d_V/d_I)$ vs. χ^* plot samples lines with $S_I \approx 0$ F]. It is quite clear from these comparisons that more sophisticated models are required.

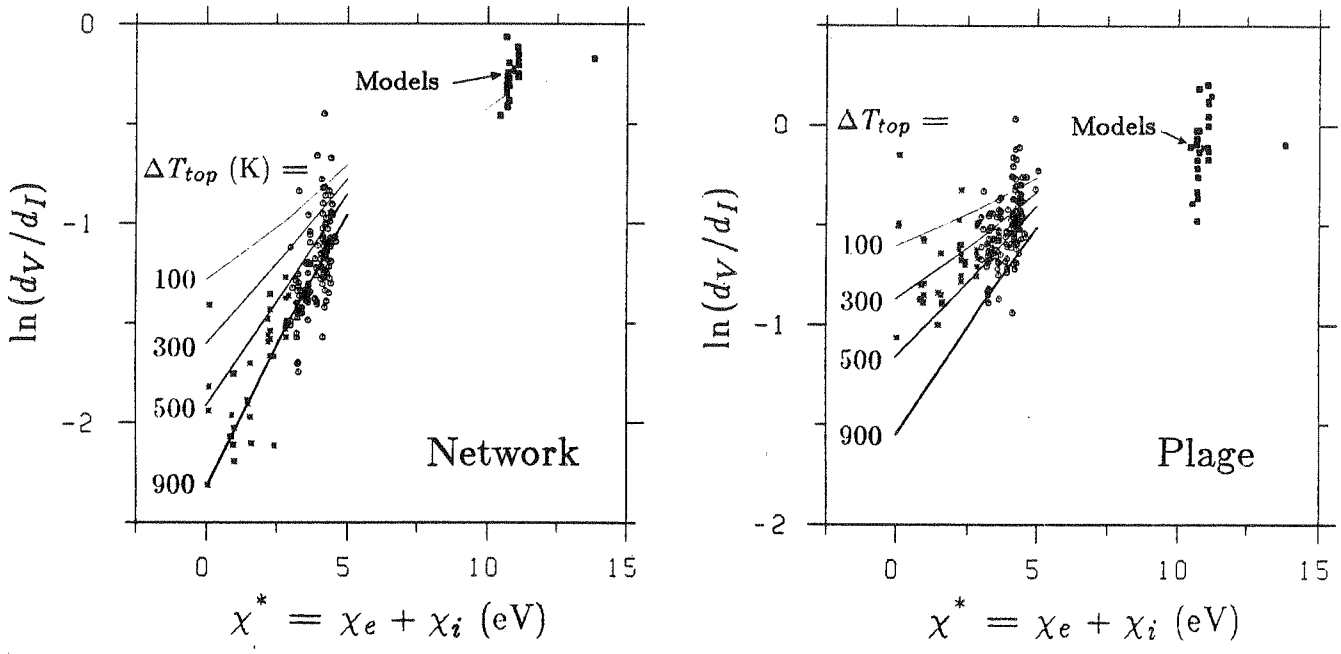

Fig. 5.6 Comparison of model calculations with observations: $\ln(d_V/d_I)$ vs. χ^*. **a** Enhanced network data reduced to the case that $S_I = 0$ and $g_{\rm eff} = 0$ using Eq. (5.1), plotted together with the curves for very weak lines calculated using the four models of Fig. 5.4. The data have been shifted such that the models provide good fits to the Fe II lines. **b** Plage data reduced to the case of $S_I = 0$ and $g_{\rm eff} = 0$, plotted together with the curves for very weak lines calculated using the four models of Fig. 5.5b. The data have been shifted such that the models provide good fits to the Fe II lines. Since the values of $\ln(d_V/d_I)$ for Fe II derived from the various models almost coincide, their locations are collectively indicated by a single arrow. Data symbols: Fe I lines with $\chi_e < 3$ eV: stars, Fe I lines with $\chi_e \geq 3$ eV: circles, Fe II lines: solid squares.

5.3. Fluxtube Temperature Structure as Determined From Line Depth Alone

5.3.1. Results

In this section we shall discuss models of $T(\tau)$ for network and plage fluxtubes derived from fitting the data in the form of $\ln(d_V/d_I)$ vs. S_I and vs. χ^* diagrams, and shall compare them with other models in the literature. The model used here is similar to the one employed in the last section (and described in Sect. 4.5.2), except that the temperature can now be specified independently at each height. Only lines with $g_{\rm eff} = 0$ are calculated (approximately forty Fe I and II lines in all per model).

Line profiles have been calculated for over a hundred different temperature stratifications with this type of model. As a first step Models with $T(\tau)$ differing from the HSRASP values only over a limited height range are calculated. The aim is to determine heights at which different lines are sensitive to the temperature. As expected, it is found that most of the Fe II lines are formed deeper in the atmosphere than the Fe I lines. This reflects the fact that the temperature increases downwards in the atmosphere, and that the Fe II spectrum arises

predominently in the hotter part of the atmosphere.

Next, model calculations with the aim of determining $T(\tau)$ through best fits to the line depths are carried out. No attempt is made to fit the line widths, since that would require some assumption regarding the velocity structure inside the fluxtube to be made. This problem will be dealt with in the next Section. An interesting result is that the best fit temperature stratification is not unique, with different models giving similar fits to the data. $T(\log \tau_{5000})$ of two such models which reproduce our network data equally well (models 3E and 6N) are plotted in Fig. 5.7a, together with the common network and plage model of Stenflo (1975), Hirayama's network model B (1978), the filigree model of Koutchmy and Stellmacher (1978), the common filigree and faculæ model of Stellmacher and Wiehr (1979), and the HSRASP.

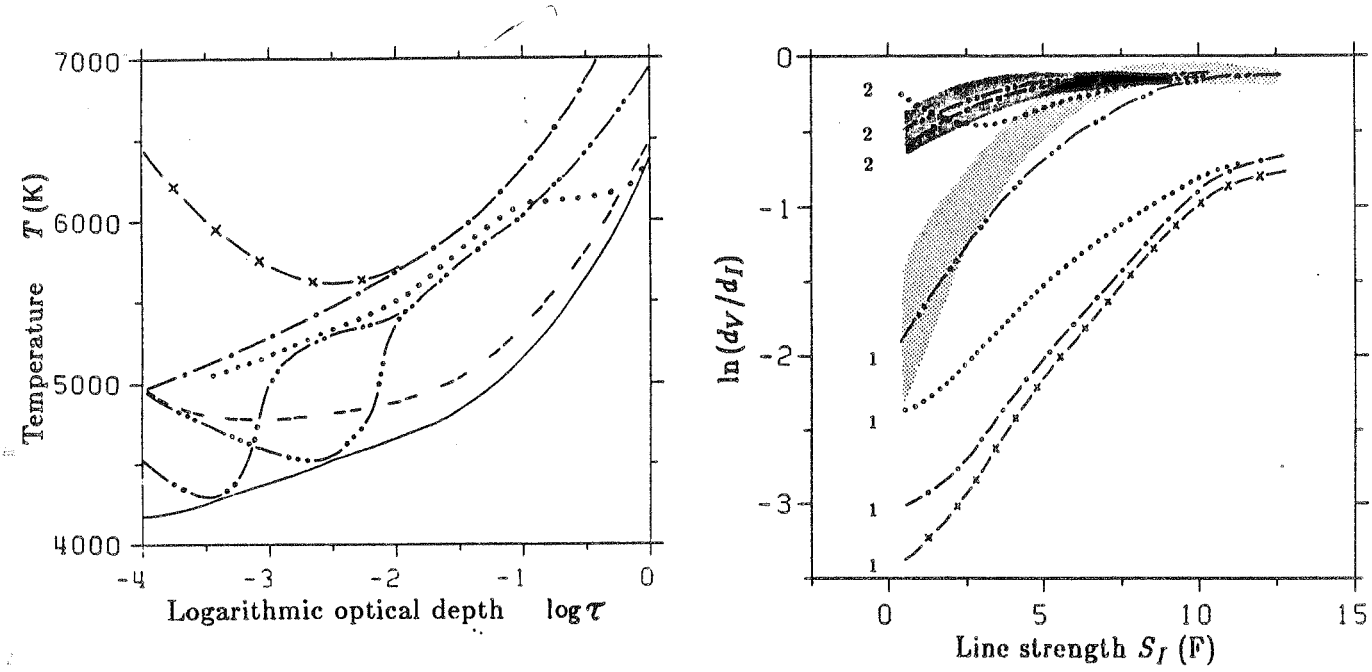

Fig. 5.7 a Temperature stratification of some empirical models of fluxtubes in the network. The HSRA (solid line) has been plotted for comparison. Stenflo (1975): - - - -, Hirayama (1978) model B: · · · ·, Koutchmy and Stellmacher (1978): — × —, Stellmacher and Wiehr (1979): — · —, Solanki (1984), model 3E: — · · —, model 6N: — · · · —. b $\ln(d_V/d_I)$ vs. S_I for network data (light shading: Fe I, $\chi_e < 3$ eV; dark shading: Fe II), and the models listed in the caption of Fig. 5.7a. Model curves labeled '1' refer to Fe I, those labeled '2' refer to Fe II.

How these models compare with the data is illustrated in Fig. 5.7b, where $\ln(d_V/d_I)$ is plotted vs. S_I for the data obtained in the network (light shading: observed Fe I lines reduced to $g_{\rm eff} = 0$, dark shading: observed Fe II lines, also reduced to $g_{\rm eff} = 0$), and for lines calculated using some of the models shown in Fig. 5.7a. The symbols used for each model are the same in both plots. In order to keep Fig. 5.7b from getting too crowded the Fe II curve of Koutchmy and Stellmacher (1978) which is very similar to the curve resulting from the Stellmacher and Wiehr (1979) model together with the curves of Stenflo's (1975) model have not been plotted. However, the results of Stenflo's model can be seen in Fig. 5.8b, which is discussed below. The results of the models 3E and 6N lie so close together that they are both represented by the same curves.

Fig. 5.8a shows $T(\tau)$ for the HSRASP and a set of plage models: Stenflo's (1975) model, the active region model Z of Hirayama (1978), the facular model of Chapman (1979), the model of Stellmacher and Wiehr (1979) and two models giving good fits to our active region plage data (6K and 6P). The plage data are compared with the results of the model calculations in Fig. 5.8b. To avoid crowding, the results of the common facular and filigree model of Stellmacher and Wiehr (1979) have not been repeated from Fig. 5.7b.

Finally, in Fig. 5.9 the different models are compared with the data in the $\ln(d_V/d_I)$ vs. χ^* diagram. Data from a network region, reduced to $S_I = 0$ and $g_{\rm eff} = 0$, and the models of Stenflo (1975), Hirayama (1978, model B), Koutchmy and Stellmacher (1978), Chapman (1979), Stellmacher and Wiehr (1979), and our network models 3E and 6N are plotted. These last two models give very similar results for this diagram as well, so that again

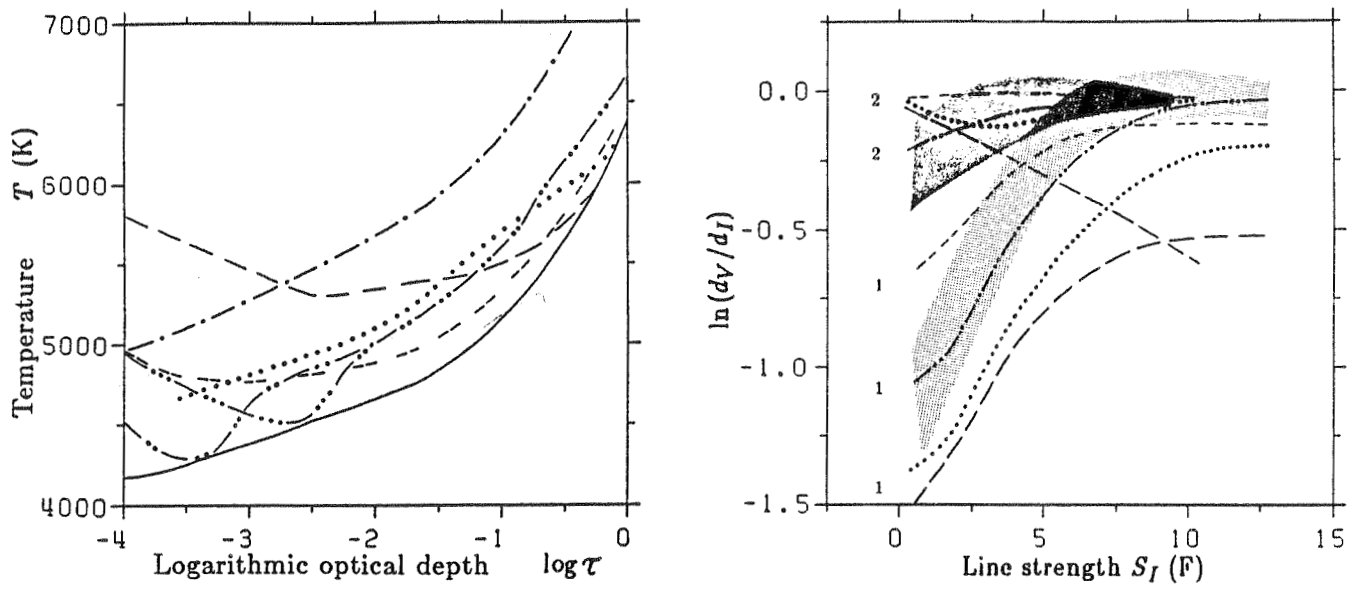

Fig. 5.8 a Temperature stratification of some empirical models of plage fluxtubes and the HSRA (solid line). Stenflo (1975): - - - -, Hirayama (1978) model Z: · · · ·, Chapman (1979): — —, Stellmacher and Wiehr (1979): — · —, Solanki (1984), model 6K: — · · —, model 6P: — · · · —. **b** $\ln(d_V/d_I)$ vs. S_I for plage data (light shading: Fe I, $\chi_e < 3$ eV; dark shading: Fe II), and the models listed in the caption of Fig. 5.8a. Model curves labeled '1' refer to Fe I, those labeled '2' refer to Fe II.

only one curve has been plotted. The model curves have been shifted in such a way that they all reproduce the Fe II data equally well.

Fig. 5.9 $\ln(d_V/d_I)$ reduced to $S_I = 0$ and $g_{\rm eff} = 0$ vs. χ^* for network data (light shading: Fe I, dark shading: Fe II) and the models listed in the caption of Fig. 5.7a.

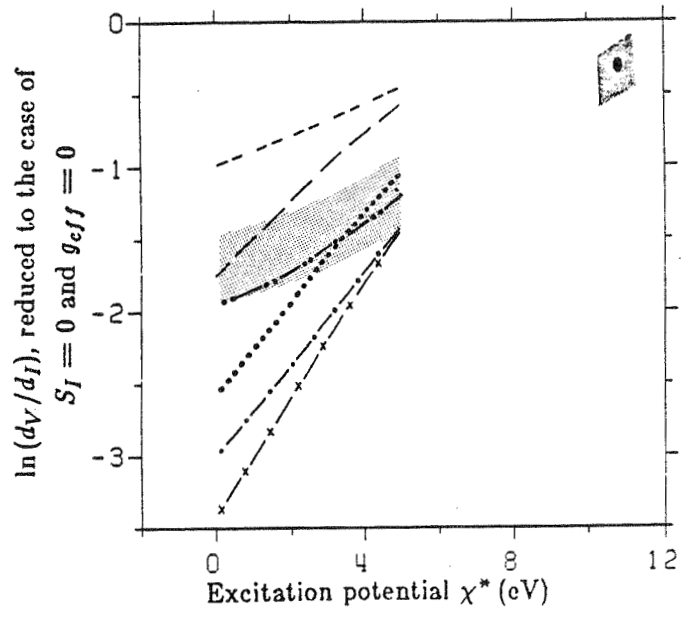

5.3.2. Discussion

In the following we list some comments on the figures and the models presented above.

- The large spread of the model curves in Figs. 5.7b and 5.8b is evidence for the temperature sensitivity of the $\ln(d_V/d_I)$ vs. S_I diagram. It also reflects the different types of data on which the various models are based. Usually the data come from more or less high spatial resolution Stokes I or continuum observations (and sometimes both), the exceptions being Stenflo (1975), who also used the Stokes V profiles of two lines, and models presented in this thesis. The models using both Stokes I and V represent just the magnetic regions

of the solar photosphere, whereas a usually unknown amount of light coming from non–magnetic regions has to be compensated for when only Stokes I data are used. One component 'average facula' models have not been included, since they represent averages of the magnetic and non–magnetic components of active regions and thus cannot be directly compared to our models. The facular model of Muller (1975) is not defined for sufficiently small τ values to allow Fe I line profiles to be calculated with it properly, and it has therefore also been excluded.

- It is confirmed that the fluxtubes in the observed network and plage regions have different temperature structures, with network fluxtubes having higher temperatures in their lower regions. Hirayama (1978) also postulated different temperatures for what he calls 'facular granules' in the network and in plages, which we interpret to signify fluxtubes. Some problems remain with this interpretation, since Hirayama requires the magnetic field strength to be larger *outside* his facular granules than inside them.

- Although the temperature structures of the two best fit plage models, 3E and 6N, look very different at first sight, they have certain important features in common. The structure of the models below their respective temperature minima is very similar, so that model 6N differs from model 3E mainly due to the fact that its temperature minimum is shifted outwards to a smaller τ value. The approximate shape of $T(\tau)$ remains the same. In particular a pronounced depression in T is needed at some τ value, where the fluxtube approaches the temperature of the surroundings at equal optical depth, in order to reproduce the data correctly. The same comment is also valid for the best fit network models 6K and 6P. The question of whether this depression is real or is an artifact of the model assumptions is discussed in Sect. 5.5.

- The models are rather uncertain below $\log\tau = -1$.

5.4. Fluxtube Temperature Determined From the Full Line Profile

The model calculations presented in the last section were able to reproduce the line depths of the I_V profiles, as represented by the $\ln(d_V/d_I)$ vs. S_I and $\ln(d_V/d_I)$ vs. χ^* plots. However, no attempt was made to model the line widths, as given for example by the $v_{D_V} - v_{D_I}$ vs. S_I diagram. Indeed Fig. 5.3 showed that in the absence of velocity broadening the calculated lines are too narrow as compared to the observed profiles.

In this section we shall follow the analysis of Solanki (1986) and present an attempt to determine the $T(\tau)$ stratification by fitting the complete line profile. In order to do this the calculated profiles have to be artificially broadened by velocity in the fluxtube. We approximate this broadening mechanism by a macroturbulence and height independent microturbulence velocity. More details on the velocities involved, their magnitude and interpretation are given in Chapter 7. At this point, it suffices to say that a description involving macroturbulence is particularly simple to employ, since the effects of temperature and velocity on the line profile are not as strongly coupled as for example when using a microturbulence velocity alone. The line profiles are first calculated for a certain $T(\tau)$ model without additional velocity (or with just a height independent microturbulence), and are then broadened by the desired amount, by convoluting them with a macroturbulence velocity profile of a given form.

If we wish to determine $T(\tau)$ from a fit to the full line profile, then we are no longer independent of the velocity structure. The differentiation between $T(\tau)$ determination and the velocity determination is therefore somewhat artificial. However, since physically they are two quite different quantities, we will discuss each individually (temperature in this chapter, velocity in chapter 7). The fits to the line profiles etc. will be discussed in this chapter, so that only the derived velocity structure remains to be discussed in chapter 7.

In addition to the velocity broadening, there is another difference to the model calculations described in the previous sections of this chapter, namely that the physically somewhat more realistic model described in Sect. 4.5.3 is used. Furthermore, the strongest lines in our sample have a non-negligible contribution from the atmosphere above the temperature minimum. To keep the chromospheric temperature rise from falsifying the LTE calculations, the HSRASP temperature structure has therefore been modified above the temperature minimum, so that its $T(\tau)$ is parallel to that of the Holweger and Müller (1974) LTE solar atmosphere model above $\tau = 10^{-4}$. This gives quite reasonable quiet Sun line profiles, even for the strongest lines considered.

5.4.1. Line Profiles in the Quiet Photosphere

Since the full line profile is now used, and since, if we neglect its asymmetry, the mean photospheric Stokes I profile can be reproduced relatively well using a mixture of macro- and depth independent microturbulent broadening (e.g. Smith et al., 1976; Nordlund, 1978; Holweger et al., 1978), we shall attempt another fit to the quiet Sun line profiles. For the microturbulence velocity a constant 0.8 km sec^{-1} is chosen as suggested by Blackwell and Shallis (1979) for the HSRA. Following Smith et al. (1976) a macroturbulent velocity distribution having the shape of a Voigt function $H(a_{\rm mac}, \xi_{\rm mac})$ ($a_{\rm mac}$ is the ratio of 'damping' to 'Doppler' width and $\xi_{\rm mac}$ is the 'Doppler' width of the macroturbulent velocity profile, see Sect. 2.2.3 for a definition of the Voigt profile) is then convoluted with the calculated line profile. The two free parameters per line are varied to give a best fit to the observed line parameters. We illustrate the resulting fits in Figs. 5.10a and b for calculations with $\delta_\Gamma = 2.5$. In Fig. 5.10a the line depth, d_I, is plotted vs. line strength, S_I. The solid curve represents synthetic Fe I lines with $\chi_e = 1.5$ eV, the dashed curve represents synthetic Fe I lines with $\chi_e = 4$ eV, and the dot-dashed curve represents synthetic Fe II lines. In Fig. 5.10b the line widths at the four chord levels $0.1d_I$, $0.3d_I$, $0.5d_I$, and $0.7d_I$ above line bottom are respectively plotted against S_I. A fit of comparable quality can be achieved with $\delta_\Gamma = 1$ as well, the only difference being that the derived macroturbulence velocities are somewhat different.

It will be noticed that the fit is not always perfect. For example, at the $0.1d_I$ chord between $S_I = 5$ F and 10 F only the Fe I data with $\chi_e \geq 3$ eV are well reproduced by the calculated profiles between $S_I = 5$ F and 10 F, the calculated Fe I, $\chi_e < 3$ eV and Fe II lines being too narrow. The lines with $S_I > 10$ F are not well reproduced at all four chords either. The main factor leading to this discrepancy is departure from LTE since for these lines, although their equivalent width is not greatly changed from LTE to NLTE, their *shape* is affected the most of all the lines (cf. Solanki and Steenbock, 1987). The $(a_{\rm mac}, \xi_{\rm mac})$ values derived for the quiet photosphere will be discussed in greater detail in chapter 7.

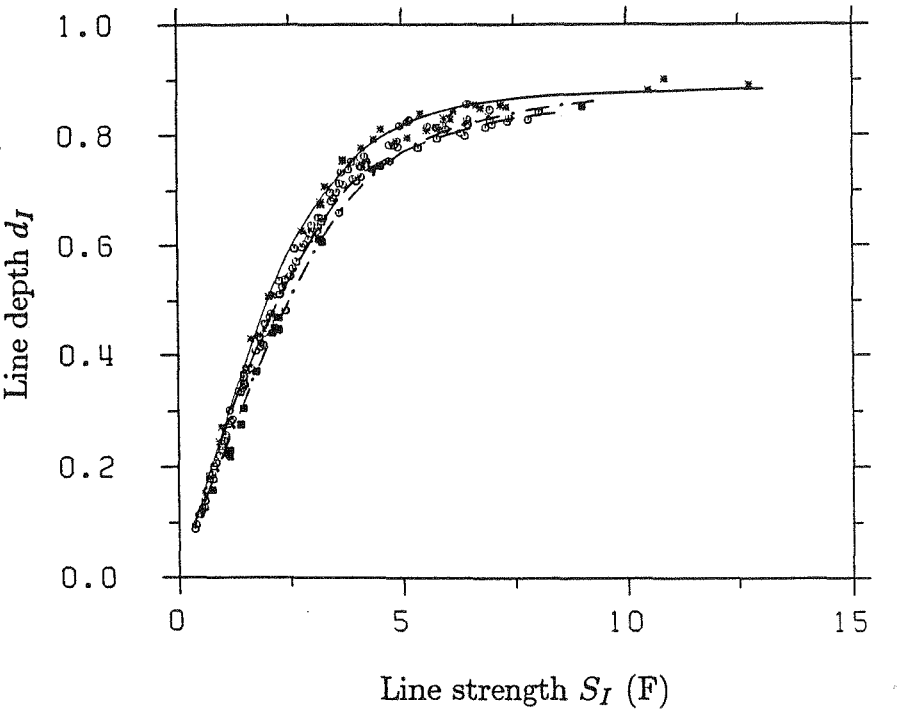

Fig. 5.10 a d_I vs. S_I for Fe I and II lines in the quiet photosphere. The symbols have the same meaning as in Fig. 5.6. The three curves are model calculations based on the HSRA. Solid curve: Fe I lines with $\chi_e = 1.5$ eV, dashed curve: Fe I lines with $\chi_e = 4$ eV, dot-dashed curve: Fe II lines with $\chi_e = 3$ eV. Empirical damping factor: $\delta_\Gamma = 2.5$.

In addition to the thirty hypothetical lines, the ten Fe I and II lines selected in Sect. 4.5.3 and listed in Table 4.4 have also been used. The observed and calculated quiet Sun Stokes I profiles of four of them, Fe I 5127.7 Å, 5247.1 Å, 5383.4 Å, and Fe II 5414.1 Å are shown in Fig. 5.11. The fit to these four lines is average in quality compared to the other six lines.

5.4.2. Fluxtube Temperature Structure

First a test is made to see if the improved model described in Sect. 4.5.3 still gives too narrow line profiles in the absence of velocity broadening. In Fig. 5.12 $v_{D_V} - v_{D_I}$ is plotted against S_I for observed and calculated spectral lines. The I_V data are from a network region, the Stokes I data are taken from a very quiet region (to avoid

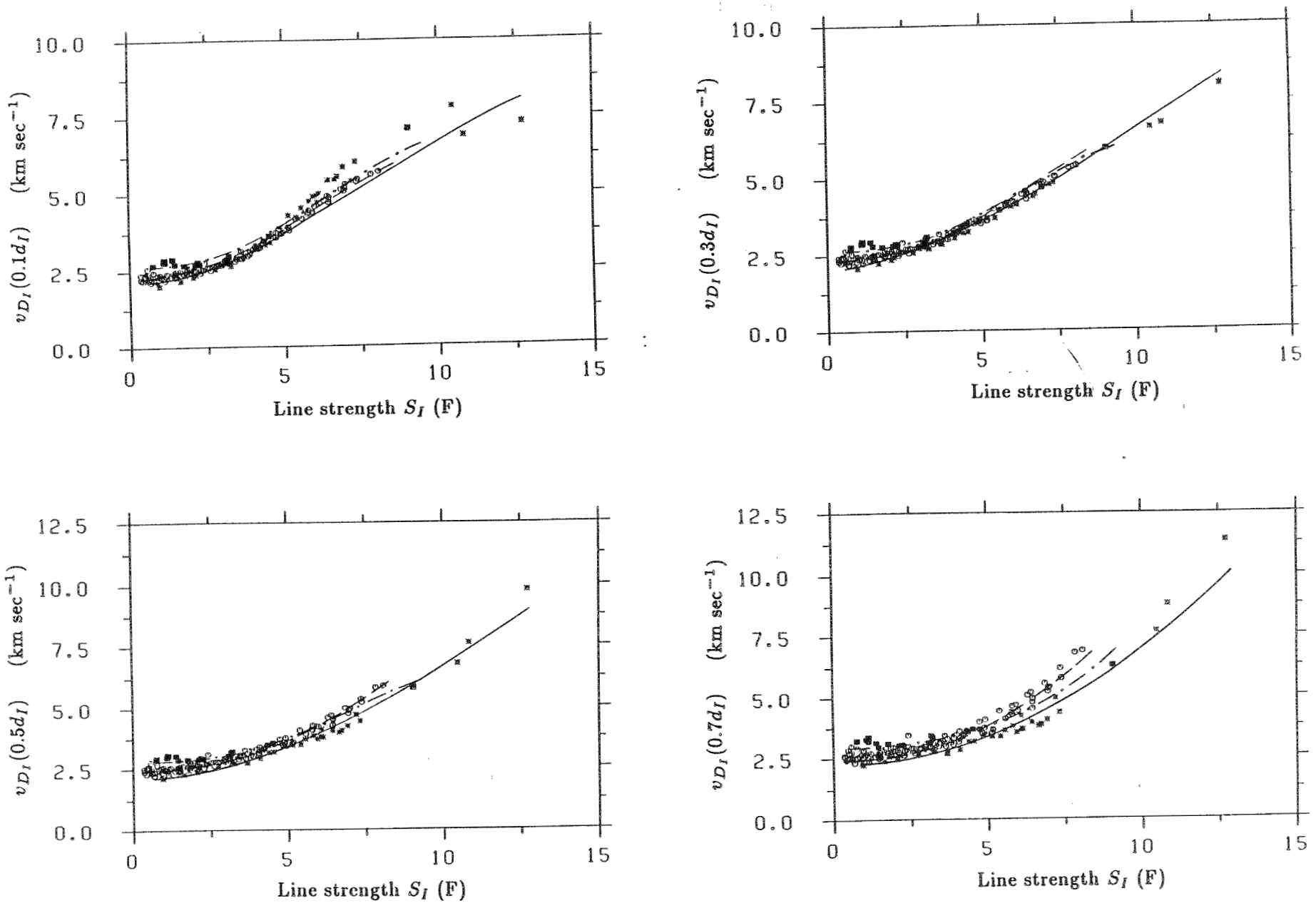

Fig. 5.10 b The four sub-figures show $v_{D_I}(0.1d_I)$ vs. S_I, $v_{D_I}(0.3d_I)$ vs. S_I, $v_{D_I}(0.5d_I)$ vs. S_I, and $v_{D_I}(0.7d_I)$ vs. S_I respectively. Here $v_{D_I}(0.1d_I)$ is the line width of Stokes I at a level $0.1d_I$ above line bottom etc., expressed in velocity units in terms of the Doppler width of a Gaussian having the same width as Stokes I at the respective level. Quiet Sun data and model calculations based on the HSRA. The data and the model results are denoted by the same symbols and curves as in Fig. 5.10a.

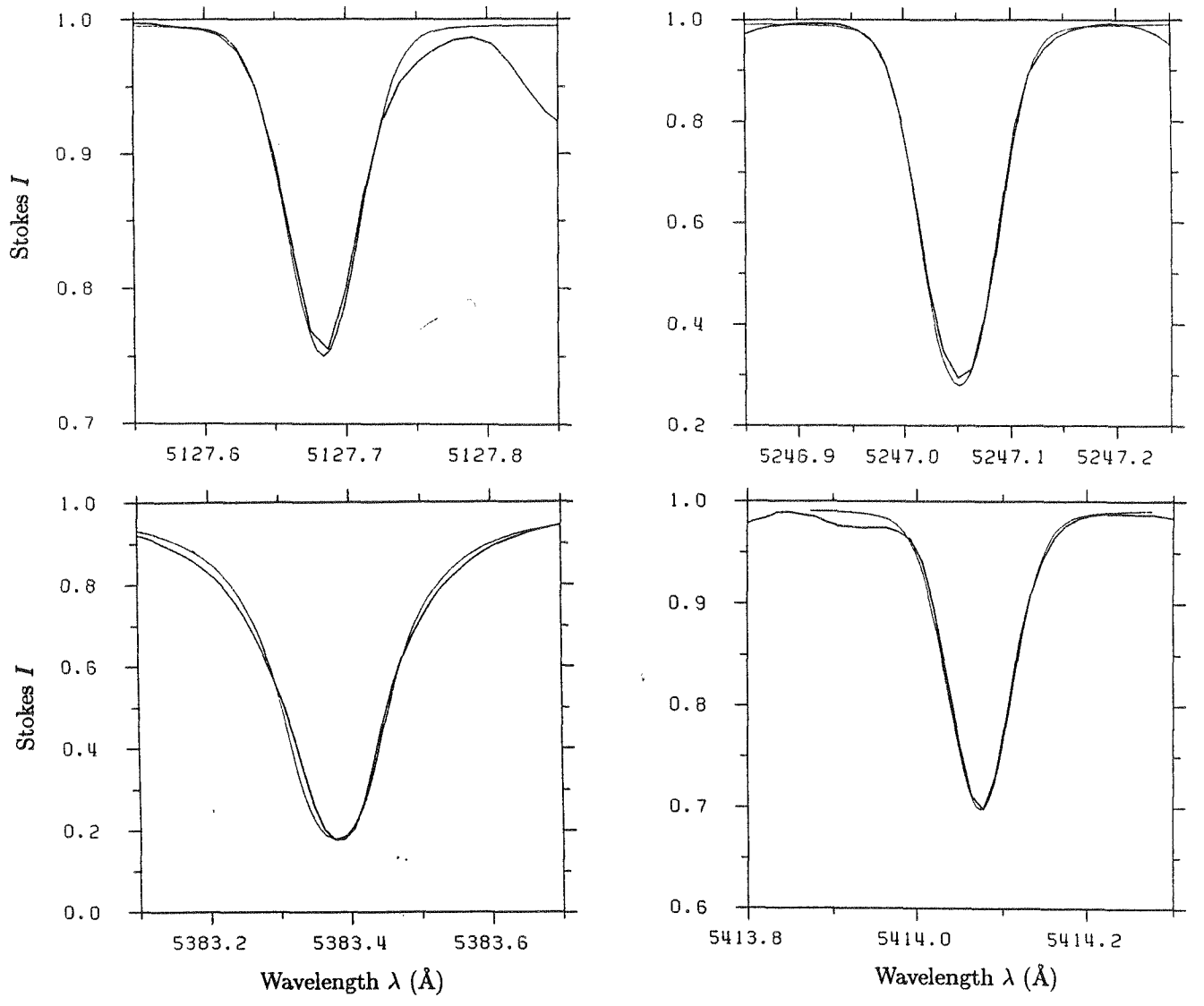

Fig. 5.11 Stokes I profiles of Fe I 5127.7 Å, 5247.1 Å, 5383.4 Å, and Fe II 5414.1 Å on the quiet Sun. Observations: thick curves; synthetic profiles: thin curves.

contamination of Stokes I by light from magnetic elements), and the model curves are produced by subtracting the v_{D_I} values calculated in Sect. 5.4.1 from the line widths of the profiles of a model with no internal velocity (reproducing $\ln(d_V/d_I)$ of network data). The solid, dashed, and dot-dashed calculated curves correspond to lines with the same atomic parameters as in Fig. 5.10. The data have been reduced to the case of $g_{\rm eff} = 0$ using the $v_{D_V} - v_{D_I}$ version of the regression Eq. (4.48). In accordance with the results of Sect. 5.2.1, the model curves lie below the data, specially for the medium strong lines. In addition, again in agreement with Sect. 5.2.1, the relative positions of the model curves and data points of different excitation lines also differ from each other. The experience gained with the models discussed in Sect. 5.2 and 5.3, as well as with a smaller grid based on the improved models suggests that the I_V line widths and depths cannot be simultaneously reproduced for any fluxtube temperature stratification if the synthetic profiles are not broadened by velocity. Within our grid of models this statement is found to be valid for both tested values of δ_Γ, i.e. $\delta_\Gamma = 1$ and $\delta_\Gamma = 2.5$. However, by including a macroturbulent broadening, models can be constructed which reproduce both the line depth and the line width for network, respectively plage data.

Harvey et al. (1972) have previously noted that the measured V profiles of Fe I 5250.2 Å are broader than the calculated ones. They had to artificially broaden the calculated profiles to make them match the data. They interpreted this broadening as due to a spread in the magnetic field strength. Indeed for only one V profile, it is not possible to distinguish between broadening due to velocity or a magnetic field. However, with many lines of various $g_{\rm eff}$ we can test the two hypotheses. Most of the lines in our sample have Landé factors near 1 and

are therefore not so sensitive to magnetic broadening. Furthermore, in Figs. 5.8 and 5.12 the data have been reduced to the case of $g_{\rm eff} = 0$, so that the residual broadening has to be mainly due to velocity.

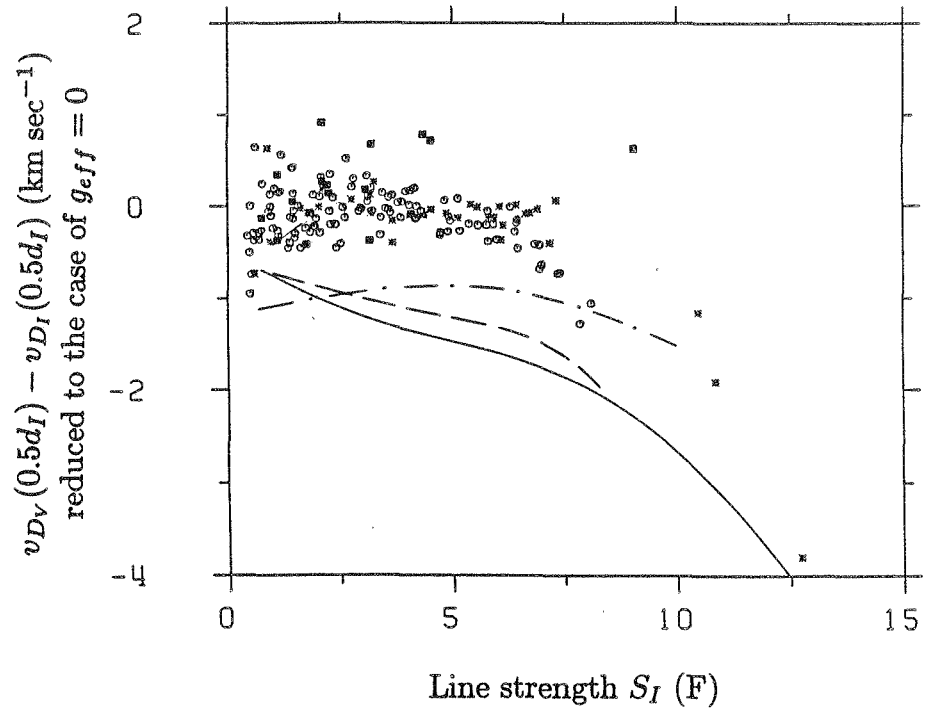

Fig. 5.12 $v_{D_V} - v_{D_I}$, reduced to the case of $g_{\rm eff} = 0$, plotted vs. S_I. Symbols as in Fig. 5.10a. The data are from a network region and the calculations are based on a network fluxtube model. The calculated profiles are unbroadened by any velocity. $\delta_{\Gamma} = 2.5$.

As a starting point for a better model, the models found to give a good fit to the $\ln(d_V/d_I)$ vs. S_I plot in Sect. 5.3 are chosen. However, for a number of reasons, these models have to be modified. Firstly, they were derived from fits to the line depths only, without taking the line widths into account, so that when the calculated profiles are convoluted with a macroturbulence to reproduce the observed line widths, the good fit to the line depths is lost. Secondly, the photospheric lines were fitted by using a depth dependent *micro*turbulence alone in the calculations described in the last section. The microturbulence inside the fluxtube was assumed to be simply some fixed fraction (typically 0.5 – 0.7) of the photospheric microturbulence. Since we do not assume any microturbulence at all inside the fluxtube in this section, this will also change the inferred temperature structure. Finally, the inclusion of atmospheric layers above the temperature minimum in the model changes the calculated profiles of the strongest lines somewhat.

However, some basic characteristics of the earlier models remain. For example, the difference between the temperature of fluxtubes in the plage and network regions studied, which was discovered earlier, is confirmed by the new models. The network fluxtubes are again observed to be hotter than plage fluxtubes, specially in the lower regions. The depression in temperature at some τ value, where it falls almost to the quiet Sun value at that τ, found as a unifying characteristic in the earlier models is still visible, although it is decidedly weakened. The ambiguity in temperature structure, as determined by Fe I and II lines alone, still appears to be present, although we have not carried out such extensive test calculations as in the previous Section.

The temperature structures of network and plage models producing the best fit line profiles are shown in Fig. 5.13 as a function of τ_{5000}, the continuum optical depth at 5000 Å. The HSRASP temperature structure is also shown for comparison.

How such a model (network), combined with macroturbulence broadening, reproduces the $v_{D_V} - v_{D_I}$ vs. S_I and the $\ln(d_V/d_I)$ vs. S_I data from a network region is shown in Fig. 5.14a and b. A fit of similar accuracy has also been obtained for the plage data. In addition, these models can reproduce the $\ln(d_V/d_I)$ vs. χ^* diagrams with a similar accuracy as the models described in Sect. 5.3. All in all, the fits achieved by these models, although not perfect, are of reasonable accuracy. For further improvements, additional data containing better information on

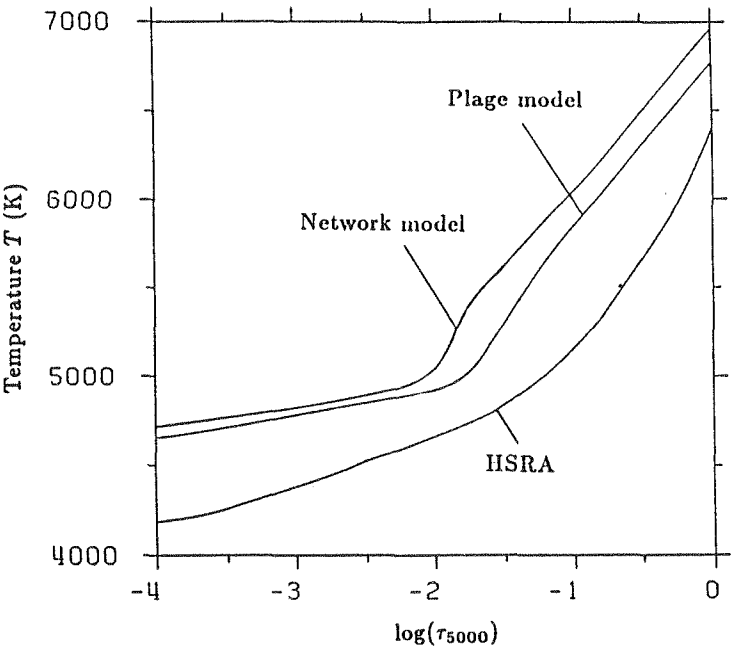

Fig. 5.13 The temperature T in K vs. the logarithm of the optical depth $\log(\tau_{5000})$ for the HSRASP and for a model each of fluxtubes in the network and in active region plages.

levels below $\log\tau = -1$ and above $\log\tau = -3$, as well as improved modelling techniques (1.5-D radiative transfer etc.) are required. On a longer term basis, NLTE effects should be included as well, as is evident from the NLTE test-calculations of Solanki and Steenbock (1987). The empirical damping correction factor does not have a large effect on the determined temperature structure, both $\delta_\Gamma = 1$ and $\delta_\Gamma = 2.5$ giving approximately similar $T(\tau)$ values. A few models have also been calculated with a combination of macroturbulence and depth independent microturbulence. It is found that as long as $\xi_{\rm mic} \leq 1$ km sec^{-1}, no significant change in the temperature structure is required. As will be shown in chapter 7, values of $\xi_{\rm mic}$ larger than 1.5 are excluded by the data, so that a constant $\xi_{\rm mic}$ should not greatly influence the determined temperature structure.

As an additional illustration to how the models reproduce the data, Fig. 5.15 shows the I_V profiles, observed in a plage, of the three Fe I lines at 5127.7 Å, 5247.1 Å, and 5383.4 Å and the Fe II 5414.1 Å line, together with their calculated Stokes I profiles from the best fit plage model. Fe II 5414.1 Å and Fe I 5383.4 Å are the two worst fit I_V profiles in our sample of ten lines, whereas the other two figure among the better reproduced lines. These ten I_V profiles have been normalised using the same $\langle B\rangle$ as is used to normalise the $\ln(d_V/d_I)$ curve. The correspondence for all ten lines is quite reasonable, considering the fact that some distortion of the I_V profile due to noise and Stokes V asymmetry is bound to occur. The Fe I 5250.2 Å line is also reproduced with an accuracy similar to Fe I 5247.1 Å, a somewhat surprising result, since its large Landé factor of 3.0 would lead one to expect that the first order approximation on which the calculation of the I_V profile is based may be insufficient for this line. * The fit to the individual profiles achieved with the best network model is slightly worse. This can, at least to a large part, be explained by the smaller signal to noise ratio in the network data, which is due to the smaller filling factor and correspondingly weaker Stokes V signal. The larger asymmetry of the network Stokes V profiles may also play a role.

5.5. Discussion

Finally, let us discuss some of the results and consequences of the work presented in this chapter and remark on possible improvements, as well as on other methods of determining fluxtube temperatures from FTS data.

* This may be simply due to the fact that the magnetic field used in these models is too weak ($B(\tau=1) \approx 1400$ G). As the results of Sect. 6.3 show, a field with $B(\tau=1) \approx 2000$ G provides a better fit to the Stokes V 5250/5247 line ratio. In such a strong field the weak field approximation is no longer valid for Fe I 5250.2 Å and its I_V profile alone is no longer a valid approximation to Stokes I. However, using Eq. (4.7a) one might still be able to reproduce 5250.2 Å reasonably.

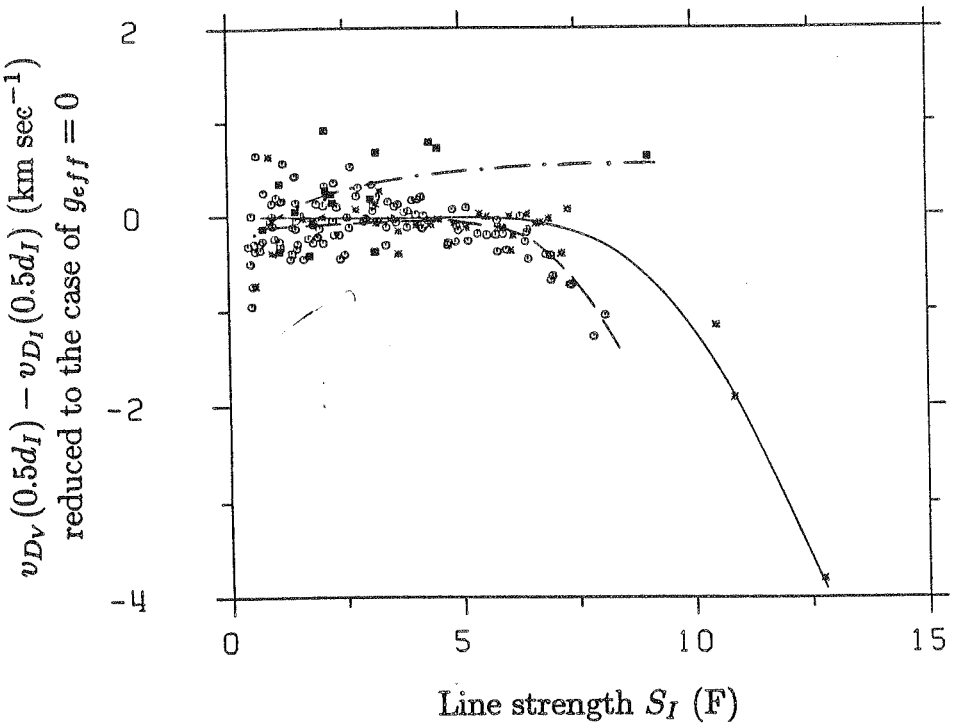

Fig. 5.14 a The same as Fig. 5.12, except that the calculated profiles have been broadened by a macroturbulence to make them match the data. The network model shown in Fig. 5.13 has been used.

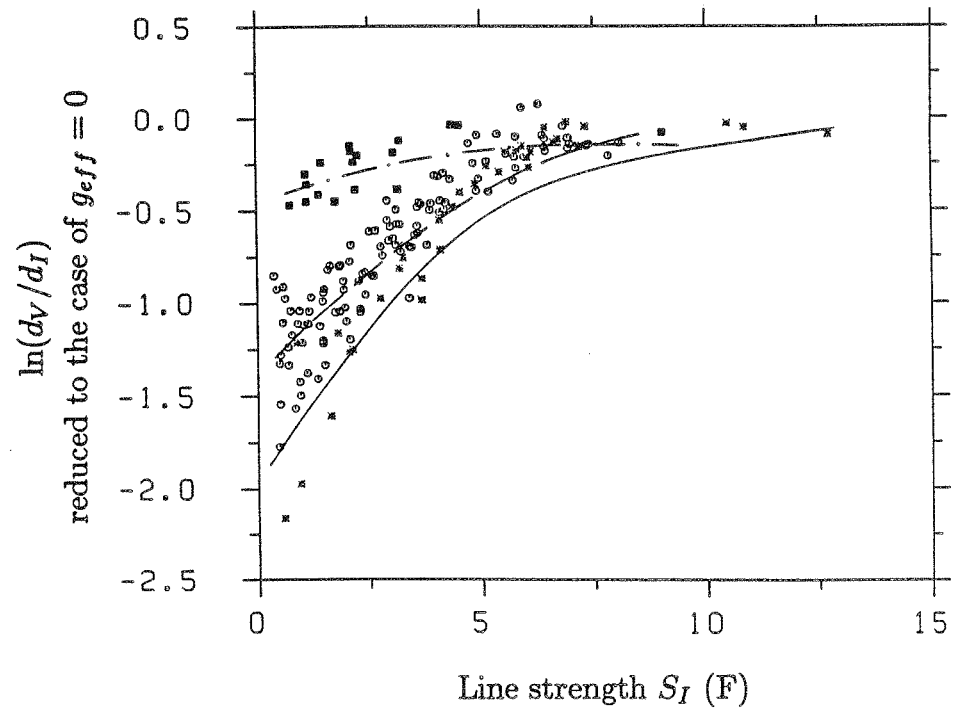

Fig. 5.14 b $\ln(d_V/d_I)$ plotted against S_I. Symbols as in Fig. 5.10a. The calculated line profiles have been convoluted with a macroturbulent velocity. The data were obtained in a network region, the model is the same as in Fig. 5.14a. $\delta_T = 2.5$.

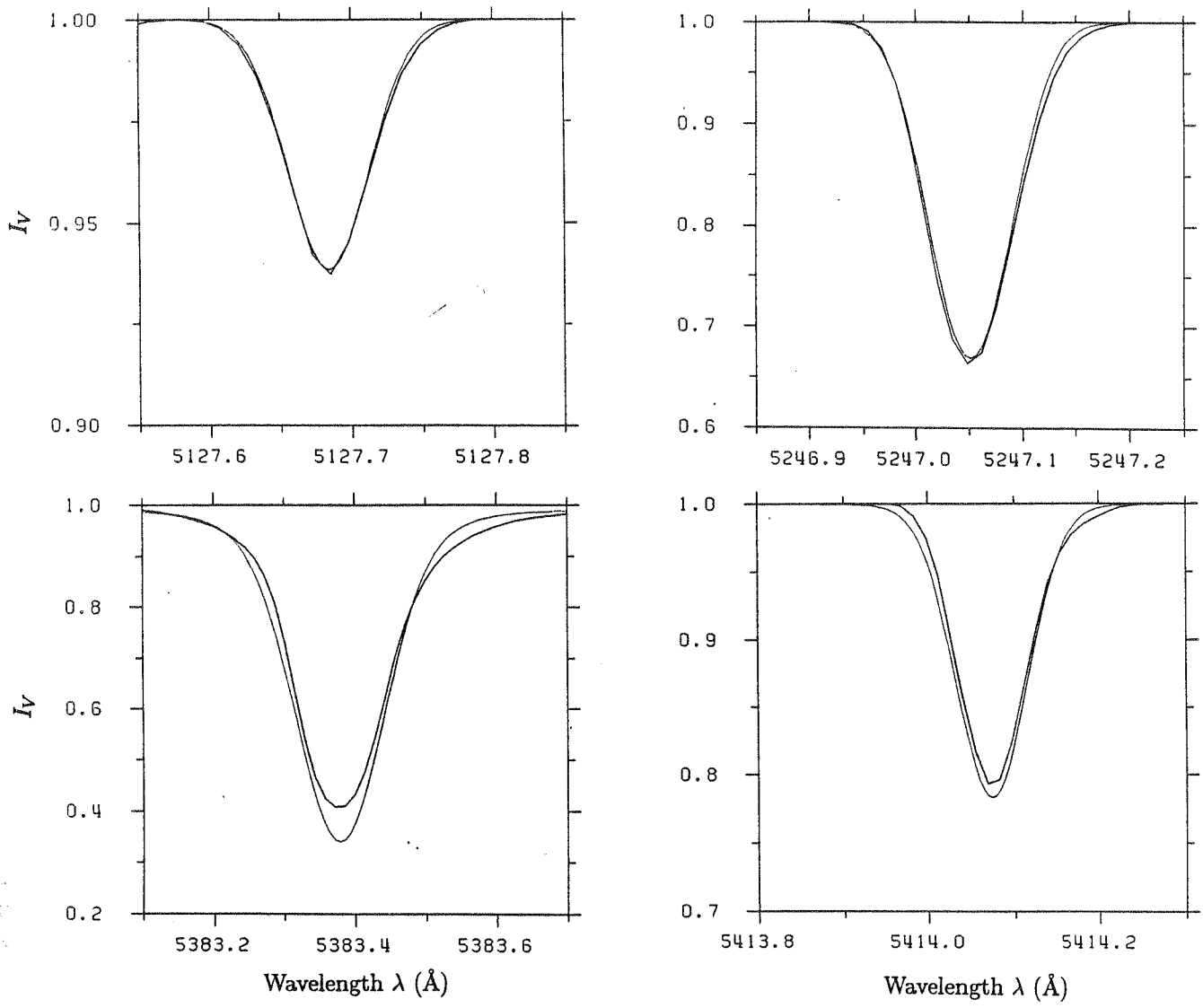

Fig. 5.15 The observed (I_V) and calculated profiles of the Fe I 5127.7 Å, 5247.1 Å, 5383.4 Å, and Fe II 5414.1 Å lines for a plage. I_V data: thick curves. Synthetic profiles: thin curves.

5.5.1. Importance of Velocity Broadening

Temperature structures determined with and without velocity broadening inside the fluxtube are quite different and consequently the inclusion of velocity broadening is important for the correct empirical modelling of fluxtube temperatures. The simple macroturbulence approach we have chosen to represent the velocity broadening in fluxtubes is certainly very primitive. Gail and Sedlmayr (1974) have calculated O I and Fe I photospheric lines with the stochastic radiative transfer equation derived by Gail et al. (1974). They find that for the quiet Sun a mesoturbulence with a correlation length of 100–300 km gives best fits to the data. They suggest that somewhat different model atmospheres may result if one uses a proper correlation length calculation instead of the traditional microturbulence/macroturbulence approach. Carlsson and Scharmer (1985) come to similar conclusions with a slightly different method. They solve the ordinary radiative transfer equation for a Ca II model atom for stochastic velocity distributions with the very fast and efficient NLTE technique of Scharmer (1981) and Scharmer and Carlsson (1985). This suggests that future calculations with better approximations of the velocity need to be carried out. Since we do not expect the velocity to be completely stochastic in fluxtubes it may be better to use some model of waves or oscillations. However, all such approaches increase the complexity of the problem tremendously.

5.5.2. Difference Between Plage and Network Fluxtube Temperature

The fluxtube temperature is different in the plages and in the network regions modelled in this chapter, with the network fluxtubes being hotter than those in active region plages. This temperature difference is particularly marked in the lower layers of the fluxtube. However, we wish to stress that this result is based only on the analysis of five regions. A much larger statistical sample will be required to test its general validity. Below, we discuss some of the explanations which have been proposed for this effect.

One possibility is that fluxtubes in plages are generally larger and therefore cooler than in the network. Such a temperature dependence on radius is supported by theoretical models. For example the larger diameter fluxtube calculated by Knölker et al. (1985), is less bright than the smaller diameter fluxtubes calculated by Deinzer et al. (1984b). Kalkofen et al. (1986), on the other hand, find for fluxtubes with radii $20\,\mathrm{km} \lesssim R \leq 90\,\mathrm{km}$, that the internal temperature *increases* with increasing radius at $\tau = 1$. Another possibility is that fluxtubes in active region plages and in the quiet network have the same diameters, but their number densities in the former are considerably larger. This would mean that the non-magnetic surroundings of the fluxtubes become cooler in plages due to the radiative losses into the larger number of fluxtubes present. Each individual fluxtube would then be able to draw less energy from its surroundings, so that it would remain cooler and darker than a fluxtube in the network (Schüssler, 1985; 1987). This cooling of its surroundings by a (single) fluxtube has been demonstrated by Spruit (1977) and Deinzer et al. (1984b). Empirical evidence for such a decrease in temperature between fluxtubes is presented by Hirayama et al. (1985), who deduce a decrease of 1% in the continuum intensity of the non-magnetic parts of active regions, by comparing their observations of the average (low resolution) continuum contrast of faculæ (0.1% near disk centre) with the high resolution observations of the continuum contrast of facular points by Muller and Keil (1983). Schüssler and Solanki (1987) also present indirect evidence for a lower continuum intensity in the non-magnetic surroundings of magnetic elements (they observe a decrease of over 10% in a strong plage).

Yet another possible explanation is based on the observations of Schoolman and Ramsey (1976), who describe what they call the 'dark component of the photospheric network'. While not significantly darker than the photosphere in the continuum (i.e. no visible pores!), this component appears to show an increased equivalent width of the Ca I 6103 Å line. Tarbell and Title (1977) confirm its existence with the Fe I 5250.2 Å line. They also suggest that its presence may be correlated with that of nearly horizontal magnetic fields, although the evidence for this is very indirect. It may be possible that one or more such elements were present in the resolution element during our plage observations. This would lower the observed average fluxtube temperature. However, the origin of such cooler regions remains unexplained.

Is there other observational evidence suggesting a difference in temperature between the fluxtubes in high and low filling factor regions? Stenflo and Harvey (1985) plot the Stokes I line depth of Fe I 5250.2 Å vs. the Stokes V amplitude of that line (their Fig. 8). The simplest interpretation would be that they plot the combined temperature and magnetic weakening vs. filling factor. Thus a decrease in the fluxtube temperature with increasing filling factor should show up as a non-linear curve in such a plot. Unfortunately, a correct interpretation is considerably more involved, since the Stokes V amplitude is also greatly affected by temperature weakening. It is therefore very difficult to reach definite conclusions from such diagrams without detailed model calculations. The same is true for all the other diagrams of this type published in the literature, e.g. Simon and Zirker (1974), who find a non-linear relationship between $\delta I/I_0$ in the core of Fe I 6302.5 Å and the average magnetic field $\langle B \rangle$ determined from the same line. Frazier (1977) observes strong changes as a function of filling factor, not only in the absolute intensity, but also in the *shape* of facular line profiles. He concludes that this is due to a continuous change in the $T(\tau)$ of fluxtubes with α. Finally, as already noted in Sect. 5.3.2, Hirayama (1978) also derives two different temperature models for plage and network fluxtubes.

5.5.3. Artifacts of One-Dimensional Models

One dimensional models, which reproduce the FTS polarimeter data, all show a more or less marked dip in the temperature at some τ value. According to Holweger (1985), this may be an artifact of the one dimensional approach. The dip is mainly due to the fact that the Fe II lines are formed in the hotter parts of the photosphere. In a one dimensional model hot and cold regions can only be segregated vertically. However, in a two dimensional model hot and cold regions of the fluxtube can co-exist beside each other, so that the Fe I and II lines may be formed at nearly the same level in the atmosphere. The Fe II lines being formed, e.g., near the hot walls of the fluxtube (if they really are hot; see the discussion of hot cloud vs. hot wall models by Schüssler, 1987, and also

the paper by Schatten et al., 1986), the Fe I lines in the cooler interior. Only future two dimensional models can decide this issue.

5.5.4. Some Limits of and Possible Extensions to the $T(\tau)$ Models

The temperature structure cannot be uniquely determined from Fe I and II data at disk centre alone. In particular, the τ of the temperature dip found in all the models which reproduce the data cannot be derived with certainty (Sect. 5.3). Perhaps data with less noise may be able to differentiate better between such models.

In addition, disk centre observations of Fe I and II lines in the visible are only sensitive to the temperature in the optical depth range $-3 \lesssim \log\tau \lesssim -1$. $T(\tau)$ for τ beyond these limits has only a minor influence on the profiles of the Fe I and II lines used. The $T(\tau)$ structures shown in Fig. 5.13 are therefore uncertain beyond these limits. The exact limits themselves depend on the temperature structure (for example in his models Chapman, 1977, finds the lines to be formed at $\tau \geq -1$), and for Stokes V, Q, and U also on the magnetic field. Extensive calculations of contribution functions to Stokes V and Q are required to delineate the τ interval over which the models are certain.

It may be possible to determine $T(\tau < 10^{-3})$ from the centre to limb variation of the Fe I and II Stokes V profiles used for the disk centre analysis. A first step in this direction has been taken by Stenflo et al. (1987a) when they plot the 'thermal line ratio' of two Stokes V profiles as a function of $\mu = \cos\theta$. As Landi Degl'Innocenti and Landolfi (1982) have shown, the ratio of the amplitudes of two otherwise similar Stokes V profiles with different χ_e values is mainly sensitive to temperature in the fluxtube. Fig. 5 of Stenflo et al. (1987a) shows that the thermal line ratio departs significantly from the value expected in non-magnetic regions at disk centre and approaches this value near the limb. If interpreted directly, this would mean that the temperature in the fluxtube approaches the outside temperature at equal τ as we go higher in the atmosphere. However, a CLV of the fluxtube line profiles due to geometrical effects (expansion of the fluxtube, a mainly vertical velocity in fluxtubes, etc.) cannot be excluded. Furthermore, only the disk centre non-magnetic I profiles were used to calibrate this line ratio, and the CLV of the Stokes I profiles may compensate for much of the variation in the thermal line ratio when going towards the limb. Compare also with Sect. 6.3.2, where the CLV of the magnetic line ratio is shown to be largely due to changes in the line profile. Future calculations of such thermal line ratios are required to obtain more quantitative results. The behaviour of the Stokes V line ratio is in accordance with the decrease in facular line weakening observed near the limb by Stellmacher and Wiehr (1973). The CLV data of Frazier (1971) also show a slight trend towards decreasing contrast in the Fe I 5250.2 Å line core with decreasing μ. The interpretation of such unpolarized data is, however, even more involved than of our Stokes V CLV.

Some estimates of $T(\tau > 10^{-1})$ are available from continuum contrast measurements. However, the results vary considerably from one investigation to another. Disk centre continuum contrasts of active region plages have been published by among others, Schmahl (1967), Frazier (1971), and Stellmacher and Wiehr (1973), all of whom find values between 1.01 and 1.02 for $I_c(\text{Facula})/I_c(\text{Photosphere})$. We write $I_c(\text{Facula})$ instead of $I_c(\text{Fluxtube})$ to stress the fact that these continuum observations cannot resolve the fluxtubes and thus measure an intensity averaged over the magnetic elements and their non-magnetic surroundings. Muller (1975), with somewhat better spatial resolution finds contrasts closer to 1.05. Chapman (1970), on the other hand, sees no contrast at disk centre, and Tarbell and Title (1977) find that the continuum contrast decreases as the amount of flux in their resolution elements increases and actually drops below 1 for flux $\gtrsim$ 150 G, although they (indirectly) exclude pores and sunspots from their analysis. From the differential photometry of faculæ in two pieces of very pure continuum, Foukal et al. (1981) conclude that faculæ are darker than their surroundings near $\tau = 1$. However, Foukal and Fowler (1984) find that for their estimated spatial resolution of 3–4″, faculæ are brighter than the quiet photosphere by approximately 0.1% ($= \Delta I/I$). They conclude that a better interpretation of the results of Foukal et al. (1981) would be that the temperature *gradient* in faculæ and the quiet photosphere is different. Foukal and Duvall (1985) also stress this interpretation, and show that the temperature gradient near $\tau = 1$ in faculæ is smaller than in the quiet Sun. Skumanich et al. (1975) find an approximately linear relation between continuum contrast and average field strength in their resolution element, such that $\Delta I_c/I_c$ increases by 0.9% for $\Delta\langle B\rangle = 100$ G. Extrapolating to 1000 G this give $I_c(\text{Facula})/I_c(\text{Photosphere}) = 1.09$. In a similar manner Frazier and Stenflo (1978) infer continuum contrasts of upto 1.18 by compensating for their limited spatial resolution through the use of additional information from polarimeter measurements. It should be noted that this method, although superiour to simply taking the measured continuum contrast at face value, probably still gives only a lower limit to the true contrast of the magnetic element, since it cannot compensate for the dark rings around

the fluxtubes, which are expected on both theoretical and observational grounds. Finally, recent evidence for a high continuum contrast of fluxtubes in an active region plage has been presented by Schüssler and Solanki (1987), who infer $I_c(\text{Fluxtube})/I_c(\text{Photosphere}) \gtrsim 1.4$ from a combination of strong plage FTS data and model calculations.

For the quiet network, the number of continuum contrast observations is considerably smaller. Koutchmy (1977) gives a value of 2.0 for one bright point, while Muller and Keil (1983) find values between 1.3 and 1.5 for a number of bright points. In both investigations attempts are made to correct for the effects of seeing.

The $I_c(\text{FT})/I_c(\text{HSRA})$ at 5000 Å for the two fluxtube models shown in Fig. 5.13 are approximately 1.2 for the plage and approximately 1.4 for the network model. The latter is compatible with the results of Muller and Keil (1983) and Schüssler and Solanki (1987), while the former is close to the compensated value published by Frazier and Stenflo (1978).

A more reliable method of determining $T(\tau)$ for $\tau > 10^{-1}$ is probably to use Stokes V profiles observed in the IR, in the wavelength range 1.5μ–1.7μ which possesses the twin advantages of little terrestrial absorption and a minimum in the solar continuum opacity. In this wavelength range H^- bound–free opacity is considerably smaller than at its maximum around 8000 Å, while the H^- free–free opacity, which increases towards the far infrared, is still small (cf. Mihalas, 1978, p. 103). Spectral lines in the IR have been previously used to model the deeper layers of sunspots (e.g. Van Ballegooijen, 1984)

5.5.5. NLTE Effects

Effects due to departures from LTE have been neglected completely in this chapter. Such effects have only been taken into account in very few investigations concerning fluxtubes. Rees (1969) and Domke and Staude (1973) studied the general influence of NLTE on the Stokes profiles in a magnetic field. Later Stenholm and Stenflo (1977, 1978) and Owocki and Auer (1980) concentrated on the effects of 2-D radiative transfer in non-plane parallel geometry, as typifies fluxtubes. As far as the influence of fluxtube temperature on the departure from LTE of iron lines is concerned, only Solanki and Steenbock (1987) have studied this using various models including those derived in Sect. 5.4.2. They find that the higher temperature inside fluxtubes increases the NLTE effects, with the difference in temperature between the $\tau = 1$ and the $\tau \approx 10^{-2}$ levels being of particular importance (since it determines the difference in the temperatures of the UV radiation field and the local electron pool, cf. Rutten, 1987). Conversely, the larger NLTE effects also lead to wrong temperature determinations, with the temperature being generally overestimated in LTE models (Rutten and Kostik, 1982). This shows the strong need for self-consistent NLTE empirical models of fluxtube temperature.

5.5.6. Stokes Q as a Temperature Diagnostic

Additional constraints on the fluxtube temperature can be set by making use of the Stokes Q profile as well. As pointed out in Sect. 4.2.3., the Stokes Q σ–π asymmetry results from a combination of saturation and Zeeman splitting. The main physical parameters of the fluxtube affecting it are therefore T and B. It is also affected by velocity broadening and slightly by the angle of the magnetic field to the line of sight γ. At first glance it may therefore appear that it is quite hopeless to determine the temperature from this parameter. However, the magnetic field strength, the velocity broadening and γ can be determined relatively unproblematically via the line ratio technique, the width of Stokes V (or I_V) and the ratio of Stokes Q to Stokes V, respectively. Since Fe I lines are weakened for increasing T, their saturation also decreases, and so does the σ–π asymmetry of Stokes Q. Thus the Stokes Q asymmetry can serve as an independent temperature indicator. One advantage is that it is basically a single line method and can also be applied when the broad spectral coverage of an FTS is not available. More to this technique is to be found in Solanki et al. (1987).

6. Magnetic Fields

"... the radical element responsible for the continuing thread of cosmic unrest is the magnetic field."

E.N. Parker (1979)

6.1. Introduction

Hale (1922a,b) first presented evidence for distinct magnetic features outside sunspots, when he published the discovery of average fields of approximately 200–300 G in what he termed 'invisible sunspots'. With improvements in instrumentation, the lower limit of measurable non-sunspot fields kept on decreasing. Thus by 1960 the field strengths in bright regions (i.e. Network, Plages, etc.) were found to lie in general between 1–200 G for the spatial resolution of usually 5″–10″ possible at that time (Babcock and Babcock, 1952, 1955; see also the review by Babcock, 1963).

During the 1960s indications accumulated that the true field strengths outside sunspots are in general considerably larger than the average field measured with low spatial resolution. Thus Sheeley (1966) detected field strengths of between 200 and 700 G in small non-sunspot features from magnetograms of quiet and active regions. Sheeley (1967) measured a field strength of approximately 350 G via the shift in the σ components of Fe I 5250.2 Å. In active regions Beckers and Schröter (1968a) measured fields of between 400 and 1400 G in what they termed 'magnetic knots' or 'micropores'. They carried out a rough correction for stray light (i.e. finite spatial resolution) and estimated the diameters of the knots to be approximately 1.3″. They also observed regions which show line weakening, but no magnetic field. However, Simon and Zirker (1974) found no evidence for such structures and suggested that these are magnetic regions with fluxes below the detection limit of Beckers and Schröter. Grigorjev (1969) and Abdussamatov and Krat (1969) also observed such magnetic knots and measured field strengths ranging from 100 to 650 G.

So far all these observations had been carried out with spatial resolutions worse than 1″. It is therefore not surprising that most values of the field strength thus determined lie below the values generally accepted today. The reason the spatial resolution is so important is that the magnetograph (or any other polarimeter for that matter) measures only the line of sight flux, which is proportional to the field strength averaged over the resolution element, and not the true field strength of an unresolved magnetic region.

As noted above, Beckers and Schröter (1968a) had assumed that the magnetic elements they observed were unresolved. Other measurements also hinted at the unresolved nature of the magnetic elements. Thus Stenflo (1966) and Severny (1967) made multiple scans of a given region with varying aperture sizes and found that the magnetic field strength increased with decreasing aperture. However, their smallest aperture was only 7 (arc sec)^2. Clearly, indirect model-independent methods of determining the magnetic field strength were required. A first step in this direction was taken when Stenflo (1968) described how the possibly filamentary structure of the magnetic field influences the interpretation of magnetograph recordings. Harvey et al. (1972) used least squares fits to observed Stokes V profiles to determine different parameters of magnetic elements. Their best fit gave an average field strength of 500 G with a scatter of ±500 G. They also found a higher field strength fit of lesser quality. Later, Stenflo (1973) was able to reproduce their observations quite well with a strong field fluxtube. Howard and Stenflo (1972) and later Frazier and Stenflo (1972) determined that over 90% of the magnetic flux is concentrated into magnetic filaments (i.e. fluxtubes) from an analysis of magnetograms in 5250.2 Å and 5232.9 Å. They do not give any value for the filamentary magnetic field. Frazier and Stenflo (1972) also found evidence for a so called 'interfilamentary field' with a small field strength of approximately 0.5–5 G, when averaged over an aperture of $2.4 \times 2.4''$. This weak diffuse field has a polarity opposite to that of the concentrated field. Livingston and Harvey (1971) have also presented some evidence for a weak field of 2–3 G strength *when averaged over their 5″ resolution element.* Of course a few small fluxtubes with large field strengths could also give such a signal, so that this last observation does not provide any hard evidence for the presence of truly weak fields. The same authors also find some statistical evidence for a quantisation of magnetic flux (Livingston and Harvey, 1969). This observation has, however, not been subsequently confirmed.

Stenflo (1973) introduced a very powerful technique for determining the true magnetic field strength of the

unresolved fluxtubes. The so-called line-ratio technique ideally uses two lines which are identical except for their Landé factors. If the fields were intrinsically weak then the amplitudes of their V profiles (or the ratio of their V at any given wavelength) would be equal to the ratio of their Landé factors. For strong fields this is no longer true and the departure of the ratio of the V profiles from the ratio of the Landé factors is a direct measure of the field strength. It is important to realize that the (at that time quite poorly known) thermal properties of fluxtubes do not affect the results of this technique. Neither is it sensitive to stationary flows in the fluxtubes, by virtue of the choice of two similar lines.† Fortunately, two such lines exist in the visible solar spectrum at 5250.2 Å ($g = 3$) and 5247.1 Å ($g_{\rm eff} = 2$), both belonging to multiplet 1 of neutral iron. From the ratio of these two lines Stenflo (1973) found that the peak field strength of the fluxtubes lies between 1600 and 2300 G for different horizontal distributions of the field strength (all of them with a rapid decline towards the boundaries of the fluxtubes).

The results of Stenflo (1973) were confirmed by Harvey and Hall (1975) who observed the Fe I 15648.5 Å line in the IR. This line, a Zeeman triplet with $g = 3$ (Litzén, 1976), is almost completely split in a field of approximately 1 kG, since Zeeman splitting $\sim \lambda^2 B$, while line broadening is approximately $\sim \lambda$. Harvey and Hall inferred field strengths of between 1200 and 1700 G (see also Harvey, 1977). Chapman (1974) presented various arguments (but no new observations) in favour of a unique magnetic field strength of the order of 1500–2000 G at the level at which photospheric lines are formed. Further confirmation came when Tarbell and Title (1977) used the Fourier technique developed by Title and Tarbell (1975) and Tarbell and Title (1976) to determine magnetic field strengths in regions with average vertical magnetic field strengths $\langle B \rangle > 125$ G. They found 1000 G $\lesssim B \lesssim$ 1800 G, with B being almost independent of $\langle B \rangle$ in their data. $B/\langle B \rangle$ ranges from 3 to 12 despite their high spatial resolution of 1.5″. They concluded from this that Simon and Zirker (1974) saw only bunches of fluxtubes when they reported that the magnetic regions had diameters 1–3″ across. Wiehr (1977, 1978) extended the line ratio method of Stenflo (1973) to include three lines, Fe I 6302.5 Å ($g = 2.5$), 6336.8 Å ($g_{\rm eff} = 2.0$), and 6408.0 Å ($g_{\rm eff} = 1.0$). He also used the radiative transfer code of Wittmann (1974) instead of the previously used Milne-Eddington solution. He deduced field strengths in the range 1200–1700 G from these measurements. He also measured the field by placing three different exit slits in the wings of Fe I 6173 Å and obtained magnetic field values between 1500 and 2200 G. However, this method is more model dependent than the line ratio technique. Finally, Wiehr (1978) also claimed to have found evidence that fluxtubes are inclined by 55° towards the west.

Koutchmy and Stellmacher (1978) found field strengths of 1000–1500 G from fits of model profiles to $I + V$ and $I - V$ profiles of Fe I 6301.5 Å and 6302.5 Å observed with 0.75–1″ resolution. Frazier and Stenflo (1978) obtained a field strength of 960 G from the line ratio technique for a rectangular cross-section of the magnetic field. Finally, Stenflo and Harvey (1985) studied the dependence of the line ratio 5250/5247 on filling factor. They found only a weak dependence (in agreement with the results of Tarbell and Title, 1977), with the field strength increasing from 800 to 1140 G when the filling factor increases by a factor of 6. Theoretically, the observed field strengths could be reproduced, for example, by the calculations of convective collapse of Spruit (1979), who found that surface fields in the collapsed state should lie in the range: $1280 < B < 1650$ G.

In Sects. 6.2 and 6.3, we discuss work on fluxtube field strengths by Solanki and Stenflo (1984, 1985), Stenflo et al. (1987a), and Solanki et al. (1987), while in Sect. 6.4 we examine the influence of finite spectral resolution on field strengths and filling factors determined from Stokes V.

6.2. Field Strengths and Filling Factors From a Regression Analysis

Using a statistical analysis of Fe I lines it is possible to determine the magnetic field strength in fluxtubes *without the need for radiative transfer calculations*. We start by noting that Zeeman splitting in fluxtubes mainly broadens the I_V profiles and decreases their depths. We may regard this as the Zeeman saturation effect of the Stokes I profile. These changes in the I_V profiles are (for not too large values of $g\lambda B$) linearly proportional to the Zeeman splitting of the lines. By carrying out regressions of the form of Eqs. (4.48) and (4.50) one should be able to disentangle this effect of the magnetic field from effects of the temperature etc. Since we use $v_{D_V} - v_{D_I}$ and $\ln(d_V/d_I)$ of Fe I lines only for the determination of the field, the regression equations are somewhat simpler than the ones shown in Sect. 4.4.2. We therefore present below the exact regression equations used here. All

† We show in Sect. 6.3.2, however, that the results of the line ratio analysis depend quite strongly on the velocity broadening of the line (turbulence broadening).

lines are assumed to be Zeeman triplets. For more details see Sect. 4.4.2.

$$v_{D_V} - v_{D_I} = x_1 + x_2 S_I + x_3 S_I^2 + x_4 v_0 \chi_e + x_5 g_{\rm eff}^2 \lambda^2 / v_0, \tag{6.1}$$

and

$$\ln(d_V/d_I) = x_1 + x_2 S_I + x_3 S_I^2 + x_4 \chi_e + x_5 \chi_e S_I + x_6\, g_{\rm eff}^2 \lambda^2 / v_0^2. \tag{6.2}$$

For the further analysis, and to enable a crude interpretation of our data, we use the two component model introduced in chapter 4. Thus the photosphere is assumed to consist of a magnetic component, covering a fraction α of the surface and a non–magnetic component covering the remaining fraction $(1-\alpha)$. It is assumed that within the magnetic component the field strength, B, is constant and that in the non–magnetic component $B = 0$.

To derive a simple analytical relation between field strength B in the fluxtube and the coefficient x_5 in the $v_{D_V} - v_{D_I}$ regression equation, we use our two–component model for a longitudinal magnetic field, and assume the line profile to be Gaussian and the Zeeman splitting to be much smaller than the line width. We furthermore assume that in the case of zero Landé factor, the line depth in the magnetic regions is δ times the line depth outside the fluxtubes ($\delta < 1$ in the case of line weakening), but that the line width is unchanged (this last assumption is approximately fulfilled by all but the strongest Fe I lines, as Fig. 4.11 shows). Finally, we assume the continuum intensity inside and outside the fluxtubes to be equal. With these assumptions, using the Taylor expansion Eq. (4.8) and the definition Eq. (4.10) of I_V, we find

$$B = \frac{(3x_5)^{1/2}}{kc}(1 - 3\delta\alpha)^{-1/2}, \tag{6.3}$$

where $k = 4.67$ km^{-1} G^{-1}, and c is the speed of light. The factors 3 in Eq. (6.3) appear because the magnetic broadening of I_V and I are due to the second terms in their respective Taylor expansions and the numerical coefficients of the two relevant terms differ by a factor of 3. Intuitively, we would expect I_V to be broadened much les by a magnetic field than the Stokes I profile arising from the same region, since it is a better approximation of the unsplit I profile.

The interpretation of the x_6 term in Eq. (6.2) is very similar to that of the x_5 term in Eq. (6.1). Notice, however, that the dependence of this term on line width goes with $1/v_0^2$ as compared with the $1/v_0$ dependence of the x_5 term of Eq. (6.1). Making the same assumptions as were made for the derivation of Eq. (6.3) the following dependence of $\ln(d_V/d_I)$ on the magnetic field is found:

$$\ln(d_V/d_I) = \ln\delta + \alpha(1-\delta) - \frac{1}{3}\frac{v_H^2}{v_D^2}(1 - 3\delta\alpha), \tag{6.4}$$

where α and δ have the same meaning as in Eq. (6.3), v_D is the line width (which we have assumed equal for I_V and Stokes I, in agreement with the observations for most lines), and v_H is the Zeeman broadening expressed in velocity units. The first two terms on the right hand side of Eq. (6.4) are independent of the magnetic field and of line parameters if the lines chosen are of approximately the same strength and excitation potential. Thus only the last term is of consequence for the determination of the magnetic field strength. For the choice of regression terms used in Eq. (6.2) it gives a relation between the magnetic field and regression coefficient x_6 identical to that of Eq. (6.3) if we replace x_5 by x_6:

$$B = \frac{(3x_6)^{1/2}}{kc}(1 - 3\delta\alpha)^{-1/2}. \tag{6.5}$$

Table 6.1 is a compilation of the magnetic field strengths and filling factors of the five regions observed close to disk centre near the height at which the weakest Fe I lines are formed. The magnetic field strength B has first been determined from regression coefficient x_5 using Eq. (6.3), and from coefficient x_6 using Eq. (6.5) with $\alpha = 0$ (columns 2 and 3). The use of $\alpha = 0$ in Eqs. (6.3) and (6.5) corresponds to the assumption that the Stokes I profiles are unaffected by the magnetic field. This is true to first order, since the I_V profile is much more strongly affected than Stokes I. The averages of the derived values of B have then been corrected through multiplication by $(1-\alpha)^{-1/2}$ assuming $\delta = 1/3$ (a value suggested by the exploratory model calculations for weak, low excitation Fe I lines), and using α values determined as described below (column 5). This is only a rough guess for δ and larger values may be nearer to the truth. However, this term does not greatly affect the determined B.

The field strengths thus determined are larger than those obtained with the line ratio technique and a constant field. This may be due to the fact that the field strengths in Table 6, being based on the assumption of small Zeeman splitting, are less accurate than those determined from the line ratio. Note, however, that the field strength determined with this technique refers to the height at which the weakest lines are formed (since we reduce to $S_I = 0$ in the regression). Since this is deeper in the atmosphere than the height of formation of 5250, we would expect a somewhat larger field strength. This follows from the generally accepted theoretical models of fluxtubes, all of which predict a field strength decreasing with height. One purpose of Table 6.1 is to show that the Zeeman broadening and saturation are similar in plages and the network, indicating similar actual field strengths in these different structures in accordance with the results of Tarbell and Title (1977) and Stenflo and Harvey (1985). This conclusion of similar field strength is also supported by Fig. 6.1, which illustrates the dependence of $\ln(d_V/d_I)$ and $v_{D_V} - v_{D_I}$ on the respective Zeeman broadening terms of Eqs. (6.1) and (6.2) after the dependence on S_I and χ_e has been removed.

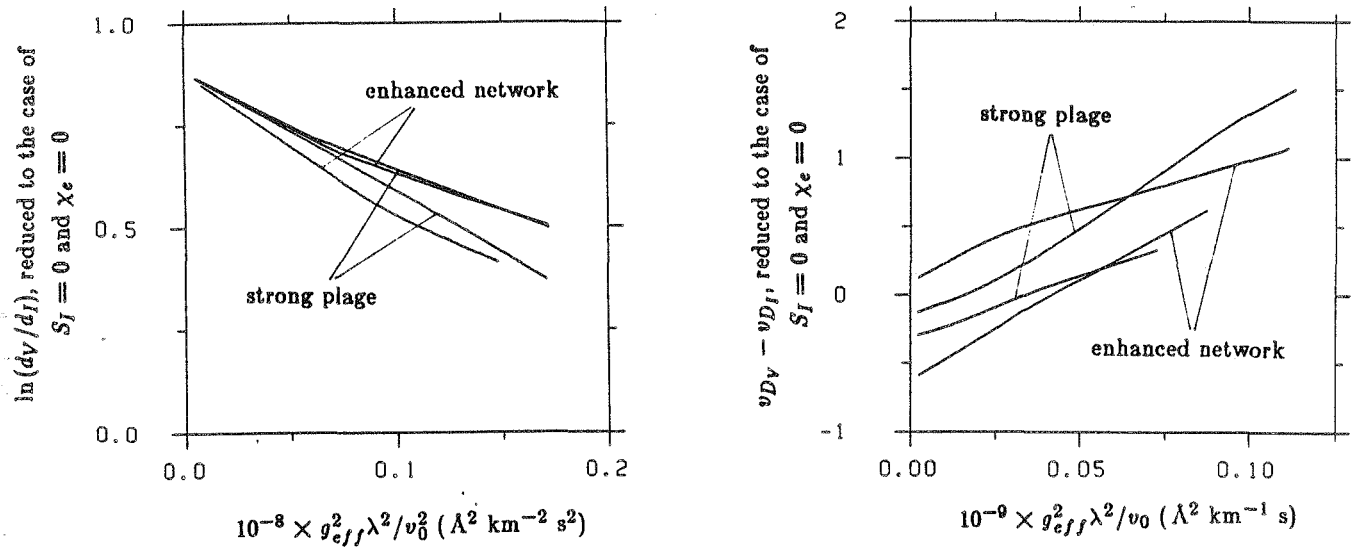

Fig. 6.1 a Smoothed averages of $\ln(d_V/d_I)$ vs. $g_{\rm eff}^2\lambda^2/v_0^2$, reduced to the case that $S_I = 0$ and $\chi_e = 0$, for two network and two plage regions. Note the approximately equal gradients of all four curves. The curves of the two plages have been shifted vertically in order to facilitate comparison. b Smoothed averages of $v_{D_V} - v_{D_I}$ vs. $g_{\rm eff}^2\lambda^2/v_0$, reduced to the case that $S_I = 0$ and $\chi_e = 0$, for the same regions as in Fig. 6.1a. The curves are all unshifted.

Recall, that when calculating the I_V profile we assumed that $\langle B \rangle = 1$ (Sect. 4.2.4), so that d_V is too large by a factor $B\alpha$. The magnetic filling factors, α, of the observed regions can therefore be readily determined from the amount by which the empirical curves in the $\ln(d_V/d_I)$ vs. S_I plot have to be vertically shifted to fit the model curves, and from the magnetic field strengths. The α values thus determined are lower limits, since any depolarization in the telescope reduces the height of the V profiles and therefore the derived value of α. Stenflo and Harvey (1985) have suggested that there is a still unexplained calibration error of a factor of two in all the polarization data of 1979 (cf. Sect. 4.2.4).

Table 6.1

Type of region	B_{x_5} (G) from (6.3) for $\alpha = 0$	B_{x_6} (G) from (6.5) for $\alpha = 0$	Average B_x (G) corrected for α	Estimated α (%)
Enhanced network	1700	1690	1720	3.0
Enhanced network	1230	1490	1390	4.4
Enhanced network	1540	1320	1465	6.1
Strong plage	1260	1560	1515	28.9
Strong plage	1460	1540	1625	32.0

This method is subject to a relatively large model dependence when using Fe I lines alone. The additional use of Fe II makes this procedure largely model independent, since all the model $\ln(d_V/d_I)$ vs. S_I curves for the ionised species lie close together. The uncertainty in the α values resulting from their model dependence is no more than a few percent, and is comparable to the uncertainty caused by the scatter of the Fe II data points. If we multiply the derived α values with a factor of two to account for an instrumental calibration error in accordance with Stenflo and Harvey (1985), we find values for the magnetic filling factor between 3 and 32%. These filling factors are listed in column 5 of Table 6.1.†

Note that it has been implicitly assumed throughout this section, that the continuum intensity inside fluxtubes is the same to the one outside. The effect of fluxtube temperature and continuum intensity on the magnetic flux determined from a magnetograph has been discussed by Grossmann-Doerth et al. (1987). A higher continuum intensity inside the fluxtube will decrease the determined α values, as is discussed in detail by Schüssler and Solanki (1987). Note that we can make the results of this section independent of $\delta_c = I_c^{\text{fluxtube}}/I_c^{\text{photosphere}}$ by replacing α by $\alpha\delta_c$ throughout. On the other hand it has also been assumed that the fields are vertical, which in general tends to give us a lower limit for α (and also for B). We have also neglected the possible cancellation of polarities in the resolution element, which would influence α, but should not affect B.

In Sect. 6.4.2 we shall investigate the influence of spectral smearing on filling factors determined from Stokes V. We also wish to point out that the statistical method can be used to determine filling factors from Stokes I alone, if some assumptions are made regarding the true field strength, or if it is determined via some other method (cf. Brandt and Solanki, 1987, for an application).

6.3. Magnetic Field Strength From the Line Ratio Technique

6.3.1. Centre to Limb Variation of the Stokes V Line Ratio: Observations

The line ratio technique of Stenflo (1973) has been briefly described in the introduction to this chapter. Further details are to be found in, e.g., Stenflo (1973, 1976), Frazier and Stenflo (1978), and Stenflo and Harvey (1985). We refer to these papers for more information.

The CLV (i.e. μ dependence) of the Stokes V line ratio of Fe I 5250.2 Å to Fe I 5247.1 Å has been previously measured by, e.g., Frazier and Stenflo (1978), who, however, did not analyse these measurements in detail. Howard and Stenflo (1972), Frazier and Stenflo (1972) and Gopasyuk et al. (1973) have measured and discussed the CLV of the ratios of other lines, which are not as useful as the 5250/5247 line ratio for determining magnetic field strengths.

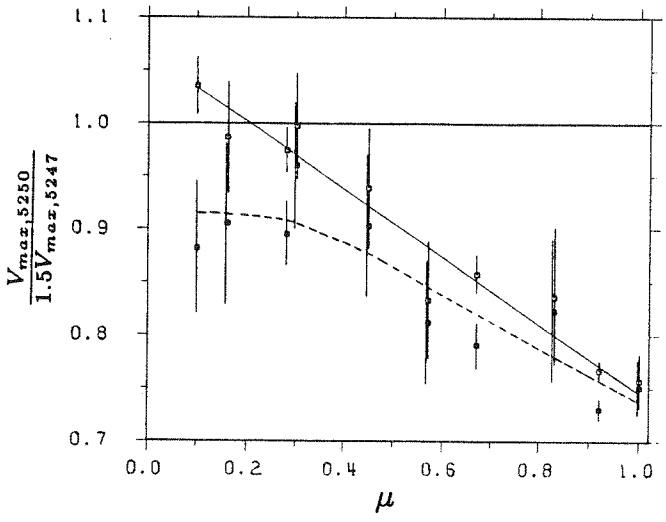

Fig. 6.2 Centre to limb variation of the 5250/5247 Stokes V amplitude line ratio. Filled squares and dashed curve represent the directly determined line ratio, while the open squares and solid curve show the line ratio reduced to the case of zero filling factor, using the regression equation (6.6).

† The filling factors published by Solanki and Stenflo (1984) are approximately a factor of two smaller than in Table 6.1 due to an error in that paper. We have also taken into account the exact positions of the observed regions on the solar disk.

In Fig. 6.2 we plot the CLV of the Stokes V line ratio of 5250/5247. The filled squares represent the orignal data, and the dashed line is a cubic spline fit. The equivalent Stokes Q line ratio also contains information on the magnetic field strength. However, we shall not discuss it further here, referring to Stenflo et al. (1987a) and Solanki et al. (1987) for more information. Since, for a weak field, we would expect the V amplitudes of the two lines to have the same ratio as their Landé factors, we have divided by this ratio in order to normalise the figure to unity for weak fields. The Stokes V line ratio clearly approaches unity when going towards the limb. The obvious interpretation is that this is due to a rapid decrease in field strength with height. However, it may also be possible that changes in the line profiles when going from disk centre to the limb may lead to a similar behaviour. Indeed Stenflo et al. (1987b) found that a part of this increase is actually due to a change in line width with μ. Furthermore, the increasing strength of the π-component with increasing γ may also be of consequence. In Sect. 6.3.2 we shall test these hypotheses quantitatively with a one dimensional model. Further effects may arise due to the 2-D geometry of fluxtubes. Such effects will be analysed in a future investigation using the model presented in chapter 9.

Another parameter which also influences the positions of the data points in Fig. 6.2 is the filling factor. As demonstrated by Stenflo and Harvey (1985), the line ratio of (5250/5247) is somewhat dependent on filling factor. This leads to the suggestion that at least part of the scatter of the points around the cubic spline fit (dashed curve) is due to the different filling factors of the observed regions. This suggestion is supported by the similarity between these departures from the dashed curve and Fig. 3.1, where the amplitudes of Stokes V of Fe I 5250.2 Å are plotted, which are a measure of the filling factor.

The following regression equation represents a first attempt to separate the μ and α dependences of the V line ratio. It is assumed that the line ratio depends linearly on both μ and $a(5250)/\mu$ (which is approximately proportional to α for vertical fields).

$$\frac{a(5250)}{1.5a(5247)} = x_0 + (x_1 + x_2\mu)(1 + x_3 a(5250)/\mu). \tag{6.6}$$

Here x_0, x_1, x_2, and x_3 are the regression coefficients. This regression is used to reduce the data to the case of $\alpha = 0$ (the solid line and the open squares in the figure). The fact that this curve becomes larger than one, which appears unphysical, suggests that this regression equation overestimates the effect of the filling factor. However, the few data do not warrant the construction of a more complex regression equation. Note, however, that 1.5-D radiative transfer calculations of the line ratio in cylindrical models which conserve flux with height can lead to line ratios greater than unity (Solanki and De Martino, in preparation)

6.3.2. Centre to limb variation of the Stokes V Line Ratio: Model Calculations

In this section we present calculations of the Stokes V line ratio of 5250/5247 which include a number of improvements with respect to previous calculations. Firstly, we use a radiative transfer code to calculate the line profiles. Most previous calculations of the line ratio have been made with the simple Unno (1956) or Rachkovsky (1967) theory, the exception being the calculations of Wiehr (1978). Secondly, we calculate the CLV of the line ratio. Thirdly, we use both a model with constant field (like all previous authors) and one based on the thin fluxtubes approximation, i.e. with a magnetic field decreasing rapidly with height (cf. Sect. 4.5.1). Fourthly, we test for the sensitivity of the line ratio on temperature by calculating it for both the HSRA and the plage model derived in Sect. 5.4.2. Fifthly, we also include the influence of macroturbulence broadening on the line ratio.

Fig. 6.3 shows the CLV of the Stokes V 5250/5247 line ratio data, as well as model calculations. The solid curves are the results of calculations using the plage model described in Sect. 5.4.2 with a magnetic field calculated using the thin tube approximation. For the upper curve the magnetic field strength at $\tau = 1$, $B(\tau=1) = 1400$ G, for the lower curve $B(\tau=1) = 2000$ G. The magnetic field vector is assumed to be vertical to the solar surface, i.e. $\cos\gamma = \mu$. No macroturbulence broadening has been assumed so far. As far as microturbulence is concerned we make use of one of the results of chapter 7, namely that the microturbulence inside the fluxtubes is similar to that outside at disk centre. Extrapolating from there, we assume that this is true for all μ values. The CLV of the microturbulence, as determined from Fe I lines in the quiet photosphere, has been given by Simmons and Blackwell (1982). The $\xi_{\rm mic}$ values of Simmons and Blackwell increase linearly with decreasing μ, except for their last point at $\mu = 0.2$, which has a considerably larger microturbulence than would be obtained from a linear extrapolation from the other points. For our calculations upto $\mu = 0.1$ we have to extrapolate from their values. Keeping in mind that Simmons and Blackwell feel that the value at $\mu = 0.2$ is considerably less certain than the

rest we have decided (for this rough analysis) to leave this value aside and extrapolate linearly from the rest of the points. We therefore adopt the following dependence of $\xi_{\rm mic}$ on μ:

$$\xi_{\rm mic} = -0.69\mu + 1.61 \qquad \text{for} \quad 0.1 \leq \mu \leq 1.0. \tag{6.7}$$

Keeping in mind that μ decreases as we approach the limb this signifies an increase when going towards the limb.

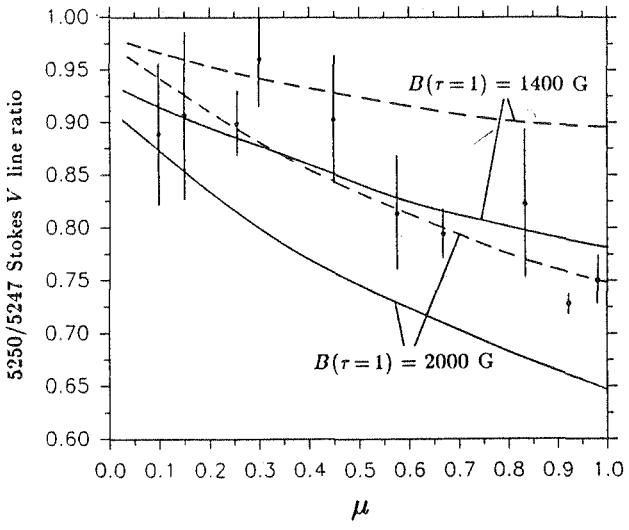

Fig. 6.3 CLV of the 5250/5247 amplitude line ratio. Filled circles: observational data. The vertical lines are error bars. Solid curves: Calculated line ratios for lines unbroadened by any macroturbulence. The magnetic fields have been calculated using the thin tube approximation, with B = 1400 and 2000 G at $\tau = 1$ as marked in the figure. Dashed curves: line ratios calculated for the same models, but now for V broadened by a macroturbulence so as to match the widths of the observed profiles.

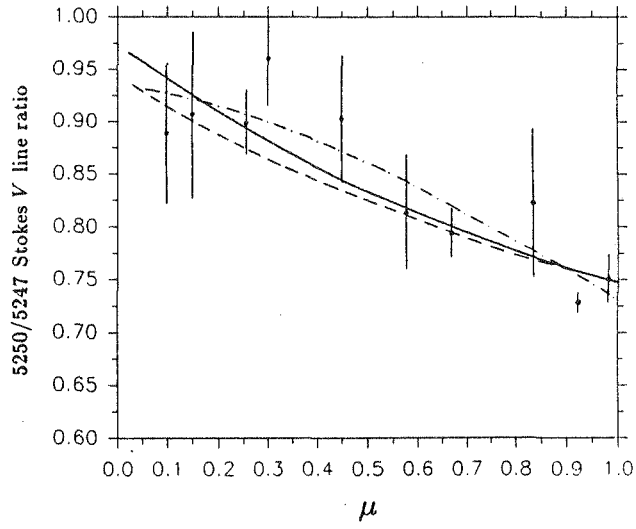

Fig. 6.4 CLV of 5250/5247 amplitude line ratio. Solid circles: observational data. Curves: line ratio determined from synthetic V profiles which have been broadened by macroturbulence to match the data. Solid curve: thin tube magnetic field with $B(\tau = 1) \approx$ 2000 G, plage temperature model. Dashed curve: constant magnetic field, B = 1140 G, plage temperature model. Dot-dashed curve: constant magnetic field, B = 1300 G, HSRA.

The solid curves in Fig. 6.3 gives the impression that the 1400 G model provides the better fit to the data. However, a comparison of the complete calculated Stokes V profiles with the observations clearly shows that the former are much too narrow, in agreement with the conclusions of chapter 5. We assume that the rest of the broadening is due to macroturbulence, which is consistent with the approach presented in chapters 5 and 7. For disk centre we can use the broadening given in Table 7.1, but for positions nearer the limb a more detailed determination is necessary.

So far no determinations of the macroturbulent broadening in fluxtubes away from disk centre have been carried out. We shall use quiet Sun values as a starting point for our determination in fluxtubes. The macroturbulence in the quiet photosphere for disk centre and near the limb has been given by Holweger et al. (1978). We interpolate linearly in their data to obtain the following relation for the CLV of the macroturbulence

$$\xi_{\rm mac} = -0.78\mu + 2.08 \qquad \text{for} \quad 0.1 \leq \mu \leq 1.0. \tag{6.8}$$

These values from the literature have been used to broaden the Stokes I profiles calculated with the HSRA without a magnetic field, which have then been compared with the data. Since the data were all obtained in active regions, the fits are not quite ideal. In particular the line depths of the observed profiles are smaller than of the calculated ones. However, for the 52471.1 Å line the line widths matched rather well. For Fe I 5250.2 Å the magnetic broadening is appreciable and does not allow good fits.

From a comparison of observed to calculated V profiles, values of $\xi_{\rm mac}^V$ (i.e. $\xi_{\rm mac}$ determined from Stokes V) between 2.0 and 2.5 km sec^{-1} have been obtained, with no clear dependence on μ visible. Thus, in contrast to Stokes I, the macroturbulence broadening does not increase towards the limb. But neither does it decrease, a somewhat surprising result, when one bears in mind that mass motions in fluxtubes are expected to be mainly vertical. However, we cannot reach definite conclusions regarding the velocity structure from just these two lines. A future statistical analysis of the type carried out by Pantellini (1986), combined with radiative transfer calculations may be able to clarify this point. We also wish to stress that the fits to the observed Stokes V profile shapes are not of very good quality. Firstly, due to the asymmetry of the observed V, but secondly also because the central portion of the observed V profiles is much flatter than that of the calculated profiles. This is suggestive of the influence of the finite thickness of the fluxtube, as evident from the 1.5-D calculations of Solanki and De Martino (in preparation).

Let us return to the Stokes V line ratio. In Fig. 6.3 the dashed curves are the calculated line ratios for the broadened profiles. The upper curve is again obtained from the thin tube model with $B(\tau = 1) = 1400$ G, the lower curve from $B(\tau = 1) = 2000$ G. Now it is the model with the higher field strength which gives the better fit. Within the scatter it fits the data quite well and suggests that the thin tube approximation is a reasonable assumption, and the magnetic field decreases with height.

However, before concluding anything on the height dependence of the magnetic field, we must first test this diagram for its sensitivity to magnetic field gradients. We have therefore also calculated profiles for a series of models with constant magnetic fields. The resulting 5250/5247 line ratio vs. μ curve of one such model ($B = 1140$ G = constant) is shown in Fig. 6.4 (dashed line) together with the corresponding curve of the thin tube model with $B(\tau = 1) = 2000$ G. The two models give identical results for $\mu = 1$, and they diverge slightly when going towards the limb. This difference is, however, exceedingly small. In particular, it is considerably smaller than the scatter of the data. We therefore conclude that it is presently not possible to determine the height variation of the magnetic field from the CLV of the line ratio. This is in contrast to the results of Stenflo et al. (1987b), who used a simple model of the Zeeman splitting of these lines to infer a considerable decrease in field strength when going from the centre to the limb. There are two possible explanations for this insensitivity to the magnetic field gradient. The first is that it is effects of the changes in line shape which dominate the CLV of the line ratio. The increasing width of the lines near the limb simulates the presence of a weaker field and the increasing relative strength of the π-component with increasing γ also contributes to the change in the line ratio (as can be seen from some straightforward manipulations of the Unno (1956) solutions; cf. Solanki et al., 1987, for more details). Although the simple model of Stenflo et al. (1987b) does take into account the increase in line width, it neglects the increasing importance of the π-component near the limb. This is the main reason for the difference of its results to those of the radiative transfer calculations presented here. Line profile effects are certainly important, but they may not be able to explain the complete effect. Another possibility is that against the generally established notion that lines are formed higher up near the limb, this is not true for fluxtubes. Calculations of the heights of formation in fluxtubes are of great importance to settle this question. Finally, we must not forget that these are only one dimensional model calculations and the finite thickness of fluxtubes may affect the results considerably.

The dot-dashed line in Fig. 6.4 is the CLV of the line ratio calculated with the HSRA and $B = 1300$ G = const. The difference to the other two curves is once more less than the scatter in the data. A field strength of 1300 G gives a somewhat lower line ratio at $\mu = 1$, but produces a better fit for this temperature model to the CLV. We conclude that the line ratio is rather insensitive to the temperature, as is expected, with a temperature difference of 400–500 K giving only a small difference of ≈ 150 G in the determined magnetic field. Comparing the three curves in Fig. 6.4 with each other shows that the difference between the curves with different magnetic field gradients is of the same order as the difference between the curves with different temperatures. It will therefore not be possible to use this diagram for the determination for the height dependence of the magnetic field, even with data of much better signal to noise ratio, unless the temperature structure in fluxtubes is very well known.

6.4. Finite Spectral Resolution and the Determination of Field Strength and Filling Factor

6.4.1. Motivation

In their quest for better data, solar observers have often opted for increased spatial and temporal resolution at the cost of a certain amount of spectral resolution. As long as the observations are limited to measurements of spectral intensity (Stokes I), this usually does not present a serious problem (except for the detailed analysis of the line profile, its bisector, and related studies, Livingston and Huang, 1987). The profile is broadened, the line depth is reduced, but the equivalent width and the core wavelength remain relatively unaffected. The situation changes dramatically for the cases when circularly polarized spectra (Stokes V) are required, e.g. for problems relating to the diagnostics of the properties of solar magnetic fluxtubes. Not only are the amplitude and asymmetry of a Stokes V line profile affected by changes in spectral resolution, but also the areas of both its wings, and the wavelength of its zero-crossing. Furthermore, different lines are not affected in the same way, which means that the ratio of two Stokes V profiles to each other is also changed. Another reason why the magnitude of the observed effect on Stokes V is generally larger than on Stokes I is due to the circumstance that with most instruments, the measurement of Stokes V requires wide slits to get a good signal to noise ratio while maintaining high temporal and/or spatial resolution. Even in the optimum spectral lines the Stokes V amplitude seldom exceeds a few percent of the continuum intensity when observing outside sunspots.

In this section we shall consider the effects of spectral smearing on the amplitudes and areas of the Stokes V profile (→ filling factors) of Fe I 5250.2 Å, as well as on the ratio of Fe I 5247.1 Å to Fe I 5250.2 Å (→ field strength). Stokes V profiles from our very high spectral resolution data of 1979 will be taken as the starting point. The effects of low spectral resolution will be numerically simulated by convoluting these observed line profiles with model instrumental profiles. We shall also try to find some Stokes V parameters which are insensitive to the spectral resolution.

In later chapters we shall use this technique to study the effects on the zero-crossing wavelength of Stokes V and on its asymmetry.

6.4.2. Description of the Technique and the Input Data

We have used data with very high spectral resolution as our starting point, and have simulated the effect of a finite entrance slit width and finite grating resolution by convoluting the data with an instrumental spectral profile. Using instrumental profiles of slightly different shapes we have also been able to get an impression of how large the effect of the profile shape is on the results. A Gaussian is often an acceptable represention of the entrance slit profile, whereas a Voigt function is a reasonable approximation of the theoretical sinc^2 profile of a perfect spectrograph (cf. Unsöld, 1955; Allen, 1973). Allen and Unsöld also give the following relation between v, the width of the Gaussian at the point where its value has fallen to $1/e$ (i.e. the Doppler width), and the entrance slit full width, s: $v = 0.41s$. For a perfect spectrograph with infinitely narrow entrance and exit slits the relations given by Allen are $v = 0.43l$, and $a = 0.33$, where l is the resolving distance (i.e. the distance from the central maximum to the first minimum), and v and a are the 'Doppler width' and 'damping constant' of a Voigt profile. If a photoelectric detector is used, then its finite width (acting as an exit slit) also has to be accounted for. Ideally the apparatus function resulting from the entrance slit and grating should be convolved with the rectangular profile of the exit slit. Usually, we have used a Gaussian profile (see below), as well as Voigt profiles with 'damping contants' $a = 0.1$ and $a = 0.2$ (see chapter 2 for a definition of the Voigt profile), as the total instrumental profile. With this approximation the entrance and exit slit widths v_1 and v_2 combine to form a total 'Doppler width' $v_{\mathrm{tot}}^2 = v_1^2 + v_2^2$. However, when discussing the line-centre-magnetogram technique in chapter 7 we have also used a rectangular exit slit profile. No attempt has been made to model asymmetric spectrograph profiles.

The reason why we have chosen these approximate profile shapes instead of theoretically more exact ones involving convolutions between sinc^2 and rectangular functions, is that different ratios of entrance to exit slit width and spectrograph resolving power result in different instrumental profile shapes which can only be described by introducing a larger number of free parameters. We feel that such a detailed analysis lies beyond the scope of the present investigation, for the following reasons. Firstly, the theoretical apparatus function can differ considerably from the profile of a real instrument, which can be asymmetric, with grating and lense defects

also contributing significantly to it (Unsöld, 1955; von Alvensleben, 1957). Secondly, as shall be apparent from the results in Sect. 6.4.3, the shape of the apparatus function generally plays a minor role, compared to other parameters like its width, or the asymmetry of Stokes V, etc.

In the following discussions the results are always expressed as a function of v. The relation between v and the often used full width at half maximum of the corresponding Gaussian is: FWHM$= 1.665v$. The actual numerical convolution has been carried out using Fourier transforms and the convolution theorem, but the convolution integral has also been evaluated directly to test the accuracy of the code. The results from both methods are almost identical. For example, the induced zero-crossing wavelength shifts differ by less than 5 m sec^{-1}.

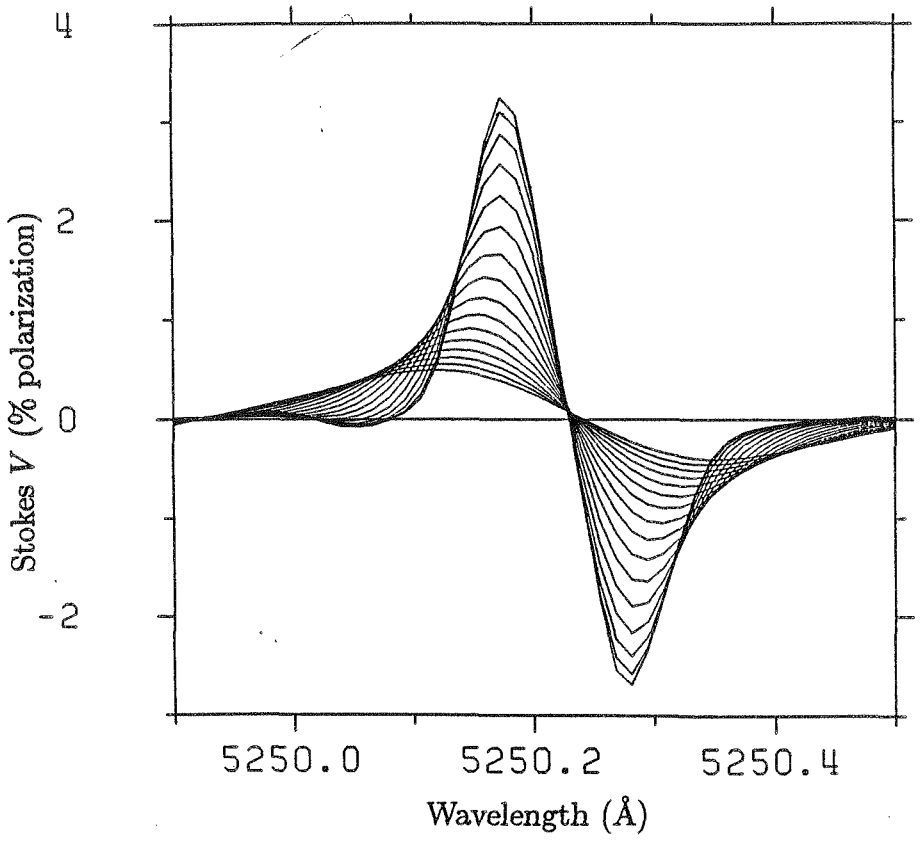

Fig. 6.5 Stokes V profile of Fe I 5250.2 Å for different amounts of spectral smearing. The highest and narrowest profile represents the original FTS data. The other profiles have been convoluted with increasingly broader Gaussians representing instrumental smearing. The broadest Gaussian has v = 150 mÅ, where v is the e-folding width ('Doppler' width).

The technique described above has been used on the Fe I 5250.2 Å and 5247.1 Å profiles in the data from 1979. The Fe I 5250.2 Å line has been chosen since it was, and still is, one of the most widely used lines for polarimetric observations of all kinds, e.g. for magnetograph observations and for magnetic field strength determinations using the line ratio technique. It is also free of obvious blends out to about 0.2 Å in both wings. Thus it is included in the lists of lines selected by Stenflo and Lindegren (1977) and by Rutten and van der Zalm (1984) as unblended after passing several stringent tests. The reason why this last point plays a role is that through spectral smearing the line gets considerably broadened, and other neighbouring lines, not blended with it, may start to overlap as the smearing increases. However, in order to be certain that the neighbouring lines do not influence the analysis presented here, their Stokes V profiles have been artificially reduced to zero for most of the calculations. Due to this precaution, the results presented in this section should be applicable to any line with a similar profile to Fe I 5250.2 Å and with no close neighbouring lines or blends. In Fig. 6.5 the Stokes V profile of Fe I 5250.2 Å is shown convoluted with different Gaussian instrumental profiles having widths, v, ranging from 0 mÅ (corresponding to the original FTS spectrum; the highest and narrowest profile in the figure) to 150 mÅ (the flattest and broadest profile). The width of the instrumental Gaussian has been increased in steps of 10 mÅ.

6.4.3. Infuence of Spectral Smearing on Amplitude and Area of Stokes V

One of the qualitative results is readily visible from Fig. 6.5; the amplitude of the Stokes V profile decreases rapidly with increasing spectral smearing. The quantitative form of this decline is shown in Fig. 6.6, where the Stokes V amplitude, normalised to its value for the fully resolved profile, i.e. $(a_b(v) + a_r(v))/(a_b(v=0) + a_r(v=0))$, has been plotted vs. v, the width of the instrumental profile. a_b and a_r are defined in Sect. 4.4.1. The three curves in Fig. 6.6 correspond to the three different model instrumental profile shapes chosen: the Gaussian (solid line), the Voigt profile with 'damping constant' $a = 0.1$ (dashed line), and the Voigt profile with $a = 0.2$ (dot-dashed line). These profiles will be represented in the same manner in the remaining figures, unless it is explicitly stated otherwise. As mentioned in Sect. 2, the main reason for choosing different profile shapes was to get an idea of how large the effect of the profile shape is on the results, and not to try to fit the profile of a particular instrument to high accuracy. Fig. 6.6 shows that the amplitude decreases more rapidly when the wings of the instrumental profile are more pronounced. Although this effect is not negligible, it is nevertheless small compared to the effect of increasing v, and supports the assumption that the exact profile shape is not very important. The curves obtained from the network and active region profiles are practically identical, and have therefore not been plotted separately. It should be noticed that for lines narrower than Fe I 5250 (for example lines with smaller $g_{\rm eff}$ values, which have smaller Zeeman broadening) the effect will be even larger (cf. the results of spectral smearing on the line ratio method in Sect. 6.4.4). We conclude that only filling factors determined by procedures which account for finite spectral resolution, e.g. from the ratio of V amplitude to $\mathrm{d}I/\mathrm{d}\lambda$ at the same wavelength, should not be appreciably affected by spectral smearing.

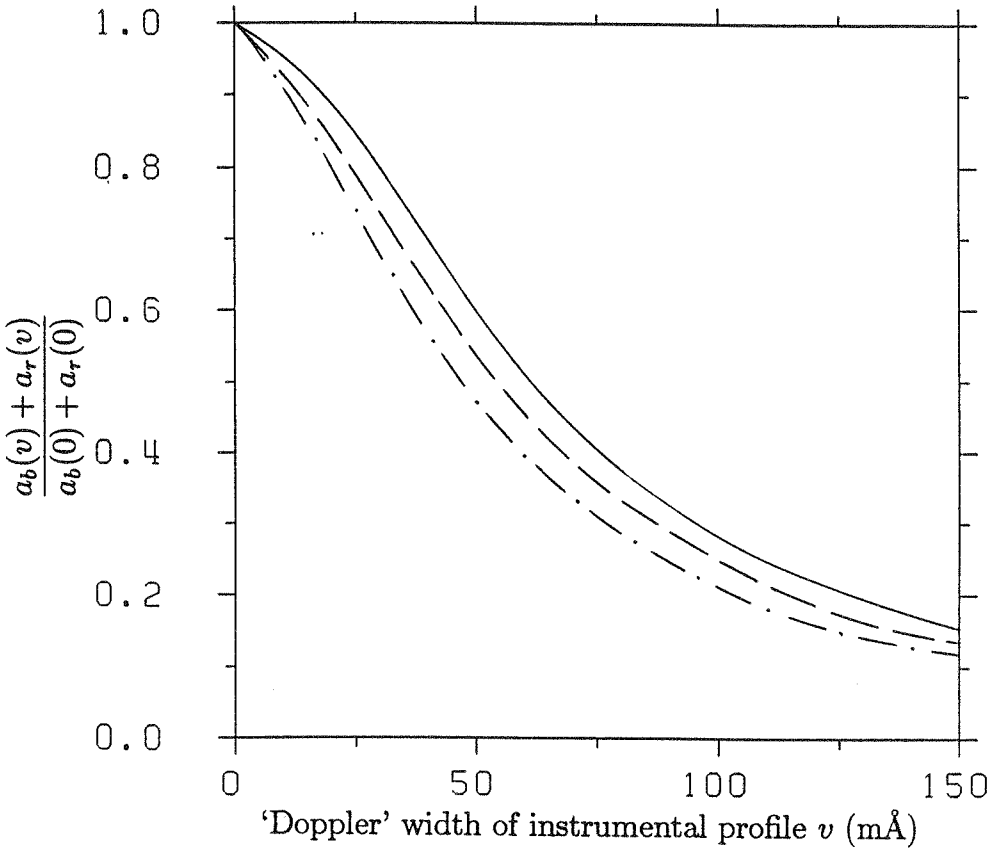

Fig. 6.6 Sum of the absolute blue and red amplitudes of Stokes V vs. 'Doppler' width v (in mÅ) of the instrumental profile. The Stokes V amplitude has been normalised to its value at $v = 0$. Solid curve: Gaussian apparatus function. Dashed curve: Voigt apparatus function with damping constant, $a = 0.1$. Dot-dashed curve: Voigt apparatus functon with $a = 0.2$. The curves represent the Fe I 5250.2 Å line in active plage as well as network regions.

Fig. 6.7 shows the total Stokes V area, normalised to its value for the fully resolved profile, i.e. $(A_b(v) + A_r(v))/(A_b(v=0) + A_r(v=0))$, plotted against v. A_b and A_r are also defined in Sect. 4.4.1. The curves for the network and plage are again too similar to warrant plotting separately.

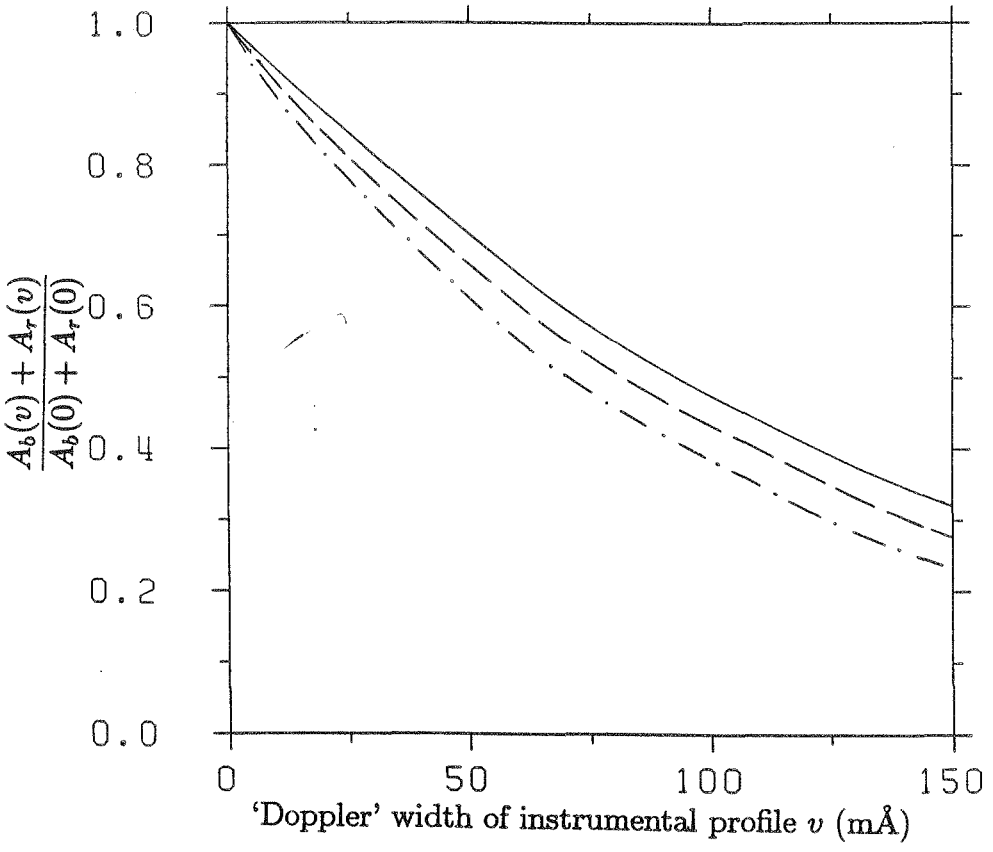

Fig. 6.7 Sum of the absolute blue and red areas of Fe I 5250.2 Å Stokes V (normalised to its value at $v = 0$) vs. v. The three curves represent the same profile shapes as in Fig. 6.6. Network and active plage regions give identical curves.

The decrease in Stokes V area is not quite as strong as the decrease in Stokes V amplitude, but is still considerable. This decrease has a simple intuitive explanation. Due to the instrumental broadening the two wings of Stokes V overlap and cancel each other increasingly, thus producing the observed result. Physically this is related to the fact that the absolute areas of the two Stokes V wings play a role very similar to that of the line depth of the I profile, and *not* to that of its equivalent width, as can be easily understood by recalling that it is the area of the I_V profile (cf. Sect. 4.2) which corresponds to the equivalent width. Indeed, the equivalent width of the I_V profile, W_V, was found to change by approximately 20% between $v = 0$ and 150 mÅ for a Gaussian instrumental profile, when neighbouring lines are not removed. This is a much smaller variation than that of A_b or A_r. Part of this change in W_V may be due to the fact that the area asymmetry of Stokes V is a function of v as well, and the renormalisation needed, therefore also depends on v. However, part of the effect is due to the circumstance that as the line broadens it becomes more difficult to determine W_V accurately. Integration has to be terminated where the neighbouring lines start to interfere. In particular for a Voigt instrumental profile the resulting decrease in W_V is significant. A way out of this dilemma is to use the line strength of the I_V profile, S_V, defined as the area of the lower half of the line. We find that for a Gaussian instrumental profile S_V decreases by less than 10% between $v = 0$ and $v = 150$ mÅ. For the range $0 \leq v \leq 50$ mÅ the decrease is less than 1%. S_V is therefore a quantity, which can be used to determine the filling factor almost independently of the spectral resolution used.

6.4.4. Influence of Spectral Smearing on Stokes V Line Ratio

One would naively expect that if one chooses two lines which are practically identical in every other respect except in the Landé factor (like the Fe I lines at 5247.1 and 5250.2 Å), the ratio of their Stokes V amplitudes would not depend on the spectral resolution, or at least not do so strongly. However, the large effect of the macroturbulence on the line ratio found in Sect. 6.3.2 suggests that we must expect a similar influence due to

spectral smearing. The larger Landé factor of Fe I 5250.2 Å means that for a kilogauss field its Stokes V profile will be somewhat broader than the Fe I 5247.1 Å line, due to Zeeman saturation (cf. Fig. 4 of Stenflo and Harvey, 1985). Its amplitude will therefore be less strongly affected by spectral smearing than that of the narrower Fe I 5247.1 Å line. As a result, a decrease in spectral resolution will change the ratio between the V amplitudes of the two lines, such that the Fe I 5250.2 Å line gets stronger with respect to the Fe I 5247.1 Å line. Fig. 6.8 shows the predicted effect. The Stokes V amplitude of the Fe I 5250.2 Å line divided by 1.5 times the Stokes V amplitude of the Fe I 5247.1 Å line, or $(a_b(5250) + a_r(5250))/((a_b(5247) + a_r(5247)) \times 1.5)$, is plotted vs. v. On the right hand side of the figure a few values of the magnetic field, based on the Milne-Eddington calculations of Stenflo and Harvey (1985), are marked. The amplitude ratio increases steadily with decreasing spectral resolution, with the consequence that the deduced field strength decreases with increasing v, if the effect of spectral smearing is not accounted for in the interpretation.

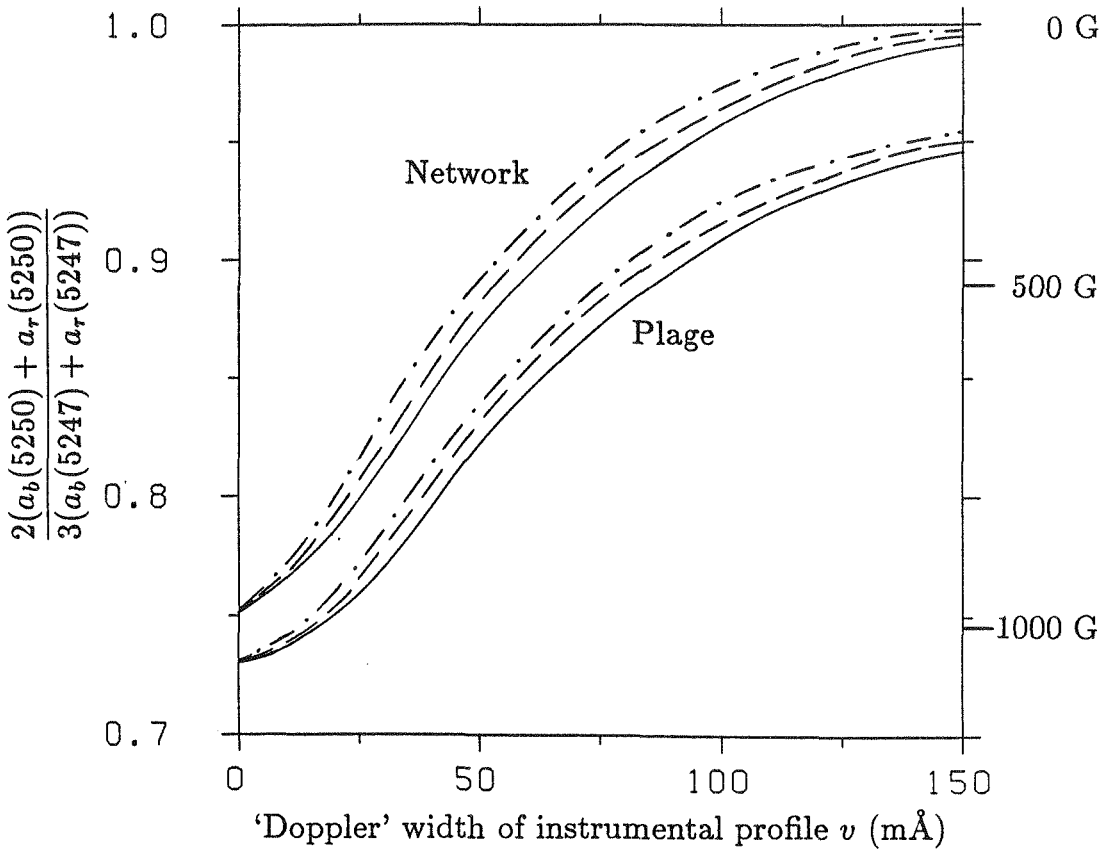

Fig. 6.8 2/3 times the ratio of the Stokes V amplitudes of Fe I 5250.2 Å and Fe I 5247.1 Å vs. v. Upper three curves: Network. Lower three curves: Plage. For some values of the line ratio the deduced field strength has been marked on the right side of the figure.

For very large v the line ratio asymptotically approaches the value one, as is expected from theoretical considerations, since for a very strongly smeared, i.e., extremely broadened profile, the Zeeman splitting is always much smaller than the line width so that Stokes V behaves like in the weak field case. We have tested the behaviour of the amplitude line ratio for v values upto $v = 500$ mÅ and have found it to behave as predicted. It should be noted, however, that we carefully removed the neighbouring lines to both Fe I 5250.2 Å and 5247.1 Å, since their presence would no longer allow a comparison with the theoretical prediction.

This effect may explain the difference in line ratio between Stokes V profiles obtained with the Kitt Peak McMath grating spectrometer (spectral resolution approximately 20 mÅ) and the FTS, as pointed out by Stenflo and Harvey (1985). Once more the shape of the instrumental profile plays only a minor role.

In most cases, however, the line ratio technique has been applied to magnetograph observations obtained with fixed exit slits (e.g. Stenflo, 1973; Wiehr, 1978). Let us denote the apparent field strengths of Fe I 5250 and

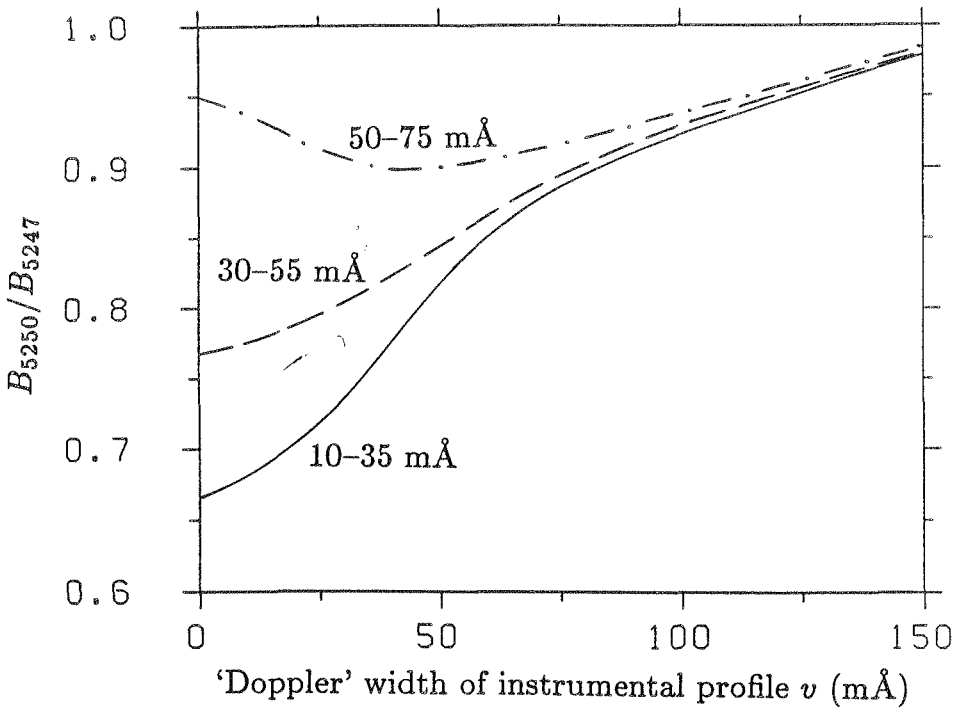

Fig. 6.9 B_{5250}/B_{5247} vs. v. B_{5250} is the signal from a magnetograph slit placed in the wings of Fe I 5250.2 Å. Solid curve: magnetograph slit 10–35 mÅ from line centre. Dashed curve: 30–55 mÅ. Dot-dashed curve: 50–75 mÅ.

5247 evaluated according to the assumption of a weak field by B_{5250} and B_{5247} respectively. Thus

$$B_{5250} \sim \frac{\int_{\lambda_{b_1}}^{\lambda_{b_2}} V_{5250}\, d\lambda - \int_{\lambda_{r_1}}^{\lambda_{r_2}} V_{5250}\, d\lambda}{g_{5250}\left(\int_{\lambda_{b_1}}^{\lambda_{b_2}} \frac{\partial}{\partial\lambda} I_{5250}\, d\lambda - \int_{\lambda_{r_1}}^{\lambda_{r_2}} \frac{\partial}{\partial\lambda} I_{5250}\, d\lambda\right)}\,, \tag{6.9}$$

where V_{5250} and I_{5250} are the spectrally smeared Stokes V and I profiles of the Fe I 5250.2 Å line, g_{5250} the Landé factor, and $\lambda_{b_{1,2}}$ and $\lambda_{r_{1,2}}$ the wavelengths of the edges of the exit slit windows in the blue and red line wings, respectively. Thus the integrals in the denominator can be directly evaluated, to become: $I_{5250}(\lambda_{b_2}) - I_{5250}(\lambda_{b_1}) - I_{5250}(\lambda_{r_2}) + I_{5250}(\lambda_{r_1})$. An analogous expression applies for the Fe I 5247.1 Å line.

Fig. 6.9 illustrates the dependence of the B_{5250}/B_{5247} line ratio on the width v of the Gaussian instrumental profile for each of three (rectangular) magnetograph slits of equal width at the positions 10–35 mÅ (solid line), 30–55 mÅ (dashed line), and 50–75 mÅ (dot-dashed line) on either side of the zero-crossing wavelength. These three slit positions were used by Stenflo (1973).

We have also tested the effect of spectral smearing on the line ratio without removing the neighbouring lines. In this case the amplitude line ratio can actually become larger than unity (upper solid curve in Fig. 6.10). This result for $v \gtrsim 100$ mÅ is due to the fact that Fe I 5247.1 Å gets slightly more blended with increasing spectral smearing than Fe I 5250.2 Å. The dashed curve is the line ratio of only the blue wings of these two lines, while the dot-dashed curve is the line ratio of the red wings. The blending in Fe I 5247.1 Å is stronger than in Fe I 5250.2 Å in both wings, but mainly in the blue wing. Note that in contrast to Stokes I, the V profile gets weakened by blends.

6.5. Conclusions

In this chapter we have presented a method for obtaining the true field strength in fluxtubes from Stokes V, which does not rely on radiative transfer calculations. The kilogauss fields found by previous investigators (cf. Sect. 6.1) are confirmed. We have also outlined a procedure for determining the filling factor in a relatively model independent manner although some problems still remain with telescope depolarization and the true continuum

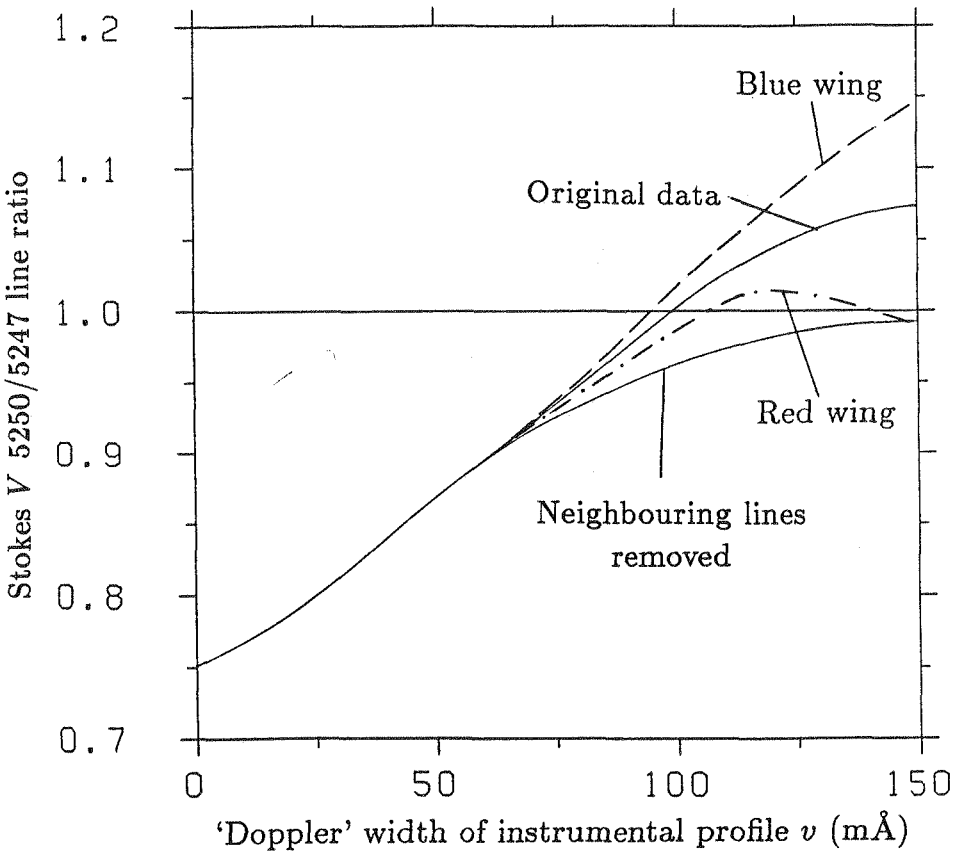

Fig. 6.10 2/3 times the ratio of the Stokes amplitude of Fe I 5250 Å and Fe I 5247.1 Å vs. v. Lower solid curve: Line ratio after removing the neighbouring lines. Upper solid curve: line ratio when neighbouring lines are not removed. Dashed curve: line ratio of blue wing only (neighbouring lines not removed). Dot-dashed curve: line ratio of red wing only (neighbouring lines not removed).

intensity in fluxtubes. The filling factor turns out to be one of the most difficult parameters to determine with certainty. In Sect. 6.3 we have examined the CLV of the 5250/5247 line ratio. Model calculations show that the observed CLV of this parameter can be reproduced equally well by a constant magnetic field of 1100–1300 G or a magnetic field decreasing with height, as determined with the thin tube approximation with $B(\tau = 1) \approx 2000$ G. The strong influence of macroturbulent broadening on the line ratio has also been demonstrated. If the lines are broadened then higher field strengths are required to give a particular line ratio.

The fact that the CLV of the 5250/5247 line ratio cannot provide information on the height variation of the magnetic field raises the question of whether there are other possible methods of obtaining such information. One possibility is the CLV of the IR line Fe I 15648.5 Å. Stenflo et al. (1987b) have been able to determine the height variation of the magnetic field directly from the splitting of this line, and find a decrease with height. However, in view of the results presented in this chapter, we require radiative transfer calculations of this line to settle this question. Fortunately, there are also other indicators which suggest that the field strength really does decrease with height. An example is the comparison of the fields derived at *disk centre* from the IR line (1400 G) and in the visible (1000–1200 G). Since the IR line is formed deeper in the atmosphere than the lines in the visible (due to a minimum in continuum opacity near 1.6 μ), this amounts to a height gradient as well. At disk centre the π-component should not play a major role, unless the fields are strongly tilted.

Another interesting result derived from the IR line is that the σ-components of its V profile are individually considerably broader than the complete I profile, cf. Fig. 6.11. Two possible explanations exist for this observation. Firstly, the magnetic field may have a range of field strengths distributed horizontally, either across the diameter of each individual fluxtube or varying from fluxtube to fluxtube. The other possiblity is that velocity broadening is responsible for this large Stokes V width. This question may be decided in a future investigation additionaly involving model calculations of this and other lines in the IR with smaller Landé factors.

We have seen the importance of changes in the line profile for the line ratio. It is therefore also necessary to investigate the line ratio calculated using 1.5-D radiative transfer (i.e. radiative transfer along many lines of

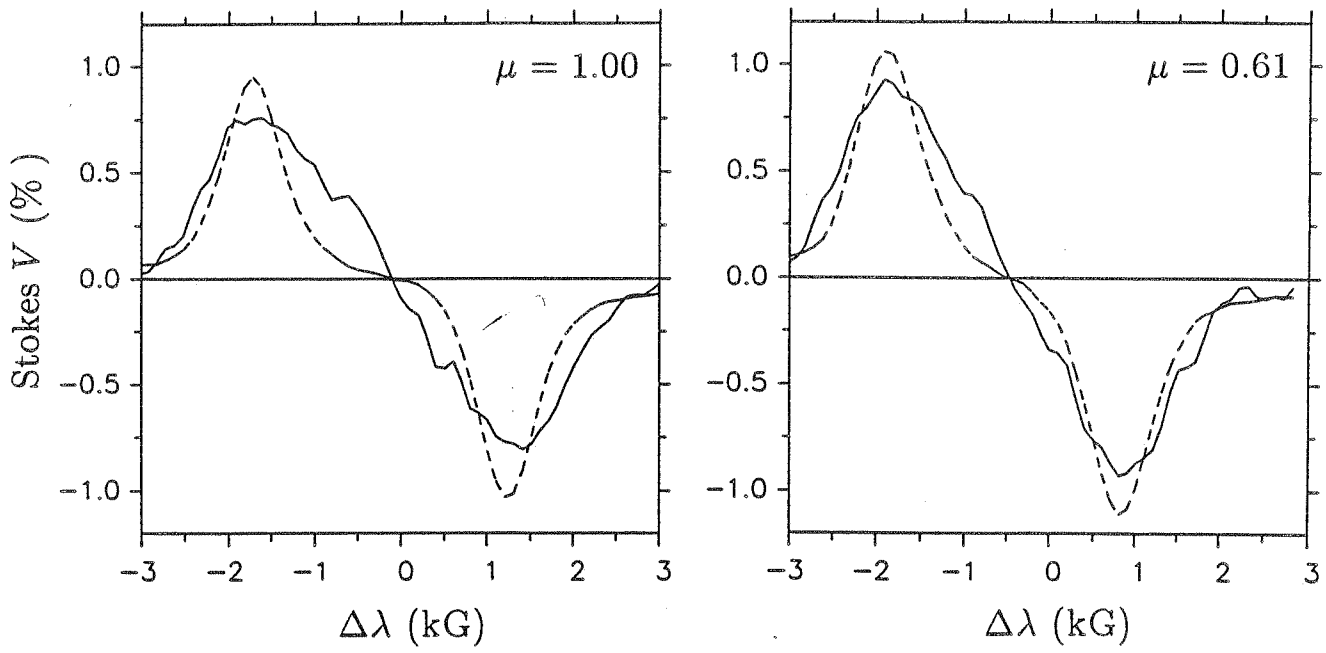

Fig. 6.11 Comparison between observed (solid curve) and computed (dashed curve) Stokes V profiles at $\mu = 1.00$ and 0.61. The computed Stokes V profile is determined by subtracting two shifted Stokes I profiles from each other. Thus the difference in width of the individual components of the two profiles is a measure of the difference in width between the I profile and a single σ-component of the V profile. The relative wavelength scale has been transformed into kG units (based on a Landé factor of 3.0).

sight with subsequent averaging of the emergent profiles) in a 2-D fluxtube model. In particular, away from disk centre the line of sight contains a magnetic contribution over only a small part of its length. The results of such calculations will be presented in a future publication (Solanki and De Martino, in preparation).

Throughout this chapter we have neglected low lying canopies whose presence has been suggested by Giovanelli (1980), Giovanelli and Jones (1982), and Jones and Giovanelli (1983). A recent review of canopy observations has been given by Jones (1985). Can our observations set any new limits on the heights of such canopies? Canopies in the photosphere would, due to the rapid expansion of the fluxtubes, cause the field strength to drop drastically. We should therefore expect the line ratio to become unity in the presence of a sufficiently low lying canopy. We find no sign for the existence of such canopies in any of our observations. The approach of the line ratio to unity near the limb is naturally explained by changes in the line profile (even for a strong constant field). This result is in agreement with the findings of Giovanelli and Jones who see such canopies mainly in chromospheric lines.

7. Mass Motions

Πάντα ῥεῖ

Ἡράκλειτος

7.1. Introduction

Mass motions, like the other basic properties of magnetic fluxtubes, have been extensively studied, both theoretically and observationally. In the following brief review we shall restrict ourselves to the literature on motions in the photospheric layers of fluxtubes.

Theorists have discovered a number of mechansims for producing mass motions in fluxtubes and have analysed the properties and the influences of such motions. Ribes and Unno (1976), Unno and Ribes (1979), Schüssler (1984a), and Hasan and Schüssler (1985) have studied the effects of steady flows on the properties and stability of fluxtubes. Parker (1978) first studied the convective instability in small fluxtubes produced by downflows. Others to study the convective instability are Webb and Roberts (1978), Spruit (1979), Spruit and Zweibel (1979), and Unno and Ando (1979). Venkatakrishnan (1983, 1985) and Hasan (1984, 1985) calculate the convective collapse fully dynamically, and Hasan (1984, 1985) finds that the convective collapse of fluxtubes gives rise to oscillatory motions within them as predicted by Spruit (1979). Nordlund (1983) has carried out convective collapse calculations in three dimensions. Venkatakrishnan (1986) has studied the resonant oscillatory motions induced in fluxtubes by external pressure fluctuations. Overstable oscillations in fluxtubes have also been examined by Hasan (1986). The wave modes possible in fluxtubes when the effects of gravity are included have been investigated (in a linear analysis) by e.g. Defouw (1976), Roberts and Webb (1978, 1979), Spruit (1981a), Rae and Roberts (1982), and Roberts (1983). Finally, Hollweg et al. (1982) calculate the propagation of Alfvén waves non-linearly, while Herbold et al. (1985) calculate the non-linear amplitudes of longitudinal waves from the photosphere to the transition region, including the production of shocks.

Mass motions play an important role for fluxtubes and their surroundings. Examples are the heating of the fluxtube atmosphere by downflows (Hasan and Schüssler, 1985), the stabilization of fluxtubes by vortical flows, and their destabilization by downflows (Schüssler, 1984a), and the heating of the Chromosphere and Corona by fluxtube waves (e.g. Herbold et al., 1985).

Early observational work with a spatial resolution of usually a couple of arc seconds, both in polarized and unpolarized light, suggested the presence of downflows of the order of 0.5 km sec^{-1} co-spatial with the magnetic field, at supergranule boundaries (e.g. Frazier, 1970; Skumanich et al., 1975) and in active regions (e.g. Giovanelli and Ramsay, 1971; Howard, 1971). Further references to such observations are given in Sect. 7.3.1. Giovanelli and Slaughter (1978) have carried out an extensive empirical study of steady flows inside small fluxtubes by measuring the zero-crossing wavelength of the Stokes V profiles (relative to their Stokes I wavelengths) of a number of lines formed at different heights in the atmosphere, and so have been able to determine the height variation of downflow velocity. They find that the velocity increases rapidly with depth, being negligible in the chromosphere and increasing to 1.6 km sec^{-1} near the $\tau = 1$ level of the photosphere. Wiehr (1985a) also finds redshifts of the Stokes V profile compared to Stokes I of between 0 and 2 km sec^{-1} for the Fe I 8468.4 Å line in different magnetic elements. Frazier and Stenflo (1978) also observed large downflows correlated with the magnetic field, but also found some indirect evidence indicating that these downflows may be located in the immediate surroundings of the fluxtubes. Such a ring of downflowing material surrounding the fluxtube appears in the self-consistent model calculations of Deinzer et al. (1984b) as well.

To keep the fluxtubes from draining the corona on a timescale of minutes Giovanelli (1977) proposed a mechanism for the inflow of matter into fluxtubes, based on the diffusion of neutral atoms across the field lines. This process, which is driven by the horizontal gradient in gas pressure, works most efficiently near the temperature minimum. However Hasan and Schüssler (1985) point out that the use of realistic diffusion coefficients (collision cross-sections) leads to very small flows, of the order of 10 m sec^{-1} (see also Schüssler, 1986).

In contrast to the observations mentioned above, Stenflo and Harvey (1985) observe only redshifts smaller than 0.3 km sec^{-1} of the zero-crossing of the Stokes V profiles of Fe I 5250.2 Å and 5247.1 Å, with respect to

the core wavelengths of the simultaneously obtained Stokes I profiles. If the wavelengths of the corresponding I profiles are corrected for the effects of convective motions according to Dravins et al. (1981), then they find that the V profiles are actually *blueshifted* by 0.0 to 0.3 km sec^{-1} (the blueshift increases with the amount of magnetic flux). Brants (1985b) also finds no evidence for net flows in faculæ in an emerging flux region from high spatial resolution observations in Fe I 6302.5 Å. Recently, Koutchmy and Stellmacher (1987) have also not found any downflows larger than 0.25 km sec^{-1} in a network element. There are therefore conflicting claims in the literature regarding the presence of downflows in fluxtubes. Furthermore, all previous authors determine the shifts of Stokes V relative to Stokes I, and there are still some problems left with the precise core wavelengths of Stokes I profiles in active regions. Kaisig and Schröter (1983) find that the cores of six Fe I lines formed in active regions are blueshifted compared to their wavelengths in purely non-magnetic regions by approximately 0.05–0.25 km sec^{-1}. On the other hand, the observations of Livingston (1982) suggest that the active region profile of the Fe I 5250.6 Å line has a relative *core* blueshift of the order of 0.01–0.02 km sec^{-1} (although at equal intensity the active region profile is always redshifted as compared to the quiet Sun profile), while Cavallini et al. (1985) observe active region relative redshifts of the order of 0.05–0.2 km sec^{-1} for 3 Fe I lines. Preliminary results of Brandt and Solanki (1987) for a number of lines observed in regions with filling factor $\lesssim 11\%$ suggest that the lowest bisector points coincide to within ± 1 mÅ. Finally Miller et al. (1984) find that the line cores of three Fe I lines observed at supergranular boundaries lie within ± 0.02 km sec^{-1} of the cores of these lines in the quiet photosphere. All these measurements are limited to a few medium strong Fe I lines. The wavelengths of Fe II lines and of most Fe I lines have not been studied at all in active regions. In the light of these uncertainties we shall determine Stokes V zero-crossing shifts for a large number of lines, both with respect to the simultaneously measured Stokes I core wavelengths, and to laboratory wavelengths. The need for measurements of Stokes V line shifts without reference to Stokes I is intensified by the fact that the Stokes V zero-crossing wavelength need not correspond exactly to the wavelength of the Stokes I line core in the presence of a complicated velocity field.

There has also been some observational evidence for the presence of non-stationary motions in fluxtubes. A correlation between fluctuations in the magnetic field and the velocity of the five minute oscillations was first presented by Tanenbaum et al. (1971). Time series of the Stokes V zero-crossing wavelength shifts have been obtained by Giovanelli et al. (1978). Although they failed to detect oscillatory motions besides the five minute oscillations in their time series, this does not imply the absence of all other oscillatory motions in fluxtubes. Their spatial resolution of $2.5'' \times 3.5''$ means that they probably observed a number of fluxtubes simultaneously, and could therefore detect only those oscillations in which all the fluxtubes were oscillating in phase. Five minute oscillations with amplitudes ranging between 0.1 and 0.25 km sec^{-1} have also been observed by Wiehr (1985a). In addition, he presents observations of large changes in Stokes V zero-crossing wavelength, amplitude, and asymmetry on a time scale of a few minutes, which appear to be independent of the five minute oscillations. However, an instrumental source for these observations cannot be ruled out (magnetic region passing in and out of the resolution element). Brants (1985b) finds a scatter of greater than ± 1 km sec^{-1} in the velocity amplitudes derived from Stokes V in faculæ, at least part of which he claims is not due to noise.

There are different methods of obtaining information on fluxtube velocities in the absence of spatially and temporally resolved spectra. Stokes V zero-crossing shifts are mainly sensitive to stationary flows, or, to be more exact, to stationary flows in the majority of fluxtubes in the resolution element. The shape of the Stokes V profile, in particular the asymmetry between its blue and red wings, is sensitive to velocity gradients along the line of sight. The width of the I_V profile (cf. Sect. 4.2 for a definition) is sensitive to horizontal, vertical, and temporal variations in velocity inside fluxtubes, or from one fluxtube to another. In this chapter we will present results based on the analysis of the zero-crossing shift (Sect. 7.2, from Solanki, 1986 and Stenflo et al., 1987a, b) and the I_V line width (Sect. 7.4, from Solanki, 1986). Observations and a simple discussion of the Stokes V asymmetry, whose interpretation is more involved, are presented separately in chapter 8. In Sect. 7.3 the results of Sect. 7.2 are compared with older observations of Stokes V zero-crossing shifts and a possible explanation for the discrepancies between the various downflow velocities is given (from Solanki and Stenflo, 1986).

7.2. Zero-crossing Wavelength Shifts

7.2.1. Absolute Wavelengths

The determination of absolute zero-crossing wavelengths requires that the measured wavelengths be corrected for any error in calibration of the wavelength scale, for gravitational redshifts, and for the relative motion between the observer and the observed region. Only the data obtained in 1979 have been reduced to an absolute Wavelength scale. Since the 1984 data were obtained closer to the limb, and the solar rotation correcton increases rapidly near the limb, the uncertainty in position of the entrance hole of the FTS makes any correction a dangerous procedure for these data (cf. Stenflo et al., 1987b). In addition, the exact position of the rotation axis was not noted during the observations. A possible future solution may be to apply Livingston's method employing the Mg Ib line to the CLV data in the visible spectral range.

The instrumental wavelength scale has been, whenever possible, checked by comparing the wavelengths of atmospheric lines taken from Pierce and Breckinridge (1973) with the wavelengths of these lines in our spectra. For two spectra it is possible to use the telluric O_2 lines between 6278 Å and 6307 Å. Of these, the lines found to be unblended by Balthasar et al. (1982) have been chosen. According to these authors the wavelengths of these lines should be stable to within 15 m sec^{-1}. Caccin et al. (1985), on the other hand, warn that pressure induced shifts and asymmetries of O_2 lines make them of questionable use as absolute wavelength standards. For two other spectra the 5420.6 Å and 5422.9 Å lines of H_2O are used, in the absence of anything better. One spectrum contains no suitable atmospheric absorptions. However, according to Brault (1978) the FTS wavenumber scale should be accurate to 0.0001 cm^{-1}, and indeed, the FTS wavelength scale is found to reproduce the telluric absorption lines to within 0.05 km sec^{-1} in all the spectra in which these are present.

Next, the gravitational redshift of 0.636 km sec^{-1} is subtracted from the wavelengths, and finally the relative motion between the observer and the observed region is compensated for. This motion may be thought of being composed of a number of components (Howard and Harvey, 1970), the most important of which near disk centre are due to the rotation of the earth around its own axis, its orbital motion around the Sun, and solar rotation. The velocity due to the first two components is calculated using a code described by Balthasar (1984). The limiting factor for the accuracy of these calculations is probably the smearing of the order of 50 m sec^{-1} introduced by the long integration times of the observations. Its main effect would be to broaden the lines slightly, but due to the asymmetry of Stokes V it may also cause a small shift of the zero-crossing wavelength, which will however be much smaller than 50 m sec^{-1}(cf. Sect. 7.3.2). The rotation rate of the solar magnetic features has been studied by e.g. Stenflo (1974). His values of the rotational velocity at different latitudes are used to compensate for solar rotation. The main uncertainty in the wavelength shift due to solar rotation is introduced by the imprecise knowledge of the position of the FTS entrance hole on the solar surface (cf. chapter 3). As an additional check on solar rotation the Stokes I core wavelength of a strong line, whose core is formed above the layer of granular motion and should therefore be unaffected by it, e.g. Mg I 5172.7 Å, is determined and compared to laboratory wavelengths. The difference between its solar (from Pierce and Breckinridge, 1973) and laboratory (from Moore, 1972) wavelength is 638 m sec^{-1} which compares very well with the gravitational redshift of 636 m sec^{-1}, which is the only expected shift if granular influences are absent. This method has been outlined by Livingston (1983). However, the relatively broad core of this line limits the accuracy of the measurement of its core wavelengths.

The total uncertainty, in the Stokes V zero-crossing shifts relative to the laboratory wavelengths, resulting from all the different sources, is estimated to be about ± 0.25 km sec^{-1} for the four data files with $\mu > 0.9$ which contain telluric lines.

7.2.2. Stokes V Zero-crossing Shift at Disk Centre

In this section the Stokes V zero-crossing shifts of the lines from Tables 4.1 and 4.2 are analysed, both with regard to laboratory wavelengths and to the wavelengths of Stokes I profiles observed simultaneously in the same region.

In Fig. 7.1a the Stokes V zero-crossing shift relative to the laboratory wavelength, v_V, is plotted vs. S_I for a plage region. We define

$$v_V = c\frac{(\lambda_V^* - \lambda_{\rm lab})}{\lambda_{\rm lab}}, \tag{7.1}$$

where c is the velocity of light, λ_V^* is the zero-crossing absolute wavelength of Stokes V, and $\lambda_{\rm lab}$ is the laboratory

wavelength of the line. The stars represent Fe I lines with excitation potential of the lower level $\chi_e < 3$ eV, the circles represent Fe I lines with $\chi_e \geq 3$ eV, and the filled squares Fe II lines. These symbols shall retain their meanings throughout the following figures. The scatter is mostly due to noise in the data and to inaccuracies in the laboratory wavelengths, but some is of solar origin (see below). In particular the larger scatter of the Fe II data, as compared to Fe I, is probably due to inconsistencies in the laboratory wavelengths of the ionised species, since a similar scatter has also been observed for Stokes I alone by Dravins et al. (1986) who first proposed this interpretation. The solid curve represents the smoothed mean of the Fe I data.

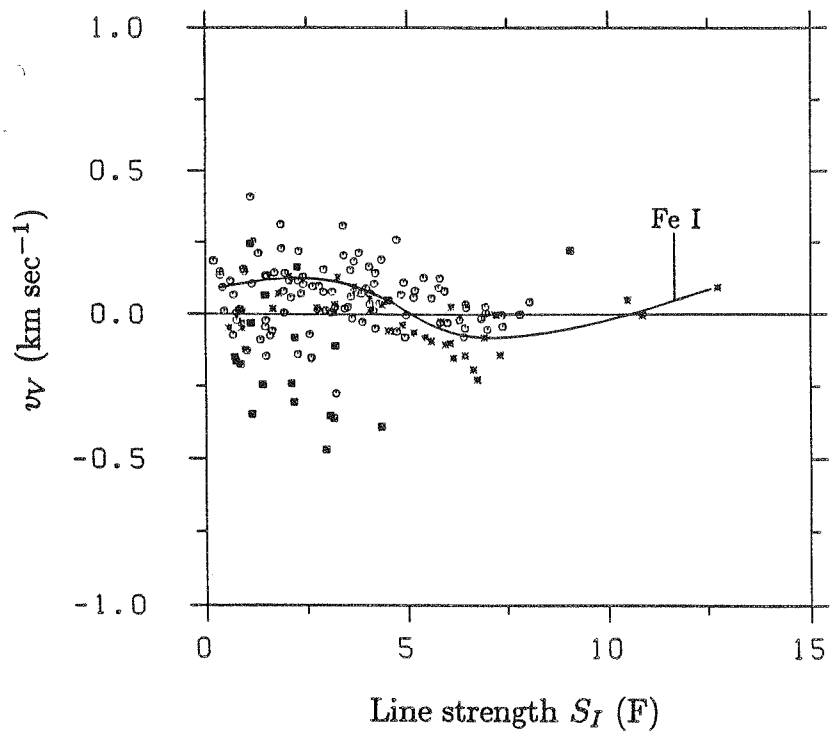

Fig. 7.1 a v_V vs. S_I, i.e. the difference, in velocity units, between Stokes V zero-crossing absolute wavelength and the laboratory wavelength, vs. the line strength of the Stokes I profile, S_I. Plotted are the unblended Fe I and II lines in an FTS spectrum of an active region plage. In this and the following figures, the stars represent Fe I lines with $\chi_e < 3$ eV, the circles Fe I lines with $\chi_e \geq 3$ eV, and the filled squares Fe II lines. The solid curve is a smoothed mean of the Fe I data.

Fig. 7.1b shows the smoothed mean v_V curves of the Fe I lines of four regions (marked *a*, *b*, *c*, and *d* in this and the following figures), again plotted vs. S_I. Due to the uncertainty in its position on the solar disk and the absence of telluric lines to serve as a wavelength standard, the fifth observed region has not been included. Note that in three regions the mean curves are blueshifted for some values of S_I and redshifted for other values. If we interpret Stokes V zero-crossing shifts as steady flows, then both up- and downflows should be present at different heights in these regions! One of the regions appears to show a downflow of around 0.15 – 0.2 km sec^{-1}, but within the error margin given in Sect. 7.2.1 all the data are compatible with an *absence* of global up- or downflows in small magnetic fluxtubes, in contrast to the results of a number of previous studies (e.g. Giovanelli and Slaughter, 1978; Harvey, 1977; Wiehr, 1985a).

The arrows on the right hand side of Fig. 7.1b mark the zero-crossing shifts of the Mg Ib lines at 5172 Å and 5183 Å for the two spectra in which these lines are present (regions *b* and *c*). These lines have strengths of approximately 38 F and 47 F respectively, after correcting for the blends in their wings. They also give upper limits of approximately 250 m sec^{-1} for any net flows inside fluxtubes. This increases our confidence in the absolute wavelength values determined. The fact that the strong Mg Ib lines and the much weaker Fe I lines are equally unshifted is completely contrary to the results of Giovanelli and Slaughter (1978), who find increasing redshift with decreasing line strength. This contradiction cannot be accounted for by any mistake in our absolute wavelength determination, since it is based only on the *relative* shifts between different simultaneously observed lines.

It is of interest to note that the curves representing the four regions all have a similar shape. Again, this shape is not affected by the uncertainty of 0.25 km sec^{-1} derived in Sect. 7.2.1, since that does not apply to the relative shifts between the lines of the same region. Medium strong lines are slightly blueshifted compared to weak and very strong lines. Surprisingly therefore, the lines with largest amplitude asymmetry (see Fig. 8.5) also have the largest blueshifts. However, the noise in the data is relatively large and we require further evidence before accepting such a dependence of Stokes V wavelength shifts on line strength. This additional evidence is

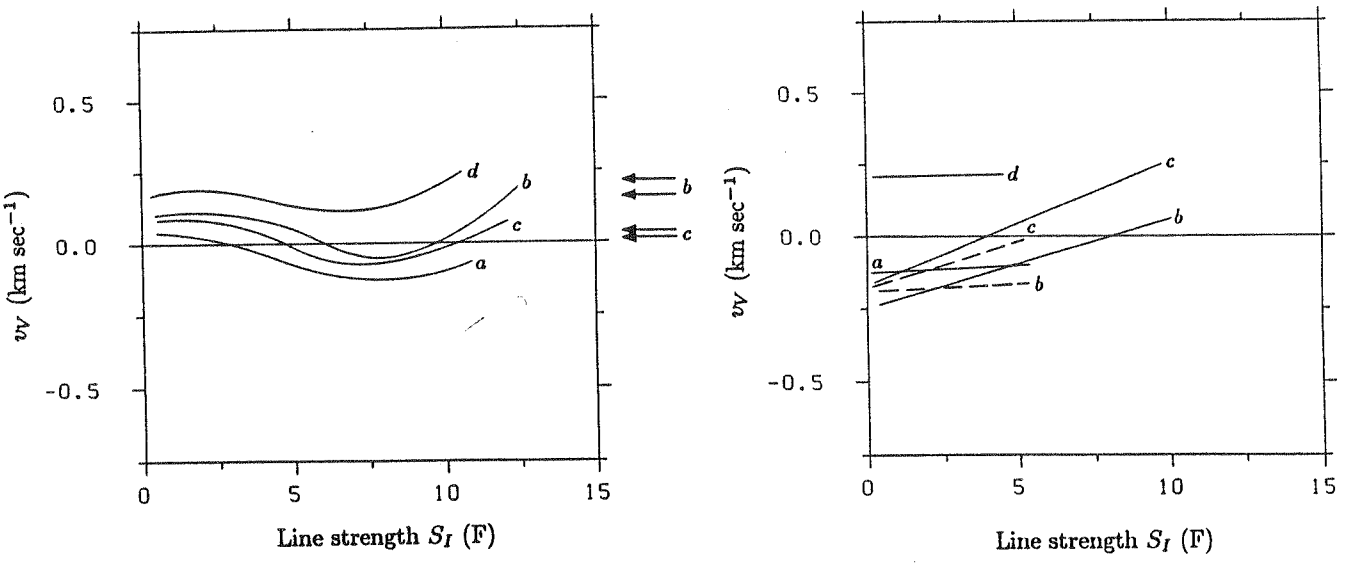

Fig. 7.1 b v_V vs. S_I for the smoothed mean curves of the Fe I lines formed in two active plages and in two network regions. The arrows denote the v_V values of the Mg Ib lines at 5172.7 Å and 5183.6 Å in two of the regions. The regions are denoted by the letters *a*, *b* (strong plage), and *c*, *d* (enhanced network). These letters mark the same regions in Figs. 7.1c and 7.3 as well. **c** v_V vs. S_I for the least-squares fits to the Fe II data of four regions (solid lines). The dashed lines are the least-squares fits to the data of two regions containing the strong Fe II 4923.9 Å line, if it is neglected.

provided by the regression analysis carried out below.

In order to see if the Stokes V wavelength shifts are also dependent on other quantities besides the line strength, we carried out a regression of the following form (for Fe I lines only):

$$v_V = x_1 + x_2 S_I + x_3 S_I^2 + x_4 \chi_e v_{D_I} + x_5 g_{\rm eff} \lambda_I^2 / v_{D_I} + x_6 \langle g_{\rm eff} \rangle \lambda_I^2 / v_{D_I}. \tag{7.2}$$

This simple regression equation is not meant to be unique or exhaustive, but is rather thought of as being the simplest one describing the dependence of v_V on the line strength, S_I, the excitation potential, χ_e, the effective Landé factor, $g_{\rm eff}$, and the wavelength, with reasonable accuracy. $\langle g_{\rm eff} \rangle$ in Eq. (2) signifies the average Landé factor of the sampled lines. The effects of adding further terms were studied, but were too small to warrant their retention. Instead of λ_I, S_I and v_{D_I} the respective parameters of the I_V profile can also be used without changing the results substantially. Unlike the regressions carried out for line width and line depth by Solanki and Stenflo (1984, 1985) (cf. chapter 4), no unique form of the x_5 (Zeeman splitting) term is obvious here from theoretical considerations. Different forms of the x_5 and x_6 (wavelength) terms were therefore tried, but again the results were not changed noticeably.

Besides the expected dependence on S_I (with x_2 being negative and x_3 positive), we found only a slight dependence of v_V on $g_{\rm eff}$ (at the level of 1.5–2σ), a marginal dependence on the wavelength, and a small but noticeable dependence on χ_e (at the level of 2–4σ for the different regions). An increase in redshift with increasing χ_e is observed. This is consistent with the shape of the v_V vs. S_I curve, since for equal line stength, lines with higher excitation potential are formed deeper in the atmosphere, and should have line shifts comparable to those of weaker low excitation potential lines. This is an additional indication that the dependence of v_V on S_I is real, and is not some artifact of the instrument or the data reduction procedure. This trend of $v_V(\chi_e)$ does not continue to Fe II lines, and they have been left out, since their inclusion in the regression analysis would have necessitated a more complex form of Eq. (7.2) with more free parameters.

The regression reduces the scatter of the points in Fig. 7.1a only slightly. We therefore conclude that it is mostly due to noise in our data and to inconsistencies and scatter in the laboratory wavelength measurements.

Fig. 7.1c shows the least squares fits for v_V of the Fe II lines in the same four regions as in Fig. 7.1b. The letters *a*, *b*, *c*, and *d* refer to the same four regions as in Fig. 7.1b. The dashed curves are the least-squares fits for two regions containing the strong Fe II 4923.9 Å line ($S_I \approx 9.3$ F), when it is not included in the fitting

procedure. A comparison of Fig. 7.1c to 7.1b suggests that the weaker Fe II lines are blueshifted compared to Fe I lines of equal strength thus reversing the trend of increasing redshift with increasing χ_e shown by the Fe I lines. This result explains why Eq. (7.2) is insufficient to handle Fe I and II simultaneously.

Next let us look at the shifts of Stokes V relative to the Stokes I profiles measured simultaneously in the same region. Fig. 7.2 shows

$$v_{VI} = c\frac{(\lambda_V - \lambda_I)}{\lambda_I} \tag{7.3}$$

for a network region, plotted against the Stokes I line depth, d_I. The scatter is again mostly due to noise, which now has a contribution from the uncertainties in solar Stokes I instead of from laboratory wavelengths. The dashed curve represents the smoothed mean of the Fe I data. The dashed straight line is a least-squares fit to the Fe II data. The large relative redshift of the weak Stokes V lines is of course due to the increasing blueshift of the Stokes I profiles for decreasing line depth. Also shown are the 'corrected' smoothed mean curves for both Fe I and II (drawn solid). These are obtained from the original curves by subtracting the granular blueshifts of the Stokes I profiles from them. The values of the Fe I blueshifts have been taken from Dravins et al. (1981), the blueshifts of Fe II from Dravins and Larsson (1984). These authors list quiet Sun mean blueshifts of groups of Fe I, respectively Fe II, lines having different line depths, wavelengths, and excitation potentials. The reason d_I was chosen as the abscissa instead of S_I is because the average Stokes I blueshifts given by Dravins et al. (1981) and Dravins and Larsson (1984) are ordered by line depth. The use of quiet Sun values to compensate for Stokes I wavelength shifts in a network region needs to be justified. Miller et al. (1984) find that at supergranule boundaries the Stokes I wavelengths are very similar to those on the quiet Sun. This is what one would expect if the filling factor, α, is small. For the network region plotted in Fig. 7.2 the filling factor is approximately 6% (Sect. 6.2), which is probably small enough for the Stokes I core wavelengths to remain largely unaffected by the magnetic field. Finally, even if the quiet Sun wavelengths may not be ideal for the task, the absence of any large body of such data from active regions makes them the only reasonable choice.

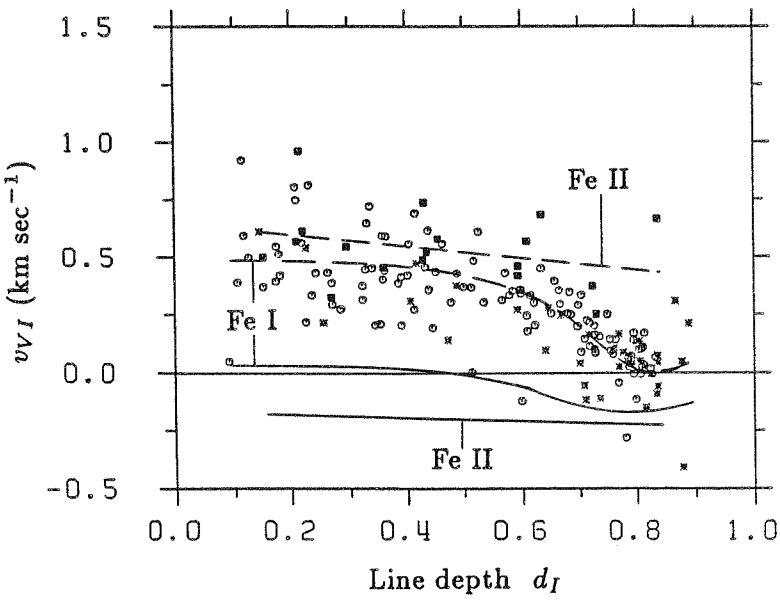

Fig. 7.2 v_{VI}, the difference, in velocity units, between Stokes V zero-crossing wavelength and the Stokes I core wavelength, vs. d_I, the line depth of Stokes I. The data are from an enhanced network region. The dashed curves denote the smoothed mean of the Fe I data, respectively a least-squares fit to the Fe II data (as marked in the figure). The solid curves are obtained from the dashed ones by removing the granular blueshift of the Stokes I profiles.

Fig. 7.3a shows the *un*compensated mean Fe I v_{VI} curves of all five regions. Applying the quiet Sun Stokes I blueshift compensations to these data results in the curves shown in Fig. 7.3b. The arrows on the right side of these figures mark v_{VI} of the Mg Ib lines at 5172 Å and 5183 Å. Since their Stokes I core wavelengths are expected to be practically unaffected by granular motions, no blueshift compensation has been carried out, and the arrows are at the same positions in Figs. 7.3a and b. A dependence of Stokes V wavelength shift (relative to Stokes I) on the filling factor is clearly evident, with the regions of small magnetic flux having Stokes V profiles showing practically no relative shifts at all, while the two plage regions show an average blueshift of approximately 250 m sec^{-1}. This is in general agreement with what Stenflo and Harvey (1985) found for the Fe I 5250.2 Å line. We find no support for such a trend from the v_V curves in Fig. 7.1b (which is not too surprsing, since its magnitude lies at the limit of the accuracy of the absolute wavelengths). A simple explanation for this behaviour of v_{VI} is that the Stokes V wavelengths remain unaffected by increasing filling factor, while the granular blueshift of the

Stokes I profiles decreases progressively with increasing filling factor (perhaps due to magnetic suppression of convection near the fluxtubes), in accordance with the results of Cavallini et al. (1985) for three Fe I lines. This interpretation appears to be supported by Wiehr's (1985a) observation that when scanning across a plage, the Stokes I profile is shifted, but the Stokes V wavelength remains unaffected. The use of the quiet Sun Stokes I blueshift values is therefore not justified for strong plages. However, the three regions with filling factor $\lesssim 7\%$ support the conclusion reached from the v_V data that only flows with small amplitudes are present in fluxtubes. They actually suggest an upper limit of about 200 m sec^{-1} on the velocities of such flows.

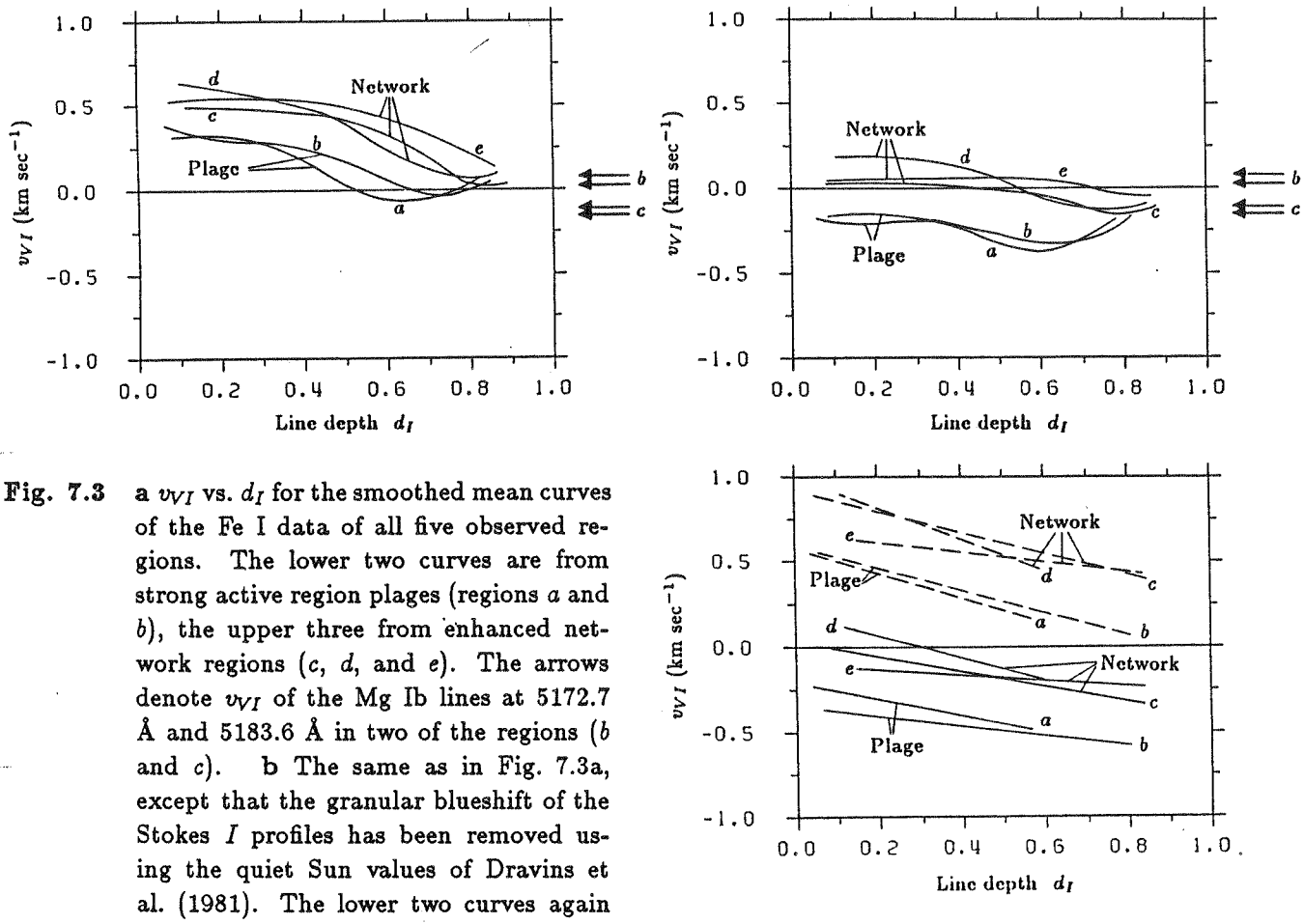

Fig. 7.3 a v_{VI} vs. d_I for the smoothed mean curves of the Fe I data of all five observed regions. The lower two curves are from strong active region plages (regions *a* and *b*), the upper three from enhanced network regions (*c*, *d*, and *e*). The arrows denote v_{VI} of the Mg Ib lines at 5172.7 Å and 5183.6 Å in two of the regions (*b* and *c*). b The same as in Fig. 7.3a, except that the granular blueshift of the Stokes I profiles has been removed using the quiet Sun values of Dravins et al. (1981). The lower two curves again represent active regions. c v_{VI} vs. d_I for the least-squares fits of the Fe II lines in the five observed regions. Dashed lines: original data. Solid lines: the data after compensating for the Stokes I blueshift.

Fig. 7.3c shows the uncompensated (dashed) and compensated (solid) least-squares fits to the Fe II v_{VI} data. The average Fe II Stokes I granular blueshifts are considerably larger than the Fe I blueshifts according to Dravins and Larsson (1984) and Dravins et al. (1986), being of the order of 600–800 m sec^{-1}. The two lowest curves in each group again belong to the two active region plages, suggesting that the granular blueshift of the Fe II Stokes I profiles, like that of the Fe I profiles, is reduced in active regions. The corrected v_{VI} values of Fe II lines again lie close to zero. They have a slight tendency to lie bluewards of the Fe I lines, confirming the trend suggested by the v_V data.

The comparison of the derived v_V and v_{VI} values also provides us with a method to check whether our data are grossly affected by the five minute oscillations, since v_V is susceptible to them, while v_{VI} is not (under the assumption that both Stokes I and V are shifted by approximately the same amount by them). From the similarity of the results of the analyses of v_V and v_{VI} (at least for the regions with low filling factor), we conclude that the five minute oscillations do not significantly affect the results of this section, as is expected due to the

relatively long integration times of our observations.

As the main result of this section we can set an upper limit on the Stokes V zero-crossing shifts of about ± 250 m sec^{-1} in both the network and active region plages. If such shifts are interpreted as being due to steady flows in magnetic fluxtubes, then the down- or upflow velocities have to be less than this value. Our data is therefore compatible with an absence of steady flows in small magnetic fluxtubes.

7.2.3. Centre to Limb Variation of Stokes V Zero-crossing Shifts

The 1984 data allows us to determine the CLV of the zero-crossing shift. We follow Stenflo et al. (1987a, b) and present such results for three Fe I lines. Fig. 7.4 shows the CLV of v_{VI} for Fe I 5250.2 Å (filled squares) and Fe I 5247.1 Å (stars) along with their standard errors. The absolute shift v_V of the 1984 data has not been determined due to the problems described in Sect. 7.1. The solid curve in the diagram is the negative value of the *absolute* wavelength shift of Stokes I profiles of the undisturbed, non-magnetic atmosphere induced by the solar granulation. It has been derived from the data of Balthasar (1984), and represents the actual "zero-level" to which the observed points should be referred to in order to represent real net velocities. The super-gravitational redshift of the Stokes I profiles near the limb can be explained by horizontal motions in the granulation, as was first evinced by Beckers and Nelson (1978). Nordlund (1984) has presented detailed calculations of the CLV of Stokes I line shifts of a number of lines including Fe I 5250.2 Å with results similar to the observations of Balthasar. Balthasar (1985) has given an intuitive explanation based on projection effects of up and downflows, composed of hot and cool material, respectively.

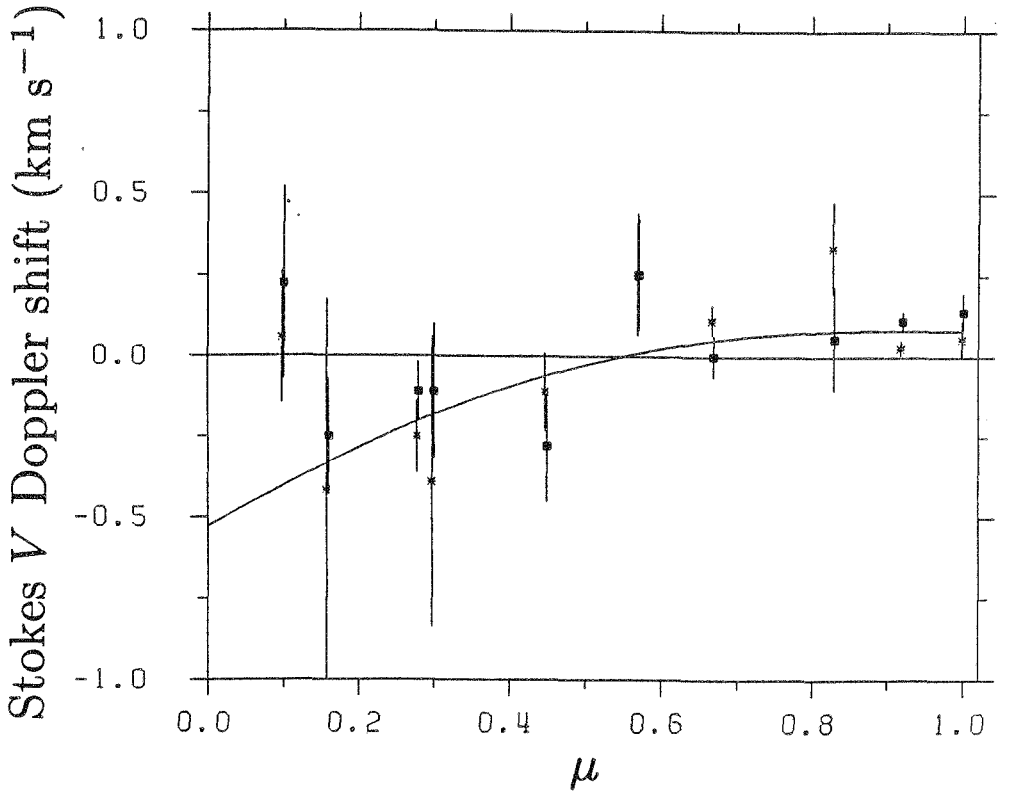

Fig. 7.4 CLV of v_{VI} for Fe I 5250.2 Å (filled squares) and Fe I 5247.1 Å (stars). The solid curve is the absolute wavelength shift with reversed sign of the non-magnetic Stokes I profile derived from the data of Balthasar (1984). It represents the corrected zero-level for the Stokes V Doppler shifts.

Fig. 7.4 shows that within the error limits, there are no significant net mass flows in fluxtubes, for all disk positions (if we disregard the questionable observation at $\mu = 0.1$). The scatter of the points around the "Balthasar zero-line" curve is typically 0.2 km sec^{-1}. Thus the CLV of v_{VI} for these two lines in the visible supports the conclusion reached in the last section from v_{VI}, that downflows in fluxtubes are smaller than 0.20 km sec^{-1}.

Flow velocities in the deeper layers of small magnetic fluxtubes can be determined from the Stokes V zero-crossing shifts of weak lines near 1.6μ. Fig. 7.5 shows the CLV of v_{VI} of the IR line Fe I 15648.5 Å. The 1.0 km sec^{-1} redshift at disk centre of the V profile of this line is considerably higher than for comparable lines in the visible and decreases only slowly to a smaller value ($\lesssim 0.4$ km sec^{-1}) near the limb. On the other hand, it is a factor of two smaller than the value given by Harvey (1977) for the same spectral line. The explanation for this discrepancy, according to Harvey (1985b), lies in the fact that the earlier measurements are inferior to the newer FTS observations, and may have been affected by systemetic error.

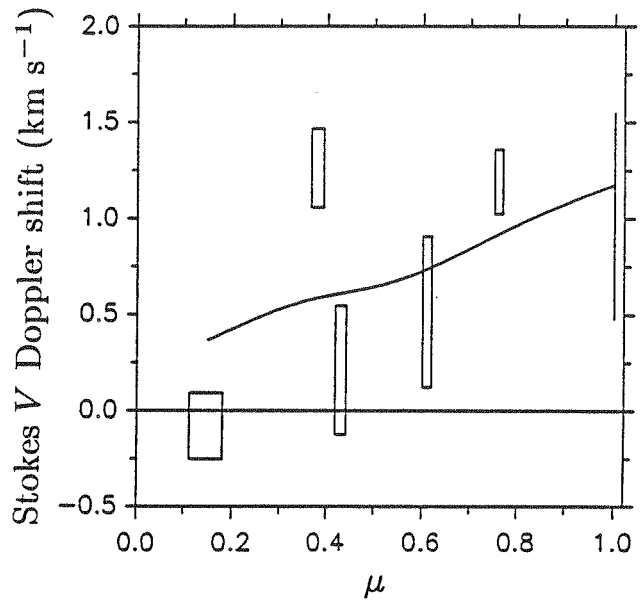

Fig. 7.5 CLV of v_{VI} for the Fe I 15648.5 Å line. The solid curve is a cubic spline fit.

Before drawing any conclusions regarding downflows in the deeper layers of fluxtubes it is necessary to subtract the blueshift of the Stokes I profile used as a wavelength standard. At visible wavelengths enough determinations of the granulation-induced blueshift exist (at least in quiet regions) to allow this to be carried out without any problems. The facts are quite different in the IR. Since no determinations of the absolute wavelength exist, we have to use indirect evidence to obtain a rough estimate of the line shift. The main difference between the weak 15648.5 Å line and the Fe I lines in the visible is that the IR line if formed much deeper down in the photosphere, near the level of $\log\tau(5000\text{Å}) = 0$ (Harvey, 1985b), where the influence of the granulation is larger, leading to a larger Stokes I blueshift. This conclusion is supported by the fact that Fe II lines, which are formed deeper in the atmosphere than Fe I lines, have much larger blueshifts (0.8 km sec^{-1} with a scatter of 0.4 km sec^{-1} according to Dravins and Larsson, 1984). Thus we expect the Stokes I profile of Fe I 15648.5 Å to have a granular blueshift of at least this magnitude. For lines in the visible the blueshift increases with increasing *depth* of formation, as established by Balthasar (1985) for lines formed in the range $-1 < \log\tau < -5$, where τ is the continuum optical depth at 5000 Å. If we make a linear extrapolation of his results to $\log\tau = 0$, the estimated depth of formation of the IR line, we obtain a blueshift of 900–1000 m sec^{-1}, comparable to our measured apparant Stokes V redshift.

In view of this evidence, it appears possible that the true Stokes V wavelength shift of Fe I 15648.5 Å does not differ greatly from zero. However, it is necessary to obtain measurements of absolute wavelengths in the IR before making any more definite statements.

7.2.4. Comparison With Transition Zone Velocities

Steady flows (i.e. flows having timescales of an hour or more) have been observed in the transition region over both the quiet and active photosphere. For quiet regions at disk centre Gebbie et al. (1981) find spatially averaged RMS velocities of about ±4 km sec^{-1} in C IV. Above active regions the observed velocities are larger, being of the order of ±5 to ±10 km sec^{-1} near disk centre in C IV (Athay et al., 1982). Both upward and downward flows have been observed, with downflows predominating. A correlation between photospheric magnetic field structure and transition region flow velocity also appears to exist. Over shorter timescales velocities with amplitudes of 15 – 20 km sec^{-1} or even higher have been reported (Dere et al., 1981; Feldman et al., 1982). For the rest of this

section we shall suppose that these flows are predominantly localised in magnetic structures having fluxtubes as their photospheric footpoints.

Assuming that the motions in active regions are mainly along magnetic field lines we can use the observed transition zone velocities to calculate the photospheric velocities in magnetic elements of a unipolar region from the conservation of mass. This requires a knowledge of the density in the transition region. Estimates of the electron density, n_e, in active regions have been made from O IV lines, which are formed at temperatures just slightly higher than C IV. However, depending on the method used quite different estimates of n_e are obtained, ranging from $n_e \approx (1\text{–}2) \times 10^{10}$ cm^{-3} (Hayes, 1985) to $n_e \approx 8 \times 10^{10}$ cm^{-3} (Feldman and Doschek, 1978).

An upper limit for the velocity in the photosphere is obtained by using the higher values of the transition region velocities and electron densities. The total transition zone mass density, ρ, is then determined for $n(\mathrm{H})/n_e = 0.77$ (McWhirter et al., 1975). By taking the corresponding value of ρ in the photosphere from the HSRA (Gingerich et al., 1971) a value of less than 0.5 m sec^{-1} is obtained for the steady flow velocity at the height of the temperature minimum ($\tau = 10^{-4}$).

So far the expansion of magnetic elements with height has not been taken into account. A limit can be set on this expansion by comparing the velocities measured in the active transition region and the upper bounds for photospheric fluxtube velocities derived in this paper. Thus one finds that the magnetic filling factor in the transition region can be up to 400 times larger than at the temperature minimum level for the parameters selected above. If the lower value of the transition zone density is assumed this upper limit will be correspondingly larger.

We therefore conclude that the limit set on the photosphere fluxtube flow velocity in this paper is easily compatible with both the large observed transition zone velocities and a dramatic chromospheric expansion of fluxtubes, the presence of which has been proposed on theoretical (e.g. Gabriel, 1976), as well as on observational grounds (e.g. Jones, 1985). However, at the present stage this is by no means a stringent limit and much greater accuracy in the measured photospheric line shifts is required if better limits on fluxtube expansion are to be set in this manner. A detailed comparison between transition-region and *chromospheric* velocities in active regions has been carried out by Mein et al. (1985).

7.3. Comparison With Previous Studies: The Importance of High Spectral Resolution

7.3.1. Where Have All the Downflows Gone ?

The polarimetric data presented in this chapter, as well as the analysis of Stenflo and Harvey (1985) of data obtained with the Kitt Peak McMath vertical grating spectrometer point to an absence of downflows larger than approximately 250 m sec^{-1}, at least in the layers where the Fe I and II lines in the visible spectral range are formed. This result is supported by the indirect evidence of Cavallini et al. (1986), who model the Stokes I bisectors in active regions by superposing quiet Sun profiles, the I_V profiles from fluxtubes and symmetrical profiles. The third profile is required due to the inhibition of convection by the magnetic field. Cavallini et al. find that they are able to reproduce the observed bisectors only if the fluxtube profiles are unshifted.

On the other hand, until recently it was generally accepted that considerable downflows exist within small solar magnetic fluxtubes. A number of authors have found a correlation between magnetic fields and downflows measured in *unpolarized* light (e.g. Beckers and Schröter, 1968a,b; Frazier, 1970; Simon and Zirker, 1974; Skumanich et al., 1975; Tarbell and Title, 1977; Frazier and Stenflo, 1978, to name but a few). However, due to the small linear dimensions of magnetic elements, these observations cannot distinguish between the fluxtube interior and the non-magnetic surroundings, although Frazier and Stenflo (1978) report some evidence for the downflows to have a cross-section larger than the magnetic element. Evidence for downflows inside fluxtubes obtained directly from Stokes V has to our knowledge been limited to a smaller number of studies by Giovanelli and Ramsay (1971), Harvey (1977), Giovanelli and Brown (1977), Giovanelli and Slaughter (1978), Wiehr (1985a), and Scholier and Wiehr (1985).

How can these conflicting results be reconciled with each other? It was first pointed out by Stenflo et al. (1984) that if Stokes V is observed with low spectral resolution, then due to its asymmetry, with the blue amplitude and area dominating over the red amplitude and area of most lines near disk centre (see chapter 8), the observed zero-crossing wavelength will be apparently shifted towards the red. This effect has been quantitatively

analysed by Solanki and Stenflo (1986) whose discussion we shall generally follow in this section. The procedure used for the calculation of the instrumental smearing of the line profile has been outlined in Sect. 6.4. We shall now present its effects on the Stokes V zero-crossing wavelength.

7.3.2. Influence of Instrumental Smearing on Zero-crossing Wavelength

In this section we will discuss the effects of the instrumental broadening described in Sect. 6.4.2 on the zero-crossing of Fe I 5250.2 Å, and will also discuss the effects of finite spectral resolution on Giovanelli's line-centre-magnetogram technique.

Fig. 7.6 shows the change in zero-crossing wavelength, $\lambda_V(v) - \lambda_V(0)$, in m sec^{-1}, as a function of the Doppler width of the instrumental profile v. The increase in λ_V is due to the Stokes V asymmetry. Since the blue wing of Stokes V is stronger than its red wing, more of the blue polarity survives spectral smearing and the resulting cancellation of polarities, thus pushing the zero-crossing towards the red. Due to the larger asymmetry in our enhanced network Stokes V data, the induced zero-crossing shift is larger for the network than for the strong plage. The effect depends only slightly on the shape of the instrumental profile.

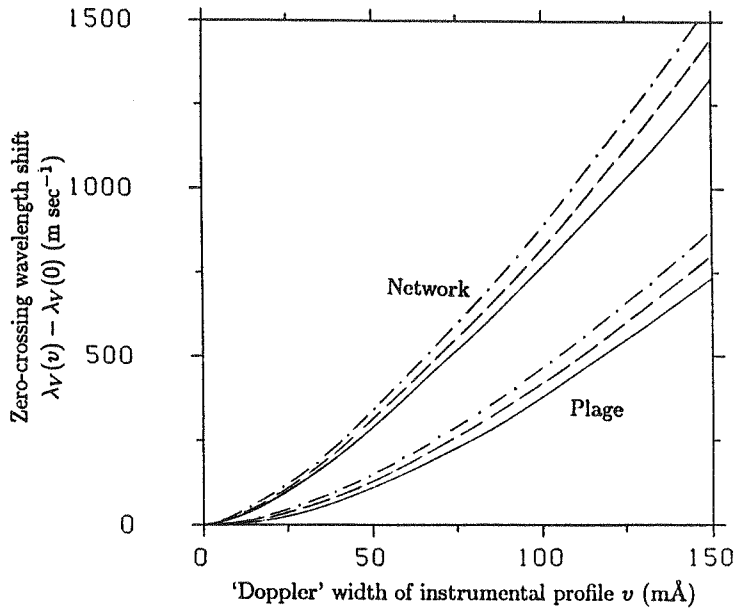

Fig. 7.6 $\lambda_V(v) - \lambda_V(v = 0)$ in velocity units vs. v, the e-folding width of the apparatus function. The upper set of curves represents the induced zero-crossing shift for network data smeared with profiles of different shapes. The lower set of curves represents plage data. Solid line: Gaussian apparatus function. Dashed line: Voigt apparatus function with damping constant, $a = 0.1$. Dot-dashed line: Voigt apparatus function with $a = 0.2$.

Often the Stokes V redshift is only measured relative to the Stokes I core wavelength, which means that we also have to consider the effect of decreased spectral resolution on Stokes I. We have therefore convoluted Stokes I with the same instrumental profiles used to smear Stokes V. The main results obtained by all four methods of determining the I wavelength described in Sect. 4.4.1 are similar to each other: The Stokes I profile is shifted only slightly as a result of spectral smearing, as compared to the shift of Stokes V. The shift increases continuously towards the blue for the enhanced network line profile, and reaches a value of approximately -230 m sec^{-1} for $v = 150$ mÅ for a Gaussian apparatus function. Note that this shift is relative to the original unsmeared FTS Stokes I profile. It should be compared with the $+1330$ m sec^{-1} by which Stokes V is shifted through the same amount of smearing. For the active region plage, the Stokes I profile first shifts towards the red until it reaches a maximum of about $+60$ m sec^{-1} at $v = 70$ mÅ, before reversing the trend and shifting towards the blue. It finally reaches a blueshift of approximately -110 m sec^{-1} at $v = 150$ mÅ. The difference in behaviour of the plage and network wavelengths reflects the difference in the shape of the Stokes I profiles of such regions. This is also reflected in their bisectors (cf. Cavallini et al., 1985). We do not wish to place too much emphasis on the details of the exact run of the Stokes I core wavelength with v, since even for relatively large spectral smearing the shifts can be so small that noise in the signal may dominate. However, the main result remains unaffected by this uncertainty: The Stokes I shifts, induced by low spectral resolution, are small compared to similarly induced Stokes V shifts.

Next let us turn to the line-centre-magnetogram technique pioneered by Giovanelli and Ramsay (1971),

and later used by Giovanelli and Brown (1977) and Giovanelli and Slaughter (1978) to measure downflows, and by Giovanelli et al. (1978) to measure oscillations. Its principle is simple. Instead of placing two exit slits in the wings of the line, a single exit slit is placed near the centre of the line. For a completely anti-symmetric Stokes V profile, the circular polarization signal disappears when the magnetograph slit is exactly centred at the zero-crossing wavelength, due to the cancellation of polarities.

However, for an asymmetric profile this is no longer the case, and the line-centre-magnetogram technique will give spurious line shifts, depending on the size of the exit slit and the spectrograph resolution (determined by the grating and entrance slit). Fig. 7.7 shows the zero-crossing wavelength shift in m sec^{-1} plotted vs. the width of the magnetograph slit (in mÅ) for data from the enhanced network. The lowest curve represents the original FTS data, the other curves are the results for data smeared by Gaussians (representing the spectrograph and entrance slit) with v = 10, 20, 30, 40, 50, and 60 mÅ, respectively, in the order of increasing redshift (upwards in the figure). The effects of changing the different parameters are clearly visible from the figure, and need not be described further. The results for the active region plage are similar, although the induced shifts are somewhat smaller, due to the smaller asymmetry of the plage Stokes V profile. It should be noted that in order to model the line-centre-magnetogram technique we have used a rectangular exit slit (instead of the usual Gaussian instrumental profile).

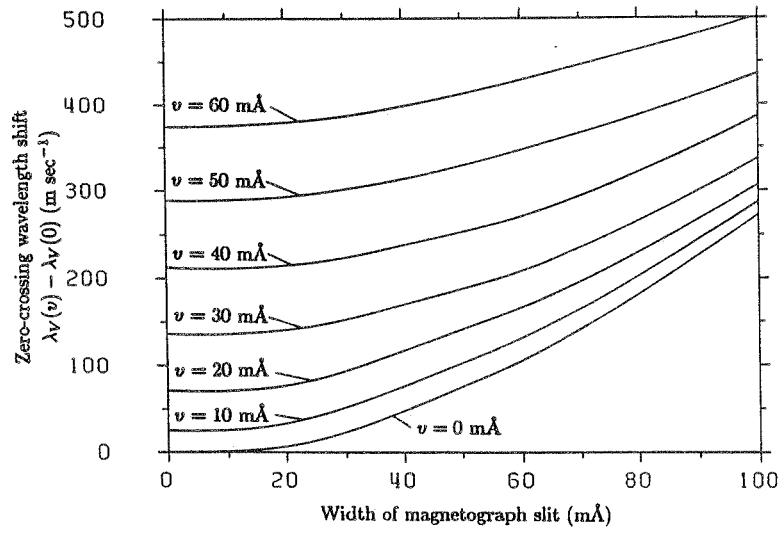

Fig. 7.7 Zero crossing shift of the Fe I 5250.2 Å line, induced by using the line centre magnetogram technique vs. full width of the magnetograph exit slit. From the bottom to the top the curves mark profiles broadened by Gaussian apparatus functions (representing spectrograph entrance slits) with e-folding width v = 0, 10, 20, 30, 40, 50, and 60 mÅ. The diagram represents the enhanced network.

7.3.3. Reproducing Some Observations of Stokes V Zero-crossings in the Literature

Giovanelli and Ramsay (1971) and Giovanelli and Brown (1977) observed the Ca I 6102.7 Å line with the Culgoora instrument. Instead of a grating spectrograph they used a tunable Fabry-Pérot filter. The width at half maximum of its transmission band is given by Ramsay et al. (1970) as 59 mÅ at 6100 Å. They (Giovanelli and co-workers) measured downflow velocities of around 0.5 km sec^{-1} relative to the Stokes I wavelength of the quiet Sun. After correcting for the blueshift of Stokes I (Giovanelli and Slaughter, 1978; Dravins et al., 1981) a downflow velocity of approximately 300–350 m sec^{-1} remains.

Since the Ca I 6102.7 Å line is present in our spectra (in one enhanced network and one plage scan), we have been able to carry out the simulations directly on its profile. Four different forms of the Fabry Pérot filter function hav been chosen: A rectangle, a Gaussian, a Voigt profile with a = 0.1, and a Voigt profile with a = 0.2. Of these the Voigt profiles probably approximate of the filter function best, due to its extended wings (Brault, 1982). The *full* width at half maximum of all four profiles is fixed at 60 mÅ, as suggested by the data of Ramsay et al. (1970). The zero-crossing shifts induced by these instrumental profiles are (in the order in which they were mentioned above) 60 m sec^{-1}, 130 m sec^{-1}, 150 m sec^{-1}, and 180 m sec^{-1}. All these shifts, except the one produced by the unrealistic rectangular profile, are sufficient to explain the difference between the earlier results (assuming that they are based on Stokes V profiles of similar asymmetry) and those presented in Sect. 7.2, within their 250 m sec^{-1} error margin. However, the residual redshift after subtracting these fictitious shifts, is still larger than 150–200 m sec^{-1} except for the Voigt filter function with a = 0.2. This could represent a small downflow, or a small line shift produced by asymmetries in the up and downflow phase of an oscillation, but

there are other possible explanations as well. The amount of parasitic light (defined as light which is transmitted outside the 'normal' instrumental profile of the filter) is quite large for the Culgoora filter according to Ramsay et al. (1970). This is illustrated by the fact that whereas the relative depth of the Ca I 6102.7 Å line in the Jungfraujoch Atlas (Delbouille et al., 1973) approaches 80 % , it is only slightly more than 50 % in the results presented by Ramsay et al. (1970), to whom the exact nature of this parasitic light was unknown. Its effect on the Stokes V profile remains an unknown factor whose importance we cannot judge. Giovanelli and Brown (1977) also mention that the filter transmission varies with position in the field of view. It is therefore possible that the effective filter function is broader in their actual measurements (which were carried out away from the centre of the field of view). When the filter half width is increased from 60 to 80 mÅ in our simulations, the four profiles, rectangular, Gaussian, Voigt ($a = 0.1$), and Voigt ($a = 0.2$), give the following shifts: 110, 200, 220, and 250 m sec^{-1} respectively. For the last three profiles the residual observed shift is now smaller than 100–150 m sec^{-1}. Yet another possibility is that the mean asymmetry of the Stokes V profiles in their observed regions is different from the FTS profiles we have used.

Giovanelli and Slaughter (1978) used the Kitt Peak vacuum telescope and magnetograph for their observations of downflow. Their entrance and exit slits measured 0.17 mm and 1.3 mm respectively. The intrinsic resolution of the spectrograph corresponded to 0.03 mm. The dispersion was 0.28 Å/mm for the IR lines Ca II 8542 Å, Fe I 8688 Å, and C I 9111 Å, and 0.165 Å/mm for Mg I b_1 5183 Å (Harvey, 1985b). These values correspond to a 47.6 mÅ entrance slit and a 364 mÅ exit slit for the IR lines, 28 and 215 mÅ, respectively, for the Mg I b_1 line.

We have simulated this instrumental setup by first convoluting a spectral line with a Gaussian representing the entrance slit, and then convoluting the resulting profile with a rectangular function representing the exit slit. Broadening due to the grating is neglected. We have carried out the above procedure on the strong Mg I b_1 line directly (it being present in the same FTS scans as Fe I 5250.2 Å), as well as on the Fe I 5250.2 Å line, instead of the weak IR lines measured by Giovanelli and Slaughter which are not present in our spectra.

The Stokes V profile of the Mg I b_1 line is shifted by less than 100 m sec^{-1} towards the red through the instrumental smearing. This is due to the large width of this line. Since the Fe I 5250 Å line has a much smaller wavelength than the IR lines used by Giovanelli and Slaughter, we assume that the spectral exit slit width was the same as for the Mg I b_1 line, and not the larger value of the IR lines. In this way, at least part of the difference in width between the profiles, due to the different wavelengths, can be taken into account. Even with the smaller slit widths, fictitious redshifts of 900 m sec^{-1} and 1400 m sec^{-1} are induced for the plage and network profiles, respectively. These values are substantially larger than those observed by Giovanelli and Slaughter (1978), who find the largest downflow for the C I 9111 Å line, with a value of approximately 600–800 m sec^{-1}, after correction for Stokes I blueshift. This difference may be due to smaller asymmetries of the line profiles they measure, as compared with the Fe I 5250 Å line. Since the IR profiles are not contained in our data, we cannot check this. In any case, our simulations easily reproduce the magnitude of the observed zero-crossing shifts.

Wiehr (1985a) has used the Locarno Gregory telescope (Wiehr et al., 1980), with the entrance slit in the form of a circular hole having an angular diameter of 8″, corresponding to a linear diameter of 1 mm. The dispersion of his spectrograph was 0.232 Å/mm, which results in a spectral width of the entrance slit of 232 mÅ (Wiehr, 1985b). Assuming that the spectrograph itself has infinite resolving power, the instrumental profile is found to be a Gaussian with $v = 92$ mÅ. From Fig. 6 we see that the redshift induced by such a resolution is 300–350 m sec^{-1} for the active region profile of Fe I 5250.2 Å, and 650–700 m sec^{-1} for the enhanced network profile. Wiehr observed in isolated Ca II plage elements which correspond more closely to our enhanced network elements than to a strong active region plage. We can check this by comparing the Stokes V asymmetry of Wiehr's line profiles with ours, since the asymmetry is the primary cause of the induced redshift. We find that the average amplitude asymmetry of Wiehr's observations is $\langle a_b/a_r \rangle = 1.69$. If corrected for spectral degradation this gives $\langle a_b/a_r \rangle(v = 0) = 1.86$ (cf. Fig. 6), which is closer to the asymmetry of our network observations than to our plage observations. If we also take into account the fact that the wavelength of the Stokes I profile with which Wiehr compares the Stokes V wavelength is blueshifted by 150–350 m sec^{-1} (Dravins et al., 1981), the total fictitious redshift becomes of the order of 800–1000 m sec^{-1}, which compares very well with the 900 m sec^{-1} average redshift he measures.

Of course the Fe I 5250.2 Å line which we have studied here differs in some respects from the Fe I 8468.4 Å line used by Wiehr (1985a). Firstly, Fe I 8468.4 Å is broader than Fe I 5250.2 Å due to the wavelength dependences of the Doppler and Zeeman broadenings. This reduces the effect of the Stokes V asymmetry. On the other hand, the Fe I 5250.2 Å line has a larger Landé factor than Fe I 8468.4 Å ($g = 3$ vs. $g = 2.5$) which

should redress the balance somewhat. Also, we have not included the effects of spectral smearing on the Stokes I profile in our analysis. Although this effect is small, for a network region it would result in a blueshift of the order of 100 m sec^{-1}, which would increase the fictitious relative Stokes V redshift by that amount. Finally, the zero-crossing shift increases rapidly with the Stokes V asymmetry of the spectral line, and we have not taken into account the fact that Wiehr's Stokes V average observed asymmetry is substantially larger than ours for the Fe I 5250.2 Å line ($\langle a_b/a_r \rangle = 1.86$ for Wiehr's data vs. 1.47 for our network profile).

Scholier and Wiehr (1985) find a redshift of Stokes V relative to Stokes I in three magnetic regions and a blueshift in only one region (region D in their Fig. 8). However, according to Pahlke and Wiehr (1986), the analysis of a number of further regions has yielded an average shift of all the regions very close to zero. We therefore conclude that the Stokes V observations in the literature are all compatible with a *mean* downflow velocity of less than 250 m sec^{-1} throughout the photospheric layers of fluxtubes, with the possible exception of the IR measurements of Harvey (1977), or the results of the IR line presented in Sect. 7.2.3, so that some downflow may still be present in the deepest layers of fluxtubes. Circumstantial evidence points to the downflows being small there as well. However, measurements of absolute wavelengths are required in the infrared to decide this question conclusively.

7.4. Fluxtube Velocity Amplitudes Derived from Line Broadening

In this section we shall analyse the I_V profile, whose width is determined by thermal Doppler broadening, radiative and collisional damping, Zeeman splitting, and mass motion induced Doppler broadening. Using simple representations of fluxtubes we shall model the profiles of Fe I and II lines and obtain a value for the rms velocity in fluxtubes by comparing them with observed I_V profiles.

7.4.1. Velocity Structure in the Quiet Photosphere

As pointed out in Sect. 5.4.1, it is necessary to model the quiet Sun profiles before attempting to determine fluxtube properties. Following Evans et al. (1975), Smith et al. (1976), Holweger et al. (1978), and Nordlund (1978) among others, we assume that the photospheric velocity structure can be described by a combination of micro- and macroturbulence velocity. We assume a Gaussian distribution for the microturbulence velocity and convolute it with the thermally produced Gaussian to obtain the absorption coefficient profile (cf. Eq. (2.20)). $\xi_{\rm mic}$ is used to represent the Doppler width of the microturbulence distribution. A depth independent $\xi_{\rm mic} = 0.8$ km sec^{-1} is chosen, as suggested by Blackwell and Shallis (1979) for the HSRA. The macroturbulence broadening is represented by a distribution in the shape of a Voigt function $H(a_{\rm mac}, \xi_{\rm mac})$. $\xi_{\rm mac}$ is the 'Doppler' width of the macroturbulence velocity distribution and $a_{\rm mac}$ is the ratio of its 'damping' to 'Doppler' width (cf. Eq. (2.21)). The macroturbulent velocity distribution is multiplied to the calculated emergent line profile which makes it particularly simple to apply.

Using the modified HSRASP the observed quiet Sun Stokes I line widths and depths are fitted as illustrated in Sect. 5.4.1 (Fig. 5.10). For the details of the fitting procedure we refer to that chapter and restrict ourselves here to discussing the empirically determined velocity structure. Fig. 7.8 shows the parameters of the macroturbulence profile as a function of S_I. $\xi^I_{\rm mac}$, i.e. $\xi_{\rm mac}$ deduced from the Stokes I profile, is plotted in Fig. 7.8a, and $a^I_{\rm mac}$ in Fig. 7.8b. The solid curves represent $\xi^I_{\rm mac}$, respectively $a^I_{\rm mac}$, as determined from Fe I lines with $\chi_e < 3$ eV, the dashed curves $\xi^I_{\rm mac}$ and $a^I_{\rm mac}$ from Fe I lines with $\chi_e \geq 3$ eV, and the dot-dashed curves $\xi^I_{\rm mac}$ and $a^I_{\rm mac}$ from Fe II lines. It should be noted that the rms velocity (for $a^I_{\rm mac} = 0$) is $\xi^I_{\rm mac}/\sqrt{2}$. * We also wish to point out that the $\xi^I_{\rm mac}$ and $a^I_{\rm mac}$ curves of Fe II are interpolated between $S_I = 5$ F and $S_I = 9$ F due to the absence of unblended Fe II lines in that range of line strengths. This part of these curves is therefore dotted in Fig. 7.8 and in subsequent figures. The line parameters are sensitive to changes in $\xi^I_{\rm mac}$ at a level of about 0.1–0.2 km sec^{-1}, although the sensitivity is smaller for the strongest lines. The sensitivity to $a^I_{\rm mac}$ is of the order of 0.05–0.1. For smaller $a^I_{\rm mac}$ the fit to the five parameters is still quite good, and even $a^I_{\rm mac} = 0$ reproduces the data reasonably well. The values of $\xi^I_{\rm mac}$ and $a^I_{\rm mac}$ needed to reproduce the observed profiles are compatible with those used by Smith et al. (1976) and Nordlund (1978) for a smaller number of lines.

In Sect. 5.4.1 the fits to the full profiles of a selected group of lines is shown. Table 7.1 gives the $\xi^I_{\rm mac}$

* Due to an oversight this factor of $1/\sqrt{2}$ was forgotten by Solanki (1985). All the numbers in the section on velocities and in Fig. 2 of that paper should therefore be reduced by this factor in order to match the text.

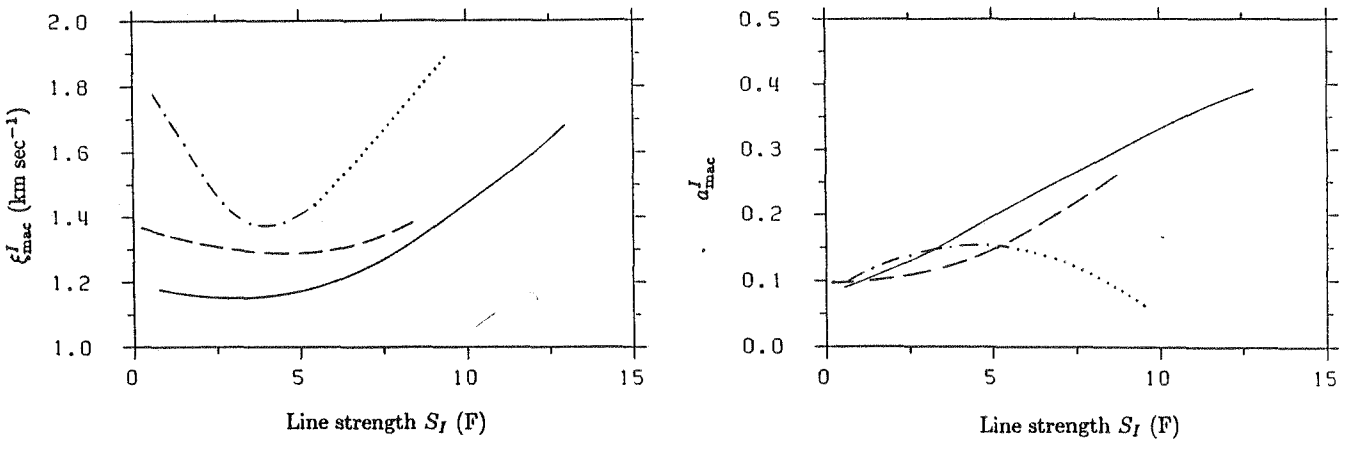

Fig. 7.8 a ξ^I_{mac}, the width of the 'Doppler core' of the macroturbulent velocity profile, as derived from Stokes I profiles observed in a quiet region, plotted vs. S_I. The ξ^I_{mac} values derived from Fe I lines with $\chi_e < 3$ eV are denoted by the solid curve, the ξ^I_{mac} values derived from Fe I, $\chi_e \geq 3$ eV lines by the dashed curve, and ξ^I_{mac} from Fe II by the dot-dashed curve. The Fe II curve is dotted between $S_I = 5$ and 9 F to indicate that it is interpolated in that region. $\delta_T = 2.5$. b a^I_{mac}, the ratio of 'damping' to 'Doppler' width of the macroturbulent velocity profile plotted vs. S_I for the quiet Sun. The symbols have the same meaning as in Fig. 7.8a.

and a^I_{mac} values determined from each line. The first two columns of Table 7.1 contain the identification (ion) and solar wavelength of the ten lines, the third column lists the excitation potentials, the fourth column their line strengths in a quiet region. The fifth and sixth columns list ξ^I_{mac} and a^I_{mac} respectively, while the seventh column lists ξ^V_{mac} values needed to broaden the individual line profiles. ξ^I_{mac} and a^I_{mac} from Table 7.1 compare reasonably well with the values shown in Fig. 7.8 for lines of equal strength and similar excitation potential, which were obtained from fitting the line parameters alone.

Table 7.1

Ion	λ (Å)	χ_e (eV)	S_I (F)	ξ^I_{mac} (km sec^{-1})	a^I_{mac}	ξ^V_{mac} (km sec^{-1})
Fe I	5048.44	3.96	3.68	1.4	0.15	2.1
Fe I	5083.34	0.96	6.63	1.2	0.12	3.3
Fe I	5127.68	0.05	0.93	1.1	0.08	1.5
Fe II	5197.57	3.23	4.39	1.2	0.15	2.9
Fe I	5247.06	0.09	3.53	1.3	0.10	1.9
Fe I	5250.22	0.12	3.51	1.3	0.13	1.9
Fe I	5293.96	4.14	1.42	1.4	0.05	1.3
Fe I	5383.38	4.31	8.12	1.1	0.20	3.3
Fe II	5414.07	3.22	1.40	1.8	0.07	2.0
Fe I	5445.05	4.39	5.76	1.3	0.10	2.8

7.4.2. Macroturbulent Velocity in Fluxtubes Without Microturbulence

Fig. 5.12 and the pertinent text in Sect. 5.4.2 illustrate the need for velocity broadening of spectral lines in fluxtubes, the calculated line profiles being much narrower than the observed profiles. Since our knowledge of the velocity structure inside fluxtubes is extremely rudimentary, we have decided, as a first step, to limit ourselves to determining the approximate rms velocity amplitudes involved, without modelling flows or oscillations in detail. Following the approach outlined in Sect. 4.2 for unpolarised radiation coming from the quiet photosphere, we shall assume that the non-thermal, non-magnetic line broadening inside fluxtubes is produced by macro- and microturbulent velocities. In this section we assume that macroturbulence alone is the broadening agent, and

defer the study of the effects of adding a height independent microturbulent velocity until the next section. We must stress, that the use of a macroturbulent (and later also of a microturbulent) velocity does not signify that we assume the presence of true turbulent or convective motion inside fluxtubes. Rather, we use the turbulence velocity approach as a simple, convenient, and effective method of determining the line of sight amplitude of what may in reality be a highly complicated velocity field. Since the data, which we use to empirically determine the velocities, were obtained near disk centre (only the observations obtained in 1979 are used in this section), and fluxtubes are expected to be nearly vertical due to buoyancy, the distortion resulting from geometrical effects should be small, and the line of sight velocity amplitude should be a good approximation of the total velocity amplitude. It must be borne in mind, however, that due to the averaging over time and over a number of fluxtubes, motions limited either to a small fraction of the fluxtubes in the resolution element, or to short timescales may have a negligible effect on the observed line width. However, line broadening can also capture motions which would not give rise to any Stokes V asymmetry, or to a net wavelength shift.

As remarked earlier, the determination of velocity and temperature in fluxtubes is closely coupled and consequently a part of the calculations have already been discussed in chapter 5. In particular the fits to the line profiles are illustrated there. We shall therefore restrict ourselves to simply presenting and discussing the velocity structure in fluxtubes.

The synthetic line profiles are broadened by convoluting them with a macroturbulence profile similar to the one chosen in Sect. 7.4.1, with one difference, $a^V_{\rm mac} = 0$ throughout. Noise and the proxiity of neighbouring lines usually make damping wings in Stokes V very hard to measure accurately (one should keep in mind that $v \sim \partial I/\partial\lambda$, which is small in the damping wings of the line), so that, to the degree of accuracy we are interested in, $a^V_{\rm mac}$ can usually be neglected.

To see how strongly the empirical $\xi^V_{\rm mac}$ values depend on the assumed temperature structure, a number of models with different $T(\tau)$ functions were calculated with temperatures ranging from 200 K higher than the photospheric value at equal τ, to approximately 1000 K higher in the part of the atmosphere where the lines of interest are formed. Some models (with too low temperatures) resulted in a part of the lines being too broad to be compatible with the observations even without velocity broadening, but for the rest of the models, despite differences in detail, the velocities obtained were surprisingly similar. Within the above temperature range, which is wide enough to encompass the temperature structures of almost all empirical fluxtube models, the $\xi^V_{\rm mac}$ values remain constant to within, on the average, ± 0.5 km sec^{-1}. The sensitivity of $\xi^V_{\rm mac}$ to the temperature is a function of the line strength, with the $\xi^V_{\rm mac}$ values derived from the weakest lines being constant to within 0.1–0.2 km sec^{-1}, whereas for the strongest Fe I lines $\xi^V_{\rm mac}$ can vary by up to ± 1.5 km sec^{-1} within this temperature range. This dependence on line strength may be explained by the increasing sensitivity of line width on temperature with the increasing importance of saturation effects.

The maximum values of $\xi^V_{\rm mac}$ for plage data and $\delta_\Gamma = 1$ vary between 3.2 and 4.4 km sec^{-1} for Fe I lines with $\chi_e = 1.5$ eV, between 2.5 and 3.5 km sec^{-1} for Fe I lines with $\chi_e = 4$ eV, and between 3.6 and 4.9 km sec^{-1} for the Fe II lines. The general trend for all the models being for the velocity amplitude to increase with increasing line strength for the weak and medium strong lines ($S_I \lesssim$ 8–10 F), but to even out and eventually to decrease again for the strongest lines. The $\xi^V_{\rm mac}$ values for the network show a similar trend, but are lower than the velocities found in plages by, on the average, 0.3–0.5 km sec^{-1}, if we assume the *same temperature structure* for the fluxtubes in both regions. The difference in velocity is only an artifact of this assumption of equal temperature and disappears when a realistic temperature model of the fluxtubes is used.

We shall now concentrate on the velocity structures derived with the fluxtube temperature models discussed in Sect. 5.4.2. In Fig. 7.9 $\xi^V_{\rm mac}$ is plotted vs. S_I, for both the best fit plage and network models. Since the plage velocities are almost the same as the velocities in the network fluxtubes, only one curve has been drawn for each group of lines. The scatter in the data limits the accuracy of our $\xi^V_{\rm mac}$ curves to approximately ± 0.3–0.5 km sec^{-1}. The relative values of $\xi^V_{\rm mac}$ for the Fe I low χ_e, high χ_e, and Fe II lines are consistent with Fig. 5.12. The large difference in line widths between the Fe II data and profiles calculated from velocity free models gives rise to a large $\xi^V_{\rm mac}$. For high excitation Fe I lines, on the other hand, the data and model curves in Fig. 5.12 lie relatively close together, so that $\xi^V_{\rm mac}$ for those lines is small.

A comparison of Fig. 7.9 with Fig. 7.8a shows strikingly, that the dependence of the velocity on line strength in the fluxtube is quite different from that in the photosphere. The initial value of $\xi^V_{\rm mac}$ is roughly similar to $\xi^I_{\rm mac}$, but becomes considerably larger than $\xi^I_{\rm mac}$ for larger S_I. However, one should keep in mind that for the quiet Sun we used a Voigt function for the velocity distribution, so that the $\xi^I_{\rm mac}$ values cannot be directly compared to $\xi^V_{\rm mac}$. We shall return to this point in Sect. 7.5.

Fig. 7.10 illustrates the effect on $\xi^V_{\rm mac}$ of increasing the damping constant by a factor of 2.5. As expected, the weak lines remain virtually unaffected by this change while the $\xi^V_{\rm mac}$ values for the strong lines are considerably reduced. Small differences between $\xi^V_{\rm mac}$ of the weak lines result from the fact that the temperature has to be changed slightly between models with different δ_Γ to retain the quality of the fit to the $\ln(d_V/d_I)$ plot. The velocities obtained now from the strong lines in the network are larger than those found in the plage regions. This is consistent with the case of $\delta_\Gamma = 1$ (Fig. 7.9), since the increase in damping constant will more strongly broaden the lines in the plage, these being less weakened than their network counterparts due to the lower temperature in the plage. Models with $\delta_\Gamma = 2.5$ reproduce the data somewhat better than models with $\delta_\Gamma = 1$ and Fig. 5.14 actually shows the results of such models. From Figs. 7.9 and 7.10 we see that the photospheric sound speed (9–10 km sec^{-1}) is larger than the maximum rms velocity in fluxtubes (3–3.5 km sec^{-1}) by a factor of about 3. This result is consistent with the initial assumption that the hydrodynamic structure of the fluxtubes is not critically affected by any motions occuring inside them.

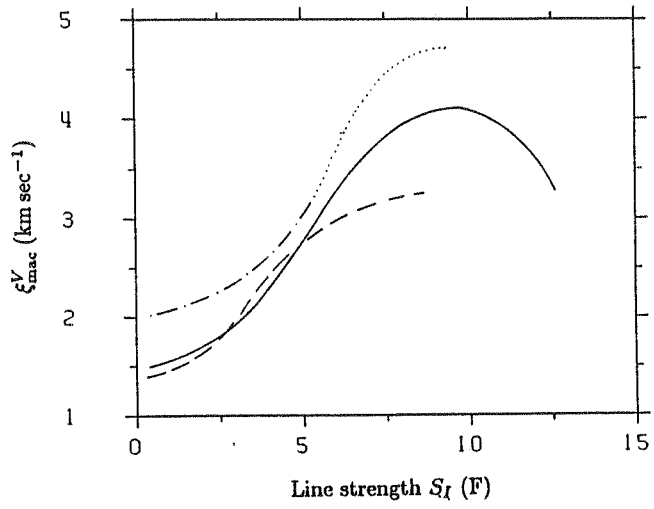

Fig. 7.9 $\xi^V_{\rm mac}$, the macroturbulence velocity derived from the I_V profile, vs. S_I. Plotted are the results for both network and plage data, if $\xi_{\rm mic} = 0$, and $\delta_\Gamma = 1$. $a^V_{\rm mac} = 0$ is assumed for all fluxtube models. Symbols as in Fig. 7.8a.

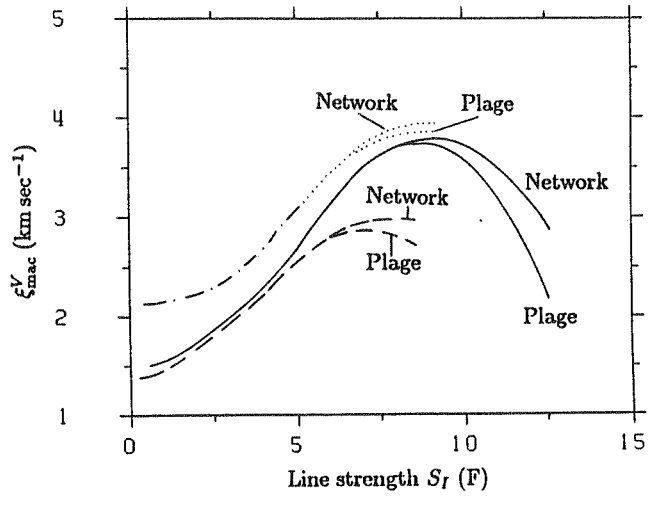

Fig. 7.10 $\xi^V_{\rm mac}$ vs. S_I with $\xi_{\rm mic} = 0$, and $\delta_\Gamma = 2.5$. The different groups of lines are denoted as in Fig. 7.8a. The lower curve for each group of spectral lines represents a plage region, the upper curve a network region.

Again full profile comparisons for the ten lines in Table 4.4 have been carried out. The $\xi^V_{\rm mac}$ values used to broaden the synthetic profiles are listed in the final column of Table 7.1 ($a^V_{\rm mac} = 0.0$ and $\delta_\Gamma = 2.5$). These values lie quite close to those derived from hypothetical lines of the same strength, which are shown in Fig. 7.10. The Fe I 5250.2 Å line is also reproduced with an accuracy similar to Fe I 5247.1 Å, a somewhat surprising result, since its large Landé factor of 3 would lead one to expect that the first order approximation on which the calculation of the I_V profile is based may be insufficient for this line.

Could these non-thermal line broadenings have a non-solar source? The line broadening induced by changes in relative observer–source velocity is negligible ($\approx$ 50 m sec^{-1}, Sect. 7.2.1). This is also true of smearing due to finite spectral resolution. Anyway, both these processes affect I_V and Stokes I equally and therefore have no influence on our analysis. Also, no difference is seen between the velocities determined from the full line profiles (I and I_V fitted individually) and the $v_{D_V} - v_{D_I}$ vs. S_I diagram (difference in I and I_V profiles fitted), suggesting that non-solar effects of this type cannot be the cause. We have seen that the renormalisation of the continuum of I_V necessitated by the area asymmetry of Stokes V, does not have a large effect on its half width (Sect. 4.4.3). Another possibility is that the first order approximation, on which the I_V profile is based, is not accurate enough for the detailed analysis of the line widths. If this were the case, then we would expect the line widths of the I_V profiles to be strongly dependent on their Landé factors, since the quality of the approximation is better, for smaller ratios of Zeeman splitting to Doppler width of the line. The dependence of I_V line width on Landé factor has been studied in Sect. 6.2, where we find that the widths of the I_V profiles increase with Landé factor exactly

as expected in the presence of a kilogauss magnetic field. This, and the fact that the same $\xi^V_{\rm mac}$ value is required to reproduce the observed profiles of Fe I 5250.2 Å and Fe I 5247.1 Å (cf. Table 7.1) leads us to conclude that the anomalously large I_V line widths have a solar origin. Even if the I_V profile does begin to deviate somewhat from Stokes I for the lines with largest splitting, the test calculations in Sect. 4.2.6 have shown that this deviation is such that the derived velocities would tend to be *underestimated.*

7.4.3. Effects of Adding Microturbulence

The observed Stokes V asymmetry (cf. Chapter 8) suggests that at least a part of the motions in magnetic fluxtubes may be non-uniform over the typical range of formation of a spectral line. This non-uniform component may be better approximated by microturbulence than by macroturbulence. Therefore, we shall describe the results of some fluxtube model calculations which use a mixture of microturbulence and macroturbulence. In principle it is possible to fit a line profile with either a mixture of macroturbulence and depth independent microturbulence, or with a depth dependent microturbulence alone (Holweger et al., 1978). However, no new physical insight is gained by using the second approach, and it is considerably more time consuming to carry out, since all the line profiles have to be recalculated for each trial depth dependence of the microturbulence, instead of simply being convoluted with different velocity profiles after being calculated only once for each chosen temperature structure, as is the case for the macroturbulence. We have therefore restricted ourselves to the case of a depth *in*dependent microturbulence.

Fig. 7.11 shows the effect of introducing a depth independent microturbulent velocity, $\xi_{\rm mic}$, on the macroturbulence $\xi^V_{\rm mac}$. Fig. 7.11a shows $\xi^V_{\rm mac}$ as derived by fitting the Fe I, $\chi_e < 3$ eV data with Fe I, $\chi_e = 1$ eV lines calculated for models with $\xi_{\rm mic} = 0$, 0.5, 1 and 1.5 km sec^{-1} respectively. $\delta_\Gamma = 2.5$ for all four models, and the temperature structure is also the same for all the models. The data are from a network region. As expected, $\xi^V_{\rm mac}$ decreases as $\xi_{\rm mic}$ is increased. For weak lines the decrease is such that $(\xi^V_{\rm mac})^2 + (\xi_{\rm mic})^2$ remains approximately constant, so that the total turbulent velocity remains unchanged. For the strong lines this is no longer the case. There $\xi^V_{\rm mac}$ decreases much faster, and the total turbulent velocity also decreases. This is due to the fact that increasing $\xi_{\rm mic}$ increases the strength of the lines. This increase, and the associated increase in line width is strongly dependent on the equivalent width of the line, being largest for lines with $W_\lambda \approx 80$ mÅ at disk centre (Holweger et al., 1978). Although the strongest Fe I lines in our sample have large equivalent widths on the quiet Sun ($W_\lambda > 100$ at disk centre), and according to Holweger et al. (1978) should not be strongly affected by the microturbulence, they are weakened in fluxtubes and thus come into the range of lines having a large sensitivity to $\xi_{\rm mic}$. Fig. 7.11a also shows that assuming $\xi_{\rm mic}$ to be the same at all heights, 1.5 km sec^{-1} is the largest value it can have at disk centre, since for this value of $\xi_{\rm mic}$, $\xi^V_{\rm mac}$ falls to zero for both the weakest and the strongest Fe I lines. $\xi_{\rm mic}$ values larger than that would cause these lines to be broader than the observed values, even for $\xi^V_{\rm mac} = 0$. Although we have tested this result for only one temperature structure, the relative insensitivity of the widths of weak lines to temperature means that it should retain its validity for a reasonable range of temperatures.

Figs. 7.11b and 7.11c are similar to Fig. 7.11a, except that they show the results derived from the Fe I lines with $\chi_e = 4$ eV and the Fe II lines respectively. The high excitation Fe I lines also give a maximum $\xi_{\rm mic}$ value of 1.5 km sec^{-1}, but the Fe II lines would allow for higher microturbulence velocities.

We can improve on the limit for $\xi_{\rm mic}$ simply by observing how well the model curves fit the $v_{D_V} - v_{D_I}$ vs. S_I and $\ln(d_V/d_I)$ vs. S_I data simultaneously. We find that the data as represented by these plots are best reproduced by the models with $\xi_{\rm mic} = 0.5$ km sec^{-1} and 1.0 km sec^{-1}, which give fits marginally better than those shown in Fig. 5.14.

For plage data the effect of $\xi_{\rm mic}$ is qualitatively the same. The resulting maximum value for $\xi_{\rm mic}$ is again 1.5 km sec^{-1}, and $\xi_{\rm mic}$ between 0.5 and 1.0 km sec^{-1} once more gives the best fit to the data. It therefore appears that whereas the macroturbulence velocity inside the fluxtubes can reach values considerably higher than in the quiet photosphere, the microturbulence velocity is of the same order.

7.5. Discussion and Conclusions

In this chapter we have attempted to empirically determine velocities in the photospheric layers of small solar magnetic fluxtubes. In order to achieve this aim we have mainly made use of the velocity information contained

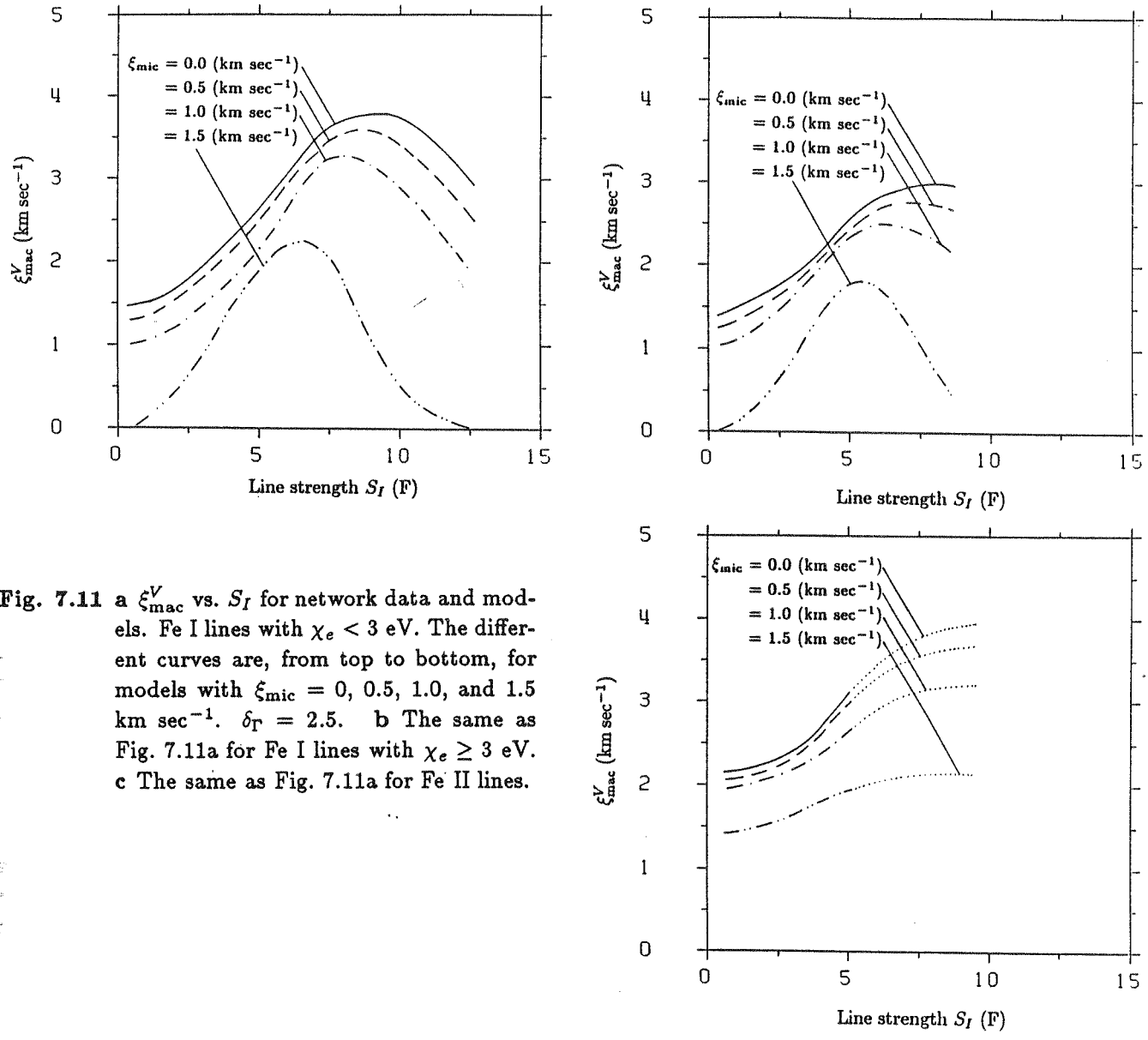

Fig. 7.11 a ξ^V_{mac} vs. S_I for network data and models. Fe I lines with $\chi_e < 3$ eV. The different curves are, from top to bottom, for models with ξ_{mic} = 0, 0.5, 1.0, and 1.5 km sec^{-1}. $\delta_T = 2.5$. b The same as Fig. 7.11a for Fe I lines with $\chi_e \geq 3$ eV. c The same as Fig. 7.11a for Fe II lines.

in two parameters derived from the Stokes V profile; its zero-crossing wavelength, λ_V, and the half-width, v_{D_V}, of the integrated V profile, I_V. λ_V is mainly sensitive to 'global' flows; global in the sense that the majority of the fluxtubes in the observed region show a line of sight flow in the same direction over most of the integration time of the observations. v_{D_V}, on the other hand, is mainly sensitive to vertical velocity gradients and (statistical) fluctuations of the velocity in space or time, as may result for example from oscillations or waves in a fluxtube, or from the presence of different flow velocities in a number of fluxtubes.

We find no zero-crossing shifts larger than approximately ± 250 m sec^{-1} in any of the observed regions (including both active region plages and network elements near disk centre) for a large sample of unblended Fe I and II lines, as well as the Mg Ib lines at 5172 Å and 5183 Å. This allows us to set an upper limit of this amount on steady up- and downflow velocities in magnetic fluxtubes. The limit in accuracy of approxiately 250 m sec^{-1} is imposed by uncertainties in the determination of the absolute wavelength of the V profiles, and partly also by the scatter in the data points. This limit is totally *independent* of the wavelength of the simultaneously measured Stokes I profile, since it results from the comparison of absolute Stokes V wavelengths with the laboratory wavelengths of the respective lines.

A small dependence on line strength, Landé factor, and excitation potential of the Stokes V zero-crossing shift is observed, suggesting that the true line shifts are not exactly zero for all the lines. However, they remain much smaller than the large redshifts reported in a number of previous studies (e.g. Giovanelli and Slaughter, 1978; Wiehr, 1985a). We explain the discrepancy between the results of this and some previous studies by

taking the difference in spectral resolution between the various observations into account. The smearing of the Stokes V profiles due to insufficient spectral resolution, when combined with their asymmetry, leads to fictitious redshifts. By using the approximate instrumental parameters which have been used to observe the large downflows reported in the literature, we are able to reproduce the observed downflows to a reasonable degree of accuracy. All observations of Stokes V zero-crossing wavelength, with one possible exception are therefore consistent with the upper limit of 250 m sec^{-1} for downflows. The possible exception is the IR line Fe I 15648.5 Å for which we find a downflow velocity of approximately 1 km sec^{-1} with respect to Stokes I. However, the granular blueshift of the I profile of this line has not been measured directly. Indirect evidence suggests that it is of the same order as the observed Stokes V relative redshift, which would thereby be cancelled. The observational case for large downflows inside fluxtubes is therefore considerably weakened and from a theoretical point of view no need for *large* flows inside fluxtubes appears to exist as well, as has been argued for example by Durrant (1977). Schüssler (1986) estimates the velocity of the downflow induced by mass inflow into the tube due to diffusion across the field lines. He finds that downflows of the order of 10 m sec^{-1} are expected for fluxtubes with radii of around 100 km, which is perfectly compatible with our results. The siphon flow mechanism has been discussed as a possible source of downflows by Hasan and Schüssler (1985), who conclude that it is unlikely to give rise to appreciable net downflows in small fluxtubes. Furthermore, Ribes et al. (1985) find that a downflow velocity increasing with depth, as suggested by Giovanelli and Slaughter (1978), results in line profiles of a shape quite incompatible with the observations.

We therefore conclude that the mean steady flow velocity in the photospheric layers of small magnetic fluxtubes is smaller than approximately 250 m sec^{-1}, in both active region plages and the network. This limit is compatible with the substantial velocities observed in the transition region above active regions, even in the presence of magnetic canopies. Of course our analysis does not rule out the possibility of strong flows occuring inside fluxtubes under certain circumstances, for example in connection with their convective collapse, our observations being restricted to mature active regions and the enhanced network.

The comparison between λ_V and Stokes I core wavelengths, λ_I, for many lines near disk centre tends to confirm the conclusion that if stationary flows are present at all inside fluxtubes, then they are small. It suggests that their velocity is less than approximately 200 m sec^{-1}. It also provides support for the observation of Cavallini et al. (1985) that the granular blueshift of Stokes I is reduced by 100–200 m sec^{-1} in active regions.

Centre to limb observations of v_{VI} of two lines in the visible also support the absence of downflows. The CLV of v_{VI} of the IR line Fe I 15648.5 Å gives somewhat ambivalent information on downflows in the deepest layers of fluxtubes. Due to the uncertainty in the granular blueshift of the Stokes I profile of this line, downflows upto about 0.5 km sec^{-1} cannot be completely ruled out at the level of $\tau_{5000} \approx 1$ in the fluxtube. However, the construction of a self-consistent fluxtube model, which has a downflow in the relatively dense layers arouund $\tau = 1$ but is stationary above that poses major problems.

How are the small observed Stokes V shifts to be interpreted, if lines with positive as well as negative wavelength shifts may occur in the same region? The dependence of line shift on line strength, wavelength and excitation potential is well known for the Stokes I profile, and has been convincingly explained by the correlated velocity and temperature structure of the convective cells associated with granules (Dravins et al., 1981). We suggest that the wavelength shifts observed for the Stokes V profiles may be the result of a similar mechanism. Of course, due to the strong magnetic field in fluxtubes all motions must be along the field lines, so that convective motions must be replaced by oscillations. These oscillations (or waves) will require respectable amplitudes and a correlation between flow velocity and temperature, even if, like the five minute oscillations, they are coherent in all the fluxtubes of an observed region. This requirement is set by the long integration times of our observations, which ensure that the five minute oscillations are practically averaged out. The present analysis hints at the danger of interpreting small shifts ($\lesssim 300$ m sec^{-1}) of the Stokes V profile of a single line as being evidence for a stationary up- or downflow inside a fluxtube, since lines with positive and negative shifts may be present in the same observed region, and also since even data with such long integration times and gathered over such a large region as ours still show a significant scatter.

That fluxtubes are not totally devoid of mass motions, also follows from the analysis in the second part of this paper, where line profiles calculated in a fluxtube model atmosphere are compared with the data. It is found that a broadening due to velocity is required in order to reproduce the observations. We have approximated the velocity field influencing the polarized light by assuming it to be composed of Gaussian macro- and microturbulent velocity profiles. We stress once more that we do not thereby imply the presence of true turbulence or of convective motion inside the fluxtubes. Macro- and microturbulence have only been chosen due to their effectiveness and

simplicity of use. Total *rms* turbulent velocities of between approximately 1 and 3.5 km sec^{-1} are derived from the I_V spectra, depending on the strength and the excitation potential of the line. Interestingly, plage and network model I_V profiles require essentially the same amount of velocity broadening to fit the data (if the appropriate temperature models are used), suggesting that the velocity structures of fluxtubes in the two types of regions are very similar.

The dependence of $\xi_{\rm mac}$ on the line strength is quite different for the magnetic and the non-magnetic data. This is best illustrated in Fig. 7.12, where the difference between $\xi^V_{\rm mac}$ for a network fluxtube and $\xi^I_{\rm mac}$ for the quiet Sun is plotted vs. S_I. Both $\xi^I_{\rm mac}$ and $\xi^V_{\rm mac}$ have been determined using models with $\xi_{\rm mic} = 0.8$ km sec^{-1} and $a_{\rm mac} = 0$. We are therefore comparing like with like (at the cost of a slightly worse fit to the quiet Sun data than with $a^I_{\rm mac} \neq 0$). As expected, $\xi^V_{\rm mac}$ is larger than $\xi^I_{\rm mac}$ for most of the lines. The near similarity in $\xi^I_{\rm mac}$ and $\xi^V_{\rm mac}$ for the weak lines is probably only due to their relative insensitivity to velocity broadening due to, e.g., velocity gradients. One problem with such a comparison, specially for the Fe I lines, is that since they are considerably weakened inside the fluxtube, their sensitivity to velocity broadening is also changed. This could falsify the picture given by Fig. 7.12 somewhat. However, since for most lines the sensitivity decreases as they are weakened, this would tend to *under*estimate $\xi^V_{\rm mac} - \xi^I_{\rm mac}$, so that the effect may in reality be even larger.

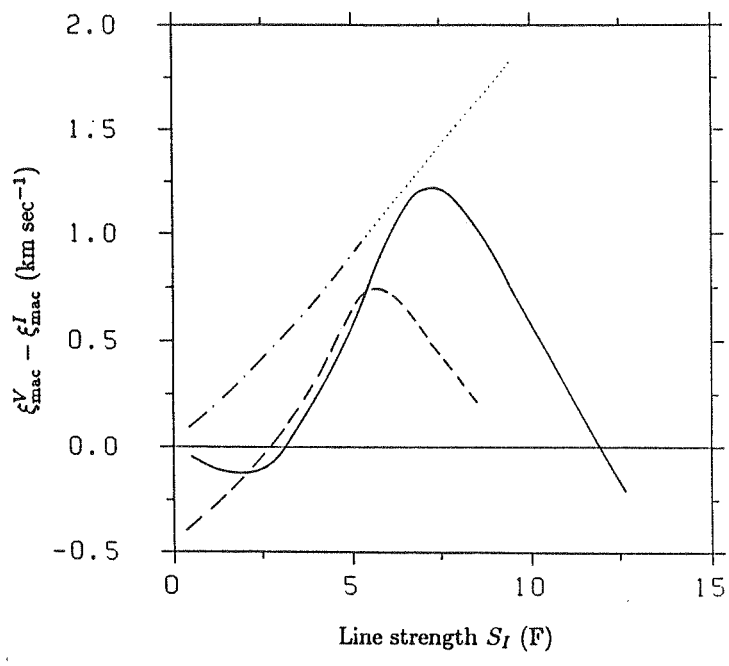

Fig. 7.12 $\xi^V_{\rm mac} - \xi^I_{\rm mac}$ vs. S_I, i.e. the macroturbulence velocity excess in the I_V data compared to the Stokes I data as a function of the line strength. Symbols are the same as in Fig. 7.8a.

We have also studied the influence of the fluxtube temperature structure on the empirically determined velocity, and find that within reasonable limits of the temperature variation (i.e. over a range of about 800 K at a fixed τ value), the macroturbulence velocity remains on the average constant to within ± 0.5 km sec^{-1}.

Calculations based on the assumption that part of the velocity in the fluxtube is better represented by a microturbulence show the expected decrease in $\xi^V_{\rm mac}$ with increasing $\xi_{\rm mic}$. The data place an upper limit of 1.5 km sec^{-1} on $\xi_{\rm mic}$ in fluxtubes, assuming that it is height independent. Best values for $\xi_{\rm mic}$ appear to lie between 0.5 and 1.0 km sec^{-1}.

In Sect. 7.4.2 it is shown that the large I_V line widths are not an artifact of the method of data analysis, the long integration times, or the spectral resolution. They are therefore of solar origin. An obvious solar source are the ubiquitous five minute oscillations. These have been measured in Stokes V by Giovanelli et al. (1978) who find amplitudes of about 0.25 km sec^{-1} for lines formed in the photosphere, and by Wiehr (1985a), who reports amplitudes of 0.1–0.25 km sec^{-1} for the Fe I 8468 Å line. These amplitudes are considerably smaller than the values of $\xi^V_{\rm mac}$ we find here, so that we are led to conclude that other mass motions besides the ones induced by the five minute oscillations have to be present in small fluxtubes. However, from the line broadening analysis alone, we cannot differentiate between the effects of a steady flow with a vertical or horizontal velocity gradient, oscillations or waves within single fluxtubes, or steady flows with different flow velocities in different fluxtubes.

By combining the main results of Sects. 7.2 and 7.4, we see that motions are present in fluxtubes which strongly broaden the spectral lines, but do not significantly shift them. Oscillations, waves, or a distribution of

up- *and* downflows in different fluxtubes (for example via a siphon flow between two fluxtubes connected by a loop) could explain the observations within the context of a (multicomponent) one-dimensional model. Motions outside the fluxtubes may also broaden the Stokes V profiles, even at disk centre, if we take their expanding geometry into account. However, the large difference in $\xi^V_{\rm mac}$ and $\xi^I_{\rm mac}$ (illustrated in Fig. 7.12) would appear to limit their contribution to the total velocity induced line broadening. However, it is possible that the velocity field in the immediate surroundings of fluxtubes differs considerably from the average over a larger portion of an active region.

The presence of motions with such large amplitudes means that non-radiative heating may play an important role even in the deep layers of the fluxtube photosphere (cf. Hasan and Schüssler, 1985). Such motions will also have to be taken into account in the empircal modelling of fluxtubes, since their neglect could lead to false values of the empirically determined temperature structure (see also chapter 5).

Finally, we wish to point out that the present work is exploratory in nature, and contains a number of shortcomings. Firstly the accuracy of the absolute wavelengths of Stokes V can be increased in future FTS observations. This would allow the setting of stronger constraints on downflow velocities in fluxtubes. Certainly more work will have to be done in the infrared as well. The large width of the wings of the Fe I 15648.5 Å Stokes V profile compared to the corresponding I profile, illustrated in Fig. 6.11, may be due to large amplitude non-stationary motions. However, further work will be needed to decide this question. The macro/microturbulence approach has its shortcomings, as has been pointed out by Gail and Sedlmayr (1974) and Carlsson and Scharmer (1985). Therefore calculations with a proper model of the motions in fluxtubes need to be carried out.

8. Stokes V Asymmetry

8.1. Brief Review

First indications of an asymmetry between the areas of the blue and red wings of Stokes V have been provided by the broad-band observations in circular polarization of sunspots by Illing et al. (1974a, b, 1975). In their first paper they measure the centre to limb variation (CLV) of $\int V/I\,\mathrm{d}\lambda$ (bandwidth 100 Å) over the $\mu = cos\theta$ range $0.95 \geq \mu \geq 0.37$, and find that the broad-band circular polarization peaks near $\mu = 0.74$ where it can reach values of $1\text{–}2 \times 10^{-3}$. They also find that most of a typical sunspot shows the same sense of polarization with a slow variation in the degree of polarization (they call this region 1), while a smaller portion shows rapid (spatial) changes in sign of $\int V/I\,\mathrm{d}\lambda$ (region 2 in their nomenclature). In their second paper, they note that the sign of $\int V/I\,\mathrm{d}\lambda$ in region 1 is correlated to the sign of the sunspot magnetic field polarity. They also speculate that region 2 may correspond to regions of small scale magnetic field reversal. Finally, in their third paper they investigate the spectral dependence of the magnitude of broad-band circular polarization, and also discuss possible mechanisms for its production. They find that $\int V/I\,\mathrm{d}\lambda$ of region 1 decreases when going from the green to the yellow part of the spectrum. The behaviour of region 2 is more ambivalent.

Further measurements of broad-band circular polarization in sunspots are presented by Kemp and Henson (1983). They extend the spectral coverage of such observations to a range extending from 3700 Å in the UV to 4.5 μ in the IR, and find a sharp drop in $\int V/I\,\mathrm{d}\lambda$ from the UV through the visible, a modest peak at 1.66 μ and then a further decline upto 4.5 μ. Their spectral resolution is 5 Å.

A number of explanations have been considered for these observations. Illing et al. (1975) rule out continuum circular polarization (produced by a mechanism described by Kemp, 1970) as a possible source of the observed $\int V/I\,\mathrm{d}\lambda$. For the field strengths of a few kG found in sunspots Kemp (1970) and Kemp et al. (1970) predict a circular polarization level of 10^{-5} in the continuum, while Illing et al. and later Kemp and Henson measure values of 10^{-3} (averaged over lines and the continuum). This continuum effect only becomes important for very large field strengths, as found on white dwarfs (see Angel, 1977, 1978 for a review).

The strong imbalance in splitting pattern exhibited by some molecular transitions and the resulting imbalance in the two circular polarization components can also lead to broad-band circular polarization. Harvey (1973b) has observed this molecular effect for the CN(0,0) band in sunspots. It has played an important role for the determination of magnetic field strengths in white dwarfs (Angel and Landstreet, 1974). A detailed theoretical calculation is presented by Illing (1981), who can reproduce the order of magnitude of the broad-band observations of Illing et al. under certain assumptions.

The remaining mechanisms for producing broad-band circular polarization are based on asymmetries of atomic Stokes V profiles. In particular the areas of the blue and red wings have to be different, i.e. $\Delta A = A_b - A_r \neq 0$ (cf. Sect. 4.4.1 for further definitions of Stokes V asymmetry). As shown in Sect. 2.4.2, the Stokes V profile for an atomic transition is exactly antisymmetric in a static atmosphere in LTE (see also Auer and Heasley, 1978; Landi Degl'Innocenti and Landi Degl'Innocenti, 1981). Therefore, one of these conditions must be violated in order to produce atomic Stokes V profiles which give rise to a net $\int V/I\,\mathrm{d}\lambda$

The mechanism preferred by Illing et al. (1975) is based on the presence of a correlated gradient in velocity and magnetic field along the line of sight. The Stokes V profiles of ordinary atomic spectral lines can then become asymmetric and give rise to broad-band circular polarization. A more detailed description of this mechanism is given in Sect. 8.4. It nicely explains the spectral dependence of $\int V/I\,\mathrm{d}\lambda$ of spot region 1 (since the spectral line density decreases from the green to the yellow) and the correlation between the sign of $\int V/I\,\mathrm{d}\lambda$ and magnetic field polarity. Auer and Heasley (1978) point out, that if the line of sight is not parallel to the magnetic field (i.e. $\gamma \neq 0°, 180°$), then a velocity gradient alone is sufficient to produce an area asymmetry in Stokes V.

In the following we briefly discuss some other analyses of Stokes V asymmetry involving velocity gradients. Grigorjev and Katz (1975) calculate all four Stokes parameters in the presence of both magnetic and velocity field gradients (of a simple parameterised form) and produce asymmetric Stokes V profiles. Landman and Finn (1979) carry out radiative transfer calculations of the Stokes parameters in a two dimensional sunspot model

(with the magnetic field calculated self-similarly via Schlüter-Temesvary theory). They choose the following set of parameters: $B_z(r=0,z_0) \approx 3200$ G, $B'_z(r=0,z_0) \approx 1$ G km^{-1} and velocity v given by

$$\mathbf{v} = \pm 2 \times 10^{-5} \frac{\mathbf{B}}{\rho} \quad \text{km sec}^{-1}, \tag{8.1}$$

where ρ is the gas density and the point $(r = 0, z_0)$ refers to the centre of the spot at its surface. They find qualitative agreement with the observations of Illing et al. but get too small values of the net circular polarization. Makita (1981) presents observational evidence that the observed broad-band polarization is due to atomic spectral lines by showing that when these are spectrally masked the circular polarization signal disappears. He also argues that both strong magnetic and velocity field gradients are required to reproduce the observed $\int V/I \, \mathrm{d}\lambda$ in sunspots. Landi Degl'Innocenti and Landolfi (1983) analyse the effects of a velocity gradient on Stokes V and Q via the response function. Like Auer and Heasley they keep the magnetic field independent of height. Ribes et al. (1985) calculate Stokes V line profiles of thirteen photospheric lines for four theoretical models incorporating gradients in both magnetic field and downflow (cf. Unno and Ribes, 1979 for a description of these models). They compare the calculated profiles of Fe I 5247.1 Å and Fe I 5250.2 Å with the observed profiles of these lines taken from Stenflo et al. (1984). It is evident from the figures of Ribes et al. (1985) that none of these models produce profiles which resemble the data.

Finally, Kemp et al. (1984) propose atomic orientation as a method for producing Stokes V asymmetry. Briefly, the mechanism rests on the fact that atoms become 'aligned' when excited anisotropically by a stream of particles or by (not necessarily polarized) anisotropic radiation. In a magnetic field, the alignment develops into orientation, i.e. the atoms acquire a finite orbital angular momentum L_z along the field lines. Kemp et al. (1984) present both theoretical and laboratory evidence for the existence of asymmetric Stokes V profiles produced by this mechanism. They briefly and qualitatively discuss the application of this process to produce broad-band circular polarization in sunspots. Landi Degl'Innocenti (1985b) discusses the application of this idea to small fluxtubes. However, he requires a velocity inside the fluxtube (and therefore a velocity gradient with respect to the non-magnetic surroundings from where the light enters the tube in his model) to produce a Stokes V area asymmetry.

8.2. Observations

8.2.1. Disk Centre Observations

First observations of the asymmetry of solar atomic Stokes V line profiles were presented and discussed by Stenflo et al. (1984). More detailed analyses have been published by Solanki and Stenflo (1984, 1985). In this section we shall present and discuss their results. All the data presented in this section were obtained near disk centre.

The Stokes V asymmetry is nicely illustrated in Fig. 8.1 in which Stokes V and $-\partial I/\partial\lambda$ for the Fe I 5247.1 Å and 5250.2 Å lines are plotted. The $-\partial I/\partial\lambda$ profile has been normalised to the blue peak of the Stokes V profile, and is almost antisymmetric. In particular, the areas of the blue and red wings of $-\partial I/\partial\lambda$ are exactly equal. If the areas of the wings were different, the integration would result in different continuum levels for Stokes I, which is never observed.

A comparison of $-\partial I/\partial\lambda$ to Stokes V shows that the latter has a very asymmetric form, with both the amplitudes and areas of the blue and red wings being different, i.e. $\Delta a \neq 0$ and $\Delta A \neq 0$. The parameters of the absolute asymmetry, ΔA and Δa, are defined in Sect. 4.4.1.

Let us now consider the amplitude asymmetry of the Stokes V profiles of the Fe I lines listed in Table 4.1. Fig. 8.2a shows the absolute amplitude asymmetry, Δa, for an active region plage plotted vs. the Stokes I line strength, S_I. The large scatter of the points can be reduced significantly by using the regression expression,

$$\Delta a = x_1 + x_2 S_I + x_3 S_I^2 + x_4 S_I^3 + x_5 S_I \chi_e, \tag{8.2}$$

to subtract the dependence on excitation potential. The result is shown in Fig. 8.2b. The dependence of Δa on the wavelength and on Landé factor has also been studied by adding further terms to Eq. (8.2), but no dependence on either quantity has been found, for which reason these terms have been discarded again.

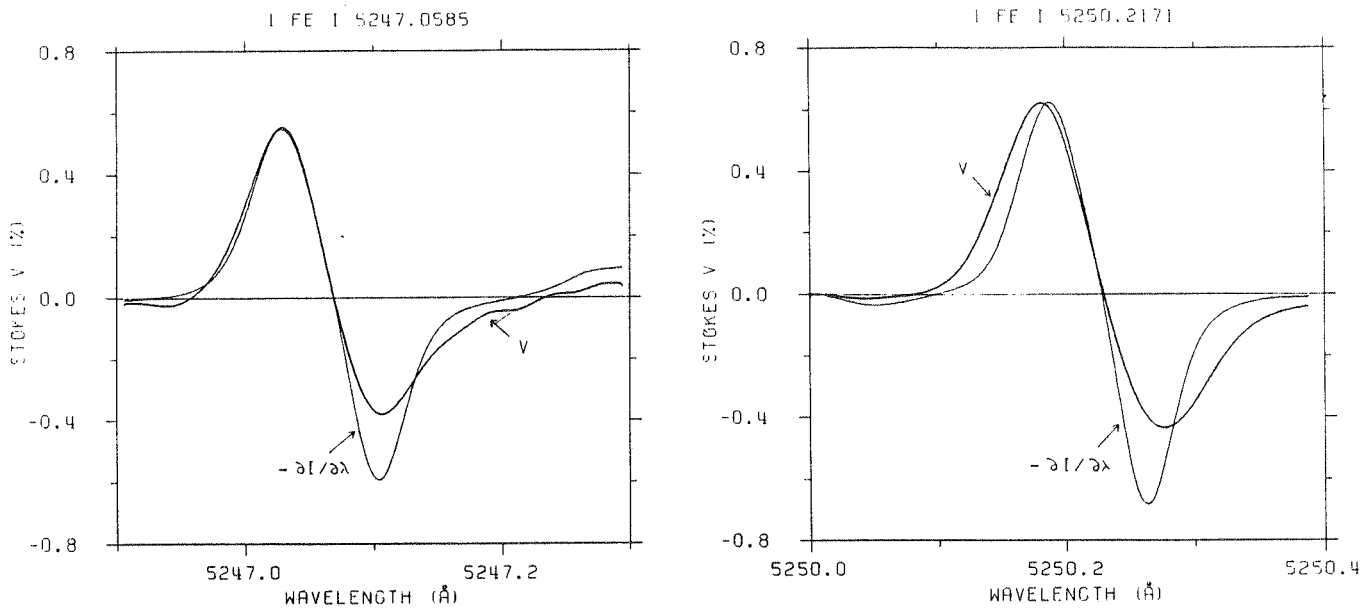

Fig. 8.1 Stokes V (thick curve) and $\partial I/\partial\lambda$ (thin curve) of the Fe I 5247.1 Å and 5250.2 Å lines, based on data recorded in an enhanced network element near disk centre. The $\partial I/\partial\lambda$ curves have been normalised to the amplitudes of the blue wings of the respective Stokes V curves. Note the pronounced asymmetry between the blue and the red wings of Stokes V.

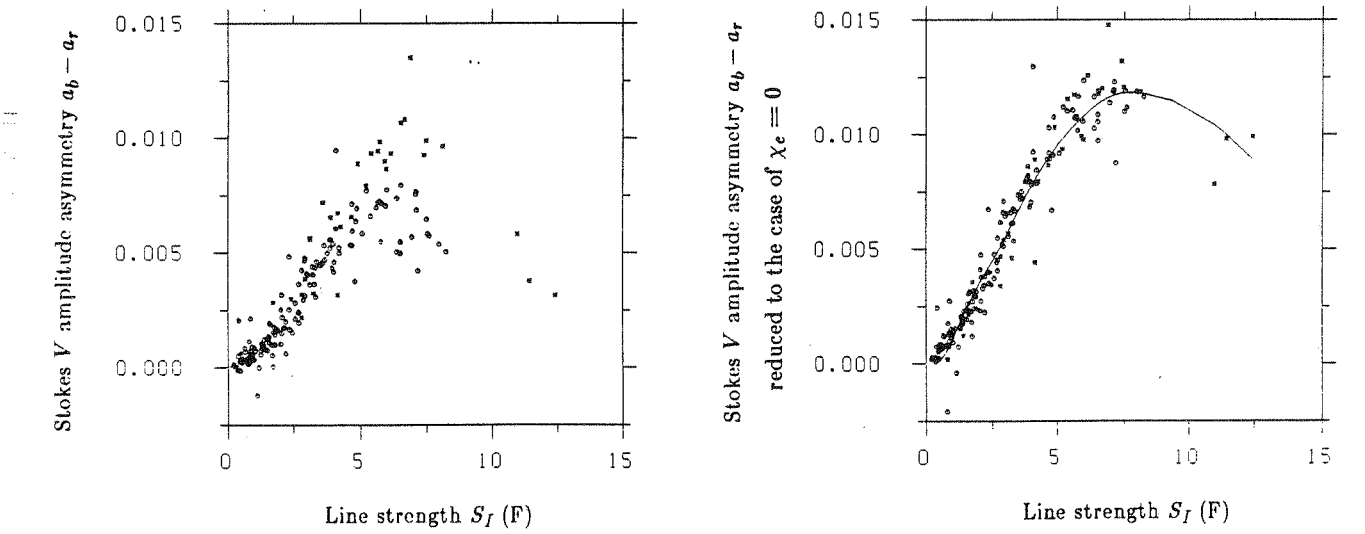

Fig. 8.2 Absolute amplitude asymmetry, $\Delta a = a_b - a_r$, plotted vs. I line strength, S_I. a_b and a_r are the amplitudes of the blue and red wings of V. a Raw data for a plage region. b The same data reduced to the case that $\chi_e = 0$ using Eq. (8.2). The smoothed average (cubic spline) is drawn as well.

Fig. 8.3a and b show the relative area and amplitude asymmetries, δA and δa (see Eqs. (4.47) for the definitions), for an active region plage plotted as functions of S_I. The solid curves drawn through the data points are smoothed averages (cubic spline fits). Note the different shapes of the two curves. The relative area asymmetry actually becomes negative for the strongest lines of our sample, while the relative amplitude asymmetry remains positive. The different shapes of the δA and δa curves suggest that slightly different mechanisms are responsible for producing them, as is intuitively clear. The amplitude asymmetry of any one particular line depends only on the maximum V amplitudes and is therefore sensitive to only a limited height range, whereas the area asymmetry, being an integral quantity, is sensitive to a much larger range of heights.

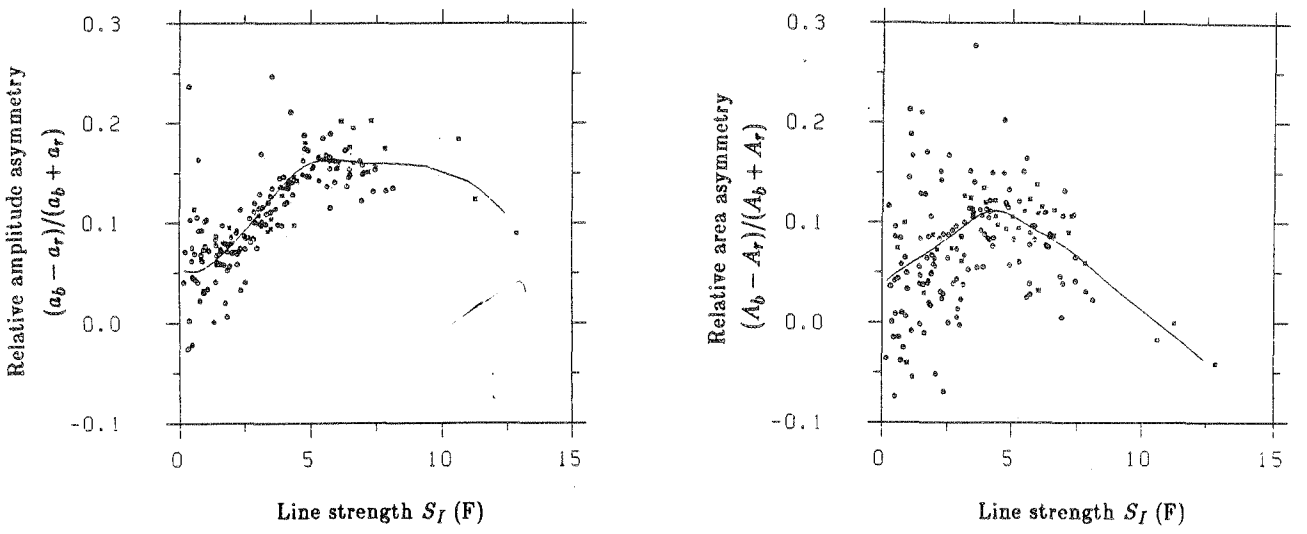

Fig. 8.3 a Relative amplitude asymmetry, $\delta a = (a_b - a_r)/(a_b + a_r)$, vs. S_I for a plage. b Relative area asymmetry, $\delta A = (A_b - A_r)/(A_b + A_r)$, vs. S_I for the same plage as in Fig. 8.3a. The solid curves are smoothed averages (cubic splines).

Due to the difference in $\langle B \rangle$ between the network and the active region plages, which leads to a difference in amplitude of the V profiles, it is impossible to compare the absolute asymmetries of the active and quiet regions without prior knowledge of the average magnetic field. The relative asymmetries, however, are on the same scale and can accordingly be compared easily. They are plotted for both the plage and network regions in Fig. 8.4. The relative asymmetry appears to be slightly smaller for the plage than the network regions, although the scatter is quite large.

Fig. 8.4 The shaded areas are bounded by the envelopes of the smoothed relative amplitude (dark shading) and area (light shading) asymmetry curves of all the regions observed in 1979, plotted vs. S_I. The dashed line running between the amplitude asymmetry envelopes is a boundary between the curves of the plage and network regions. The smoothed plage curves lie below this line whereas the network curves lie above it.

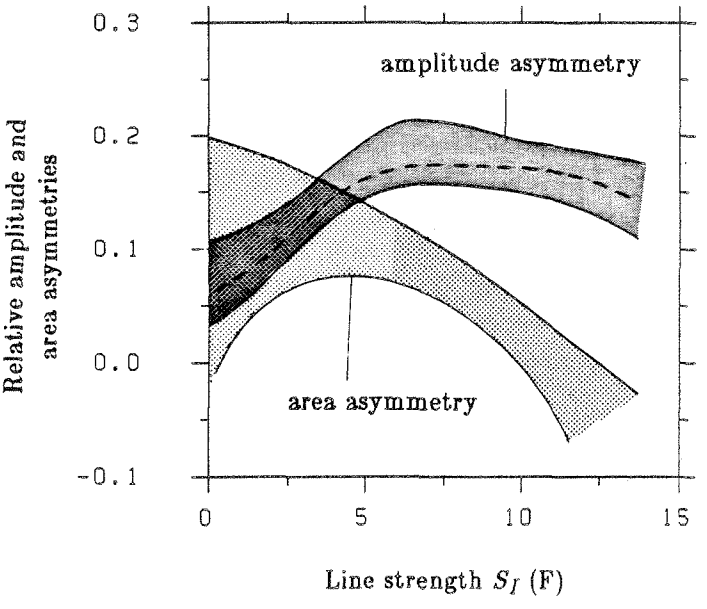

In Fig. 8.5 Δa is plotted vs. S_I for both Fe I and II lines. The areas with light shading indicate the location of Fe I points with $\chi_e \geq 3$ eV, the areas with intermediate shading Fe I lines with $\chi_e < 3$ eV, and the areas with dark shading Fe II lines.

As pointed out in Sect. 4.4.2, the Fe II I_V profiles have widths larger than expected from an extrapolation of the $v_{D_V} - v_{D_I}$ vs. χ_e dependence of the Fe I lines. A similar dependence is observed for Δa. The Fe II lines are more asymmetric than expected from the Fe I lines. This similarity in behaviour of $v_{D_V} - v_{D_I}$ and Δa of lines of different χ^* suggests a relationship between the width of I_V and the asymmetry of V. As we have seen

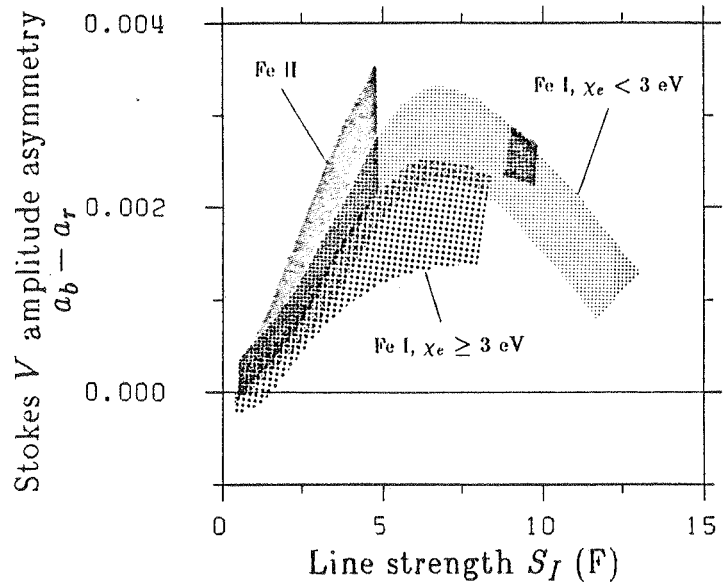

Fig. 8.5 Δa vs. S_I for an enhanced network region. The lightly shaded portions indicate the location of Fe I lines with $\chi_e \geq 3$ eV, the intermediately shaded portions Fe I lines with $\chi_e < 3$ eV, and the darkly shaded portions Fe II lines.

in chapters 5 and 7 the width of I_V is strongly influenced by velocity broadening, so that this correlation points towards a relationship between asymmetry and velocity. We shall discuss such a relationship in greater detail in Sect. 8.4.1.

We have checked that our observed asymmetries are not caused by instrumental effects and really represent fluxtube physics on the Sun. Thus, for instance the polarity of the observed magnetic field does not affect the behaviour of the Stokes V asymmetry. The predominance of the amplitude and area of the blue wing of Stokes V over the red wing applies to both positive and negative polarity regions. This means that the broad-band circular polarization produced by our asymmetric profiles shows the same relative relationship to the magnetic polarity as found by Illing et al. (1974b). It also excludes the possibility that the instrument somehow favours one sense of circular polarization over the other. Furthermore, the absence of a strong wavelength dependence of the Stokes V asymmetry suggests that the effects of possible differential chromatic properties of any of the optical elements have not infiltrated our results.

For Fe I lines around 5250 Å a similar value of the Stokes V asymmetry was found with the vertical grating spectrograph of the McMath telescope (Stenflo and Harvey, 1985), with which a much larger number of magnetic regions could be sampled. Therefore Stokes V asymmetry is not an artifact of the FTS. The results also do not depend on the time of day, and are thus uncorrelated to the position of the obliquely reflecting heliostat mirror.

Since the original discovery, other observations of Stokes V asymmetry have also been published. Wiehr (1985a) has observed Stokes V of Fe I 8468.4 Å near disk centre with the Locarno Gregory telescope, and also finds an asymmetry of the type described above, as do Scholier and Wiehr (1985). Further confirmation comes from the broad-band observations of the full solar disk and of its north and south hemispheres by Kemp et al. (1987). Their measurements are compatible with the broadband signal obtained from the FTS data by Stenflo (1984b) who integrated over 50 Å running windows. In particular, the spectral dependence of the broad-band circular polarization of the two data sets is remarkably similar, suggesting that the signal of Kemp et al. (1987) is mainly due to lines. Since observations with completely independent telescopes and instrumental techniques have yielded a similar Stokes V asymmetry, we conclude that this asymmetry is real.

8.2.2. Centre to Limb Variation of the Stokes V Asymmetry

In Fig. 8.6 the CLV of the Stokes V asymmetry of a few selected lines is represented. Fig. 8.6a shows the relative area asymmtry δA for Fe I 5250.2 Å (filled squares) and Fe I 5247.1 Å (stars). The thick and thin curves are smoothed means of Fe I 5250.2 Å and 5247.1 Å respectively. The δA values of the nearby lines Fe I 5250.6 Å and Cr I 5247.6 Å have also been checked and have been found to closely resemble those of the plotted lines. Surprisingly, δA changes sign near $\mu = 0.4$, so that near the limb it is negative. This means that the area of the red Stokes V wing becomes larger than the area of the blue wing. The fact that four spectral lines in three different spectra exhibit this negative asymmetry means that it is not a fluke, or due to noise. Therefore, near the limb δA of these medium strong lines behaves more like the strongest lines near disk centre. Whether this

effect is due to the greater height of formation near the limb, or is due to the change in the angle of the line of sight cannot be decided as yet.

Fig. 8.6b shows the relative amplitude asymmetry δa for the four lines mentioned above. Since Fe I 5247.1 Å and Fe I 5250.2 Å behave differently in this figure, all four lines have been plotted. One can see that, for an unknown reason, it is Fe I 5247.1 Å whose behaviour is anomalous. We shall therefore disregard Fe I 5247.1 Å during the following discussion. The solid line is a smoothed mean curve for the Fe I 5250.2 Å data points. For $\mu > 0.4$ the behaviour of δa is very similar to that of δA. However, near $\mu = 0.4$ δa simply drops to zero while δA becomes negative.

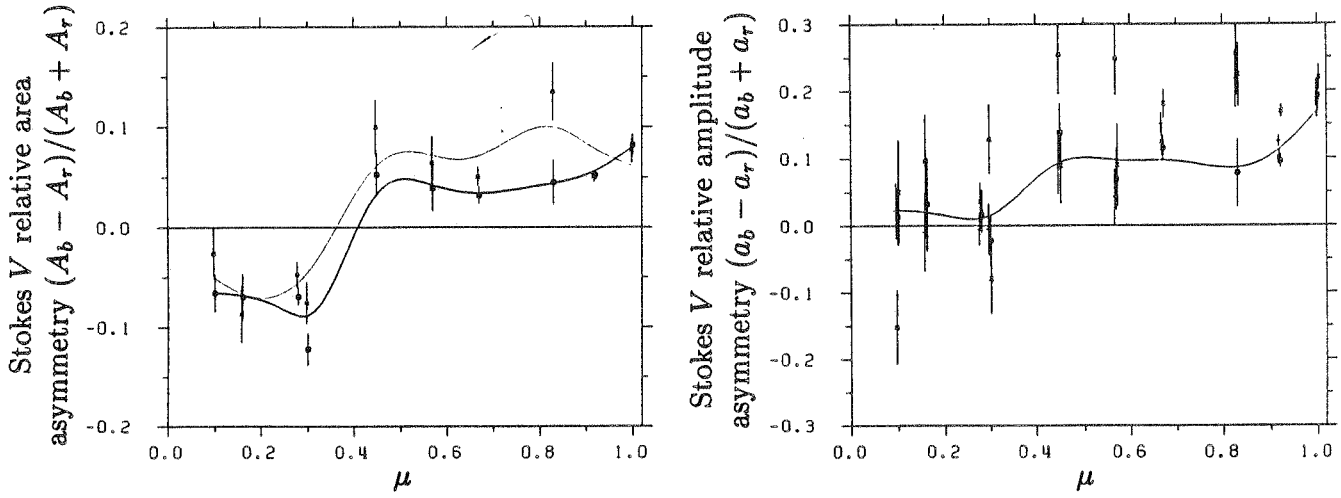

Fig. 8.6 Centre to limb variation (CLV) of four lines near 5250: Fe I 5247.1 Å (stars), Cr I 5247.6 Å (pluses), Fe I 5250.2 Å (filled squares), Fe I 5250.6 Å (crosses). a Relative area asymmetry δA. Thick curve is a smoothed spline fit to 5250.2 Å, the thin curve to 5247.1 Å. b Relative amplitude asymmetry δa. Thick curve is a smoothed spline fit to 5250.2 Å.

Another line for which the CLV of the Stokes V asymmetry has been studied is the Fe I line at 15648.5 Å. Figs. 8.7a and b show its δA and δa values respectively, as a function of μ. Due to the weakness of this line, the error bars are considerably larger than for e.g. Fe I 5250.2 Å. Inspite of this, the IR line appears to have a considerably smaller δA near disk centre, which becomes sizeably negative when going towards the limb. However, the large error boxes would also allow this line to have a small or vanishing δA throughout. The amplitude asymmetry is small as well (compare with $\delta a \approx 10\%$ for Fe I 5250.2 Å at $\mu = 1$), but shows a tendency to increase slightly towards the limb. It is negative for all μ. Once more, observations with a better S/N ratio are required to give more definite results. A statistical analysis of further lines in the IR may also shed some more light on this. The small δA and δa values of Fe I 15648.5 Å are in accordance with the small asymmetries of lines of similar strength in the visible.

8.3. Effects of Spectral Smearing on Stokes V Asymmetry

The Stokes V asymmetry is also affected by spectral smearing. Fig. 8.8 shows the change in Stokes V relative area asymmetry δA induced by changing v. The asymmetry increases dramatically with v for both the enhanced network and active region observations. We explain this result by noting that as the profiles are smeared, equal amounts of each polarity are cancelled, so that the net polarization (the numerator of δA, $A_b - A_r = \Delta A$) remains the same (giving the contribution of the line to the broadband polarization in the limit of $v \to \infty$), but the sum of the absolute areas of the Stokes V wings (the denominator $A_b + A_r$) decreases (cf. Fig. 6.7). The quantity δA is therefore bound to increase with increasing spectral smearing.

Indeed $A_b - A_r$ is found to be constant within our numerical accuracy of a couple of percent, in the range $0 \leq v \leq 150$ mÅ for different solar regions and instrumental profile shapes. This resolution independence of $A_b - A_r$ is reflected by the fact that the curves of Fig. 8.8 are almost inversely proportional to the curves in Fig. 6.7. However, although $A_b - A_r$ is independent of spectral resolution, it is strongly dependent on the filling

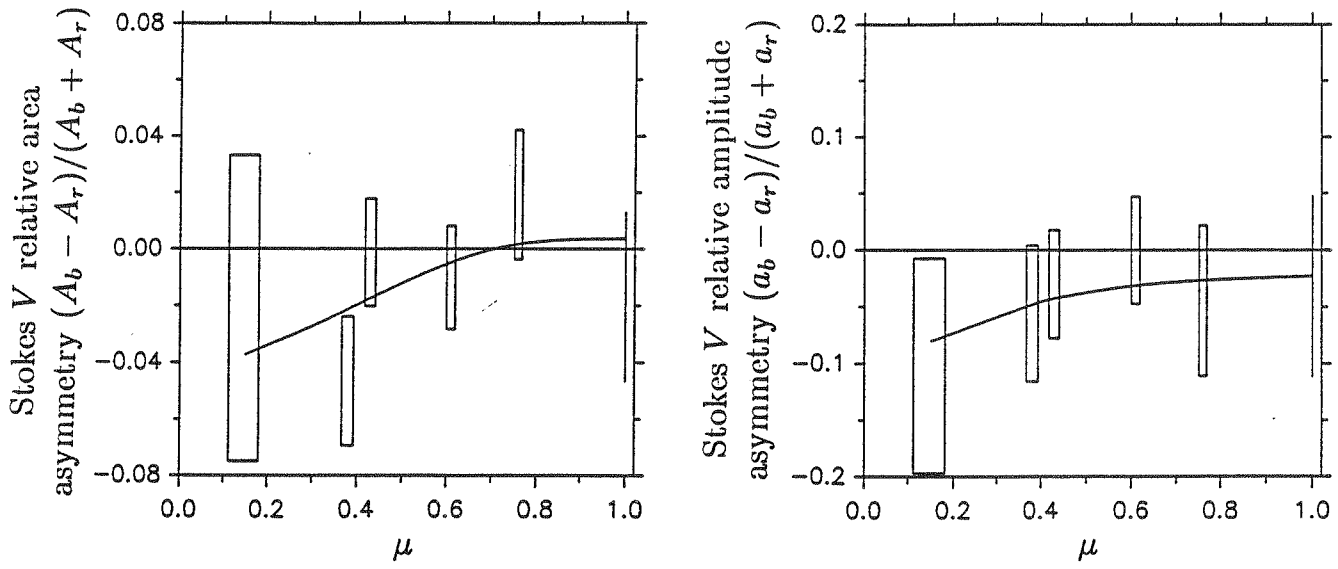

Fig. 8.7 CLV of the asymmetry of Fe I 15648.5 Å. The solid curves are cubic spline fits. **a** Relative area asymmetry δA. **b** Relative amplitude asymmetry δa.

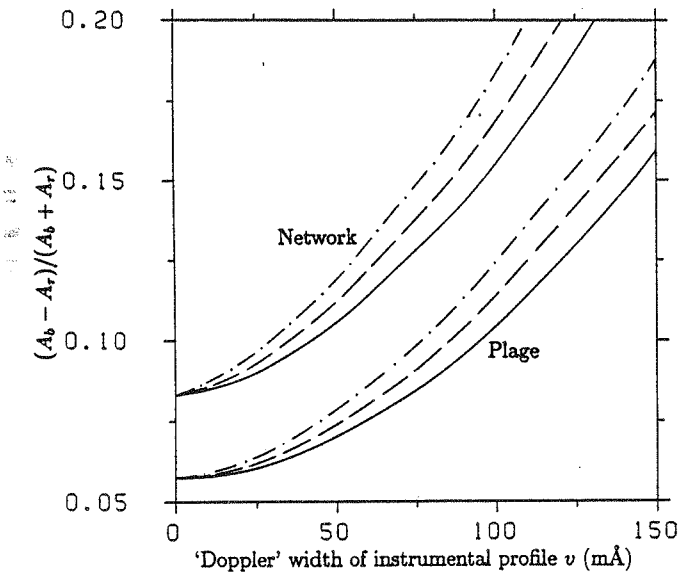

Fig. 8.8 δA of Fe I 5250.2 Å vs. v, the e-folding width of the instrumental profile. The upper set of curves corresponds to enhanced network observations, the lower set to observations made in an active region plage. Solid line: Gaussian apparatus function. Dashed line: Voigt apparatus function (with damping constant, $a = 0.1$). Dot-dashed line: Voigt apparatus functon ($a = 0.2$).

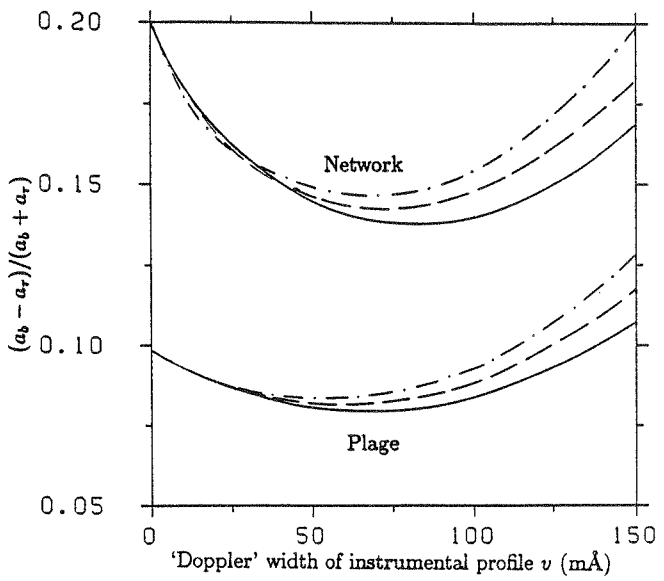

Fig. 8.9 δa of Fe I 5250.2 Å vs. v. The upper set of curves corresponds to enhanced network observations, the lower set to observations made in an active region plage. The different instrumental profile shapes are represented as in Fig. 8.8.

factor (since A_b and A_r are both approximately proportional to the filling factor), and is not particularly useful for comparisons amongst observations of different regions.

As however S_V is also approximately proportional to the filling factor and insensitive to the spectral resolution used, the quantity $(A_b - A_r)/S_V$ is practically independent of both resolution and filling factor. S_V has a different physical meaning from $A_b + A_r$, and the insignificant v dependence of $(A_b - A_r)/S_V$ which we find, is not simply an artifact, but reflects this difference.

Fig. 8.9 shows the relative amplitude asymmetry, δa, as a function of v. The behaviour of this quantity is more complicated, but can nevertheless be understood in general terms, by considering the following three effects: Firstly, $a_b + a_r$ decreases strongly with v (Fig. 6.6). This tends to increase the relative amplitude asymmetry. Secondly, the absolute amplitude asymmetry, $a_b - a_r$, decreases initially even more rapidly with v, which is quite contrary to what is observed for the area asymmetry. The main reason for this rapid decrease is that the blue peak, being narrower than the red peak, is more strongly affected by spectral smearing, so that a_b decreases faster than a_r, approaching the latter asymptotically. For large v both peaks are so broad that this effect becomes small, allowing the relative amplitude asymmetry to increase again. Thirdly, due to the overlapping and partial cancellation of the blue and red wings and also due to the general broadening of the Stokes V profile, the blue and red maxima move apart, and no longer necessarily represent the same part of the line. This affects both $a_b - a_r$ and $a_b + a_r$. However, this last effect is difficult to isolate, so that we cannot judge its importance for the overall behaviour of δa.

In contrast to the case of the area asymmetry, the S_V normalised amplitude asymmetry $(a_b - a_r)/S_V$ is not a useful parameter, being strongly resolution dependent. This is because $a_b - a_r$ depends so strongly on v while S_V does not.

8.4. Interpretation of Stokes V Asymmetry

8.4.1. Correlation Between Stokes V Asymmetry and Velocity Broadening

In order to interpret the asymmetric Stokes V line profiles observed in small fluxtubes, let us briefly recall the interpretations proposed for the broad-band circular polarization in sunspots. Of course we can immediately rule out the interpretations involving polarization of the continuum or asymmetric molecular lines, since our spectrally resolved observations clearly show that atomic Stokes V profiles are asymmetric. Two possible mechanisms remain: velocity gradients and atomic orientation. In this section we present some evidence favouring the former mechanism. It follows from these observations than any broad-band circular polarization observed outside sunspots will be due to the asymmetry in atomic Stokes V profiles. The same is most probably also true for sunspots (recall the observations of Makita, 1981). Stokes V observations with high spectral resolution in sunspots are therefore very desirable.

A comparison of Fig. 7.9 with Fig. 8.5 suggests a correlation between the velocity broadening represented by $\xi^V_{\rm mac}$ and the absolute amplitude asymmetry Δa. We would now like to place this analysis on a more quantitative footing. Fig. 8.10 shows $\xi^V_{\rm mac}$ (derived assuming $\xi_{\rm mic} = 0$) plotted vs. $a_b - a_r$, both quantities having S_I as a parameter. The S_I values 0, 2.5, 5, 7.5, 10, and 12.5 F are marked by notches in the curves. For the Fe II lines the point at $S_I = 9.3$ F is marked instead of $S_I = 7.5$ F. The Fe II curve between $S_I = 5$ F and $S_I = 9.3$ F is dotted to indicate that it is interpolated between these values. The asymmetry data and $\xi^V_{\rm mac}$ values are for an enhanced network region. The model for which $\xi^V_{\rm mac}$ is derived, is the best fit network model with $\xi_{\rm mic} = 0$ and $\delta_\Gamma = 2.5$. The peculiar hook-like shape of the curves is due to the decrease in asymmetry and $\xi^V_{\rm mac}$ above $S_I \approx 7$–8 F, and is without deeper significance, being only an artifact of plotting the data with S_I as a parameter. The straight line is a least-squares fit to the three curves. A straight line fit to the data is also suggested by comparing Fig. 7.9 with Fig. 8.5.

The correlation coefficient for these two quantities is 0.85 (on a scale ranging from -1 to $+1$, with ± 1 meaning perfect correlation, and 0 a total absence of correlation), which is high enough to suggest the existence of a simple linear relation between the fluxtube velocity amplitudes, as determined from the line broadening, and the asymmetry of Stokes V, specially if we take the rather large errors, indicated by the error box in the lower right of the figure, into account. Its size is primarily dictated by the considerable scatter in the asymmetry values of the different lines.

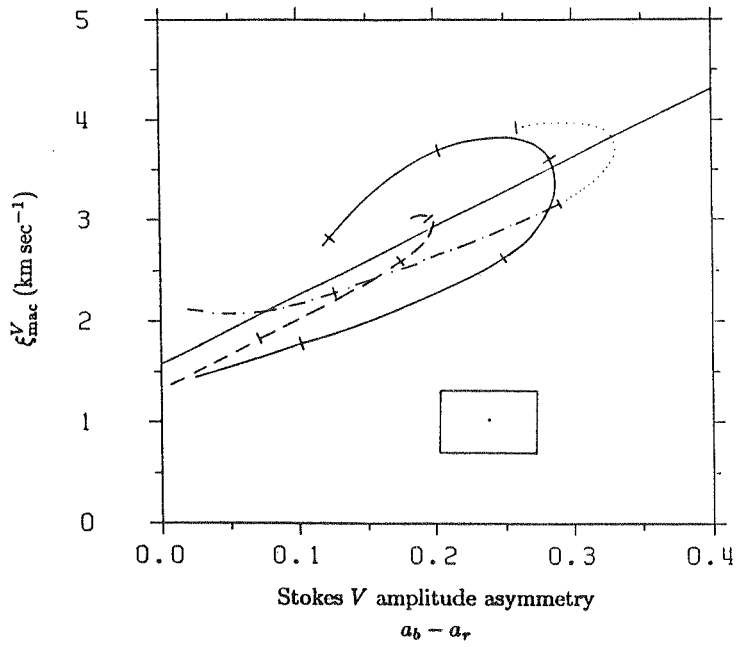

Fig. 8.10 Macroturbulence velocity in the fluxtubes $\xi^V_{\rm mac}$ vs. $a_b - a_r$. The curves are plotted with S_I as a parameter. Its value is marked by notches every 2.5 F. An error box is plotted at lower right. Fe I lines with $\chi_e < 3$ eV are denoted by the solid curve, Fe I lines with $\chi_e \geq 3$ eV by the dashed curve, and the Fe II lines by the dot-dashed curve.

It is interesting to note that the asymmetry tends to disappear for very weak lines, while the velocity broadening does not. The least squares fit gives $\xi^V_{\rm mac} = 1.6$ km sec^{-1} for $a_b - a_r = 0$.

The foregoing analysis clearly demonstrates that a relationship exists between Stokes V asymmetry and the velocity in fluxtubes. However, the nature of such velocities is not quite clear. Auer and Heasley (1978) have shown that for one dimensional LTE models velocity *gradients* are required. These may be coupled with a magnetic field gradient. The velocity gradients may be produced by a steady flow, or they may be the result of oscillations or of waves inside the fluxtube. Finally, if we consider the expanding geometry of fluxtubes, then flows *outside* the fluxtube may cause an asymmetry of Stokes V. In the next Sections we consider the case of steady flows in one dimensional fluxtubes observed at disk centre.

8.4.2. Stokes V Asymmetry Produced by Velocity Gradients: General Considerations

Since Stokes V asymmetry has also been observed at disk centre and fluxtubes are expected to be nearly vertical due to buoyancy, the mechanism proposed by Auer and Heasley (1978), which does not involve a magnetic field gradient and works only for $\gamma \neq 0$, is less likely to be the cause, at least near disk centre. In addition, Makita (1981) has pointed out that this mechanism is much less efficient at producing an asymmetry than the one originally proposed by Illing et al. (1975) involving both a velocity and a magnetic field gradient along the line of sight. In the following we shall therefore consider the mechanism of Illing et al. in greater detail. Of course, for the general case of $\gamma \neq 0$ and $\mathrm{d}B/\mathrm{d}\tau \neq 0$ the asymmetry is caused by a combination of the two effects, which are both automatically taken into account by radiative transfer codes. An advantage of the Auer and Heasley mechanism is that it allows an analytical solution. We shall, therefore, later use it to show that the area asymmetry disappears for very weak lines.

Fig. 8.11 illustrates schematically how Stokes V asymmetry can be produced in a very simple model consisting of two plane parallel slabs lying on top of each other. We assume that $\mu = 1$ and that the magnetic field is vertical. Then the radiative transfer equations for circular and linear polarization decouple and we can consider right and left circularly polarized light independently (Stepanov, 1958a, b; Stenflo, 1971). In the bottom frame (i) $\eta_\pm$, the ratio of the line to continuum absorption coefficients for right and left circularly polarized light, are shown at a depth in the atmosphere where the magnetic field strength, B, is large and the velocity, $v \approx 0$. In the second lowest frame (ii) $\eta_\pm$ are shown higher up in the atmosphere where B is small and v is large and positive. We use the usual sign convention: $v(\tau) > 0$ for downflows. The third frame from the bottom (iii) shows the emergent profiles $I_\pm(\tau = 0)$ (i.e. the intensity profiles of right and left circularly polarized light coming from inside the magnetic element) and finally the top frame (iv) shows the corresponding Stokes V profile, $V = I_+ - I_-$. The difference between the areas of I_+ and I_-, and therefore also the asymmetry in Stokes V is produced by a combination of saturation effects and gradients in $v(\tau)$ and $B(\tau)$. In reality, light from the non-magnetic surroundings is mixed with $I_\pm$, but when creating Stokes V this non-fluxtube light does not contribute, so that

we need not include it in Fig. 8.11. λ_0 is the laboratory wavelength of the line, λ_V the actual zero-crossing wavelength of Stokes V. Note the redshift, $\lambda_V - \lambda_0$ of Stokes V in Fig. 8.11. As is suggested by the figure, it is the combined *gradients* of B and v which are important for the production of the asymmetry. In particular, the absolute value of v has no effect on the asymmetry, so that we can write

$$v(\tau) = v_0 + v_1(\tau) = v(\tau_0) + (v(\tau) - v(\tau_0)) , \tag{8.3}$$

with τ_0 chosen such that the contribution function of the line is approximately zero there. $v_0 = v(\tau_0)$ is an arbitrary constant velocity as far as the asymmetry is concerned. Note, however, that this is not true for B_0 [if we write in analogy to Eq. (8.3): $B(\tau) = B_0 + B_1(\tau)$], since the magnetic field affects the line profile in a completely different manner.

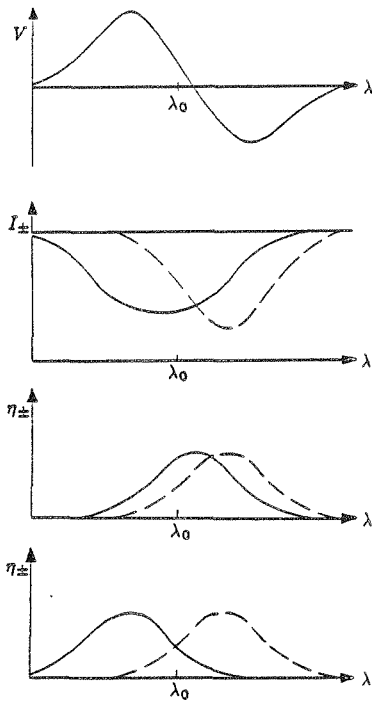

Fig. 8.11 Bottom frame: $\eta_\pm$ (absorption coefficients for right and left circularly polarized light) deep in the atmosphere. Second lowest frame: $\eta_\pm$ higher in the atmosphere. Third lowest frame: $I_\pm$, the emergent intensity profiles for the two polarizations. Topmost frame: $V = I_+ - I_-$.

Fig. 8.11 also illustrates another simple point. Near disk centre for all but the very strongest lines the observed asymmetry is always such that the blue wing of Stokes V dominates over its red wing, i.e. $\delta a > 0$ and $\delta A > 0$. In order to reproduce the the sign of δA correctly,

$$\frac{\mathrm{d}|B(\tau)|}{\mathrm{d}\tau}\frac{\mathrm{d}v(\tau)}{\mathrm{d}\tau} < 0 \tag{8.4}$$

must be true in the region of the formation of these lines at disk centre. The fact that only the absolute value of $B(\tau)$ is important, while the sign of $v(\tau)$ also plays a role is again due to the different ways in which v and B affect the line profile.

Eq. (8.4) has some straightforward, but interesting consequences. If $\mathrm{d}|B(\tau)|/\mathrm{d}\tau > 0$ (i.e. magnetic field strength *decreasing* with geometrical *height*), then for a downflow the velocity must decrease with τ, while for an upflow it must increase with τ. In the former case we expect the resulting Stokes V profile to be in general redshifted, while in the latter case we commonly expect a blueshift. Of course, it is always possible to choose v_0 in Eq. (8.3) such that the emergent line profile shows no shift relative to its rest wavelength. However, if we want to interpret $v(\tau)$ as a stationary flow inside fluxtubes then we must require that the sign of v does not change at any height in the fluxtube photosphere. Since the possible $v_1(\tau)$ values are constrained by the observed asymmetry, this additional condition greatly limits the choice of v_0. Thus it may no longer be possible to reproduce both the observed profile shape and zero-crossing shift with a stationary flow. In the next section we present the results of some model calculations which test this point. In order not to be unduly restrictive we shall also accept $v(\tau)$ functions which retain their sign only over the height range over which the calculated lines show any sensitivity to the velocity.

The crude model presented above suggests that very weak lines, with their absence of saturation, should have Stokes V profiles with disappearing area asymmetry. This can be proved analytically for the model of Auer and Heasley (1978), which assumes a static Milne-Eddington atmosphere with constant field strength B overlain by a thin moving layer with the same field strength and the velocity v.

In the notation of chapter 2, and using the expression for the unnormalised Stokes V profile in a Milne-Eddington atmosphere, we obtain for the (unnormalised) V profile emerging from the underlying static layer (if we neglect magnetooptical effects; cf. Eq. 2.66)

$$V = -\frac{B_{\nu_0}\beta_0\mu}{D}\eta_V(0), \tag{8.5}$$

where $\eta_V(0)$ is the absorption coefficient for a static atmosphere (i.e. with stationary velocity, $v = 0$), and

$$D = (1+\eta_I(0))^2 - \eta_Q^2(0) - \eta_U^2(0) - \eta_V^2(0). \tag{8.6}$$

The linearised change in the V profile caused by the thin moving layer is

$$\Delta V = \frac{\Delta\tau B_{\nu_0}\beta_0}{D}\left(\eta_V(v)\left(1-\frac{D}{\beta_0\mu}\right) + \eta_V(v)\eta_I(0) - \eta_V(0) - \eta_V(0)\eta_I(v)\right), \tag{8.7}$$

where $\eta_V(v)$ and $\eta_I(v)$ represent the line absorption coefficients in the moving layer of velocity v. The final emergent profile is then

$$V_{\rm tot} = V + \Delta V = \frac{\Delta\tau B_{\nu_0}\beta_0}{D}\left(\eta_V(v)\left(1-\frac{D}{\beta_0\mu}\right) + \eta_V(v)\eta_I(0) - \eta_V(0)\eta_I(v) - \eta_V(0)\left(1+\frac{\mu}{\Delta\tau}\right)\right). \tag{8.8}$$

For a very weak line with $\eta_I \ll 1$ and $\eta_V \ll 1$ we have $D \approx 1$, $\eta_V(v)\eta_I(0) \ll \eta_V(v)$, and $\eta_V(0)\eta_I(v) \ll \eta_V(0)$, so that Eq. (8.8) reduces to

$$V_{\rm tot} = \Delta\tau B_{\nu_0}\beta_0\left(\eta_V(v)\left(1-\frac{1}{\beta_0\mu}\right) - \eta_V(0)\left(1+\frac{\mu}{\Delta\tau}\right)\right). \tag{8.9}$$

The emergent V profile is therefore a sum of two profiles which are antisymmetric about $x = \lambda - \lambda_0 = 0$ and $x = v$, respectively. Although the profile shape need not be antisymmetric, it will not exhibit any *area* asymmetry, since it is the sum of antisymmetric profiles (cf. Sect. 2.4.2).

In view of this result we would expect in Fig. 8.4 the weak lines to show no asymmetry. This does not appear to be the case in this figure, but we hasten to add that the scatter is very large for the smallest lines (in particular in the relative asymmetry, because we divide by the small area) and not too much weight should be given to those lines in this figure. Compare also with Fig. 8.3b, where this scatter is directly visible and the small offset of the mean curve at $S_I = 0$ is brought into relation.

It follows from the above discussion, that according to this model, the Stokes V area asymmetry is due to a combination of Zeeman splitting, saturation, and velocity gradient. This is in contrast to the σ-π area asymmetry of Stokes Q (Sect. 4.2.3), which is a result of Zeeman splitting and saturation alone.

8.4.3. Test Calculations of Stokes V Asymmetry Using Stationary Flows

In this and the following section we present numerical calculations of Stokes V profiles including their asymmetry. Initially, we investigate the diagnostic contents of the Stokes V asymmetry and see how well the simple picture presented in the last section compares to the results of numerical radiative transfer calculations. Later we quantitatively test the hypothesis that the observed Stokes V asymmetry is caused by stationary downflows inside fluxtubes by comparing the numerical results with the data. All calculations have been performed at disk centre assuming vertical fluxtubes. Only one line of sight along the fluxtube axis has been considered (i.e. $\gamma = 0°$).

Restricting $B(\tau)$ and $v(\tau)$ to functions linear in τ, we have tested how the asymmetry of a line is influenced by its strength, excitation potential, and Zeeman splitting. Constant B and v gradients are chosen, since lines of different strengths and excitation potentials are formed at different heights in the atmosphere and this choice makes certain that all lines are treated approximately equally. In the following we list some of the results.

- We find that δA always has the signs predicted by Eq. (8.4) in Sect. 8.4.2 for both up- and downflows.
- Whereas δA is always positive for $\mathrm{d}|B|/\mathrm{d}\tau > 0$ and $\mathrm{d}v/\mathrm{d}\tau < 0$, δa can be either positive or negative. Its value depends on the exact velocity gradient and on the spectral line. Thus for diagnostic purposes δA is better for determining the outline of the velocity structure, while the amplitude, is more sensitive to the details.
- δA is only weakly dependent on the Landé factor for the cases we have tested. Lines, with otherwise equal properties and with Landé factors ranging from 0.5 to 3.0 have been tested. This also suggests that the absolute value of B is not of dominating importance. It is possible that the last result is an artifact of the limited number of model calculations.
- δa is somewhat dependent on Landé factor, although the dependence is not clearly defined for the models we have calculated.
- The area asymmetry increases strongly with the amount of saturation in the line. For lines of equal excitation potential, this means that δA increases rapidly with increasing S_I. This result is in agreement with the discussion of Sect. 8.4.2.
- δa also shows an increasing tendency to become positive as the amount of saturation increases, but this trend is less clear cut.
- For a given line and an otherwise unchanged atmosphere, an increase in temperature leads to a decrease in the calculated asymmetry of that line. This effect is small for Fe II lines and markedly larger for Fe I. It increases dramatically with *decreasing* excitation potential (for lines of equal strength in the original atmosphere), and is mainly due to the temperature weakening and the associated decrease in saturation of the lines.
- The shapes of the lines calculated with linear $v(\tau)$ are not in the least similar to the observations, even if we use a $B(\tau)$ calculated via the thin tube approximation. For example synthetic Fe I 5250.2 Å profiles have $\delta A > 0$ but $\delta a < 0$, while the observations show that both δA and δa are positive.

8.4.4. Comparison With Observations

In this section we attempt to match spectral lines calculated with a model containing a stationary downflow to the data. We have tried to simultaneously reproduce the asymmetry of four lines selected from Table 4.4, namely Fe I 5250.2 Å, 5127.7 Å, 5083.3 Å, and Fe II 5197.6 Å. The first three are low χ_e Fe I lines with strongly different S_I values, while 5197.6 Å is an Fe II line slightly stronger than 5250.2 Å. We use a number of temperature models: the plage and network models derived in chapter 5, a model with $T(\tau)$ similar to that of Chapman (1979), and models with $T = T_{\mathrm{HSRA}} + \Delta T$, where $\Delta T = 400$ K and 800 K, and $\Delta T \neq \Delta T(\tau)$. Initially we chose the magnetic field as calculated with the thin tube approximation, with $B(\tau = 1) = 2000$ G, as suggested by the results of chapter 6. Later $B(\tau)$ was allowed to be specified freely in an attempt to reproduce the lines better. No constraints have been placed on the $v(\tau)$ structure throughout. We first determined $v(\tau)$ [and later also $B(\tau)$] by trying to reproduce one particular line profile, usually Fe I 5250.2 Å, and then calculated the other profiles with the same atmosphere and velocity structure.

In Fig. 8.12 we have plotted the observed and calculated profiles of the four selected lines. The observations were obtained in an active region plage (FTS4) and the calculations were made using the plage temperature model derived in chapter 5. Since we are at the moment only interested in the line shape, the synthetic profiles have been shifted and multiplied by factors to make them match the data.

Although 5127.7 Å can be reproduced reasonably well simultaneously with 5250.2 Å, the synthetic 5083.3 Å profile does not fit the data at all. While the calculated values of the relative area asymmetry, $\delta A(5127) = 0.7\%$, $\delta A(5250) = 5.1\%$, and $\delta A(5083) = 28.1\%$, increase steadily with line strength, in accordance with the results of the test calculations of Sect. 8.4.3, this is not true for the observed values, with $\delta A(5127) = -1.8\%$, $\delta A(5250) = 5.3\%$, and $\delta A(5083) = 5.2\%$. The δA of the calculated profiles of 5250.2 Å and 5127.7 Å lie within the error in the data, but the observed profiles of 5250.2 Å and 5083.3 Å have approximately equal relative asymmetry which leads to a mis-match between the data and the calculations because the observed asymmetry does not increase steadily with line strength as the model requires. The relative behaviour of these lines is similar for the other tested models as well, none of which reproduces the data better.

We also tried improving the fit to 5083.3 Å alone, but the fit to 5250.2 Å then begins to deteriorate. Only 5127.7 Å remains almost unchanged, due to its relative insensitivity to velocity gradients. Actually, 5083.3 Å poses considerable problems by itself, since the shape of its complete V profile is very difficult to reproduce. In

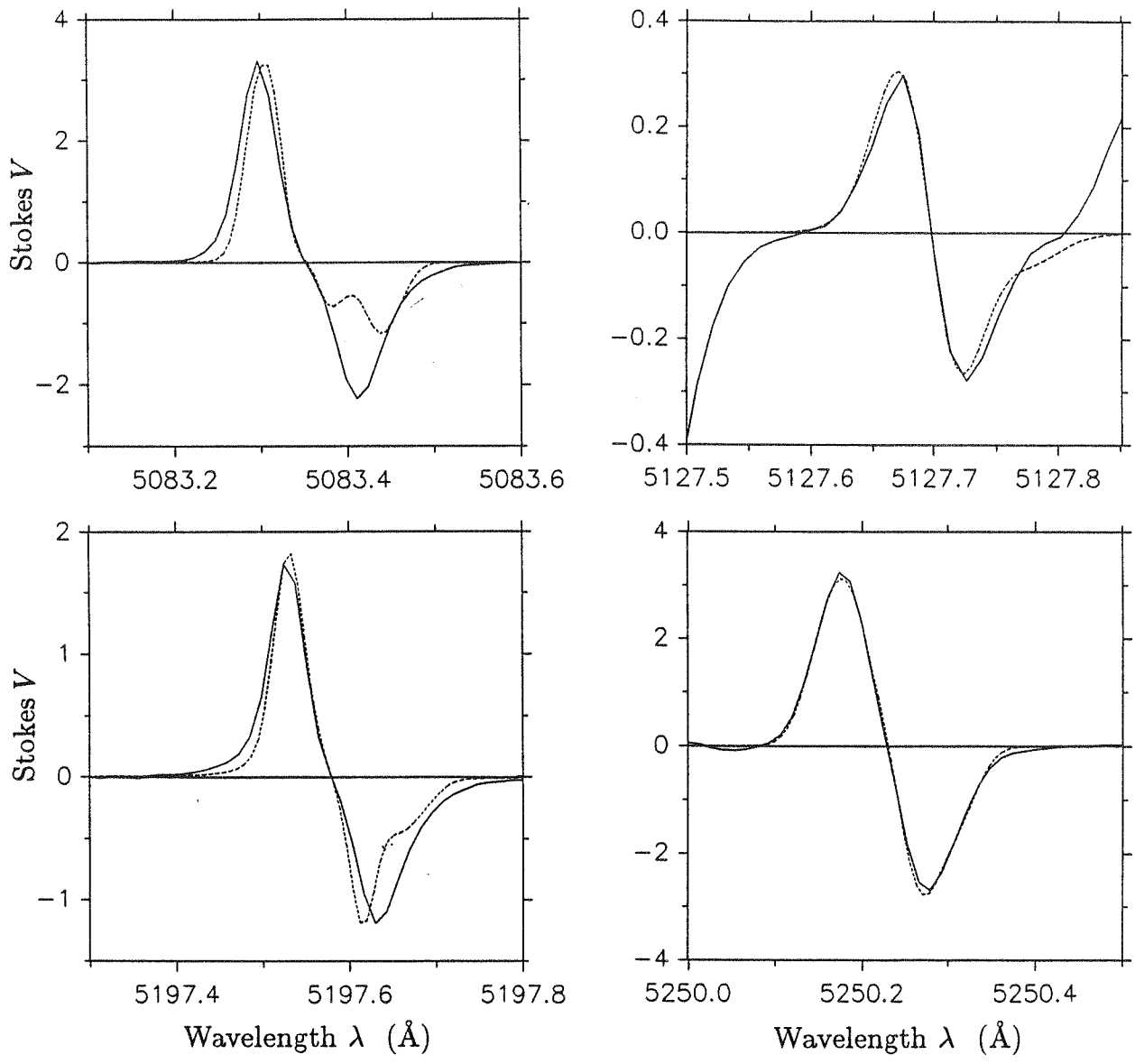

Fig. 8.12 Profiles of Fe I 5083.3 Å, Fe I 5127.7 Å, Fe II 5197.7 Å, and Fe I 5250.2 Å, as observed in an active plage (solid curves) and calculated (dashed curves) using a stationary downflow, which is chosen such that the Fe I 5250.2 Å profile is reproduced. The calculated profiles have been shifted and normalised to the observations.

order to check whether this problem is due to a hidden blend, or some other peculiarity of this particular line, we have also briefly used the Fe I 5127.3 Å line, which has an excitation potential and line strength similar to 5083.3 Å. However, 5127.3 Å also exhibits the same problems.

The difficulty is due to the fact that the observed asymmetry of the strong low excitation lines requires the presence of relatively small velocity gradients, while, at the same time, these lines are also considerably velocity broadened (chapter 7). In fact, such lines have nearly the largest velocity broadening of all the Fe I lines. Therefore, if a stationary flow with a small gradient is chosen as the only velocity in the fluxtube, then the line width cannot be reproduced. If, on the other hand, we try to reproduce the large width with only a velocity gradient, an immense value is required and the asymmetry becomes much too large.

A possible way out of this dilemma is to use a combination of stationary velocity with a small vertical gradient and a turbulence velocity, composed for example of a micro- and a macroturbulence. The former produces the asymmetry, while the latter gives the line the required width. Although the resulting profile does not yet have the right shape, it is considerably closer to the observed profile than if any one of the mechanisms is used alone. Nonetheless a stationary flow inside the fluxtube cannot by itself account for the profile of Fe I 5083.3 Å.

When using the velocity derived by fitting Fe I 5250.2 Å to calculate Fe II 5197.6 Å we find that this line also has a too large asymmetry compared to the observed profile ($\delta A_{\rm calc} = 11.4\%$ for the plage model, while $\delta A_{\rm obs} = 4.4\%$), although the amplitude asymmetry is similar to the observed one (Fig. 8.12). The factor of two larger asymmetry of the calculated Fe II 5197.6 Å line profile compared to that of Fe I 5250.2 Å is mainly due to the fact that the former is considerably less weakened by the higher temperature of the fluxtube model.

We have also observed that all the good fits to the shape of Fe I 5250.2 Å, involving only a stationary downflow, have a zero-crossing wavelength shifted towards the red by a value greater than approximately 0.9 km sec^{-1}. A shift is induced by the requirement that the velocity must retain the same sign over the whole photosphere. Note that we reduce the shift to a minimum by setting $v = 0$ just below the height at which the line starts to become sensitive to the velocity gradient. This choice is somewhat unrealistic since, due to mass conservation, the velocity cannot disappear completely. Therefore, the observational constraint that the Stokes V zero-crossing shift is less than 0.25 km sec^{-1} (chapter 7) also speaks strongly against a purely stationary flow being the source of the Stokes V asymmetry. The argument that, since asymmetry and zero-crossing shift of 5250.2 Å cannot be reproduced simultaneously by stationary flows, these cannot be the main cause of Stokes V asymmetry in fluxtubes has been invoked earlier by Pahlke and Solanki (1986).

The zero-crossing shift can be reduced still further if we use a turbulence velocity to produce a part of the line broadening. Thus by broadening the 5250.2 Å line with a mixture of micro- and macroturbulence of amplitude $\sqrt{\xi_{\rm mic}^2 + \xi_{\rm mac}^2} \approx 1.5$–$2.0$ km sec^{-1} we have been able to obtain a zero-crossing shift as small as 0.4–0.5 km sec^{-1}, which is considerably closer to the upper bound of 0.25 km sec^{-1} set by the observations in chapter 7. However, the additional turbulent velocity implies that we no longer have a pure downflow.

Finally, if we accept that the temperature in the network is higher than in the plage (as suggested by the analysis of chapter 5), we have the paradoxical situation that the higher temperature leads to smaller asymmetries of the synthetic profiles in the network for a given velocity and magnetic field structure, but the observed asymmetries can be considerably larger than in the plage. Thus, we have been able to reproduce the observed network profile of 5250.2 Å with the network model of chapter 5 only by increasing both the velocity and the magnetic field gradients significantly.

8.5. Conclusions

In the present chapter we have presented extensive observational evidence for Stokes V asymmetry, a brief overview of the various mechanisms proposed to produce it, and a detailed discussion, including model calculations, of the simplest of these mechanisms involving a stationary flow with a height gradient inside the fluxtubes. A comparison of the calculated profiles to the observations highlights the limitations of this mechanism. The following three arguments summarize the case against a stationary flow as the sole responsible agent for the observed asymmetry.

- We are unable to reproduce the profiles (δA values) of e.g. Fe I 5250.2 Å and Fe I 5083.3 Å, or Fe I 5250.2 Å and Fe II 5197.6 Å simultaneously.
- We are unable to reproduce the asymmetry and the line-width of Fe I 5083.3 Å simultaneously.
- We are unable to reproduce the asymmetry and the zero-crossing shift of Fe I 5250.2 Å simultaneously.

We therefore conclude that *stationary* flows inside fluxtubes are not the main contributors to the asymmetry in the Stokes V profiles. This result is indirectly supported by the calculations of Ribes et al. (1985) who have calculated line profiles for the theoretical fluxtube models of Unno and Ribes (1979) which contain stationary downflows. The resulting profiles also do not match the data at all.

Do these arguments imply that velocities are ruled out as the source of V asymmetry altogether? We believe not. Firstly, there is the indirect empirical evidence for a connection between asymmetry and velocity broadening presented in Sect. 8.4.2. Secondly, as the detailed modelling in chapters 5 and 7 has shown, large amplitude mass motions are present in fluxtubes, which broaden the lines considerably, but do not significantly shift them. Due to the strong vertical (and, for a small fluxtube, also horizontal) stratification, gradients in velocity and magnetic field along the line of sight are bound to occur. Thus the velocity will automatically tend to produce some asymmetry in the line profiles. However, the velocity structure will be considerably more involved than the simple $v(\tau)$ profiles considered here. For the purposes of empirical modelling it may be represented as the sum of many individual (stationary) $v(\tau)$, so that Stokes V profiles calculated for a large number of $v(\tau)$ will have to be summed up to give a resultant which can be compared to the observations. One problem with this approach

is the large number of free parameters which makes a purely empirical analysis impractical and requires that a physically self-consistent and dynamical model of fluxtubes be used. This is beyond the scope of the present investigation.

The assumptions made in the present work, one line of sight with a stationary velocity, are quite restrictive. Thus it is possible that in reality velocities outside the fluxtube also play a role in producing the asymmetry. We conclude that, although stationary flows inside fluxtubes can, to our mind, be ruled out as the dominating source of Stokes V asymmetry, the broader question of whether velocity is the main source of δA, or if the optical pumping mechanism of Kemp et al. (1984) plays the major role still cannot be decided at present.

9. An Expansion Model

9.1. Introduction

A rich literature exists on theoretical models of small magnetic fluxtubes. A variety of approaches and approximations for determining the magnetic structure of a fluxtube with height have been tried, some of which are listed below. Many models employ the so-called "thin tube approximation" or "slender tube approximation", where the internal magnetic field, pressure, temperature etc. are assumed to be uniform across the cross-section. The magnetic field is also supposed to be purely axial and unrestrained by tension forces. Examples of such models are given by Parker (1955, 1979, 1982a, b), Defouw (1976), Roberts and Webb (1978, 1979), Unno and Ribes (1979), Meyer et al. (1979), Spruit (1981a, b), Hasan and Schüssler (1985), Ferrari et al. (1985), and Kalkofen et al. (1986) among many others. Such models have been used to investigate mass motions in fluxtubes, their stability, and possible heating mechanisms. Most empirical models of small fluxtubes are also of this type including the ones presented in this thesis. Potential and force-free field models of small fluxtubes have been constructed by Spruit (1976), Browning and Priest (1982, 1983), Simon et al. (1983), and Van Ballegooijen (1985a). Van Ballegooijen has also calculated Stokes profiles in such models, while Caccin and Severino (1979) have determined the continuum signature of Spruit's model. A further class of models has been introduced by Schlüter and Temesvary (1958) and is based on the so-called similarity assumption, where the magnetic field is assumed to have a cross-sectional shape independent of height. Self-similar models of small fluxtubes have been calculated by Wilson (1977a, b), Solanki (1982), and Osherovich et al. (1983). Chapman and Gingell (1984) have calculated the continuum contrast of the last named of these models. Deinzer et al. (1983, 1984a, b) have published fully self-consistent MHD models in two dimensional slab geometry (including an energy equation and the effects of the fluxtube on its surroundings), while Knölker et al. (1985, 1987) have used the same method to calculate slightly thicker tubes. Steiner et al. (1986) have calculated models of small fluxtubes based on the self-consistent method of Pneuman and Kopp (1971), including a current sheet. Finally, Nordlund (1983, 1985, 1986) has presented dynamical 3-D fluxtube models. Schüssler (1987) has compared some of these theoretical models with the observations in detail.

In this chapter a theoretical model is presented which includes the effects of magnetic tension, but which, at the same time, is simple enough to serve as the basis of future empirical analyses of fluxtube properties. The radiative transfer calculations of Van Ballegooijen (1985a, b) suggest that the geometry of fluxtubes is quite important for the spectrum, and a (simple) 2-D model is therefore required to carry out such calculations. This has been confirmed by De Martino (1986) and Solanki and De Martino (in preparation). This model also serves to study another effect, which has so far received only little attention, namely the merging of fluxtubes. We expect that any discrete set of fluxtubes will merge into larger field distributions if we go high enough into the atmosphere, since an unobstructed fluxtube will expand indefinitely with height.

The merging problem has so far been considered consistently only for entire network and plage regions, under the assumption of a potential field (Gabriel, 1976; Anzer and Galloway, 1983a, b). Spruit (1984) has studied the effect of fluxtube merging on wave amplitudes, but does not calculate the merging height self-consistently. We wish to investigate the structure and merging of individual small fluxtubes instead of the behaviour of whole ensembles of them, and also to attack the problem from an MHD standpoint. Since both the thin tube approximation and the similarity assumption lead to problems (no internal structure for the thin tube approximation, fixed horizontal variation of the magnetic field for similarity theory which is incompatible with the merging of fluxtubes), and a full MHD solution is too extensive for our later requirement of a model with which to empirically determine fluxtube properties, we use an expansion technique to solve the MHD equations.

The MHD equations are expanded in a power series about the axis of the fluxtube. The zero-th order solution is then the thin tube approximation, and higher order terms take into account the finite width of the fluxtube. We shall solve the equations to second order. A similar expansion approach has been suggested by Browning and Priest (1982, 1983). This chapter is based on the work of Pneuman et al. (1986).

9.2. Basic Equations

If we neglect the transport of energy, then a magnetised gas with infinite conductivity (and a magnetic permeability of 1) in an external constant gravitational field can be described in the MHD approximation by the equation of continuity, divergence freedom of $\mathbf{B}$, the momentum transport equation, and the equation of state of an ideal gas

$$\frac{\partial \rho}{\partial t} + \nabla(\rho \mathbf{v}) = 0, \tag{9.1}$$

$$\nabla \mathbf{B} = 0, \tag{9.2}$$

$$\rho \frac{\mathrm{d}\mathbf{v}}{\mathrm{dt}} = \rho g - \nabla P + \frac{1}{4\pi}(\nabla \times \mathbf{B}) \times \mathbf{B} + \mathbf{F}, \tag{9.3}$$

$$P = \rho \mathcal{R} T / m_{\mathrm{p}}, \tag{9.4}$$

where ρ is the density, $\mathbf{v}$ the velocity vector, $\mathbf{B}$ the magnetic field vector, g the acceleration due to gravity, $\mathbf{F}$ the vector of the viscous force per unit volume, P the gas pressure, $\mathcal{R}$ the universal gas constant, and m_p the mean particle mass.

For the stationary structure of a solar magnetic fluxtube in the absence of flows (cf. Sect. 7.2) we need use only the magnetohydrostatic approximation, and the above set of equations reduces to

$$\nabla \mathbf{B} = 0, \tag{9.5}$$

$$\nabla P = \frac{1}{4\pi}(\nabla \times \mathbf{B}) \times \mathbf{B} + \rho g, \tag{9.6}$$

$$P = \rho \mathcal{R} T / m_{\mathrm{p}}. \tag{9.7}$$

We now assume that the fluxtube is rotationally symmetric around the vertical z-axis, i.e. we reduce the problem to two dimensions. Let r, θ, and z be ordinary cylindrical coordinates. In this geometry Eqs. (9.5) to (9.7) become

$$4\pi \frac{\partial P}{\partial r} = B_z \left(\frac{\partial B_r}{\partial z} - \frac{\partial B_z}{\partial r} \right) - \frac{B_\theta}{r} \frac{\partial}{\partial r}(r B_\theta), \tag{9.8}$$

$$0 = \frac{B_r}{r} \frac{\partial}{\partial r}(r B_\theta) + B_z \frac{\partial B_\theta}{\partial z}, \tag{9.9}$$

$$4\pi \left(\frac{\partial P}{\partial z} + \frac{P}{H} \right) = -B_r \left(\frac{\partial B_r}{\partial z} - \frac{\partial B_z}{\partial r} \right) - B_\theta \frac{\partial B_\theta}{\partial z}, \tag{9.10}$$

$$0 = \frac{1}{r} \frac{\partial}{\partial r}(r B_r) + \frac{\partial B_z}{\partial z}, \tag{9.11}$$

where B_r, B_θ, and B_z are the three compontents of the magnetic field, and H the scale height defined by

$$H(z) = \frac{k T(z) R_\odot^2}{G m_p M_\odot}, \tag{9.12}$$

k being Boltzmann's constant, T the temperature, $R_\odot$ the solar radius, G the gravitational constant, and $M_\odot$ the solar mass. Fig. 9.1 illustrates some of the basic quantities.

Further calculations are simplified by transforming Eqs. (9.8)–(9.11) into non-dimensional form. To this end we define the following non-dimensional quantities

$$x = r/H^*, \tag{9.13}$$

$$y = z/H^*, \tag{9.14}$$

$$\mathbf{b} = \mathbf{B}/B^*, \tag{9.15}$$

$$p = P/P^*, \tag{9.16}$$

$$\sigma = T/T^*, \tag{9.17}$$

where B^*, P^*, and T^* are the values of B, P, and T at the reference height $z = 0$ on the axis of the fluxtube (Fig. 9.1), and

$$H^* = \frac{k T^* R_\odot^2}{G m_p M_\odot}. \tag{9.18}$$

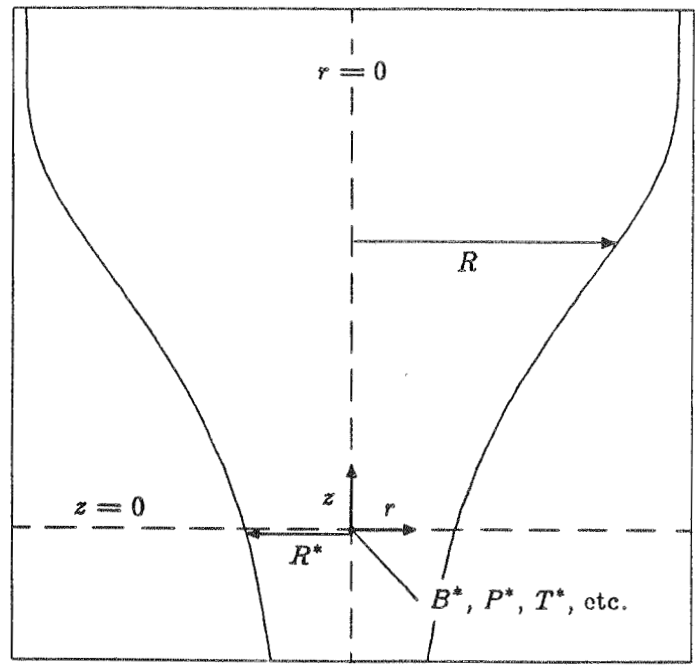

Fig. 9.1 Schematic of fluxtube geometry showing pertinent definitions.

Eqs. (9.8)–(9.11) then become

$$\beta\frac{\partial p}{\partial x} = b_z\left(\frac{\partial b_r}{\partial y} - \frac{\partial b_z}{\partial x}\right) - \frac{b_\theta}{x}\frac{\partial}{\partial x}(xb_\theta), \tag{9.19}$$

$$0 = \frac{b_r}{x}\frac{\partial}{\partial x}(xb_\theta) + b_z\frac{\partial b_\theta}{\partial y}, \tag{9.20}$$

$$\beta\left(\frac{\partial p}{\partial y} + \frac{p}{\sigma}\right) = -b_r\left(\frac{\partial b_r}{\partial y} - \frac{\partial b_z}{\partial x}\right) - b_\theta\frac{\partial b_\theta}{\partial y}, \tag{9.21}$$

$$0 = \frac{1}{x}\frac{\partial}{\partial x}(xb_r) + \frac{\partial b_z}{\partial y}, \tag{9.22}$$

where

$$\beta = 4\pi\frac{p^*}{b^{*2}}. \tag{9.23}$$

We now expand all variables in a power series in x.

$$b_z = h_0 + h_2x^2 + h_4x^4 + \cdots, \tag{9.24}$$

$$b_r = f_1x + f_3x^3 + \cdots, \tag{9.25}$$

$$b_\theta = g_1x + g_3x^3 + \cdots. \tag{9.26}$$

We express b_z by an even series in x, while b_r and b_θ are given by odd series. This is consistent with power series expansions of potential fields and analytical force free fields (cf. Ferraro and Plumpton, 1966). For p and σ expansions containing only even terms are used as well, as suggested by the form of the Eqs. (9.19)–(9.22).

$$p = p_0 + p_2x^2 + p_4x^4 + \cdots, \tag{9.27}$$

$$\sigma = \sigma_0 + \sigma_2x^2 + \sigma_4x^4 + \cdots. \tag{9.28}$$

The gas density can be determined via the ideal gas equation (9.7) and need not concern us further in this chapter.† Now Equations (9.19) – (9.22) assume the form

$$\begin{aligned} 2\beta(p_2 + 2p_4x^2 + \cdots) = (h_0 + h_2x^2 + \cdots)\left((f_1' + f_3'x^2 + \cdots) - (2h_2 + 4h_4x^2 + \cdots)\right) \\ - (g_1 + g_3x^2 + \cdots)(2g_1 + 4g_3x^2 + \cdots), \end{aligned} \tag{9.29}$$

† It is not required for radiative transfer calculations either.

$$0 = 2(f_1 + f_3x^2 + \cdots)(g_1 + 2g_3x^2 + \cdots) + (h_0 + h_2x^2 + \cdots)(g_1' + g_3'x^2 + \cdots), \tag{9.30}$$

$$\begin{aligned}\beta\big((\sigma_0 + \sigma_2x^2 + \cdots)(p_0' + p_2'x^2 + \cdots) + (p_0 + p_2x^2 + \cdots)\big) \\ = (\sigma_0 + \sigma_2x^2 + \cdots)\Big(-(f_1x + f_3x^3 + \cdots)\big((f_1'x + f_3'x^3 + \cdots) \\ - (2h_2x + h_4x^3 + \cdots)\big) - (g_1x + g_3x^3 + \cdots)(g_1'x + g_3'x^3 + \cdots)\Big),\end{aligned} \tag{9.31}$$

$$0 = (2f_1 + 4f_3x^2 + \cdots) + (h_0' + h_2'x^2 + \cdots), \tag{9.32}$$

where the prime denotes differentiation with respect to y. Equating equal powers of x up through terms of $O(x^2)$ yields,

x^0 terms:

$$\sigma_0p_0' + p_0 = 0, \tag{9.33}$$

$$h_0(f_1' - 2h_2) - 2g_1^2 = 2\beta p_2, \tag{9.34}$$

$$2f_1g_1 + h_0g_1' = 0, \tag{9.35}$$

$$2f_1 + h_0' = 0. \tag{9.36}$$

x^2 terms:

$$\beta(\sigma_0p_2' + \sigma_2p_0' + p_2) = -\sigma_0f_1(f_1' - 2h_2), \tag{9.37}$$

$$h_0(f_3' - 4h_4) + h_2(f_1' - 2h_2) - 6g_1g_3 = 4\beta p_4, \tag{9.38}$$

$$4f_1g_3 + 2g_1f_3 + h_0g_3' + h_2g_1' = 0, \tag{9.39}$$

$$4f_3 + h_2' = 0. \tag{9.40}$$

In addition to these equations, the solution must also satisfy the boundary condition that the total pressure $P + B^2/8\pi$ does not change across the boundary (we assume a discrete boundary of the fluxtube)

$$(2\beta p + b^2)\big|_{x=a} = \Phi, \tag{9.41}$$

where

$$\Phi = (8\pi P_e + B_e^2)/B^{*2}. \tag{9.42}$$

P_e and B_e are the external gas pressure and magnetic field strength respectivley, and $a = R/H^*$ the non-dimensional radius of the tube. The external gas pressure P_e is not to be mistaken with the electron pressure denoted by the same symbol in other chapters of this thesis. Another condition for b_z is that the total amount of axial magnetic flux is conserved

$$\int_0^a b_z x\,\mathrm{d}x = \text{const.} \tag{9.43}$$

Expanding Eqs. (9.41) and (9.43) according to a (it being a special value of x) and retaining terms upto a^2 we obtain

$$(2\beta p_0 + h_0^2) + a^2(2\beta p_2 + f_1^2 + g_1^2 + 2h_0h_2) = \Phi, \tag{9.44}$$

$$h_0a^2 = a^{*2}, \tag{9.45}$$

where $a^* = R^*/H^*$.

Eq. (9.45) introduces as an additional unknown the radius of the tube $a(y)$. As remarked earlier, these calculations are carried out without an energy equation and instead the temperature is specified prior to solving the MHD equations, so that we need not consider σ_0 and σ_2 to be unknown variables. Keeping this in mind we have ten equations (9.33)–(9.40) and (9.44), (9.45) in the eleven unknowns p_0, p_2, p_4, h_0, h_2, h_4, f_1, f_3, g_1, g_1, and a. However, the variables p_4 and h_4 appear only in Eq. (9.38), so that by omitting this equation, we are left with nine equations for nine unknowns and have therefore got a closed system.

h_4 and p_4 can be determined from the other nine variables by using Eq. (9.38) and the equation resulting from the x^4 terms of Eq. (9.29), i.e.

$$\begin{aligned}\beta(\sigma_0 p_4' + p_4 + \sigma_2 p_2' + \sigma_4 p_0') = &-\sigma_0(f_1 f_3' - f_3 f_1' + 4 f_1 h_4 + 2 f_3 h_2) \\ &- \sigma_2(f_1 f_1' - 2 f_1 h_2) - \sigma_0(g_1 g_3' + g_3 g_1') - \sigma_2 g_1 g_1'.\end{aligned} \tag{9.46}$$

This procedure, although not completely self-consistent, will be used later to check whether p_4 and h_4 are small enough to ensure the validity of our solution.

We can rewrite our set of equations in such a way that p_0, f_1, g_1, p_2, h_2, and a are expressed in terms of h_0 and the prescribed temperature σ_0 and σ_2 alone. Thus

$$p_0 = \exp\left(-\int_0^y \frac{\mathrm{d}y}{\sigma_0}\right), \tag{9.47}$$

$$f_1 = -\frac{h_0'}{2}, \tag{9.48}$$

$$g_1 = g_1^* h_0, \tag{9.49}$$

$$p_2 = h_0\left(p_2^* + \int_0^y \frac{\sigma_2}{\sigma_0^2 h_0}\,\mathrm{d}y\right)\exp\left(-\int_0^y \frac{\mathrm{d}y}{\sigma_0}\right), \tag{9.50}$$

$$h_2 = -\frac{1}{4}h_0'' - g_1^{*2} h_0 - \beta\left(p_2^* + \int_0^y \frac{\sigma_2}{\sigma_0^2 h_0}\,\mathrm{d}y\right)\exp\left(-\int_0^y \frac{\mathrm{d}y}{\sigma_0}\right), \tag{9.51}$$

$$a = \frac{a^*}{\sqrt{h_0}}. \tag{9.52}$$

Furthermore, we express f_3 and g_3 as functions of h_0 and h_2. Using Eq. (9.51) it is possible to write f_3 and g_3 in terms of only one unknown, namely h_0, but the resulting expressions are complex and do not offer any new insight.

$$f_3 = -\frac{1}{4}h_2', \tag{9.53}$$

$$g_3 = h_0^2\left(g_3^* - \frac{g_1^*}{2}\int_0^y \frac{1}{h_0^3}(h_2' h_0 - 2 h_2 h_0')\,\mathrm{d}y\right). \tag{9.54}$$

It is, therefore, only necessary to determine h_0 in order to obtain all the unknowns. A differential equation for h_0 can be derived from the boundary condition Eq. (9.44). Let us first consider the case of a solitary fluxtube embedded in a non-magnetic atmosphere. By substituting Eqs. (9.47)–(9.52) into Eq. (9.44) we obtain

$$h_0'' - \frac{1}{2h_0}(h_0')^2 = \frac{2}{a^{*2}}\left(h_0^2\left(1 - \frac{\delta}{h_0}\right) + 2\beta p_0 - \frac{8\pi P_e}{B^{*2}}\right), \tag{9.55}$$

where $\delta = a^{*2} g_1^{*2}$. This is the only place where the twist of the magnetic field enters into this equation. If we take only the RHS of Eq. (9.55) and put it equal to zero, setting $\delta = 0$ as well (no initial twist), then we regain the well known thin tube approximation. In general, however, fluxtubes will be present in groups (e.g. in network elements or in active region plages) and will merge above a given height. If we have a collection of identical, vertical, and cylindrically symmetric fluxtubes which, at the reference level $y = 0$, occupy a fraction α of the area, then each of these tubes will expand with height and they will eventually merge with each other when their areas have increased by a factor $1/\alpha$. Since the internal fields of the individual fluxtubes become vertical and uniform near the height at which they merge, the breakdown in cylindrical symmetry around that level should not significantly affect our analysis. However, twisted fields have to be treated separately, since for them the field does not become vertical and uniform above any given height.

We model the merging as follows. The space between the fluxtubes is assumed to be filled with a small external seed field of magnitude B_e, which has a value B_e^* at the reference height $y = 0$. The conservation of flux relates B_e to the field strength along the fluxtube axis

$$B_e = B_e^* h_0\left(\frac{1-\alpha}{h_0 - \alpha}\right). \tag{9.56}$$

The filling factor α can be defined unambiguously in our model due to the sharp boundary. Recall that α is independent of y. It follows from Eq. (9.56) that B_e increases with height as the fluxtube expands. In particular, as the value of h_0 approaches α, B_e becomes large and mimics the effect of a neighbouring fluxtube by forcing the model tube to become straight. We wish to note that the seed field is used only as a convenient way of obtaining smooth merging. If it is chosen to be sufficiently small at the reference level its strength does not influence any of the properties of the solution such as the merging height, or the shape of the fluxtube (cf. Sect. 9.3.1).

Now, assuming the external magnetic field to have the form given by Eq. (9.56) we again carry out the substitutions made to derive Eq. (9.55) and obtain a second order non-linear differential equation for h_0,

$$h_0'' - \frac{1}{2h_0}(h_0')^2 = \frac{2}{a^{*2}}\left(h_0^2\left(1-\frac{\delta}{h_0}\right) + 2\beta p_0 - \frac{1}{B^{*2}}\left(8\pi P_e + B_e^{*2}h_0^2\left(\frac{1-\alpha}{h_0-\alpha}\right)^2\right)\right). \tag{9.57}$$

We solve this equation numerically. Before describing the method of solution and the results we first define the merging height and the external atmosphere to the fluxtube.

We consider the fluxtubes to be merged when the quantity h_0'/h_0 (a measure of how vertical the field is) becomes less than some small, arbitrary value. In practice we say the tubes are merged when

$$h_0'/h_0 \leq 0.05. \tag{9.58}$$

A short distance above this height the internal field of the fluxtube without twist (i.e. $\delta = 0$) becomes uniform ($h_2 \to 0$) and h_0 approaches the constant value

$$h_0 \approx \alpha + (1-\alpha)\frac{B_e^*}{B^*}. \tag{9.59}$$

The fluxtube is now vertical and straight, and in the limit of a vanishing seed field ($B_e^* \to 0$) its boundary lies immediately adjacent to that of its neighbours, so that the concept of individual fluxtubes loses its meaning for greater heights.

For specifying the external gas pressure, we will employ the HSRASP (cf. Sect. 4.5.1). We choose our reference level, $y = 0$, at the $\tau_{5000} = 1$ level of that model.

The actual numerical integration of Eq. (9.57) is carried out using the routine DGEAR of the IMSL (International Mathematics and Statistics Library), which is based on the backward differentiation formula method (cf. Gear, 1971, and Hindmarsh, 1974), an implicit linear multistep method. In order to carry out the integration we must specify h_0 and h_0' at $y = 0$. h_0 equals unity there by definition and h_0' is adjusted so as to make h_0 smoothly approach a constant value (given by the filling factor α) at large distances. Experience has shown that the solution of Eq. (9.57) is critically dependent on h_0'. Even slight changes cause the solution to diverge to either $+\infty$ or 0 at a finite value of y. Moreover, as we proceed to increasingly deeper layers ($y < 0$) we expect h_0 to approach the thin fluxtube solution to an ever closer degree. This means that wherever we choose our reference level to lie, the degree of depth in the physical atmosphere must be reflected in a relationship between the reference values on the right–hand–side of Equation (9.57). If the internal temperature is identical to the external temperature then, the deeper the reference level, the closer the right–hand–side initially must be to zero. This amounts to a relationship between P^*, B^*, P_e^*, B_e^*, and δ which reads

$$\Psi = 8\pi(P^* - P_e^*) - B_e^{*2} + (1-\delta)B^{*2} \approx 0 \tag{9.60}$$

if the reference level lies deep enough down in the atmosphere. Ψ is not *identically* zero because of radial variations in the base conditions. In practice, we use Equation (9.60) to determine P^*. The small difference in Ψ from zero is a weak function of a^* and is adjusted until a solution is found which is well behaved as y increases in the negative direction.

How does this approach compare to similarity theory? Major differences exist between our approach and models based on similarity theory, such as those of Schlüter and Temesvary (1958), Deinzer (1965), Yun (1970, 1971), Landman and Finn (1979), Solanki (1982), and Osherovich et al. (1983), even if we exclude the merging. The main difference results from the fact that similarity theory constrains the radial form of the magnetic field and pressure. The radial force balance can then be satisfied exactly, for any chosen temperature distribution, but the axial force balance can be achieved for only one particular horizontal temperature distribution. This

is of course unrealistic, since the horizontal temperature distribution is in general determined by the chosen energy equation. The expansion technique takes the opposite course. First the temperature is specified, either empirically or through an energy equation and then the radial variation of the field strength and pressure is calculated. As will be shown in Sect. 9.3, the field strength is found to be distinctly non-self-similar.

9.3. Discussion of Results

In Sects. 9.3.1 and 9.3.2 we study untwisted tubes, looking at the effects of twist separately in Sect. 9.3.3. Finally in Sect. 9.3.4 we compare our second order solution with the thin tube approximation and also try to estimate the significance of the fourth order terms. There are a number of free parameters in the model which can be varied. One of these is the temperature. Except for a few calculations we have kept the temperature fixed throughout this chapter, assuming the temperature inside the fluxtube to be the same as the temperature outside at equal geometrical depth (we keep $\sigma_2(y) = 0$). We might expect this to be not far from the truth when radiative coupling between the fluxtube and its surroundings is sufficiently efficient, and mechanical heating plays only a subordinate role.

9.3.1. Merging Height and Fluxtube Cross-Section

First let us examine the effect of the seed field on the fluxtube cross-section. Fig. 9.2 shows $R(z)$ for fluxtubes with different B_e^*/B^* values. If we choose the temperature as $\sigma_2(y) = 0$, $\sigma_0(y) = \sigma_{\mathrm{HSRA}}(y)$, then P^* follows directly from Eq. (9.60). In particular, in the limit of vanishing B_e^* the solution becomes independent of B^* and is determined only by a^* and α (as long as Eq. (9.60) is satisfied). We have chosen a radius of 100 km and a filling factor of 0.1. This filling factor lies between the lower values for network fields in quiet regions and the higher values corresponding to strong plages (chapter 6). The value for the radius is close to that given by Muller and Keil (1983) for facular points in continuum observations of the quiet Sun network. Since we keep the pressure uniform across the cross–section, the calculated fields are potential. As expected, the smaller the seed field strength, the closer the tube expands towards its theoretical limit

$$R_m = \sqrt{\frac{1}{\alpha}} R^*. \tag{9.61}$$

It appears from Fig. 9.2 that the merging height as defined by Eq. (9.58) is approximately independent of the strength of the seed field.

Spruit and Zwaan (1981) find that, in active regions, small fluxtubes exhibit a broad range of diameters ranging from below their best resolution up to 1.6″ (fluxtubes larger than this are seen as pores). We have therefore also studied the effect of fluxtube diameter on the merging height, although we have concentrated mostly on the so called facular elements, which according to Spruit and Zwaan (1981) have diameters $< 0.5''$. The cross-section variation and merging height for different values of R^* but a fixed filling factor of 10% is shown in Fig. 9.3. The dashed curve represents the locus of merging heights which, curiously, is essentially a linear function of R_m and, hence R^*. Since the filling factor is fixed, a larger value of R^* corresponds to fewer fluxtubes per unit surface area on the Sun. We see then that, the larger the fluxtubes, the higher the level above $\tau_{5000} = 1$ that they merge. The horizontal line in the figure represents the temperature minimum level of the HSRA which we shall consider to be the base of the chromosphere. Hence, unless the tubes are very thin (< 25 km), merging takes place in the chromosphere for this filling factor.

By combining the thin tube approximation with the conservation of magnetic flux in an isothermal external atmosphere, Spruit (1983) derived a simple expression for the merging height as a function of the other physical parameters. It reads

$$z_m = -H \ln \alpha, \tag{9.62}$$

where z_m is the merging height and H is the isothermal scale height. From the comparison of Eq. (9.61), which gives a merging height independent of R^*, with Fig. 9.3, shows that the merging height clearly increases with R^*, we conclude that the magnetic curvature forces have a significant influence on the merging height.

Next we vary α from 0.025 to 1 while keeping the radius R^* constant at 100 km. The resulting cross-sections are plotted in Fig. 9.4, with the merging height indicated by the dashed line. As expected, the merging height varies inversely with filling factor. The shape of this curve is approximately logarithmic in accordance with that

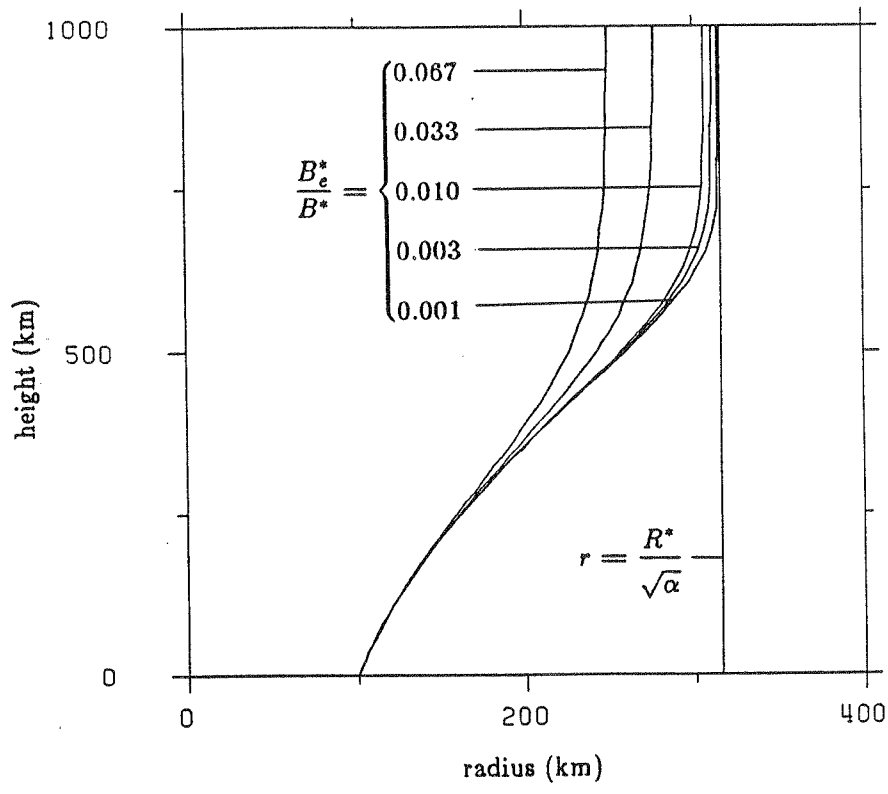

Fig. 9.2 Variation of the fluxtube cross-section with height for different values of the ratio of seed field strength (B_e^*) to the internal field strength (B^*). We have chosen an initial radius (R^*) of 100 km and a filling factor (α) of 0.1. The vertical line represents the radius for complete merging. We see that, as the seed field strength becomes infinitely small, the solution becomes essentially independent of its magnitude. Furthermore, the merging height is almost independent of the seed field strength.

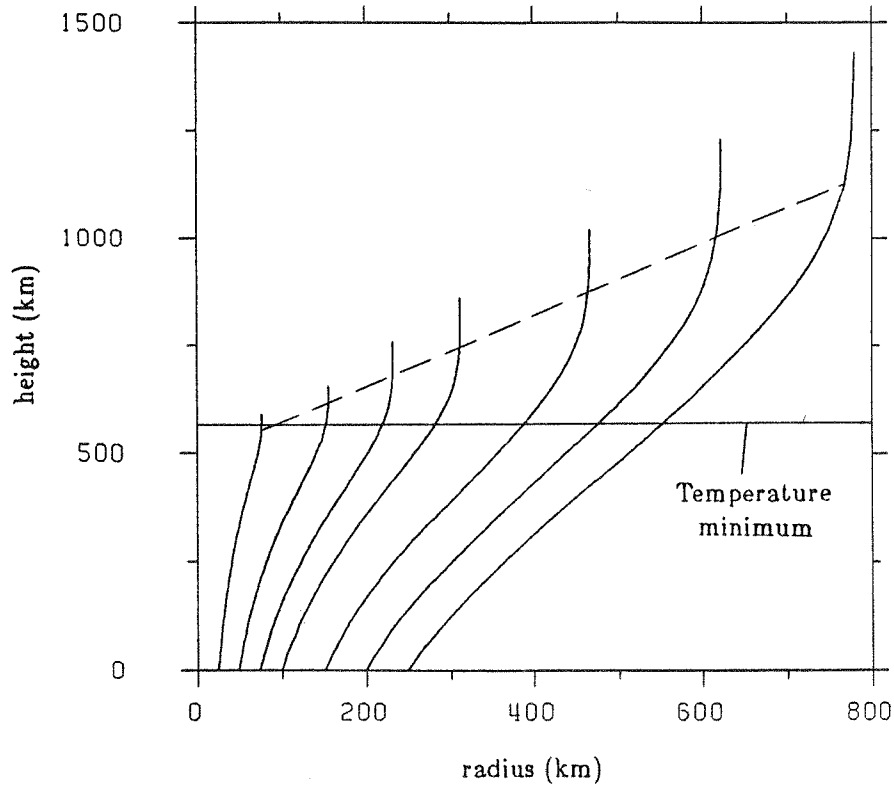

Fig. 9.3 Height variation of cross-section for different initial base diameters and a filling factor of 0.1. Here, larger base diameters correspond to fewer fluxtubes per unit volume. The horizontal line is the level of the temperature minimum and the dashed curve is the locus of the merging heights. Note that this curve is almost a straight line.

predicted by Equation (9.62), but the constant of proportionality between z_m and $\ln \alpha$ does not correspond to the appropriate scale height. For $\alpha < 0.1$, i.e., for network fields, the merging takes place in the chromosphere.

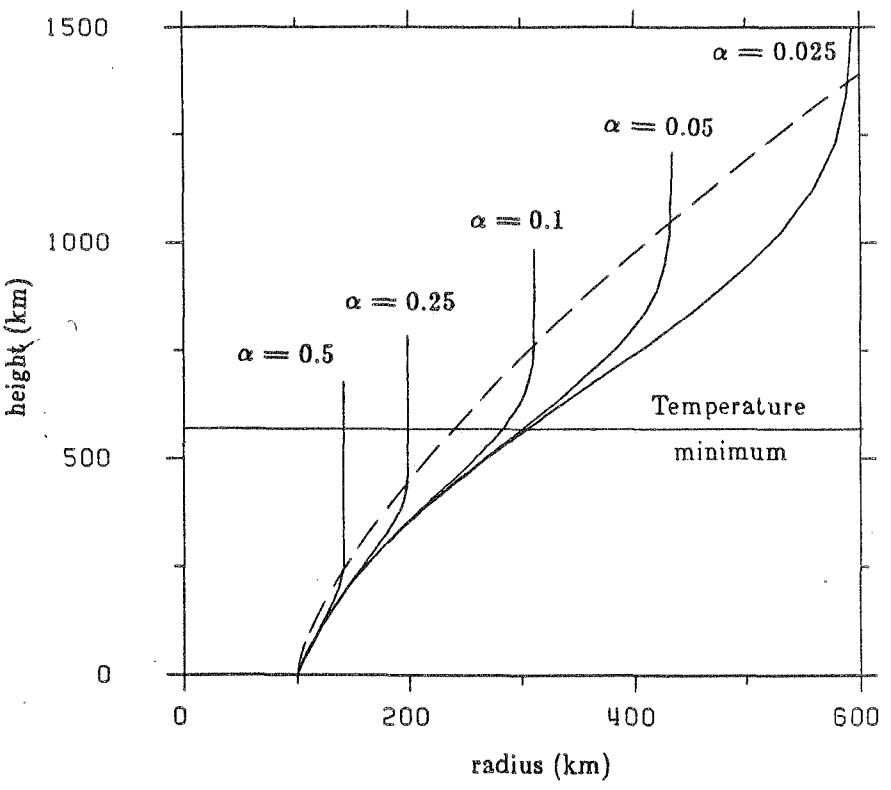

Fig. 9.4 Variation with height of the cross-section for a fixed base radius of 100 km and different values of the filling factor. As in Fig. 9.3, the dashed curve represents the locus of the merging heights.

In strong plages, however, the filling factor can be considerably larger and merging can occur in the photosphere.

Let us next vary the temperature inside the fluxtube. If the internal temperature differs from the external value, the merging height becomes dependent on B^*. We model the temperature difference in a crude manner, by supposing the ratio of the external (T_e) to internal (T_i) temperature to be a fixed value for all heights in the atmosphere (we also keep $\sigma_2 = 0$ throughout). Fig. 9.5 shows the merging height as a function of T_e/T_i for $B^* = 1300$, 1500, and 1700 G.

For $T_e/T_i < 1$, the merging height increases with increasing B^* whereas, for $T_e/T_i > 1$, the reverse is true. The reasons for this behaviour are the following. For $T_e/T_i < 1$, the internal gas pressure falls off more slowly with height than the external gas pressure and, at some height they become nearly equal. Here, the internal magnetic field must become small in order to satisfy the boundary conditions and the cross-section then becomes large enough to ensure merging. Since Equation (9.60) must be satisfied at the reference level, the internal pressure, P^*, has to be lower for larger field strengths, B^*. This means that the height at which the internal gas pressure becomes larger than the external gas pressure increases with increasing B^* resulting in a correspondingly higher merging height. Due to the presence of the seed field term in Equation (9.57), which dominates over the pressure terms near the merging height, valid solutions can be obtained even above the level at which the internal gas pressure becomes larger than the external gas pressure. Due to magnetic tension the fluxtubes do not become straight suddenly at this height, so that the merging height (defined in Section 3.1) can lie above this level. The lines in Fig. 9.5 are drawn dashed for small T_e/T_i since the low merging height and the related very rapid expansion of the tube lead the model to the limits of its validity. For $T_e/T_i > 1$, on the other hand, the internal pressure falls so rapidly with respect to the external pressure that it soon becomes unimportant. Now, the internal magnetic pressure dominates and produces more rapid expansion and quicker merging as the field strength is increased. Note that, as T_i becomes very small compared to T_e, the merging height approaches an asymptotic value independent of T_i. This is because the internal gas pressure now decreases so rapidly with height that it becomes totally unimportant not far above the reference level.

9.3.2. Internal Structure of the Fluxtube

The horizontal variation of B_z and B_r are shown at different heights in the atmosphere in Fig. 9.6. The base pressure for this model is assumed to be uniform i.e. $P_2^* = 0$. The radial variation of the field is shown at intervals of 100 km, upwards from the reference level. $T_e/T_i = 1$ for all the models discussed in this section. We see that,

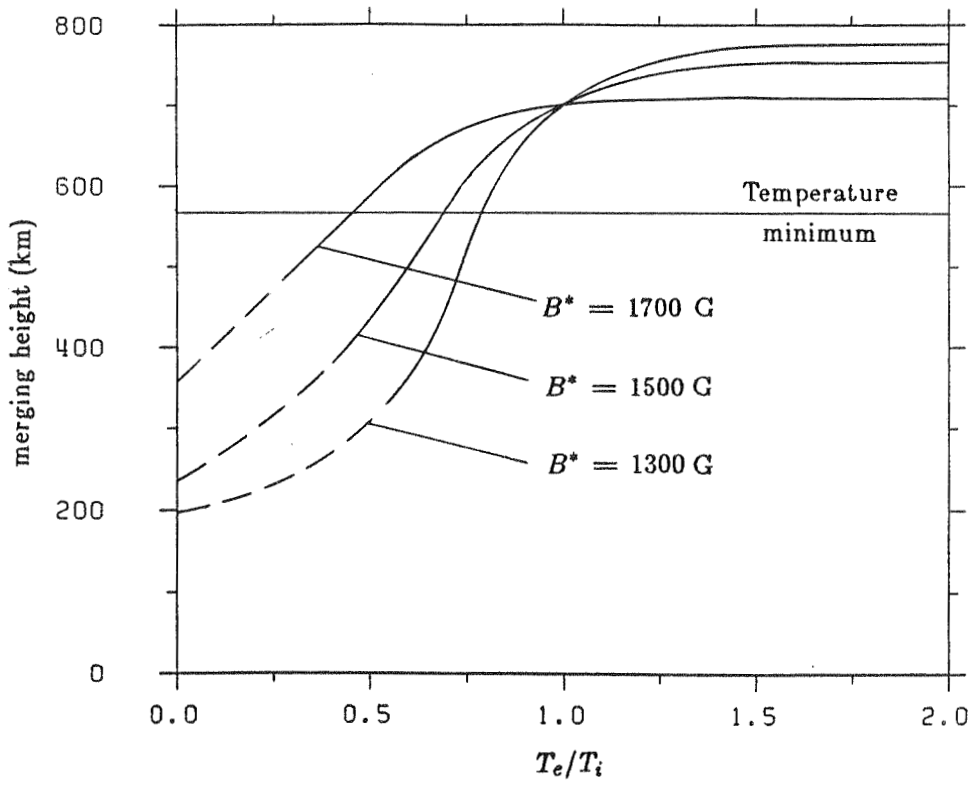

Fig. 9.5 Dependence of merging height upon ratio of external (T_e) to internal (T_i) temperature for different base magnetic field strengths.

at low heights, B_z is almost uniform, as expected from the thin fluxtube approximation. As we proceed upward the axial field becomes more nonuniform, declining outward from the center of the tube. Then, near the merging height, it becomes more uniform again and is, of course, constant after merging. This variation of B_z with radius and height is clearly *not* self–similar. Note that the correction terms to h_0 and f_1 ($x^2 h_2$ and $x^3 f_3$) are not large but also not negligible.

The case of a tube with base pressure increasing outwards, such that $a^{*2} p_2^* = 1$ is shown in Fig. 9.7. Near the reference level the magnetic field is now distinctly more non-uniform, in order to provide the ourward magnetic pressure gradient needed to balance the inward gas pressure gradient at the lower boundary. However, at and above the merging height no difference is seen with respect to the case with horizontally constant gas pressure. How can this be explained? The horizontal gradient of the gas pressure does not disappear, since as opposed to the variation of the magnetic field quantities, the gas pressure does behave self–similarly if the temperature inside the tube is the same as that outside. This can be seen by using Eqs. (9.47) and (9.50) to write the expression for the total pressure for the case of a horizontally uniform temperature ($\sigma_2 = 0$),

$$p = p_0 + x^2 p_2 + \cdots \approx (1 + x^2 p_2^* h_0) \exp\left(-\int_0^y \frac{\mathrm{d}y}{\sigma_0}\right). \tag{9.63}$$

But, from Equation (9.45) we have $h_0 = (a^*/a)^2$, so that

$$p \approx \left(1 + p_2^* a^{*2} \left(\frac{x}{a}\right)^2\right) \exp\left(-\int_0^y \frac{\mathrm{d}y}{\sigma_0}\right). \tag{9.64}$$

Obviously, this is a singular case since the self-similar property disappears if the internal and external temperatures are unequal or if the internal temperature varies with x. The above equation shows that the lateral pressure gradient persists even after the fluxtubes have merged. This means that the magnetic field cannot be exactly uniform after merging. However, the pressure declines exponentially while the magnetic field remains constant

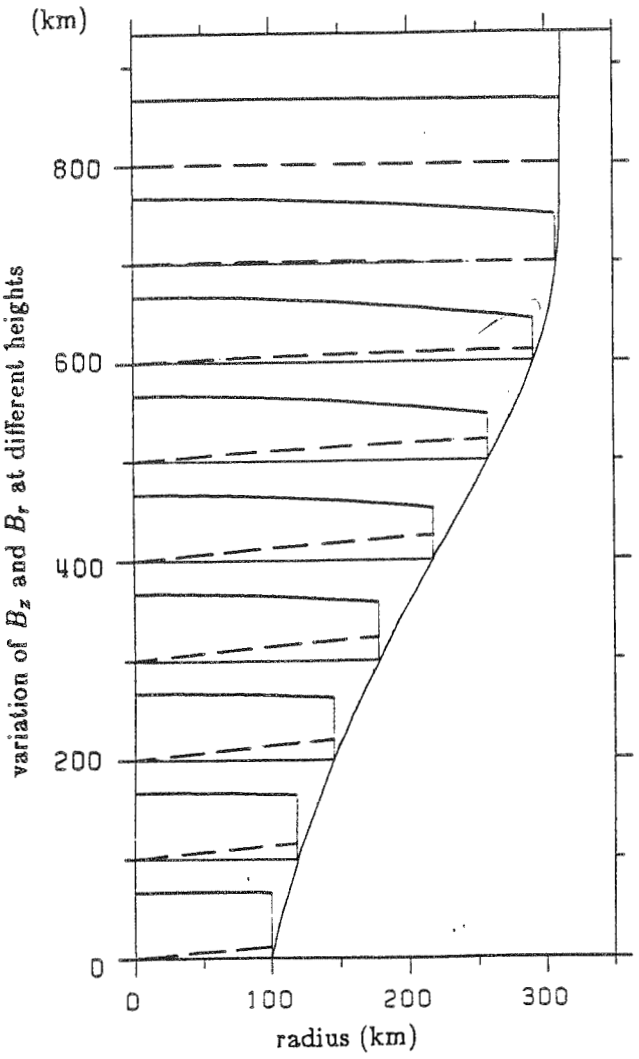

Fig. 9.6 Radial variation of B_z and B_r at different heights for a typical fluxtube of initial radius equal to 100 km and a filling factor of 0.1. For this case, the base gas pressure is taken to be uniform. To interpret this figure and others like it properly, visualize the figure of the overall fluxtube geometry to be subdivided into groups of subfigures placed at different heights in the tube. Each subfigure contains three curves. At the bottom is a horizontal line defining the height. Above it is the radial variation of B_r shown dashed and, above that, the variation of B_z (solid). As in all figures of this type, both B_z and B_r are normalized to the value of B_z on the axis. Here, the axial field at the base is essentially uniform but then begins to decline outward as the height increases. But, near the merging height, it approaches uniformity again, consistent with a uniform vertical cross-section.

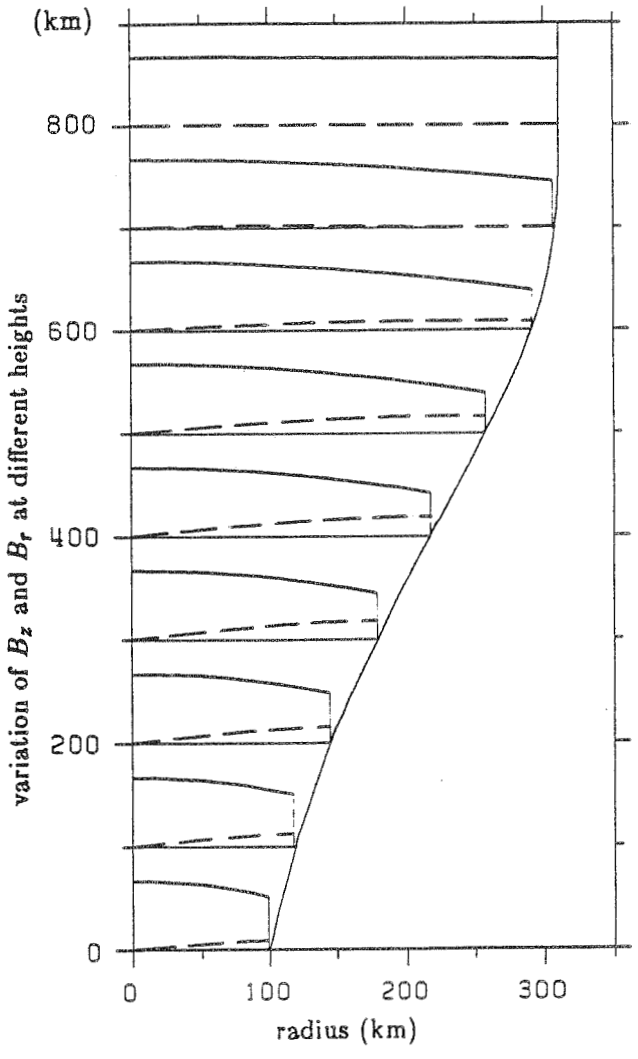

Fig. 9.7 The same as Fig. 9.6 but with a base gas pressure increasing outward from the axis. Now, the axial field is no longer uniform at the base since its pressure gradient must balance the inward gas pressure gradient. At large heights, however, the gas pressure is no longer important and the field approaches uniformity as in Fig. 9.6.

after merging, so that this non-uniformity damps out rapidly above the merging height. Even below the merging height, magnetic tension makes the field decrease considerably less rapidly than the pressure.

In Fig. 9.8 the internal magnetic field structure of a fluxtube with the pressure at the lower boundary decreasing with radius is shown. The magnitude of p_2 is chosen such that $a^{*2}p_2 = -1$. The result is as expected with the axial magnetic field now increasing outward in the lower part of the tube in order to provide the required pressure gradient. Higher up, the solution is similar to the other two cases. The independence of the radial dependence of the field on the horizontal pressure variation has already been explained further up.

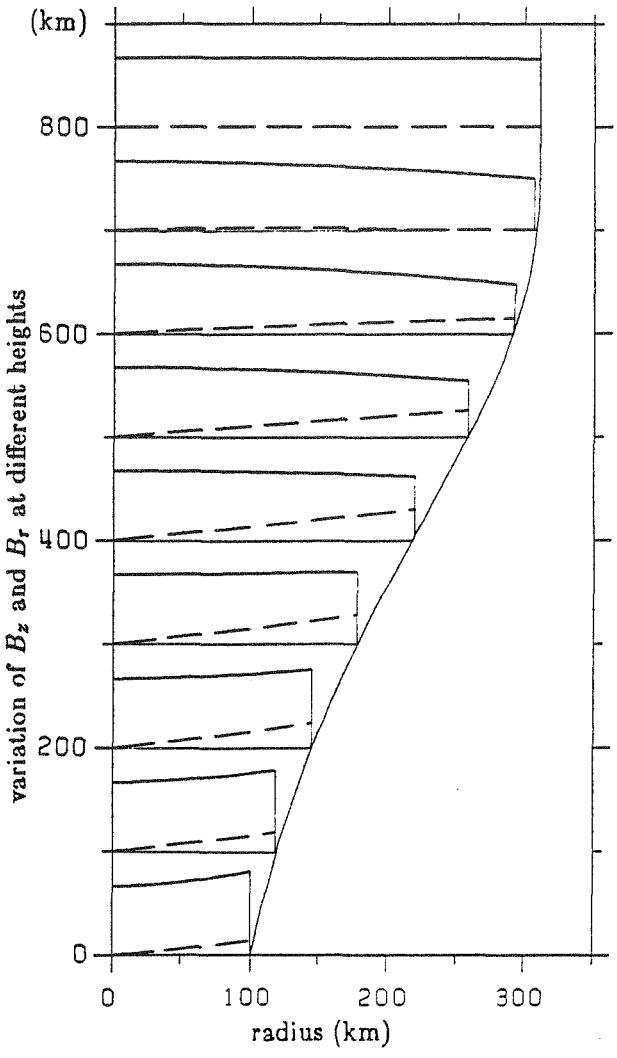

Fig. 9.8 The same as Fig. 9.6 but with the base gas pressure now decreasing outward. As expected, the axial field at the base now increases outward to counterbalance the outward gas pressure gradient but then begins to decline outward as the influence of the pressure declines. Eventually, as in the previous cases, the field becomes uniform near the merging height.

9.3.3. Fluxtube Models With a Twisted Field

Because the higher order terms in the expansion become quite large if the twist is too significant, it is safe within the context of the expansion method we are using to investigate only relatively small values of the initial twist. Nevertheless, several interesting results do emerge from the investigation of even quite small pitch angles. For initial pitch angles less than 15°, the twist has only a small effect upon the cross-section and merging height, the calculation to second order showing a slight decrease in the cross-section at greater heights as compared to the untwisted case. However, we believe this result could be spurious for the following reason: As can be seen from Eq. (9.57), the net effect of B_θ (through the term containing δ) is of the same sign as the external pressure and tends to enhance the axial field at the axis, h_0, in agreement with the results of Parker (1974). However, the flux condition correct to second order, Eq. (9.45), contains only $h_0 a^2$ and not the fourth order term in the axial field $h_2 a^4$. Because h_0 is enhanced, the final calculated cross-section from Eq. (9.52) will be underestimated without the inclusion of the fourth order term which can become significant at great heights where, in the twisted case, the radial gradient of B_z becomes large. Therefore, the result that the cross-section is slightly decreased

for increasing twist should not necessarily be taken as a contradiction to the opposite results of Parker (1974, 1976)*. It may merely show the inadaquacies of a second order expansion when the twist becomes large (as it does near the merging height). In any case, the effect on the cross-section is expected to be quite limited due to the restrictions imposed by merging. We feel that, despite this problem, some qualitative conclusions on twisted tubes can still be reached.

Since, to first order, the pitch angle of the field, η_1, is given by

$$\eta_1 = \tan^{-1} \frac{B_\theta}{B_z} = \tan^{-1} g_1^* a, \tag{9.65}$$

we see that the twist increases with height as the fluxtube broadens in accordance with the results of Parker (1974). Moreover, the number of turns per unit length along the tube remains approximately constant, i.e.

$$N \sim \frac{1}{a} \tan \eta \approx \text{const.} \tag{9.66}$$

Fig. 9.9 shows a plot of the tangent of the pitch angle as a function of height for three values of the initial twist. These curves are calculated correct to second order, i.e.,

$$\eta = \tan^{-1} \frac{g_1 a + g_3 a^3}{h_0 + h_2 a^2}. \tag{9.67}$$

The twist increases initially with height, reaches a maximum value as the fields begin to merge and then decreases again to an asymptotic constant value. It is the second order terms in Eq. (9.67) which lead to the decrease in pitch above the merging height. The decrease above the merging height of (negative valued) h_2, as the field becomes more uniform, is the dominent cause. The fact that the tube radius remains approximately constant above the merging leads to the twist showing an asymptotic behaviour high in the atmosphere, with the asymptotic value η_1 given approximately by

$$\tan \eta_1 \approx \frac{1}{\sqrt{\alpha}} \tan \eta^*, \tag{9.68}$$

where η^* is the pitch at the boundary of the fluxtube for $y = 0$. Eq. (9.66) is only approximate, since h_2 does not disappear above the merging height as is readily visible from Fig. 9.10. It should also be kept in mind that cylindrical symmetry breaks down above the merging height (since the field does not become uniform at any height above merging!), which makes the discussion of twisted tubes in that region questionable.

In Fig. 9.10 the horizontal variation of B_z and B_θ (which replaces B_r in this figure) is shown at various heights for the model with $\tan \eta^* = 0.225$. At the base $B_\theta \ll B_z$ but at greater heights B_θ becomes larger than B_z near the surface of the tube, consistent with Fig. 9.9. The reason for the strong decrease in B_z across the tube in the higher levels, even after merging, is that the azimuthal field produces an inward magnetic pressure force. Since the pressure in this model is horizontally uniform, an outward magnetic pressure force is required to balance it. Therefore with increasing height and correspondingly increasing twist B_z decreases ever more rapidly outwards.

9.3.4. Comparison With the Thin Fluxtube Approximation and the Importance of Higher Order Terms

If we set the RHS of Eq. (9.57) equal to zero, then we obtain the magnetic field structure in the thin fluxtube approximation, but now modified to include merging with a seed field. In Fig. 9.11 the shape of the fluxtube cross-section calculated with the modified thin tube approximation is compared with the cross-section of the second order expansion solution. Both thin tube and expansion models have internal temperature equal to the external temperature, $\alpha = 0.1$, no twist and uniform base pressure (this last condition is trivially fulfilled for the thin tube approximation). Tubes having four different radii are shown, namely 25, 50, 75, and 100 km. It is evident that the differences between the two solutions increase with height until they reach a maximum near the merging height. Above that level the seed field forces both tubes to behave the same. Magnetic tension evidently makes the tubes merge at a greater height. This effect increases with increasing radius, so that the second order

* Although, our analysis is quite different from that of Parker (1974, 1976) in that we specifically include the radial component, B_r, in our treatment.

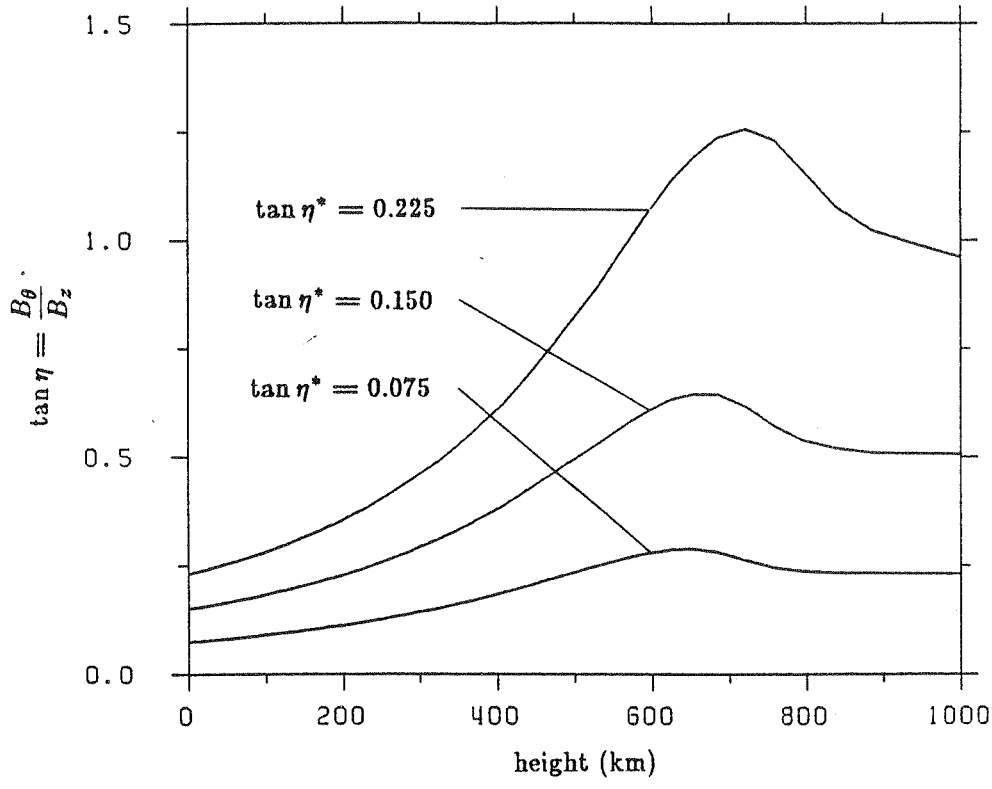

Fig. 9.9 Variation of pitch angle with height for a twisted fluxtube for different values of the initial twist at the base. For all these tubes, $R^* = 100$ km and $\alpha = 0.1$. We see that the twist increases strongly with height. But, near the merging height, it reaches a maximum and then declines to a constant value.

solution merges at ever greater heights (compare with Sect. 9.3.1), while the thin tube solutions all merge at approximately the same height, in accordance with the results of Spruit (1983).

In order to estimate the validity of our expansion technique, we plot in Fig. 9.12 the second and fourth order terms in the expansion of the axial magnetic field strength at the boundary, normalized to its value on the axis, i.e.,

$$\frac{b_z}{h_0} = 1 + \frac{h_2}{h_0}a^2 + \frac{h_4}{h_0}a^4. \tag{9.69}$$

This plot corresponds to the 'standard' model with $\alpha = 0.1$, $R^* = 100$ km, no twist, and with the temperature and pressure uniform over the cross–section. For this case, Equations (9.38), (9.46), and (9.51) yield simply

$$p_4 = 0, \tag{9.70}$$

$$h_2 = -\frac{1}{4}h_0'', \tag{9.71}$$

$$h_4 = -\frac{1}{16}h_2'' = \frac{1}{64}h_0^{(\mathrm{IV})}. \tag{9.72}$$

Near the reference level both the second and fourth order terms are small. The second order term increases in magnitude with increasing height until it starts decreasing again rapidly towards zero slightly below the merging height, which for this model lies at 750 km. The fourth order term remains small over most of the height range. Near the merging height it reflects the rapid change in h_2, since it is proportional to the curvature of h_2.

Both the fourth order terms p_4 and h_4 remain small for most of the models studied by us, including those with $p_2 \neq 0$. However, they are strongly dependent on the radius of the tube. Furthermore, h_4 may become large for tubes with large twist.

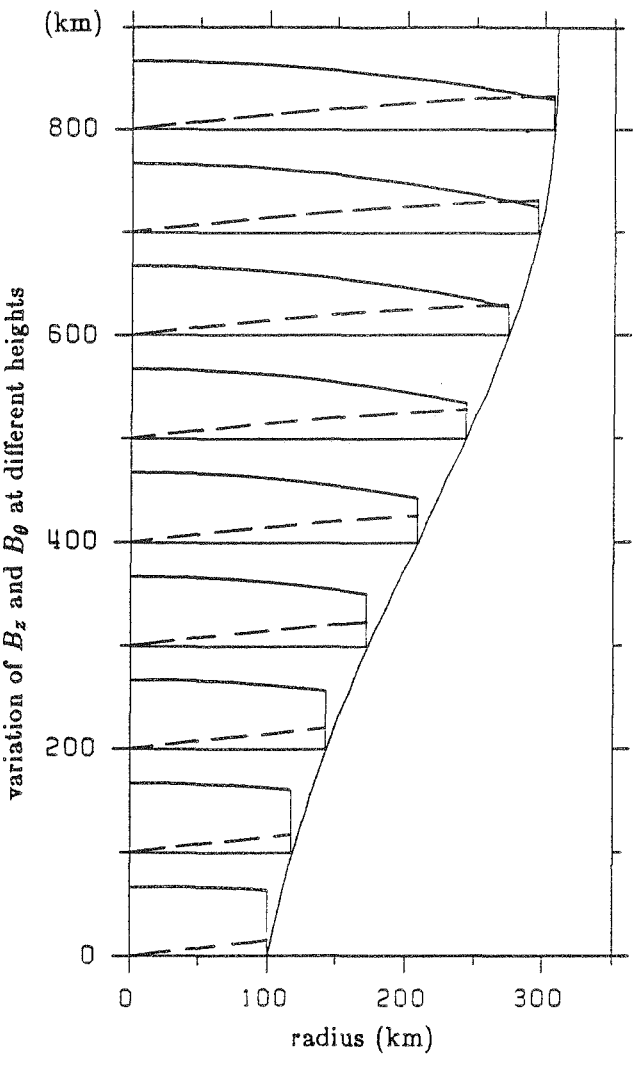

Fig. 9.10 Radial variation of B_θ (dashed) and B_z (solid) at different heights for $\tan\eta^* = 0.225$, $R^* = 100$ km, and $\alpha = 0.1$. Like Fig. 9.9 this figure also shows the strong increase in twist with height.

9.4. Conclusions

Besides the long term goal of a model to serve as a basis of empirical radiative transfer calculations, the model presented in this chapter has served two purposes. Firstly, higher order departures from the thin tube approximation due to magnetic tension have been studied. Secondly, the effects of neighbouring fluxtubes on the structure of a given fluxtube have been treated. In particular, the merging of fluxtubes has been examined in some detail. To accomplish these goals we have chosen to use an expansion technique in which the appropriate variables such as magnetic field strength, gas pressure, and temperature are expanded in power series in the radial variable, perpendicular to the tube axis. We simplify the appropriate MHD equations for the height variation of the various coefficients by equating equal powers to any ascending order of accuracy desired. If this process is carried out to second order, one ultimately obtains a nonlinear second order differential equation for the magnetic field along the axis of the fluxtube which must be solved numerically. A small seed field filling the space between the fluxtubes is used to cause the smooth merging of fluxtubes. The seed field does not affect the structure or merging of the fluxtube as long as its magnitude is small.

For untwisted tubes with internal temperature equal to the external temperature and no horizontal variation of pressure and temperature we find that the merging height increases linearly with fluxtube radius for a fixed filling factor, while for fluxtubes with a fixed diameter the merging height varies inversely with filling factor. For such fluxtubes the merging height is independent of the base field strength, whereas for tubes whose temperature differs from the temperature of the surroundings this is no longer the case. Thus for tubes which are hotter than the surrounding photosphere the merging height increases with increasing field strength, whereas for cooler fluxtubes, the reverse is true.

In general, we find that the thin fluxtube solution is quite good low in the atmosphere, but, as the tubes

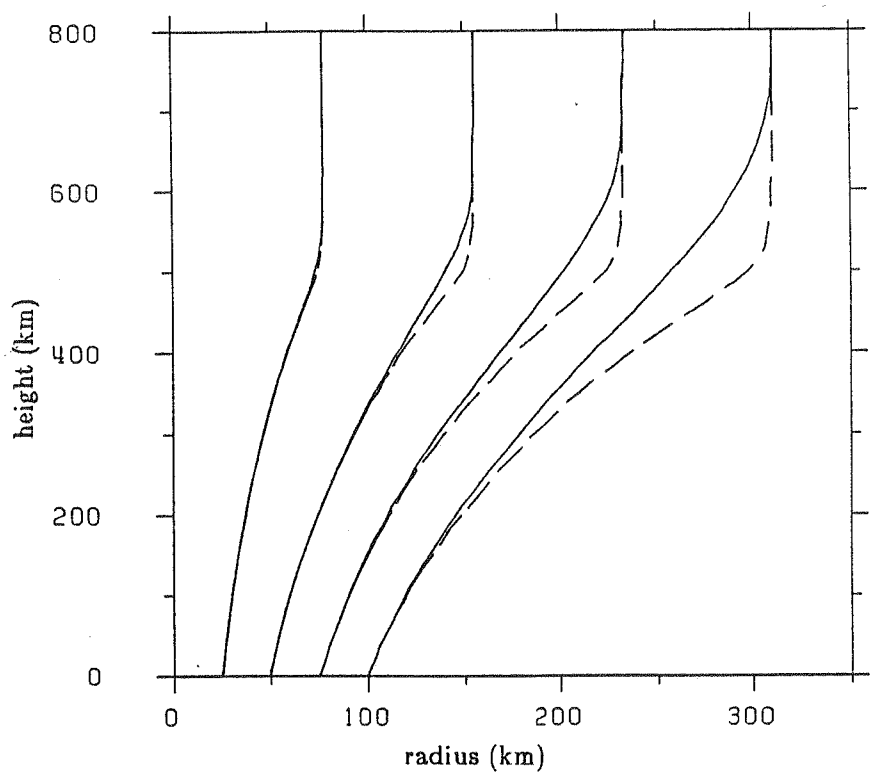

Fig. 9.11 Comparison of fluxtube cross-section obtained from our expansion technique carried to second order with the thin fluxtube approximation (dashed) also modified through the use of a seed field. The figure shows that the thin fluxtube approximation is quite good near the base but that the deviations from our model become more and more marked as the height increases.

expand, deviations soon become apparent, with the greatest departures occuring near the merging height. Our solution shows that the effects of magnetic field line curvature extends the merging to greater heights than predicted by the thin fluxtube approximation modified by the use of a seed field. However, the departures are small enough for the thin tube approximation to remain a useful tool for many applications.

The horizontal structure of the magnetic field is found to be decidedly non-self-similar for the horizontally constant temperature structure employed. For horizontally uniform base gas pressure the magnetic field starts out approximately uniform at the base, declines outwards ever more as the tube expands and finally becomes uniform again above the merging height. In contrast to self-similar solutions, which require a specific temperature structure to satisfy force balance in both directions, the expansion solution can be coupled to an energy equation, or to an empirically determined temperature structure.

Some physical implications of slightly twisted fields at the fluxtube base have been discussed. For such fields the twist does not have a large effect on the overall cross-section and merging height. In accordance with the results of Parker (1974), the pitch angle increases strongly with height due to the expansion of the tube. However, as the fields begin to merge, the pitch angle reaches a maximum and then begins to decrease towards an asymptotic value. In contrast to the untwisted fluxtube, the axial field decreases outwards from the axis even after merging. Presumably, after merging, fields of opposite polarity will come into contact with each other, resulting in magnetic reconnection which could serve to combine tubes integrally with their neighbours (Parker, 1983a).

It is generally agreed that the magnetic field of unipolar regions expands until it comes into contact with field lines coming from neighbouring regions. Different theoretical models have been proposed for this expansion (e.g. Gabriel, 1976; Anzer and Galloway, 1983b). The results from these models have been interpreted to give "canopy heights" of around 1500 km above the photosphere in quiet regions, where "canopy height" is interpreted as the height at which the atmosphere begins to be dominated by the magnetic field. On the other hand Giovanelli (1980), Giovanelli and Jones (1982), and Jones and Giovanelli (1983) have found evidence from magnetograph recordings for magnetic canopies lying between 500 and 800 km in the atmosphere, near both active and quiet network regions. They define canopies as regions of magnetic field overlying non-magnetic regions. If their interpretation of the observations is correct, then we should expect on the basis of our analysis that the individual fluxtubes would not be fully merged when the canopy begins to form, i.e. when the fields become strongly inclined.

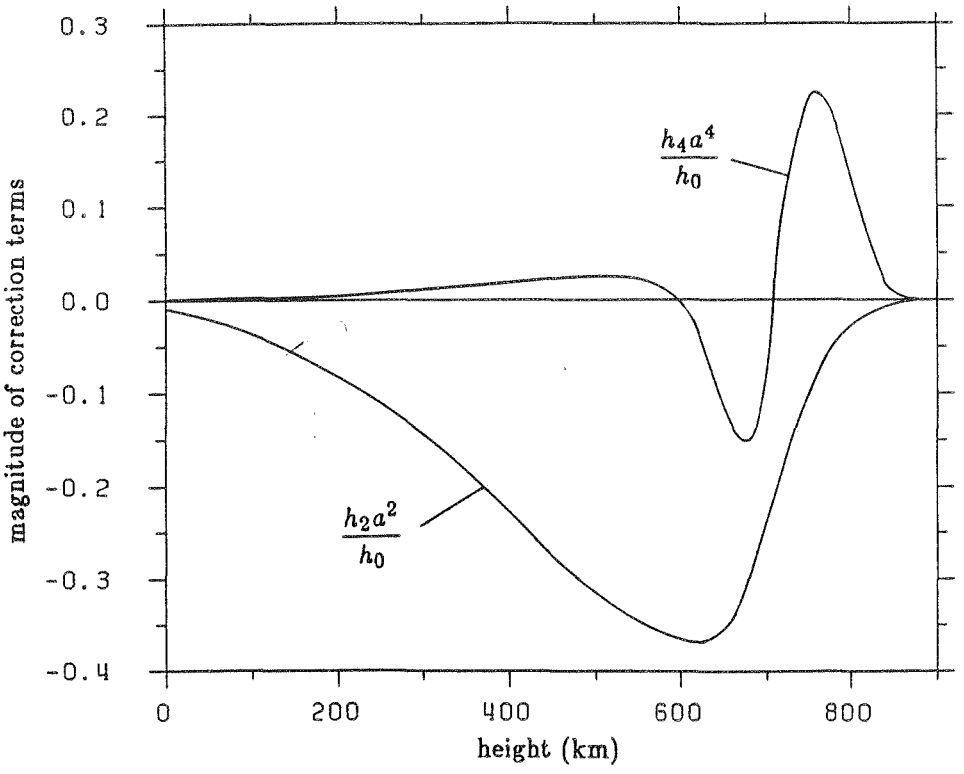

Fig. 9.12 Variation of the second and fourth order terms in the expansion for B_z with height. The curves show the ratio of these terms to the zeroth order terms. The second order term grows with height and becomes quite significant near the merging height but then drops quickly to zero. The fourth order term is very small at low heights but also increases near the height where the fields merge. This figure corresponds to our "standard" model with $R^* = 100$ km and $\alpha = 0.1$. For fluxtubes thinner than this, these terms should become correspondingly smaller.

Consequently, there clearly is a need to study the structure and merging of non-vertical fluxtubes. This need is supported by the observations of Solanki et al. (1987) that in half of the regions investigated the fluxtubes are inclined by over 10° to the vertical.

This model may in future be used to calculate Stokes line profiles and thereby to test some of the assumptions underlying past and present empirical models of solar magnetic fluxtubes. For example, it can be used to test how strongly the Stokes profiles calculated in the cylindrical geometry of the model (1.5-D calculations along many lines of sight) differ from profiles calculated in slab geometry or in a plane-parallel model. For more details see De Martino (1986) and Solanki and De Martino (in preparation). Another possible use for this model is to test the importance of magnetic tension in fluxtubes models as reflected by the Stokes profiles. Thus, by comparing the line profiles produced by the thin tube and the expansion model, it may be possible to decide whether models more sophisticated than the thin tube approximation are needed for fluxtube diagnostics. The expansion model can at a later stage also be used as the basis for empirical modelling of fluxtubes. For this purpose its simplicity can become a distinct advantage over more sophisticated models, since it can be calculated with a minimum of computer time, leading to a considerably greater flexibility.

However, in the long run, exact MHD solutions for this problem are certainly feasible. This has been demonstrated, for example, by the time-dependent relaxation technique employed by Endler (1971), Steinolfson et al. (1982), and Suess (1983) for the coronal streamer problem and by Deinzer et al (1984a, b) for fluxtubes in slab geometry. Another promising approach is the iterative method used by Pneuman and Kopp (1971) for streamers, which has recently been applied to sunspots by Pizzo (1986) and to small fluxtubes by Steiner et al. (1986).

10. Outlook

Man reist ja nicht, um anzukommen,
sondern um zu reisen

J.W. Goethe

We shall not bore the indefatigable reader who has fought his way through the last nine chapters with a summary of the results, since one is provided in the abstract. Neither shall we weary him with a discussion of their implications, such discussions are included in chapters 5 through 9. Instead, in this final chapter we shall outline some of the future perspectives opened up by this work. A number of promising avenues await exploration and the questions inviting consideration are legion. Below we list only some of the work possible in the near (and sometimes more distant) future. A part of it is already underway.

1. More data, both of high and of moderate spatial resolution, are required in order to resolve a number of problems. Some examples of open questions which can be addressed with additional moderate spatial resolution data are: *i*) What is the dependence of fluxtube properties on filling factor, the position on the solar disk, the age of an active region, the distance from a sunspot, etc.? A large sample of observations will be required to determine these dependences with any measure of certainty. *ii*) What are the properties of the deeper and the higher layers of fluxtubes? These are known only in their rudiments and their determination requires polarimetric data in chromospheric lines and at various wavelengths in the infrared. *iii*) Are fluxtubes inclined and what is their geometry? The data available to date are usually limited to Stokes I and V, but complete profiles of Stokes Q and U will also be needed in future if we want to answer this question.
2. Better diagnostic techniques are required as well. In particular Stokes Q and U are almost virgin territory as far as fluxtube diagnostics are concerned (some exceptions are to be found in Hagyard, 1985). Besides being absolutely necessary for determining the direction of the field, Stokes Q and U are also capable of serving as diagnostics for the field strength, temperature, and perhaps even velocity inside the fluxtubes. For a more detailed discussion see Solanki et al. (1987). An example is the σ-π asymmetry of Stokes Q (the summed area of the two σ-components is not equal to the area of the π-component, cf. Sect. 4.2.3). It can be used to set constraints on the temperature inside fluxtubes. A further example of the potential of Stokes Q is presented further below.

   The diagnostic potential of Stokes V has also not been used to the full. For example, the "thermal line ratio", introduced by Landi Degl'Innocenti and Landolfi (1982) and first applied by Stenflo et al. (1987a) requires further development before it can be used as a reliable guide to fluxtube temperature. In addition to new techniques, long established methods like the 5250/5247 line ratio technique of Stenflo (1973) need to be studied further. In chapter 6 we found the unexpected result that the CLV of the ratio of the V amplitudes gives only little information on the height variation of the magnetic field. However, the ratio of the full line profile of 5250/5247 at disk centre probably does contain some (model dependent) information on $B(z)$ as pointed out by Stenflo (1984a). A proper analysis would require 1.5-D calculations (since flux conservation is important). A reinterpretation of conventional 5250/5247 line ratio data has recently been presented by Semel (1986). He demonstrates that if a weak field of opposite polarity is assumed outside the fluxtubes then the observed line ratio (at disk centre) can be explained with a field strength inside the fluxtubes considerably below the generally accepted value of 1 kG. With conventional line ratio observations it is probably not possible to differentiate between the two interpretations. However, the 5250/5247 Q line ratio, being insensitive to polarity, should be able to decide between them. The Stokes Q line ratio also contains information on the height variation of the magnetic field strength. Since its π-component is formed higher in the atmosphere than its σ-components (for a not completely split line), a comparison of the 5250/5247 π and σ line ratios will give the B gradient if we know their respective heights of formation (see point 3 below). The advantage of using Stokes Q is that we see higher in the atmosphere (Stokes V is zero at the wavelength where the π-component is strongest). The proper application of this method will, however, also require 1.5-D radiative transfer calculations and ideally data with better signal to noise ratio than currently available.
3. In order to improve the diagnostics we also need to know the heights of formation of the spectral lines in fluxtubes. To this end we may use either the method of Van Ballegooijen (1985a), or of Wittmann

(1973a, 1974). Since Van Ballegooijen's method, although possessing a sounder physical foundation, gives the emission contribution function, which unfortunately mixes the contributions to the continuum and the line (cf. Gurtovenko and Sheminova, 1983; Magain, 1986; see also Fig. 4 of Van Ballegooijen, 1985a), a further investigation of both methods seems appropriate at the moment. A promising approach would be to combine Magain's definition of the line depression contribution function with Van Ballegooijen's formalism for solving the radiative transfer equations.

4. Data near $\lambda = 1.6\mu$ are crucial for determining two important and so far only very badly known parameters of fluxtubes, their temperature and their field strength near $\tau_{5000} = 1$. $T(\tau_{5000} \approx 1)$ gives the continuum intensity without the usual problems, namely limited spatial resolution and the influence of the dark ring surrounding fluxtubes (Deinzer et al., 1984b) which hamper direct observations; and the fact that only the product of continuum contrast and filling factor is measured with indirect methods (Schüssler and Solanki, 1987). Together, temperature and field strength near $\tau_{5000} = 1$ may allow constraints to be set on the possible heating mechanisms (e.g. mainly radiative or mainly mechanical heating in the deep photospheric layers of fluxtubes).
5. 1.5-D radiative transfer: Future *empirical* models must combine a 2-D MHD model of a fluxtube without energy equation (e.g. thin tube model, the expansion model of chapter 9, or the exact solution of Steiner et al., 1986) with radiative transfer along many lines of sight (1.5-D). Specially away from disk centre the effects of limited fluxtube diameter should play a major role. 1.5-D calculations of Stokes I, in conjunction with fluxtube models of varying sophistication, have been carried out by e.g. Chapman (1970), Caccin and Severino (1979), Rees and Semel (1979, they also consider Stokes V), Owocki and Auer (1980), Chapman and Gingell (1984), Deinzer et al. (1983, 1984b), and Walton (1987). So far only Van Ballegooijen (1985a) has studied the influence of the fluxtube geometry (including expansion, and finite diameter) on all four Stokes profiles.

   1.5-D radiative transfer calculations must be carried out systematically to test the difference to the present generation of 1-D models. A first step, in which the Stokes profiles from a plane-parallel, slab and cylindrical fluxtube are compared, is in preparation. Only a single fluxtube is considered, namely the standard model of chapter 9. In a second step the influence of neighbouring fluxtubes on the emergent line profiles must also be taken into account. Only slab geometry need be considered, since Stokes V is found to behave very similarly for slab and cylindrical geometry. Also, a proper combination of radiative transfer with a group of merging cylindrical fluxtubes becomes prohibitively complicated and expansive in computing time. The influence of filling factor will then no longer restrict itself to changing the amplitude of the V profiles, but will also affect the line shapes. Not only the distance between fluxtubes will play a role, but also their diameters, possibly allowing information on the true diameters of small fluxtubes to be obtained. All previous attempts have only been able to set upper limits (e.g. Mehltretter, 1974; Stenflo, 1976; Ramsey et al., 1977).
6. NLTE effects will have to be taken into account in a future calculation. This is particularly true if the continuum intensity of fluxtubes really is so high as suggested by the indirect analysis of Schüssler and Solanki (1987), since Solanki and Steenbock (1987) find that the departures from LTE increase rapidly with increasing difference in temperature between the levels at which the continuum and the lines are formed. As far as the diagnostics are concerned, it is the empirically determined temperature which is most strongly affected by NLTE, with departures from LTE mimicking a higher temperature. Therefore, an empirical model using NLTE radiative transfer of the Stokes profiles is an important (but probably distant) goal. As a first step the NLTE departure functions may be calculated without any polarization using a standard NLTE code (e.g. that described by Steenbock and Holweger, 1984; Steenbock, 1985). The Stokes code described in chapter 2 can then be used to calculate the complete Stokes vector if Eqs. (2.69) and (2.70) are incorporated. This requires only a minor change in the present code.
7. An application of the methods presented in chapter 4 to FTS spectra at various limb distances should pay rich dividents. Besides being an independent test for the temperature models developed in chapter 5 such an analysis may also provide a first (indirect) glimpse at mass-motions not observable at disk centre, e.g. Alfvén waves (Parker, 1979; these torsional waves can be excited by a whirl flow in the surroundings, which in turn is due to the bathtub effect, Nordlund, 1983; Schüssler, 1984a) or the jiggling of fluxtubes by granular motions (Parker, 1983b, 1986).
8. As the data continue to improve and the empirical models must attain ever greater complexity to interpret them properly, it becomes increasingly feasible to compare the observations directly with profiles calculated from self-consistent theoretical models (i.e. models including an energy equation, e.g. Spruit, 1976; Deinzer et

al., 1984a, b; Knölker et al., 1985, 1987; Nordlund, 1986). Particularly, when the theoretical models become more comprehensive. The present status of such models and how they compare with observations has been reviewed by Schüssler (1987).

Although the static models mentioned above are quite useful, theoretical models become inescapable when we want to study dynamic phenomena. A possible short term project would be to take model calculations of different wave modes in fluxtubes and calculate their time and/or space averaged Stokes I and V signals. A similar analysis for the non-magnetic atmosphere has recently been published by Keil and Marmolino (1986). A linear calculation (cf. Roberts, 1986) should be sufficient for the beginning. It actually has the advantage that the wave amplitudes are free parameters which can be varied to fit the observations of line broadening. Furthermore, a combination with the observed zero-crossing shifts as well as Stokes V asymmetry may even be able to select between the different wave modes.

9. By integrating running windows over our FTS spectra we can obtain the broad-band Stokes V signal of solar magnetic fluxtubes. The CLV of this signal may decide whether the broad-band circular polarization measured by Kemp et al. (1987) on the solar disk near the poles is produced by the Stokes V asymmetry in small magnetic fluxtubes or not. Their results suggest that the broad-band polarization is incompatible with the sign of the asymmetry seen at disk centre (with the blue wing being stronger than the red wing). As discussed in Sect. 8.2.2 the asymmetry changes sign close to the limb for a few medium strong lines, but the CLV of the asymmetry of all lines must be determined in order to decide whether the thin strip near the limb with opposite sign has enough weight to override the asymmetry of the major part of the solar disk.
10. The I_V profile is also susceptible to new applications. For example, it allows us to obtain an idea of the line bisector inside fluxtubes, thus opening another approach to the study of fluxtube properties, in particular their internal mass motions. The main problem in this context is the Stokes V area asymmetry and the rather rudimentary manner of removing it (Sect. 4.2.5). However, the influence on the line bisector of the renormalisation procedure, in which the blue wing of V is multiplied by $\sqrt{A_r/A_b}$ and the red wing by $\sqrt{A_b/A_r}$ prior to integration can be tested by also determining the bisectors of the profiles renormalised by multiplying only the blue wing with A_r/A_b, respectively only the red wing with A_b/A_r. The bisectors determined with these last two renormalisations delineate the two extremes within which the true bisector must lie.

    Furthermore, by substracting the suitably weighted I_V profile from the Stokes I profile observed in the same active region, it may also be possible to recreate the line profile arising solely from the *non*-magnetic environment of fluxtubes. A method for doing this with a minimum of a priori assumptions has been presented by Schüssler and Solanki (1987).
11. Finally, some of the methods developed here and elsewhere can be easily adapted and applied to stars. In particular, the regression technique pioneered by Stenflo and Lindegren (1977) can be used to measure stellar magnetic fields if data with a sufficient number of unblended lines and high enough spectral resolution are used. A first step in this direction has been taken by Mathys and Stenflo (1986), who have determined the field strength on an Ap star using this method. However, it shows most promise for solar type stars whose tangled magnetic fields cannot be studied with polarimetric methods (cf. chapter 1). The Stenflo-Lindegren technique has a considerable advantage over the usually used Robinson method, since it is considerably less sensitive to blends. Another possible diagnostic for stellar magnetic fields is the Stokes I line ratio of 5247/5250 introduced by Schüssler and Solanki (1987) to determine the product of magnetic flux and continuum contrast of solar magnetic fluxtubes.

References

Note: Numbers in brackets at the end of each reference signify the chapters in which the given reference has been quoted.

Abdusamatov, H.I., Krat, V.A.: 1969, *Solar Phys.* **9**, 420 (6)

Abramowitz, M., and Stegun, I.A.: 1970, *Handbook of Mathematical Functions*, Dover, New York, N.Y. (2,3)

Alfvén, H.: 1967, in *Magnetism and the Cosmos*, W. Hindmarsh, F. Lowes, P. Roberts, and S. Runcorn (Eds.), Oliver and Boyd, Edinburgh, p. 246 (5)

Allen, C.W.: 1973, *Astrophysical Quantities*, Athlone Press, London (4,6)

Altschuler, M.D., Newkirk, G., Jr.: 1969, *Solar Phys.* **9**, 131 (1)

Altschuler, M.D., Levine, R.H., Stix, M., Harvey, J.W.: 1977, *Solar Phys.* **51**, 345 (1)

Angel, J.R.P.: 1977, *Astrophys. J.* **216**, 1 (8)

Angel, J.R.P.: 1978, *Ann. Rev. Astron. Astrophys.* **16**, 487 (1,8)

Angel, J.R.P., Landstreet, J.D.: 1974, *Astrophys. J.* **191**, 457 (8)

Anzer, U., Galloway, D.J.: 1983a, in *Solar and Stellar Magnetic Fields: Origins and Coronal Effects*, J.O. Stenflo (Ed.), *IAU Symp.* **102**, 339 (9)

Anzer, U., Galloway, D.J.: 1983b, *Mon. Not. Roy. Astron. Soc.* **203**, 637 (9)

Arena, P., Landi Degl'Innocenti, E.: 1982, *Astron. Astrophys. Suppl. Ser.* **48**, 81 (2)

Athay, R.G., Gurman, J.B., Henze, W., Shine, R.A.: 1982, *Astrophys. J.* **261**, 684 (7)

Auer, L.H., Heasley, J.N.: 1978, *Astron. Astrophys.* **64**, 67 (2,8)

Ayres, T.R., Testerman, L., Brault, J.W.: 1986, *Astrophys. J.* **304**, 542 (1)

Babcock, H.W.: 1947, *Astrophys. J.* **105**, 105 (1)

Babcock, H.W.: 1949, *Astrophys. J.* **110**, 126 (2)

Babcock, H.W.: 1958, *Astrophys. J. Suppl. Ser.* **3**, 141 (1)

Babcock, H.W.: 1963, *Ann. Rev. Astron. Astrophys.* **1**, 41 (6)

Babcock, H.W., Babcock, H.D.: 1952, *Publ. Astron. Soc. Pacific* **64**, 282 (1,6)

Babcock, H.W., Babcock, H.D.: 1955, *Astrophys. J.* **121**, 349 (1,6)

Baliunas, S.L., Dupree, A.K.: 1982, *Astrophys. J.* **252**, 668 (1)

Baliunas, S.L., Horne, J.H., Porter, A., Duncan, D.K., Frazer, J., Lanning, H., Misch, A., Mueller, J., Noyes, R.W., Soyumer, D., Vaughan, A.H., Woodard, L.: 1985, *Astrophys. J.* **294**, 310 (1)

Baliunas, S.L., Vaughan, A.H.: 1985, *Ann. Rev. Astron. Astrophys.* **23**, 379 (1)

Balthasar, H.: 1984, *Ph.D. Thesis*, Göttingen University (7)

Balthasar, H.: 1985, *Solar Phys.* **99**, 31 (7)

Balthasar, H., Thiele, U., Wöhl, H.: 1982, *Astron. Astrophys.* **114**, 357 (7)

Bartholinus, E.: 1670, *Experimenta Crystalli Islandici Disdiaclastici Quibus mira en insolita Refractio Elegetur*, Hafniæ, Copenhagen, p. 73 and p. 174 (2)

Baschek, B., Scholz, M.: 1982, in *Landolt–Börnstein*, New Series, Vol. VI/2 b, Springer Verlag, Berlin, p. 91 (4)

Basri, G.S., Linsky, J.L.: 1979, *Astrophys. J.* **234**, 1023 (1)

Basri, G.S., Linsky, J.L., Bartoe, J.–D.F., Brueckner, G.E., Van Hoosier, M.G.: 1979, *Astrophys. J.* **230**, 924 (5)

Baym, G.: 1969, *Lectures on Quantum Mechanics*, W.A. Benjamin, Inc., Reading, MA. (2)

Beckers, J.M.: 1969a, *Solar Phys.* **9**, 372 (2,4)

Beckers, J.M.: 1969b, *Solar Phys.* **10**, 262 (2,4)

Beckers, J.M.: 1969c, *A Table of Zeeman Multiplets*, AFCRL–69–0115 (2,4)

Beckers, J.M.: 1972, *Ann. Rev. Astron. Astrophys.* **10**, 73 (1)

Beckers, J.M., Nelson, G.D.: 1978, *Solar Phys.* **58**, 243 (7)

Beckers, J.M., Schröter, E.H.: 1968a, *Solar Phys.* **4**, 142 (5,6,7)
Beckers, J.M., Schröter, E.H.: 1968b, *Solar Phys.* **4**, 165 (7)
Belvedere, G.: 1985, *Solar Phys.* **100**, 363 (1)
Bigelow, F.H.: 1889, *The Solar Corona*, Smithsonian Institute, Washington, D.C. (1)
Blackwell, D.E., Ibbetson, P.A., Petford, A.D., Shallis, M.J.: 1979, *Mon. Not. Roy. Astron. Soc.* **186**, 633 (4)
Blackwell, D.E., Petford, A.D., Shallis, M.J.: 1979, *Mon. Not. Roy. Astron. Soc.* **186**, 657 (4)
Blackwell, D.E., Shallis, M.J.: 1979, *Mon. Not. Roy. Astron. Soc.* **186**, 673 (4,5,7)
Blackwell, D.E., Shallis, M.J., Simmons, G.J.: 1980, *Astron. Astrophys.* **81**, 340 (4)
Bohr, N.: 1918, *Kopenhagener Akad.*, Part I and II (2)
Bommier, V., Leroy, J.L., Sahal-Brechot, S.: 1981, *Astron. Astrophys.* **100**, 231 (1)
Borra, E.F., Landstreet, J.D., Mestel, L.: 1982, *Ann. Rev. Astron. Astrophys.* **20**, 191 (1)
Borra, E.F., Edwards, G., Mayor, M.: 1984, *Astrophys. J.* **284**, 211 (1)
Brandt, P.N., Solanki, S.K.: 1987, in *Proc. Workshop on the Role of Fine-Scale Magnetic Fields on the Structure of the Solar Atmosphere*, Tenerife, 6–12 Oct. 1986, in press (1,4,6,7)
Brants, J.J.: 1985a, *Solar Phys.* **95**, 15 (3)
Brants, J.J.: 1985b, *Solar Phys.* **98**, 197 (3,7)
Brault, J.W.: 1978, *Osserv. Mem. Oss. Astrofis. Arcetri* **106**, 33 (3,7)
Brault, J.W.: 1982, *Phil. Trans. Roy. Soc. London* A **307**, 503 (3,7)
Brault, J.W.: 1985, in *High Resolution in Astronomy*, A.O. Benz, M.C.E. Huber, M. Mayor (Eds.), Obs. Genève, Sauverny, p. 3 (3)
Bridges, J.M.: 1973, in *Contributed Papers—11th International Conference on Phenomena in Ionized Gases*, I. Stoll (Ed.), Czech. Acad. Sci., Inst. Phys., Prague, Czech., p. 418 (4)
Bridges, J.M., Kornblith, R.L.: 1974, *Astrophys. J.* **192**, 793 (4)
Browning, P.K., Priest, E.R.: 1982, *Geophys. Astrophys. Fluid dyn.* **21**, 237 (9)
Browning, P.K., Priest, E.R.: 1983, *Astrophys. J.* **266**, 848 (9)
Brueckner, K.A.: 1971, *Astrophys. J.* **169**, 621 (4)

Caccin, B., Cavallini, F., Ceppatelli, G., Righini, A., Sambuco, A.M.: 1985, *Astron. Astrophys.* **149**, 357 (7)
Caccin, B., Severino, G.: 1979, *Astrophys. J.* **232**, 297 (9,10)
Calamai, G., Landi Degl'Innocenti, E., Landi Degl'Innocenti, M.: 1975, *Astron. Astrophys.* **45**, 297 (4)
Carlsson, M., Scharmer, G.B.: 1985, in *Chromospheric Diagnostics and Modelling*, B.W. Lites (Ed.), National Solar Obs., Sacramento Peak, NM, p. 137 (5,7)
Cavallini, F., Ceppatelli, G., Righini, A.: 1985, *Astron. Astrophys.* **143**, 116 (1,7)
Cavallini, F., Ceppatelli, G., Righini, A.: 1987, *Astron. Astrophys.* **173**, 155 (7)
Chandrasekhar, S.: 1947, *Astrophys. J.* **105**, 424 (2)
Chandrasekhar, S.: 1950, *Radiative Transfer*, Clarendon Press, Oxford (2)
Chapman, G.A.: 1970, *Solar Phys.* **14**, 315 (5,10)
Chapman, G.A.: 1974, *Astrophys. J.* **191**, 255 (6)
Chapman, G.A.: 1977, *Astrophys. J. Suppl. Ser.* **33**, 35 (5)
Chapman, G.A.: 1979, *Astrophys. J.* **232**, 923 (4,5,8)
Chapman, G.A., Gingell, T.A.: 1984, *Solar Phys.* **91**, 243 (9,10)
Chapman, G.A., Sheeley, Jr., N.R.: 1968, *Solar Phys.* **5**, 442 (1,4,5)
Clarke, D., Grainger, J.F.: 1971, *Polarized Light and Optical Measurement*, Pergamon Press, Oxford (2)
Clerke, A.M.: 1885, *A Popular History of Astronomy during the Nineteenth Century*, A. & C. Black, Edinburgh (1)
Condon, E.U., Shortley, G.H.: 1964, *The Theory of Atomic Spectra*, Cambridge University Press, London (2)
Cook, J.W., Brueckner, G.E., Bartoe, J.-D.F.: 1983, *Astrophys. J.* **270**, L89 (5)
Corinaldesi, E.: 1959, *Il Nuovo Cimento, Suppl.* **14**, 369 (2)
Corliss, C., Sugar, J.: 1982, *J. Phys. Chem. Ref. Data* **11**, 353 (4)
Crosswhite, H.M.: 1975, *J. Research N.B.S.* **79a**, 17 (4)

Dawson, H.G.: 1898, *London Math. Soc. Proc. S1* **29**, 519 (2)
Debye, P.: 1916, *Göttinger Nachr.* von 3. Juni (2)
Defouw, R.J.: 1976, *Astrophys. J.* **209**, 266 (7,9)

Deinzer, W.: 1965, *Astrophys. J.* **141**, 548 (9)
Deinzer, W., Hensler, G., Schmitt, D., Schüssler, M., Weisshaar, E.: 1983, in *Solar and Stellar Magnetic Fields: Origins and Coronal Effects*, J.O. Stenflo (Ed.), *IAU Symp.* **102**, 67 (9,10)
Deinzer, W., Hensler, G., Schüssler, M., Weisshaar, E.: 1984a, *Astron. Astrophys.* **139**, 426 (9,10)
Deinzer, W., Hensler, G., Schüssler, M., Weisshaar, E.: 1984b, *Astron. Astrophys.* **139**, 435 (1,4,5,7,9,10)
Delbouille, L., Roland, G., Neven, L.: 1973, *Photometric Atlas of the Solar Spectrum from λ 3000 to λ 10 000*, Inst. d'Astrophysique, Liège (4,7)
De Martino, S.: 1986, *Diplomarbeit*, ETH, Zürich (9)
Dere, K.P., Bartoe, J.-D.F., Brueckner, G.E., Dykton, M.D., Van Hoosier, M.E.: 1981, *Astrophys. J.* **249**, 333 (7)
Domke, H.: 1971, *Astrofizika* **7**, 39 (2)
Domke, H., Staude, J.: 1973, *Solar Phys.* **31**, 279 (2,5)
Dravins, D., Larsson, B.: 1984, in *Small-Scale Dynamical Processes in Quiet Stellar Atmospheres*, S.L. Keil (Ed.), National Solar Obs., Sacramento Peak, N.M., p. 306 (4,7)
Dravins, D., Larsson, L., Nordlund, Å.: 1986, *Astron. Astrophys.* **158**, 83 (4,7)
Dravins, D., Lindegren, L., Nordlund, Å.: 1981, *Astron. Astrophys.* **96**, 345 (4,7)
Dulk, G.A.: 1985, *Ann. Rev. Astron. Astrophys.* **23**, 169 (1)
Dunn, R.B.: 1972, *Solar Phys.* **22**, 256 (Frontispiece) (1)
Dunn, R.B., Zirker, J.B.: 1973, 33, 281 (5) Solar Physics
Durrant, C.J.: 1977, in *Highlights in Astronomy*, E.A. Müller (Ed.), Vol. **4**, part **II**, p. 267 (7)

Eddy, J.A.: 1980, in *The Ancient Sun*, R.O. Pepin, J.A. Eddy, R.B. Merrill (Eds.), Pergamon Press, New York, N.Y., p. 119 (1)
Endler, F.: 1971, *Thesis*, University of Göttingen (9)
Evans, J.C., Ramsey, L.W., Testerman, L.: 1975, *Astron. Astrophys.* **42**, 237 (7)

Faraday, M.: 1855, *Experimental Researches in Electricity*, Vol. III, Taylor and Francis, London (2)
Feldman, U., Doschek, G.A.: 1978, *Astron. Astrophys.* **65**, 215 (7)
Feldman, U., Cohen, L., Doschek, G.A.: 1982, *Astrophys. J.* **255**, 325 (7)
Ferrari, A., Massaglia, S., Kalkofen, W., Rosner, R., Bodo, G.: 1985, *Astrophys. J.* **298**, 181 (9)
Ferraro, V.C.A., Plumpton, C.: 1966, *An Introduction to Magneto-Fluid Mechanics*, Clarendon Press, Oxford (9)
Foukal, P., Duvall, T. Jr.: 1985, *Astrophys. J.* **296**, 739 (3,5)
Foukal, P., Duvall, T. Jr., Gillespie, B.: 1981, *Astrophys. J.* **249**, 394 (3,5)
Foukal, P., Fowler, L.: 1984, *Astrophys. J.* **281**, 442 (5)
Frazier, E.N.: 1970, *Solar Phys.* **14**, 89 (7)
Frazier, E.N.: 1971, *Solar Phys.* **21**, 42 (5)
Frazier, E.N.: 1977, in *Highlights of Astronomy*, E.A. Müller (Ed.), Vol. **4**, Part **II**, p. 255 (5)
Frazier, E.N., Stenflo, J.O.: 1972, *Solar Phys.* **27**, 330 (1,6)
Frazier, E.N., Stenflo, J.O.: 1978, *Astron. Astrophys.* **70**, 789 (4,5,6,7)
Fuhr, J.R., Martin, G.A., Wiese, W.L., Younger, S.M.: 1981, *J. Phys. Chem. Ref. Data*, **10**, 305 (4)

Gabriel A.H.: 1976, *Phil. Trans. Roy. Soc. London* **A281**, 339 (7,9)
Gail, H.-P., Hundt, F., Kegel, W.H., Schmid-Burgk, J., Traving, G.: 1974, *Astron. Astrophys.* **32**, 65 (5)
Gail, H.-P., Sedlmayr, E.: 1974, *Astron. Astrophys.* **36**, 17 (5,7)
Gary, D.E., Linsky, J.L.: 1981, *Astrophys. J.* **250**, 284 (1)
Gear, C.W.: 1971, *Numerical Initial Value Problems in Ordinary Differential Equations*, Prentice Hall, Englewood Cliffs, NJ (9)
Gebbie, K.B., Hill, F., Toomre, J., November, L.J., Simon, G.W., Gurman, J.B., Shine, R.A., Woodgate, B.E., Athay, R.G., Bruner, E.C., Rehse, R.A., Tandberg-Hanssen, E.A.: 1981, *Astrophys. J.* **251**, L115 (7)
Giampapa, M.S., Golub, L., Worden, S.P.: 1983, *Astrophys. J.* **268**, L121 (1)
Gilman, P.A.: 1983, in *Solar and Stellar Magnetic Fields: Origins and Coronal Effects*, J.O. Stenflo (Ed.), *IAU Symp.* **102**, 247 (1)
Gingerich, O., Noyes, R.W., Kalkofen, W., Cuny, Y.: 1971, *Solar Phys.* **18**, 347 (2,4,7)

Giovanelli, R.G.: 1977, *Solar Phys.* **52**, 315 (7)
Giovanelli, R.G.: 1980, *Solar Phys.* **68**, 49 (4,6,9)
Giovanelli, R.G., Brown, N.: 1977, *Solar Phys.* **52**, 27 (7)
Giovanelli, R.G., Jones, H.P.: 1982, *Solar Phys.* **79**, 267 (6,9)
Giovanelli, R.G., Livingston, W.C., Harvey, J.W.: 1978, *Solar Phys.* **59**, 49 (3,7)
Giovanelli, R.G., Ramsay, J.V.: 1971, in R. Howard (Ed.) *Solar Magnetic Fields, IAU Symp.* **43**, 293 (7)
Giovanelli, R.G., Slaughter, C.: 1978, *Solar Phys.* **57**, 255 (7)
Göhring, R.: 1971, in *Solar Magnetic fields*, R. Howard (Ed.), *IAU Symp.* **43**, 162 (2)
Golub, L., Maxson, C., Rosner, R., Serio, S., Vaiana, G.S.: 1980, *Astrophys. J.* **238**, 343 (1)
Golub, L., Noci, G., Poletto, G., Vaiana, G.S.: 1982, *Astrophys. J.* **259**, 359 (1)
Gopasyuk, S.I., Kotov, V.A., Severny, A.B., Tsap, T.T.: 1973, *Solar Phys.* **31**, 307 (6)
Gray, D.F.: 1984, *Astrophys. J.* **277**, 640 (1)
Grigorjev, V.M.: 1969, *Solar Phys.* **6**, 67 (6)
Grigorjev, V.M., Katz, J.M.: 1975, *Solar Phys.* **42**, 21 (8)
Grossmann-Doerth, U., Pahlke, K.-D., Schüssler, M.: 1987, *Astron. Astrophys.* in press (4,6)
Gurtovenko, E.A.: 1975, *Solar Phys.* **45**, 25 (5)
Gurtovenko, E.A., Kostik, R.I.: 1982, *Astron. Astrophys. Suppl. Ser.* **47**, 193 (4)
Gurtovenko, É.A., Sheminova, V.A.: 1983, *Astron. Zh.* **60**, 982 = *Soviet Astron.* **27**, 568 (10)
Gustafsson, B.: 1973, *Uppsala Astron. Obs. Ann.* **5**, No. 6 (2,4)

Hagyard M.J.: 1985, (Ed.), *Measurements of Solar Vector Magnetic Fields*, NASA Conf. Publ. 2374, p. 322 (10)
Hale, G.E.: 1908a, *Astrophys. J.* **28**, 100 (1)
Hale, G.E.: 1908b, *Astrophys. J.* **28**, 315 (1)
Hale, G.E.: 1913, *Astrophys. J.* **38**, 27 (1)
Hale, G.E.: 1922a, *Proc. National Acad. Sci.* **8**, 168 (1,6)
Hale, G.E.: 1922b, *Mon. Not. Roy. Astron. Soc.* **82**, 168 (1,6)
Hale, G.E., Ellermann, F., Nicholson, S.B., Joy, A.H.: 1919, *Astrophys. J.* **49**, 153 (1)
Hammer, R.: 1987, in *Proc. Workshop on the Role of Fine-Scale Magnetic Fields on the Structure of the Solar Atmosphere*, Tenerife, 6–12 Oct. 1986, in press (1)
Harvey, J.W.: 1973a, *Solar Phys.* **28**, 9 (4)
Harvey, J.W.: 1973b, *Solar Phys.* **28**, 43 (2,8)
Harvey, J.W: 1977, in *Highlights of Astronomy*, E.A. Müller (Ed.), Vol. **4**, Part **II**, p. 223 (1,6,7)
Harvey, J.W.: 1984, *FTS Polarimeter: Principles of Operation*, unpublished manuscript (3)
Harvey, J.W.: 1985a, in *Measurements of Solar Vector Magnetic Fields*, M.J. Hagyard (Ed.), NASA Conf. Publ. 2374, p. 109 (3)
Harvey, J.W.: 1985b, private communication (3,4,7)
Harvey, J.W.: 1986, in *Small Scale Magnetic Flux Concentrations in the Solar Photosphere*, W. Deinzer, M. Knölker, H.H. Voigt (Eds.), Vandenhoeck & Ruprecht, Göttingen, p. 25 (1,2)
Harvey, J.W., Hall, D.: 1975, *Bull. Amer. Astron. Soc.* **7**, 459 (1,6)
Harvey, J.W., Livingston, W.: 1969, *Solar Phys.* **10**, 283 (1,4,5)
Harvey, J.W., Livingston, W., Slaughter, C: 1972, in *Line Formation in the Presence of Magnetic Fields*, High Altitude Obs., NCAR, Boulder, CO, p. 227 (4,5,6)
Hasan, S.S.: 1984, *Astrophys. J.* **285**, 851 (1,7)
Hasan, S.S.: 1985, *Astron. Astrophys.* **143**, 39 (1,7)
Hasan, S.S.: 1986, *Mon. Not. Roy. Astron. Soc.* **219**, 357 (1,7)
Hasan, S.S., Schüssler, M.: 1985, *Astron. Astrophys.* **151**, 69 (7,9)
Hayes, M.: 1985, private communication (7)
Henze, W., Jr., Tandberg-Hanssen, E., Hagyard, M.J., Woodgate, B.E., Shine, R.A., Beckers, J.M., Bruner, M., Gurman, J.B., Hyder, C.L., West, E.A.: 1982, *Solar Phys.* **81**, 231 (1)
Herbold, G., Ulmschneider, P., Spruit, H.C., Rosner, R.: 1985, *Astron. Astrophys.* **145**, 157 (7)
Hersé, M.: 1979, *Solar Phys.* **63**, 35 (5)
Herzberg, G.: 1944, *Atomic Spectra and Atomic Structure*, Dover, New York (2)

Heyvaerts, J.: 1985, in *Future Missions in Solar, Heliospheric, and Space Plasma Physics*, E. Rolfe, B. Battrick (Eds.), ESA SP–235, p. 169 (1)
Hindmarsh, A.C.: 1974, *GEAR: Ordinary Differential Eq. System Solver*, Lawrence Livermore Lab., Report UCID-30001 (9)
Hirayama, T.: 1978, *Publ. Astron. Soc. Japan* **30**, 337 (5)
Hirayama, T., Hamana, S., Mizugaki, K.: 1985, *Solar Phys.* **99**, 43 (5)
Hollweg, J.V.: 1982, *Astrophys. J.* **257**, 345 (1)
Hollweg, J.V., Jackson, S., Galloway, D.J.: 1982, *Solar Phys.* **75**, 35 (1,7)
Holweger, H.: 1967, *Z. Astrophys.* **65**, 365 (4,5)
Holweger, H.: 1979, in *Proc. 22nd Liège International Astrophys. Symp.*, Inst. d'Astrophysique, Liège, 117 (4)
Holweger, H.: 1985, private communication (5)
Holweger, H., Gehlsen, M., Ruland, F.: 1978, *Astron. Astrophys.* **70**, 537 (5,6,7)
Holweger, H., Müller, E.A.: 1974, *Solar Phys.* **39**, 19 (4,5)
Hönl, H.: 1925, *Z. Physik* **31**, 340 (2)
Howard, R.: 1971, *Solar Phys.* **16**, 21 (7)
Howard, R., Harvey, J.W.: 1970, *Solar Phys.* **12**, 23 (7)
Howard, R.W., Stenflo, J.O.: 1972, *Solar Phys.* **22**, 402 (1,6)
Hubbard, R.: 1982, *FTS Laboratory Users Guide*, KPNO, Tucson, AZ (3)
Hubenet, H.: 1954, 1954, *Z. Astrophys.* **34**, 110 (2)
Huber, M.C.E., Sandeman, R.J.: 1986, *Rep. Prog. Phys.* **49**, 397 (2)
Hui, A.K., Armstrong, B.H., Wray, A.A.: 1978, *J. Quant. Spectrosc. Radiat. Transfer* **19**, 509 (2)
Huygens, C.: 1690, *Traité de la Lumière*, p. 75 (2)

Illing, R.M.E.: 1981, *Astrophys. J.* **248**, 358 (2,8)
Illing, R.M.E., Landman, D.A., Mickey, D.L.: 1974a, *Astron. Astrophys.* **35**, 327 (8)
Illing, R.M.E., Landman, D.A., Mickey, D.L.: 1974b, *Astron. Astrophys.* **37**, 97 (8)
Illing, R.M.E., Landman, D.A., Mickey, D.L.: 1975, *Astron. Astrophys.* **41**, 183 (8)
Irwin, A.W.: 1981, *Astrophys. J. Suppl. Ser.* **45**, 621 (2)

Johansson, S.: 1978, *Phys. Scripta* **18**, 217 (4)
Jones, H.P.: 1985, in *Chromospheric Diagnostics and Modelling*, B.W. Lites (Ed.), National Solar Obs., Sacramento Peak, NM, p. 175 (6,7)
Jones, H.P., Giovanelli, R.G.: 1983, *Solar Phys.* **87**, 37 (6,9)

Kaisig, M., Schröter, E.H.: 1983, *Astron. Astrophys.* **117**, 305 (7)
Kalkofen, W., Rosner, R., Ferrari, A., Massaglia, S.: 1986, *Astrophys. J.* **304**, 519 (5,9)
Keil, S.L., Marmolino, C.: 1986, *Astrophys. J.* **310**, 912 (10)
Kemp, J.C.: 1970, *Astrophys. J.* **162**, 169 (8)
Kemp, J.C., Henson, G.D.: 1983, *Astrophys. J.* **266**, L69 (8)
Kemp, J.C., Henson, G.D., Steiner, C.T., Beardsley, I.S., Powell, E.R.: 1987, *Nature* **326**, 270 (2,3,8,10)
Kemp, J.C., Macek, J.H., Nehring, F.W.: 1984, *Astrophys. J.* **278**, 863 (8)
Kemp, J.C., Swedlund, J.B., Evans, B.D.: 1970, *Phys. Rev. Letters* **24**, 1211 (8)
Kiepenheuer, K.O.: 1953, *Astrophys. J.* **117**, 447 (1)
Kjeldseth Moe, O.: 1968, *Solar Phys.* **4**, 267 (2)
Knölker, M., Schüssler, M., Weisshaar E.: 1985, in *Theoretical Problems in High Resolution Solar Physics*, H.U. Schmidt (Ed.), Max Planck Inst. f. Astrophys., Munich, p. 195 (5,9,10)
Knölker, M., Schüssler, M., Weisshaar E.: 1987, in *Proc. Workshop on the Role of Fine-Scale Magnetic Fields on the Structure of the Solar Atmosphere*, Tenerife, 6–12 Oct. 1986, in press (9,10)
Koutchmy, S.: 1977, *Astron. Astrophys.* **61**, 397 (5)
Koutchmy, S., Stellmacher, G.: 1978, *Astron. Astrophys.* **67**, 93 (5,6,7)
Koutchmy, S., Stellmacher, G.: 1987, in *Proc. Workshop on the Role of Fine-Scale Magnetic Fields on the Structure of the Solar Atmosphere*, Tenerife, 6–12 Oct. 1986, in press (7)
Kraft, R.P.: 1967, *Astrophys. J.* **150**, 551 (1)
Kramers, H.A.: 1927, *Atti Congresso Internationale dei Fisici, Como*, **2**, 545 (2)

Kronig, R. de L.: 1925, *Z. Physik* **31**, 885 (2)
Kronig, R. de L.: 1926, *J. Opt. Soc. America* **12**, 547 (2)

Landé, A.: 1923, *Z. Physik* **15**, 189 (2)
Landi Degl'Innocenti, E.: 1976, *Astron. Astrophys. Suppl. Ser.* **25**, 379 (2)
Landi Degl'Innocenti, E.: 1982, *Solar Phys.* **77**, 285 (2,4)
Landi Degl'Innocenti, E.: 1983, *Solar Phys.* **85**, 3 (2)
Landi Degl'Innocenti, E.: 1985a, *Solar Phys.* **99**, 1 (4)
Landi Degl'Innocenti E.: 1985b, in *Theoretical Problems in High Resolution Solar Physics*, H.U. Schmidt (Ed.), Max Planck Inst. f. Astrophys., Munich, p. 162 (8)
Landi Degl'Innocenti, E., Landi Degl'Innocenti, M.: 1972, *Solar Phys.* **27**, 319 (2)
Landi Degl'Innocenti, E., Landi Degl'Innocenti, M.: 1973, *Solar Phys.* **31**, 299 (2,4)
Landi Degl'Innocenti, E., Landi Degl'Innocenti, M.: 1981, *Il Nuovo Cimento B* **62**, 1 (2,8)
Landi Degl'Innocenti, E., Landi Degl'Innocenti, M.: 1985, *Solar Phys.* **97**, 239 (2)
Landi Degl'Innocenti, E., Landolfi, M.: 1982, *Solar Phys.* **77**, 13 (5,10)
Landi Degl'Innocenti, E., Landolfi, M.: 1983, *Solar Phys.* **87**, 221 (8)
Landman, D.A., Finn, G.D.: 1979, *Solar Phys.* **63**, 221 (8,9)
Lang, K.R.: 1974, *Astrophysical Formulæ*, Springer Verlag, Berlin (2)
Lang, K.R.: 1983, in *Solar and Stellar Magnetic Fields: Origins and Coronal Effects*, J.O. Stenflo (Ed.), *IAU Symp.* **102**, 363 (1)
Lang, K.R., Willson, R.F.: 1979, *Nature* **278**, 24 (1,2)
Leighton, R.B., Noyes, R.W., Simon, G.W.: 1962, *Astrophys. J.* **135**, 474 (1)
Leroy, J.L.: 1962, *Ann. Astrophys.* **25**, 127 (4)
Leroy, J.L.: 1985, in *Measurements of Solar Vector Magnetic Fields*, M.J. Hagyard (Ed.), NASA Conf. Publ. 2374, p. 121 (1,2)
Linsky, J.L.: 1985, *Solar Phys.* **100**, 333 (1)
Linsky, J.L., Ayres, T.R.: 1978, *Astrophys. J.* **220**, 619 (1)
Lites, B.W.: 1972, *Ph.D. Thesis*, NCAR, Boulder, CO. (4)
Lites, B.W.: 1973, *Solar Phys.* **32**, 283 (5)
Litzén, U.: 1976, *Physica Scripta* **14**, 165 (6)
Litzén, U.: 1984, private communication (4)
Livingston, W.C.: 1982, *Nature* **297**, 208 (7)
Livingston, W.C.: 1983, in *Solar and Stellar Magnetic Fields: Origins and Coronal Effects*, J.O. Stenflo (Ed.), *IAU Symp.* **102**, 149 (7)
Livingston, W., Harvey, J.W.: 1969, *Solar Phys.* **10**, 294 (5,6)
Livingston, W., Harvey, J.W.: 1971, in *Solar Magnetic Fields*, R. Howard (Ed.), *IAU Symp.* **43**, 51 (6)
Livingston, W., Huang, Y.R.: 1986, in *Proc. Solar-Stellar Facility Workshop*, Tucson, Sept. 1986, p. 1 (6)
Lockyer, N.: 1866, *Proc. Roy. Soc. London* **15**, 256 (1)

Mäckle, R., Griffin, R., Griffin, R., Holweger, H.: 1975, *Astron. Astrophys. Suppl. Ser.* **19**, 303 (4)
Magain, P.: 1986, *Astron. Astrophys.* **163**, 135 (10)
Makita, M.: 1981, in *Proc. Japan–France Seminar on Solar Physics*, F. Moriyama and J.C. Henoux (Eds.), University of Tokyo Press, Tokyo, p. 99 (8)
Marcy, G.W.: 1983, in *Solar and Stellar Magnetic Fields: Origins and Coronal Effects*, J.O. Stenflo (Ed.), *IAU Symp.* **102**, 3 (1)
Marcy, G.W.: 1984, *Astrophys. J.* **276**, 286 (1)
Marcy, G.W., Bruning, D.H.: 1984, *Astrophys. J.* **281**, 286 (1)
Marstad, N., Linsky, J.L., Simon, T., Rodono, M., Blanco, C., Catalano, S., Marilli, E., Andrews, A.D., Butler, C.J., Byrne, P.B.: 1982, in *Advances in Ultraviolet Astronomy: Four years of IUE Research*, NASA Conf. Publ. No. 2238, p. 554 (1)
Mathys, G.: 1983, *Ph.D. Thesis*, University of Liège (2)
Mathys, G., Stenflo, J.O.: 1986, *Astron. Astrophys.* **168**, 184 (1,4,10)
Mathys, G., Stenflo, J.O.: 1987a, *Astron. Astrophys.* **171**, 368 (4)
Mathys, G., Stenflo, J.O.: 1987b, *Astron. Astrophys. Suppl. Ser.* **67**, 557 (4)

Mattig, W.: 1966, in *Atti del Convegno sulle Macchie Solari*, G. Barbèra (Ed.), Firenze = *Mitt. Fraunhofer Inst. Freiburg*, Nr. 62 (2)
May, M., Richter, J., Wichelmann, J.: 1974, *Astron. Astrophys. Suppl. Ser.* **18**, 415 (4)
McMath, R.R., Mohler, O.C., Pierce, A.K., Goldberg, L.: 1956, *Astrophys. J.* **124**, 1 (5)
McWirther, R.W.P., Thonemann, P.C., Wilson, R.: 1975, *Astron. Astrophys.* **40**, 63 (7)
Mehltretter, J.P.: 1974, *Solar Phys.* **38**, 43 (1,5,10)
Mein, P., Malherbe, J.-M., Schmieder, B., Simon, G., Tandberg-Hanssen, E.: 1985, in *Chromospheric Diagnostics and Modelling*, B.W. Lites (Ed.), National Solar Obs., Sacramento Peak, NM, p. 206 (7)
Meyer, E., Schmitt, H.U., Simon, G.W., Weiss, N.O.: 1979, *Astron. Astrophys.* **76**, 35 (9)
Michard, R.: 1961, *Compt. Rend.* **253**, 2857 (2)
Middelkoop, F.: 1982, *Astron. Astrophys.* **107**, 31 (1)
Middelkoop, F., Zwaan, C.: 1981, *Astron. Astrophys.* **101**, 26 (1)
Mihalas, D.: 1978, *Stellar Atmospheres*, Freeman and Company, San Francisco (2,5)
Miller, P., Foukal, P., Keil, S.: 1984, *Solar Phys.* **92**, 33 (7)
Moore, C.E.: 1972, *A Multiplet Table of Astrophysical Interest*, National Bureau of Standards, NSRDS–NBS 40 (4,7)
Moore, C.E., Minneart, M.G.J. and Houtgast J.: 1966, *The Solar Spectrum 2935 Å to 8770 Å*, National Bureau of Standards, Washington, D.C. (4)
Morrison, N.D., Linsky, J.L.: 1978, *Astrophys. J.* **222**, 723 (5)
Muller, R.: 1975, *Solar Phys.* **45**, 105 (5)
Muller, R.: 1977, *Solar Phys.* **52**, 249 (5)
Muller, R., Keil, S.L.: 1983, *Solar Phys.* **87**, 243 (5,9)

Nordlund, Å.: 1978, in *Astronomical Papers dedicated to Bengt Strömgren*, A. Reiz and T. Andersen (Eds.), Copenhagen University Obs., p. 95 (5,7)
Nordlund, Å.: 1983, in *Solar and Stellar Magnetic Fields: Origins and Coronal Effects*, J.O. Stenflo (Ed.), *IAU Symp.* **102**, 79 (1,7,9,10)
Nordlund, Å.: 1984, in *Small–Scale Dynamical Processes in Quiet Stellar Atmospheres*, S.L. Keil (Ed.), National Solar Obs., Sacramento Peak, N.M., p. 181 (4,7)
Nordlund, Å.: 1985, in *Theoretical Problems in High Resolution Solar Physics*, H.U. Schmidt (Ed.), Max Planck Inst. f. Astrophys., Munich, p. 101 (9)
Nordlund, Å.: 1986, in *Proc. Workshop on Small Magnetic Flux Concentrations in the Solar Photosphere*, W. Deinzer, M. Knölker, H.H. Voigt (Eds.), Vandenhoeck & Ruprecht, Göttingen, p. 83 (1,9,10)
Noyes, R.W.: 1985, *Solar Phys.* **100**, 385 (1)

O'Mara, B.J.: 1976, *Mon. Not. Roy. Astron. Soc.* **177**, 551 (4)
Osherovich, V.A., Flå, T., Chapman, G.A.: 1983, *Astrophys. J.* **286**, 412 (9)
Owocki, S.P., Auer, L.H.: 1980, *Astrophys. J.* **241**, 448 (5,10)

Pahlke, K.D., Solanki, S.K.: 1986, *Mitt. Astron. Gesellschaft* **65**, 162 (8)
Pahlke, K.D., Wiehr, E.: 1986, private communication (7)
Pallavicini, R., Golub, L., Rosner, R., Vaiana, G.S., Ayres, T., Linsky, J.L.: 1981, *Astrophys. J.* **248**, 279 (1)
Pantellini, F.G.E.: 1986, *Diplomarbeit*, ETH Zürich (6)
Parker, E.N.: 1955, *Astrophys. J.* **121**, 491 (9)
Parker, E.N.: 1974, *Astrophys. J.* **191**, 245 (9)
Parker, E.N.: 1976, *Astrophys. Space Sci.* **44**, 107 (9)
Parker, E.N.: 1978, *Astrophys. J.* **221**, 368 (7)
Parker, E.N.: 1979, *Cosmical Magnetic Fields*, Clarendon Press, Oxford (6,9,10)
Parker, E.N.: 1982a, *Astrophys. J.* **256**, 736 (9)
Parker, E.N.: 1982b, *Astrophys. J.* **256**, 746 (9)
Parker, E.N.: 1983a, *Astrophys. J.* **264**, 635 (9)
Parker, E.N.: 1983b, *Astrophys. J.* **264**, 642 (10)
Parker, E.N.: 1985, *Solar Phys.* **100**, 599 (1,3)

Parker, E.N.: 1986, in *Small Scale Magnetic Flux Concentrations in the Solar Photosphere*, W. Deinzer, M. Knölker, H.H. Voigt (Eds.), Vandenhoeck & Ruprecht, Göttingen, p. 13 (4)
Phillips, M.M.: 1979, *Astrophys. J. Suppl. Ser.* **39**, 377 (4)
Pierce A.K., Breckinridge, J.B.: 1973, *KPNO Contr.* **559** (4,7)
Pizzo, V.J.: 1986, *Astrophys. J.* **302**, 785 (9)
Pneuman, G.W.: 1985, in *High Resolution in Solar Physics*, R. Muller (Ed.), Lecture Notes in Physics, Vol. 233, Springer Verlag, Berlin, p. 226 (1)
Pneuman, G.W., Kopp, R.A.: 1971, *Solar Phys.* **18**, 258 (9)
Pneuman, G.W., Solanki, S.K., Stenflo, J.O.: 1986, *Astron. Astrophys.* **154**, 231 (4,9)
Poincaré, H.: 1892, *Théorie Mathematique de la Lumière*, Vol. 2, Corré, Paris (2)
Preston, G.W.: 1971, *Astrophys. J.* **164**, 309 (4)
Proctor, M.R.E., Weiss, N.O.: 1982, *Rep. Prog. Phys.* **45**, 1317 (1)

Querfeld, C.W.: 1977, in *Measurements and Interpretation of Polarization Arising in the Solar Chromosphere and Corona*, J.O. Stenflo (Ed.), *Reports Obs. Lund* **12**, 109 (1)
Querfeld, C.W., Smartt, R.N., Bommier, V., Landi Degl'Innocenti, E., House, L.L.: 1985, *Solar Phys.* **96**, 277 (1)

Rachkovsky, D.N.: 1961, *Izv. Krymsk. Astrofiz. Obs.* **26**, 63 (2)
Rachkovsky, D.N.: 1962, *Izv. Krymsk. Astrofiz. Obs.* **28**, 259 (2)
Rachkovsky, D.N.: 1967, *Izv. Krymsk. Astrofiz. Obs.* **37**, 56 (2,6)
Rae, I.C., Roberts, B.: 1982, *Astrophys. J.* **256**, 761 (7)
Ramsay, J.V., Kobler, H., Mugridge, E.G.V.: 1970, *Solar Phys.* **12**, 492 (7)
Ramsey, H.E., Schoolman, S.A., Title, A.M: 1977, *Astrophys. J.* **215**, L41 (1,10)
Reader, J., Sugar, J.: 1975, *J. Phys. Chem. Ref. Data* **4**, 353 (4)
Rees, D.E.: 1969, *Solar Phys.* **10**, 268 (2,5)
Rees, D.E., Semel, M.D.: 1979, *Astron. Astrophys.* **74**, 1 (10)
Ribes, E., Rees, D.E., Fang, Ch.: 1985, *Astrophys. J.* **296**, 268 (7,8)
Ribes, E., Unno, W.: 1976, *Astron. Astrophys.* **53**, 197 (7)
Ridgeway, S.T., Brault, J.W.: 1984, *Ann. Rev. Astron. Astrophys.* **22**, 291 (3)
Roberts, B.: 1983, *Solar Phys.* **87**, 77 (7)
Roberts, B.: 1986, in *Small Scale Magnetic Flux Concentrations in the Solar Photosphere*, W. Deinzer, M. Knölker, H.H. Voigt (Eds.), Vandenhoeck & Ruprecht, Göttingen, p. 169 (10)
Roberts, B., Webb, A.R.: 1978, *Solar Phys.* **56**, 5 (7,9)
Roberts, B., Webb, A.R.: 1979, *Solar Phys.* **64**, 77 (7,9)
Robinson, R.D.: 1980, *Astrophys. J.* **239**, 961 (1)
Robinson, R.D., Worden, S.P., Harvey, J.W.: 1980, *Astrophys. J.* **236**, L155 (1)
Robson, R.A.: 1974, *The Theory of Polarization Phenomena*, Clarendon Press, Oxford (2)
Rogerson, J.B.: 1961, *Astrophys. J.* **134**, 331 (5)
Rosner, R.: 1986, *Mitt. Astron. Ges.* **65**, 79 (1)
Rosner, R., Golub, L., Vaiana, G.S.: 1985, *Ann. Rev. Astron. Astrophys.* **23**, 413 (1)
Rubinowicz, A.: 1918a, *Physikal. Z.* **19**, 441 (2)
Rubinowicz, A.: 1918b, *Physikal. Z.* **19**, 465 (2)
Ruland, F., Griffin, R., Griffin, R., Biehl, D., Holweger, H.: 1980, *Astron. Astrophys. Suppl. Ser.* **42**, 391 (4)
Rutten, R.J.: 1987, in *Physics of Formation of Fe II Lines Outside LTE*, R. Viotti (Ed.), *IAU Colloq.* **94**, in press (5)
Rutten, R.J., Kostik, R.I.: 1982, *Astron. Astrophys.* **115**, 104 (5)
Rutten, R.J., van der Zalm, E.B.J.: 1984, *Astron. Astrophys. Suppl. Ser.* **55**, 143 (4,6)
Rybicki, G.B.: 1972, in *Line Formation in the Presence of Magnetic Fields*, NCAR, Boulder, CO, p. 145 (2)

Saar, S.H., Linsky, J.L.: 1985, *Astrophys. J.* **299**, L47 (1)
Saar, S.H., Linsky, J.L., Beckers, J.M.: 1986, *Astrophys. J.* **302**, 777 (1)
Scharmer, G.B.: 1981, *Astrophys. J.* **249**, 720 (5)
Scharmer, G.B., Carlsson, M.: 1985, *J. Comput. Phys.* **59**, 56 (5)

Schatten, K.H., Mayr, H.G., Omidvar, K., Maier, E.: 1986, *Astrophys. J.* **311**, 460 (5)
Schlüter, A., Temesvary, S.: 1958, *Electromagnetic Phenomena in Cosmical physics*, B. Lehnert (Ed.), *IAU Symp.* **6**, 263 (9)
Schmahl, G.: 1967, *Z. Astrophys.* **66**, 81 (5)
Schmieder, B., Mein, N.: 1981, *Astron. Astrophys.* **97**, 310 (1)
Scholier, W., Wiehr, E.: 1985, *Solar Phys.* **99**, 349 (7,8)
Schoolman, S.A., Ramsey, H.E.: 1976, *Solar Phys.* **50**, 25 (5)
Schüssler, M.: 1983, in *Solar and Stellar Magnetic Fields: Origins and Coronal Effects*, J.O. Stenflo (Ed.), *IAU Symp.* **102**, 213 (1)
Schüssler, M.: 1984a, *Astron. Astrophys.* **140**, 453 (7,10)
Schüssler, M.: 1984b, in *The Hydromagnetics of the Sun*, T.D. Guyenne and J.J. Hunt (Eds.), *Proc. Fourth European Meeting on Solar Physics*, ESA SP–220, p. 67 (1)
Schüssler, M.: 1985, private communication (5,7)
Schüssler, M.: 1986, in *Small Scale Magnetic Flux Concentrations in the Solar Photosphere*, W. Deinzer, M. Knölker, H.H. Voigt (Eds.), Vandenhoeck & Ruprecht, Göttingen, p. 103 (3,7)
Schüssler, M.: 1987, in *Proc. Workshop on the Role of Fine-Scale Magnetic Fields on the Structure of the Solar Atmosphere*, Tenerife, 6–12 Oct. 1986, in press (5,9,10)
Schüssler, M., Solanki, S.K.: 1987, *Astron. Astrophys.* submitted (3,4,5,6,10)
Seares, F.H.: 1913, *Astrophys. J.* **38**, 99 (2)
Secchi, P.A.: 1872, *Die Sonne*, Verlag George Westermann, Braunschweig (1)
Semel, M.: 1986, in *Small Scale Magnetic Flux Concentrations in the Solar Photosphere*, W. Deinzer, M. Knölker, H.H. Voigt (Eds.), Vandenhoeck & Ruprecht, Göttingen, p. 39 (10)
Severny, A.B.: 1967, *Izv. Krymsk. Astrofiz. Obs.* **38**, 3 (6)
Sheeley, Jr., N.R.: 1966, *Astrophys. J.* **144**, 723 (6)
Sheeley, Jr., N.R.: 1967, *Solar Phys.* **1**, 171 (5,6)
Shenstone, A.G., Blair, H.A.: 1929, *Phil. Mag.* **8**, 765 (2)
Shine, R.A., Linsky, J.L.: 1974a, *Solar Phys.* **37**, 145 (5)
Shine, R.A., Linsky, J.L.: 1974b, *Solar Phys.* **39**, 49 (5)
Simmons, G.J., Blackwell, D.E.: 1982, *Astron. Astrophys.* **112**, 209 (4,6)
Simon, G.W., Leighton, R.B.: 1964, *Astrophys. J.* **140**, 1120 (1)
Simon, G.W., Weiss, N.O., Nye, A.: 1983, *Solar Phys.* **87**, 65 (9)
Simon, G.W., Zirker, J.B.: 1974, *Solar Phys.* **35**, 331 (5,6,7)
Sistla, G., Harvey, J.W.: 1970, *Solar Phys.* **12**, 66 (4)
Skumanich, A., Smythe, C., Frazier, E.N.: 1975, *Astrophys. J.* **200**, 747 (1,5,7)
Smith, M.A., Testerman, L., Evans, J.C.: 1976, *Astrophys. J.* **207**, 308 (5,7)
Sobel'man, I.I.: 1972, *Introduction to the Theory of Atomic Spectra*, Pergamon Press, London (2)
Solanki, S.K.: 1982, *Diplomarbeit*, ETH, Zürich (9)
Solanki, S.K.: 1984, in *The Hydromagnetics of the Sun*, T.D. Guyenne and J.J. Hunt (Eds.), *Proc. Fourth European Meeting on Solar Physics*, ESA SP–220, p. 63 (5)
Solanki, S.K.: 1985, in *Theoretical Problems in High Resolution Solar Physics*, H.U. Schmidt (Ed.), Max Planck Inst. f. Astrophys., Munich, p. 172 (7)
Solanki, S.K.: 1986, *Astron. Astrophys.* **168**, 311 (5,7)
Solanki, S.K.: 1987, in *Proc. Workshop on the Role of Fine-Scale Magnetic Fields on the Structure of the Solar Atmosphere*, Tenerife, 6–12 Oct. 1986, in press (4)
Solanki, S.K., Keller, C., Stenflo, J.O.: 1987, *Astron. Astrophys.* to be submitted (3,5,6,9,10)
Solanki, S.K., Pantellini, F.G.E., Stenflo, J.O.: 1986, *Solar Phys.* **107**, 57 (4)
Solanki, S.K., Steenbock, W.: 1987, *Astron. Astrophys.* submitted (4,5,10)
Solanki, S.K., Stenflo, J.O.: 1984, *Astron. Astrophys.* **140**, 185 (4,5,6,7,8)
Solanki, S.K., Stenflo, J.O.: 1985, *Astron. Astrophys.* **148**, 123 (4,5,6,7,8)
Solanki, S.K., Stenflo, J.O.: 1986, *Astron. Astrophys.* **170**, 120 (4,7)
Sommerfeld, A.: 1916, *Physikal. Z.* **17**, 491 (2)
Spruit, H.C.: 1974, *Solar Phys.* **34**, 277 (4)
Spruit, H.C.: 1976, *Solar Phys.* **50**, 269 (9,10)
Spruit, H.C.: 1977, *Solar Phys.* **55**, 3 (1,4,5)

Spruit, H.C.: 1979, *Solar Phys.* **61**, 363 (1,6,7)
Spruit, H.C.: 1981a, *Astron. Astrophys.* **98**, 155 (7,9)
Spruit, H.C.: 1981b, in S. Jordan (Ed.) *The Sun as a Star*, NASA SP-450, p. 385 (9)
Spruit, H.C.: 1983, in *Solar and Stellar Magnetic Fields: Origins and Coronal Effects*, J.O. Stenflo (Ed.), *IAU Symp.* **102**, 41 (9)
Spruit, H.C.: 1984, in *Small-Scale Dynamical Processes in Quiet Stellar Atmospheres*, S.L. Keil (Ed.), National Solar Obs., Sacramento Peak, NM, p. 249 (9)
Spruit, H.C., Roberts, B.: 1983, *Nature* **304**, 401 (1)
Spruit, H.C., Zwaan, C.: 1981, *Solar Phys.* **70**, 207 (9)
Spruit, H.C., Zweibel, E.G.: 1979, *Solar Phys.* **62**, 15 (7)
stststst
St. John, C.E.: 1922, *Phys. Rev.* **19**, 390 (5)
Staude, J.: 1969, *Solar Phys.* **8**, 264 (2)
Steenbock, W.: 1985, in *Cool Stars with Excesses of Heavy Elements*, M. Jaschek and P.C. Keenan (Eds.), Reidel, p. 231 (10)
Steenbock, W., Holweger, H.: 1984, *Astron. Astrophys.* **130**, 319 (10)
Steffen, M.: 1985, *Astron. Astrophys. Suppl. Ser.* **59**, 403 (2)
Steiner, O., Pneuman, G.W., Stenflo, J.O.: 1986, *Astron. Astrophys.* **170**, 126 (9,10)
Steinolfson, R.S., Suess, S.T., Wu, S.T.: 1982, *Astrophys. J.* **255**, 730 (9)
Stellmacher, G., Wiehr, E.: 1971, *Solar Phys.* **18**, 220 (4,5)
Stellmacher, G., Wiehr, E.: 1973, *Astron. Astrophys.* **29**, 13 (5)
Stellmacher, G., Wiehr, E.: 1979, *Astron. Astrophys.* **75**, 263 (5)
Stenflo, J.O.: 1966, *Arkiv. Astron.* **4**, 173 (6)
Stenflo, J.O.: 1968, *Acta Univ. Lund* **II**, No. 2 =*Medd. Lunds Astron. Obs.* **II**, No. 153 (6)
Stenflo, J.O.: 1971, in *Solar Magnetic fields*, R. Howard (Ed.), *IAU Symp.* **43**, 101 (2,5,8)
Stenflo, J.O.: 1973, *Solar Phys.* **32**, 41 (1,6,10)
Stenflo, J.O.: 1974, *Solar Phys.* **36**, 495 (7)
Stenflo, J.O.: 1975, *Solar Phys.* **42**, 79 (5)
Stenflo, J.O.: 1976, in *Basic Mechanisms of Solar Activity*, V. Bumba, J. Kleczek (Eds.), *IAU Symp.* **71**, 69 (6,10)
Stenflo, J.O.: 1978, *Rep. Prog. Phys.* **41**, 865 (1,2)
Stenflo, J.O.: 1982, *Solar Phys.* **80**, 209 (1)
Stenflo, J.O.: 1984a, *Adv. Space Res.* **4**, 5 (10)
Stenflo, J.O.: 1984b, *Applied Optics* **23**, 1267 (2,3,8)
Stenflo, J.O.: 1985, in *Measurements of Solar Vector Magnetic Fields*, M.J. Hagyard (Ed.), NASA Conf. Publ. 2374, p. 322 (4)
Stenflo, J.O., Harvey, J.W.: 1985, *Solar Phys.* **95**, 99 (3,4,5,6,7,8)
Stenflo, J.O., Harvey, J.W., Brault, J.W., Solanki, S.K.: 1984, *Astron. Astrophys.* **131**, 33 (3,4,7,8)
Stenflo, J.O., Lindegren, L.: 1977, *Astron. Astrophys.* **59**, 367 (4,6,10)
Stenflo, J.O., Solanki, S.K., Harvey, J.W.: 1987a, *Astron. Astrophys.* **171**, 305 (3,5,6,7,10)
Stenflo, J.O., Solanki, S.K., Harvey, J.W.: 1987b, *Astron. Astrophys.* **173**, 167 (3,6,7)
Stenflo, J.O., Twerenbold, D., Harvey, J.W.: 1983, *Astron. Astrophys.* **52**, 161 (3)
Stenholm, L.G.: 1977, *Astron. Astrophys.* **54**, 577 (2)
Stenholm, L.G., Stenflo, J.O.: 1977, *Astron. Astrophys.* **58**, 273 (2,5)
Stenholm, L.G., Stenflo, J.O.: 1978, *Astron. Astrophys.* **67**, 33 (2,5)
Stepanov V.E.: 1958a, *Izv. Krymsk. Astrofiz. Observ.* **18**, 136 (2,8)
Stepanov V.E.: 1958b, *Izv. Krymsk. Astrofiz. Observ.* **19**, 20 (2,8)
Stibbs, D.W.N.: 1950, *Mon. Not. Roy. Astron. Soc.* **110**, 395 (1)
Stokes, G.G.: 1852, *Trans. Camb. Philos. Soc.* **9**, 399 (2)
Suess, S.T.: 1983, *NASA Cont. Publ.*, NASA CP-2280, 183 (9)

Tanenbaum, A.S., Wilcox, J.M., Howard, R.: 1971, in *Solar Magnetic Fields*, R. Howard (Ed.), *IAU Symp.* **43**, 348 (7)
Tarbell, T.D., Title, A.M.: 1976, *Solar Phys.* **47**, 563 (6)

Tarbell, T.D., Title, A.M.: 1977, *Solar Phys.* **52**, 13 (5,6,7)
Thiessen, G.: 1952, *Z. Astrophys.* **30**, 185 (1)
Title, A.M., Tarbell, T.D.: 1975, *Solar Phys.* **41**, 255 (6)
Title, A.M., Tarbell, T.D., Simon, G.W., Acton, L., Duncan, D., Ferguson, S., Finch, M., Frank, Z., Kelly, G., Lindgren, R., Morrill, M., Pope, T., Reeves, R., Rehse, R., Shine, R., Topka, K., Harvey, J., Leibacher, J., Livingston, W., November, L.: 1986, preprint (1)
Title, A.M., Tarbell, T.D., Topka, K.P.: 1987, *Astrophys. J.* in press (1)

Uhlenbeck, G.E., Goudsmit, S.: 1925, *Naturwiss.* **13**, 953 (2)
Uhlenbeck, G.E., Goudsmit, S.: 1926, *Nature* **117**, 264 (2)
Unno, W.: 1956, *Publ. Astron. Soc. Japan* **8**, 108 (2,4,6)
Unno, W.: 1959, *Astrophys. J.* **129**, 375 (4)
Unno, W., Ando, H.: 1979, *Geophys. Astrophys. Fluid Dyn.* **12**, 107 (7)
Unno, W., Ribes, E.: 1979, *Astron. Astrophys.* **73**, 314 (7,8,9)
Unsöld, A.: 1955, *Physik der Sternatmosphären*, Springer Verlag, Berlin (2,4,6)

Vaiana, G.S.: 1983, in *Solar and Stellar Magnetic Fields: Origins and Coronal Effects*, J.O. Stenflo (Ed.), *IAU Symp.* **102**, 165 (1)
Vaiana, G.S., Cassinelli, J.P., Fabbiano, G., Giacconi, R., Golub, L., Gorenstein, P., Haisch, B.M., Harnden, F.R., Jr., Johnson, H.M., Linsky, J.L., Maxson, C.W., Mewe, R., Rosner, R., Seward, F., Topka,K., Zwaan, C.: 1981, *Astrophys. J.* **245**, 163 (1)
Van Ballegooijen, A.A.: 1984, *Solar Phys.* **91**, 195 (5)
Van Ballegooijen, A.A.: 1985a, in *Measurements of Solar Vector Magnetic Fields*, M.J. Hagyard (Ed.), NASA Conf. Publ. 2374, p. 322 (2,9,10)
Van Ballegooijen, A.A.: 1985b, in *Theoretical Problems in High Resolution Solar Physics*, H.U. Schmidt (Ed.), Max Planck Inst. f. Astrophys., Munich, p. 167 (3,9)
Vaughan, A.H.: 1983, in *Solar and Stellar Magnetic Fields: Origins and Coronal Effects*, J.O. Stenflo (Ed.), *IAU Symp.* **102**, 113 (1)
Venkatakrishnan, P.: 1983, *J. Astrophys. Astron.* **4**, 135 (7)
Venkatakrishnan, P.: 1985, *J. Astrophys. Astron.* **6**, 21 (7)
Venkatakrishnan, P.: 1986, *Solar Phys.* **104**, 347 (7)
Vernazza, J.E., Avrett, E.H., Loeser, R.: 1981, *Astrophys. J. Suppl. Ser.* **45**, 635 (5)
Vitense, E.: 1951, *Z. Astrophys.* **28**, 81 (4)
Vogt, S.S.: 1983, in *Activity in Red-Dwarf Stars*, M. Rodono, P. Byrne (Eds.), D. Reidel Publ. Co., Dortrecht, *IAU Colloq.* **71**, 137 (1)
Vogt, S.S., Penrod, G.D.: 1983a, in *Activity in Red-Dwarf Stars*, M. Rodono, P. Byrne (Eds.), D. Reidel Publ. Co., Dortrecht, *IAU Colloq.* **71**, 379 (1)
Vogt, S.S., Penrod, G.D.: 1983b, *Publ. Astron. Soc. Pacific* **95**, 565 (1)
Voigt, W.: 1913, *Physikal. Z.* **14**, 377 (2)
Von Alvensleben, A.: 1957, *Z. Astrophys.* **43**, 63 (6)
von Klüber, H.: 1947, *Z. Astrophys.* **24**, 121 (4)

Waldmeier, M.: 1961, *The Sunspot-Activity in the Years 1610–1960*, Schulthess, Zürich (1)
Waldmeier, M.: 1976, *Astron. Mitt. Eidg. Sternwarte Zürich* Nr. 346 (1)
Walton, S.R.: 1987, *Astrophys. J.* **312**, 909 (5,10)
Webb, A.R., Roberts, B.: 1978, *Solar Phys.* **59**, 249 (7)
Wiehr, E.: 1977, in *Highlights of Astronomy*, E.A. Müller (Ed.), Vol. **4**, Part **II**, p. 251 (6)
Wiehr, E.: 1978, *Astron. Astrophys.* **69**, 279 (6)
Wiehr, E.: 1985a, *Astron. Astrophys.* **149**, 217 (3,7,8)
Wiehr, E.: 1985b, private communication (7)
Wiehr, E., Wittmann, A., Wöhl, H.: 1980, *Solar Phys.* **68**, 207 (7)
Willson, R.C.: 1984, in *Solar Irradiance Variations on Active Region Time Scales*, B.J. LaBonte, G.A. Chapman, H.S. Hudson, R.C. Willson (Eds.), NASA Conf. Publ. 2310, p. 1 (1)
Wilson, O.C.: 1978, *Astrophys. J.* **226**, 379 (1)

Wilson, P.R.: 1971, *Solar Phys.* **21**, 101 (1)
Wilson, P.R.: 1977a, *Astrophys. J.* **214**, 611 (9)
Wilson, P.R.: 1977b, *Astrophys. J.* **214**, 917 (9)
Wittmann, A.D.: 1973a, *Ph.D. Thesis*, University of Göttingen (2,10)
Wittmann, A.D.: 1973b, *Solar Phys.* **33**, 107 (2)
Wittmann, A.D.: 1974, *Solar Phys.* **35**, 11 (2,6,10)
Wittmann, A.D.: 1977, *Astron. Astrophys.* **54**, 175 (2)
Wittmann, A.D.: 1986, private communication (2)
Wolf, R.: 1877, *Beobachtungen der Sonnenflecken von der Zeit ihrer Entdeckung bis auf die Gegenwart*, unpublished manuscript, ETH, Zürich (1)
Wolnik, S.J., Berthel, R.O., Wares, G.W.: 1970, *Astrophys. J.* **162**, 1037 (4)

Xanthakis, J.: 1969, *Solar Phys.* **10**, 168 (1)

Yun, H.S.: 1970, *Astrophys. J.* **162**, 975 (9)
Yun, H.S.: 1971, *Solar Phys.* **16**, 398 (9)

Zeeman, P.: 1897a, *Phil. Mag.* **43**, 226 (2)
Zeeman, P.: 1897b, *Phil. Mag.* **44**, 55 (2)
Zeeman, P.: 1897c, *Phil. Mag.* **44**, 255 (2)
Zwaan, C.: 1978, *Solar Phys.* **60**, 213 (1)
Zwaan, C.: 1983, in *Solar and Stellar Magnetic Fields: Origins and Coronal Effects*, J.O. Stenflo (Ed.), *IAU Symp.* **102**, 85 (1)
Zweibel, E.G., Bogdan, T.J.: 1986, *Astrophys. J.* **308**, 401 (1)

SUPPLEMENT

SONNIGE FERIEN!

Wie wärs mit garantiert sonnigen Ferien (24 Stunden Sonne pro Tag hautnah erleben!). Unsere leuchtenden Strände, von den Einheimischen "Plage" genannt, warten auf Sie! Kein Rummel, keine Platzprobleme, Millionen von Quadratkilometern Strand ohne einen anderen Menschen. Schauen Sie dem faszinierenden Spiel des granularen Meeres zu, verfolgen Sie das Geschick einzelner Flussröhren, oder liegen sie einfach auf dem Rücken und geniessen Sie den Anblick vom Wald der Flussröhren, der sich über Ihnen schliesst. Als Abwechslung empfehlen wir Ihnen eine Abkühlung im angenehmen Schatten einer Umbra. Und am Abend tanzen Sie zu den heissen Rythmen der vielen ausgezeichneten Bands, z.B. der weltberühmten "Los 5 Oscillationes".

Melden Sie sich heute schon an bei:
CORONA TRAVEL.
Sie finden uns am
Sonnenweg 1$\odot$,
Heliopolis.

ACHTUNG! ACHTUNG! ACHTUNG! ACHTUNG! ACHTUNG!

Damit Ihre unvergesslichen Erlebnisse in unserem Ferienparadies wirklich unvergesslich bleiben, schenken wir **jedem** Teilnehmer (KOSTENLOS) die revolutionäre, neue sphärische 360° Kamera für die endgültigen Panorama-Aufnahmen: die Photo-Sphäre, ein Produkt der Spektrum AG. Gegen ein bescheidenes Entgelt liefern wir Ihnen auch das phantastische Profi-Modell für leuchtend brilliante Farbpanoramen: die Chromo-Sphäre.

KEINE ANGST!

Wir möchten betonen, dass Sie *keine* Angst vor Terroristen zu haben brauchen. Unsere speziell ausgebildete Sicherheitskräfte werden sie effizient und mit hundert prozentiger Sicherheit schützen vor den Ellerman Bomben und den 'Coronal Bullets'.

! ! ! ! ! ALSO NICHTS WIE LOS. JETZT ANMELDEN ! ! ! ! ! !

The Stony Path to Publication

As reflected by anotated quotations

1. S.K. Solanki: 1982, in preparation
   Only a vague idea of dubious quality exists so far and nothing has actually been done yet, but it can nevertheless be quoted: That's one more for the citation index.

2. S.K. Solanki and A.N. Angel: 1983, *Astron. Astrophys.* to be submitted
   A.N. Angel, a Diploma student, has now turned up and has toiled away day and night for the last six months to produce some reasonable results from that initial, dubious idea based on assumptions which are about as solid as fresh jelly. The primary author has constructively spent the mean time at conference dinners. Oh yes, he has also decided on the journal to submit the paper to (only the best will do), once it is written. His contribution is therefore quite sufficient for him to place his name first.

3. S.K. Solanki and A.N. Angel: 1984, *Astron. Astrophys.* to be submitted
   A.N. Angel has long since left the institute (and as a result is blissfully ignorant of what shall follow), but the primary author has so far had no time to write up the results in the form of a short paper. He talks of being overworked, but could the real reason be too many conference dinners? Keep in mind the exhausting after dinner speeches.

4. S.K. Solanki and A.N. Angel: 1985, *Astron. Astrophys.* submitted
   With large helpings of fuzzy logic, a rigorous disregard of the laws of physics, a ruthless suppression of any nagging doubts, and a careful choice of words the paper has finally been completed and the great day of submission, 1.4.1985, has arrived. With an immense sigh of relief the packet with the three copies of the manuscript has been sent off to the editor. A.N. Angel, who had actually done all the work and is well acquainted with the noisy data, the inherent numerical instability of the analysis procedure, and the hopelessly muddled situation as far as the interpretation is concerned, was against publishing the "results", but as the poet so rightly wrote: "Fools rush in where angels dare not tread."

5. S.K. Solanki and A.N. Angel: 1985, *Astron. Astrophys.* to be rejected
   A rarely used quotation. At this stage only the referee knows this current status and he is not likely to quote it in this form, since it would reveal his closely guarded identity.

6. S.K. Solanki and A.N. Angel: 1985, *Astron. Astrophys.* rejected
   Another rare quotation. The rejection first plunged the primary author into a state of deepest dejection, followed by maniac outbursts of anger and a wild but fruitless search for the identity of the referee.

7. S.K. Solanki and A.N. Angel: 1986, *Astron. Astrophys.* resubmitted
   In his heart of hearts the primary author knows that this paper is not really worth the pulp for the preprints, but, after all, he spent a whole week writing it. Sufficient reason for

writing a scathing letter to the editor demanding another, more competent, referee. Note that most astronomers prefer to stick to the tried and tested "submitted" at this stage.

8. S.K. Solanki and A.N. Angel: 1986, *Astron. Astrophys.* to be rejected again

Here we go again. The second referee appears to be as heartless and incompetent as the first.

9. S.K. Solanki and A.N. Angel: 1986, *Astron. Astrophys.* rejected for the second time

What comment can do justice to the feelings of the (primary) author now? With a heavy heart he decides to forget about getting this paper published.

10. T.H.E. Devil, S.K. Solanki and A.N. Angel: 1987, *Astrophys. Junk* submitted

Enter T.H.E. Devil, professional name placer on other peoples papers, senior member of the staff of an unnamed institute and a close friend of the editor of that final refuge for the hopelessly incompetent astronomer: Astrophys. Junk (often also abbreviated simply as Ap. J.). T.H.E. Devil spies a good opportunity for advancing the cause of the two unsuccessful authors (poor devils) and naturally also of himself. The rest of the story is quite straightforward.

11. T.H.E. Devil, S.K. Solanki and A.N. Angel: 1987, *Astrophys. Junk* accepted

Within a week of submission, the card of acceptance has already arrived. A miracle, if we keep the vagaries of our so highly developed postal system in mind. We can only conclude that this referee worked really fast, or, perish the thought, that this paper was never sent to a referee.

12. T.H.E. Devil, S.K. Solanki and A.N. Angel: 1987, *Astrophys. Junk* in press

The proofs have been hurriedly corrected and sent off again. As usual, most of the corrections are necessitated not by typesetters' errors, but by faults in the submitted manuscript.

13. T.H.E. Devil, S.K. Solanki and A.N. Angel: 1987, *Astrophys. Junk* **13**, 13

The article has finally appeared and is already totally obsolete. However, although it may be rather useless as far as the advancement of scientific knowledge is concerned, it does add one more entry to the steadily growing list of publications of the authors.

And the moral of the story?

For publication inspiration can be almost completely replaced by transpiration.

How to Build a Fluxtube Model: Selected Recipes

Fluxtubes are highly decorative objects and most of us would surely wish to have one livening up the drawing room. There is, however, a practical problem in the fact that few of us have a drawing room of sufficient size. Recall that a typical fluxtube is expected to be about 100 km or more in diameter and after all we want the pretty little fluxtube in the drawing room and not the other way round. Out of this problem has arisen the fluxtube models industry which churns out scaled down versions of the real thing in large numbers. Although a host of such ready-made fluxtube models are available on the market at a wide range of prices (depending on the number of special 'realistic' features which a given model incorporates), I still feel that building a fluxtube model yourself gives a unique feeling of satisfaction which I, gentle reader, cannot bear to withhold from you. So I have put together the do-it-yourself recipes of a few almost random examples of fluxtube models. Read on, make your choice and build one, or better still, forget about making a choice and build them all.

The Baked Fluxtube

Every housewife can surprise her husband by serving a baked fluxtube for dinner. ‡ The recipe starts off simply enough: Take some dough and roll it flat. But soon comes the difficult part: Form a tube of the following shape:

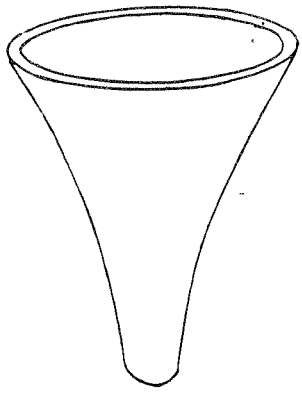

Fig. 1

and put it into the oven to bake at a typical photospheric temperature ($\approx$ 5000 K). If you are lucky then you may be able to observe any one of a number of dough instabilities occuring in your model. E.g. kink instability (Fig. 2), or fluting instability (Fig. 3), ¶ or perhaps even the big one, viz. total (convective?) collapse. In some rare cases it may happen that none of these highly

‡ In this age of enlightenment and equal rights, it could also be the other way around, the house-husband being the one doing the serving to the stressed business wife.

¶ The kink and fluting instabilities in the baking fluxtube are sometimes collectively called the Salvador-Dali effect, since their effects remind some people of his melting clocks.

engrossing and optically beautiful processes takes place and you actually end up with an intact fluxtube model. Take it from the oven, fill it to approximately half its height with ice cream, and serve it without further delay. You have now produced the famous hot-wall cool-bottom model of the fluxtube.

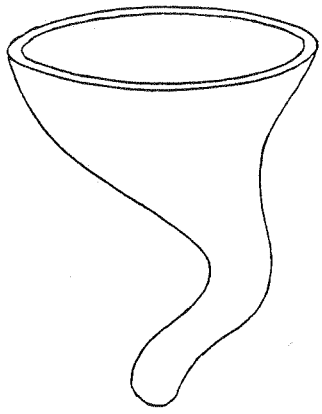

Fig. 2

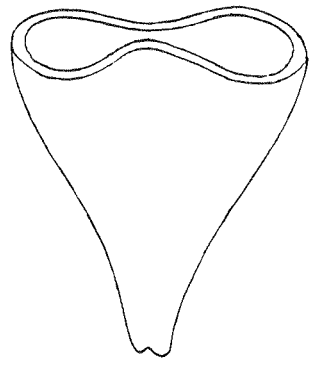

Fig. 3

The Open Air Fluxtube Model. Also Called the Show it to Your Neighbours Model

Drawing rooms have one disadvantage, they have walls. So even if you were to fill yours completely with innumerable strange and wonderous fluxtube models, your neighbours might never learn about them. And, to be honest, who makes fluxtube models just for the fun of it? If, however, you are lucky enough to possess a garden with a pond then you already have almost all the raw material in hand to make your neighbours turn spinach green with envy. You ask: How to do it? It's easy: Take some balsa wood, saw out pieces of the right shape and size, glue together and you are on your way. The first approximation of a model is schematically illustrated in Fig. 4.

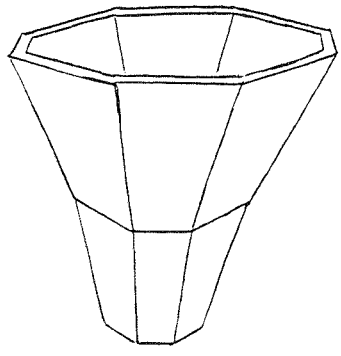

Fig. 4

With a few simple additions this model can be made considerably more realistic. For example you can add a ring of lead at the thin end of the model, so that it will float upright with the stately grace of a 15 meter yacht in a steady breeze. You now have not just any old model, but have produced a buoyant fluxtube. The beauty of this scheme is that you can play with it. By making waves in the pond you can simulate the buffeting of your tube by the surrounding granulation. There is no question that its great fun for the kids too. Be careful, however, not to add too much lead, since you don't want it to sink (with about the stately grace of, well, a lump of lead) before the amused eyes of your neighbours. Should this happen (after all nobody is perfect), then the important thing is not to bat an eyelash and state with an air of haughty confidence (or studied indifference if you prefer) that you were modelling the submergence of magnetic flux. That ought to leave them at a loss. This sophistication should be quite enough for most neighbours, but even the most hard boiled samples will give up the fight if you put a water hose into the model from the bottom. Suddenly switching the water on and off will then produce a fountain, which is a delightful approximation of that enigmatic member of the zoo of solar phenomena: the spicule.

The Josef Beuys or Pop Art Model

This one's for the arty set. Take a funnel. Balance it on its narrow end. Hey presto, that's your fluxtube. If you so wish, then you can also paint it some impossibly horrid colour and within minutes you will be the proud (?) possessor of the Andy Warhol version of the basic model which is particularly popular on the western side of the Atlantic. Note: A well known member of the jet set (an ex solar physicist) first got rich and famous when he sold such a model to the Museum of Modern Art of Schildburg for a still secret, but sickeningly high, sum.

The Permanent Model

For people who like enduring values I suggest a model out of reinforced concrete. A solid foundation for many a famous fluxtube collection has been laid with such a model. Besides being trendy and a never exhausted source of conversation with guests it can serve a useful purpose if you build one in the middle of the drawing room. For example as a support for the ceiling. As a bonus it opens up whole new possibilities when playing hide and seek. Finally, if you decide against constructing one yourself, it is also a model of how to keep the economy on a sound footing and how to keep the ever complaining building industry satisfied. Its money spinning potential has been realised with characteristic speed by the construction firms. Thus, the new sales slogan of the staid Golden House Inc. reads:

A model home needs a model fluxtube,

while the new up and coming Slick Brick Corp. is planning a crash publicity campaign having the motto:

We'll get you the flux
For just thousand bucks.

The Wine Glass Model

Take a burgundy glass. Fill it well with vintage burgundy (what else?) and place it on a table with a plain white table cloth. Take a deep look (now you know what a fluxtube looks like in Hα). Take a deep breath. Take a deep gulp (feel that downflow?). Once the burgundy is gone you will have a white-light picture of a fluxtube. Repeat the procedure until you see two models. Then the fun begins. Watch numerous instabilities and the constant jiggling motions of your model. Artificial seeing is also a possible by-product. Warning: people sometimes get addicted to this kind of model.

And then there is the merging wine glass variant: Fill many burgundy glasses and place them on the table, packed as tightly together as possible. You now have a beautiful view of a whole network element. From there on the procedure is the same as above. The advantage is that, since you do not have to refill the glasses each time, you get to the instability stage quicker.

The Computer Model

Computer models of fluxtubes are time consuming to program, expensive to run, unreliable and often outright wrong. This is why no one builds such models, except some particularly woolly minded astronomers, and all of us know enough about astronomers to realize what this means. So take the advice of an experienced hand and keep your fingers away from computer models.

Concluding Salestalk

There are still many, many more fluxtube models to be made. Lack of space does not allow me to describe such dainties as the evacuated fluxtube model starring your vacuum cleaner, or the bathtub fluxtube with the stabilizing whirl flows. If this little introduction to fluxtube modelling leaves you hungering for more information, then read my forthcoming comprehensive book entitled "The α and Ω of Fluxtube Dynamos and Other Useful Electrical Tips for Bicycle Mechanics, Plumbers, and Foolhardy Astronomers". For those who prefer slightly lighter fare, there's the "Hitchhiker's Guide to Galactic Fluxtubes", or "Zen and the Art of Solar Cycle Maintenance".